

Wing Pressure Distributions From Subsonic Tests of a High-Wing Transport Model

Zachary T. Applin and Garl L. Gentry, Jr.
Langley Research Center • Hampton, Virginia

M. A. Takallu
Lockheed Engineering & Sciences Company • Hampton, Virginia

This publication is available from the following sources:

NASA Center for AeroSpace Information
800 Elkridge Landing Road
Linthicum Heights, MD 21090-2934
(301) 621-0390

National Technical Information Service (NTIS)
5285 Port Royal Road
Springfield, VA 22161-2171
(703) 487-4650

Abstract

A wind tunnel investigation was conducted on a generic, high-wing transport model in the Langley 14- by 22-Foot Subsonic Tunnel. This report contains pressure data that document effects of various model configurations and free-stream conditions on wing pressure distributions. The untwisted wing incorporated a full-span, leading-edge Krueger flap and a part-span, double-slotted trailing-edge flap system. The trailing-edge flap was tested at four different deflection angles (20° , 30° , 40° , and 60°). Four wing configurations were tested: cruise, flaps only, Krueger flap only, and high lift (Krueger flap and flaps deployed). Tests were conducted at free-stream dynamic pressures of 20 psf to 60 psf with corresponding chord Reynolds numbers of 1.22×10^6 to 2.11×10^6 and Mach numbers of 0.12 to 0.20. The angles of attack presented range from 0° to 20° and were determined by wing configuration. The angle of sideslip ranged from -20° to 20° . In general, pressure distributions were relatively insensitive to free-stream speed with exceptions primarily at high angles of attack or high flap deflections. Increasing trailing-edge flap deflection increased suction pressures on the wing and improved flow on the flaps. The leading-edge Krueger flap significantly reduced peak suction pressures and steep gradients on the wing at high angles of attack. Installation of the empennage had no effect on wing pressure distributions. Unpowered engine nacelles reduced suction pressures on the wing and the flaps.

Introduction

Extensive research of aft-fuselage-mounted, advanced turboprop (ATP) engines on commercial aircraft has been conducted at Langley Research Center (refs. 1 and 2). Recent interest has expanded to include determination of aerodynamic characteristics for wing-mounted installations. A significant amount of wing-integration research was conducted in the 1960's and the 1970's for propeller-driven aircraft (refs. 3 and 4). Advanced turboprop aircraft have higher disk loading than propeller-driven aircraft. Low-speed integration issues such as interaction of propeller slipstream and high-lift system, stability and control, and engine-out characteristics may be more critical for wing-mounted ATP engines. These concerns led to the design and the fabrication of a high-wing model with the capability of testing the propulsion system in wing-mounted configurations.

The initial task of the research reported herein was to measure and to document the aerodynamic characteristics of the baseline (unpowered) model. This report contains wing pressure distribution data obtained from subsonic tests in the Langley 14- by 22-Foot Subsonic Tunnel.

Detailed wing surface pressure distributions are presented herein for a variety of model configurations. Limited analysis of the data ascertains the effects of certain model configurations and free-stream

flow conditions on wing surface flow behavior. The entire data set can be electronically transferred by contacting the authors.

Symbols

C_p	pressure coefficient
c_f	local flap chord, in.
c_K	local Krueger-flap chord, in.
c_v	local vane chord, in.
c_w	local cruise wing chord, in.
M	free-stream Mach number
q	free-stream dynamic pressure, psf
R	Reynolds number based on wing mean aerodynamic chord
S	wing reference area, 16.92 ft ²
x	chordwise distance aft of leading edge, in.
y	spanwise distance from model centerline, in.
z_l	ordinate on lower surface, in.
z_u	ordinate on upper surface, in.
α	angle of attack of model reference centerline (positive nose up), deg

β	angle of sideslip of model reference centerline (positive nose left), deg
δ_f	deflection angle of flap, deg
δ_K	deflection angle of leading-edge Krueger flap, deg
δ_v	deflection angle of vane, deg
Subscripts:	
f	flap
ref	reference
v	vane
w	wing
Abbreviations:	
ATP	advanced turboprop
DAS	data acquisition system
ESP	electronically scanned pressure
HT	horizontal tail
MAC	mean aerodynamic chord
Sta	station
VT	vertical tail

Model Description

The model used in this investigation was a generic, high-wing transport configuration, which was designed to be rigid for the conditions tested. The untwisted wing incorporated a full-span, leading-edge Krueger flap and a part-span, double-slotted trailing-edge flap system. The geometry of the wing and the high-lift system was identical to the semispan wing model used in reference 5. Sketches of the complete model and the starboard wing with pressure taps are shown in figure 1. Photographs of the model installed in the Langley 14- by 22-Foot Subsonic Tunnel are shown in figure 2. Sectional coordinates of the wing, the vane, the flap, and the leading-edge Krueger flap are shown in tables 1 to 3.

The trailing-edge flap system was tested at four different deflection angles ($\delta_f = 20^\circ, 30^\circ, 40^\circ$, and 60°). Table 4 shows vane and flap deflection angles that were used during the investigation. The leading-edge Krueger flap was full span and twisted. The deflection of the Krueger flap varied along the wing span because of the twist as indicated in table 4. The Krueger flap had two "cutouts," approximately 1.5 in. wide to provide clearance for pylons to mount engine simulators on the wing. These cutouts

were left open for all tests without the pylons and the nacelles (fig. 2(b)).

Four wing configurations (figs. 1(b) to 1(e)) were tested: cruise, flaps only, Krueger flap only, and high lift (Krueger flap and flaps deployed). The cruise configuration was obtained by removing the Krueger flap and stowing the trailing-edge flap system with fixed brackets. In this configuration, only exposed pressure ports were plotted to represent pressure distributions for the cruise wing. Four additional sets of trailing-edge flap system brackets were used to obtain the other deflections.

Figure 3 shows the reference points used to position the wing and the trailing-edge flap for various wing configurations. The reference points are located vertically on the component reference plane ($z = 0$) and chordwise relative to the component leading edge. The leading-edge Krueger flap is not shown, but its reference point is the lower-surface trailing edge, which is always coincident with the leading-edge of the wing with no gap.

Figures 4 to 6 show details of the inboard and the outboard segments of the trailing-edge flap system. Two flap brackets were used for each of the flap segments; the bracket stations are indicated. All flap brackets were 0.75 in. thick and had similar cross-sectional shapes: rounded leading edges, straight sides, and slab-sided trailing edges. The inboard flap segment is constant in thickness across its span and the outboard flap segment varies linearly across its span.

The pylon and unpowered engine nacelle installations are shown in figure 7. The nacelle geometry is identical for both inboard and outboard stations, but the pylon geometry changes slightly as shown.

The starboard wing had five rows of chordwise pressure taps (fig. 1(f)). The three inboard pressure stations were located in close proximity to the inboard engine nacelle mounting location. The fourth pressure station was located near the middle of the outboard flap segment, and the fifth station was located on the aileron. The wing had a maximum of 313 pressure taps; coordinates are presented in tables 5 to 9.

The empennage consisted of a T-shaped tail arrangement with an all movable horizontal stabilizer with an elevator. The vertical tail had a double-segmented rudder. All control settings were at zero for all tests.

Unpowered engine nacelles were tested in a four-engine, wing-mounted configuration. Nacelle geometry was identical to the model used in reference 6.

The nacelles were mounted at wing stations $y = 15.00$ in. and 29.00 in. A sketch of the transport model with nacelles installed is shown in figure 8. Photographs of the model with nacelles are presented in figure 9.

Test Conditions

The investigation was conducted in the Langley 14- by 22-Foot Subsonic Tunnel, which has a test section 14.50 ft high by 21.75 ft wide by 50.00 ft long (ref. 7). Tests were conducted in the closed, solid-wall test section at free-stream dynamic pressures of 20 psf to 60 psf with corresponding Reynolds numbers based on wing mean aerodynamic chord of 1.22×10^6 to 2.11×10^6 . Mach numbers corresponding to the dynamic pressures were 0.12 to 0.20 . The model was tested through an angle of attack range of -4° to 24° in 2° increments and an angle of sideslip range of -20° to 20° in 5° increments; only a representative portion of these data are contained in the report. In some cases, the maximum angle of attack was limited by model dynamic oscillations near stall. Pressure distributions are presented for angles of attack from 0° to 20° . All tests were conducted with the model positioned at or near the tunnel centerline to minimize possible wall effects. The entire data set is available on electronic files from the authors.

Angle of attack was set by the pitch drive of the model support system and was measured by an electronic inclinometer mounted inside the forward portion of the fuselage. Sideslip angle was set by the yaw drive of the model support system and was measured by an electronic counter mounted to the yaw drive. Accuracy of angle-of-attack and sideslip measurements was $\pm 0.01^\circ$ and $\pm 0.02^\circ$, respectively.

Wing, body, and wake blockage corrections, determined from reference 8, were used to correct free-stream dynamic pressure. No corrections were made to the data for tunnel flow angularity (according to reference 7, upflow is about 0.15°) or support system interference.

Data presented herein were acquired with an electronically scanned pressure (ESP) system. Each pressure tap is connected to an individual 5 psi pressure transducer, which is contained in modules of 32 transducers. The accuracy stated by the manufacturer for the pressure system is ± 0.72 psf (0.1 percent of full scale). The ESP system has the capability of online calibration for each pressure transducer to maintain a high degree of accuracy. The ESP system scans all transducers at rates up to 20 kHz and acquires all pressure data at nearly the same instant. These data are passed to the tunnel data acquisition

system (DAS) at the rate of 1 sample per second. The DAS averages 20 of these samples for each data point.

Presentation of Results

Surface pressure distributions for each wing element are presented as pressure coefficient (C_p) at nondimensional chord location. Chord locations are nondimensionalized by the local element chords at each wing station, which are presented in tables 5 to 9. Unless specified, all tests were conducted without the empennage and the engine nacelles installed.

Discussion of Results

Pressure distributions are presented at selected angles of attack for various wing configurations to support the limited analysis discussed herein. The transport model was configured in a wing and body geometry for most of the data presented in the report (horizontal and vertical tails removed and without engine nacelles). Exceptions are noted in the text and the figures. Pressure distributions are presented from $\alpha = 0^\circ$ to $\alpha = 16^\circ$ for the wing without the leading-edge Krueger flap and to $\alpha = 20^\circ$ with the Krueger flap.

Effect of Free-Stream Speed

The 14- by 22-Foot Subsonic Tunnel does not have the ability to independently vary dynamic pressure (q), Reynolds number (R), and Mach number (M). Therefore, an increase or a decrease in any one of these parameters results in a corresponding increase or decrease in the other two parameters. For this investigation, increasing dynamic pressure from 20 psf to 60 psf resulted in corresponding increases in Reynolds number from 1.2×10^6 to 2.1×10^6 , and in Mach number from 0.12 to 0.20 .

Figures 10 to 19 present the effect of increasing free-stream speed on wing pressure distributions by increasing free-stream dynamic pressure from 20 psf to 60 psf. Results for the cruise configuration (fig. 10) show no effect of free-stream speed on pressure distributions for $\alpha \leq 12^\circ$. At $\alpha = 16^\circ$, the higher free-stream speeds caused slightly increased suction pressures (more negative C_p) on the upper surface near the leading edge.

Pressure distributions for the flaps-only configuration (figs. 11 to 14) exhibited similar insensitivity to free-stream speed at low angles of attack. Slightly increased suction pressure on the upper surface of the wing near the leading edge occurred at $\alpha = 12^\circ$ for the higher free-stream speeds. Two conditions are particularly noteworthy for this wing configuration. Pressure distributions at $\alpha = 16^\circ$ for $\delta_f = 40^\circ$

and 60° (figs. 13(e) and 14(e)) indicate significant effects of free-stream speed on the wing surface flow characteristics. At $q = 20$ psf, suction peaks on the wing for the three inboard stations ($y = 11.0$ in., 19.0 in., and 22.0 in.) are greatly reduced from higher free-stream speed conditions. (Data were not available for the $q = 60$ psf for $\delta_f = 60^\circ$ condition.) Data at the two outer wing stations ($y = 43.75$ in. and 59.0 in.) implied that the flow on the upper surface of the wing was completely separated for the $q = 20$ psf condition. The flow at these two wing stations remained attached at higher free-stream speed conditions. This flow condition was probably a Reynolds number effect because the chord Reynolds number was smaller at the two outboard wing stations than at the inboard wing stations.

The Krueger-flap-only configuration results are presented in figure 15. As expected, flow on the lower surface of the Krueger flap appeared to be separated. This caused a stagnant (no flow) region on the lower surface of the wing near the leading edge. Variations in free-stream speed had virtually no effect on pressure distributions for this configuration.

Pressure distributions for the high-lift configuration (leading-edge Krueger flap on and trailing-edge flaps deployed) are presented in figures 16 to 19. For the $\delta_f = 30^\circ$ at $\alpha = 20^\circ$ condition (fig. 17(f)), wing stations $y = 11.0$ in. and 19.0 in. had less suction pressure on the wing upper surface for $q = 20$ psf than for the $q = 40$ psf case. (Data were not acquired for the $q = 60$ psf condition.) Exactly the opposite occurred at $y = 43.75$ in. station, where results at $q = 40$ psf had less suction pressure than the results at $q = 20$ psf. For the $\delta_f = 40^\circ$ at $\alpha = 20^\circ$ case (fig. 18(f)), the pressure distributions were nearly identical for the low and the high free-stream speed conditions ($q = 20$ psf and 60 psf). However, the $q = 40$ psf results were similar to those shown in figure 17(f).

Overall, each wing configuration showed sensitivity to free-stream speed at high angles of attack. The effects on the cruise and the Krueger-flap-only configurations were confined to slight changes in peak C_p values near the wing leading edge. The flaps-only and the high-lift configurations at high angles of attack and high flap deflections were very sensitive to changes in free-stream speed.

Effect of Angle of Attack

Figures 20 to 29 present the effect of angle-of-attack variation on pressure distributions for different wing configurations. Cruise configuration results (fig. 20) showed expected negative increases in C_p

with no unusual characteristics as angle of attack increased to $\alpha = 16^\circ$.

Figures 21 to 24 show the effect of angle-of-attack variation for the flaps-only configuration. Flow separation was evident on the wing of the flaps-only configuration for two conditions. Pressure distributions for the $\delta_f = 40^\circ$ and 60° conditions at $\alpha = 16^\circ$ and $q = 20$ psf indicate flow separation on the two outer stations of the wing upper surface (figs. 23(a) and 24(a)). These were the same conditions highlighted in the "Effect of Free-Stream Speed" section. Trailing-edge flap pressure distributions were relatively insensitive to changes in angle of attack except for the two conditions with flow separation on the outer wing.

The Krueger-flap-only configuration (fig. 25) showed a progressive increase in suction pressure for the outer two wing stations ($y = 43.75$ in. and 59.0 in.) as angle of attack increased. The three inboard stations showed an initial increase in suction pressure for $\alpha \leq 16^\circ$, which was followed by a decrease in suction pressure at $\alpha = 20^\circ$. Suction pressure on the Krueger flap progressively increased with angle of attack at all wing stations. Increases for the two outboard stations were larger than increases for the inboard stations.

Effect of angle of attack on pressure distributions for the high-lift configuration is presented in figures 26 to 29. Generally, suction pressure on the wing increased when angle of attack increased for $\alpha \leq 16^\circ$. The three inboard wing stations indicated a decrease in suction pressure as angle of attack was increased from $\alpha = 16^\circ$ to 20° . Station $y = 43.75$ in. typically had similar pressure distributions for $\alpha = 16^\circ$ and 20° . The outer most wing station continually increased in suction pressure with increasing angle of attack. Similar trends were observed for leading-edge Krueger-flap pressure distributions. Trailing-edge flap system pressures indicated increased sensitivity to angle-of-attack changes as flap deflection was increased, particularly for the three inboard stations. The larger flap deflections at the highest angles of attack had greatly decreased suction pressure on the upper surfaces, which indicated significant flow separation for the three inboard stations. In general, this was not the case at $y = 43.75$ in., where typically a continual increase in suction pressure with increasing angle of attack occurred.

Generally, increasing angle of attack had the predictable effect of increasing suction pressure on the upper surface of the wing. The effect of increasing angle of attack on the high-lift elements varied with the

configuration. At high angles of attack, free-stream speed effects predominated.

Effect of Sideslip Angle

The model was tested at various sideslip angles to determine the effect on pressure distributions for free-stream dynamic pressures of $q = 20$ psf and 40 psf. Data were acquired by positioning the model at a given angle of attack and conducting a sideslip angle sweep from $\beta = -20^\circ$ to 20° in 5° increments. Sideslip variation had the effect of unsweeping the starboard wing relative to the oncoming flow to $\beta \approx 10^\circ$. Since the wing leading-edge sweep is 9.57° , increases in sideslip actually produced a forward sweep of the starboard wing.

Figure 30 presents the effect of sideslip angle on cruise configuration pressure distributions. Generally, suction pressure increased as sideslip was increased from -20° to 20° ; this trend was accentuated as angle of attack was increased. The effect was greater for inboard wing stations than for outboard stations with station $y = 11.0$ in. experiencing the most sensitivity.

The flaps-only and Krueger-flap-only configurations (figs. 31 to 33, respectively) generally had trends similar to the cruise configuration. However, upper-surface flow separation was evident on the wing of the flaps-only configuration for the $\delta_f = 30^\circ$ at $\alpha = 16^\circ$ condition. Wing stations $y = 43.75$ in. and 59.0 in. appeared to have flow separation on the wing upper surface at $q = 20$ psf (fig. 31(e)), while only station $y = 59.0$ in. indicated flow separation for the $q = 40$ psf case (fig. 31(f)). Pressure distributions on the trailing-edge flap system were largely unaffected by sideslip changes with the largest changes in pressure distributions occurring on the inboard stations. Minimal effects of sideslip were observed on the Krueger-flap pressure distributions for $\alpha \leq 8^\circ$. The greatest effect of sideslip variation for the Krueger flap occurred at station $y = 11.0$ for $\alpha = 16^\circ$.

Results for the high-lift wing configuration are presented in figures 34 and 35. Inboard wing stations, again, showed the largest changes with sideslip variation. The high-lift elements showed significant variation in pressure distributions at high angles of attack.

Effect of Flap Deflection

Figures 36 and 37 show the effect of flap deflection on pressure distributions for the flaps-only and high-lift configurations, respectively. As expected, when flap deflection was increased, suction pressure

increased on the wing and the flap elements for both configurations. Flow on the flap elements, as indicated by C_p distributions, appeared to improve dramatically with increasing flap deflection.

Wing pressure distributions for the flaps-only configuration showed one anomalous characteristic at $q = 20$ psf and $\alpha = 16^\circ$ for both $\delta_f = 40^\circ$ and 60° conditions (fig. 36(g)). Flow on the wing upper surface appeared to be completely separated at the two outboard stations ($y = 43.75$ in. and 59.0 in.). These were the same conditions that were significantly affected by changes in free-stream speed and discussed in the "Effect of Free-Stream Speed" section.

Wing pressure distributions for the high-lift configuration exhibited several interesting characteristics. At $\alpha = 16^\circ$, the three inboard stations increased in suction pressure over the forward portion of the wing as flap deflection was increased from $\delta_f = 20^\circ$ to 40° , followed by a decrease in suction pressure for the $\delta_f = 60^\circ$ condition (figs. 37(g) to 37(i)). Both outboard wing stations showed continually increasing suction pressure as flap deflection was increased. The pressure distribution on the Krueger flap were generally unaffected by flap deflection changes for the three inboard stations, whereas the outboard stations were much more sensitive to changes in flap deflection.

Effect of Leading-Edge Krueger Flap

The effect of the leading-edge Krueger flap on pressure distributions was investigated and the results are presented in figures 38 to 40. The function of a leading-edge Krueger flap is to extend the angle-of-attack range of the wing. A properly designed Krueger flap has a deflection angle that would be aligned with the upwash at the leading edge. This alignment reduces the peak suction pressure on the wing, which allows operation at higher angles of attack without flow separation.

Results highlighting the effect of addition of the Krueger flap to the cruise configuration are presented in figure 38. Interestingly, the Krueger flap increased the suction pressure on the wing above that exhibited with the cruise wing configuration at $\alpha = 0^\circ$. Apparently the Krueger flap increased the wing circulation, which caused the wing loading to increase. At $\alpha = 8^\circ$, the upper-surface pressure distribution on the wing with and without the Krueger flap were nearly identical. Wing lower-surface flow was affected by the stagnant (no flow) region on the lower surface of the Krueger flap. Above $\alpha = 16^\circ$, the classical reduction in peak suction pressure on the wing occurred. Figure 38(j) particularly highlights the benefits of the Krueger flap at station 59.0 in. Without the Krueger flap installed, the wing upper

surface was separated; but with the Krueger flap installed, flow on the wing remained attached.

Figures 39 and 40 present the effect of installation of the Krueger flap to the flaps-only configuration. Nearly identical upper-surface pressure distributions on the wing with and without the Krueger flap occurred at $\alpha = 0^\circ$. At $\alpha = 8^\circ$ and above, peak suction pressure on the wing was reduced by the installation of the Krueger flap. Several examples highlighting how the Krueger flap reduced very steep pressure gradients on the wing are shown in figures 39 and 40 for $\alpha \geq 16^\circ$. Deployment of the Krueger flap appeared to eliminate flow separation on the outer two wing stations at $\alpha = 20^\circ$.

Installation of the Krueger flap reduced suction pressure on the trailing-edge flaps at $\alpha = 0^\circ$ for the $\delta_f = 30^\circ$ and 60° conditions. Pressures were largely unaffected by the Krueger flap for the $\delta_f = 30^\circ$ condition at higher angles of attack. For the $\delta_f = 60^\circ$ condition, however, trailing-edge flap suction pressures were typically reduced by the Krueger flap at higher angles of attack.

Effect of Empennage

Tests were done to determine the effect of the empennage on wing pressures, and the results are presented in figures 41 and 42 for the cruise and flaps-only ($\delta_f = 30^\circ$) configurations, respectively. The empennage appeared to have no measurable effect on wing pressures for either configuration throughout the angle-of-attack range.

The data of the cruise configuration highlight an important aspect. Data acquired for the configuration with no empennage were obtained near the beginning of the wind tunnel investigation and data for the configuration with the empennage were acquired near the end, with a great number of model changes in between. The excellent repeatability implies not only good model fidelity, but also demonstrates the ability to accurately replicate model and tunnel conditions.

Effect of Engine Nacelles

The effect of the unpowered engine nacelles on pressure distributions is presented in figures 43 and 44 for the cruise and the flaps-only ($\delta_f = 40^\circ$) configurations, respectively. The nacelles were installed at wing stations $y = 15.00$ in. and 29.00 in. The model geometry was wing and body (no horizontal or vertical tail) for both wing configurations with nacelles off. For the cruise configuration, both vertical and horizontal tails were installed with the

nacelles-on case (fig. 43). For the flaps-only configuration, only the vertical tail was installed with the nacelles-on case (fig. 44). The empennage had no effect on wing pressures; therefore, any differences shown in figures 43 and 44 can be exclusively attributed to the installation of nacelles on the wing.

Figure 43 presents the effect of nacelle installation on wing pressures for the cruise configuration. The nacelle installation caused a very slight reduction in suction pressure for the three inboard stations. There was little or no effect on pressure distributions for the outer two stations.

The effect of nacelles on wing pressures for the flaps-only configuration is presented in figure 44. At low angles of attack ($\alpha \leq 8^\circ$), the only noticeable effect was a very slight reduction in peak suction pressure on the wing for the three inboard stations. Significant changes in C_p values can be seen for the $q = 20$ psf at $\alpha = 16^\circ$ condition (fig. 44(g)), where major differences in pressure distributions appear to have been caused by installation of the nacelles. This condition was sensitive to changes in free-stream speed. The addition of nacelles may have caused changes in the flow-field of the wing that represented more than just the interference effect of the nacelles. Data at higher free-stream speeds ($q = 40$ psf and 60 psf) at this angle of attack indicate that the nacelles caused a reduction in suction pressure on the wing and the flaps for the three inboard stations and had essentially no effect on the outer two stations.

Concluding Remarks

A wind tunnel investigation was conducted on a generic, high-wing transport model in the Langley 14- by 22-Foot Subsonic Tunnel. The untwisted wing incorporated a full-span, leading-edge Krueger flap, a part-span, double-slotted trailing-edge flap system. The starboard wing had five rows of chordwise pressure taps. The trailing-edge flap was tested at four different deflection angles (20° , 30° , 40° , and 60°). Four wing configurations were tested: cruise, flaps only, Krueger flap only, and high lift (Krueger flap and flaps deployed).

Tests were conducted at free-stream dynamic pressures of 20 psf to 60 psf with corresponding chord Reynolds numbers of 1.22×10^6 to 2.11×10^6 and Mach numbers of 0.12 to 0.20. The angles of attack presented range from 0° to 20° and were determined by model configuration. The angle of sideslip ranged from -20° to 20° . This report contains data that document effects of various model configurations and free-stream conditions on wing pressure distributions.

Results of the investigation may be summarized as follows:

1. Pressure distributions were largely unaffected by free-stream speed at low to moderate angles of attack ($\alpha < 16^\circ$). Significant effects of free-stream speed were observed at high angles of attack ($\alpha \geq 16^\circ$); these effects increased as flap deflection was increased.
2. Increasing angle of attack had the general effect of increasing suction pressure on the upper surface of the wing. The effect of increasing angle of attack on the high-lift elements varied with configuration.
3. Increasing sideslip angle from -20° to 20° generally produced significant increases in suction pressure for the inboard wing stations with less effect on the outboard stations. The sensitivity of the pressure distributions on the Krueger flap and trailing-edge flaps to sideslip changes varied with wing configuration and angle of attack.
4. Increasing trailing-edge flap angle produced increased suction pressures on the wing and the flap. Improvements in flap loading were evident with increasing flap deflection. Outboard pressure stations on the Krueger flap were much more sensitive to flap angle changes than the inboard Krueger flap stations.
5. The leading-edge Krueger flap increased the maximum suction peak on the wing for the Krueger-flap-only configuration at low angles of attack. At higher angles of attack, the Krueger flap lowered the peak suction pressure on the wing, thus allowing operation at high angles of attack without flow separation.
6. Installation of the empennage had no measurable effect on pressure distributions throughout the angle-of-attack range investigated.
7. Installation of wing-mounted, unpowered engine nacelles generally caused a reduction in suction pressure on the wing and the trailing-edge flaps. The effect was significant for the inboard wing stations that were in the proximity of the nacelles and negligible for the outboard stations. The effect of the nacelles was greater for the wing with trailing-edge flaps deployed than for the cruise wing configuration.

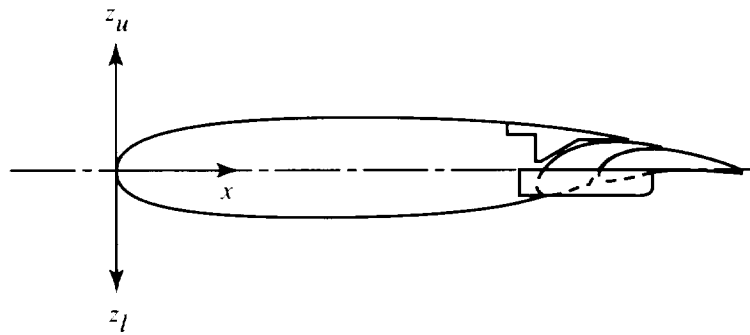
Pressure distribution data presented herein provide a quantitative assessment of aerodynamic effects due to model configuration and free-stream conditions. Examples of excellent data repeatability demonstrate good model fidelity and accurate replication of test conditions. The entire data set can be made available by electronic transfer by contacting the authors.

NASA Langley Research Center
Hampton, VA 23681-0001
October 27, 1994

References

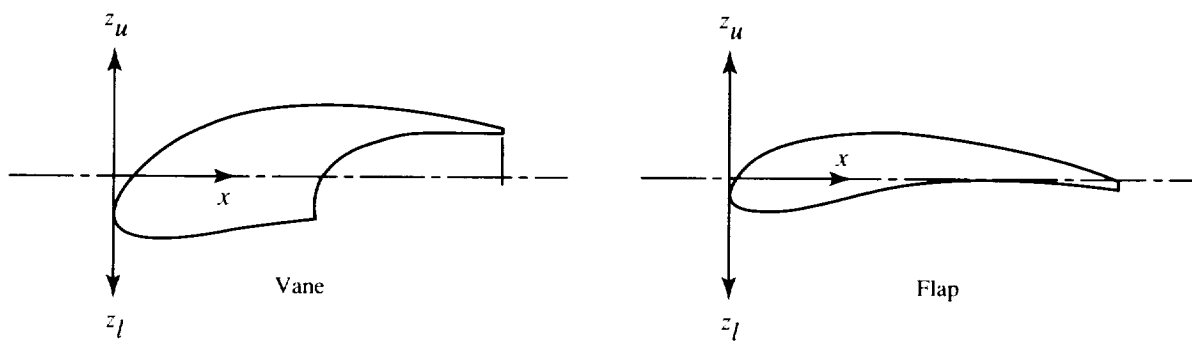
1. Applin, Zachary T.; and Coe, Paul L., Jr.: *Low-Speed Stability and Control Characteristics of a Transport Model With Aft-Fuselage-Mounted Advanced Turboprops*. NASA TP-2535, 1986.
2. Dunham, Dana Morris; Gentry, Garl L.; Manuel, Gregory S.; Applin, Zachary T.; and Quinto, P. Frank: *Low-Speed Aerodynamic Characteristics of a Twin-Engine General Aviation Configuration With Aft-Fuselage-Mounted Pusher Propellers*. NASA TP-2763, 1987.
3. Margason, Richard J.; Hammond, Alexander D.; and Gentry, Garl L.: *Longitudinal Stability and Control Characteristics of a Powered Model of a Twin-Propeller Deflected-Slipstream STOL Airplane Configuration*. NASA TN D-3438, 1966.
4. Nishimura, Y.: *An Experimental Investigation by Force and Surface Pressure Measurements of a Wing Immersed in a Propeller Slipstream. Part 2 - Surface Pressure Measurements of Wing Immersed in Propeller Slipstream*. NAE-LR-525, NRC-11062, June 1969.
5. Phelps, Arthur E., III: *Static and Wind-on Tests of an Upper-Surface-Blown Jet-Flap Nozzle Arrangement for Use on the Quiet Clean Short-Haul Experimental Engine (QCSEE)*. NASA TN D-8476, 1977.
6. Aljabri, A. S.: *Wind Tunnel Tests on a One-Foot Diameter SR-7L Propfan Model*. AIAA-87-1892, June/July 1987.
7. Gentry, Garl L., Jr.; Quinto, P. Frank; Gatlin, Gregory M.; and Applin, Zachary T.: *The Langley 14-by 22-Foot Subsonic Tunnel: Description, Flow Characteristics, and Guide for Users*. NASA TP-3008, 1990.
8. Rae, William H., Jr.; and Pope, Alan: *Low-Speed Wind Tunnel Testing, Second ed.* John Wiley & Sons, Inc., 1984.

Table 1. Coordinates of Wing



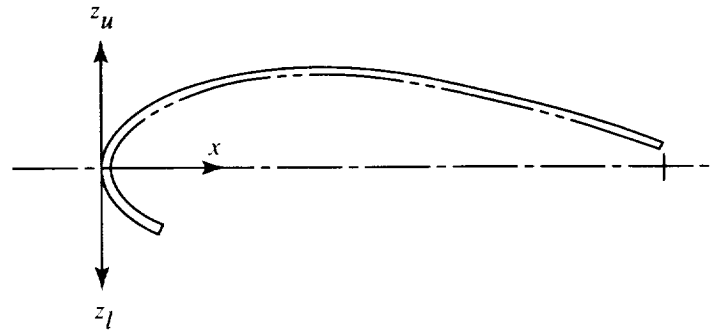
x , percent c_w	Coordinates of wing at--					
	Station 0 in.		Station 35.00 in.		Station 70.00 in.	
	z_u , percent c_w	z_l , percent c_w	z_u , percent c_w	z_l , percent c_w	z_u , percent c_w	z_l , percent c_w
0	0	0	0	0	0	0
1.25	2.96	-2.89	2.92	-3.12	2.18	-2.17
2.50	3.93	-3.74	3.97	-4.14	2.76	-2.80
5.00	5.14	-4.78	5.18	-5.34	3.48	-3.58
7.50	5.97	-5.35	5.91	-6.06	3.95	-4.09
10.00	6.57	-5.80	6.48	-6.58	4.29	-4.46
15.00	7.33	-6.38	7.33	-7.30	4.77	-4.94
20.00	7.80	-6.79	7.92	-7.77	5.08	-5.23
25.00	8.09	-7.00	8.31	-8.04	5.27	-5.41
30.00	8.23	-7.14	8.61	-8.18	5.40	-5.49
35.00	8.25	-7.24	8.80	-8.16	5.47	-5.49
40.00	8.25	-7.28	8.92	-8.05	5.50	-5.25
50.00	8.09	-7.16	8.85	-7.37	5.45	-4.98
60.00	7.53	-6.43	8.34	-5.48	5.21	-3.90
70.00	6.56	-4.57	7.36	-3.56	4.74	-1.51
80.00	5.12	-2.05	5.61	-1.30	3.96	.53
90.00	3.00	-.25	3.14	-.22	2.56	1.40
95.00	1.64	-.14	1.62	-.45	1.45	1.07
100.00	0	-.62	0	-.77	-.08	-1.14

Table 2. Coordinates of Vane and Flap



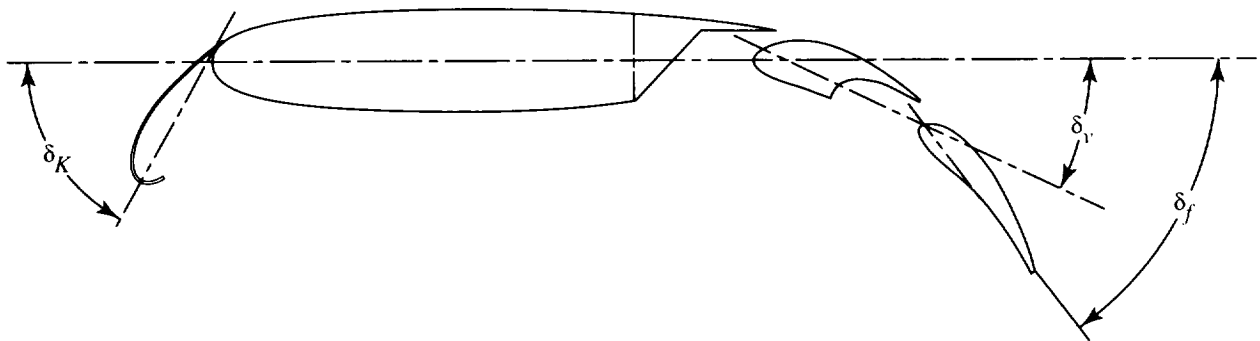
x, percent c_v or c_f	Coordinates for vane at				Coordinates for flap at			
	Station 35.00 in.		Station 52.50 in.		Station 35.00 in.		Station 52.50 in.	
	z_u , percent c_v $c_v = 0.236c_w$	z_l , percent c_v $c_v = 0.236c_w$	z_u , percent c_v $c_v = 0.233c_w$	z_l , percent c_v $c_v = 0.233c_w$	z_u , percent c_f $c_f = 0.264c_w$	z_l , percent c_f $c_f = 0.264c_w$	z_u , percent c_f $c_f = 0.262c_w$	z_l , percent c_f $c_f = 0.262c_w$
0	-12.50	-12.50	-8.00	-8.00	-4.00	-4.00	-2.50	-2.50
1.25	-6.52	-16.50	-3.50	-12.60	0	-7.38	1.50	-5.05
2.50	-4.00	-18.09	-1.48	-14.00	1.92	-8.42	3.25	-5.85
5.00	-.30	-19.49	1.65	-15.50	4.79	-8.70	5.32	-6.48
7.50	3.55	-20.20	3.90	-16.27	6.93	-8.45	6.60	-6.68
10.00	4.82	-20.48	5.75	-16.65	8.68	-7.87	7.56	-6.56
15.00	8.50	-20.13	8.90	-16.65	11.01	-6.70	9.08	-5.76
20.00	11.52	-19.19	11.25	-16.10	12.64	-5.64	10.20	-4.84
25.00	14.10	-17.98	13.11	-15.20	13.78	-4.67	11.06	-3.98
30.00	16.28	-16.51	14.65	-14.02	14.52	-3.75	11.65	-2.15
40.00	19.40	-13.82	16.92	-11.70	15.06	-2.15	12.11	-1.72
50.00	21.05	-11.50	18.10	-9.60/-2.00	14.25	-1.02	11.90	-.69
52.00	21.24	1.10	18.25	2.90				
54.00	21.42	4.10	18.33	4.80				
60.00	21.84	9.98	18.40	8.30	12.32	-.43	10.95	0
70.00	21.82	13.50	18.23	11.32	9.75	-.46	9.30	.15
80.00	21.13	15.85	17.70	12.92	6.68	-1.00	7.17	0
90.00	19.91	16.71	16.63	13.50	3.25	-1.79	4.75	-.60
100.00	18.00	16.55	15.28	13.50	-.43	-2.70	2.11	-1.45

Table 3. Coordinates of Leading-Edge Krueger Flap



x , percent c_K	Coordinates of Krueger flap at --					
	Station 0 in.		Station 35.00 in.		Station 70.00 in.	
	z_u , percent c_K $c_K = 0.17c_w$	z_l , percent c_K $c_K = 0.17c_w$	z_u , percent c_K $c_K = 0.22c_w$	z_l , percent c_K $c_K = 0.22c_w$	z_u , percent c_K $c_K = 0.175c_w$	z_l , percent c_K $c_K = 0.175c_w$
0	0	0	0	0	0	0
1.25	5.00	-5.00	5.00	-5.00	5.00	-5.00
2.50	6.95	-6.95	6.95	-6.95	6.95	-6.95
5.00	10.00	-10.00	10.00	-10.00	10.00	-10.00
7.50	12.05	-12.05	12.00	-12.05	12.00	-12.05
10.00	13.55	-13.55	13.55	-13.55	13.55	-13.55
15.00	15.60	-15.60	15.60	-15.60	15.95	-15.95
20.00	16.95		16.95		17.50	
30.00	17.90		17.90		19.20	
40.00	17.50		17.50		19.35	
50.00	16.20		16.20		18.62	
60.00	14.20		14.20		17.25	
70.00	11.60		11.60		15.30	
80.00	8.55		8.55		12.80	
90.00	5.25		5.25		9.90	
100.00	1.70		1.70		6.70	

Table 4. Deflection Angles of Leading-Edge Krueger Flap and Trailing-Edge Double-Slotted Flap



Wing station, in.	δ_K , deg	$\delta_{f'}$, deg	δ_f , deg
35.00	70	10	20
↓	↓	15	30
		20	40
		30	60
52.50	60	10	20
↓	↓	15	30
	↓	20	40
		30	60
70.00	40		

Table 5. Nondimensional Chordwise Location of Cruise Wing Pressure Taps

Location of pressure taps at—				
Station 11.00 in.; $c_w = 22.446$ in.	Station 19.00 in.; $c_w = 21.097$ in.	Station 22.00 in.; $c_w = 20.591$ in.	Station 43.75 in.; $c_w = 15.925$ in.	Station 59.00 in.; $c_w = 11.611$ in.
Upper surface				
0.000	0.000	0.000	0.000	0.000
.003	.003	.003	.002	.003
.010	.010	.010	.010	.010
.025	.025	.024	.025	.024
.050	.050	.050	.050	.050
.075	.075	.075	.075	.075
.100	.100	.100	.100	.100
.150	.151	.151	.151	.150
.300	.300	.300	.300	.300
.400	.400	.400	.400	.400
.500	.500	.500	.500	.500
.600	.601	.600	.600	.600
.700	.698	.700	.700	.697
.749	.750	.744	.749	.749
.799	.800	.800	.779	.808
Upper surface vane				.855
0.860	0.852	0.848	0.830	.904
.874	.866	.864	.847	.951
Upper surface flap				.987
0.937	0.932	0.930	0.921	.997
.981	.978	.977	.974	
.997	.995	.996	.995	
1.000	1.000	1.000	1.000	
Lower surface				
0.003	0.003	0.004	0.004	0.004
.012	.012	.013	.012	.012
.050	.050	.050	.050	.050
.100	.100	.100	.100	.101
.150	.150	.150	.150	.150
.300	.300	.300	.299	.300
.400	.400	.400	.400	.400
.488	.488	.488	.488	.500
.600	.599	.600	.599	.599
.650	.649	.650	.651	.650
Lower surface vane				.700
0.716	0.697	0.690	0.655	.750
.735	.718	.711	.678	.808
.764	.750	.743	.712	.855
Lower surface flap				.903
0.795	0.781	0.775	0.750	.951
.817	.804	.799	.776	.987
.871	.862	.858	.842	
.936	.931	.929	.921	
.979	.977	.976	.974	
.996	.995	.995	.995	

Table 6. Nondimensional Chordwise Location of High-Lift Wing Pressure Taps

Location of pressure taps at—				
Station 11.00 in.; $c_w = 22.446$ in.	Station 19.00 in.; $c_w = 21.097$ in.	Station 22.00 in.; $c_w = 20.591$ in.	Station 43.75 in.; $c_w = 15.925$ in.	Station 59.00 in.; $c_w = 11.611$ in.
Upper surface				
0.000	0.000	0.000	0.000	0.000
.003	.003	.003	.002	.003
.010	.010	.010	.010	.010
.025	.025	.024	.025	.024
.050	.050	.050	.050	.050
.075	.075	.075	.075	.075
.100	.100	.100	.100	.100
.150	.151	.151	.151	.150
.300	.300	.300	.300	.300
.400	.400	.400	.400	.400
.500	.500	.500	.500	.500
.600	.601	.600	.600	.600
.700	.698	.700	.700	.697
.749	.750	.744	.749	.749
.799	.800	.800	.779	.808
				.855
				.904
				.951
				.987
				.997
Lower surface				
0.800	0.800	0.800	0.779	0.987
.750	.750	.750	.749	.951
.700	.700	.700	.700	.903
.650	.649	.650	.651	.855
.600	.599	.600	.599	.808
.488	.488	.488	.488	.750
.400	.400	.400	.400	.700
.300	.300	.300	.299	.650
.150	.150	.150	.150	.599
.100	.100	.100	.100	.500
.050	.050	.050	.050	.400
.012	.012	.013	.012	.300
.003	.003	.004	.004	.150
				.101
				.050
				.012
				.004

Table 7. Nondimensional Chordwise Location of Krueger Pressure Taps

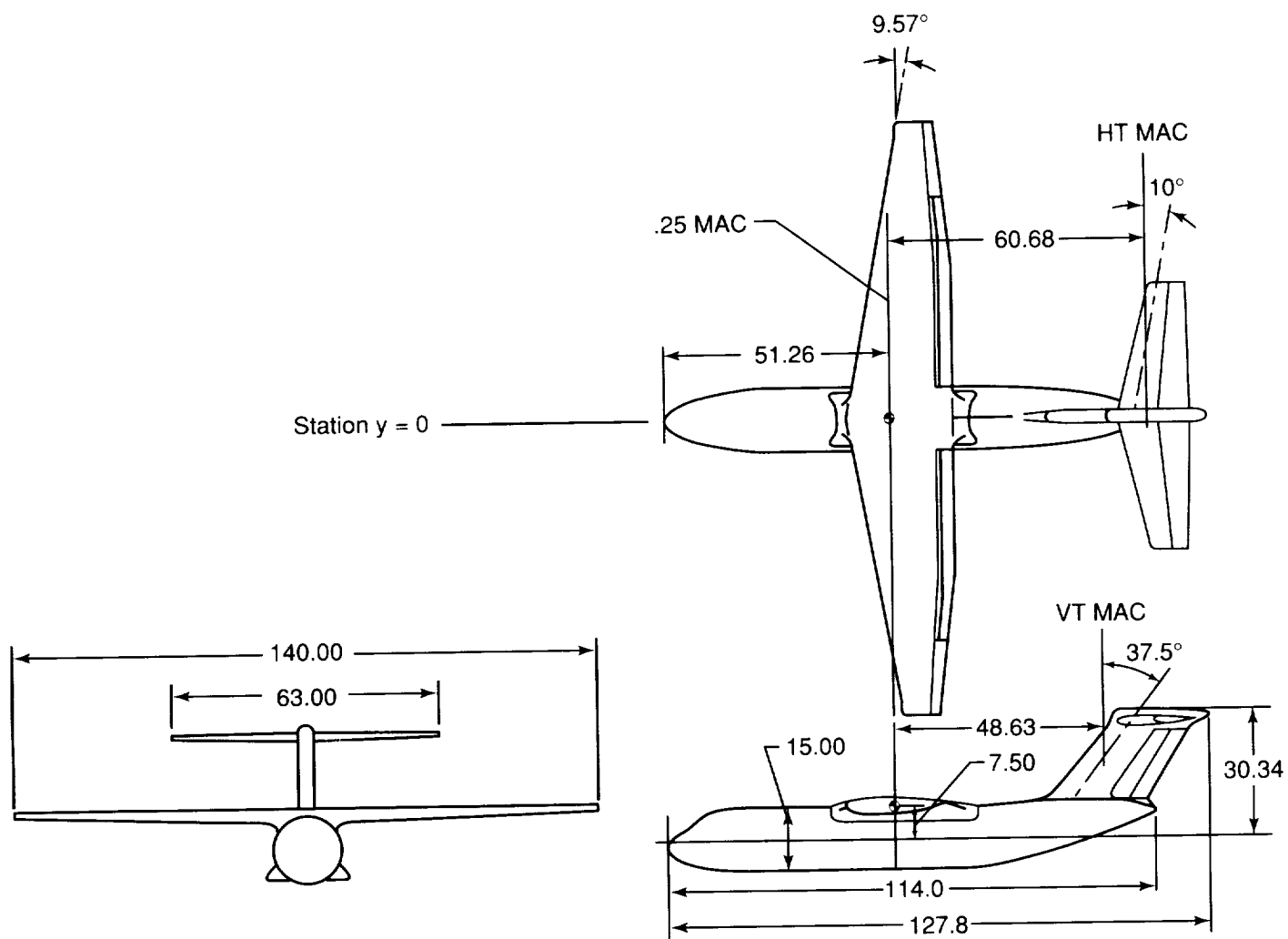
Location of pressure taps at—				
Station 11.00 in.; $c_K = 4.105$ in.	Station 19.00 in.; $c_K = 4.087$ in.	Station 22.00 in.; $c_K = 4.087$ in.	Station 43.75 in.; $c_K = 3.359$ in.	Station 59.00 in.; $c_K = 2.231$ in.
Upper surface				
0.000	0.000	0.000	0.000	0.000
.009	.012	.004	.012	.016
.047	.049	.052	.042	.066
.151	.150	.153	.136	.163
.400	.399	.403	.381	.414
.700	.700	.703	.683	.708
.897	.889	.903	.891	.897
.966	.968	.972	.962	.963
Lower surface				
0.693	0.696	0.699	0.665	0.706
.399	.407	.402	.369	.401
.100	.101	.099	.109	.090
.046	.047	.051	.055	.042
.011	.011	.005	.017	.011

Table 8. Nondimensional Chordwise Location of Vane Pressure Taps

Location of pressure taps at—			
Station 11.00 in.; $c_v = 4.342$ in.	Station 19.00 in.; $c_v = 4.342$ in.	Station 22.00 in.; $c_v = 4.342$ in.	Station 43.75 in.; $c_v = 3.734$ in.
Upper surface			
0.001	0.002	0.001	0.000
.009	.012	.016	.011
.047	.049	.055	.051
.144	.151	.151	.155
.220	.227	.228	.252
.394	.400	.402	.406
.693	.701	.703	.705
.895	.901	.901	.902
.967	.971	.973	.973
Lower surface			
0.968	0.970	0.968	0.972
.896	.901	.900	.906
.594	.599	.599	.602
.496	.498	.498	.501
.396	.400	.400	.398
.249	.250	.250	.248
.150	.147	.149	.147
.049	.048	.048	.048
.005	.013	.017	.012

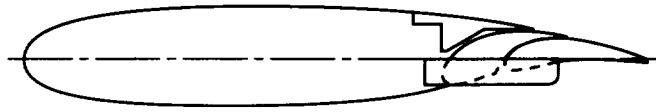
Table 9. Nondimensional Chordwise Location of Flap Pressure Taps

Location of pressure taps at—			
Station 11.00 in.; $c_f = 4.858$ in.	Station 19.00 in.; $c_f = 4.858$ in.	Station 22.00 in.; $c_f = 4.858$ in.	Station 43.75 in.; $c_f = 4.197$ in.
Upper surface			
0.011	0.006	0.004	0.002
.033	.029	.028	.025
.059	.054	.053	.050
.158	.154	.152	.151
.407	.405	.402	.402
.709	.703	.702	.700
.907	.904	.902	.898
.987	.984	.982	.979
.999	1.000	.999	1.000
Lower surface			
0.982	0.979	0.978	0.979
.904	.899	.899	.899
.703	.700	.698	.697
.402	.400	.399	.401
.153	.150	.149	.150
.053	.049	.046	.051
.018	.013	.012	.011

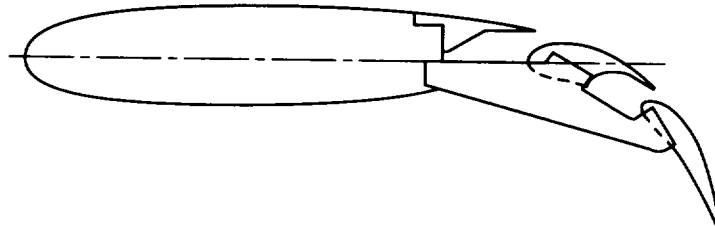


(a) Front, side, and top views.

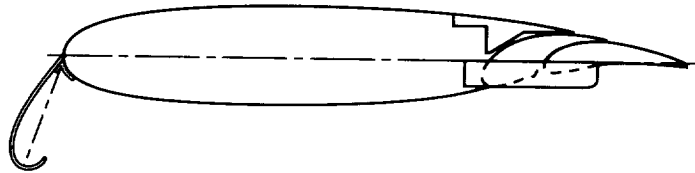
Figure 1. Sketch of generic, high-wing transport model. Linear dimensions are given in inches.



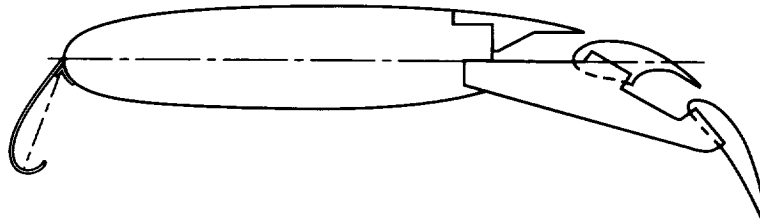
(b) Cruise wing.



(c) Flaps-only wing.

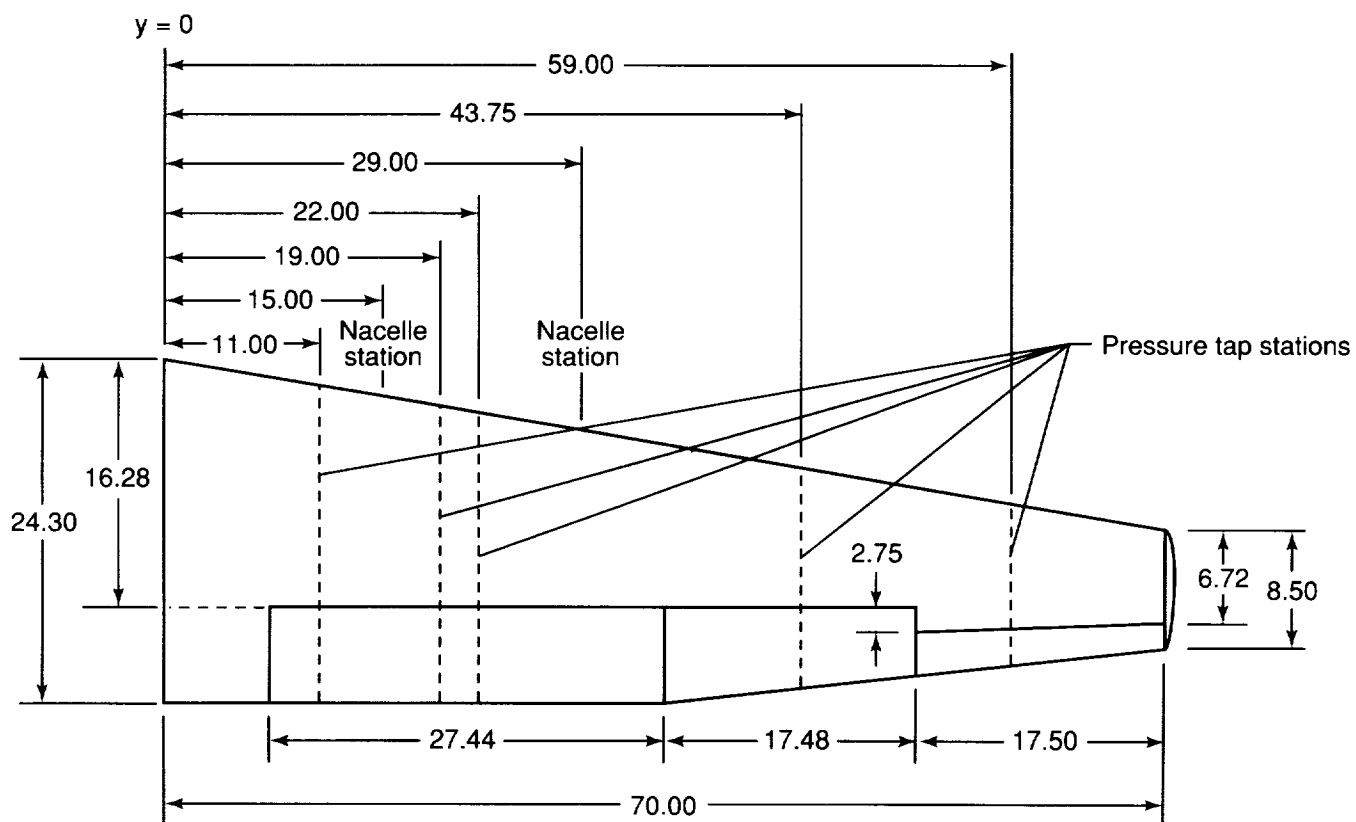


(d) Krueger-flap-only wing.



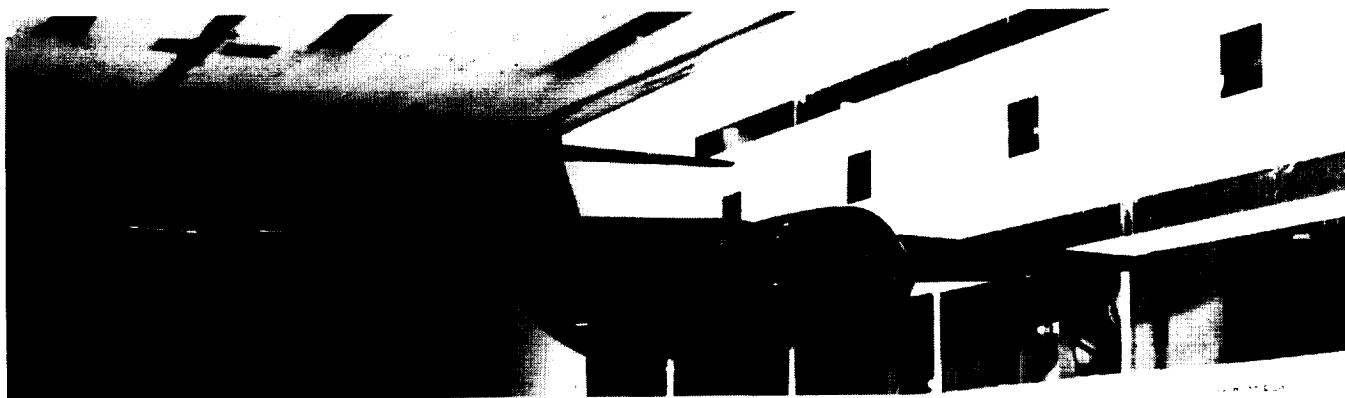
(e) High-lift wing.

Figure 1. Continued.



(f) Pressure tap and nacelle station locations on starboard wing. Dimensions are in inches.

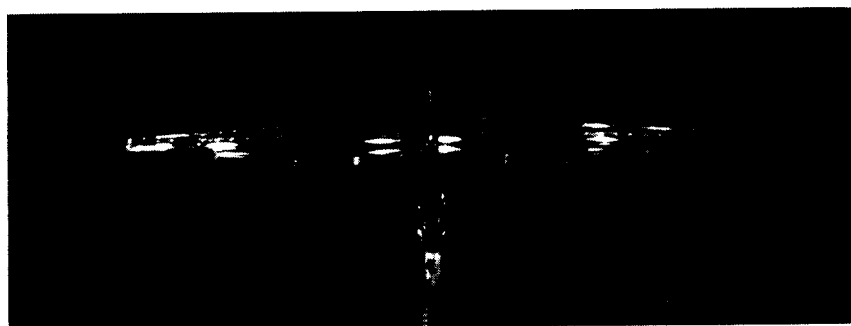
Figure 1. Concluded.



(a) Front three-quarter view.



(b) Aft three-quarter view.



(c) Aft view.

Figure 2. Generic, high-wing transport model with high-lift configuration, empennage on, and unpowered engine nacelles off installed in Langley 14- by 22-Foot Subsonic Tunnel.

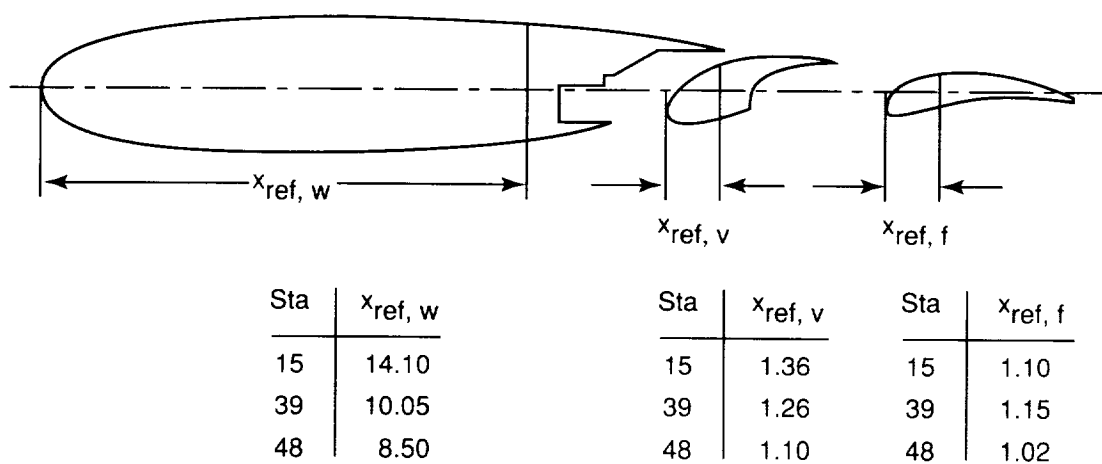
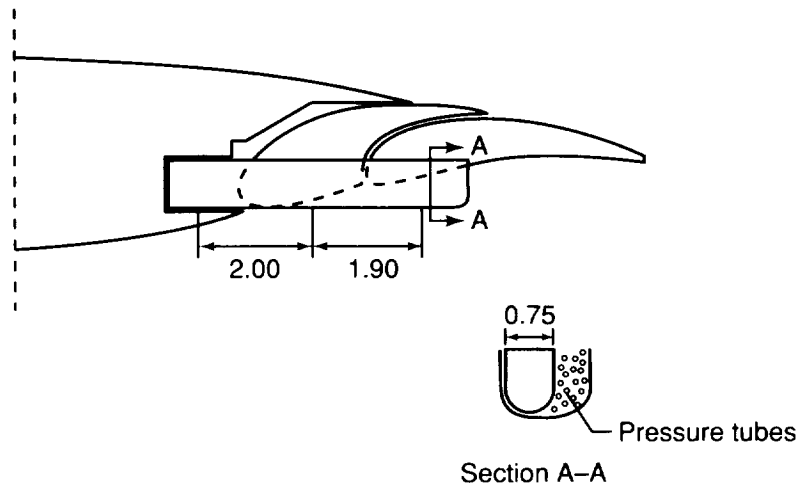
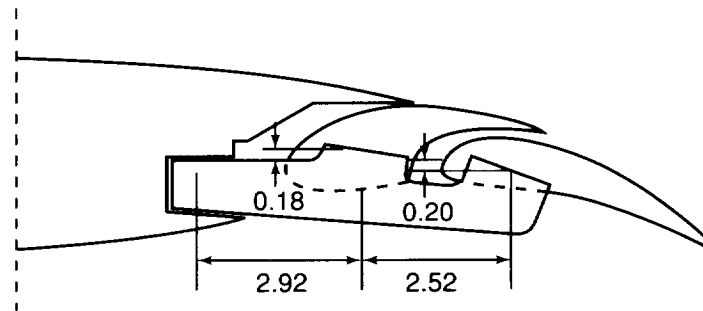


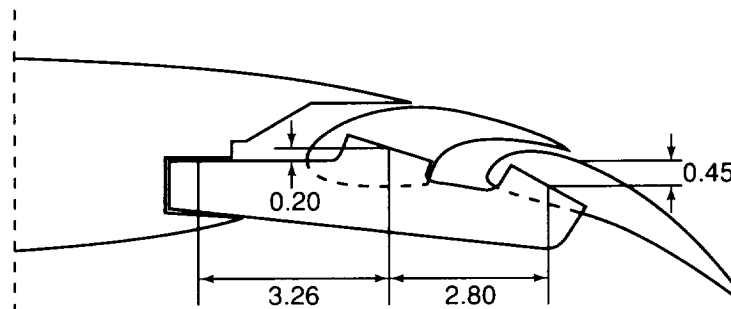
Figure 3. Location of reference points used to position high-lift system elements. Dimensions are in inches.



(a) $\delta_f = 0^\circ$.

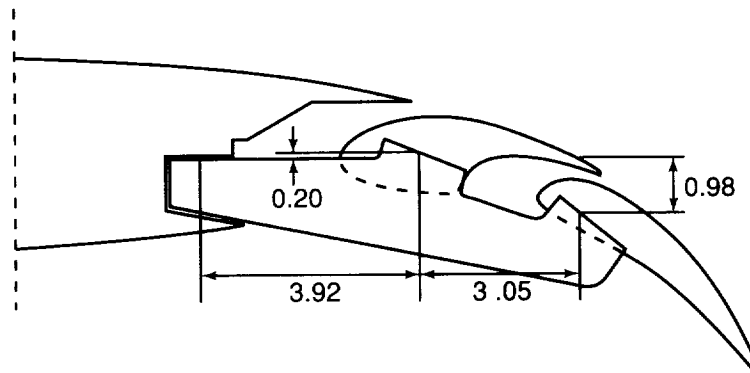


(b) $\delta_f = 20^\circ$.

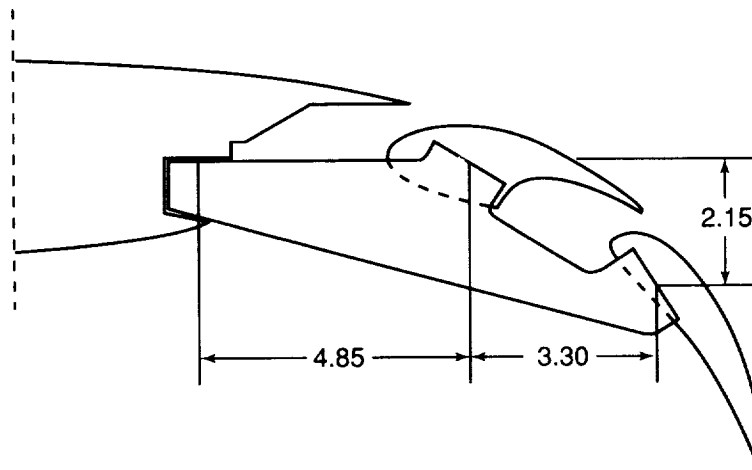


(c) $\delta_f = 30^\circ$.

Figure 4. Inboard trailing-edge flap system brackets and element locations for stations $y = 15.0$ and 29.0 in. Dimensions are in inches.

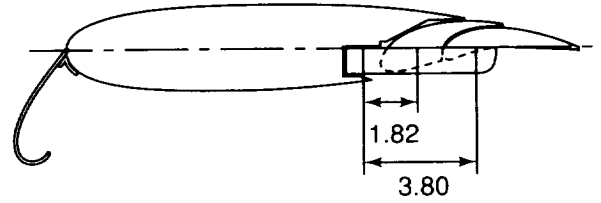


(d) $\delta_f = 40^\circ$.

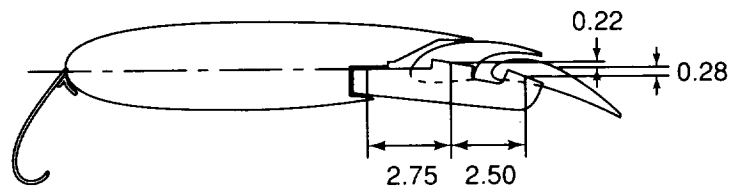


(e) $\delta_f = 60^\circ$.

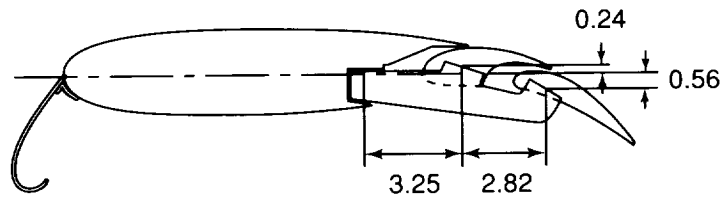
Figure 4. Concluded.



(a) $\delta_f = 0^\circ$.

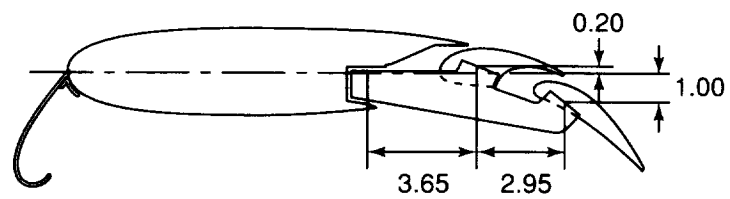


(b) $\delta_f = 20^\circ$.

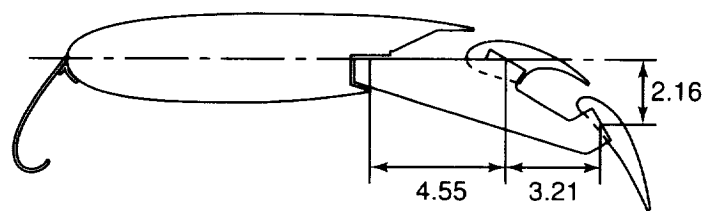


(c) $\delta_f = 30^\circ$.

Figure 5. Outboard trailing-edge flap system brackets and element locations for station $y = 39.0$ in. Dimensions are in inches.

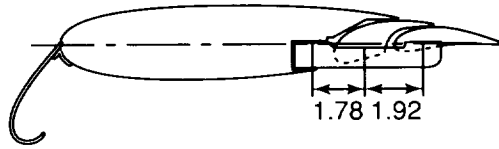


(d) $\delta_f = 40^\circ$.

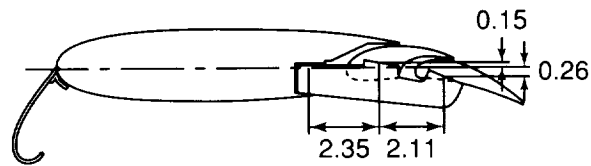


(e) $\delta_f = 60^\circ$.

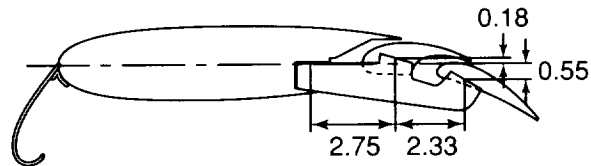
Figure 5. Concluded.



(a) $\delta_f = 0^\circ$.

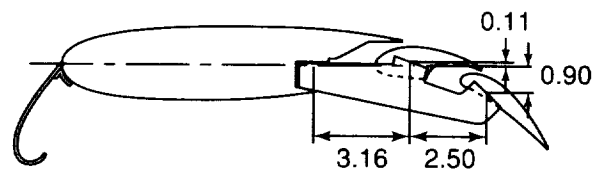


(b) $\delta_f = 20^\circ$.

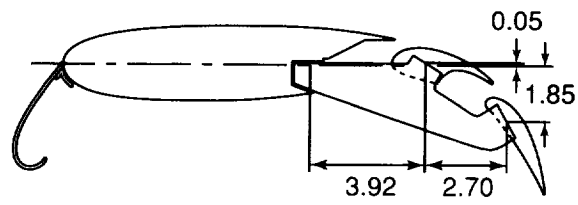


(c) $\delta_f = 30^\circ$.

Figure 6. Outboard trailing-edge flap system brackets and element locations for station $y = 48.5$ in. Dimensions are in inches.

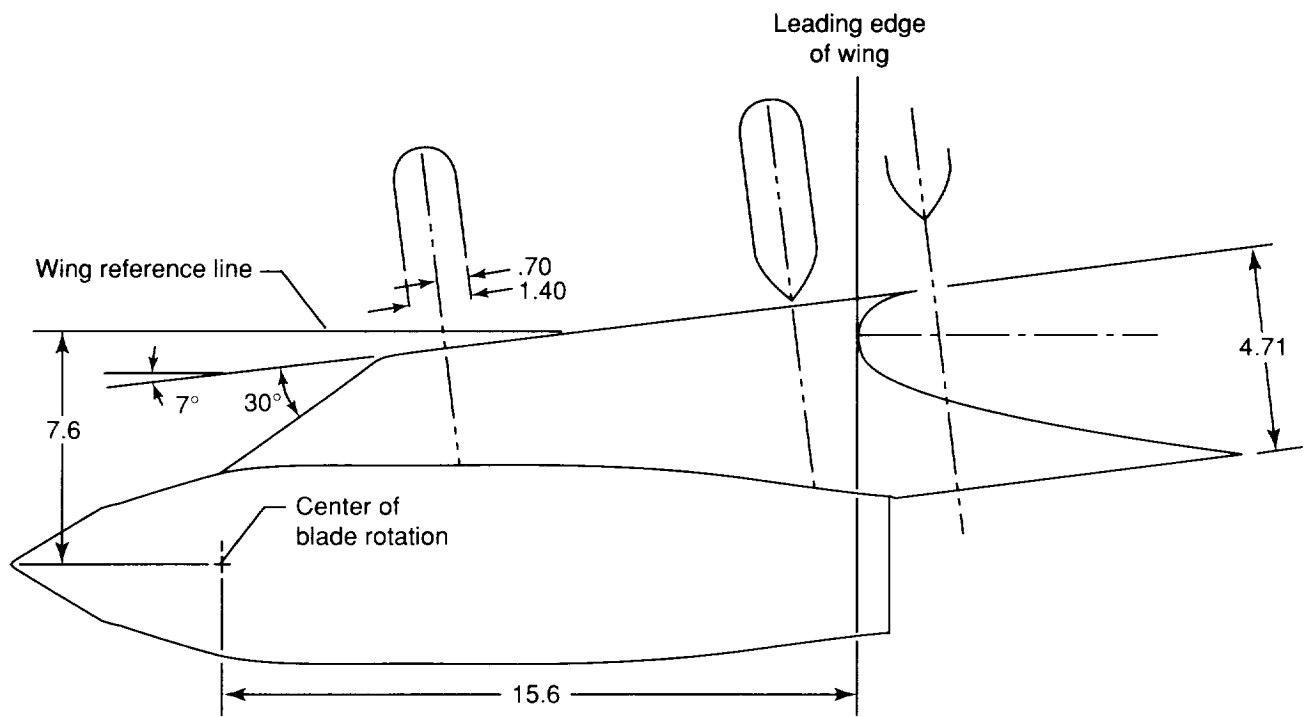


(d) $\delta_f = 40^\circ$.

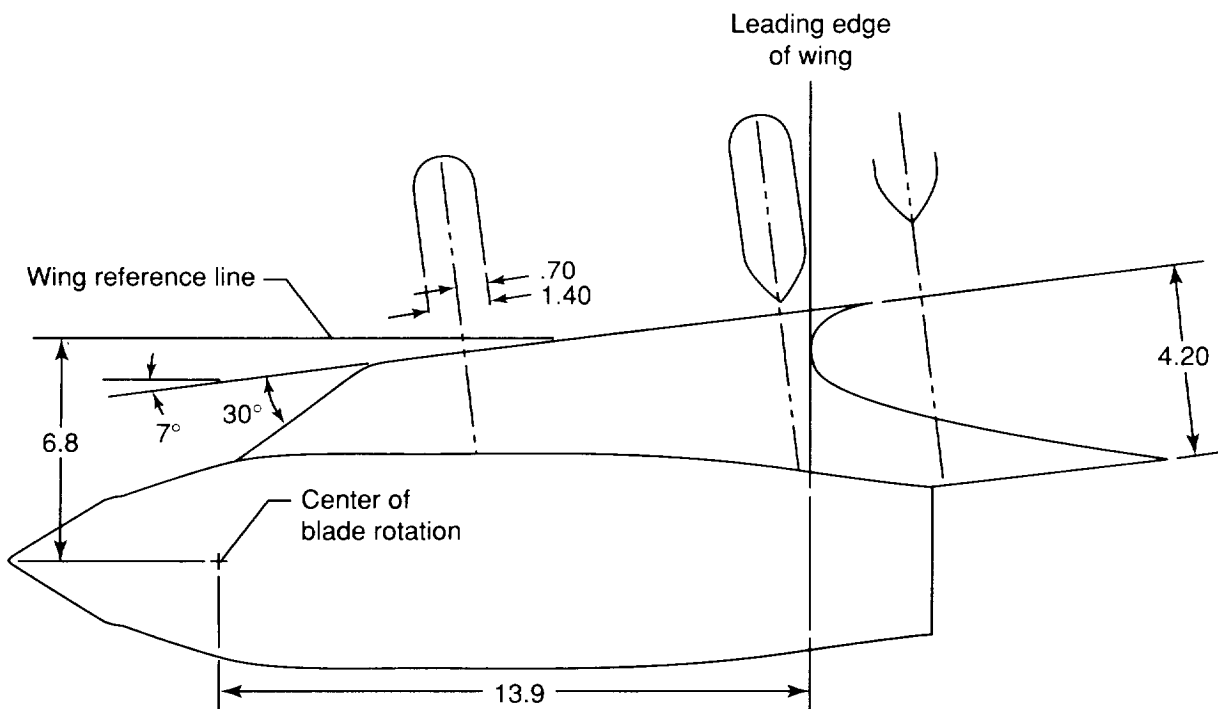


(e) $\delta_f = 60^\circ$.

Figure 6. Concluded.

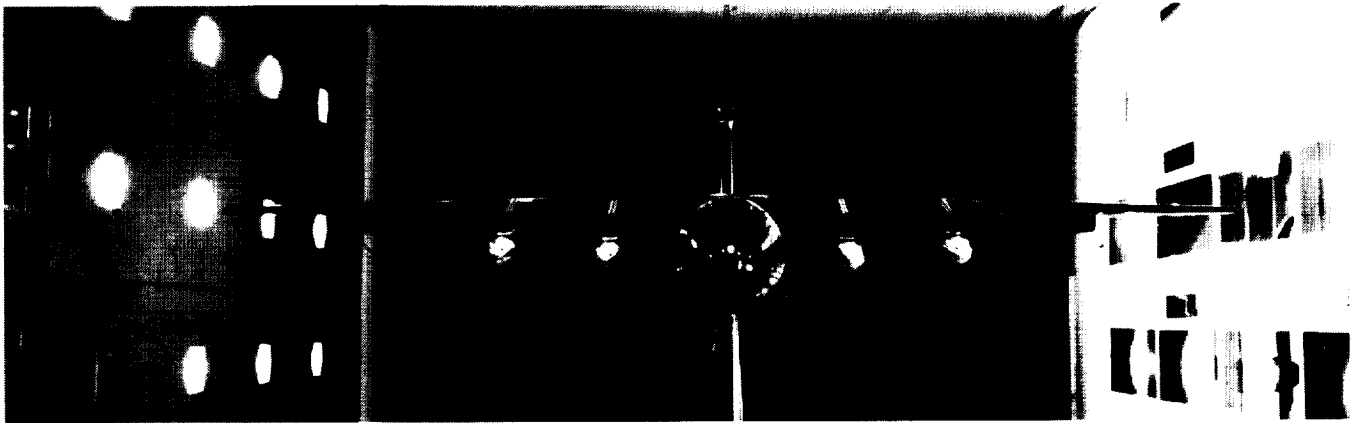


(a) Station $y = 15.0$ in.

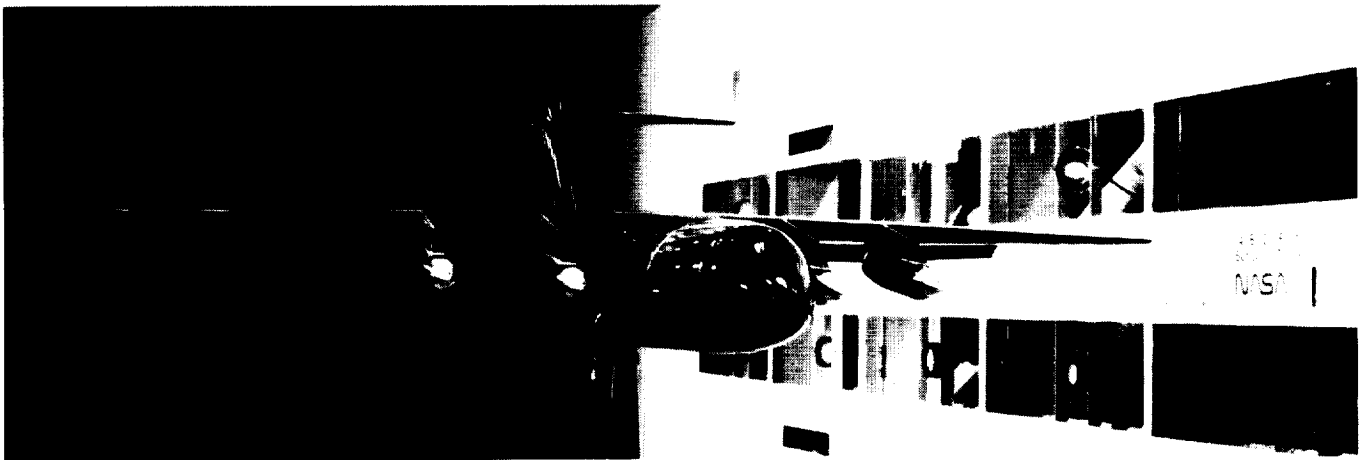


(b) Station $y = 29.0$ in.

Figure 7. Unpowered engine nacelle and pylon installation characteristics. Dimensions are in inches unless otherwise noted.



(a) Front view.



(b) Front three-quarter view.

Figure 9. Transport model with unpowered engine nacelles installed, flaps-only configuration, and empennage on.

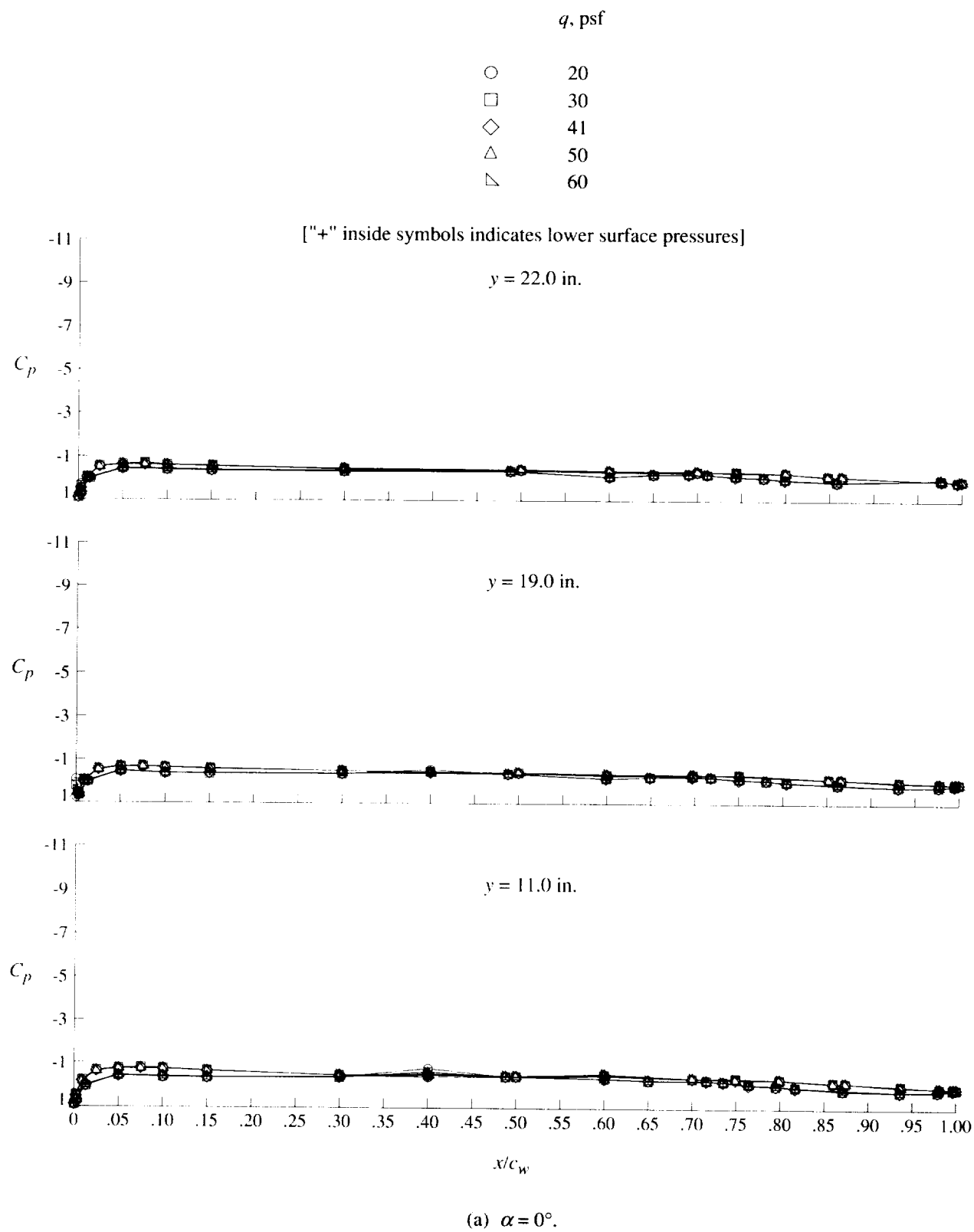


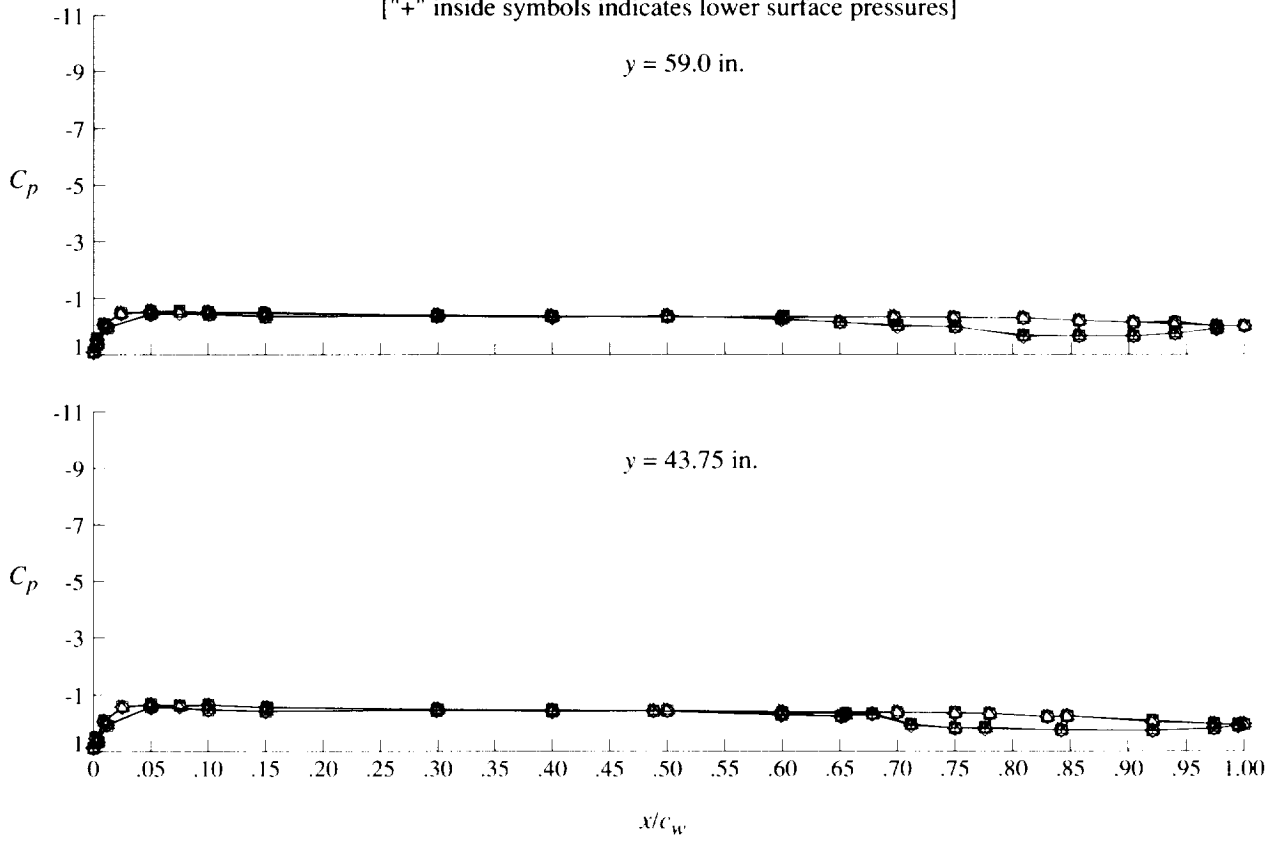
Figure 10. Effect of free-stream speed on pressure distributions for cruise configuration.

q , psf

○	20
□	30
◇	41
△	50
▽	60

["+" inside symbols indicates lower surface pressures]

$y = 59.0$ in.



(a) Concluded.

Figure 10. Continued.

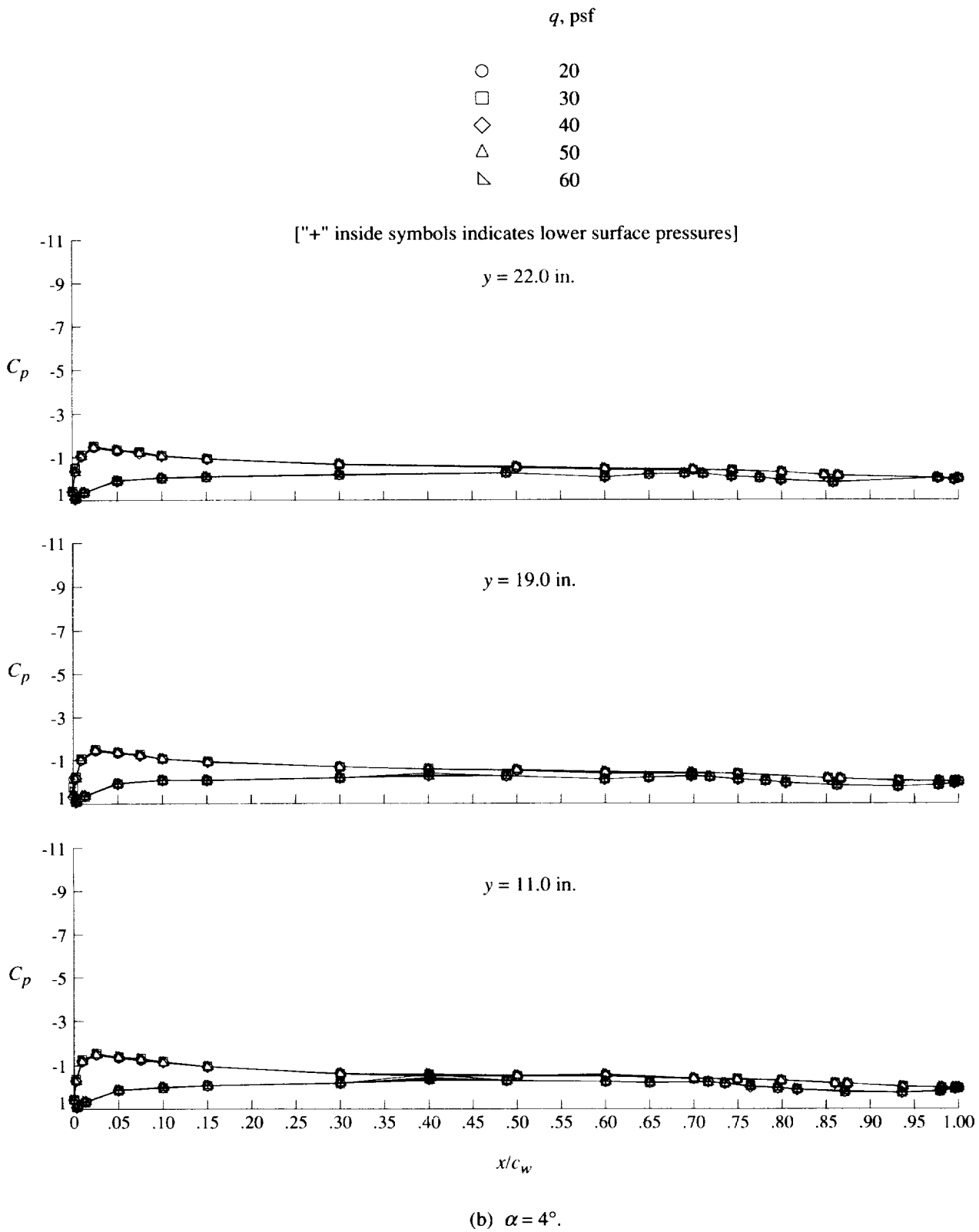


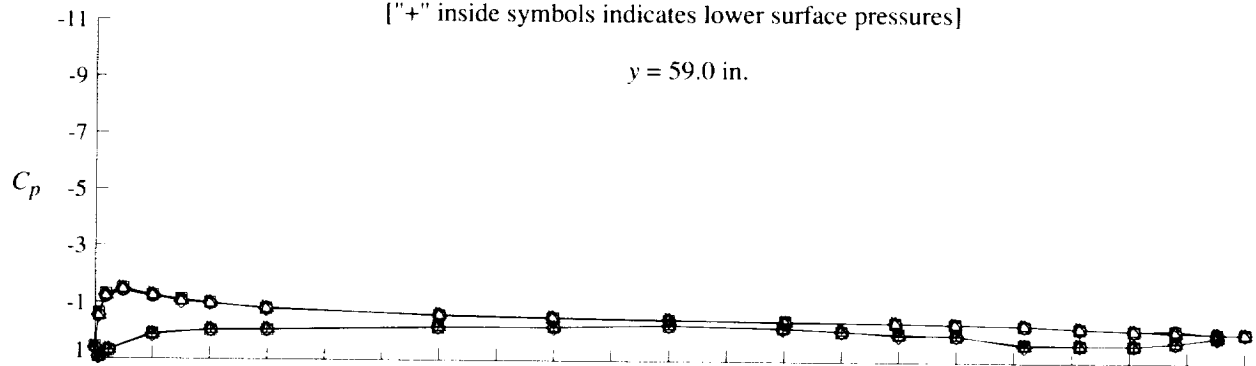
Figure 10. Continued.

q , psf

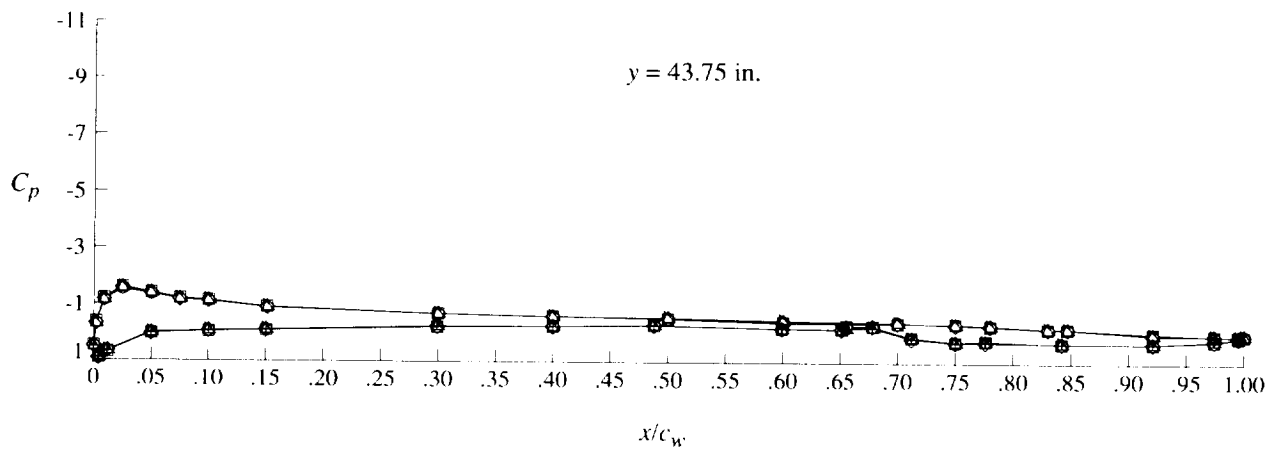
○	20
□	30
◇	40
△	50
▽	60

["+" inside symbols indicates lower surface pressures]

$y = 59.0$ in.



$y = 43.75$ in.



(b) Concluded.

Figure 10. Continued.

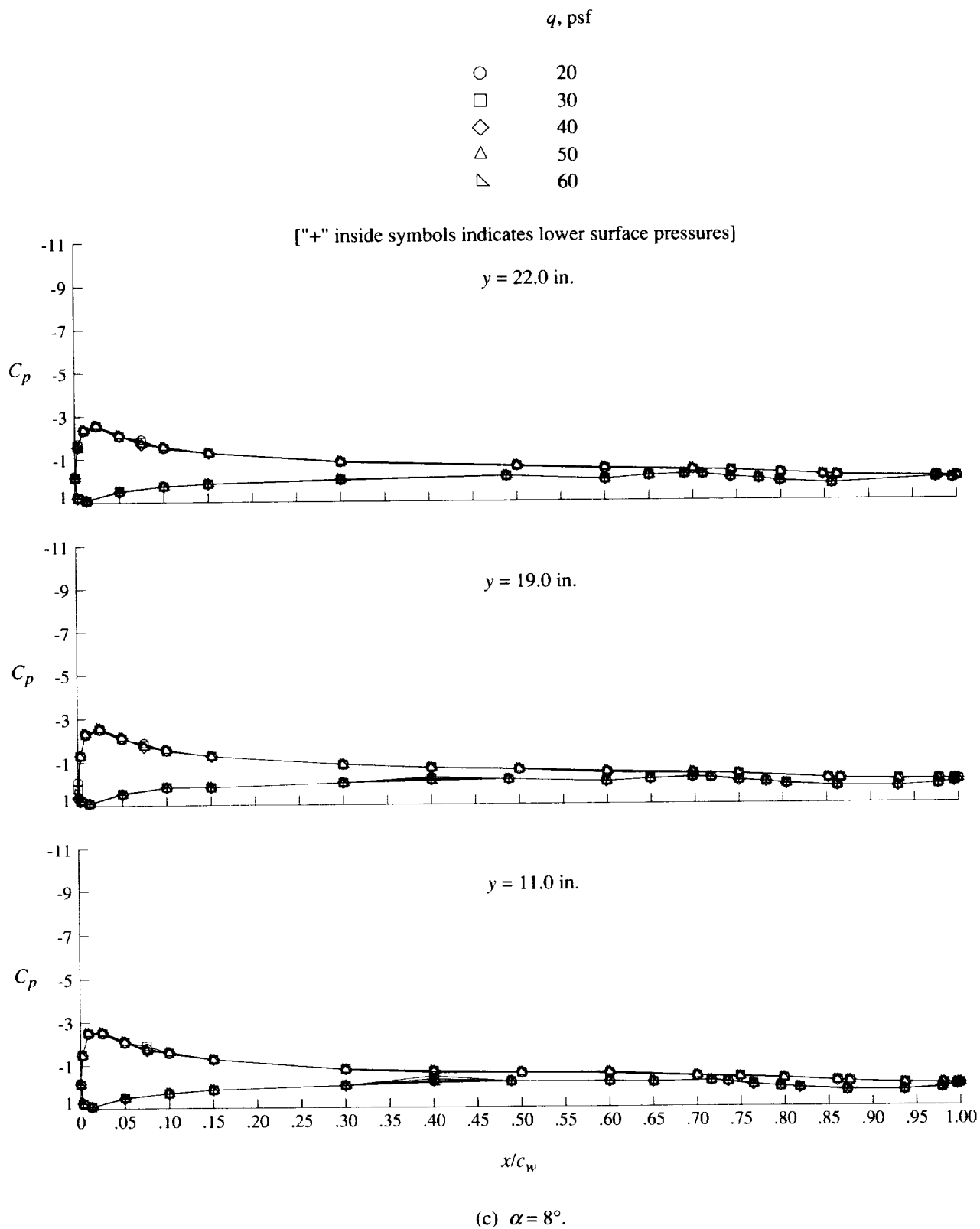
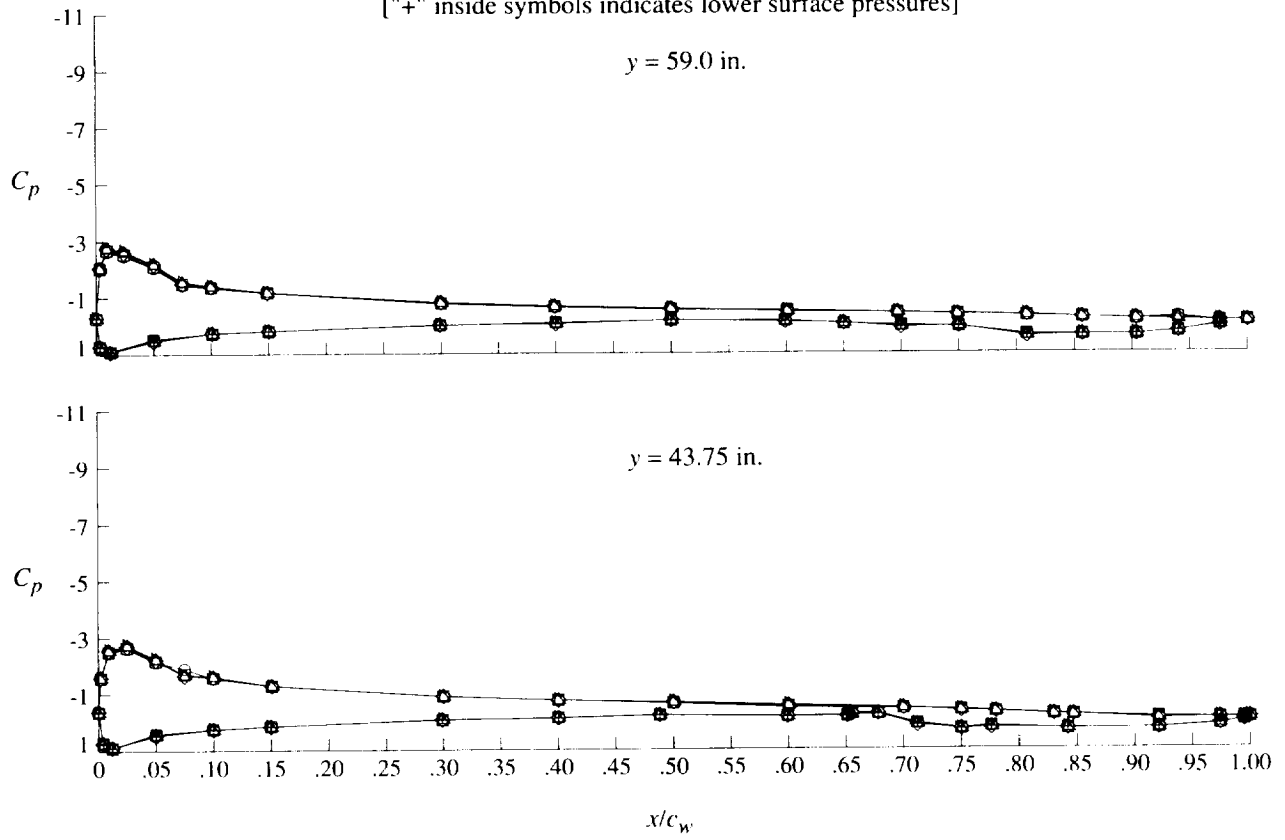


Figure 10. Continued.

q , psf

○	20
□	30
◇	40
△	50
▽	60

["+" inside symbols indicates lower surface pressures]



(c) Concluded.

Figure 10. Continued.

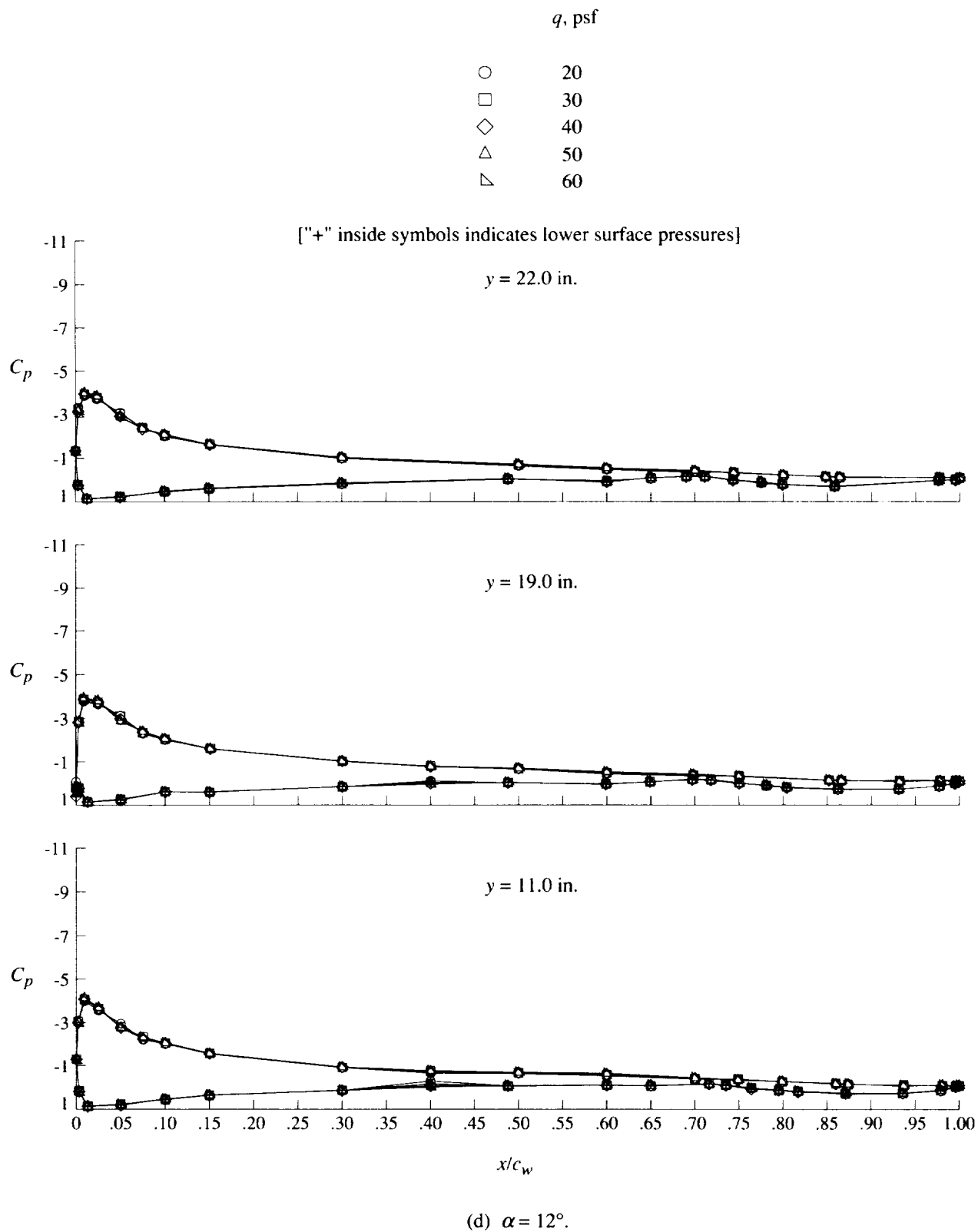
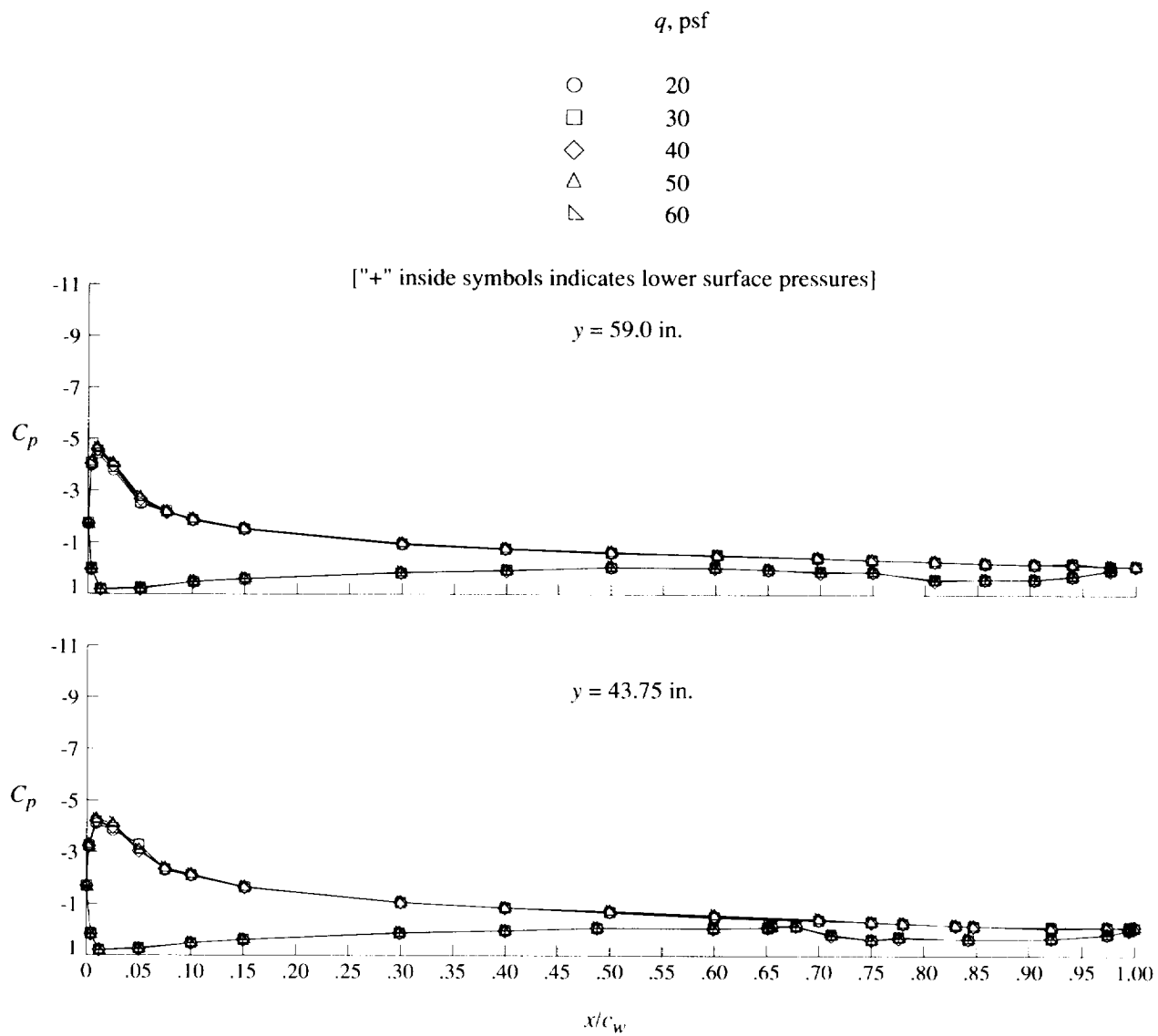


Figure 10. Continued.



(d) Concluded.

Figure 10. Continued.

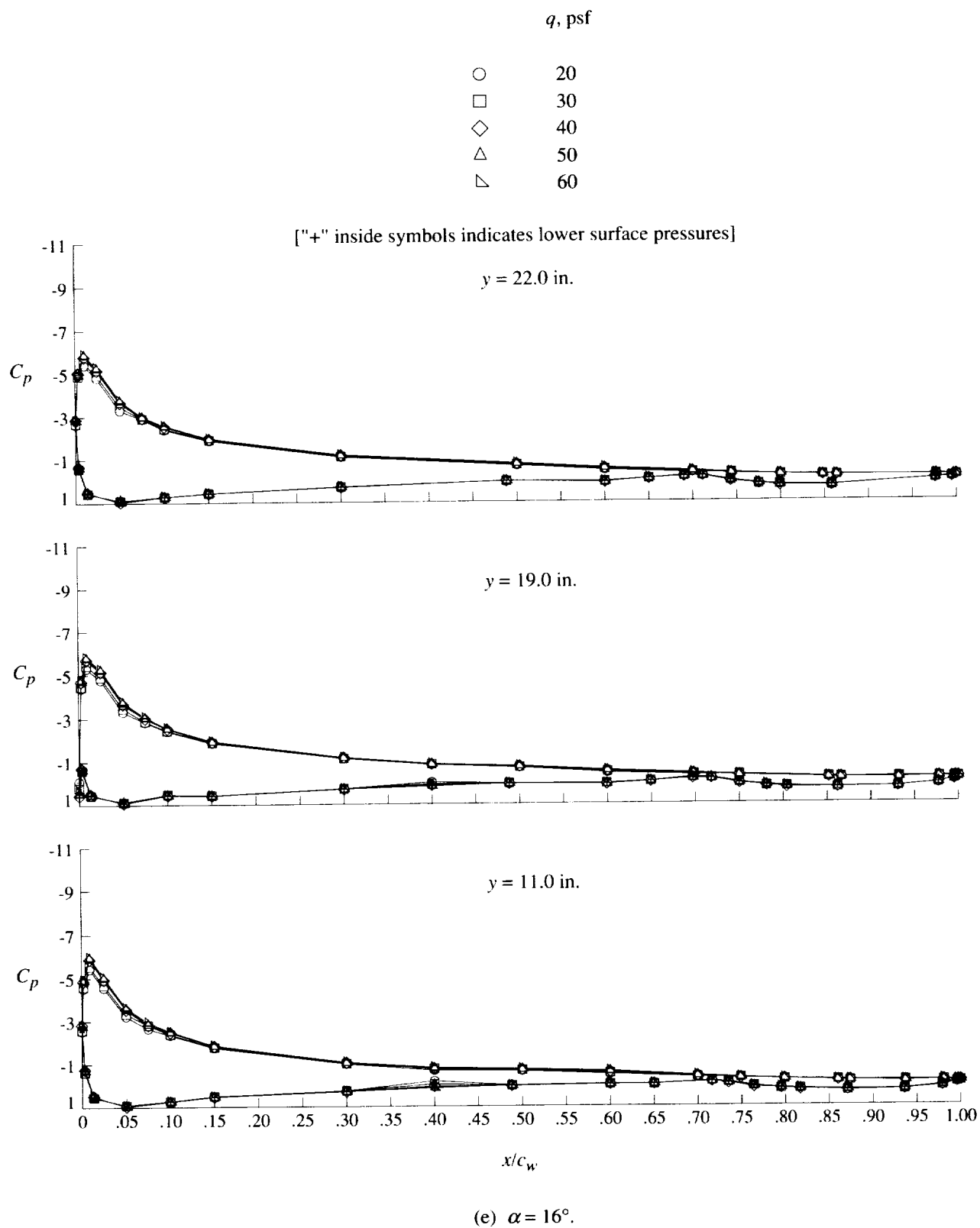
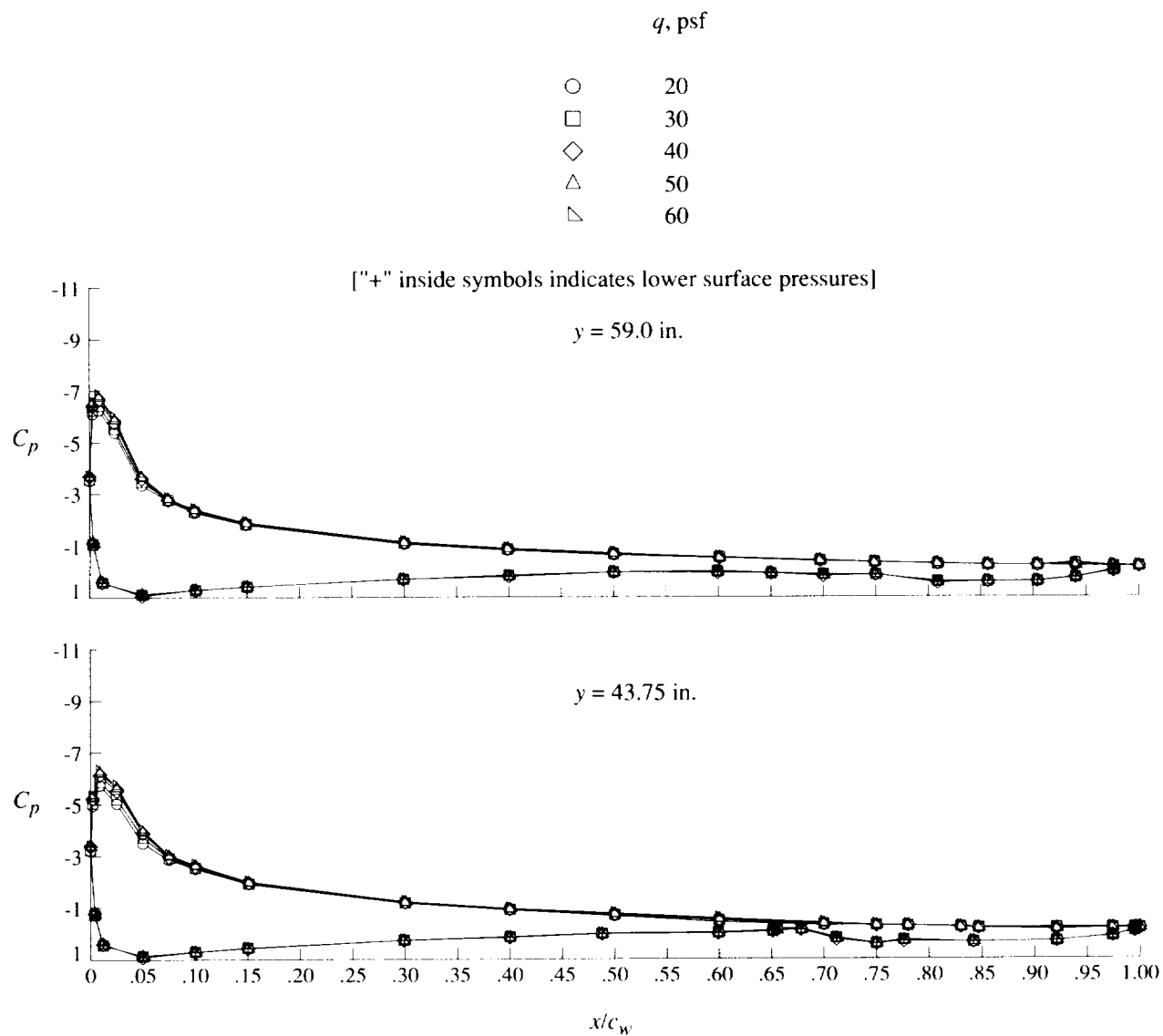


Figure 10. Continued.



(e) Concluded.

Figure 10. Concluded.

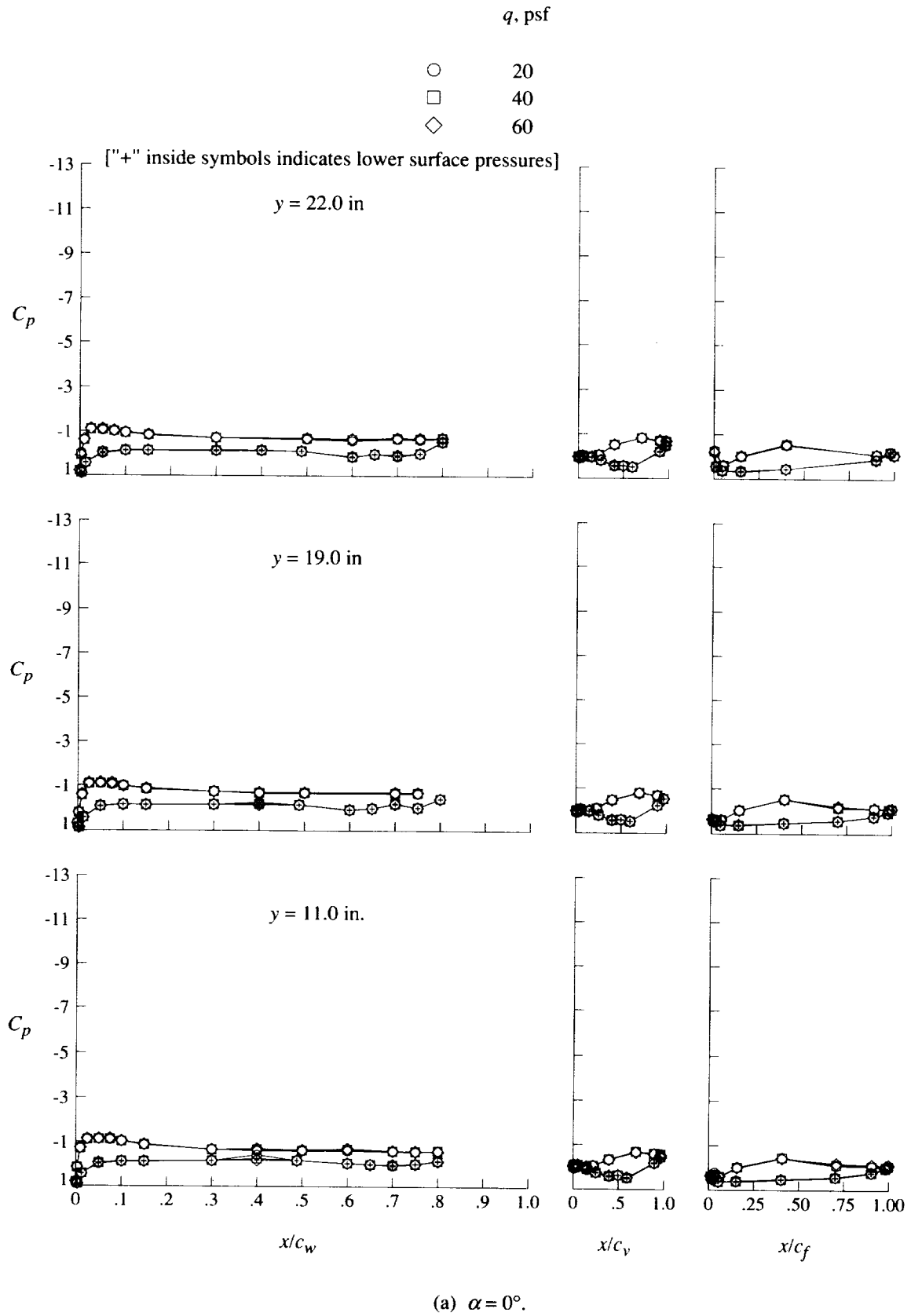
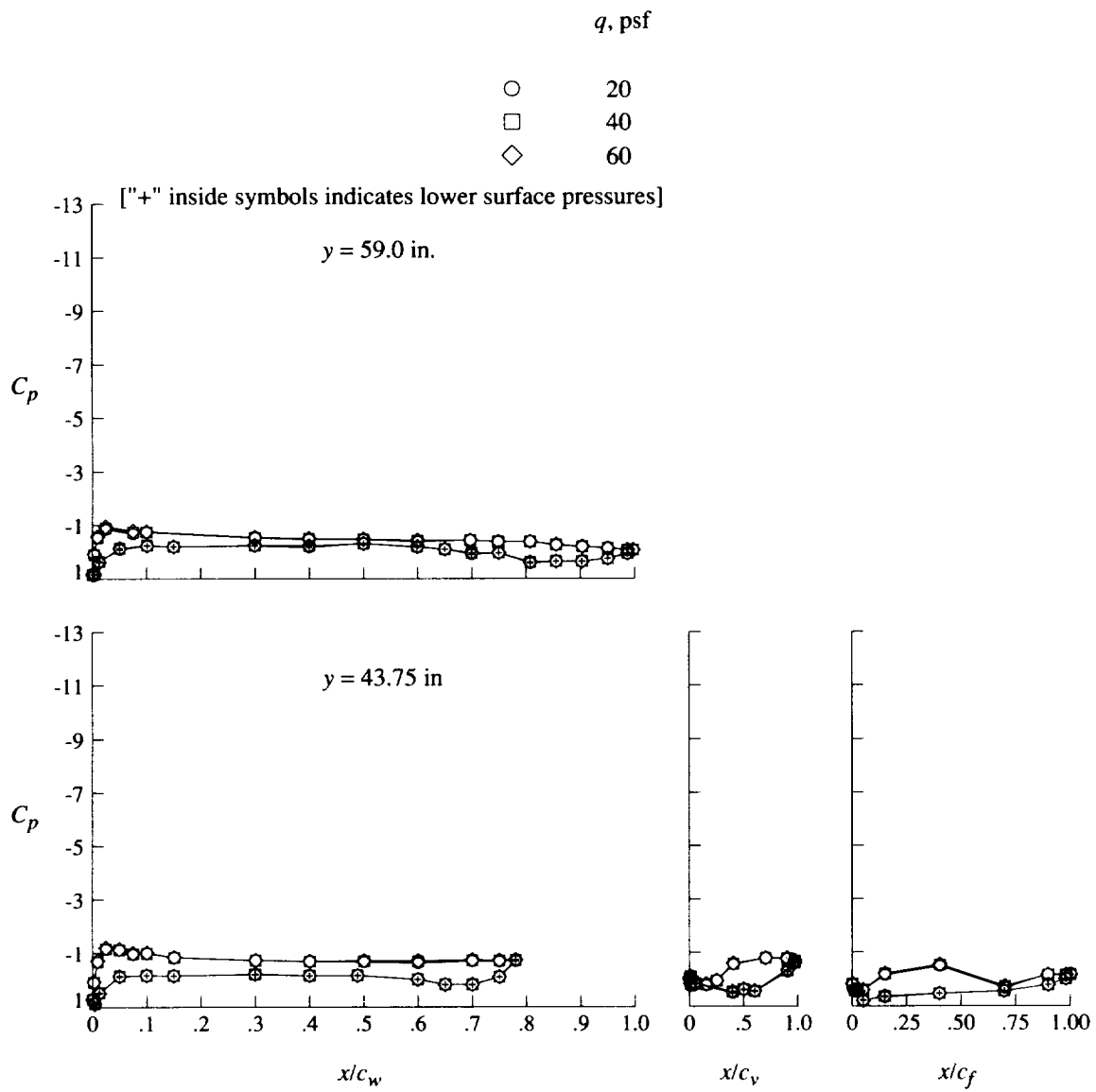
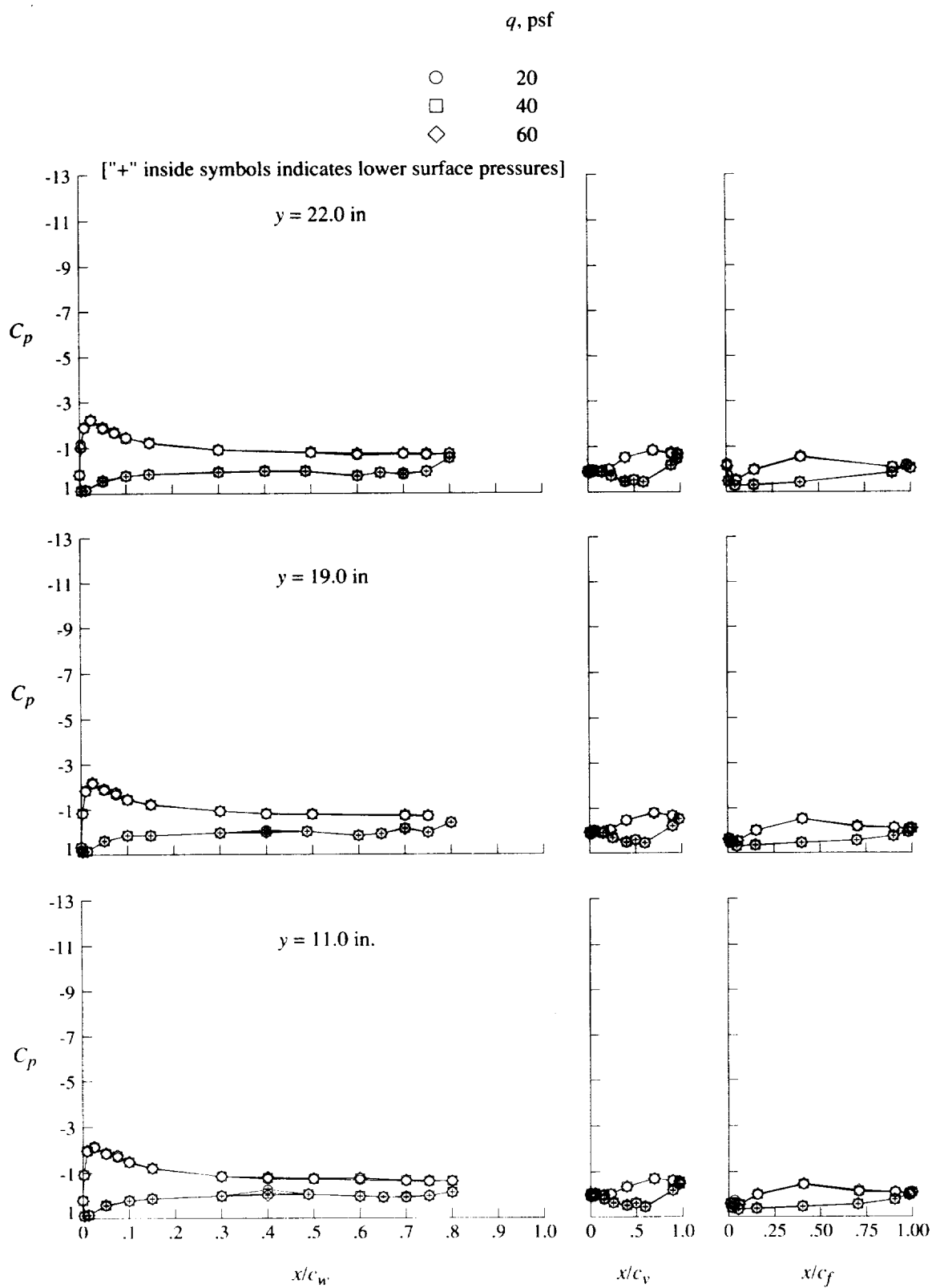


Figure 11. Effect of free-stream speed on pressure distributions for flaps-only configuration at $\delta_f = 20^\circ$.



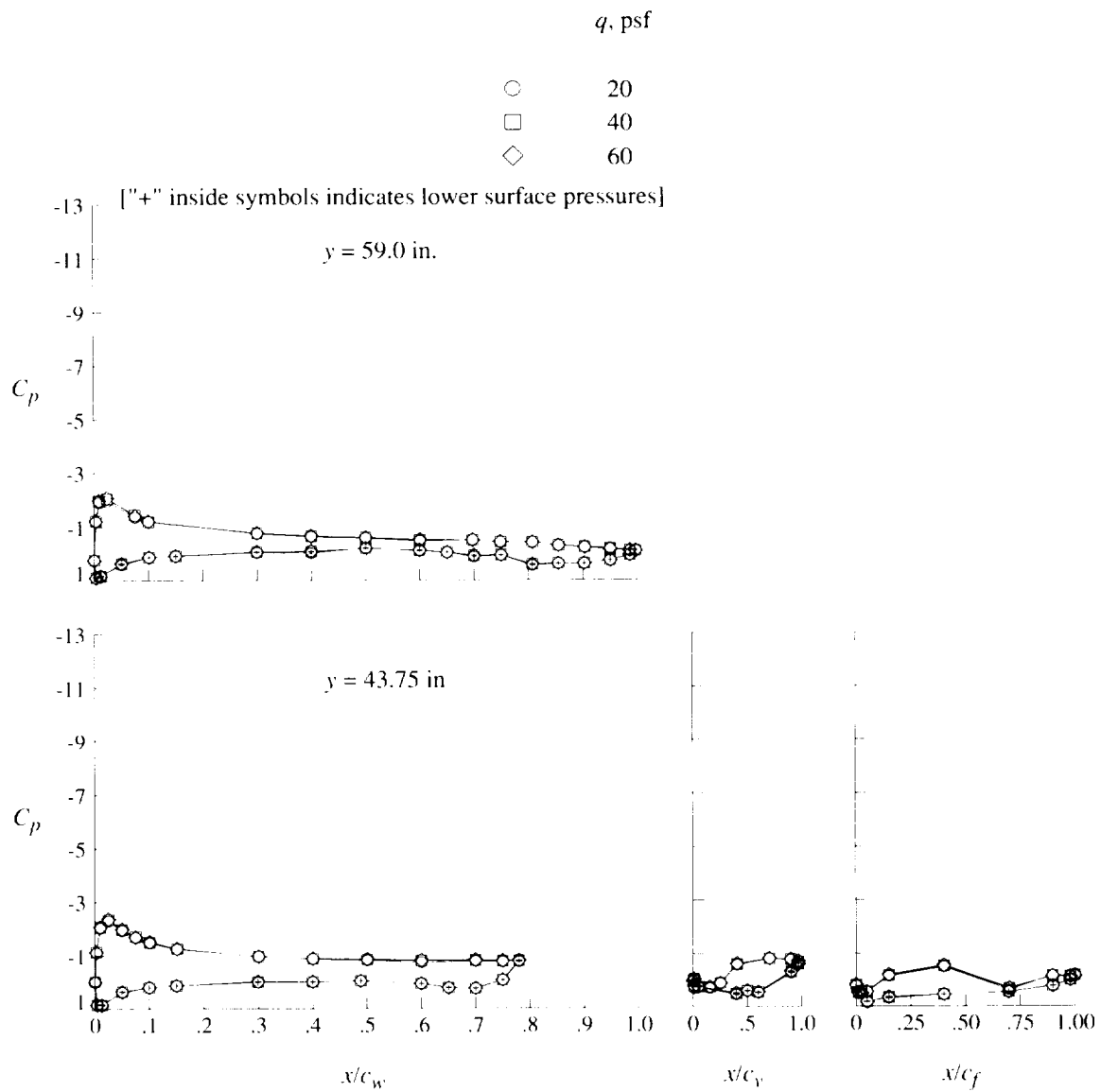
(a) Concluded.

Figure 11. Continued.



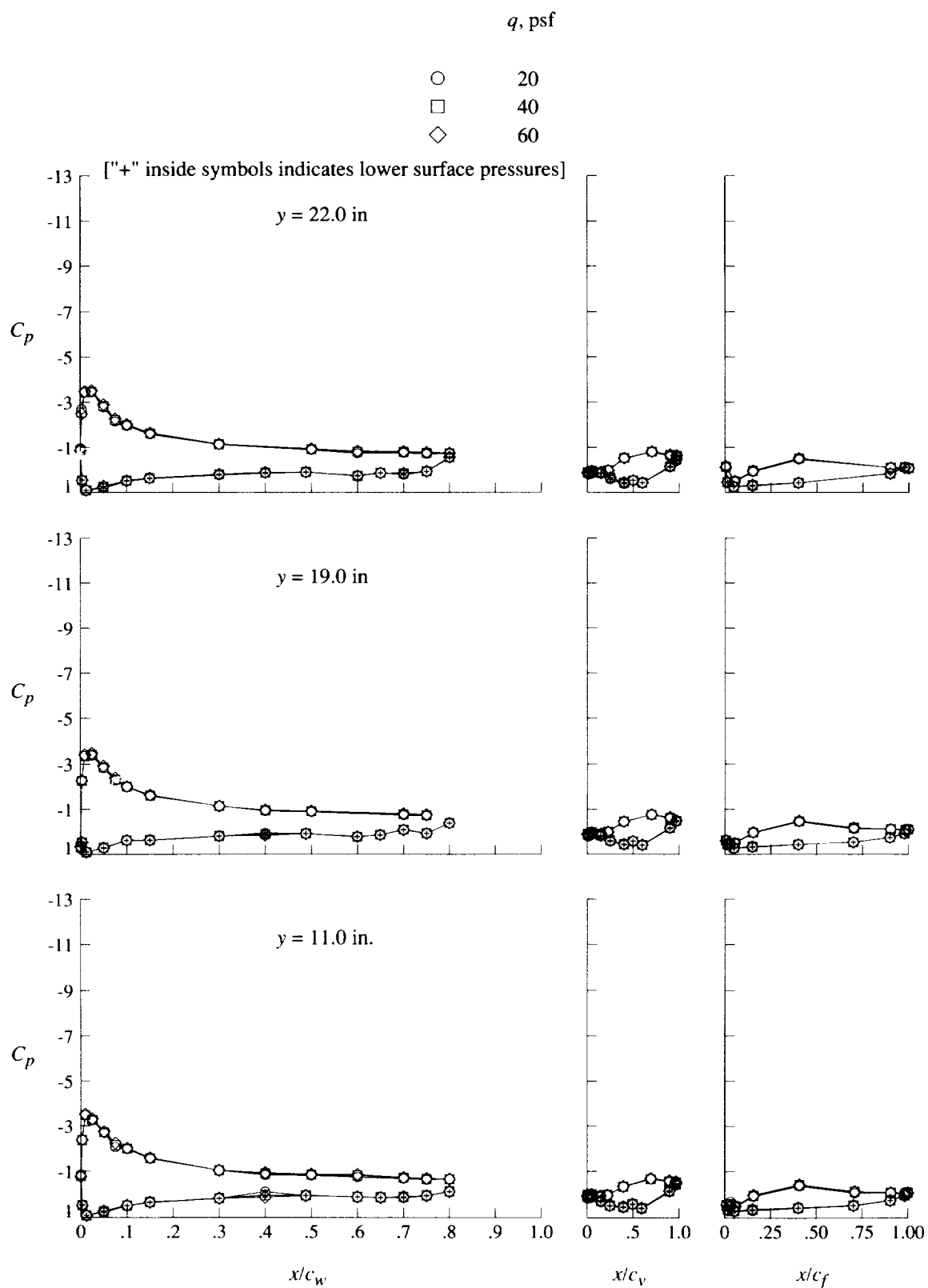
(b) $\alpha = 4^\circ$.

Figure 11. Continued.



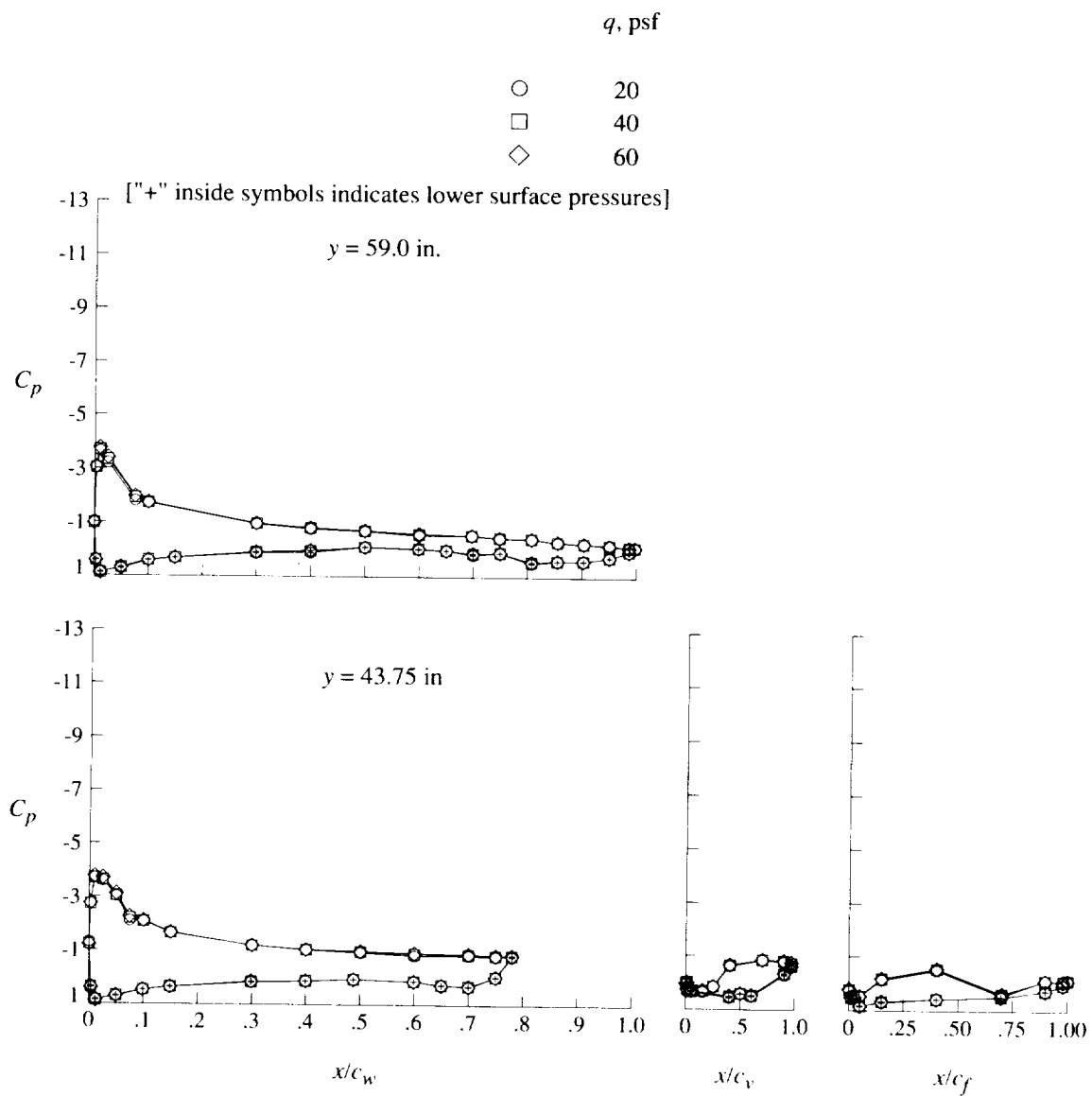
(b) Concluded.

Figure 11. Continued.



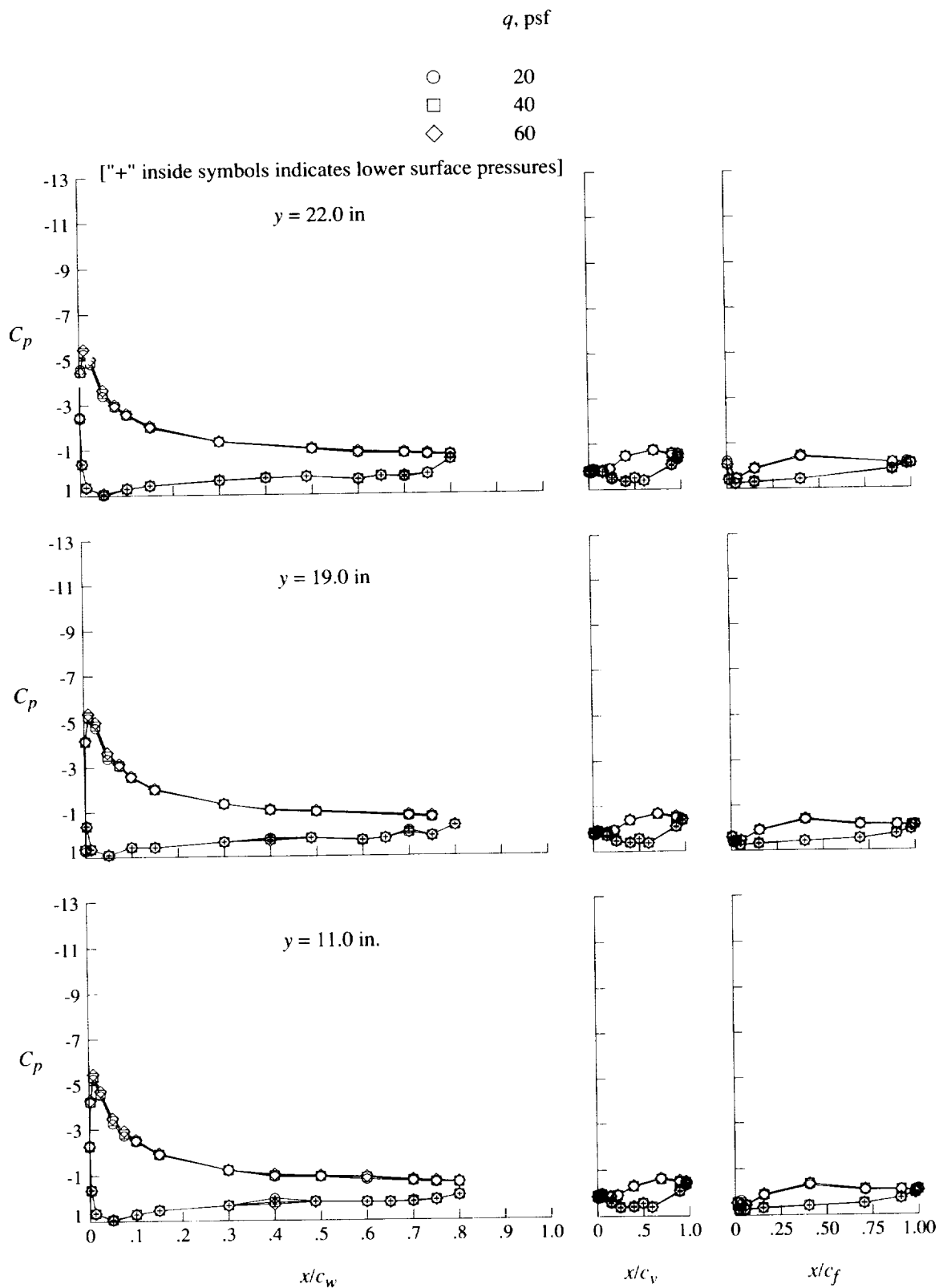
(c) $\alpha = 8^\circ$.

Figure 11. Continued.



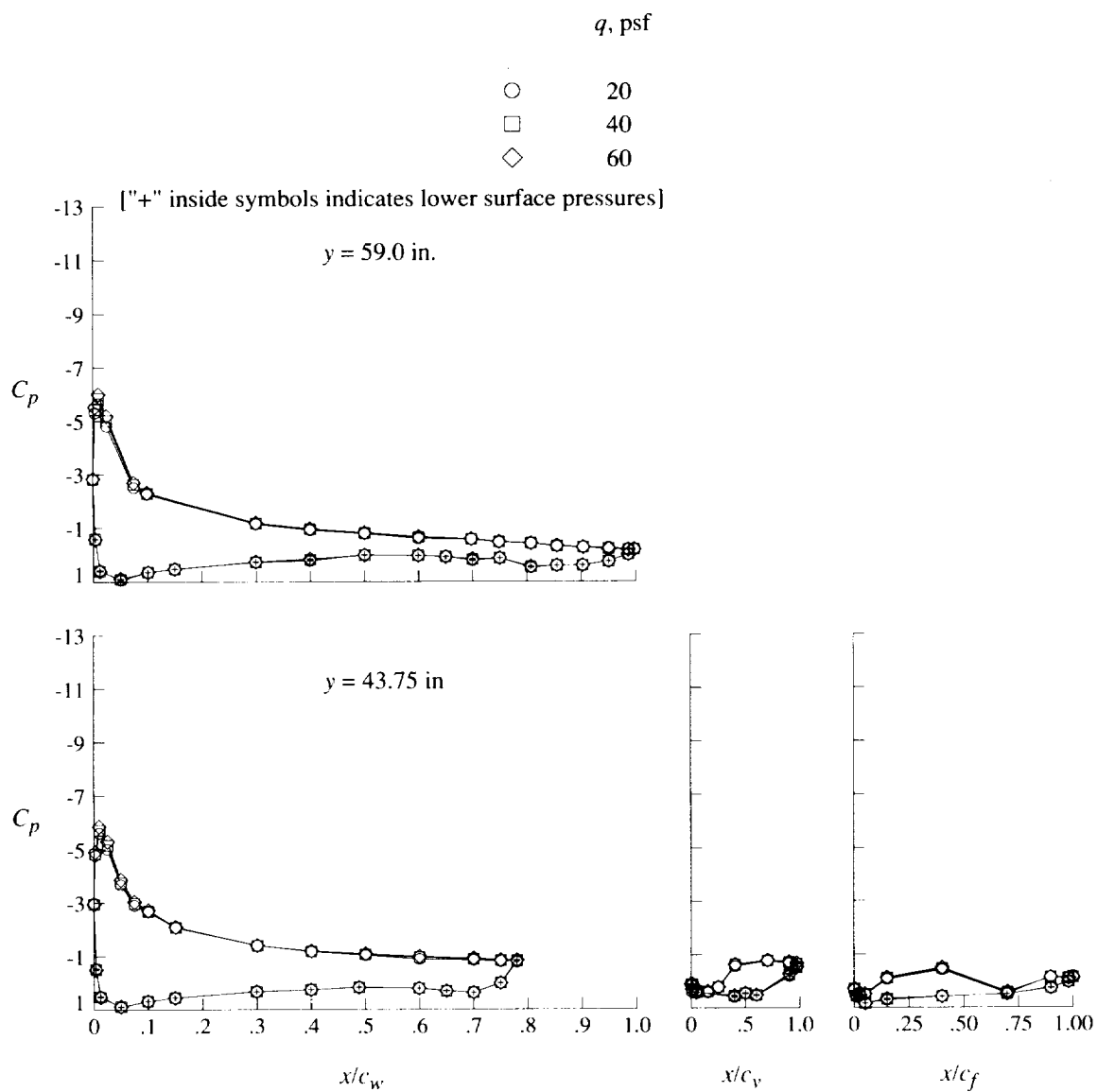
(c) Concluded.

Figure 11. Continued.



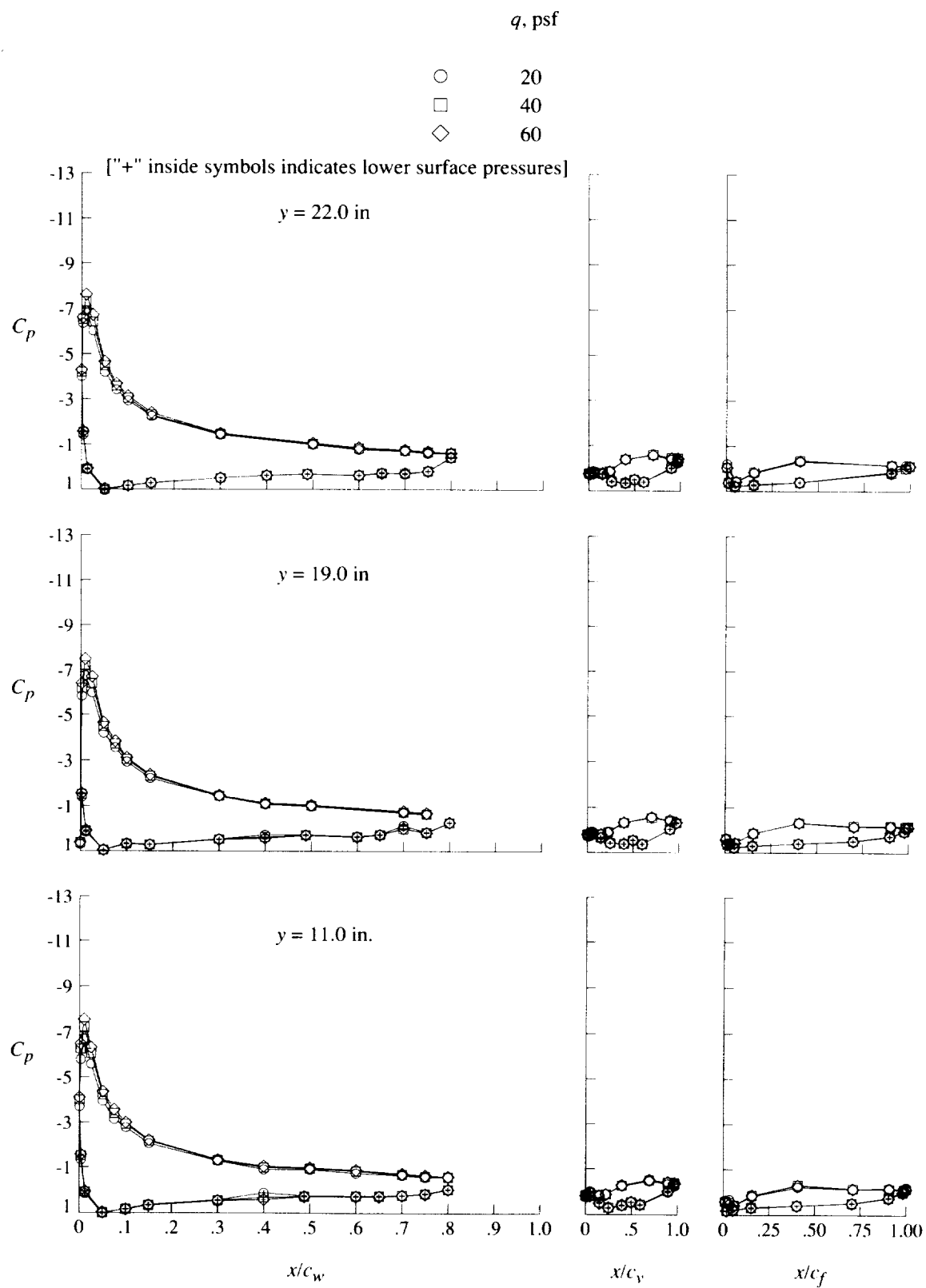
(d) $\alpha = 12^\circ$.

Figure 11. Continued.



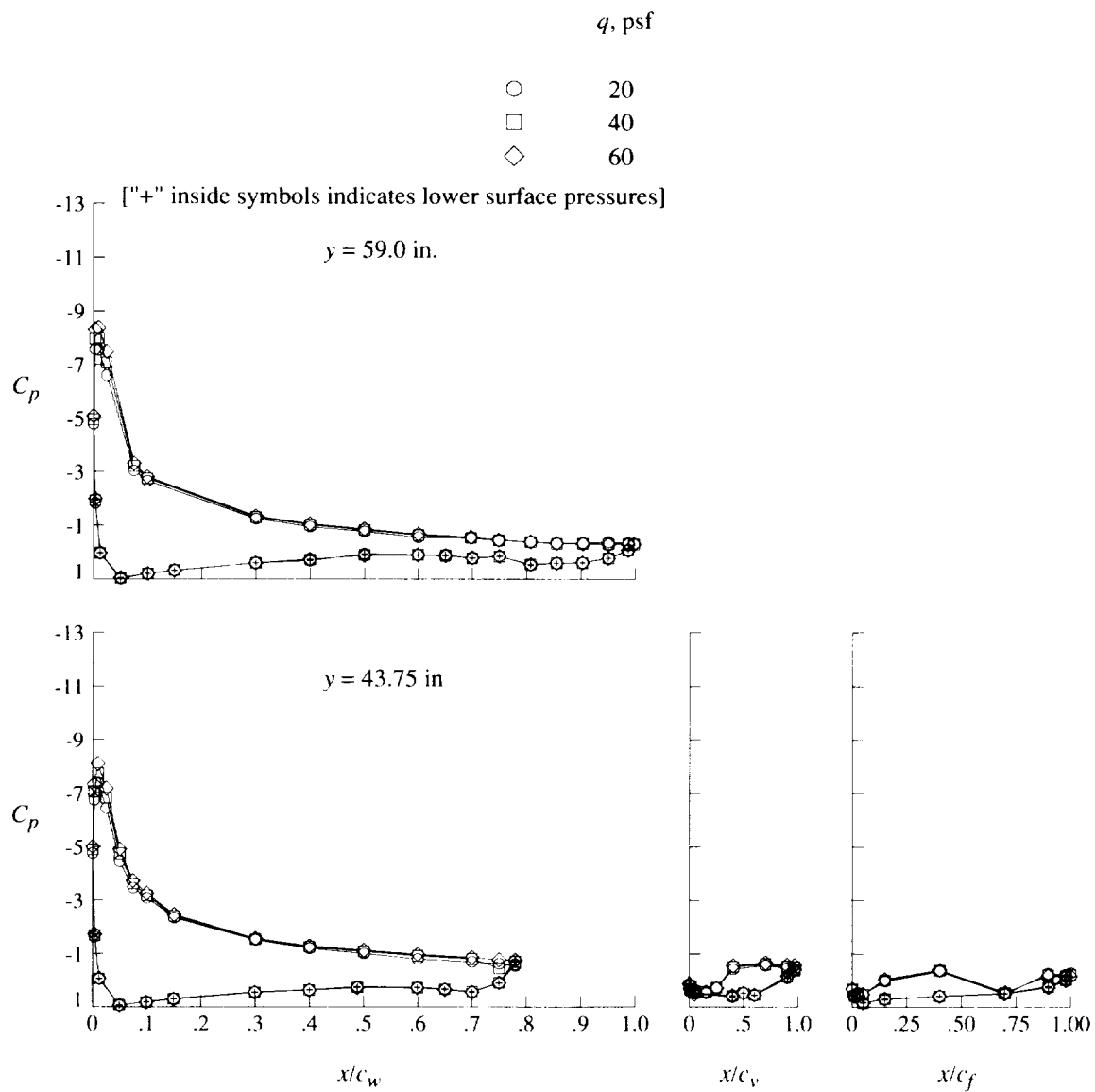
(d) Concluded.

Figure 11. Continued.



(e) $\alpha = 16^\circ$.

Figure 11. Continued.



(e) Concluded.

Figure 11. Concluded.

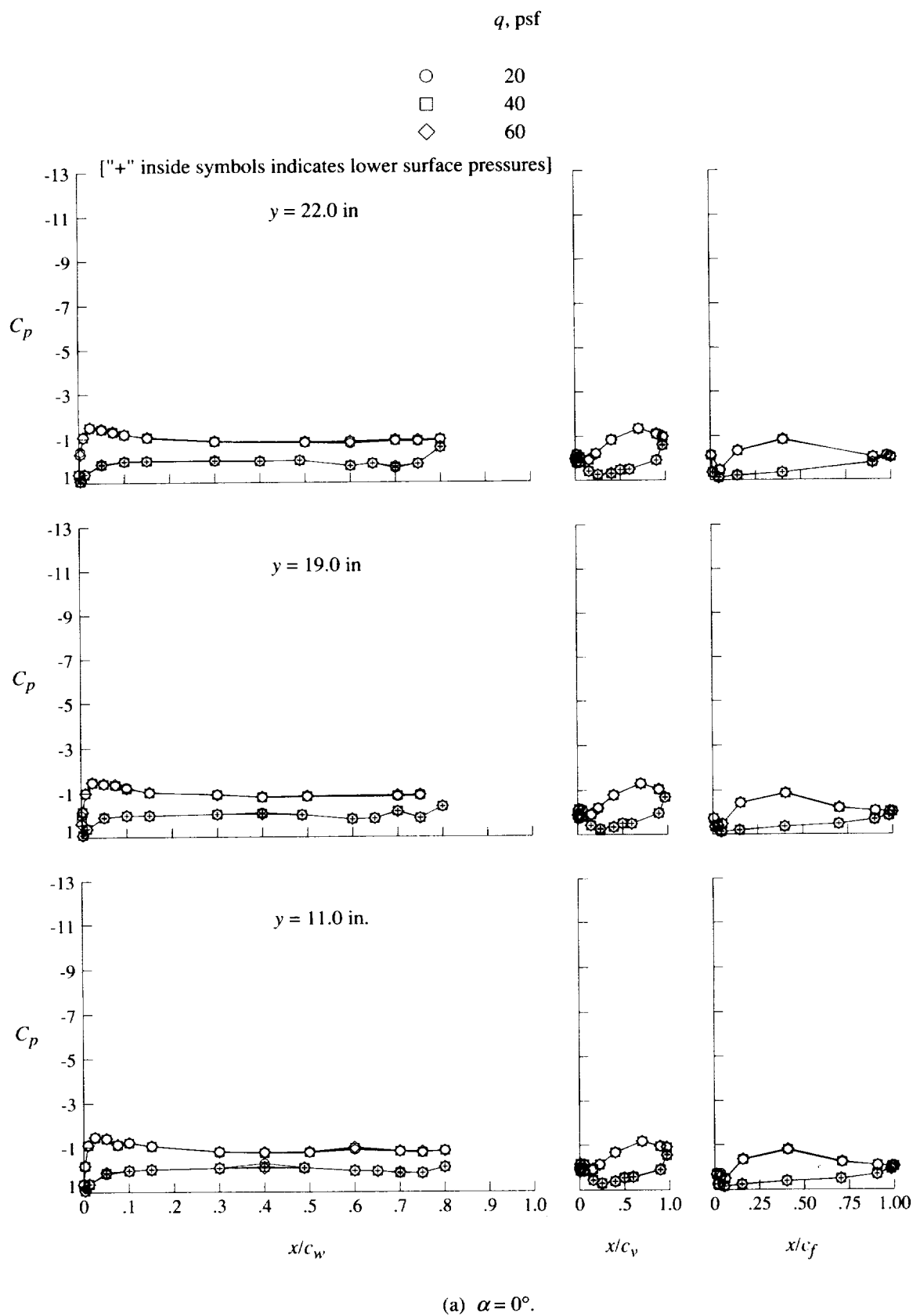
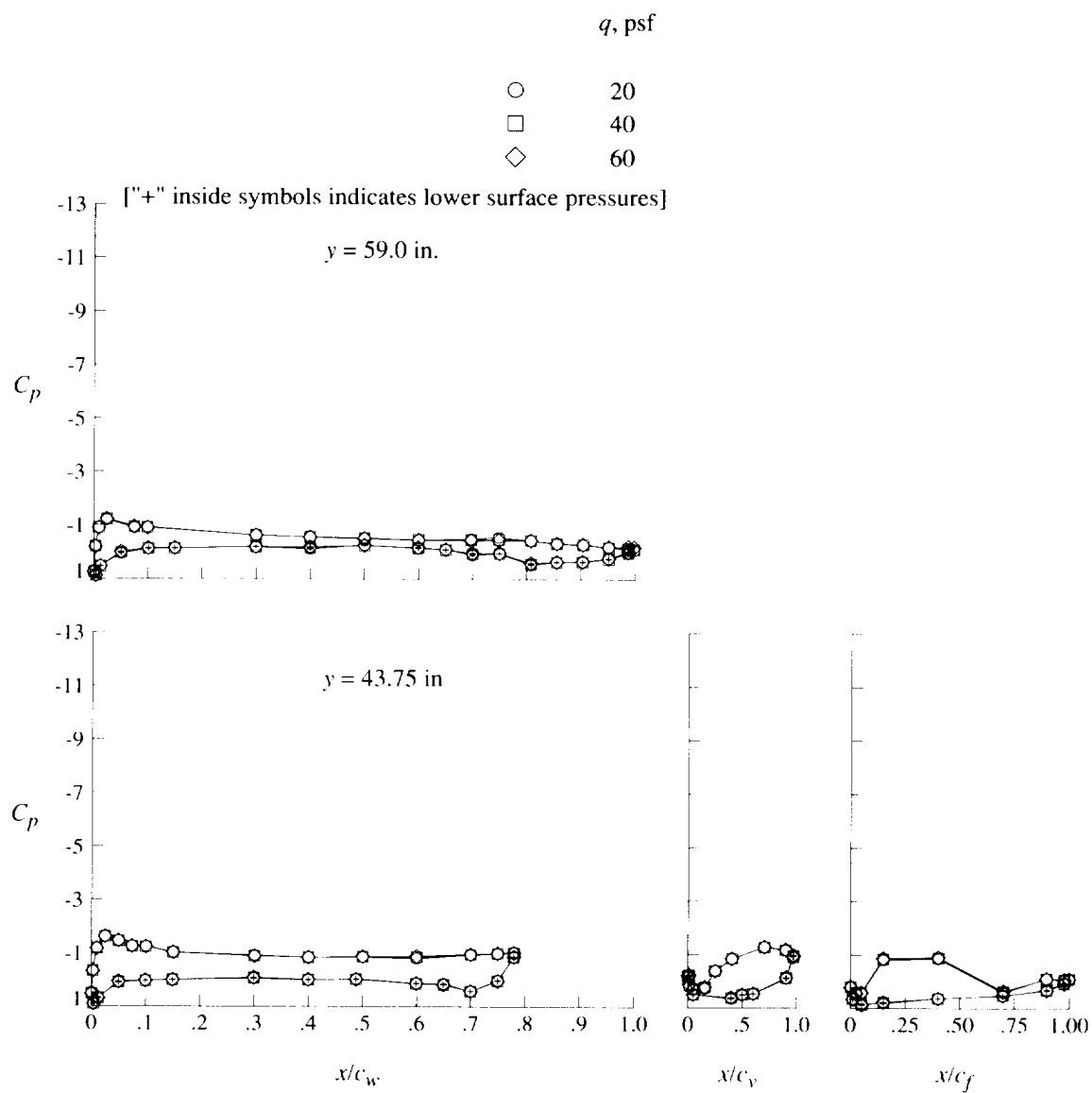
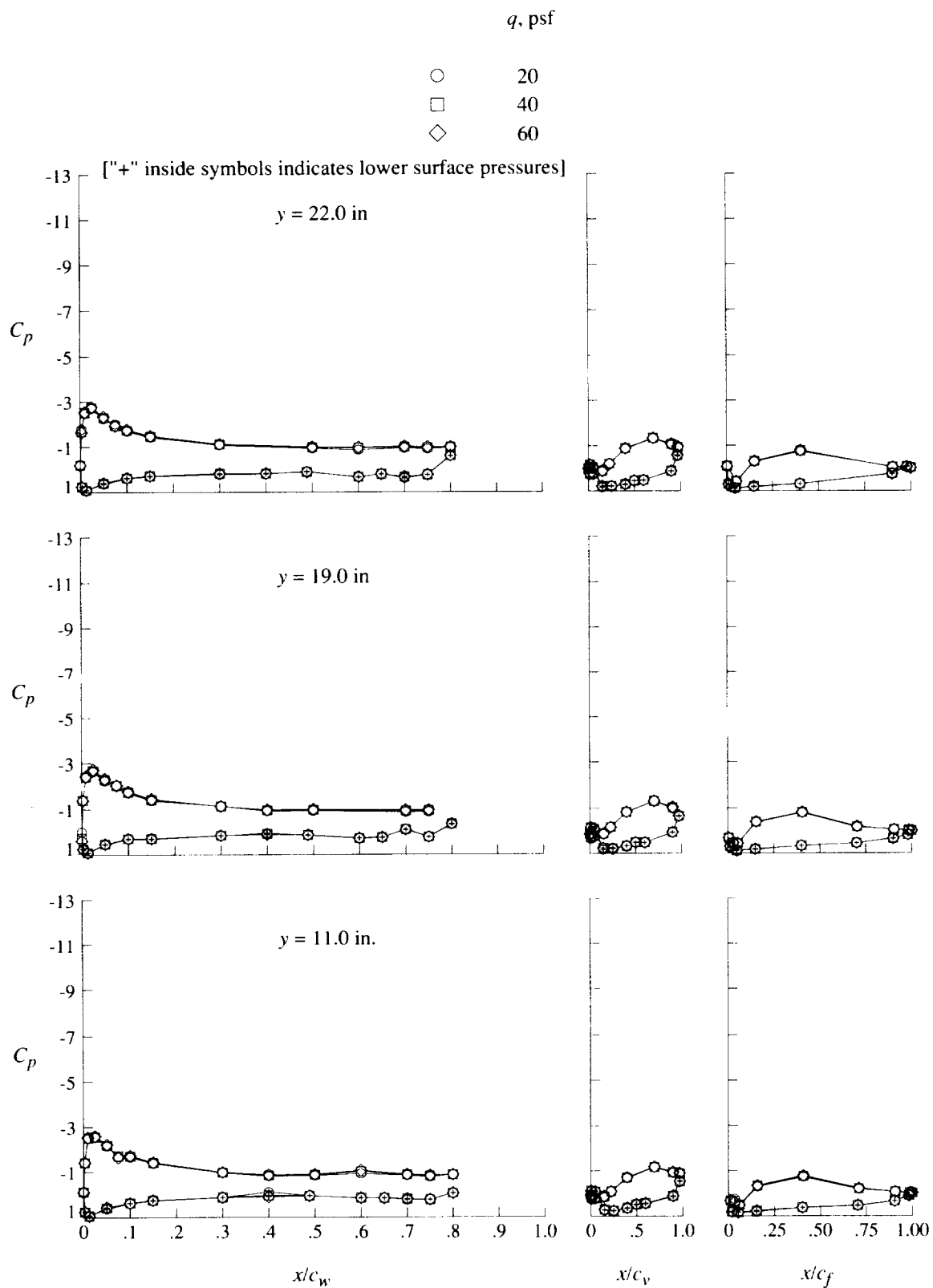


Figure 12. Effect of free-stream speed on pressure distributions for flaps-only configuration at $\delta_f = 30^\circ$.



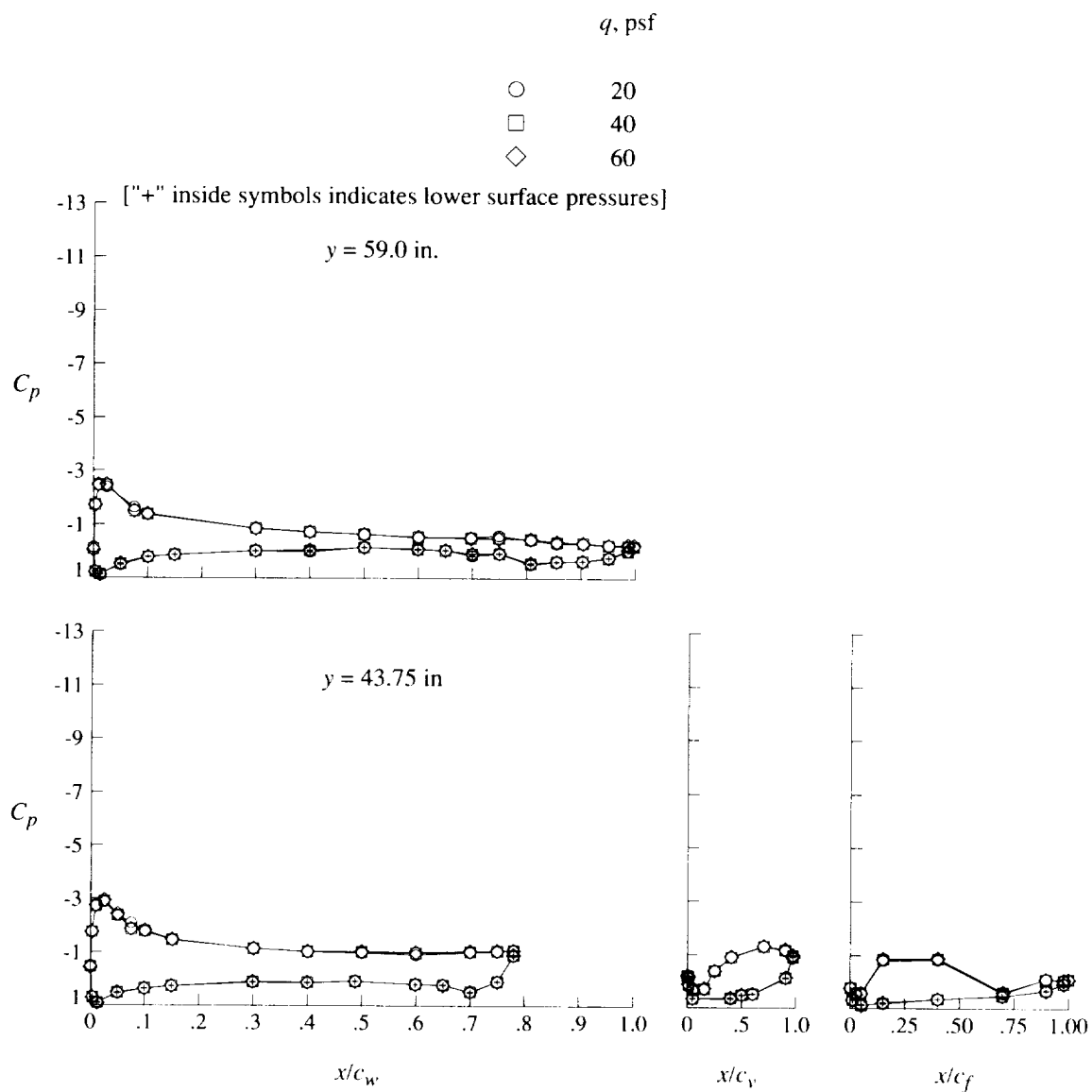
(a) Concluded.

Figure 12. Continued.



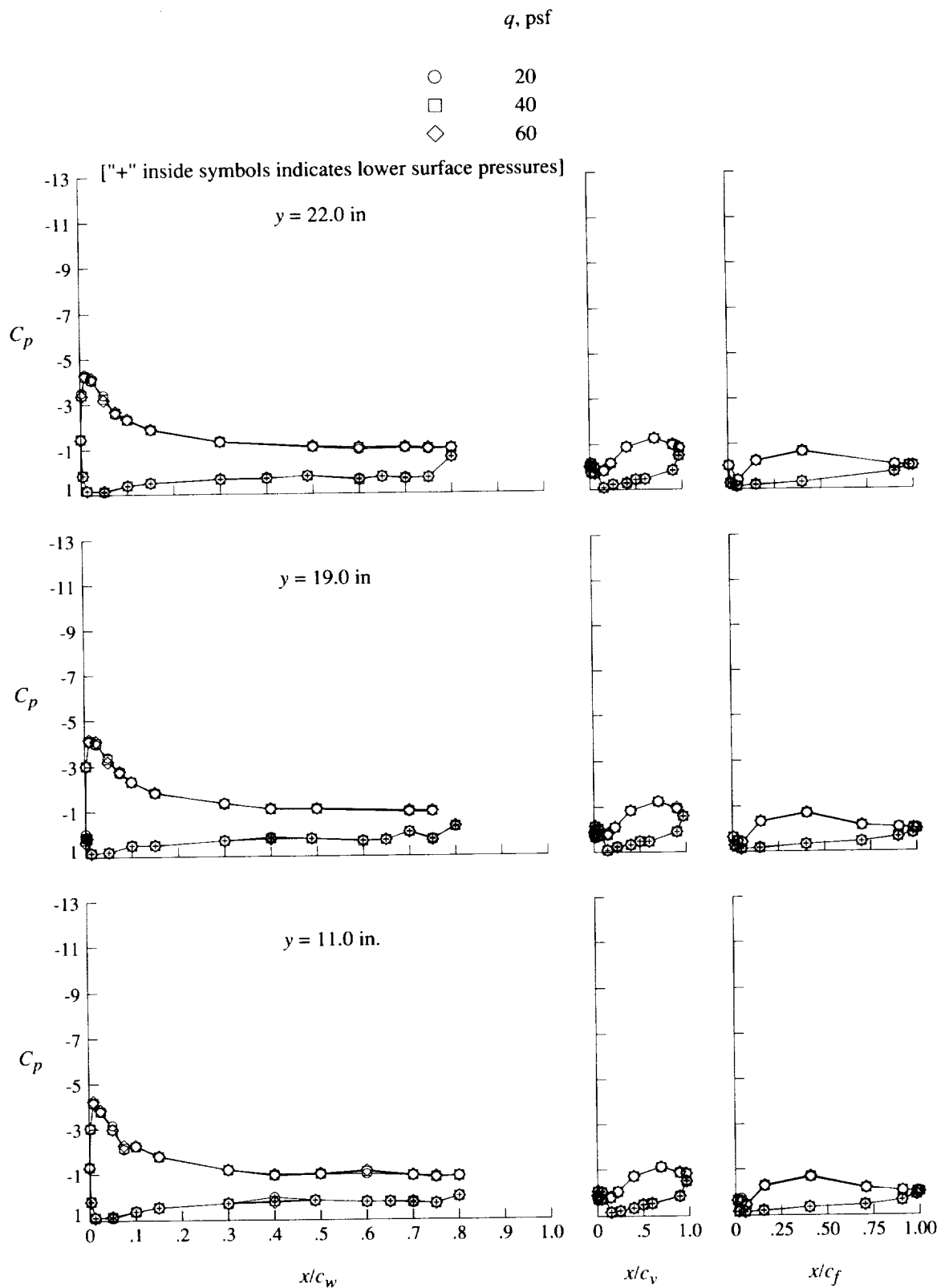
(b) $\alpha = 4^\circ$.

Figure 12. Continued.



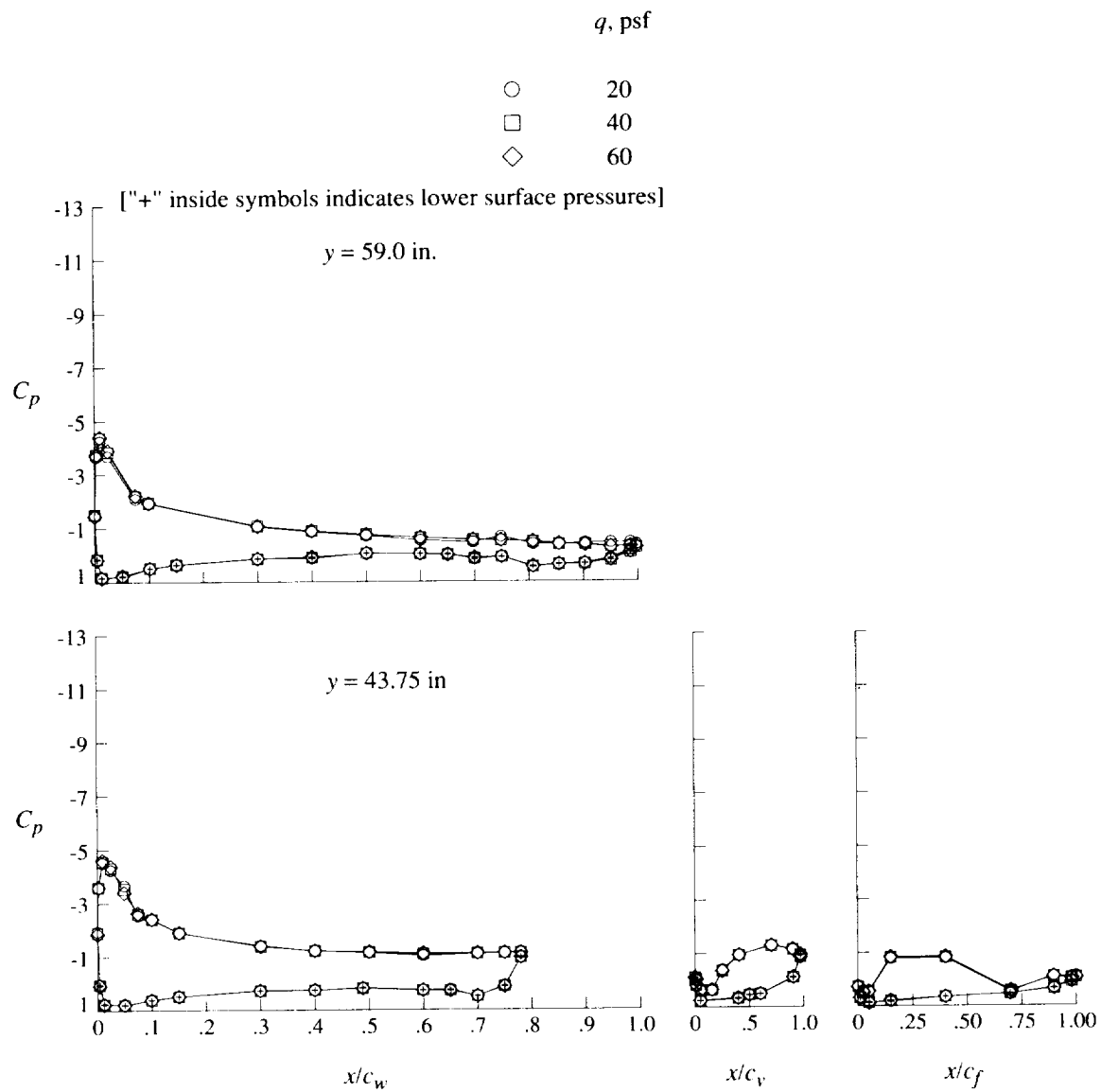
(b) Concluded.

Figure 12. Continued.



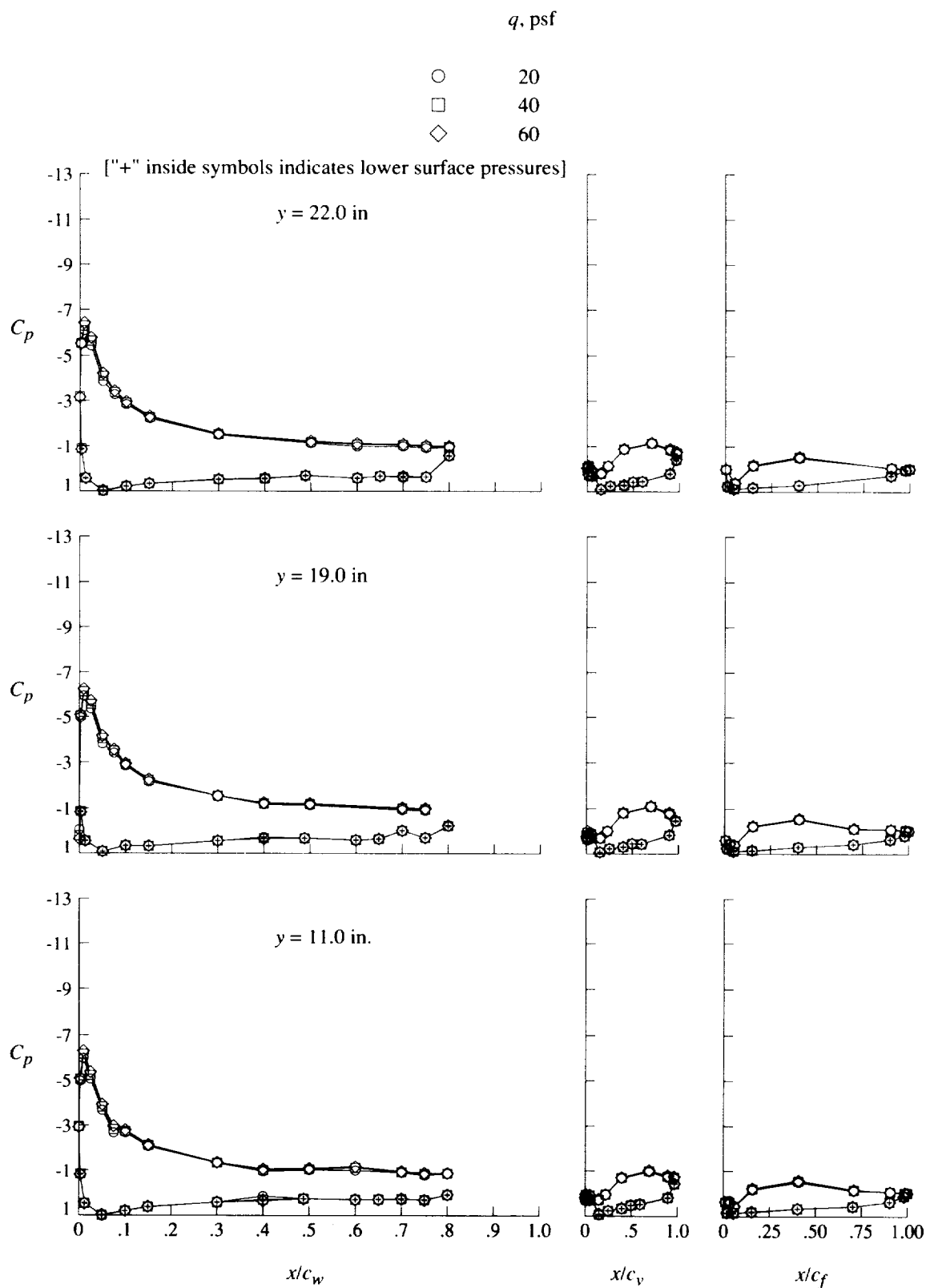
(c) $\alpha = 8^\circ$.

Figure 12. Continued.



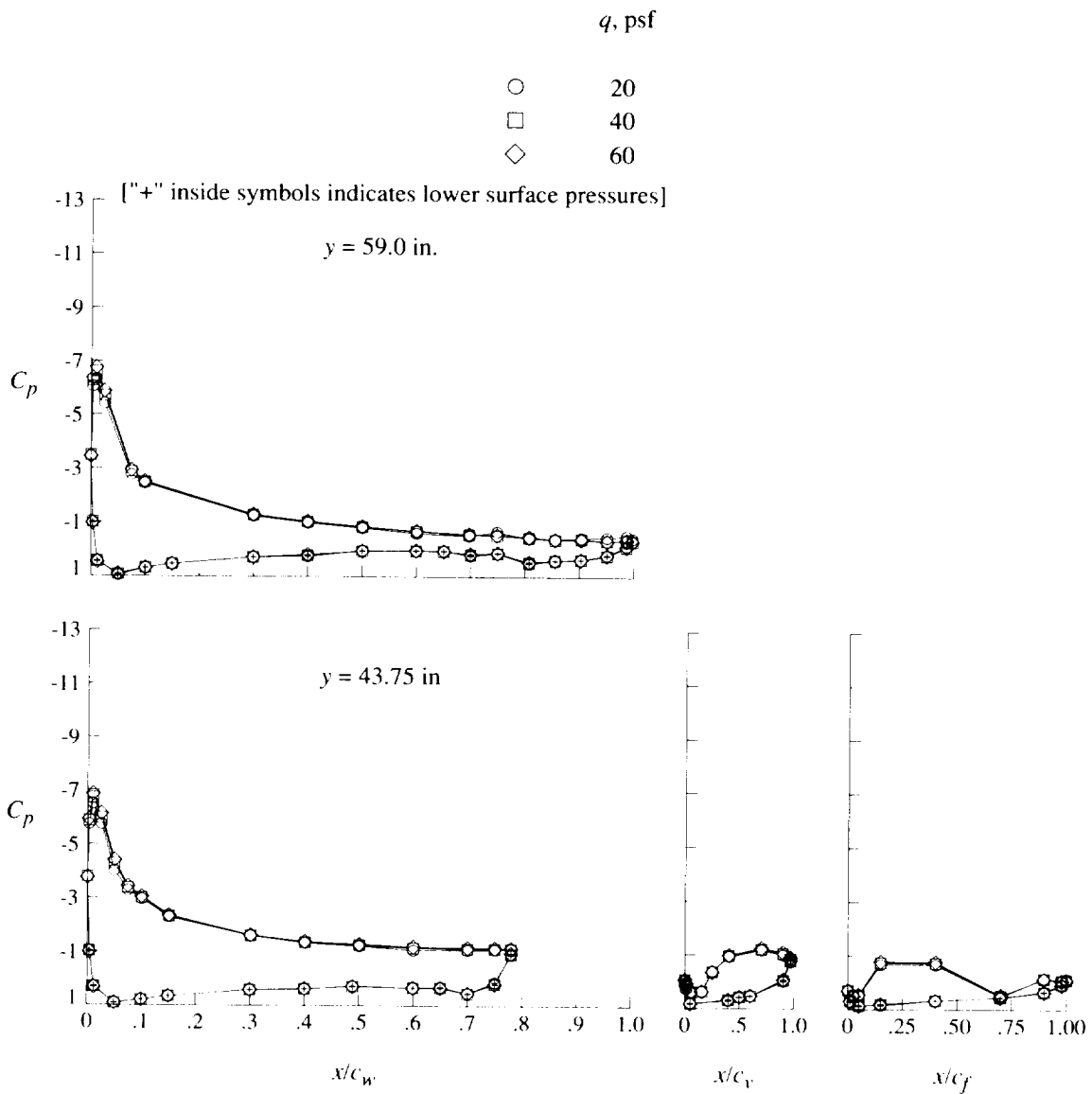
(c) Concluded.

Figure 12. Continued.



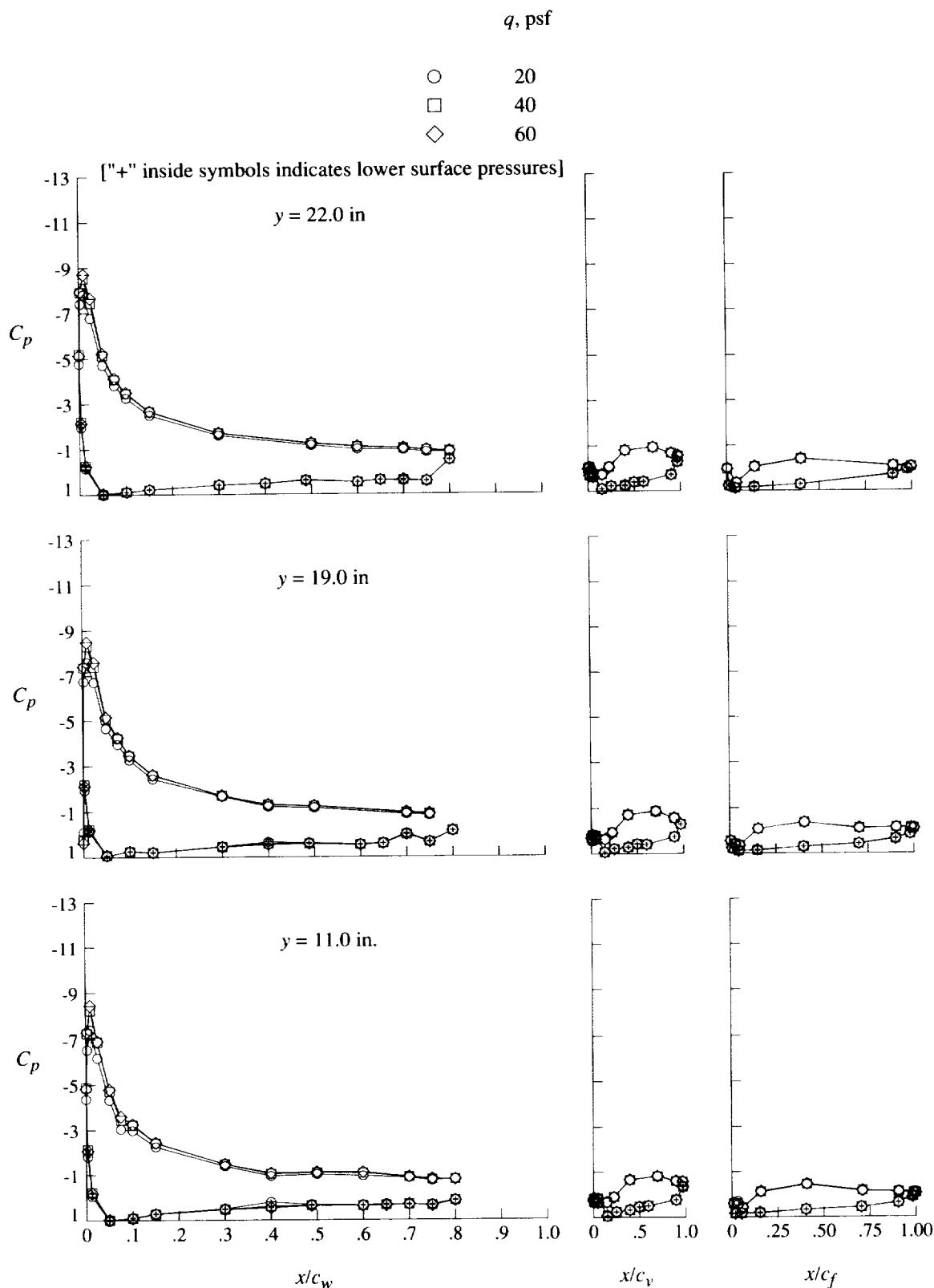
(d) $\alpha = 12^\circ$.

Figure 12. Continued.



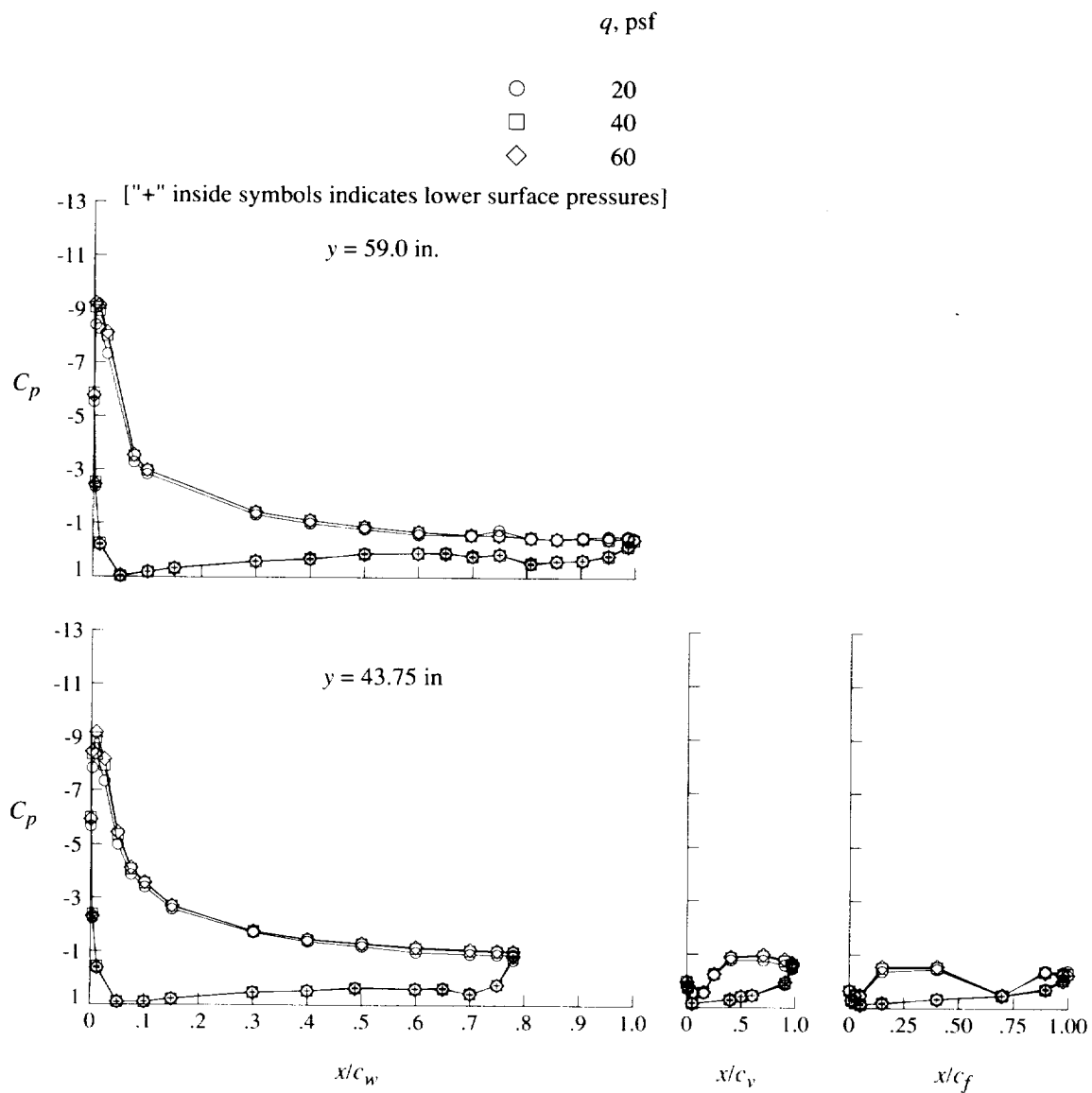
(d) Concluded.

Figure 12. Continued.



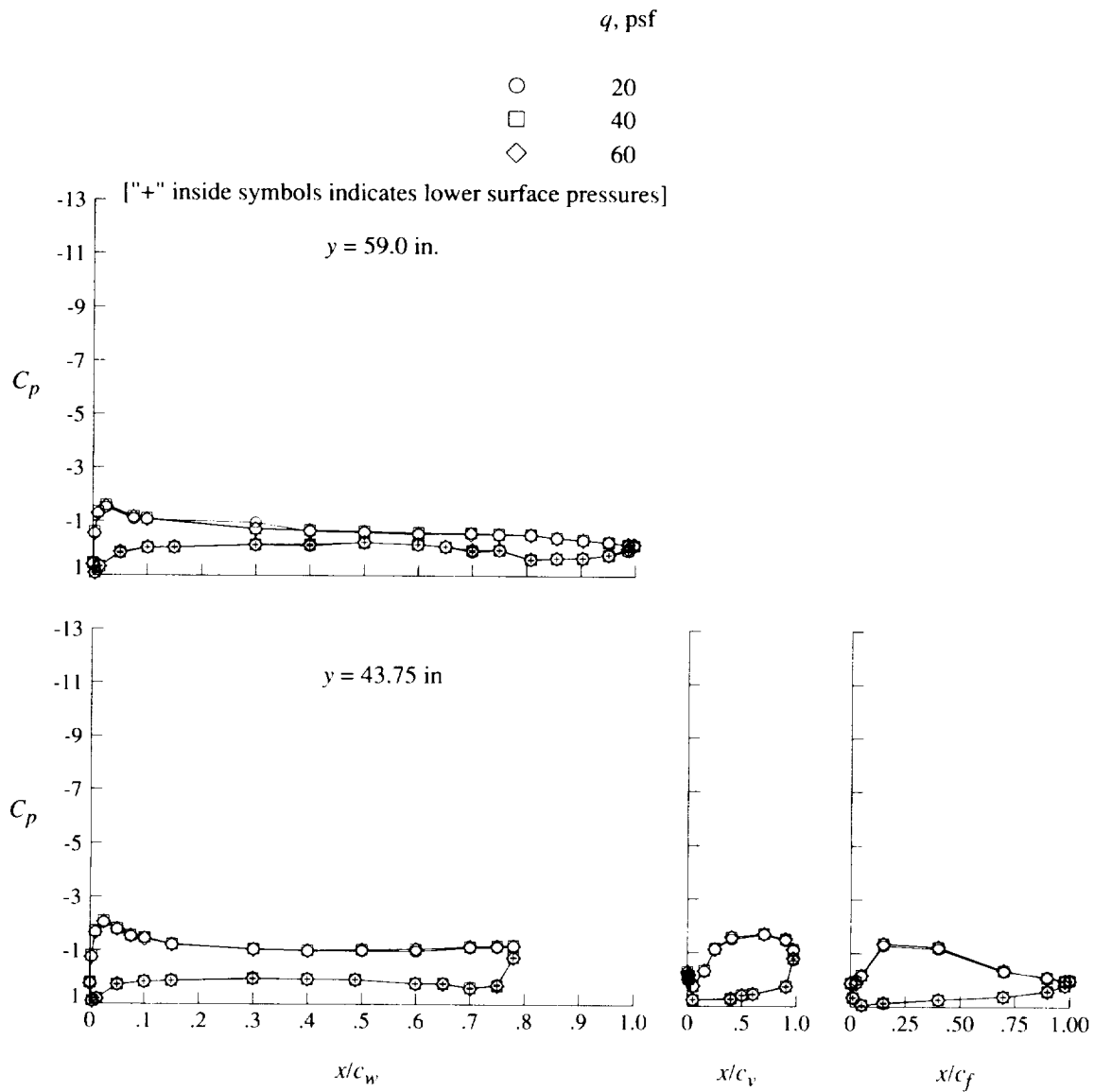
(e) $\alpha = 16^\circ$.

Figure 12. Continued.



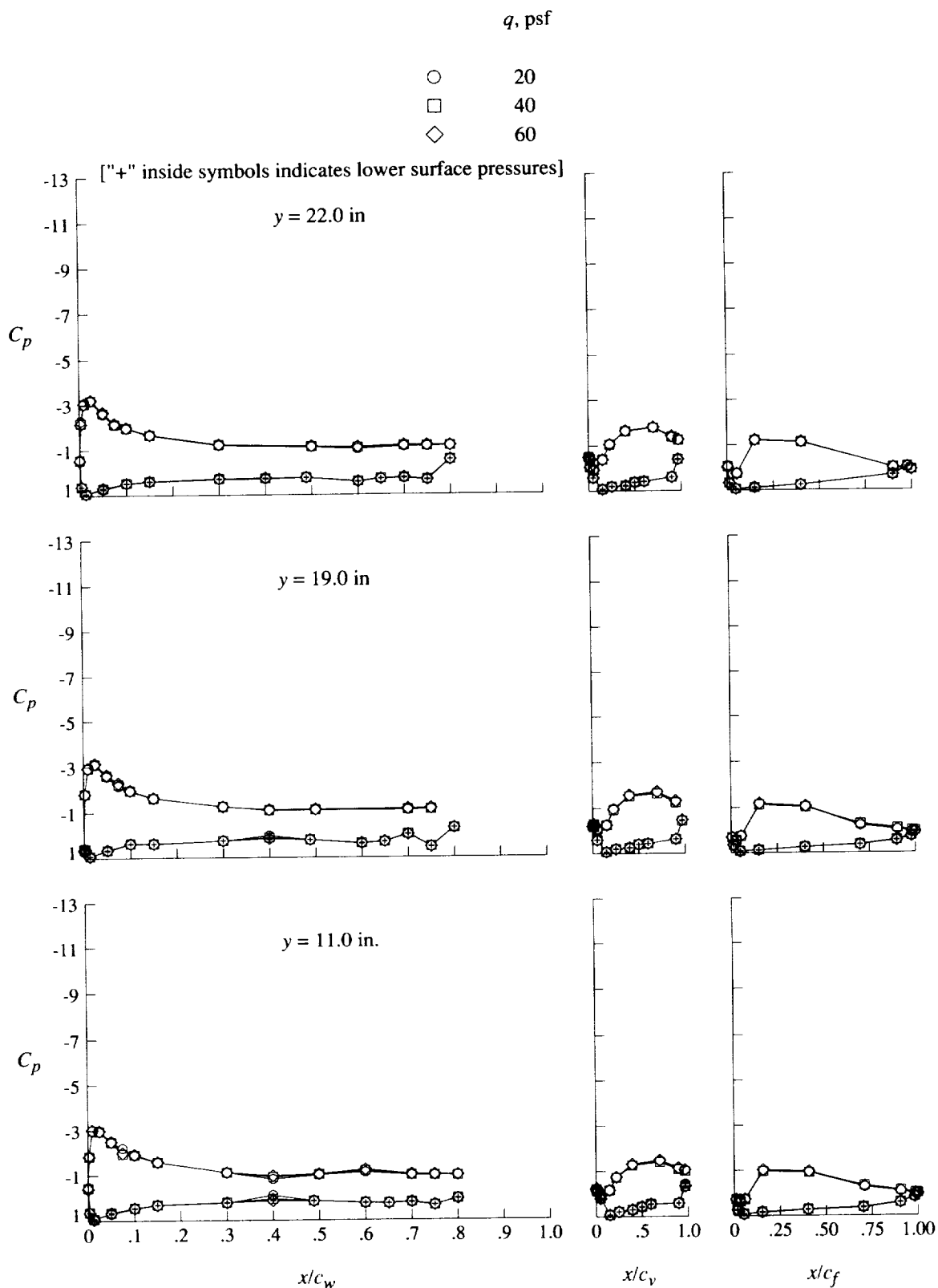
(e) Concluded.

Figure 12. Concluded.



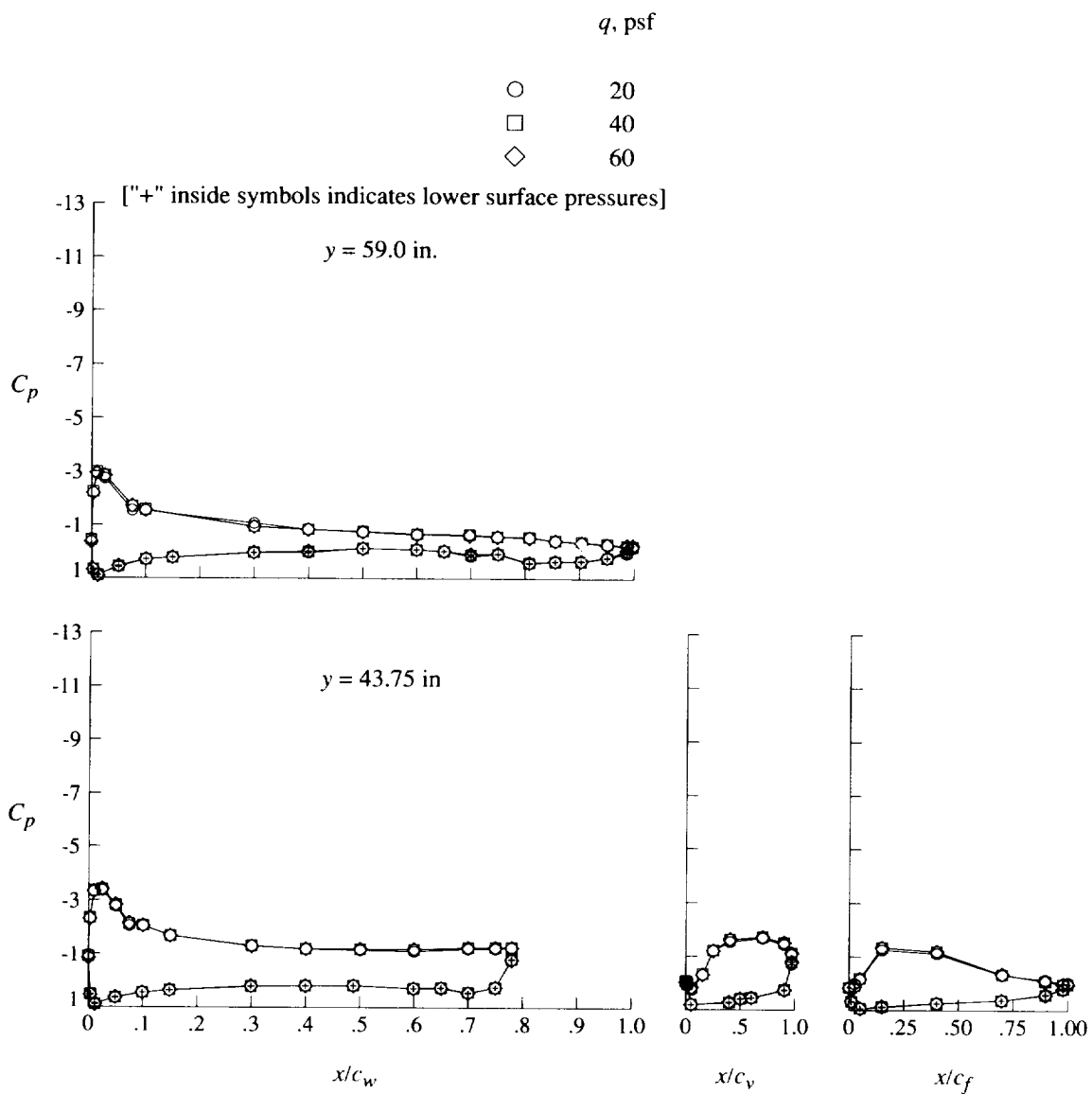
(a) Concluded.

Figure 13. Continued.



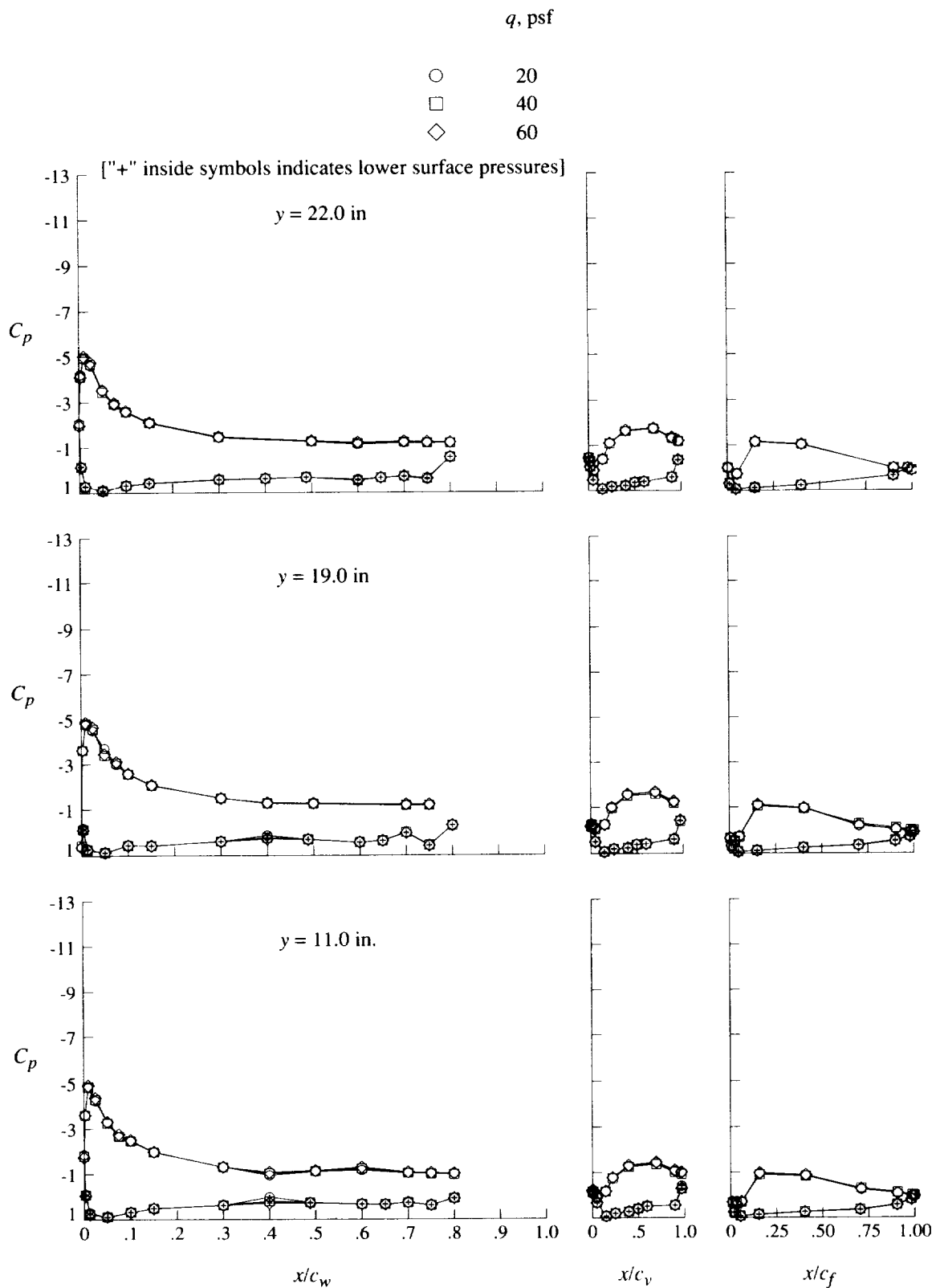
(b) $\alpha = 4^\circ$.

Figure 13. Continued.



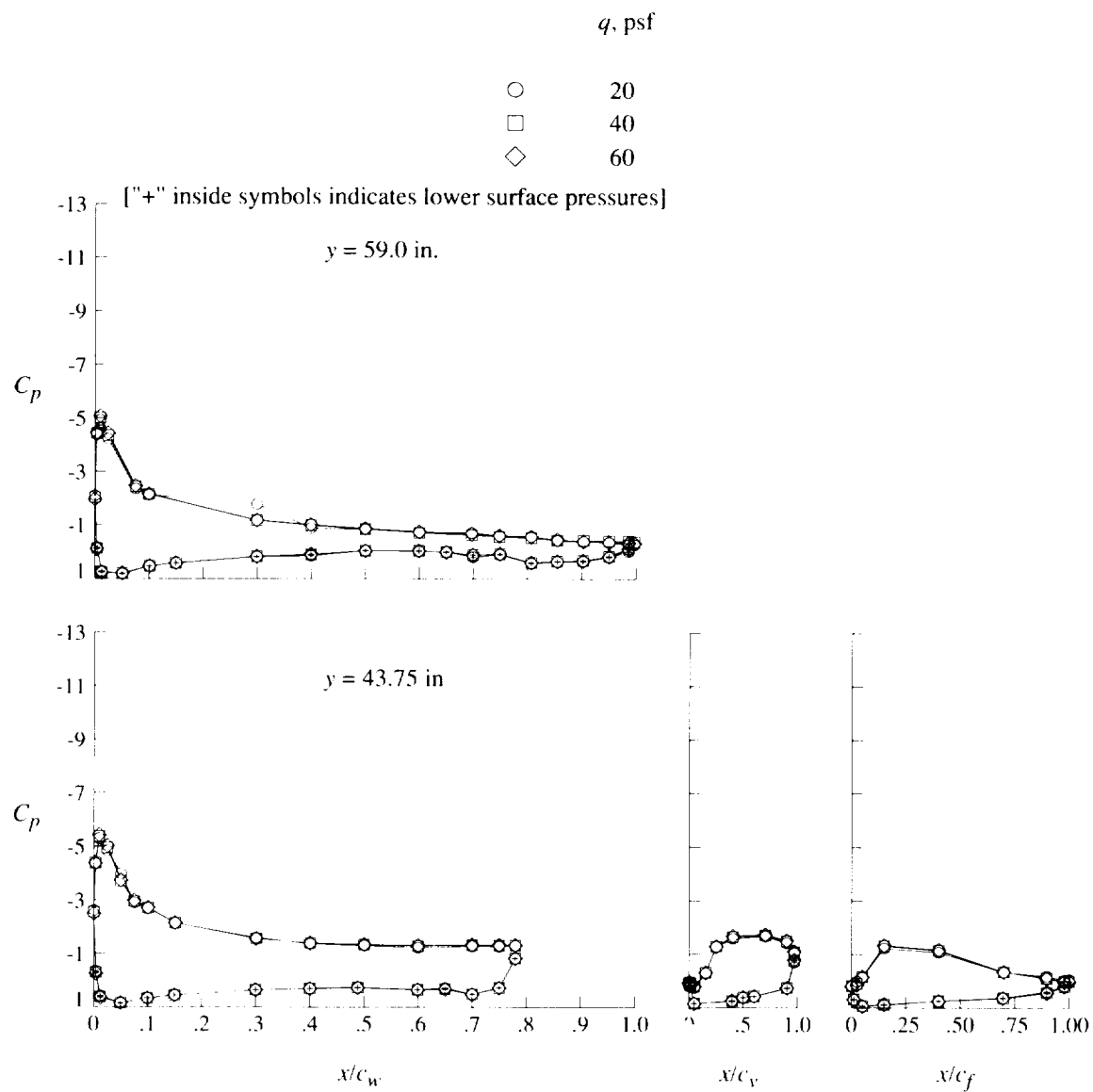
(b) Concluded.

Figure 13. Continued.



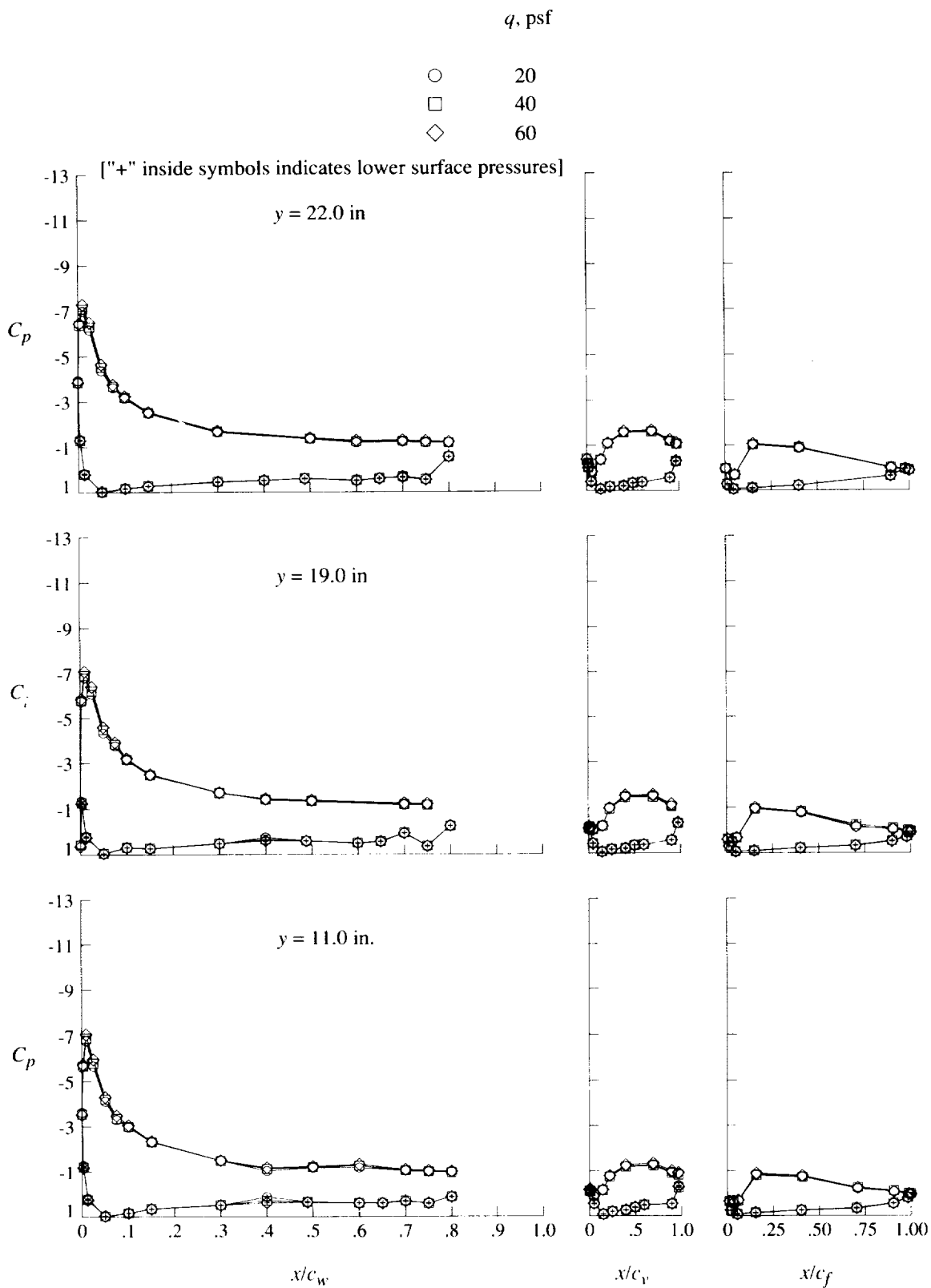
(c) $\alpha = 8^\circ$.

Figure 13. Continued.



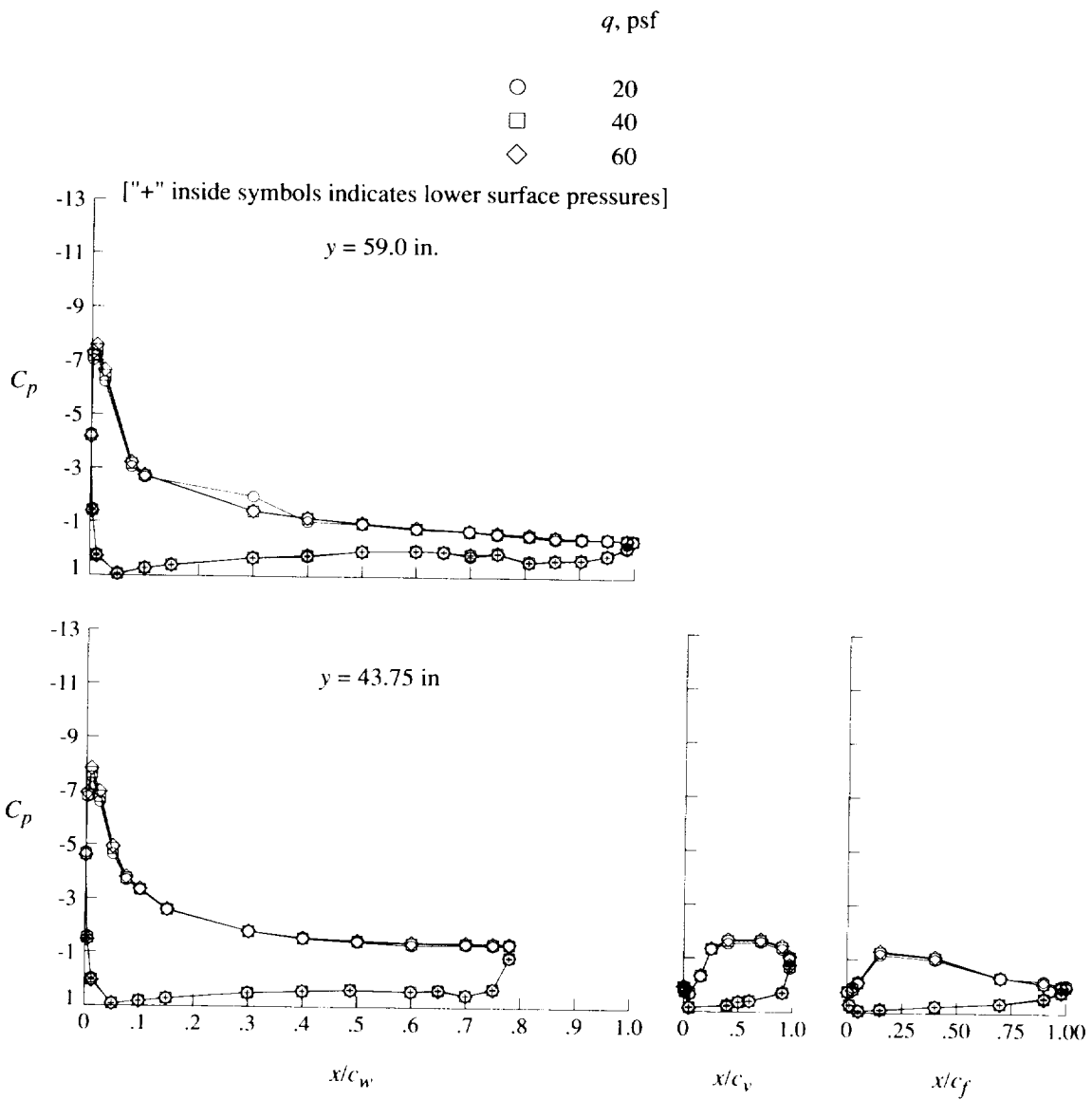
(c) Concluded.

Figure 13. Continued.



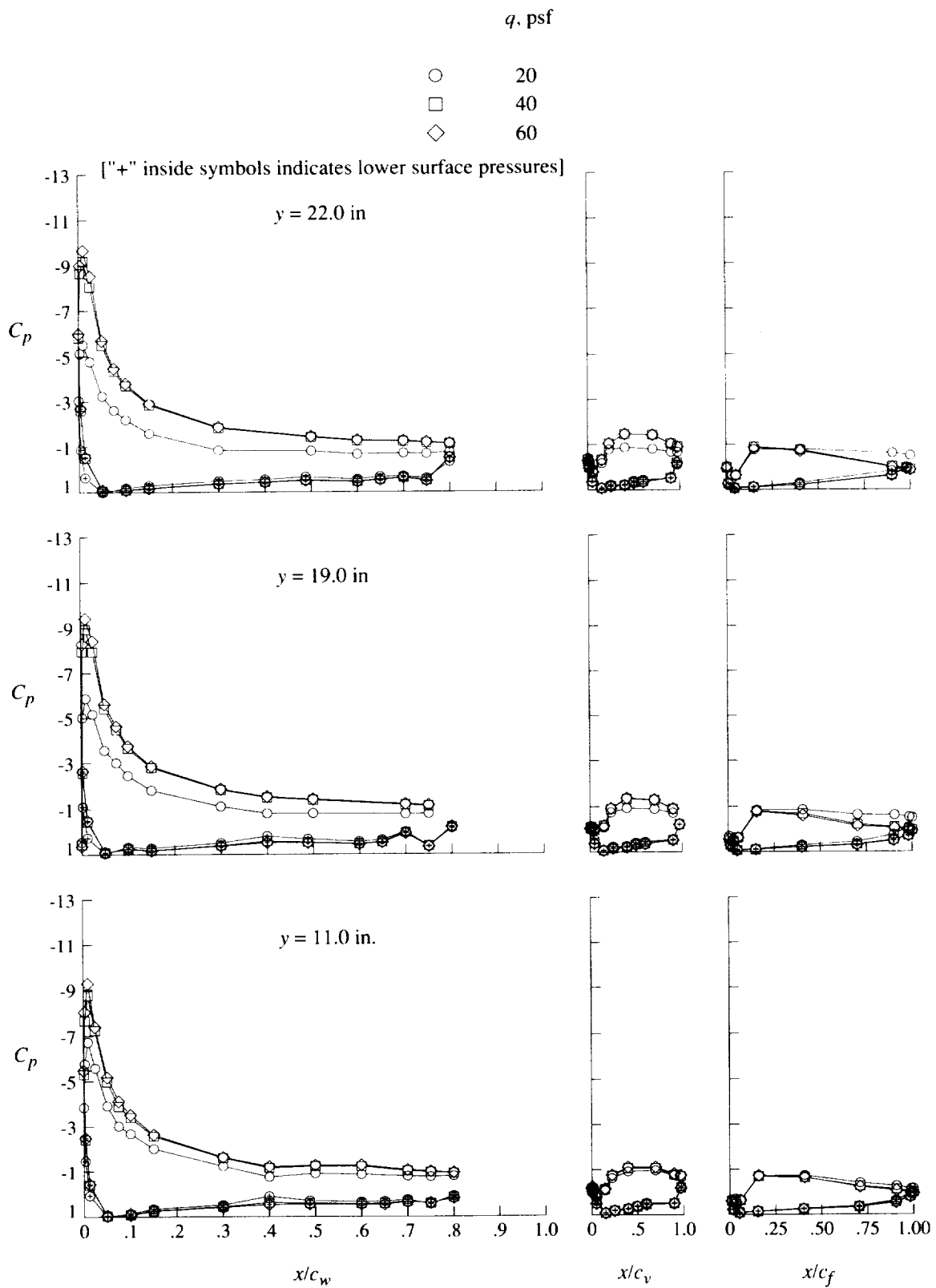
(d) $\alpha = 12^\circ$.

Figure 13. Continued.



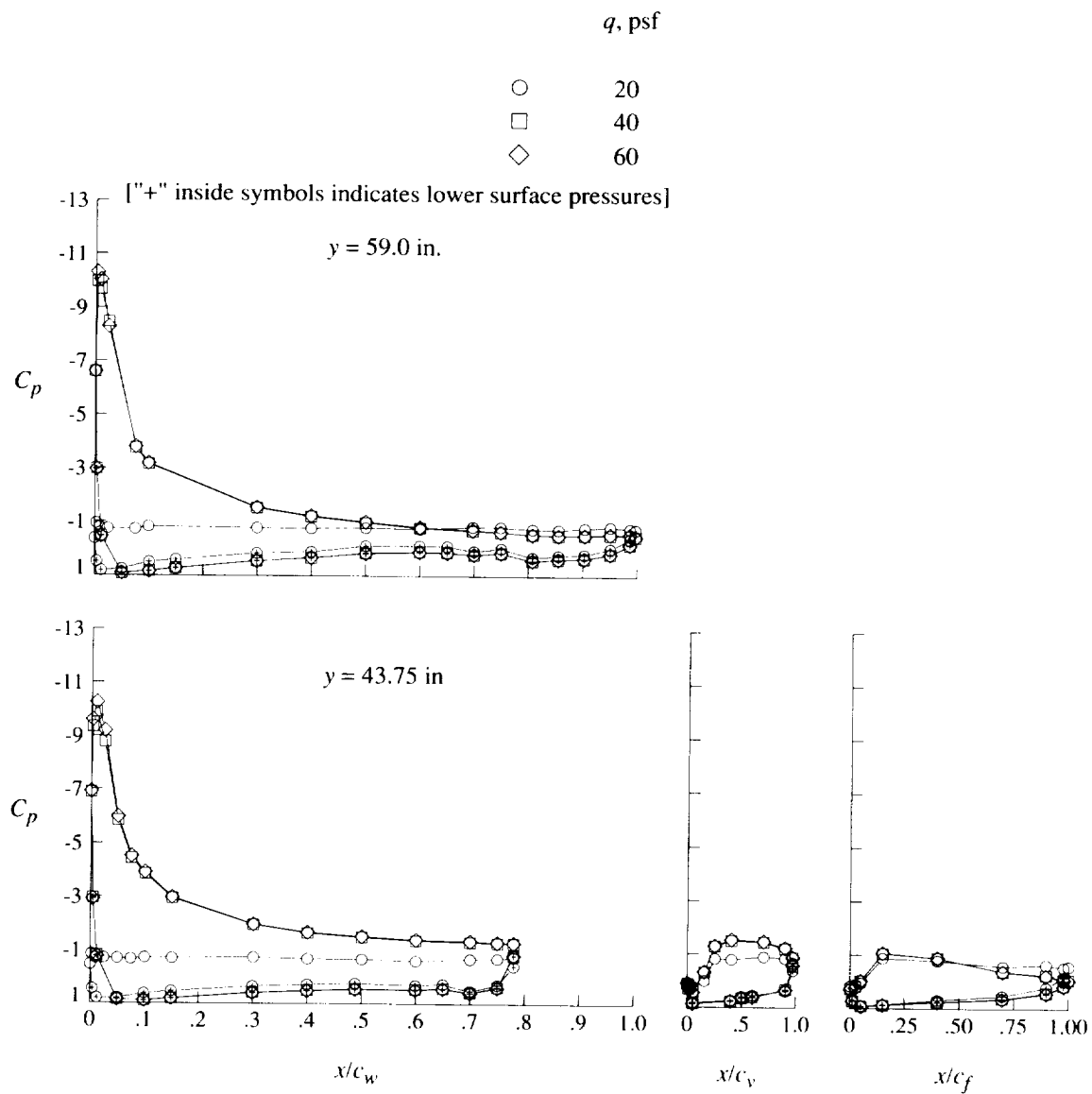
(d) Concluded.

Figure 13. Continued.



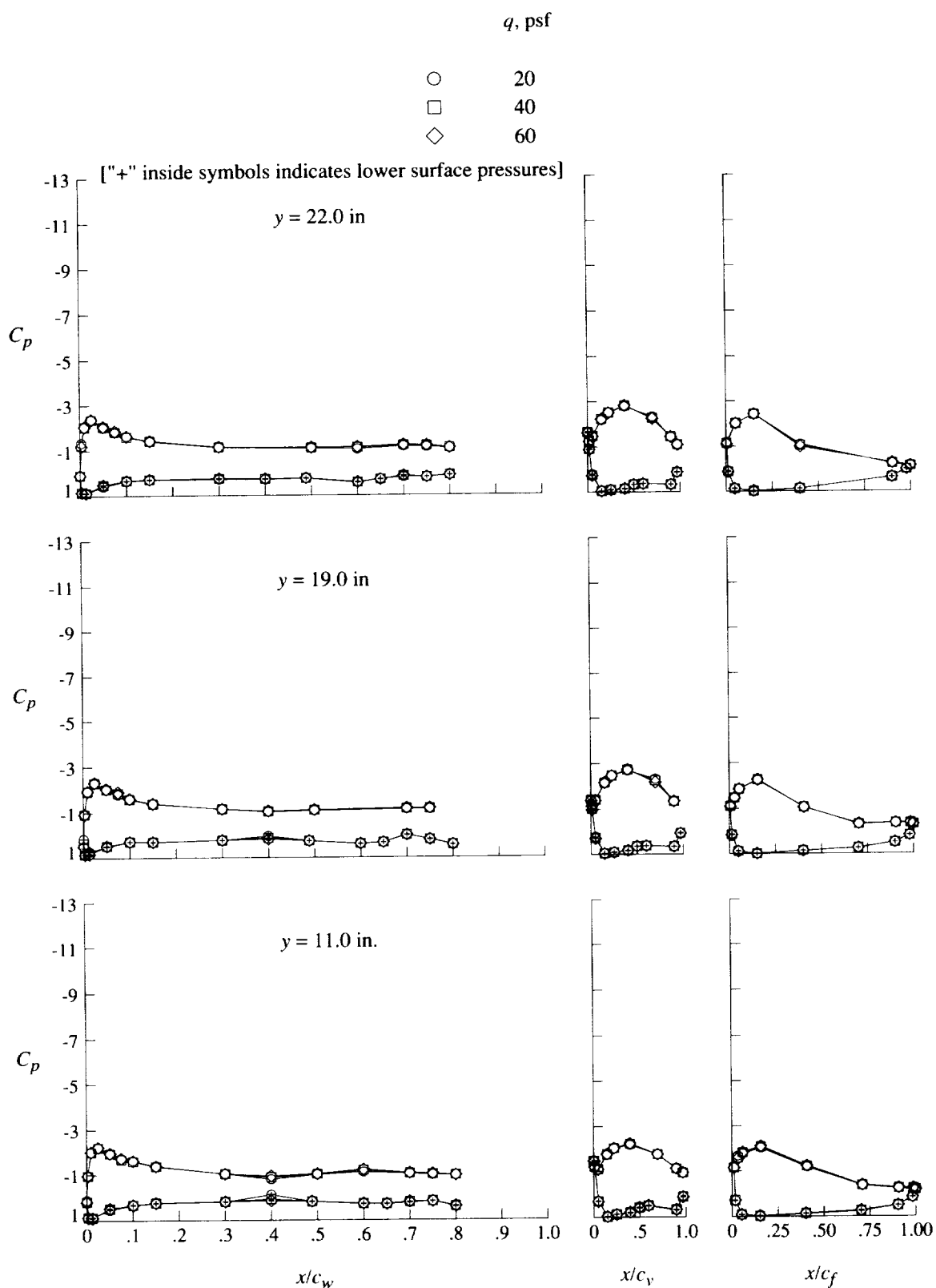
(e) $\alpha = 16^\circ$.

Figure 13. Continued.



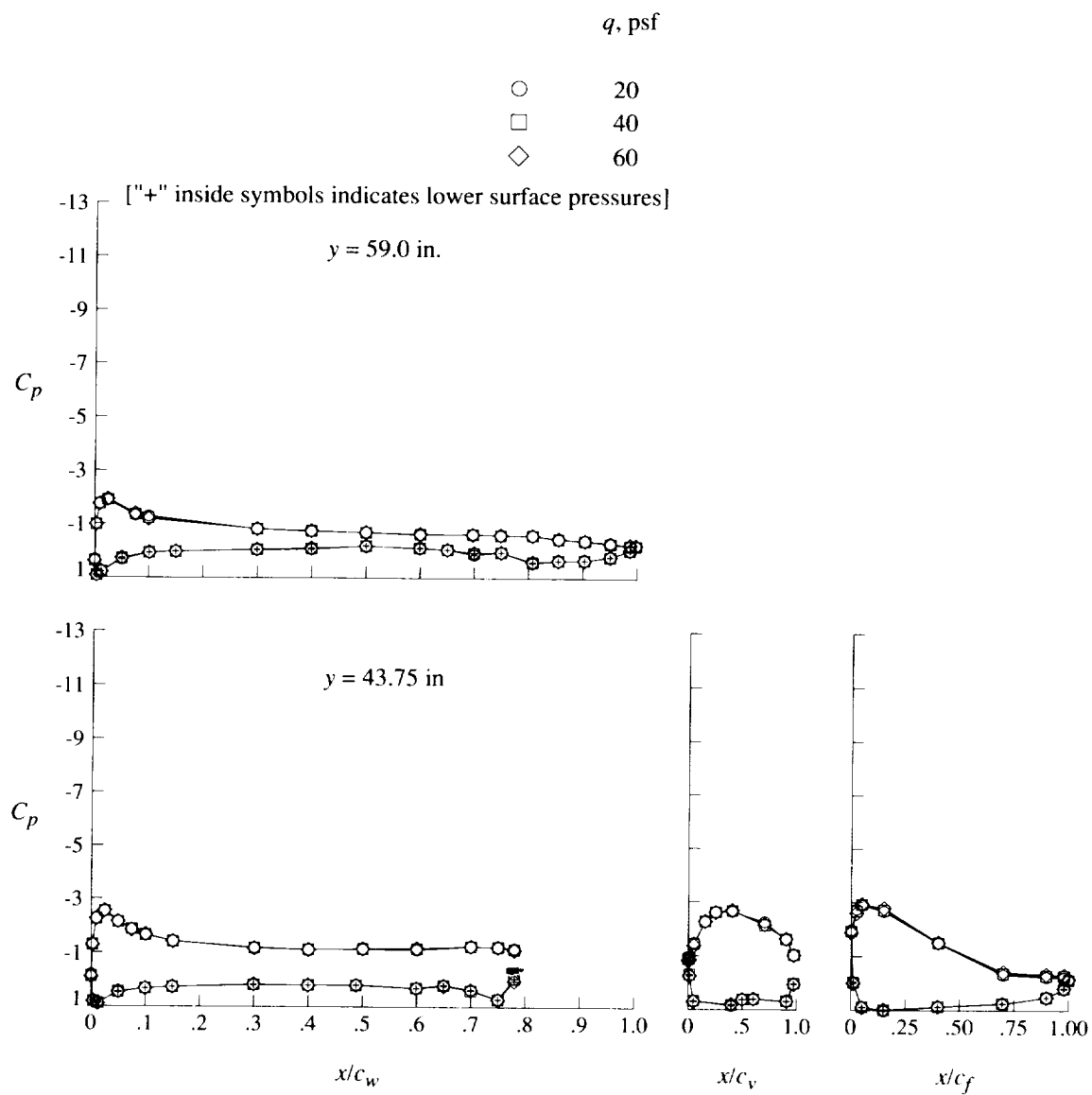
(e) Concluded.

Figure 13. Concluded.



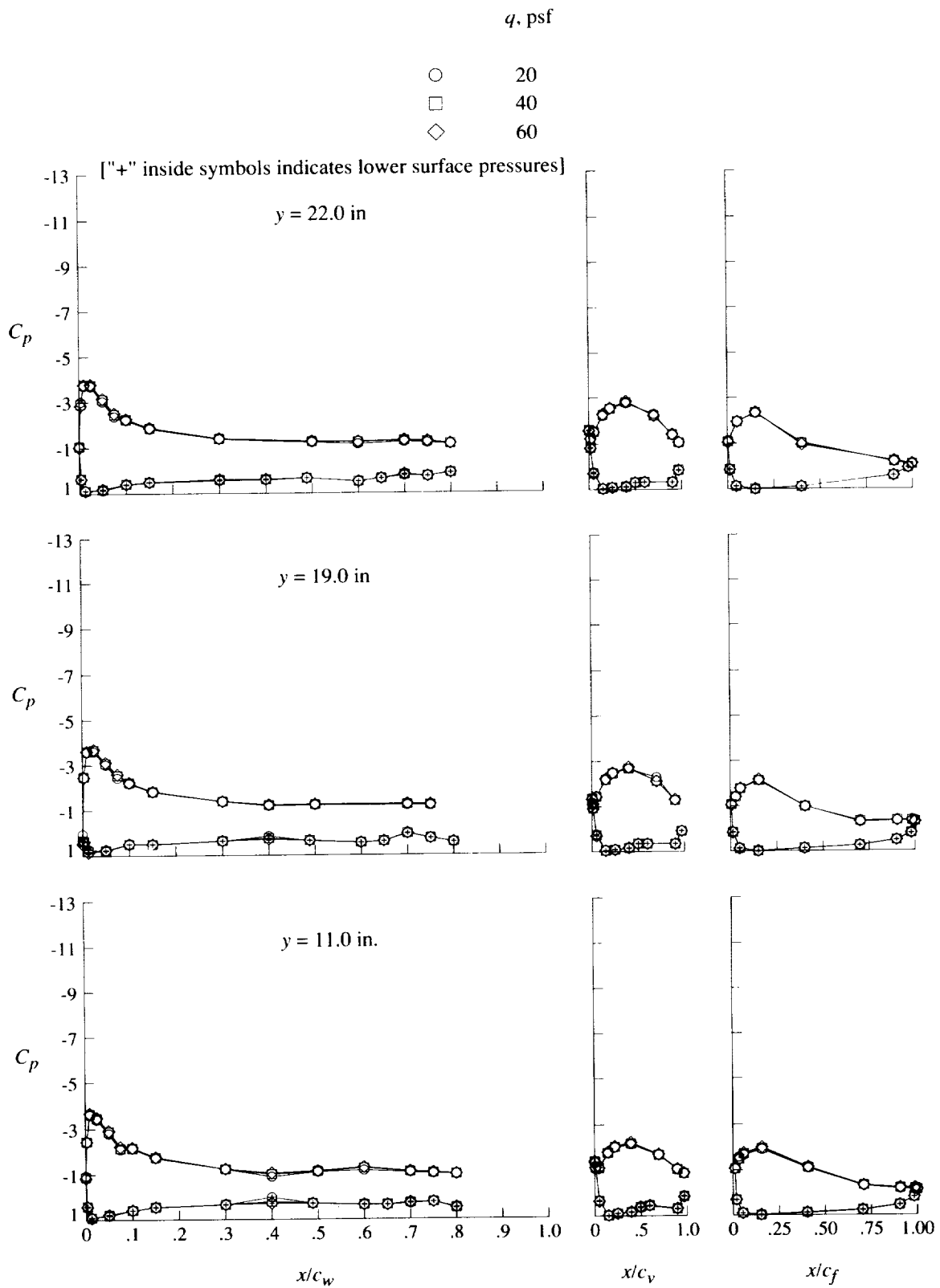
(a) $\alpha = 0^\circ$.

Figure 14. Effect of free-stream speed on pressure distributions for flaps-only configuration at $\delta_f = 60^\circ$.



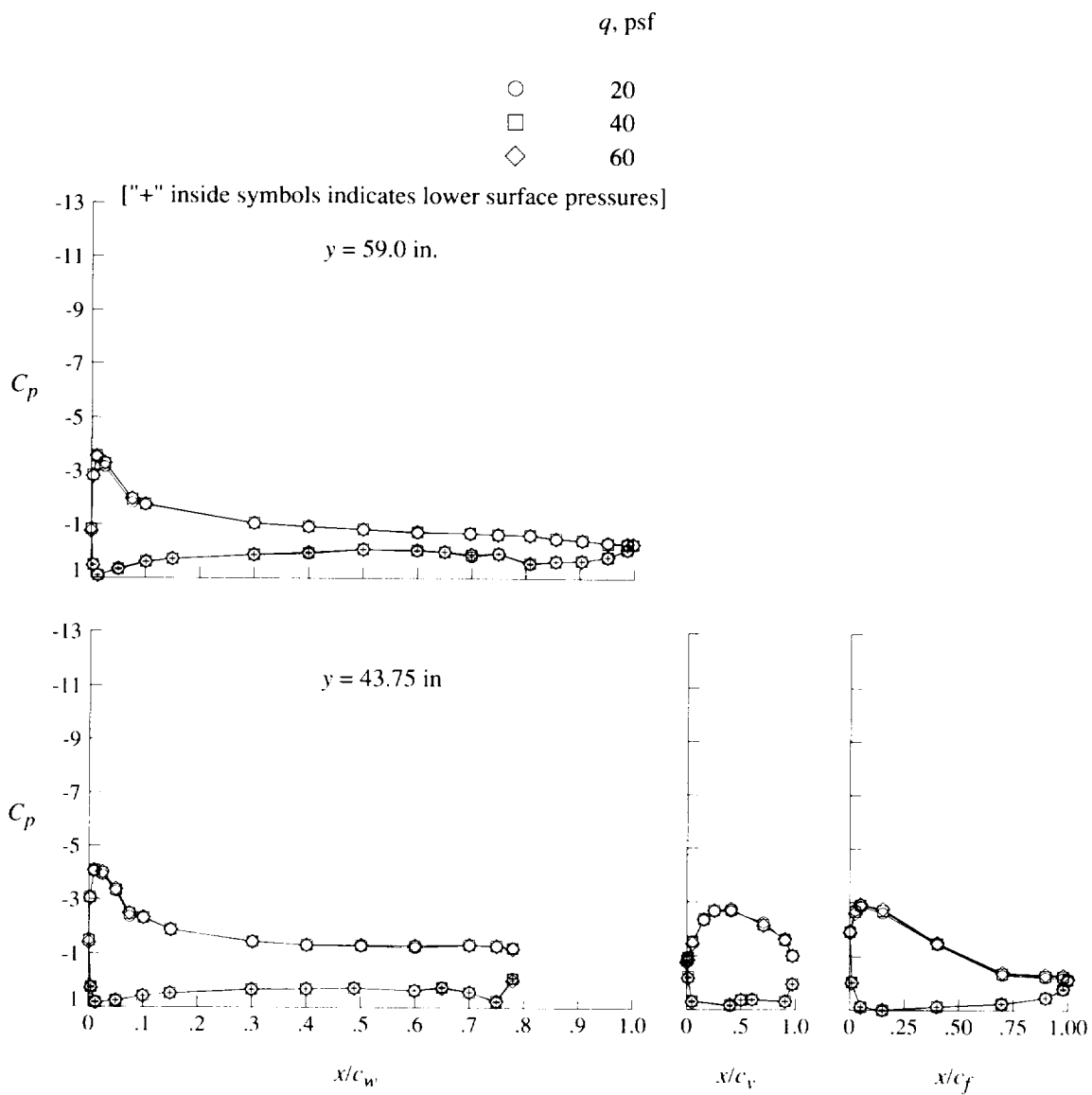
(a) Concluded.

Figure 14. Continued.



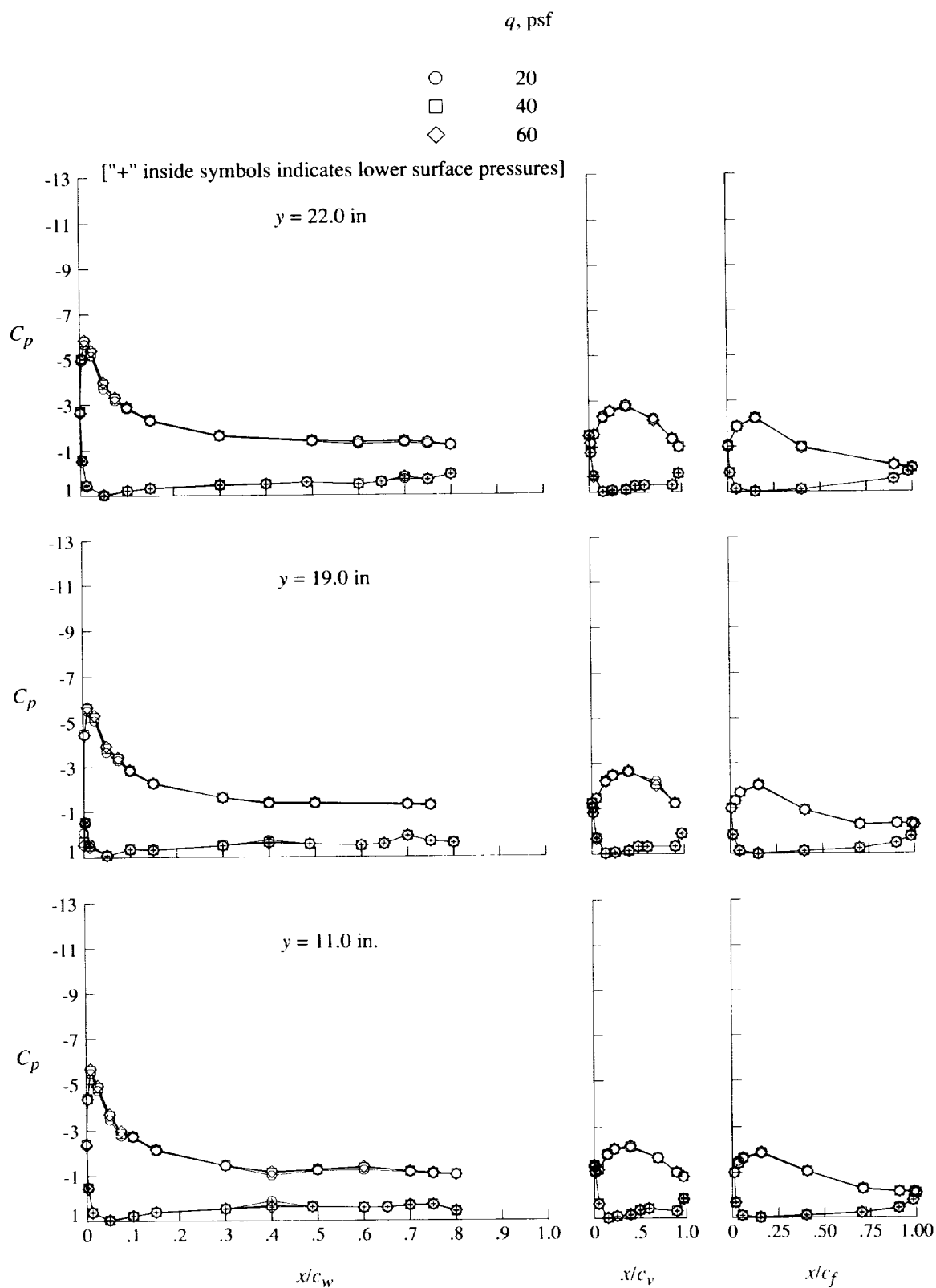
(b) $\alpha = 4^\circ$.

Figure 14. Continued.



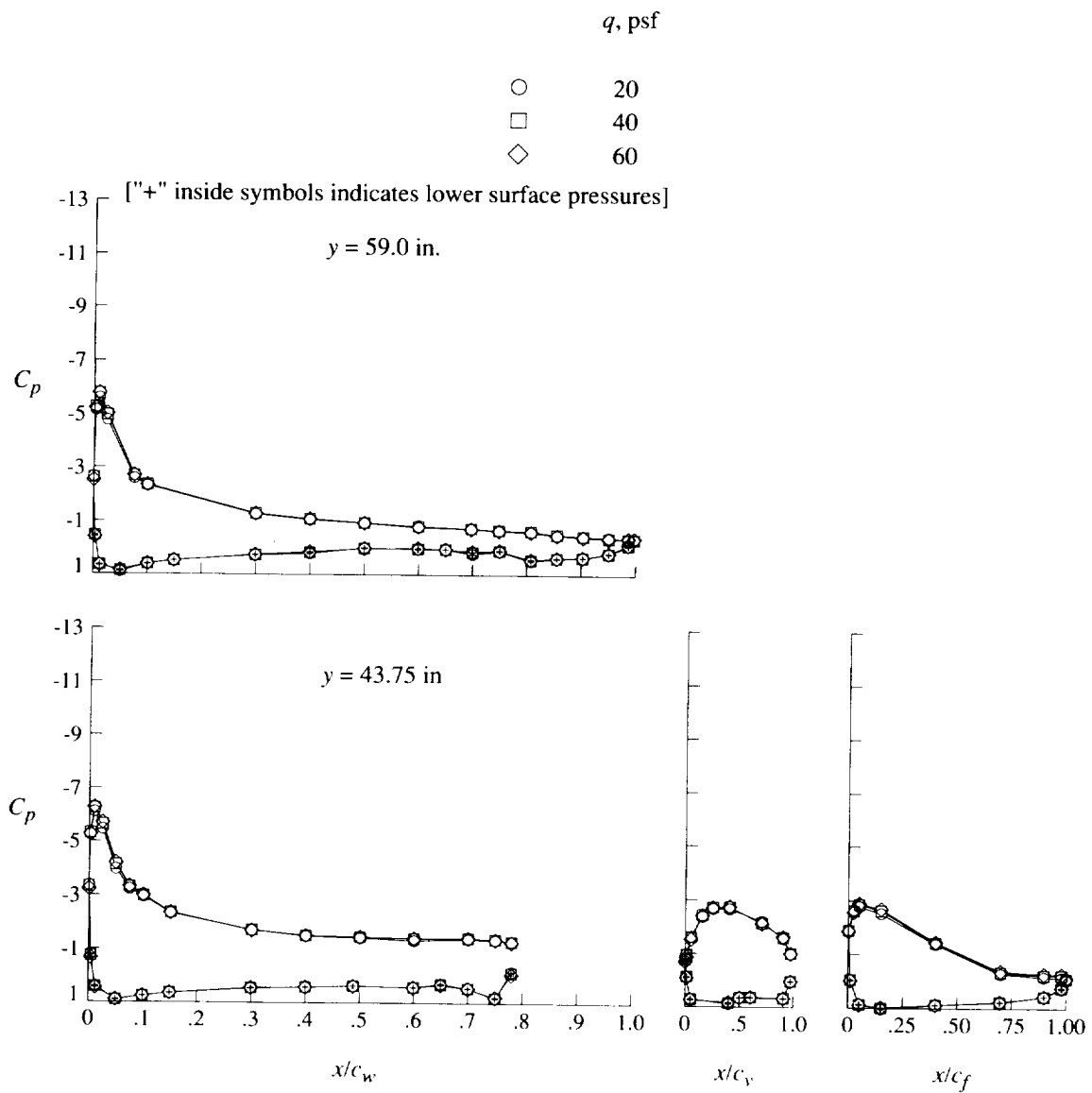
(b) Concluded.

Figure 14. Continued.



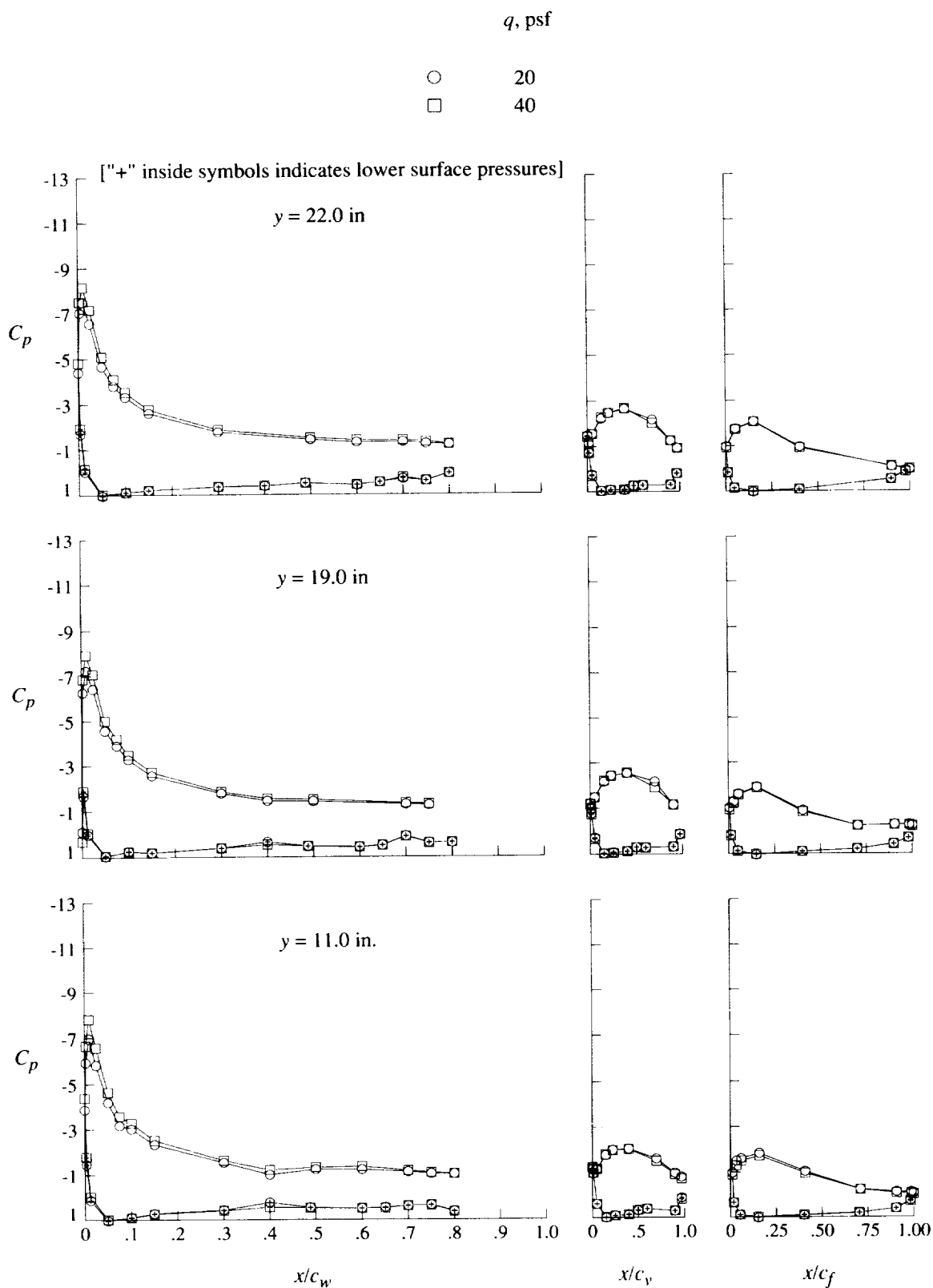
(c) $\alpha = 8^\circ$.

Figure 14. Continued.



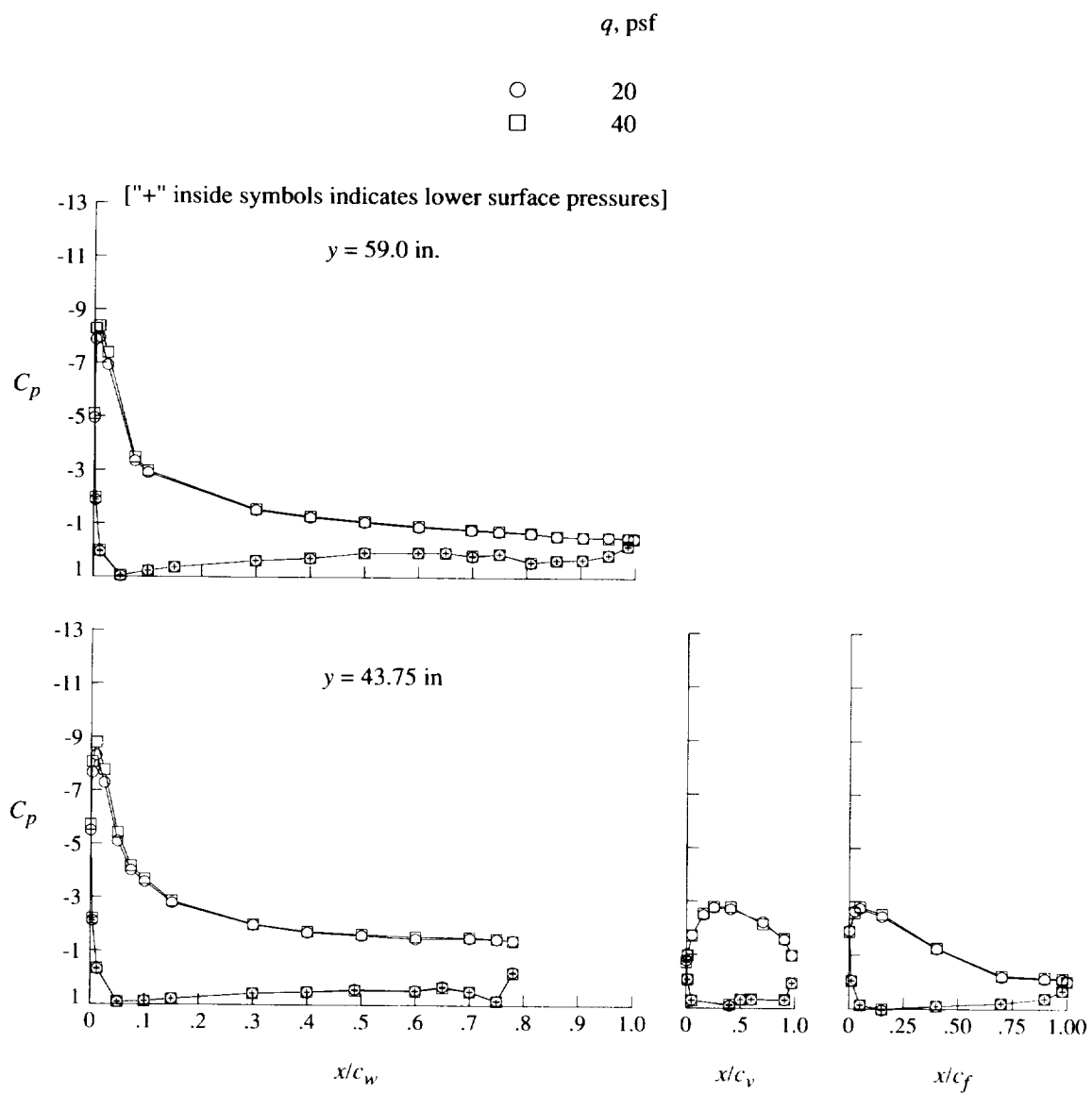
(c) Concluded.

Figure 14. Continued.



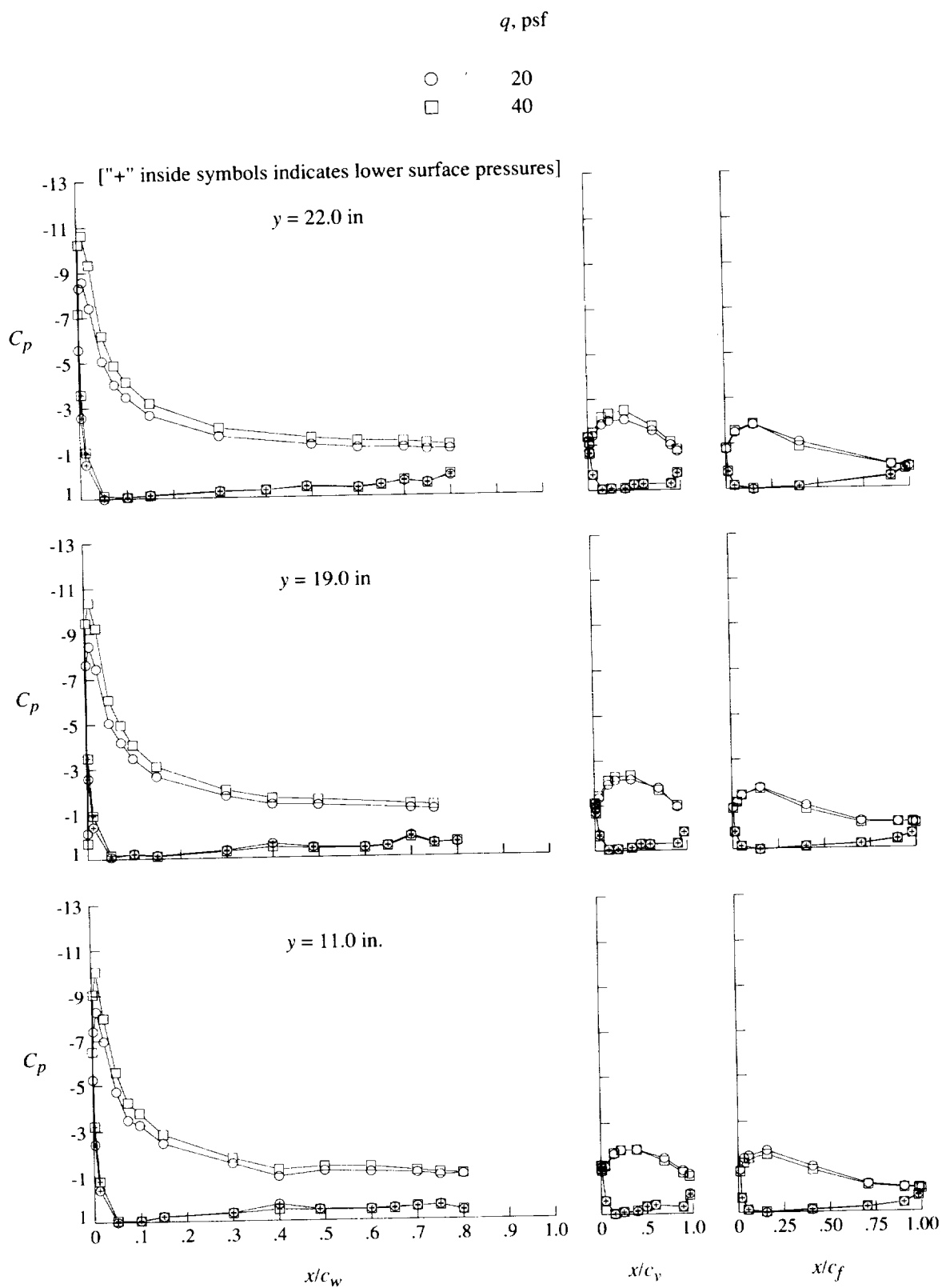
(d) $\alpha = 12^\circ$.

Figure 14. Continued.



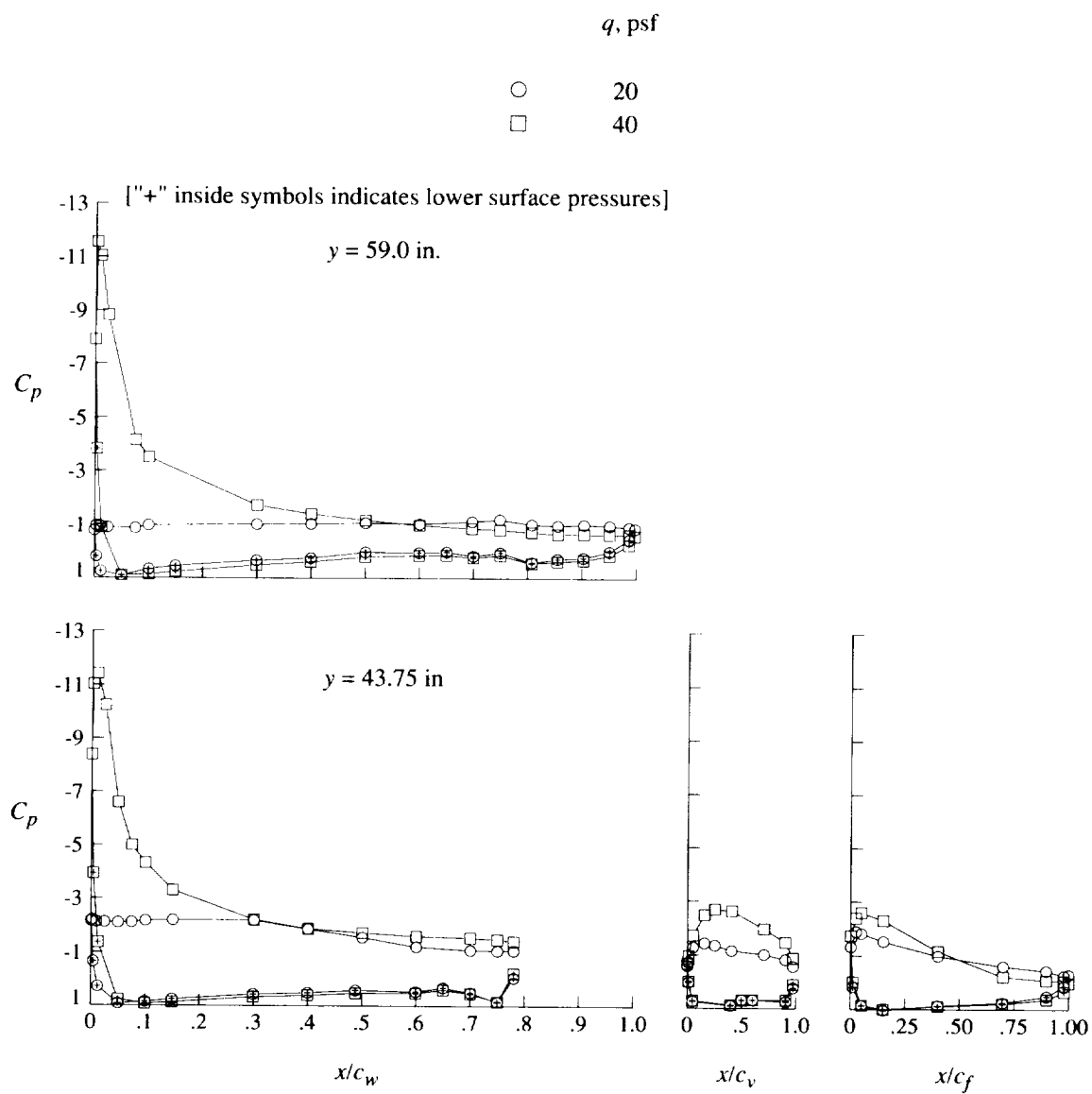
(d) Concluded.

Figure 14. Continued.



(e) $\alpha = 16^\circ$.

Figure 14. Continued.



(e) Concluded.

Figure 14. Concluded.

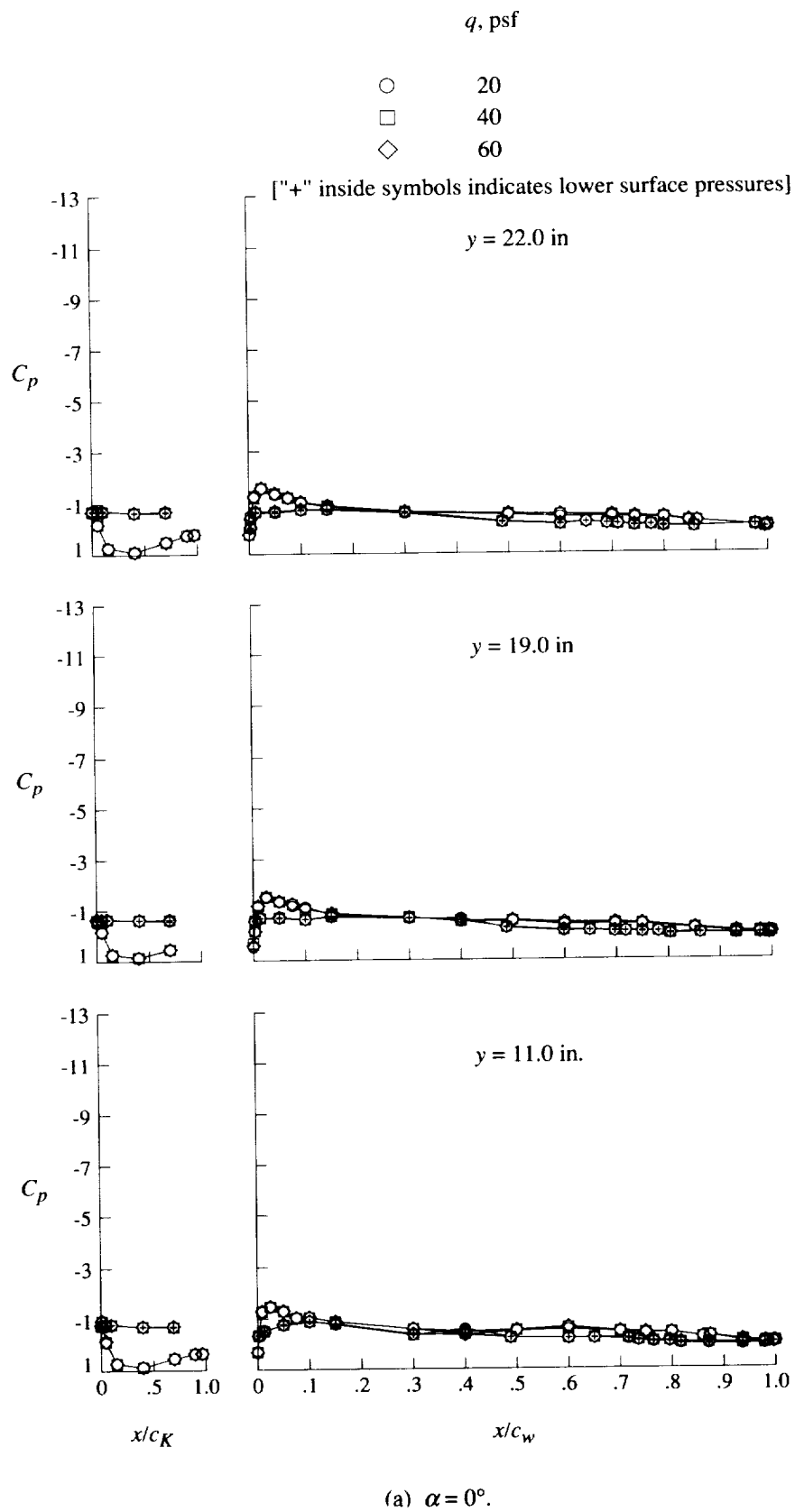
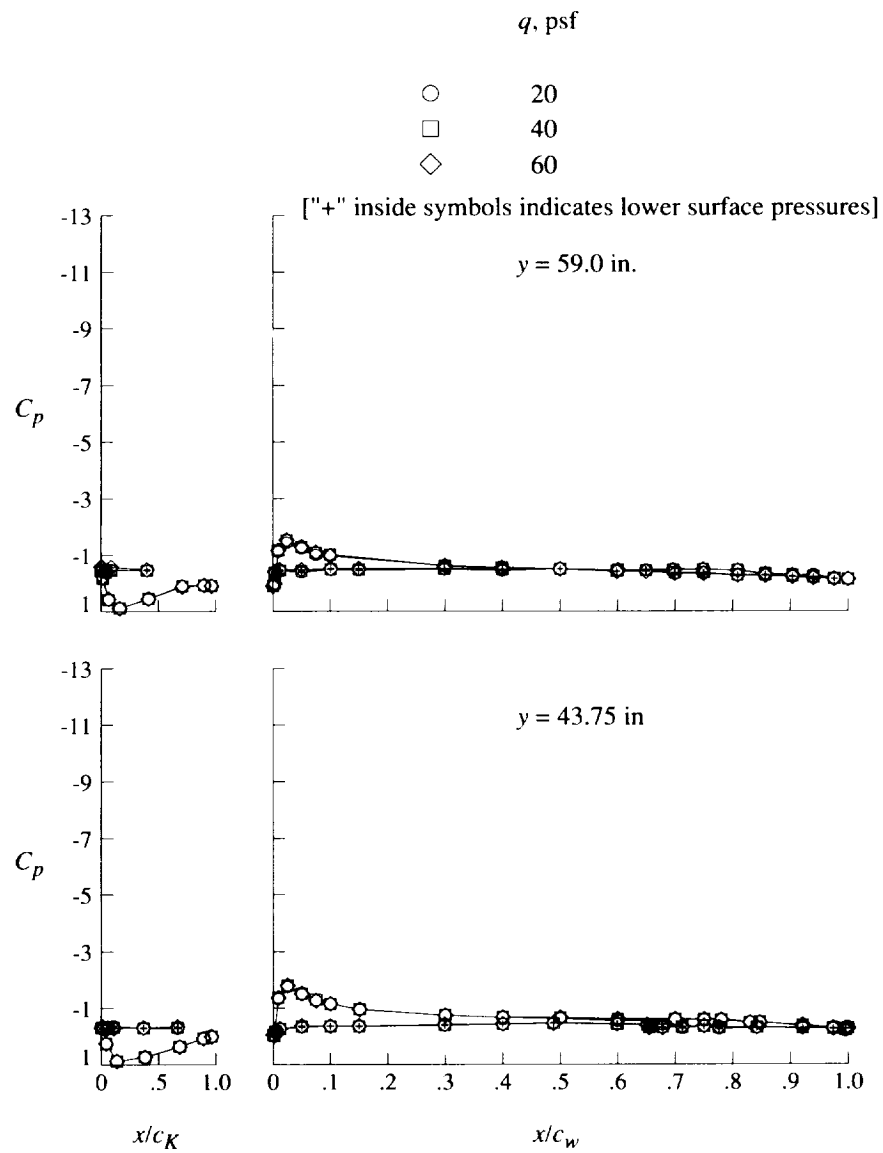
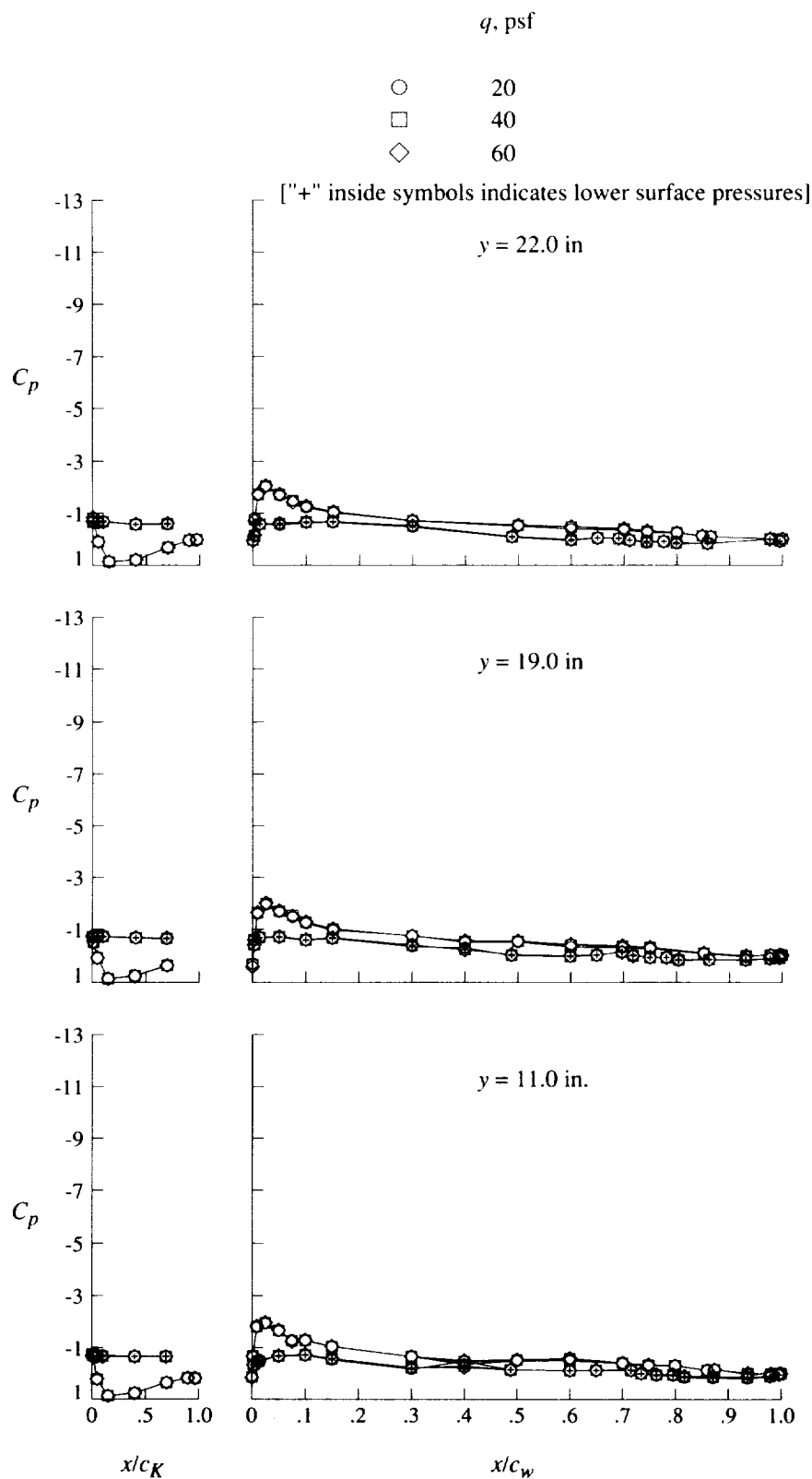


Figure 15. Effect of free-stream speed on pressure distributions for Krueger-flap-only configuration.



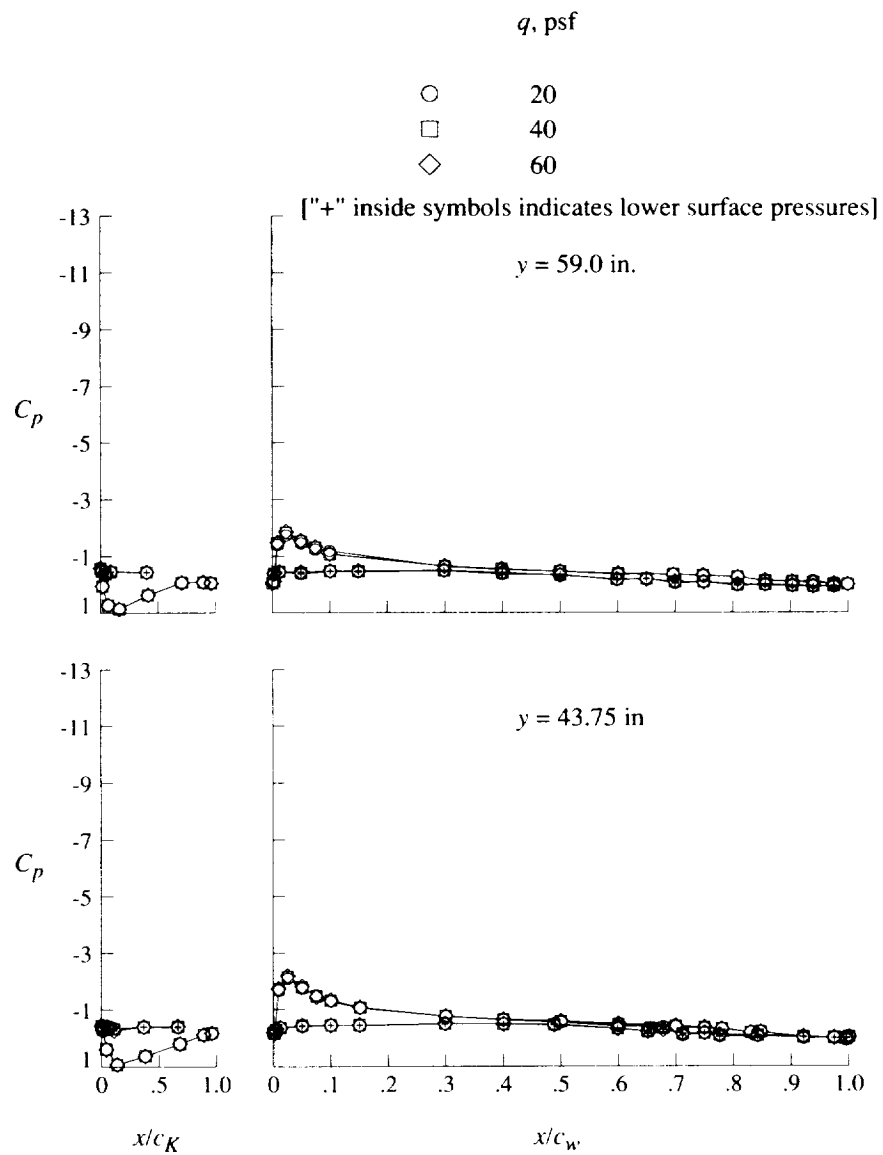
(a) Concluded.

Figure 15. Continued.



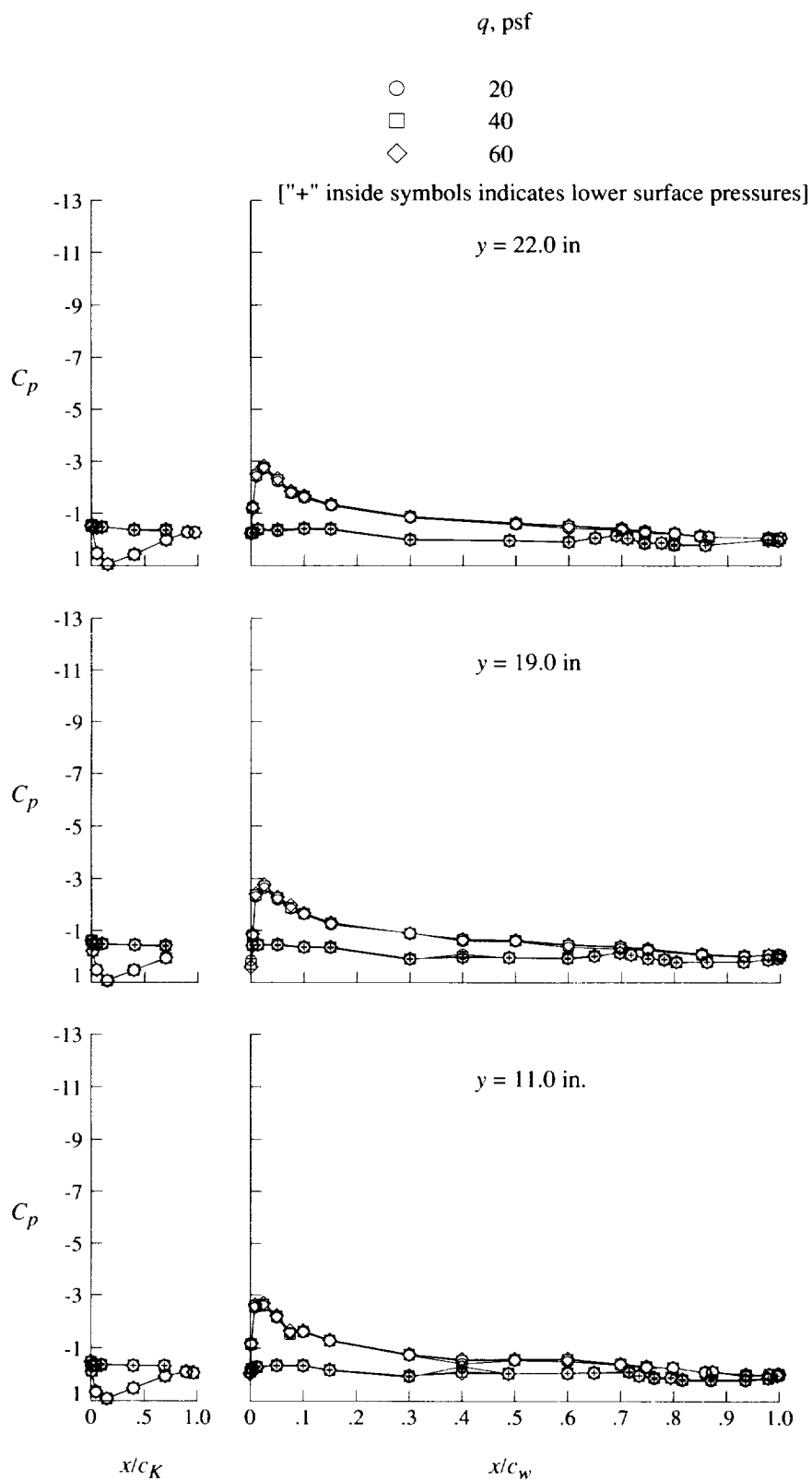
(b) $\alpha = 4^\circ$.

Figure 15. Continued.



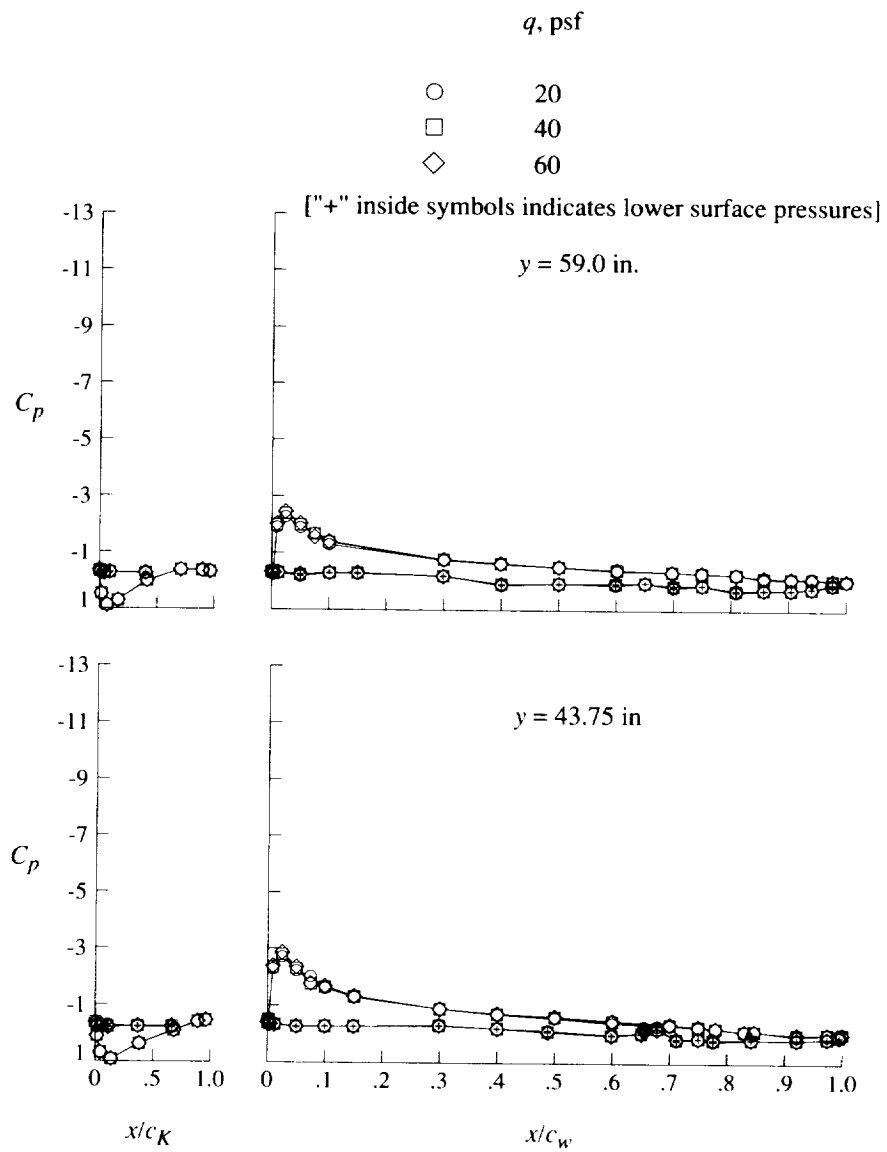
(b) Concluded.

Figure 15. Continued.



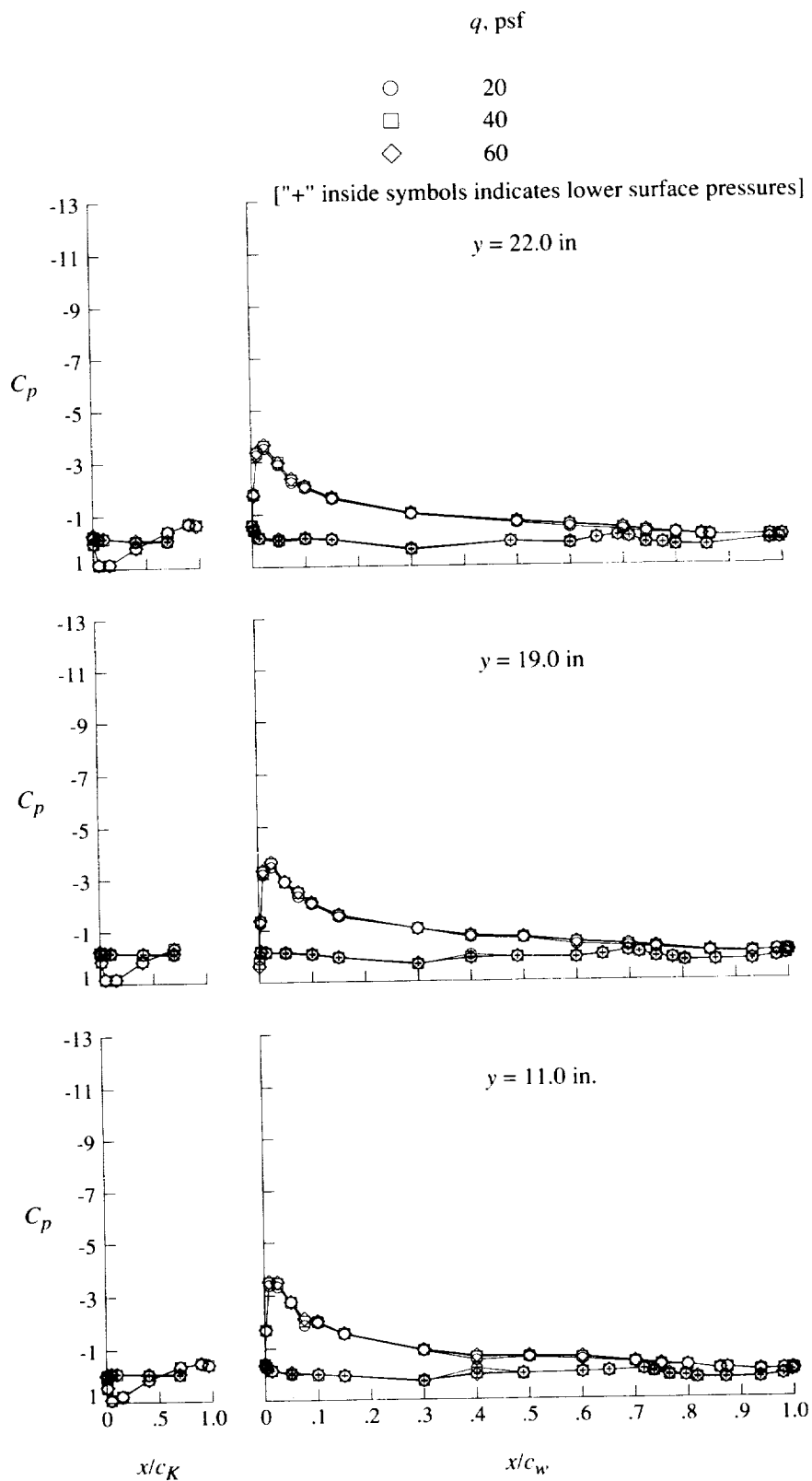
(c) $\alpha = 8^\circ$.

Figure 15. Continued.



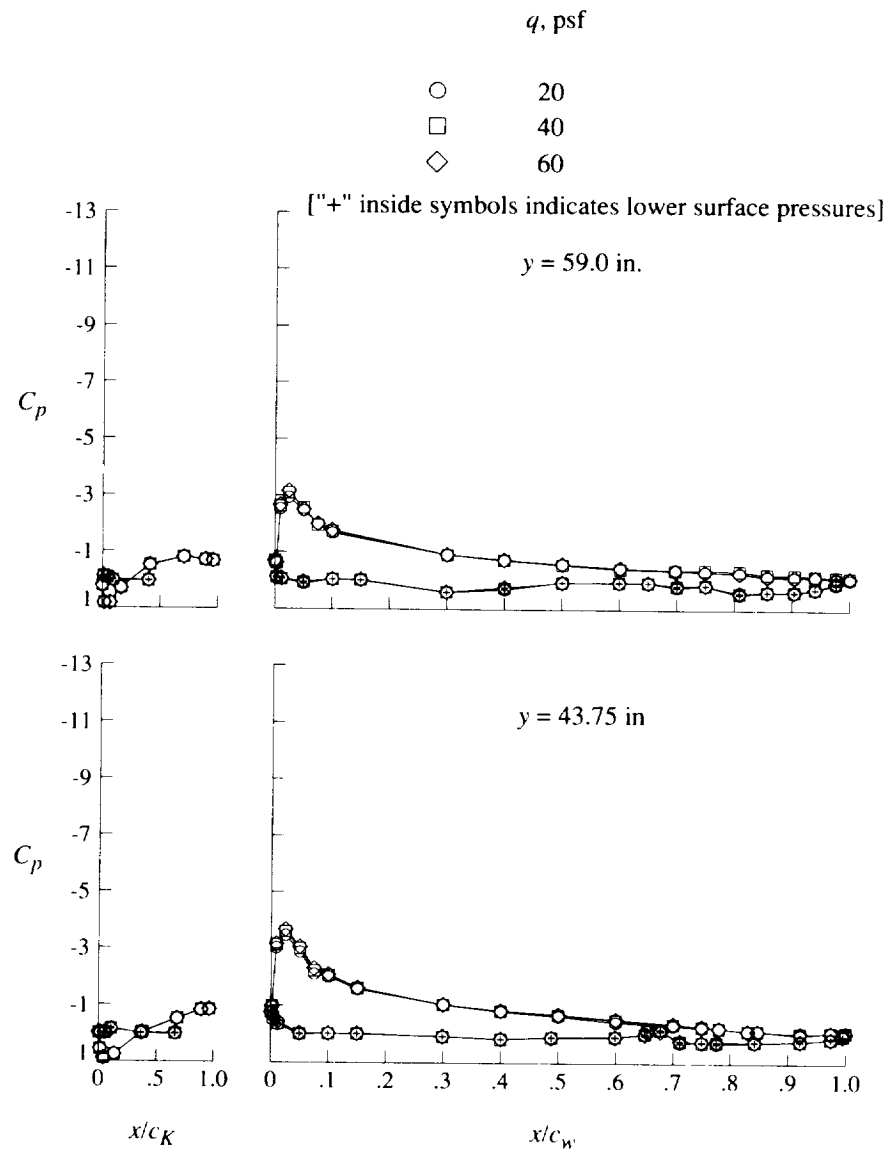
(c) Concluded.

Figure 15. Continued.



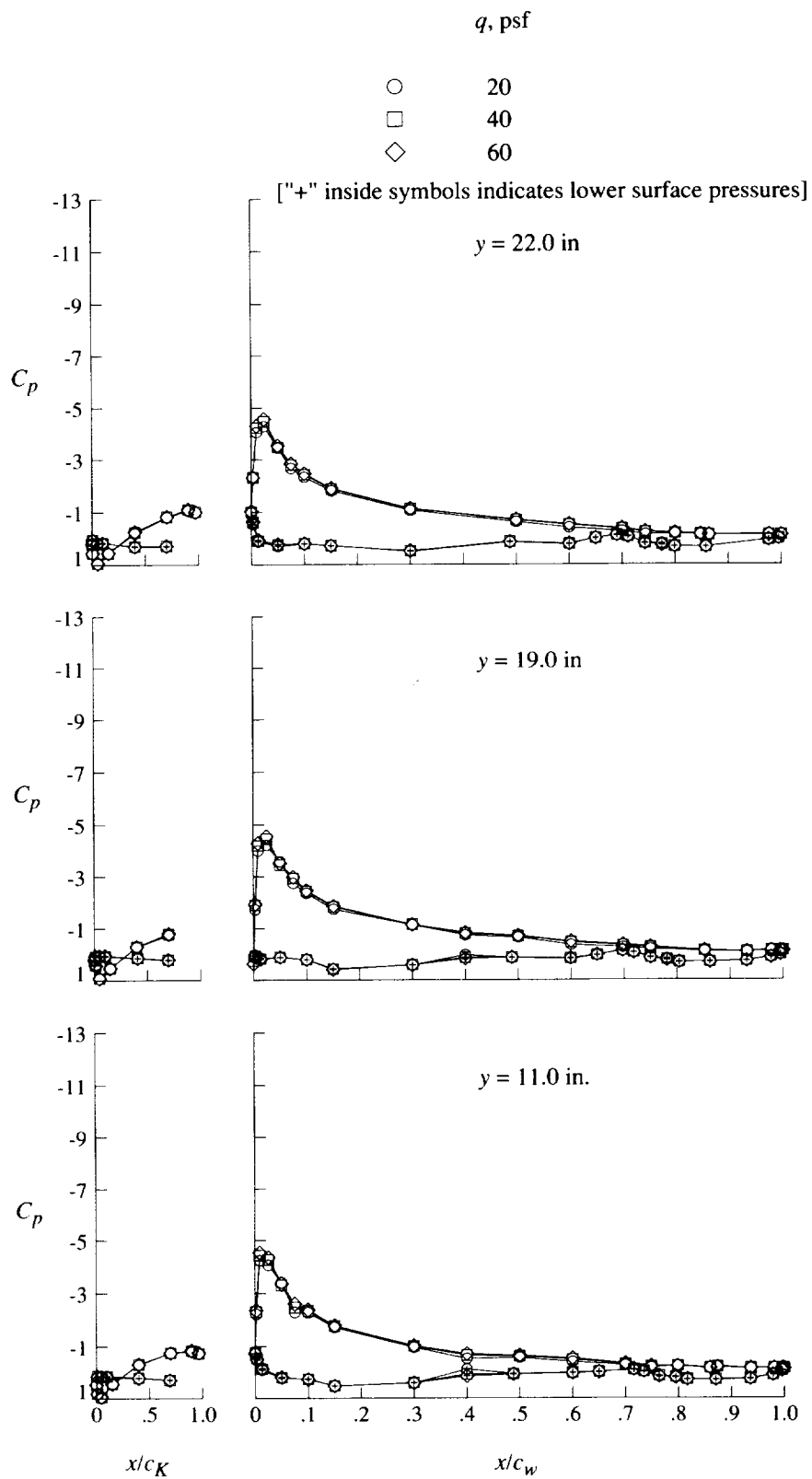
(d) $\alpha = 12^\circ$.

Figure 15. Continued.



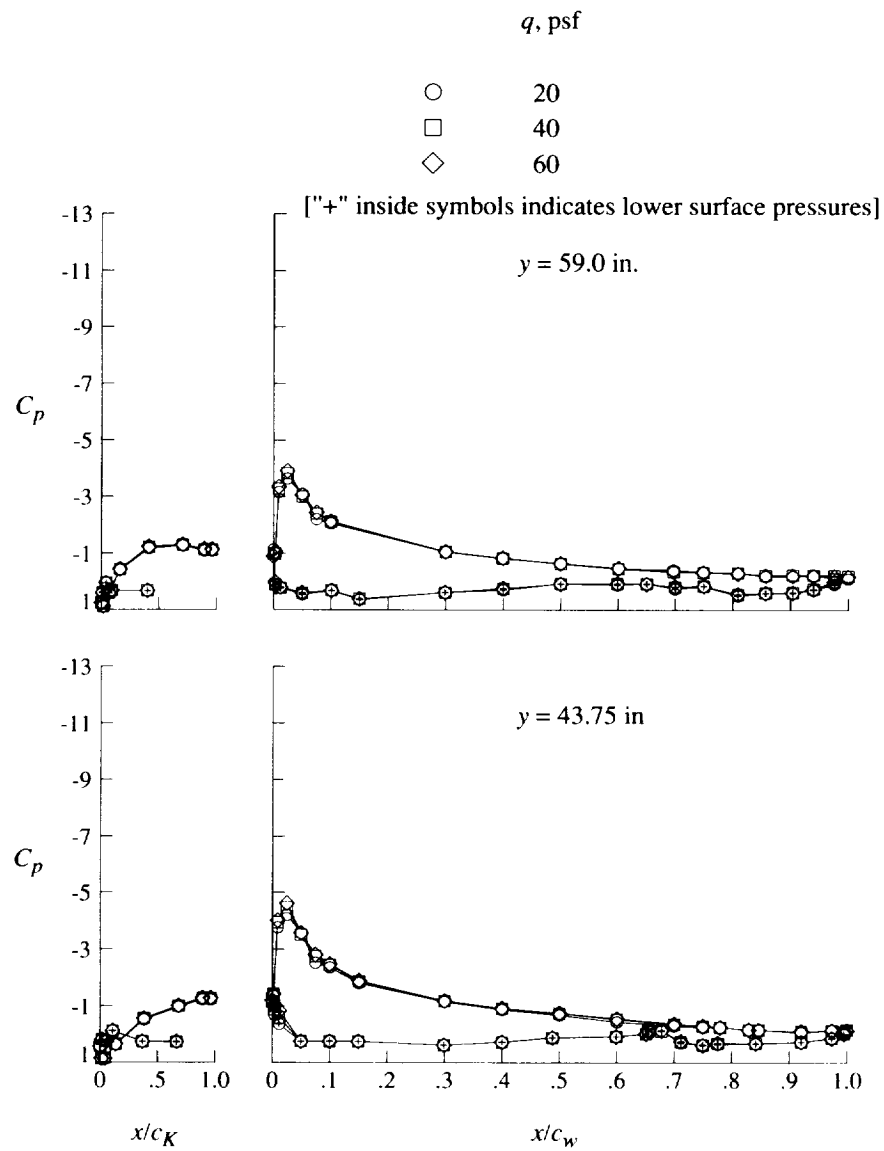
(d) Concluded.

Figure 15. Continued.



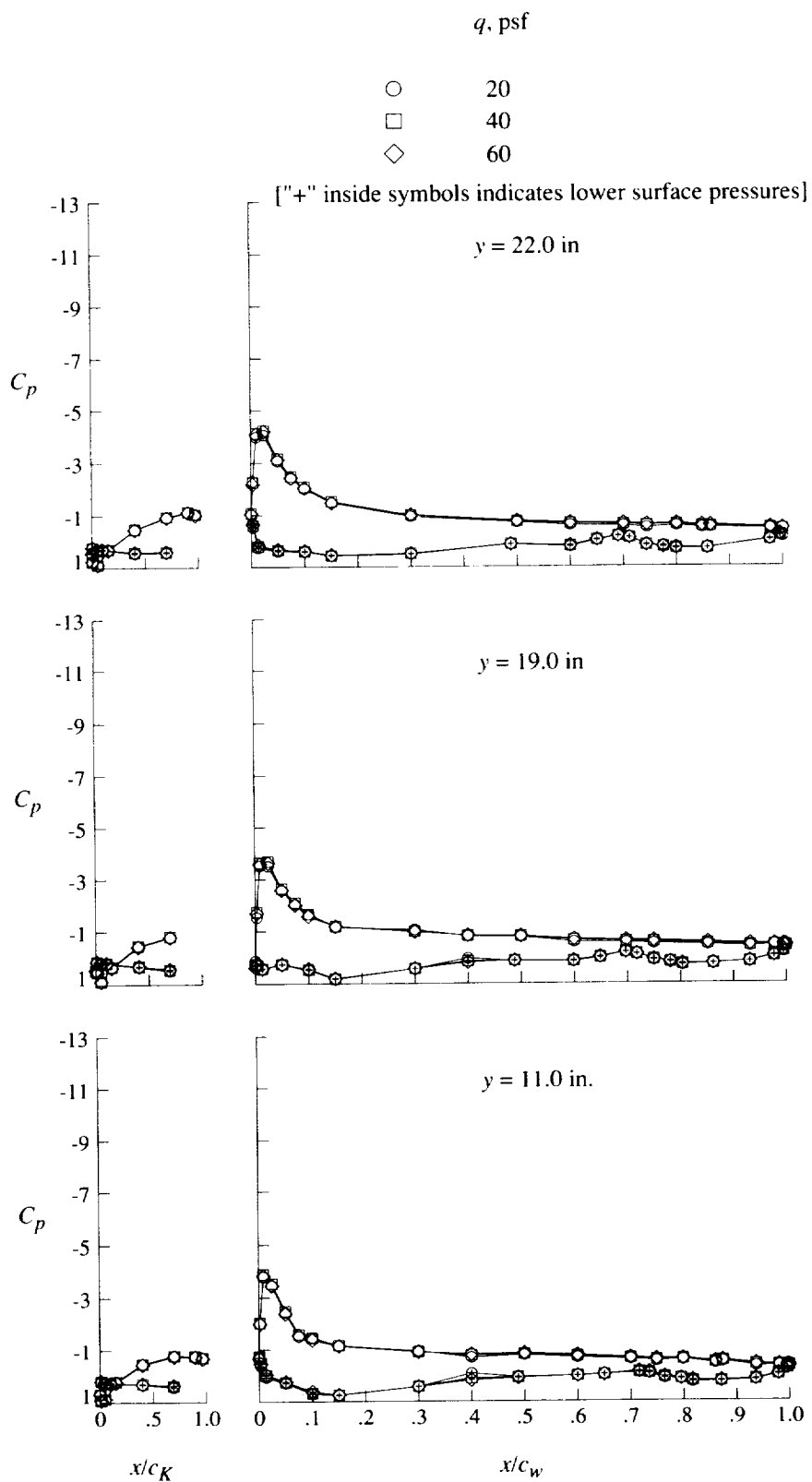
(e) $\alpha = 16^\circ$.

Figure 15. Continued.



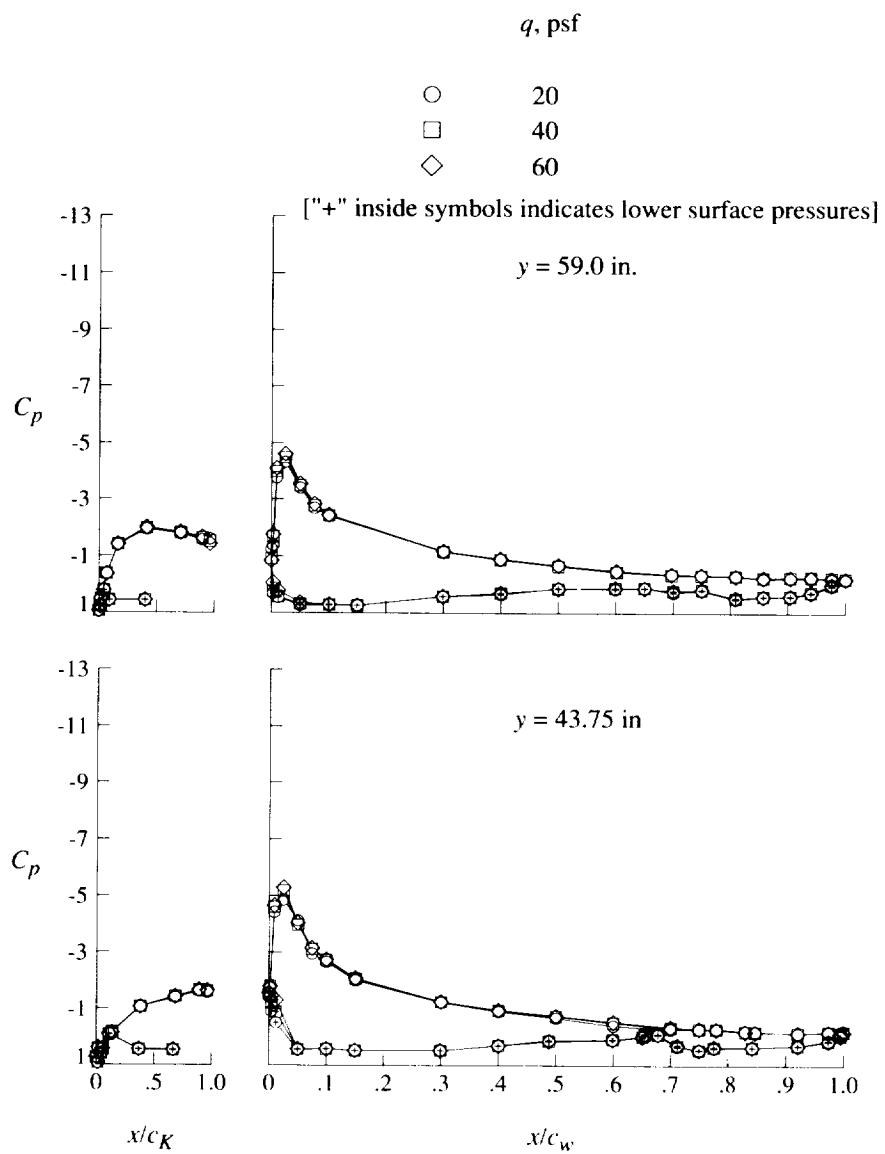
(e) Concluded.

Figure 15. Continued.



(f) $\alpha = 20^\circ$.

Figure 15. Continued.



(f) Concluded.

Figure 15. Concluded.

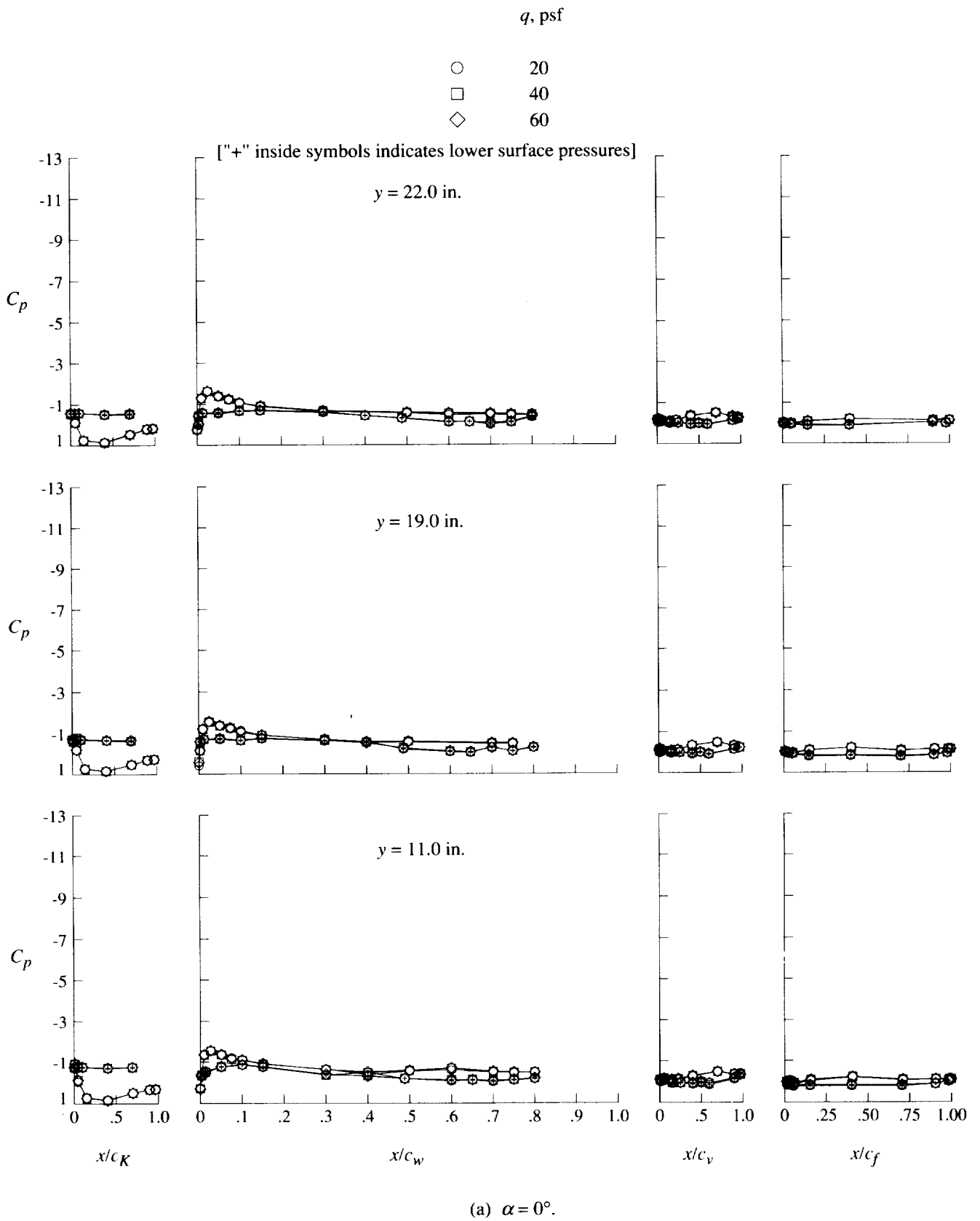
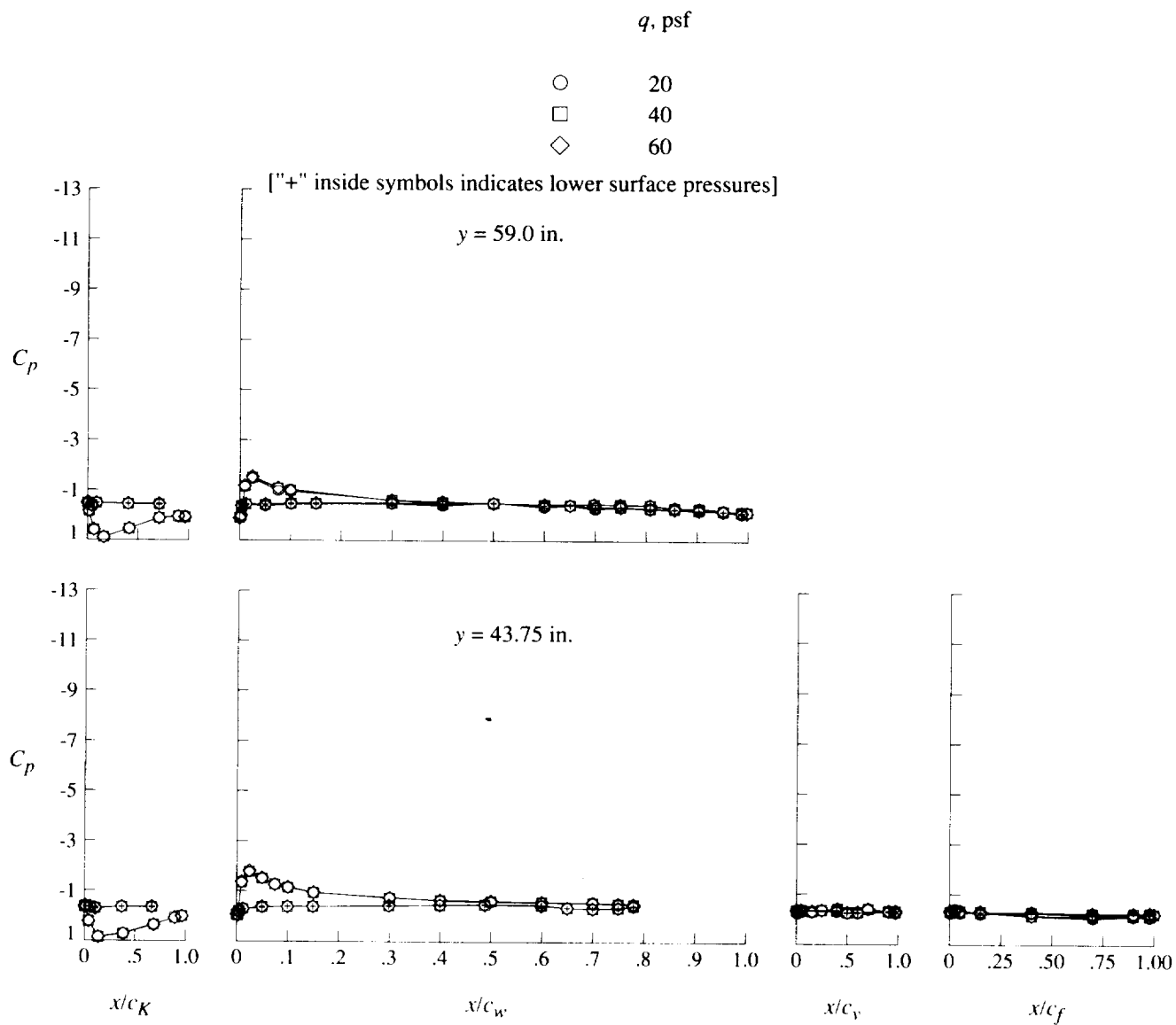


Figure 16. Effect of free-stream speed on pressure distributions for high-lift configuration at $\delta_f = 20^\circ$.



(a) Concluded.

Figure 16. Continued.

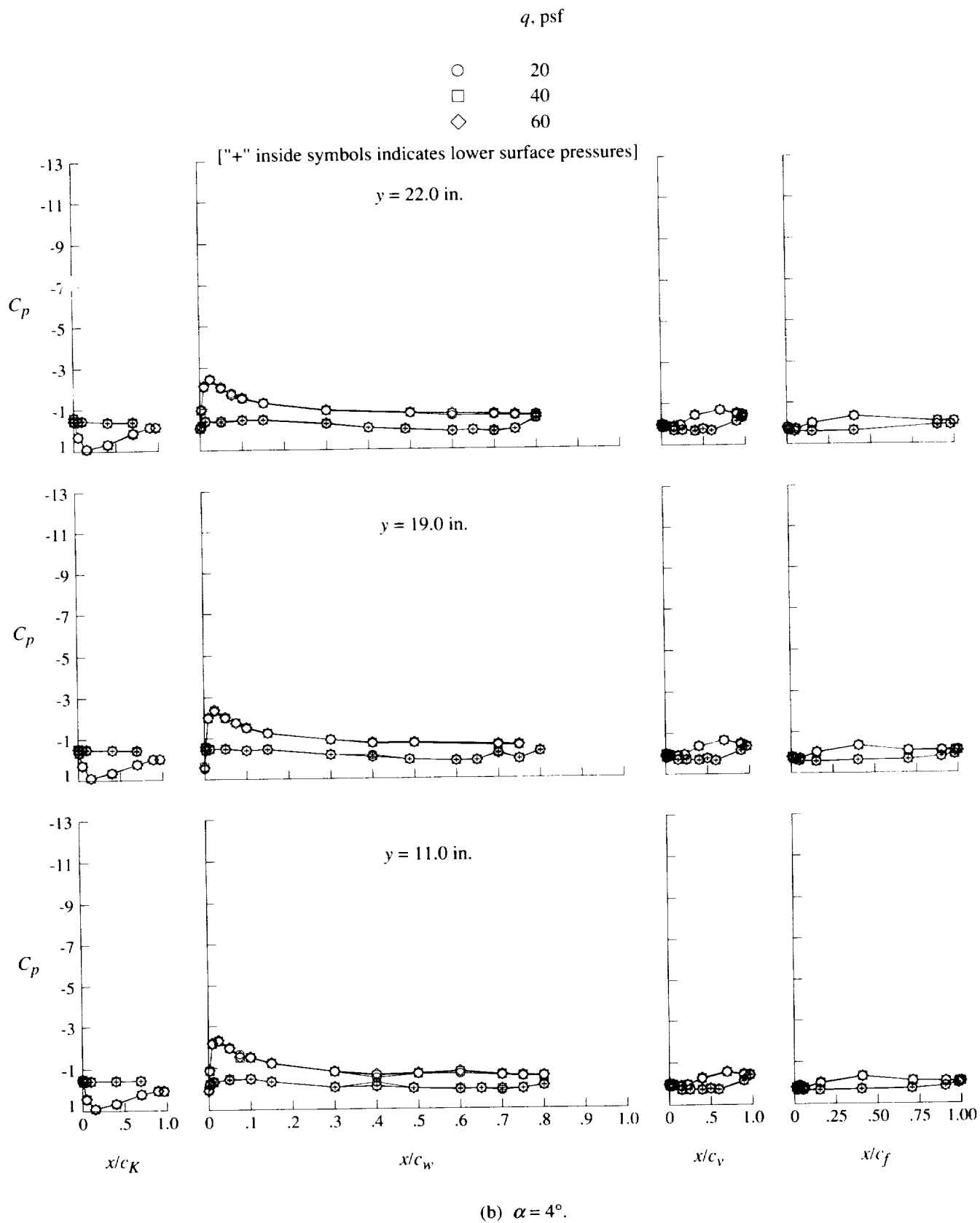
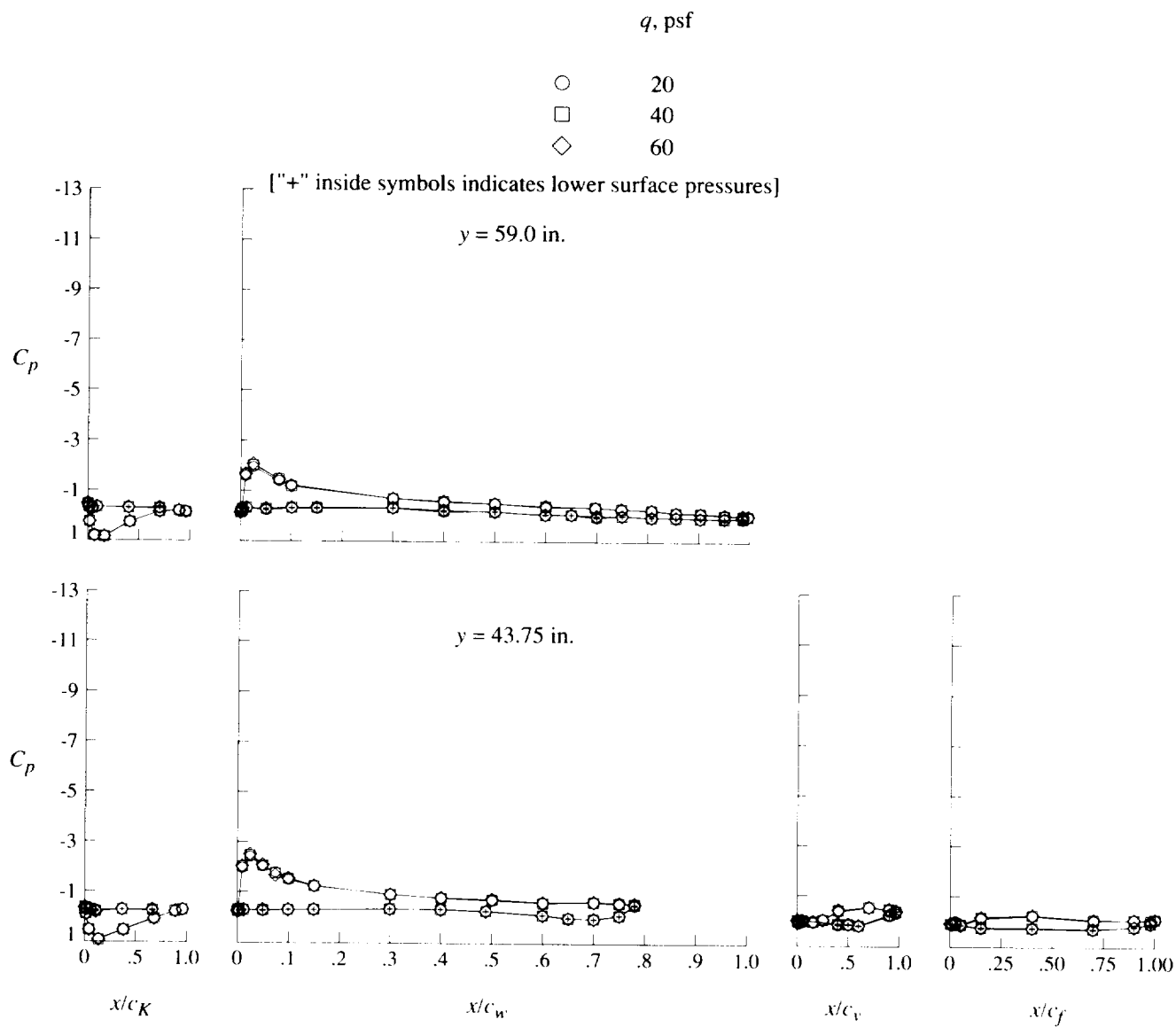
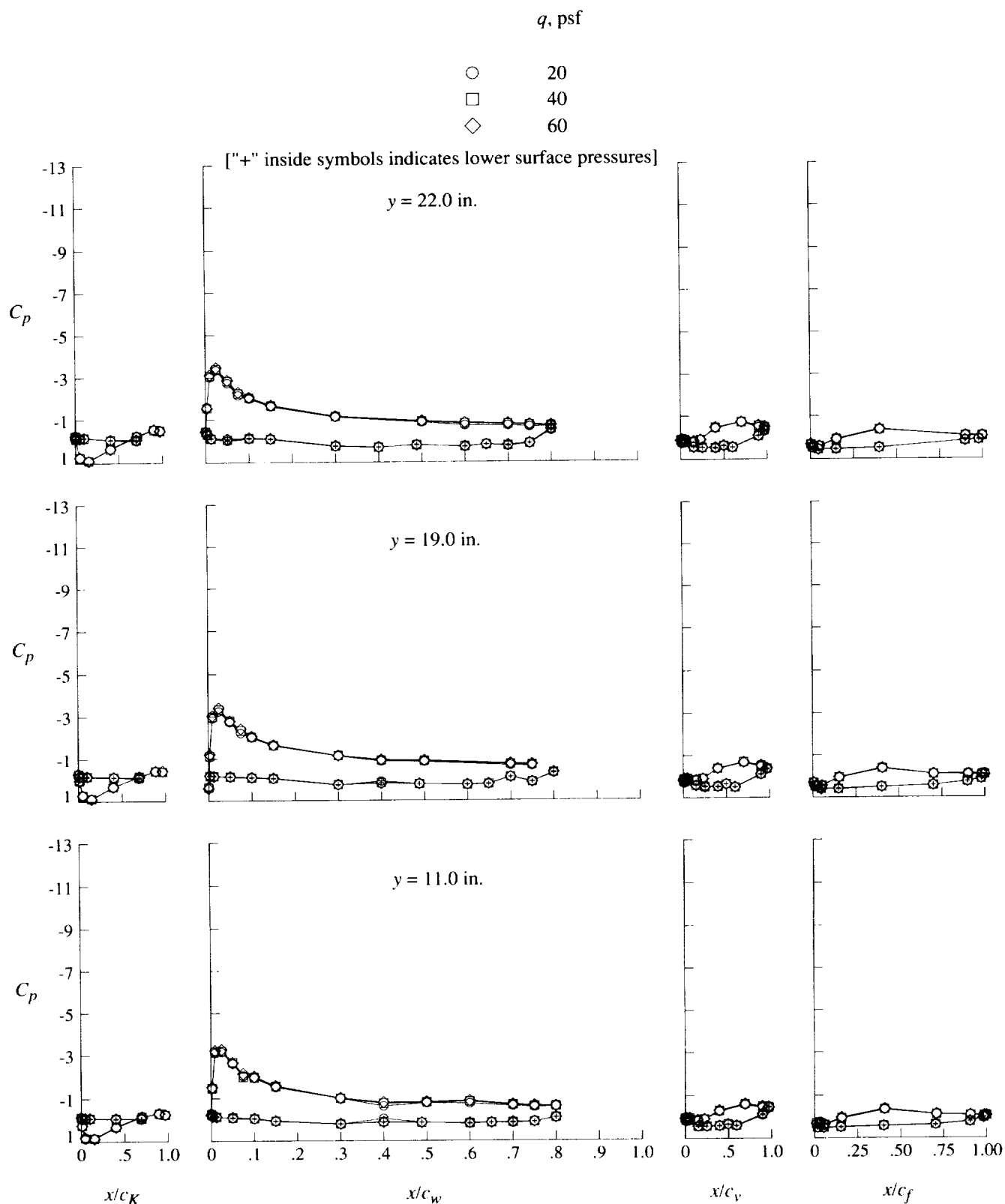


Figure 16. Continued.



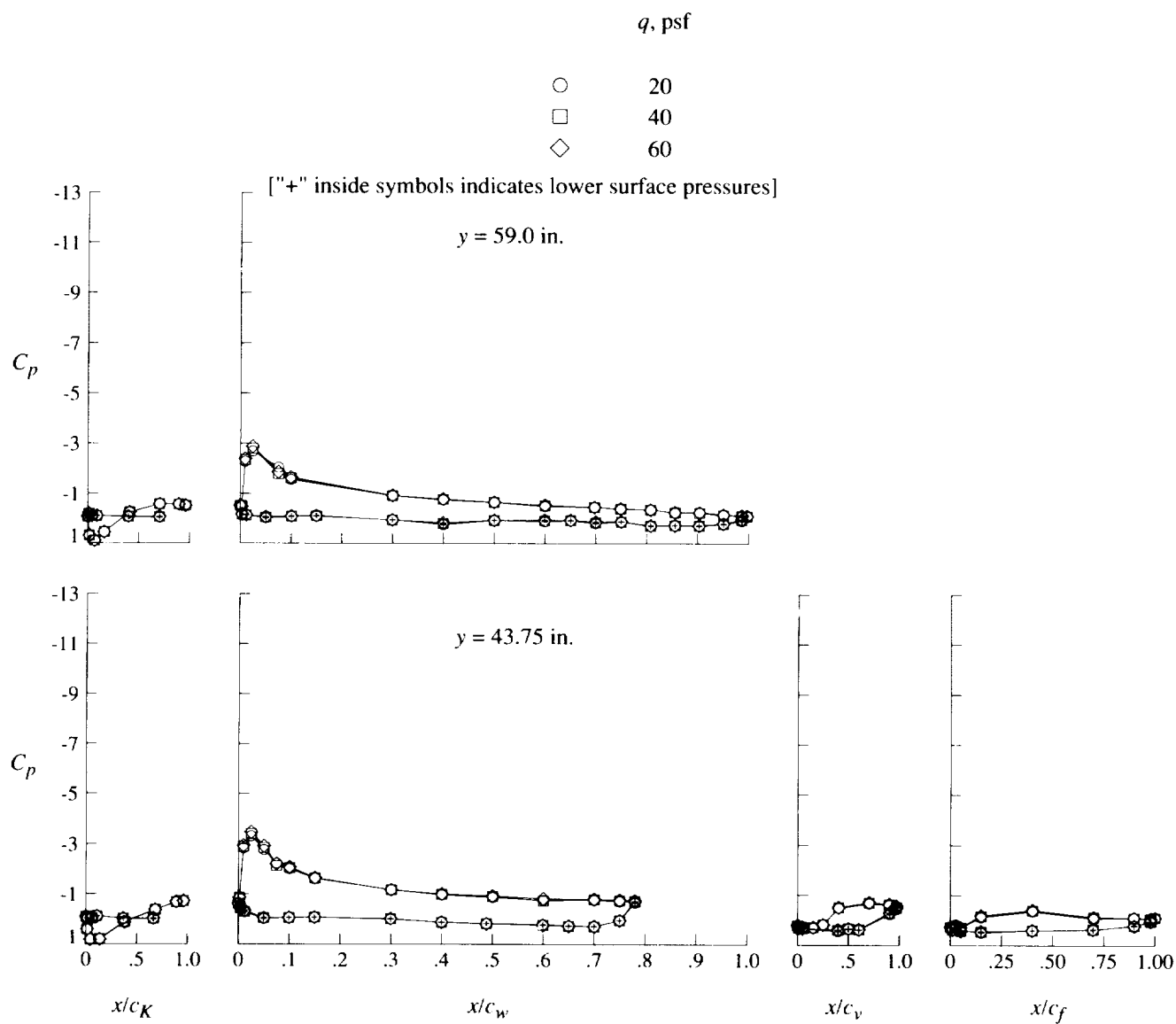
(b) Concluded.

Figure 16. Continued.



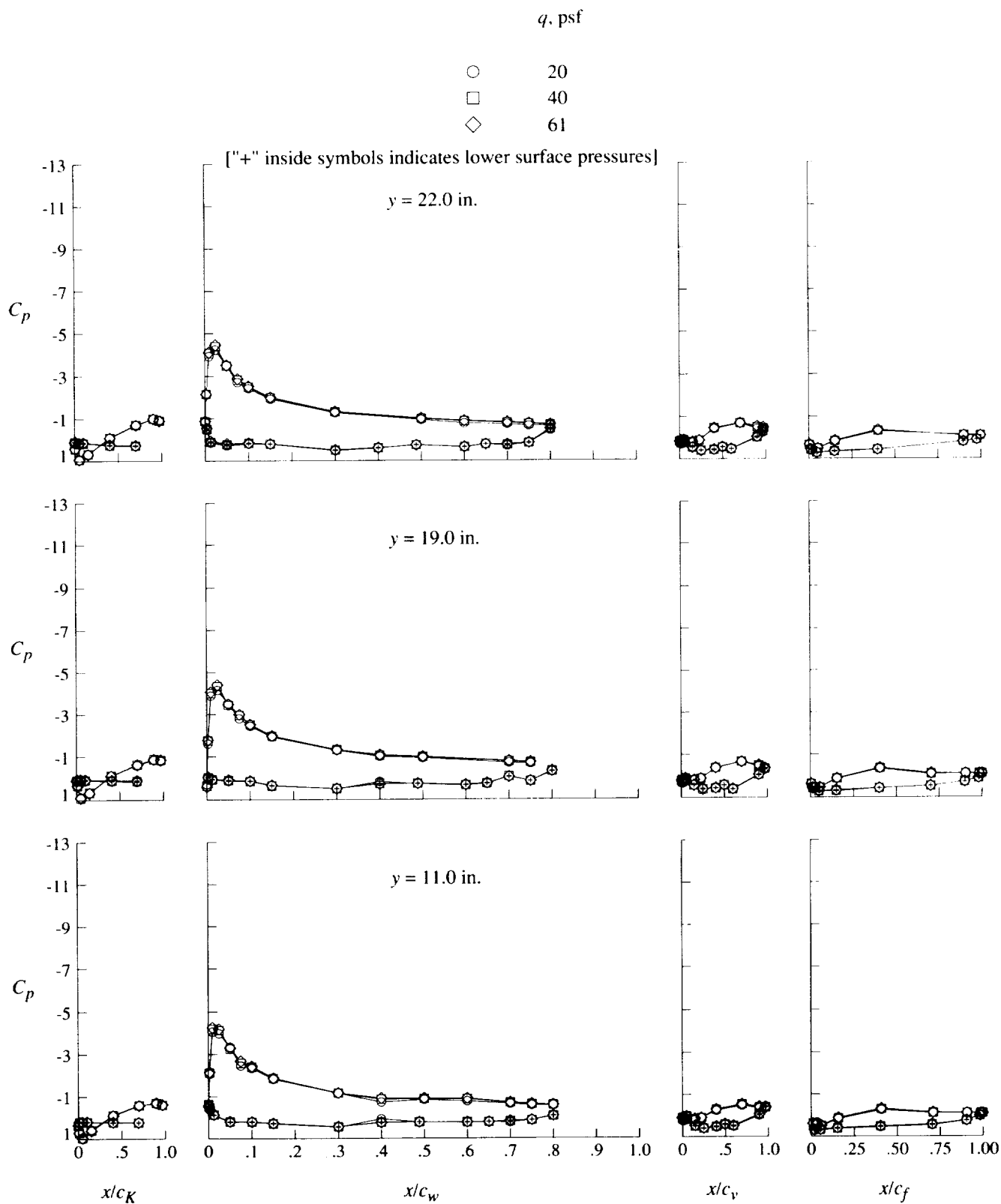
(c) $\alpha = 8^\circ$.

Figure 16. Continued.



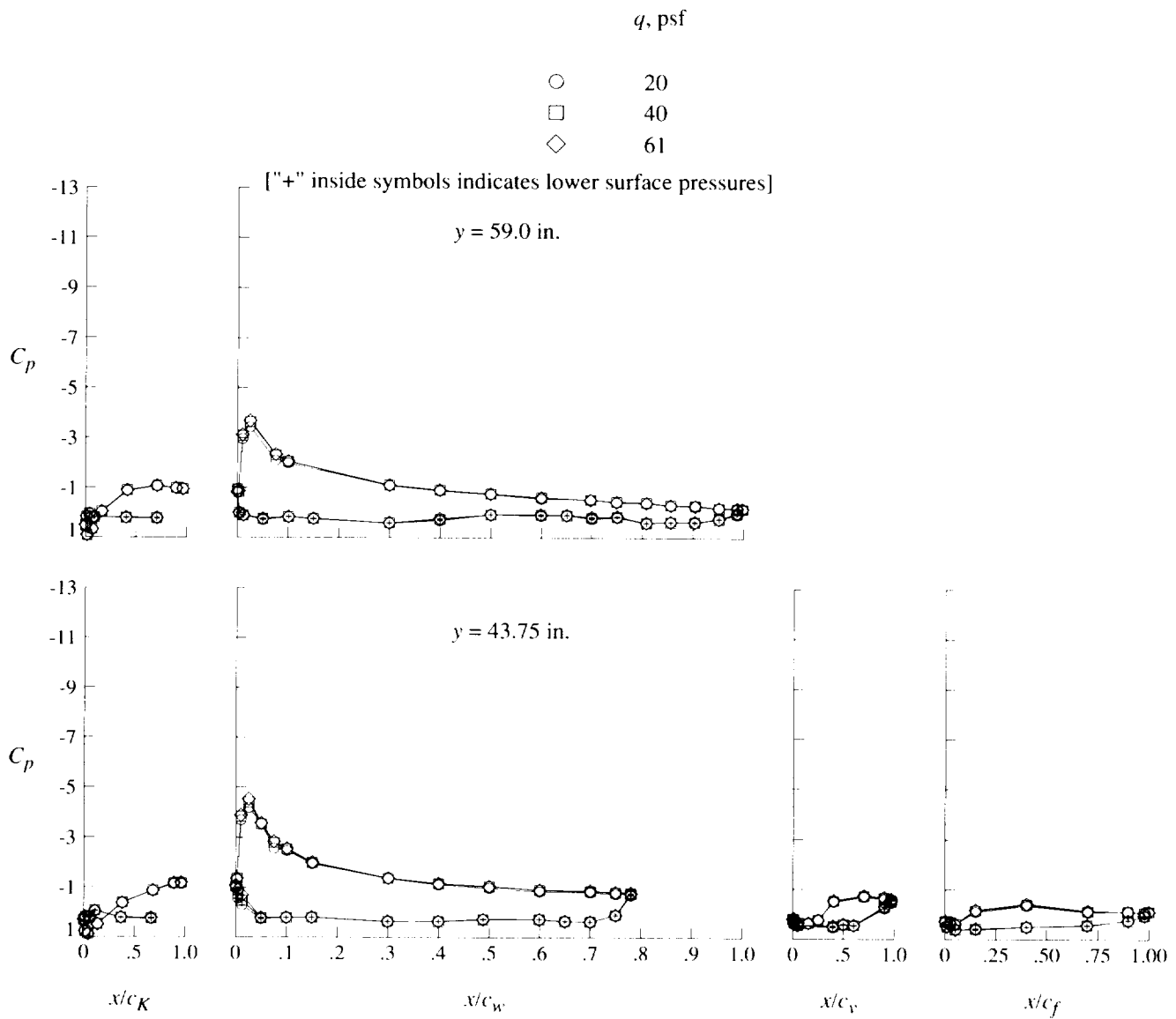
(c) Concluded.

Figure 16. Continued.



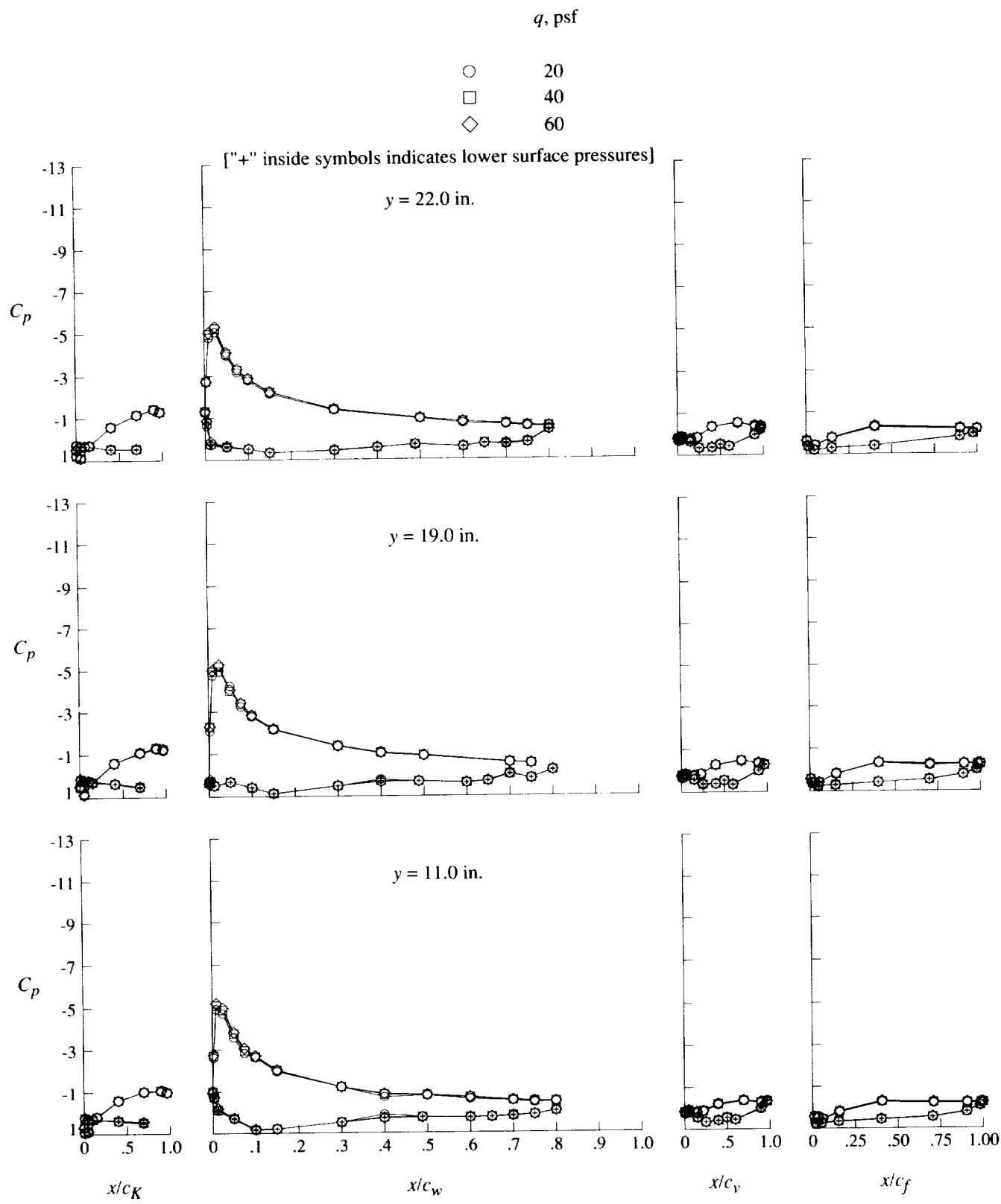
(d) $\alpha = 12^\circ$.

Figure 16. Continued.



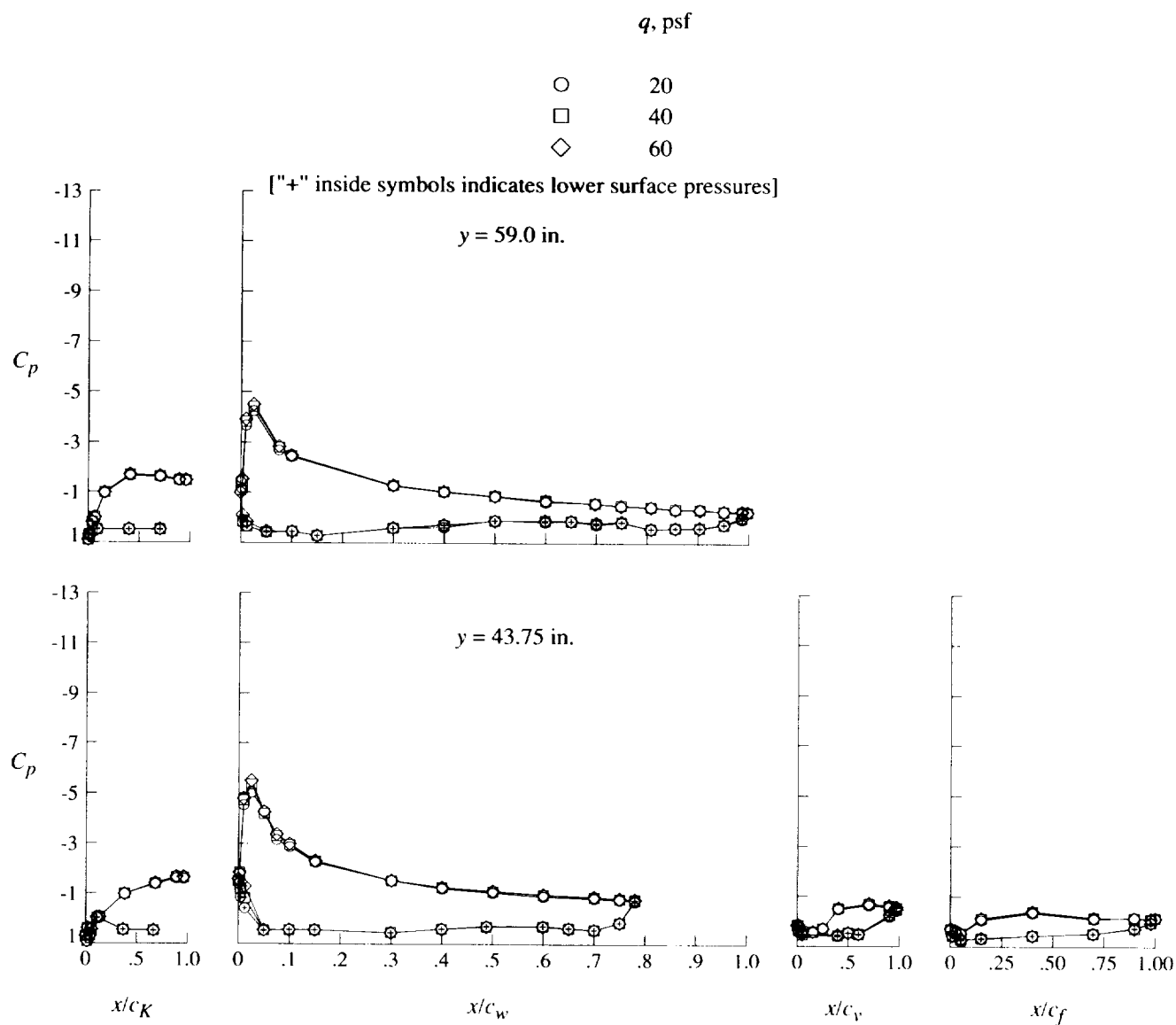
(d) Concluded.

Figure 16. Continued.



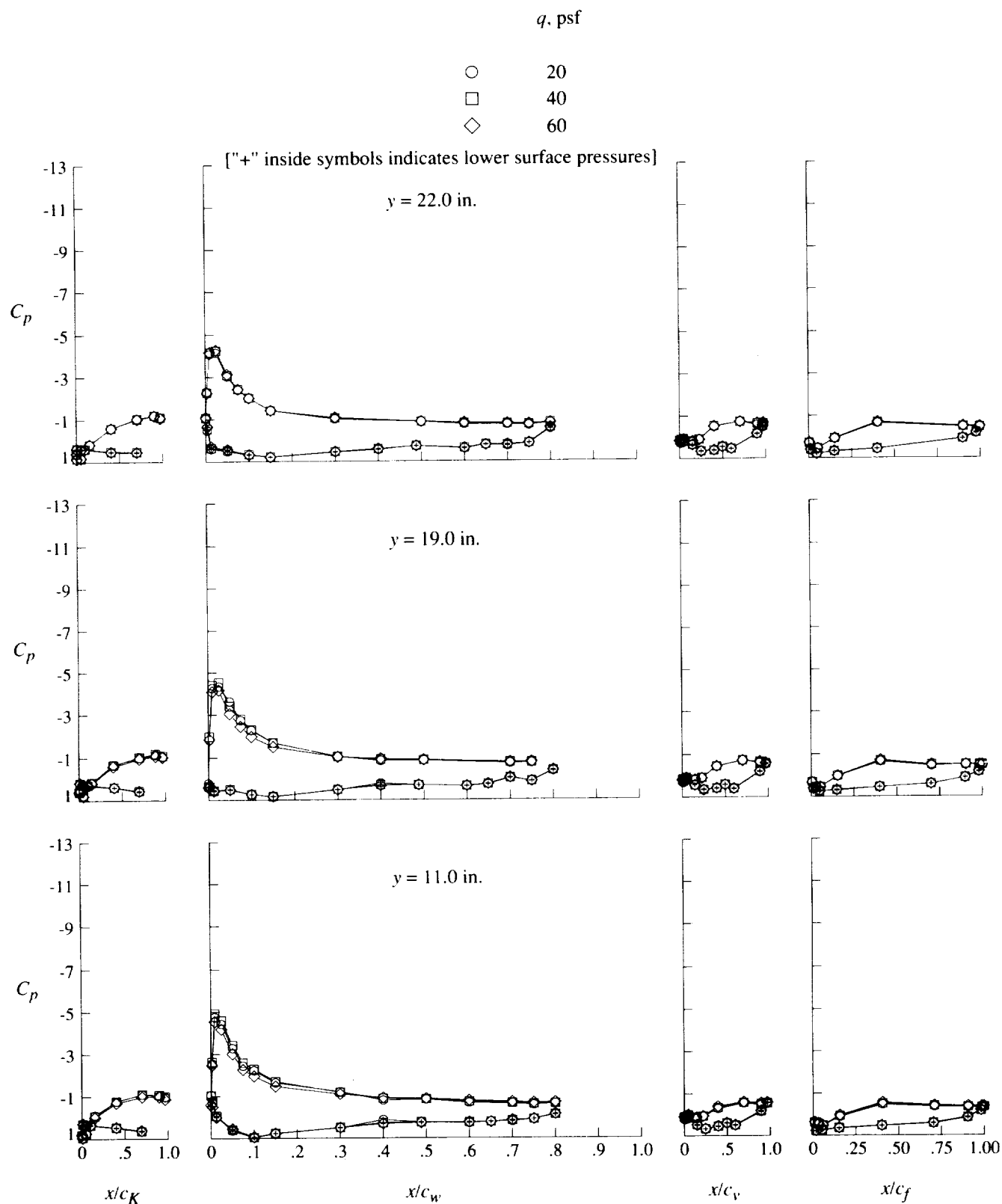
(e) $\alpha = 16^\circ$.

Figure 16. Continued.



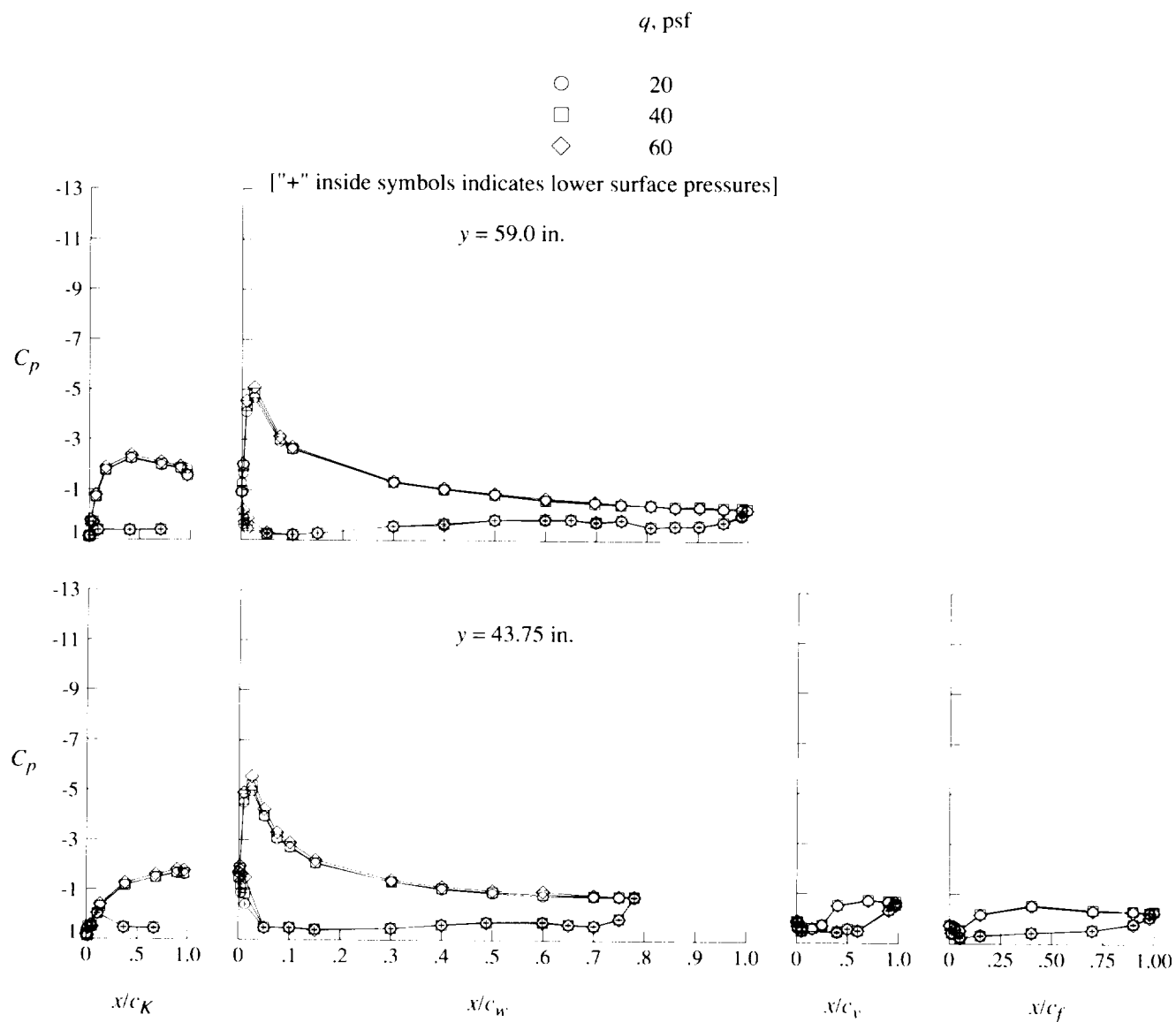
(e) Concluded.

Figure 16. Continued.



(f) $\alpha = 20^\circ$.

Figure 16. Continued.



(f) Concluded.

Figure 16. Concluded.

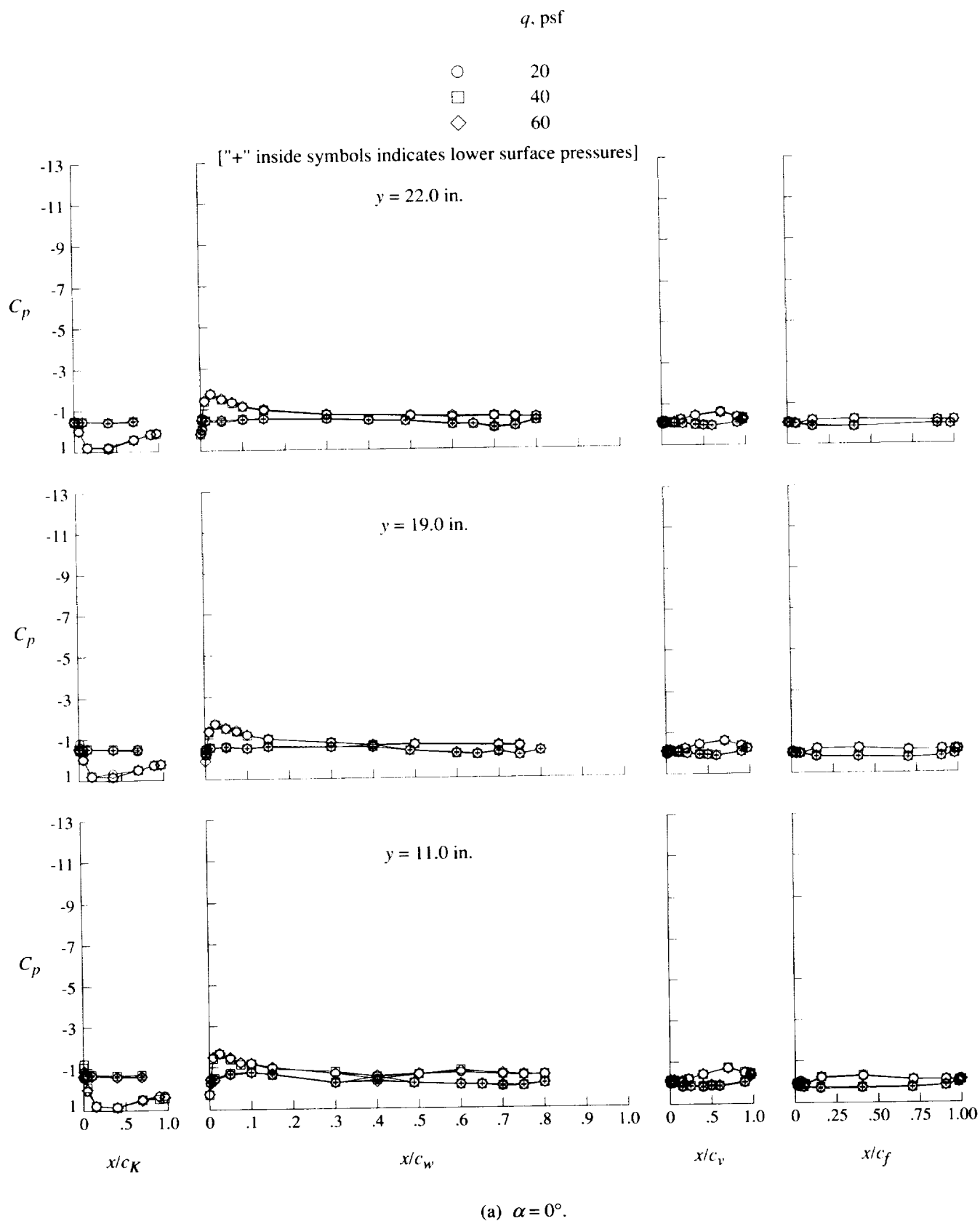
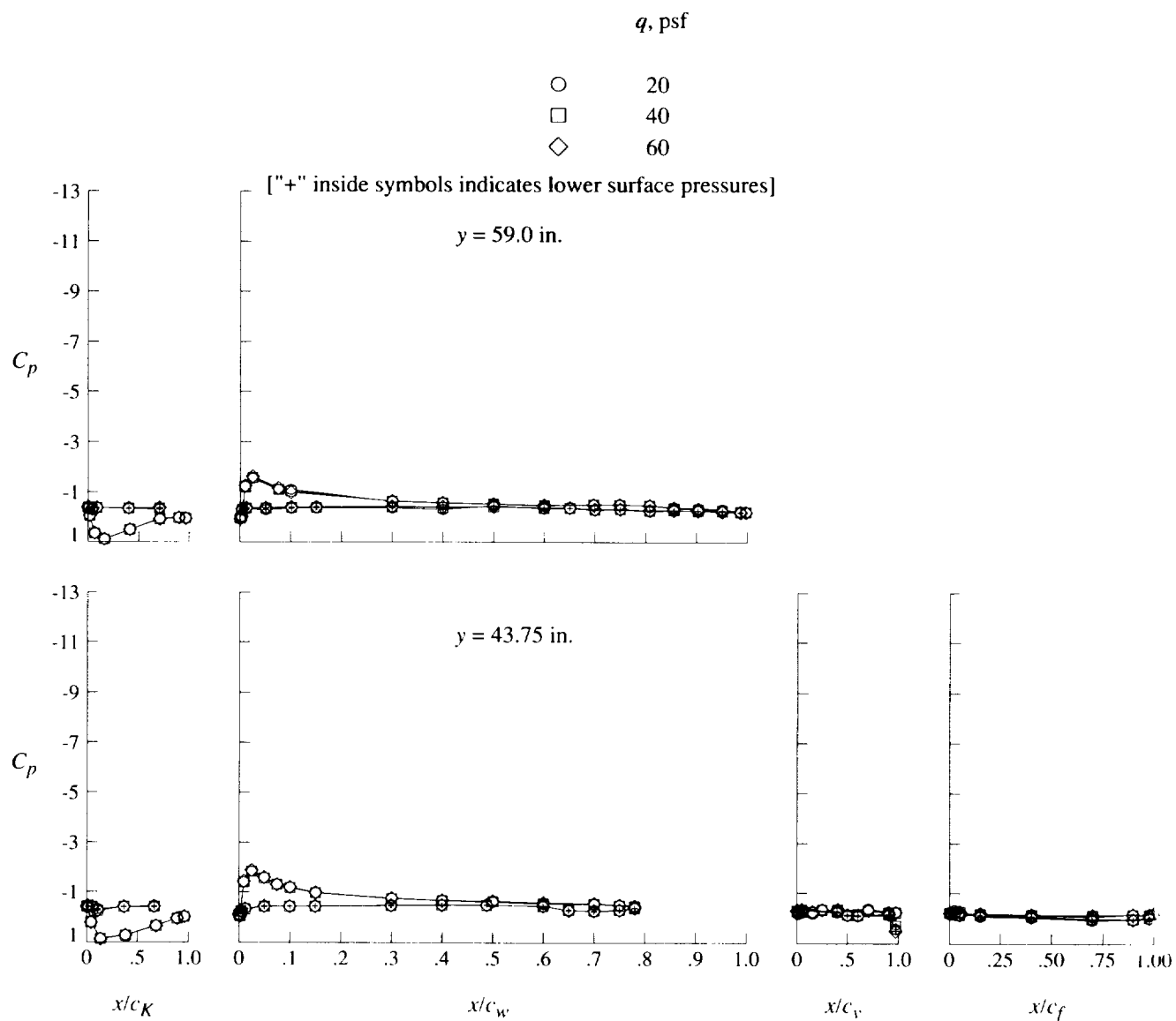


Figure 17. Effect of free-stream speed on pressure distributions for high-lift configuration at $\delta_f = 30^\circ$.



(a) Concluded.

Figure 17. Continued.

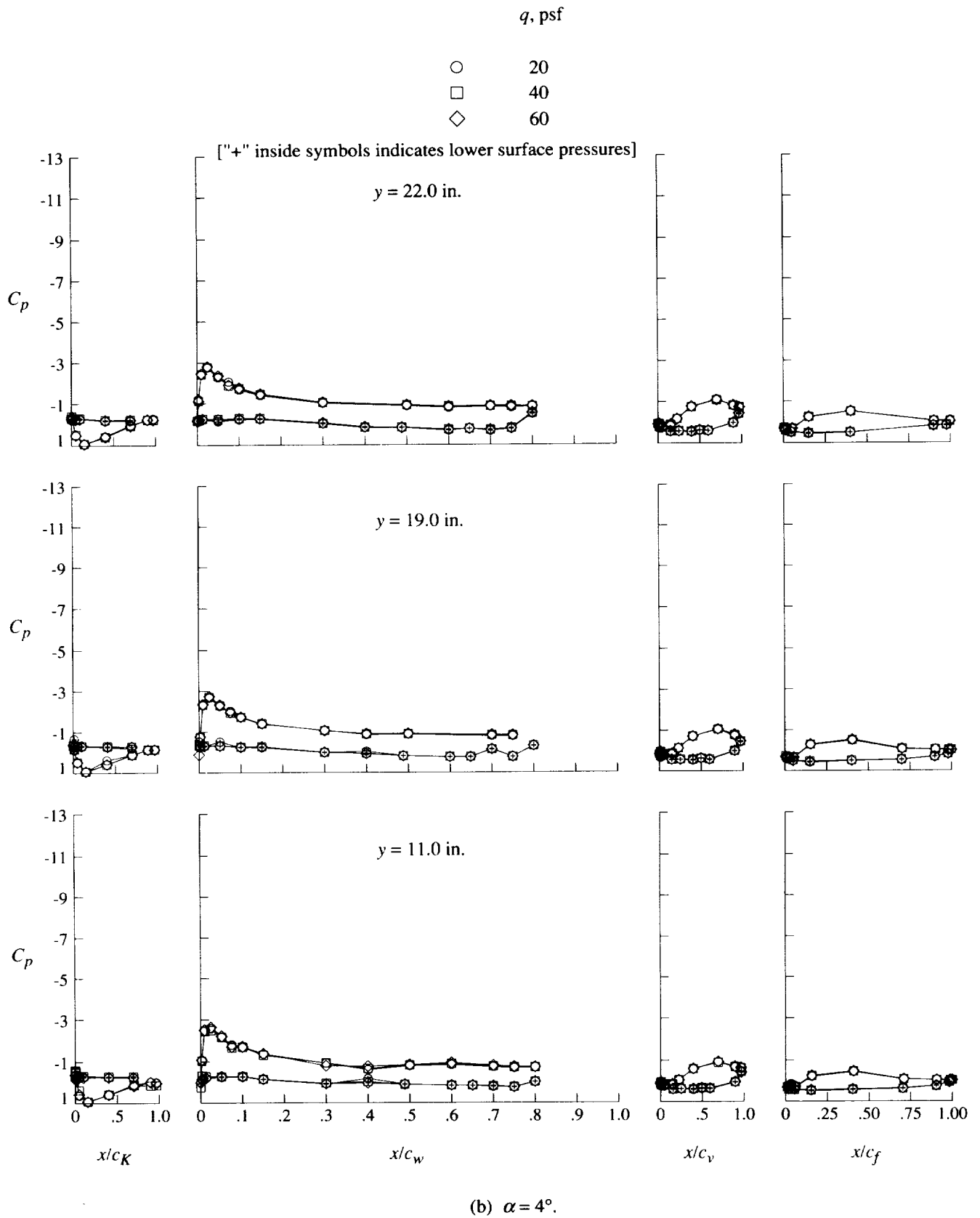
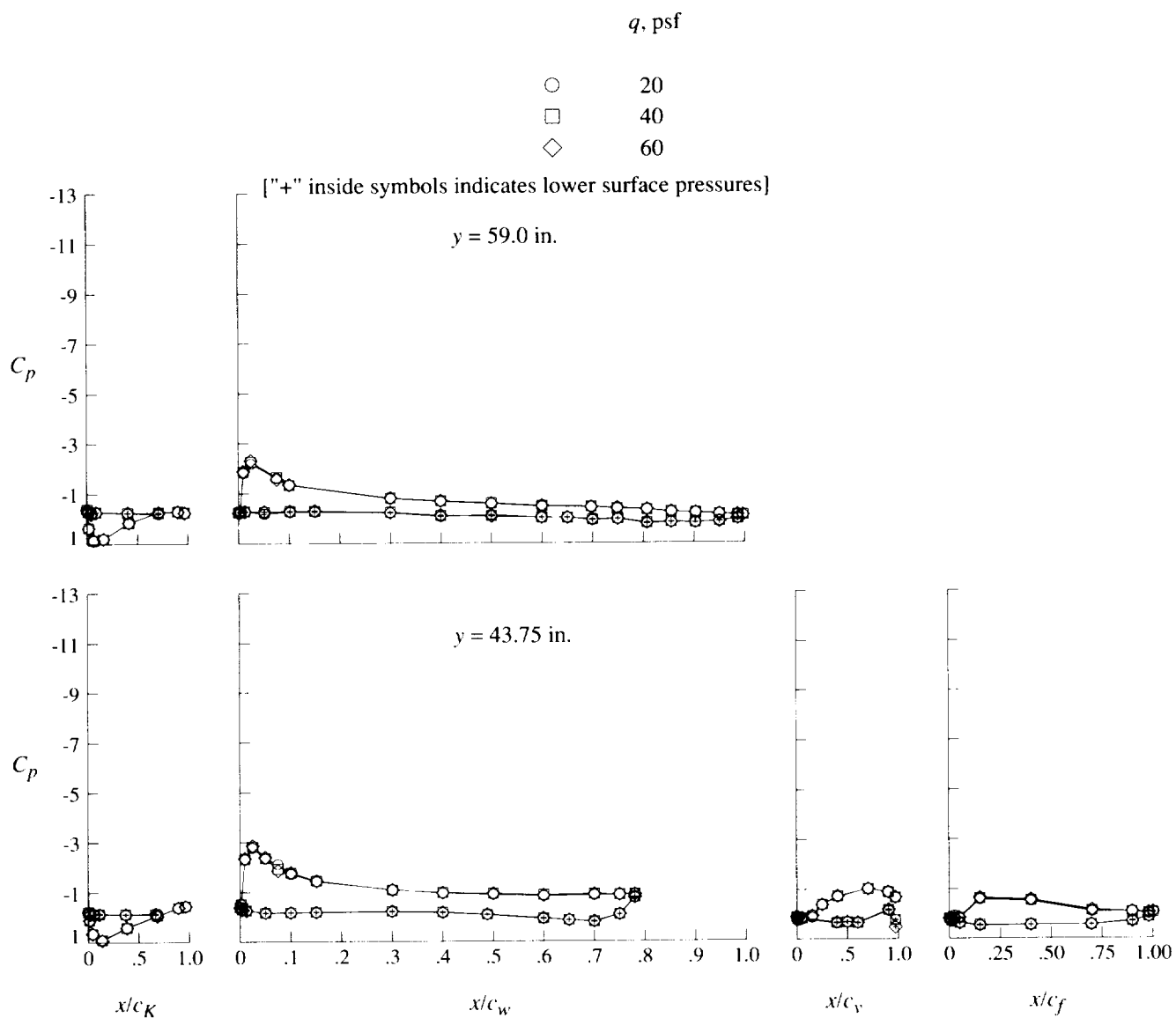
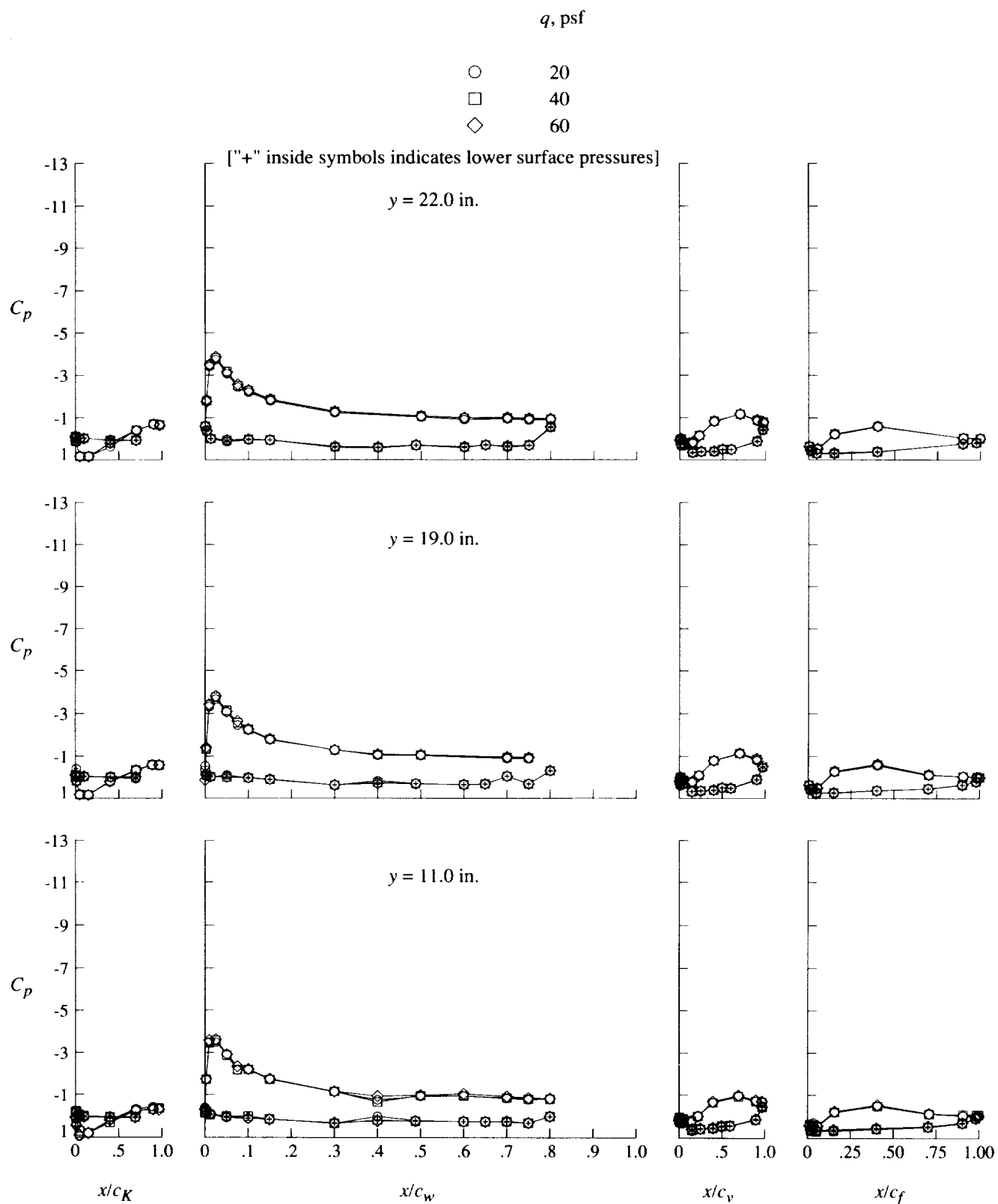


Figure 17. Continued.



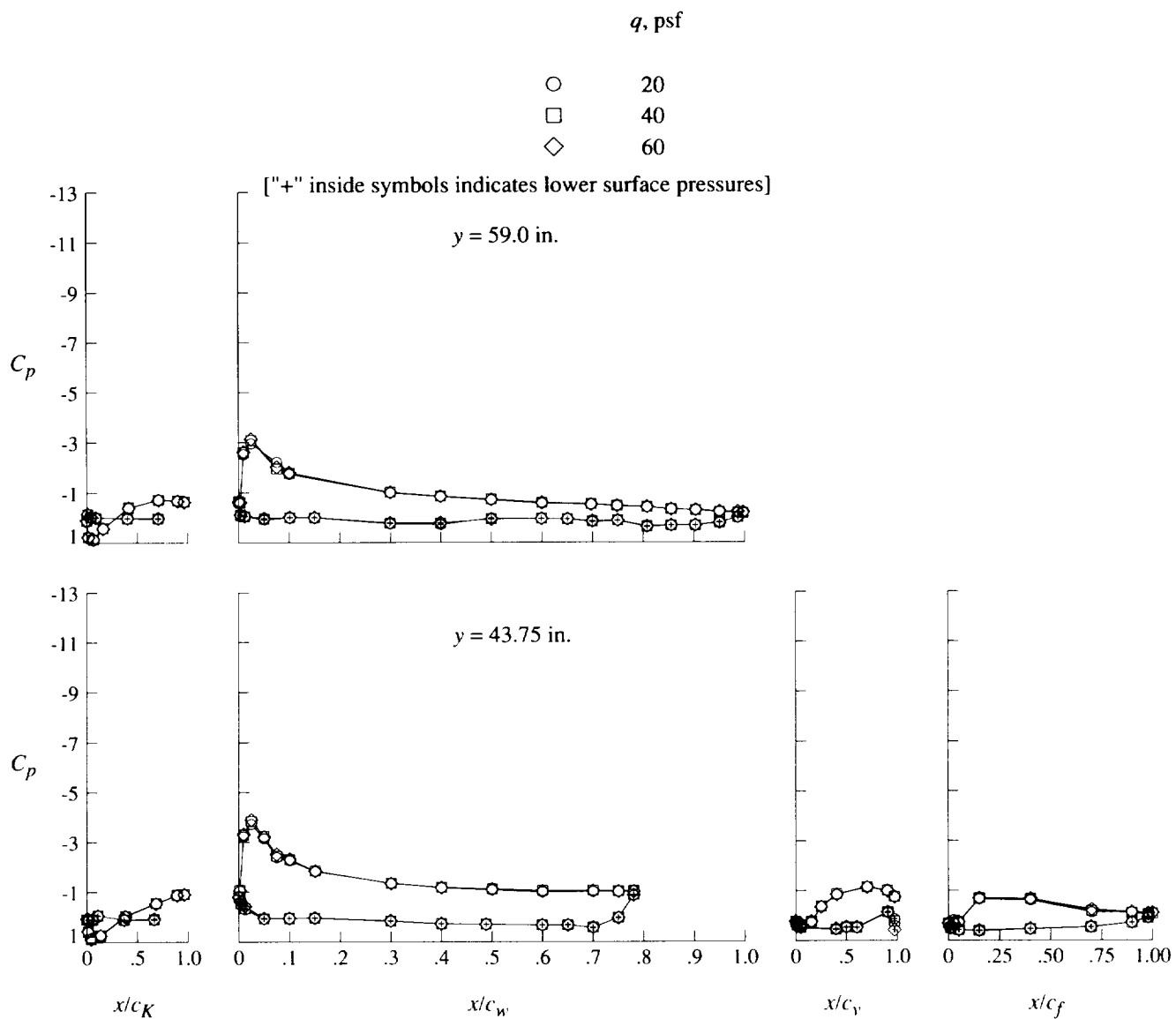
(b) Concluded.

Figure 17. Continued.



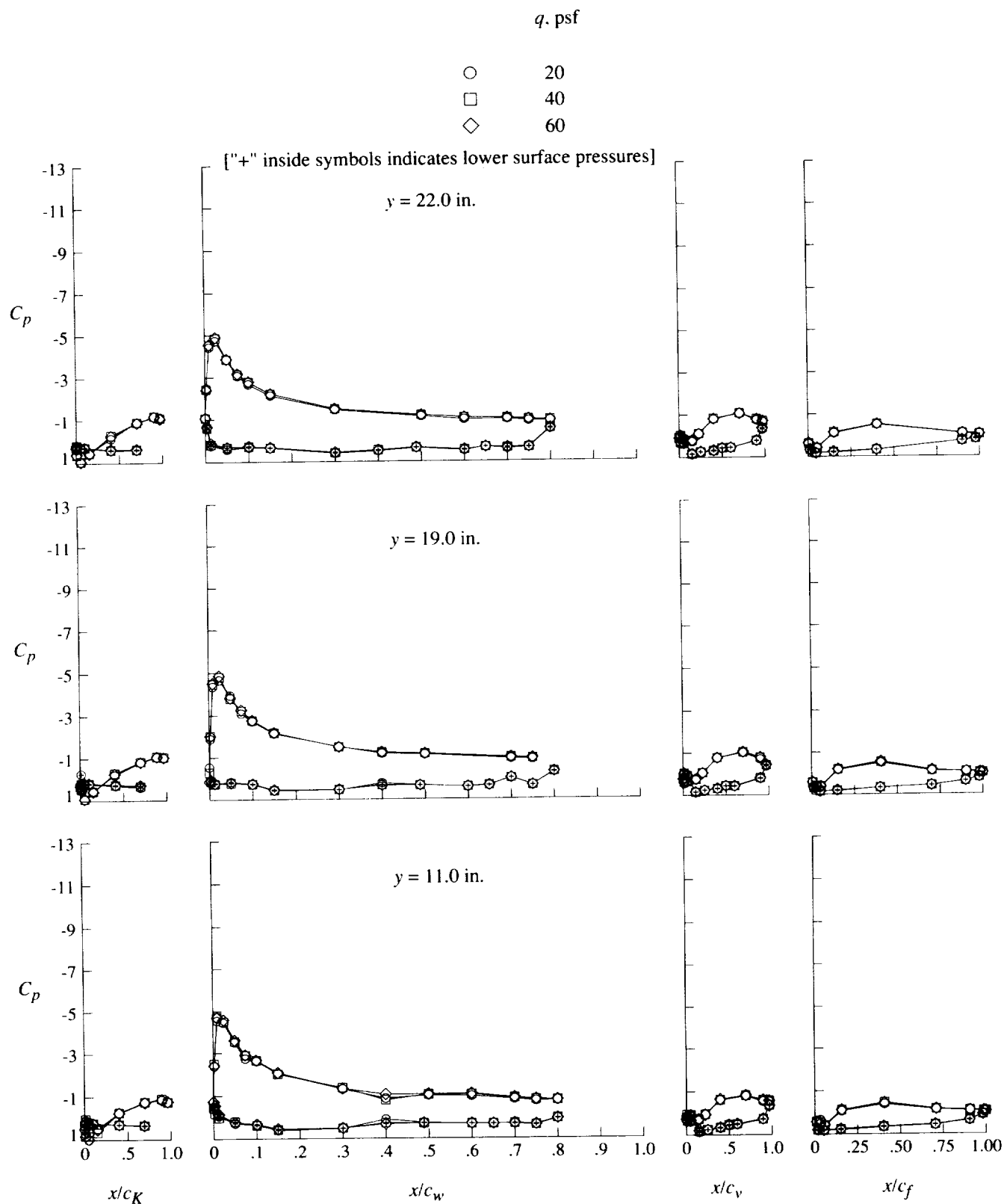
(c) $\alpha = 8^\circ$.

Figure 17. Continued.



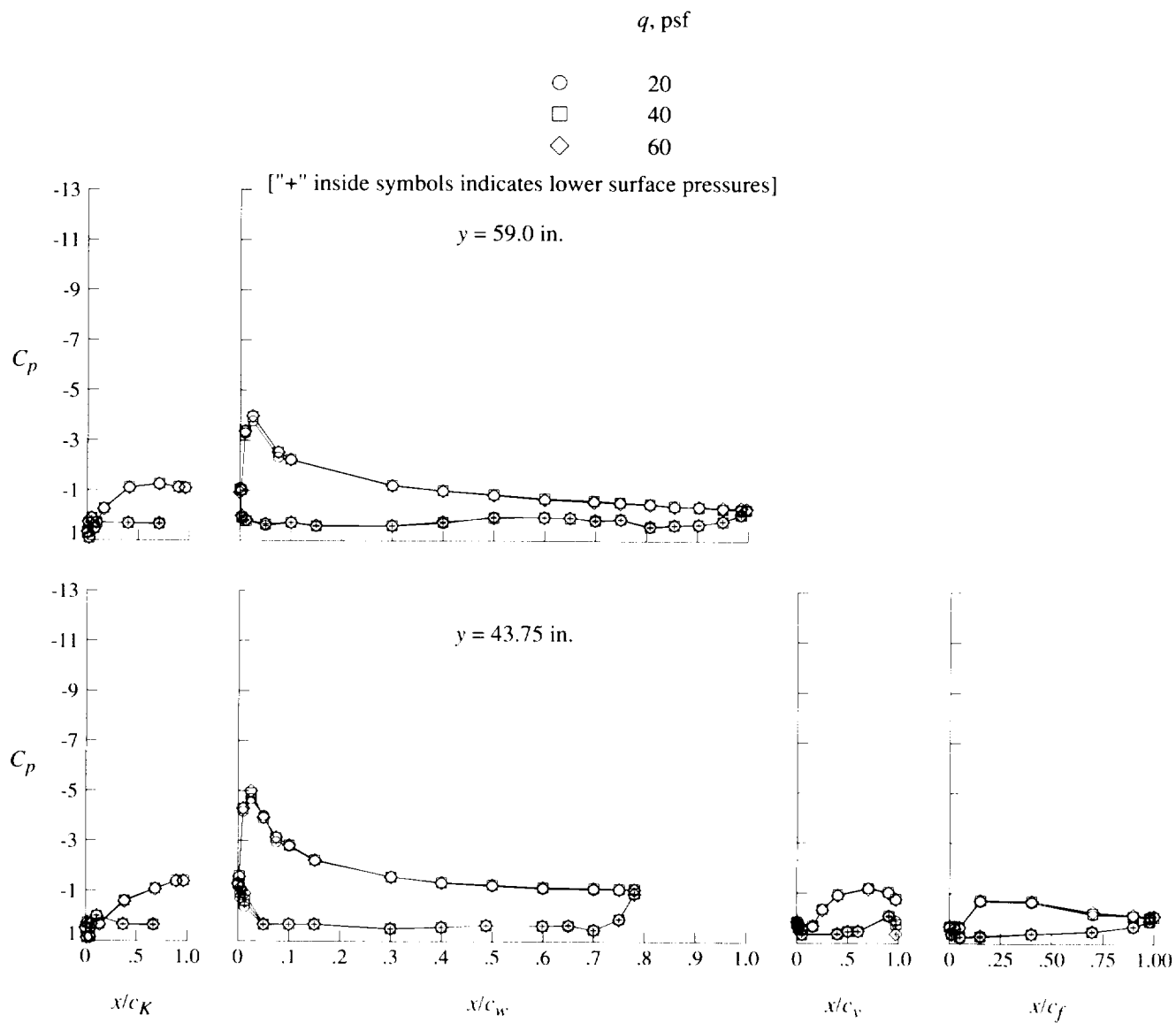
(c) Concluded.

Figure 17. Continued.



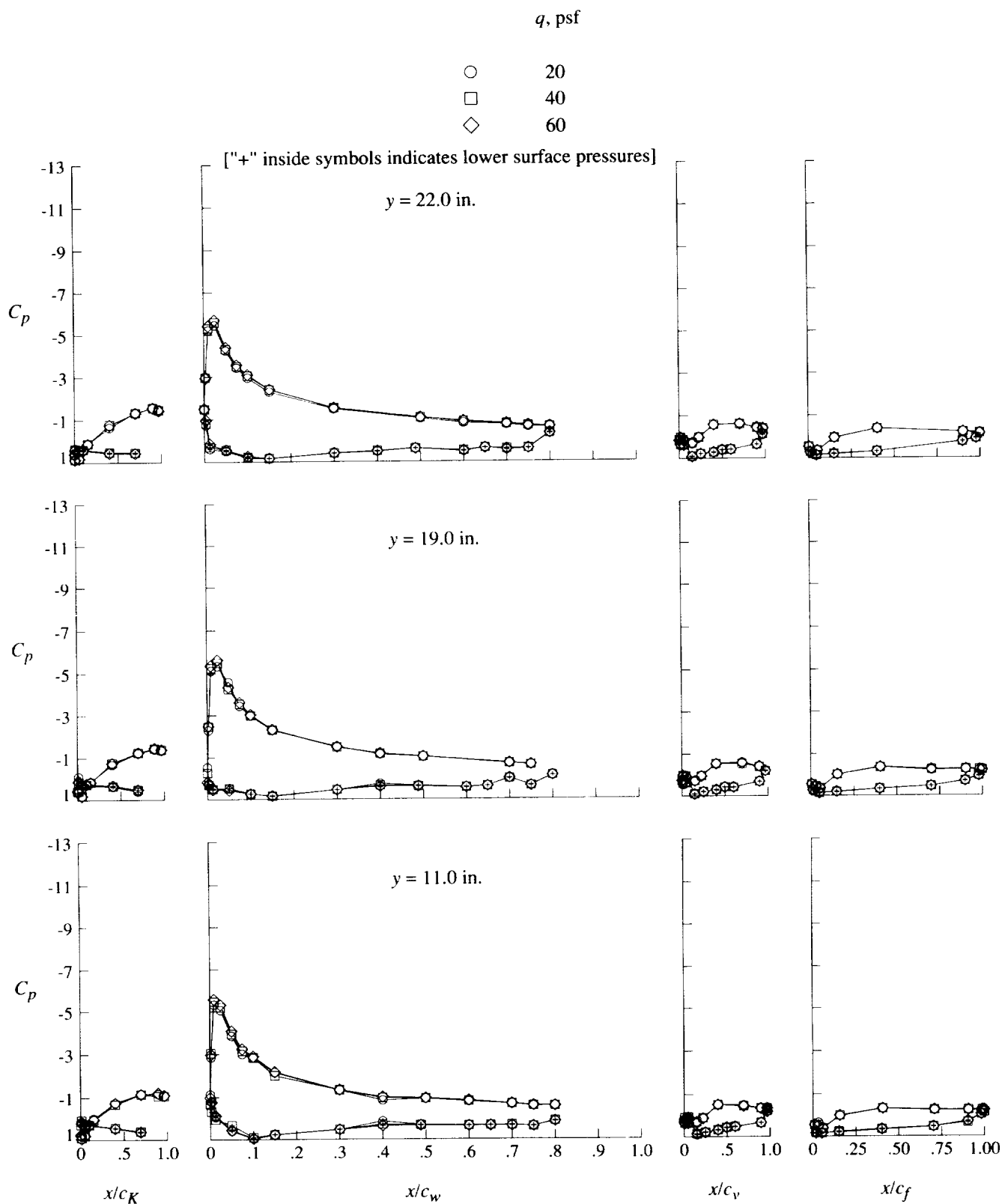
(d) $\alpha = 12^\circ$.

Figure 17. Continued.



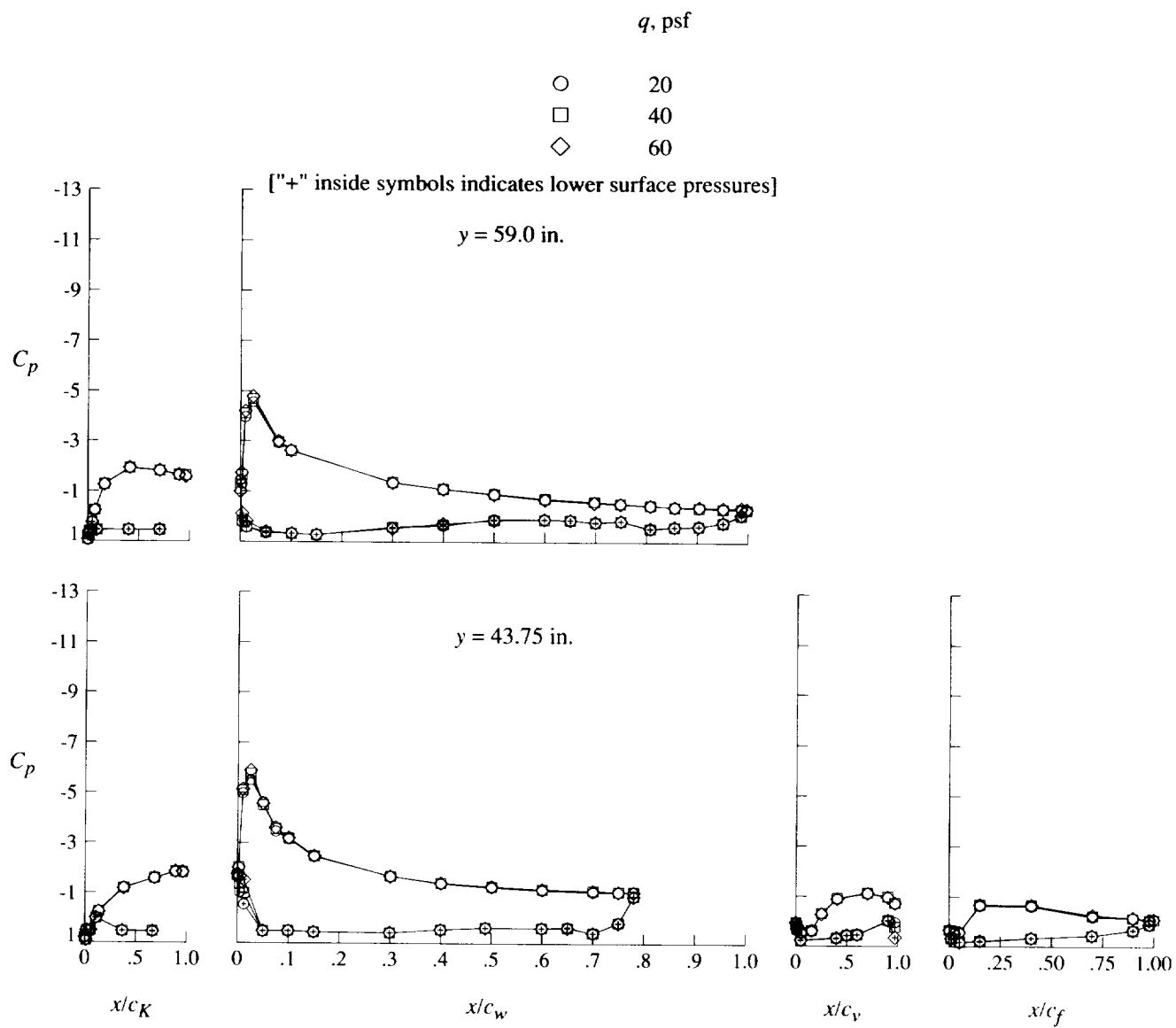
(d) Concluded.

Figure 17. Continued.



(e) $\alpha = 16^\circ$.

Figure 17. Continued.



(e) Concluded.

Figure 17. Continued.

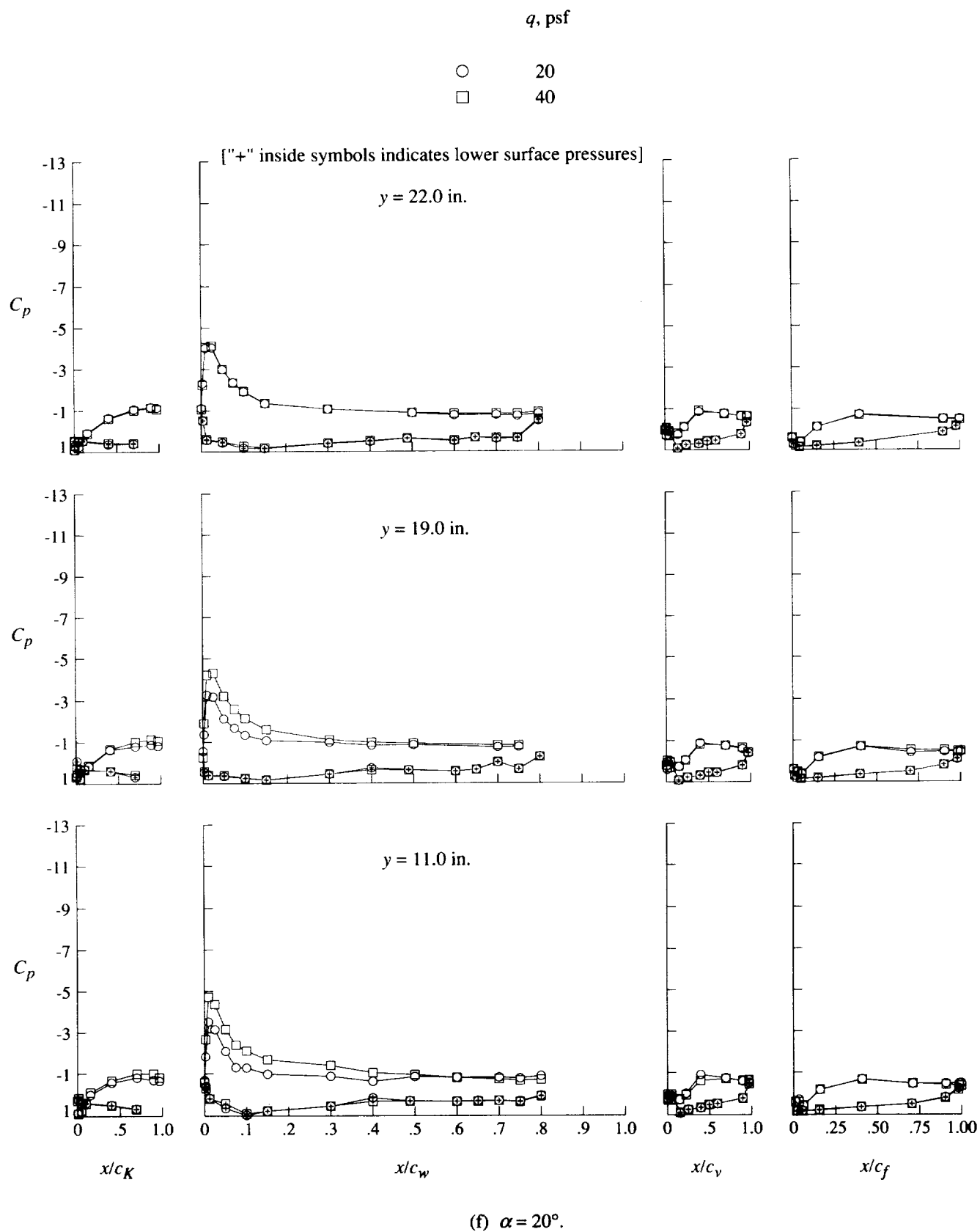
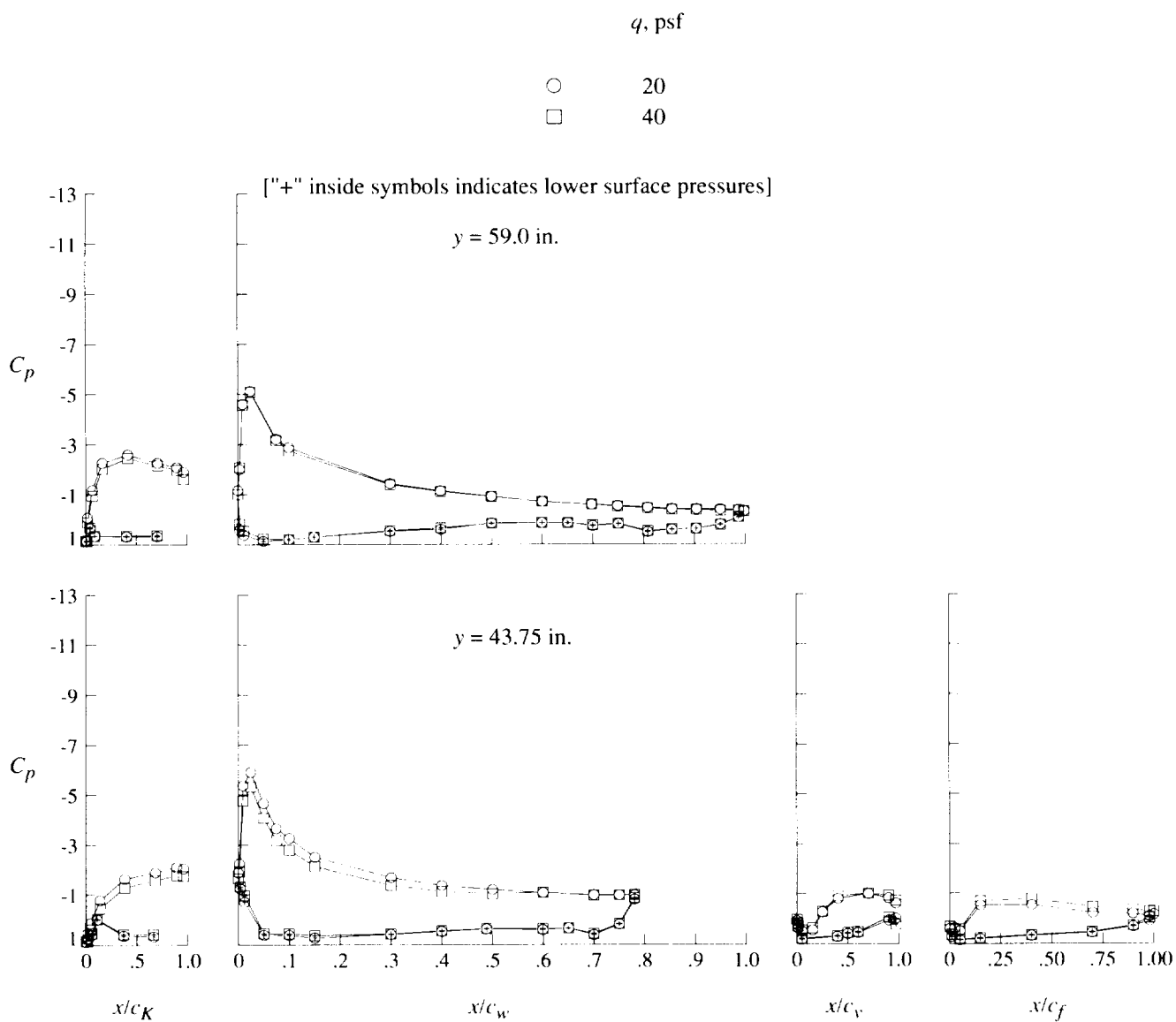


Figure 17. Continued.



(f) Concluded.

Figure 17. Concluded.

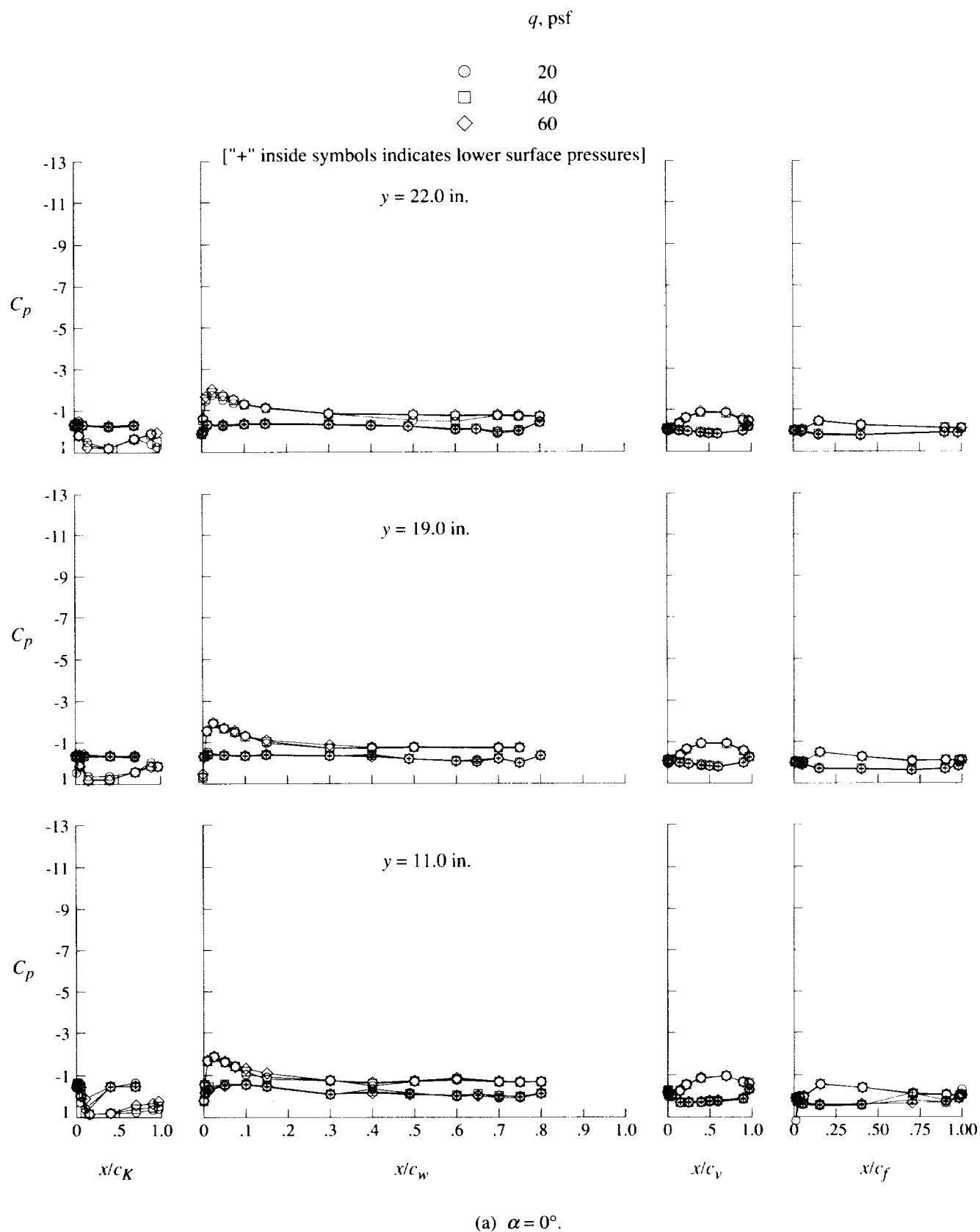
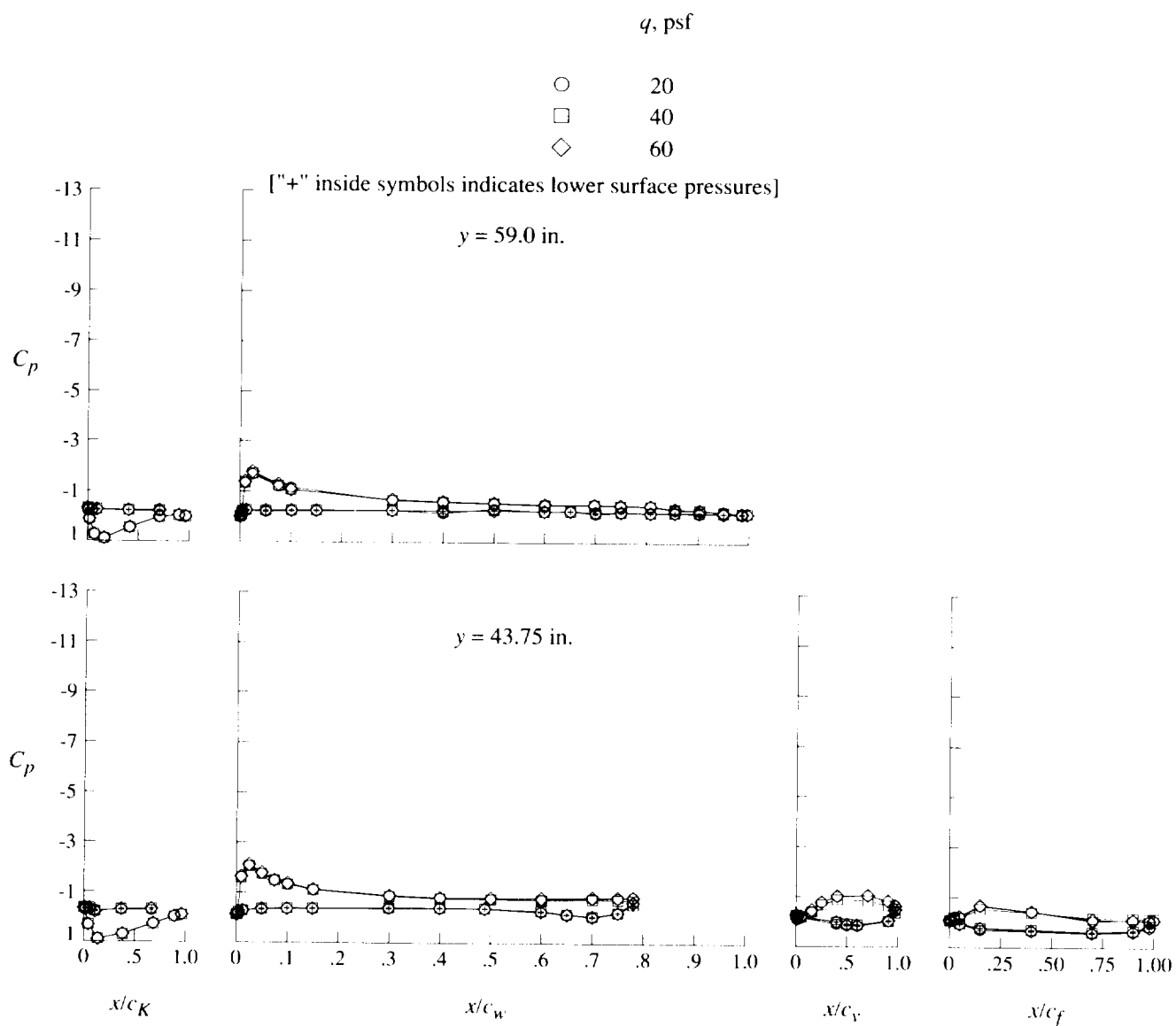
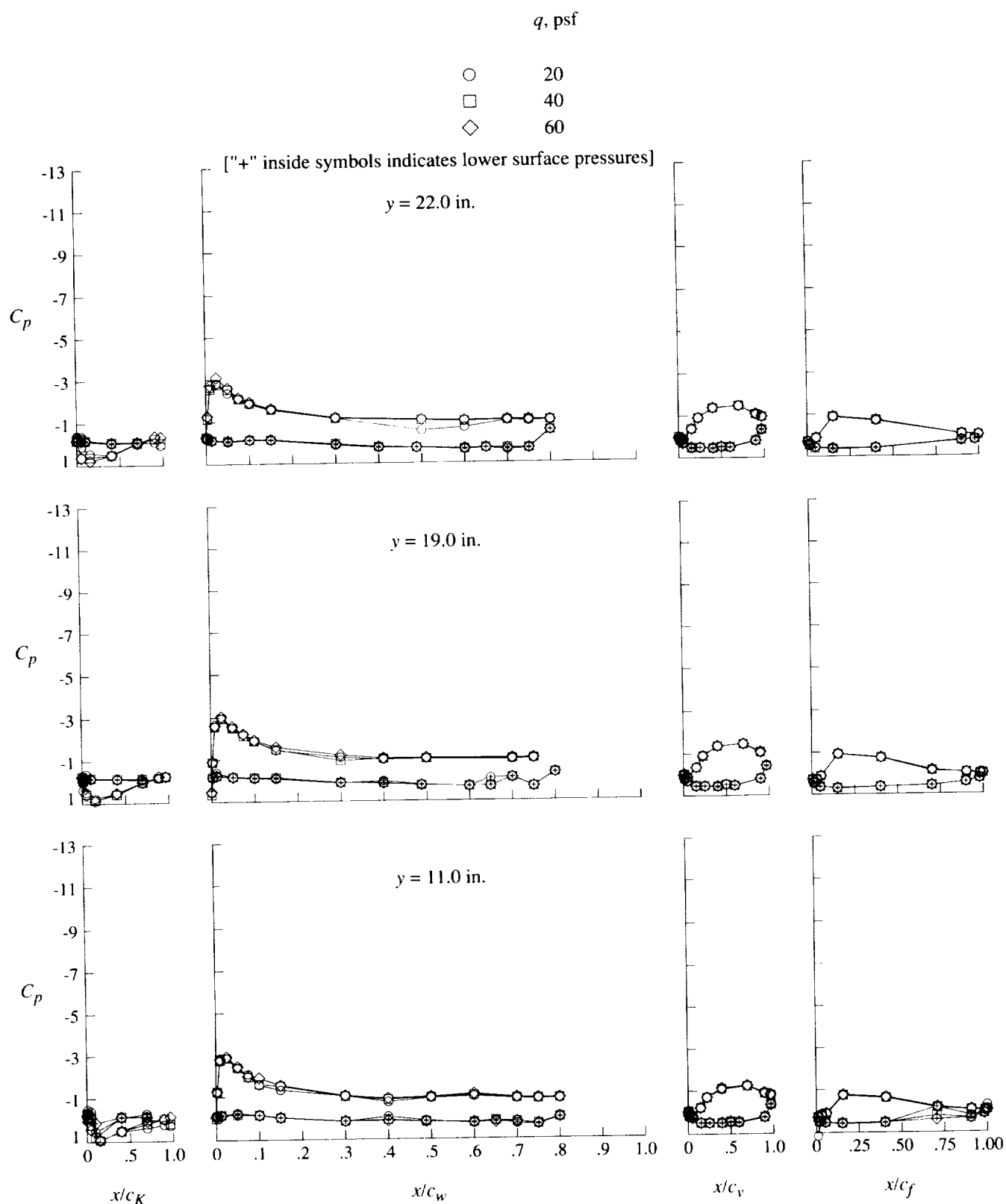


Figure 18. Effect of free-stream speed on pressure distributions for high-lift configuration at $\delta_f = 40^\circ$.



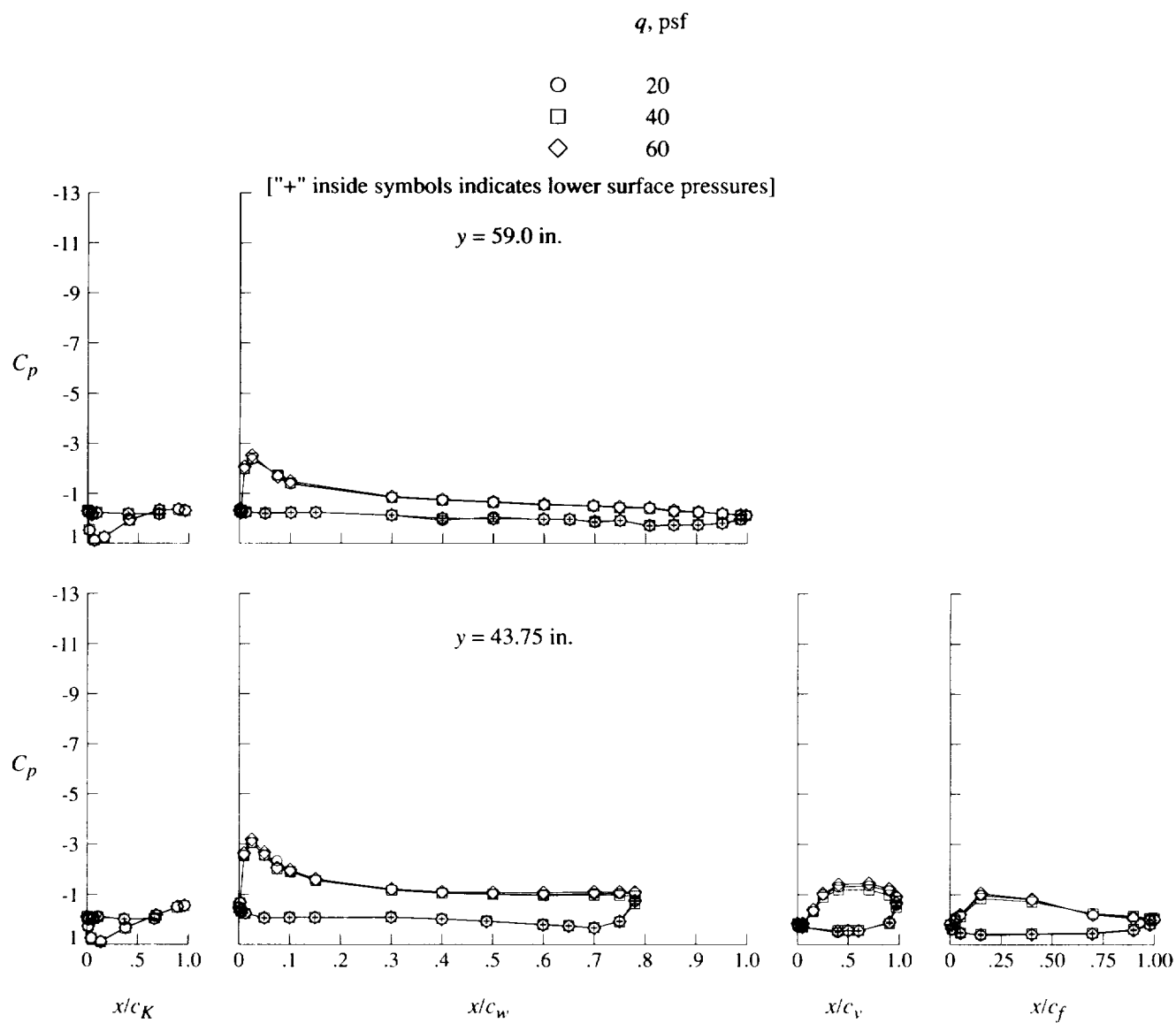
(a) Concluded.

Figure 18. Continued.



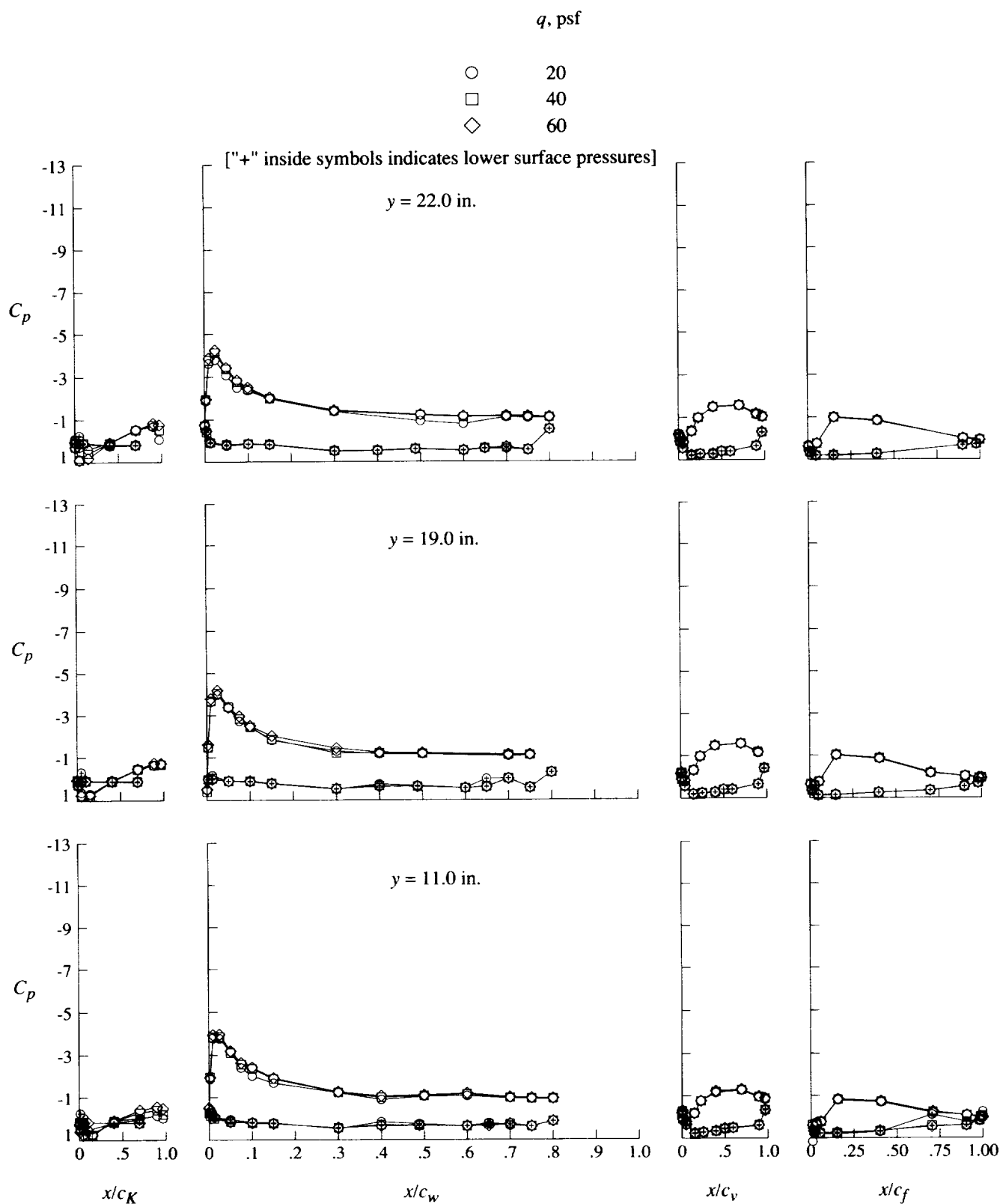
(b) $\alpha = 4^\circ$.

Figure 18. Continued.



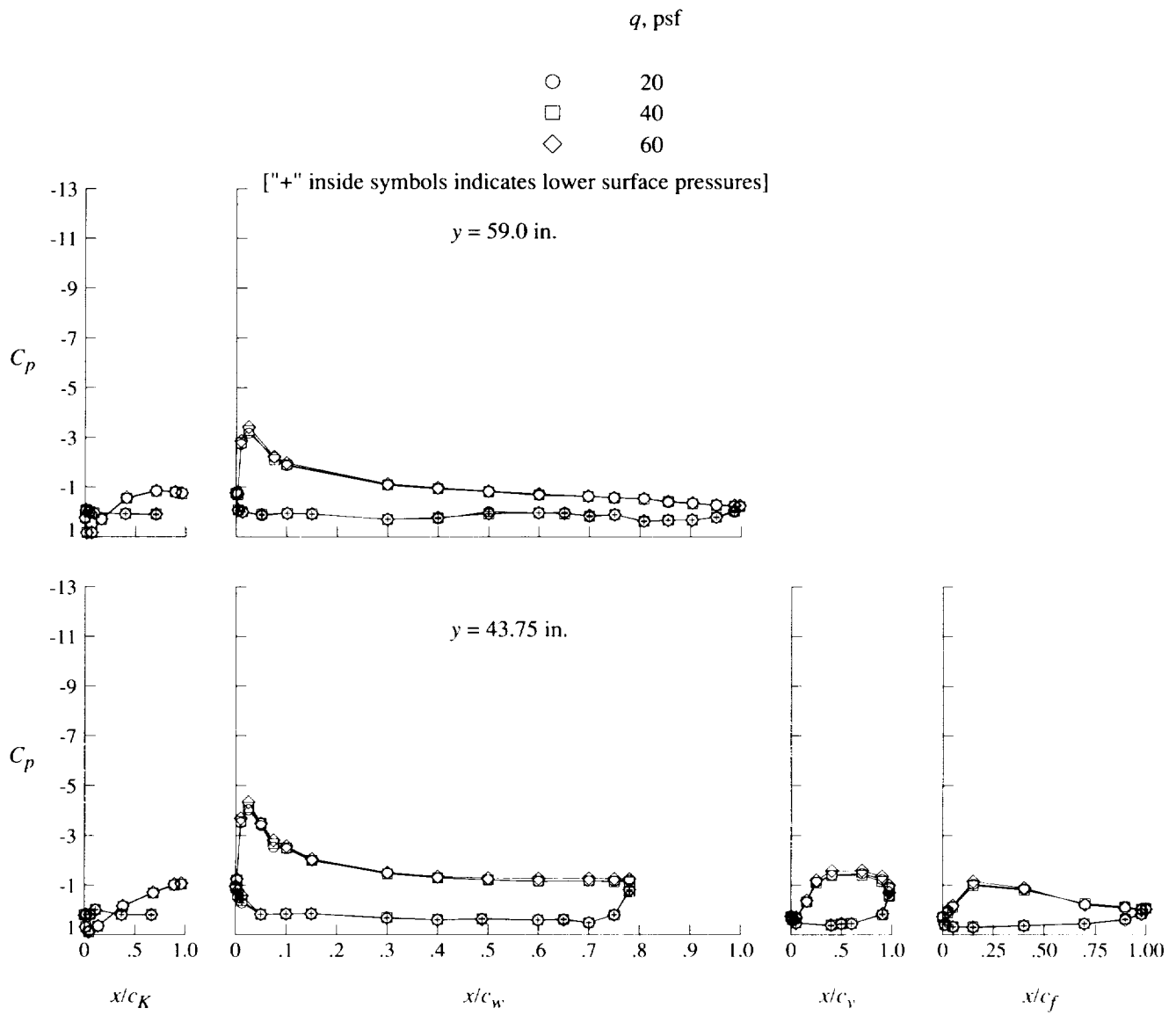
(b) Concluded.

Figure 18. Continued.



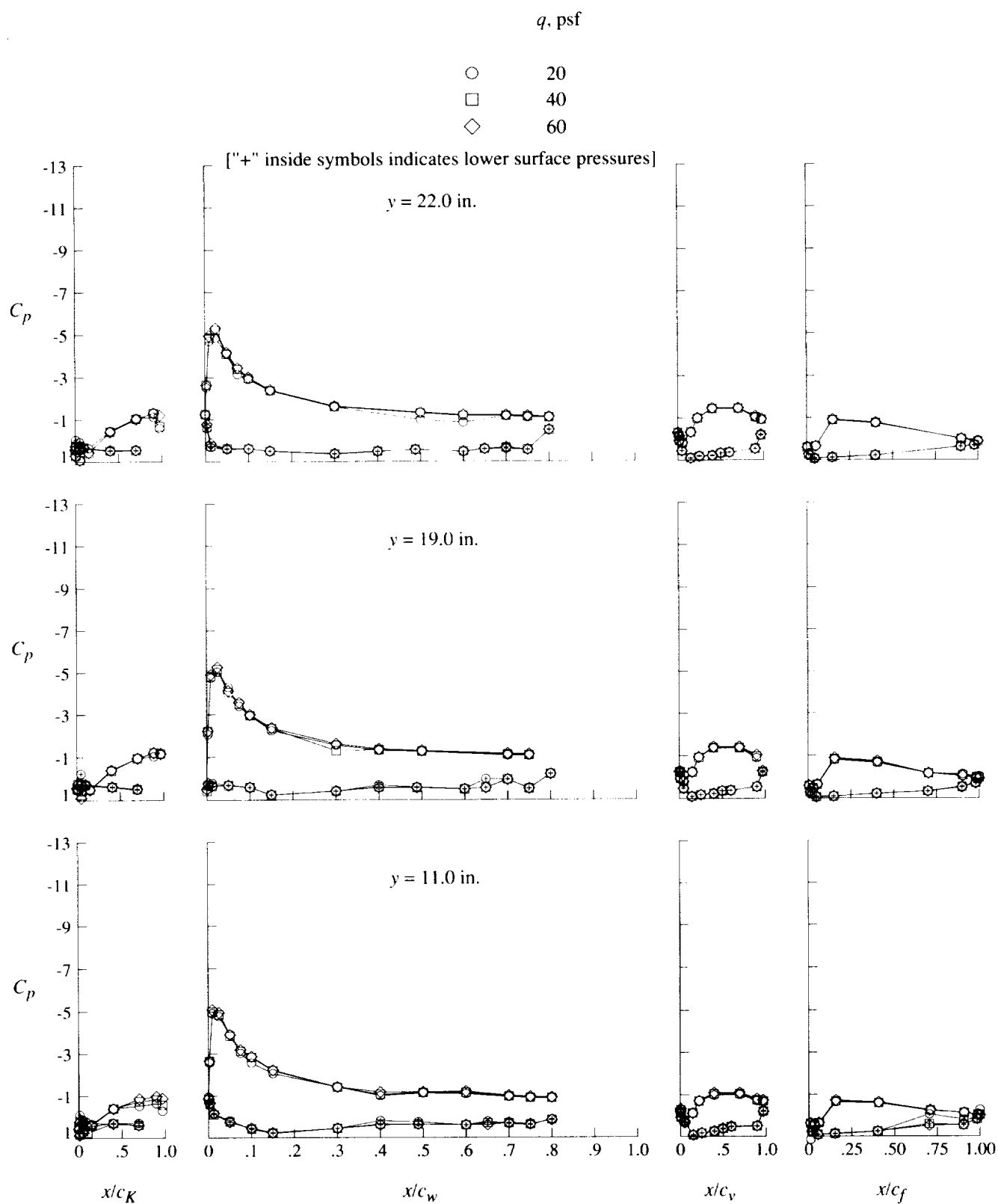
(c) $\alpha = 8^\circ$.

Figure 18. Continued.



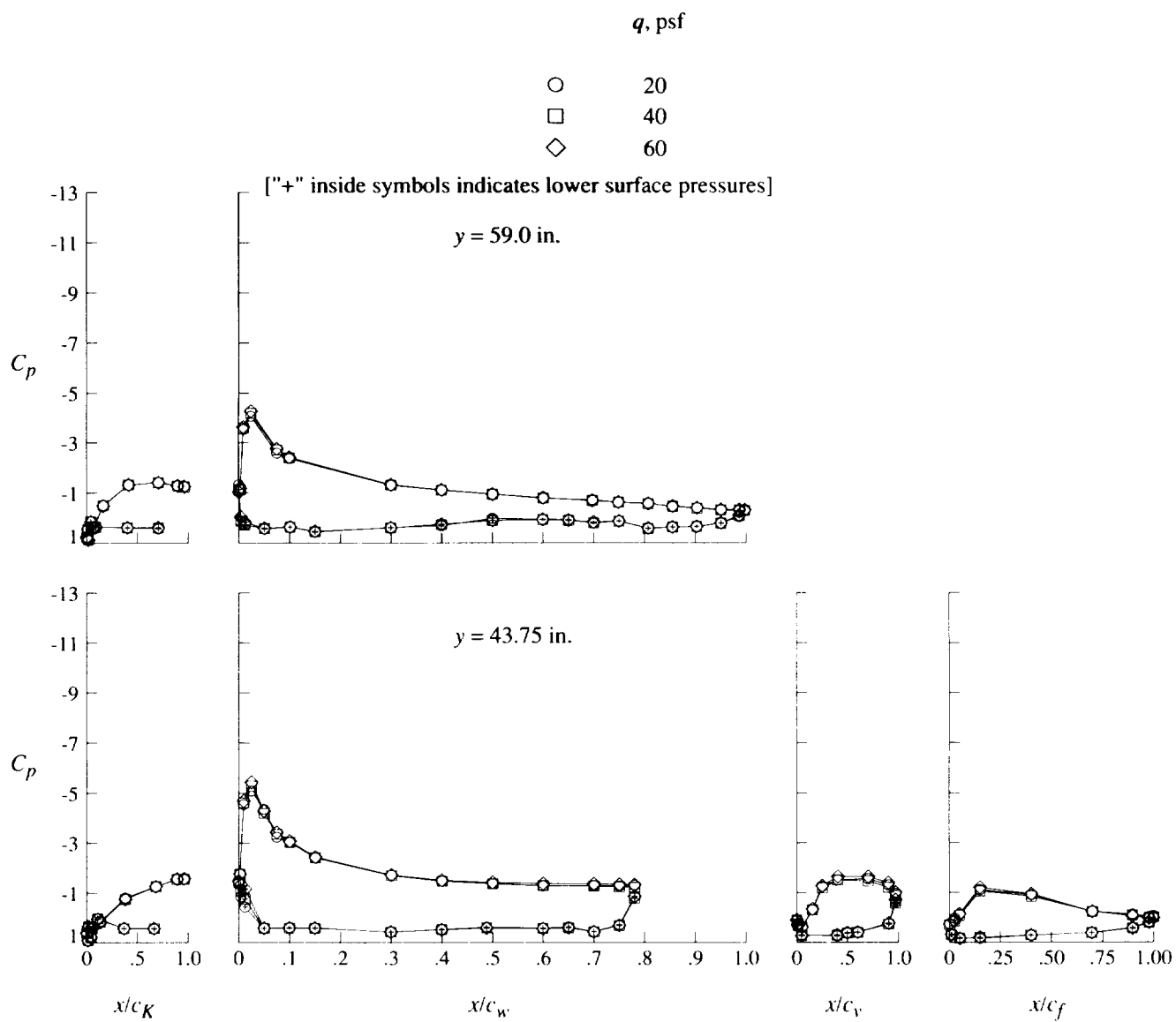
(c) Concluded.

Figure 18. Continued.



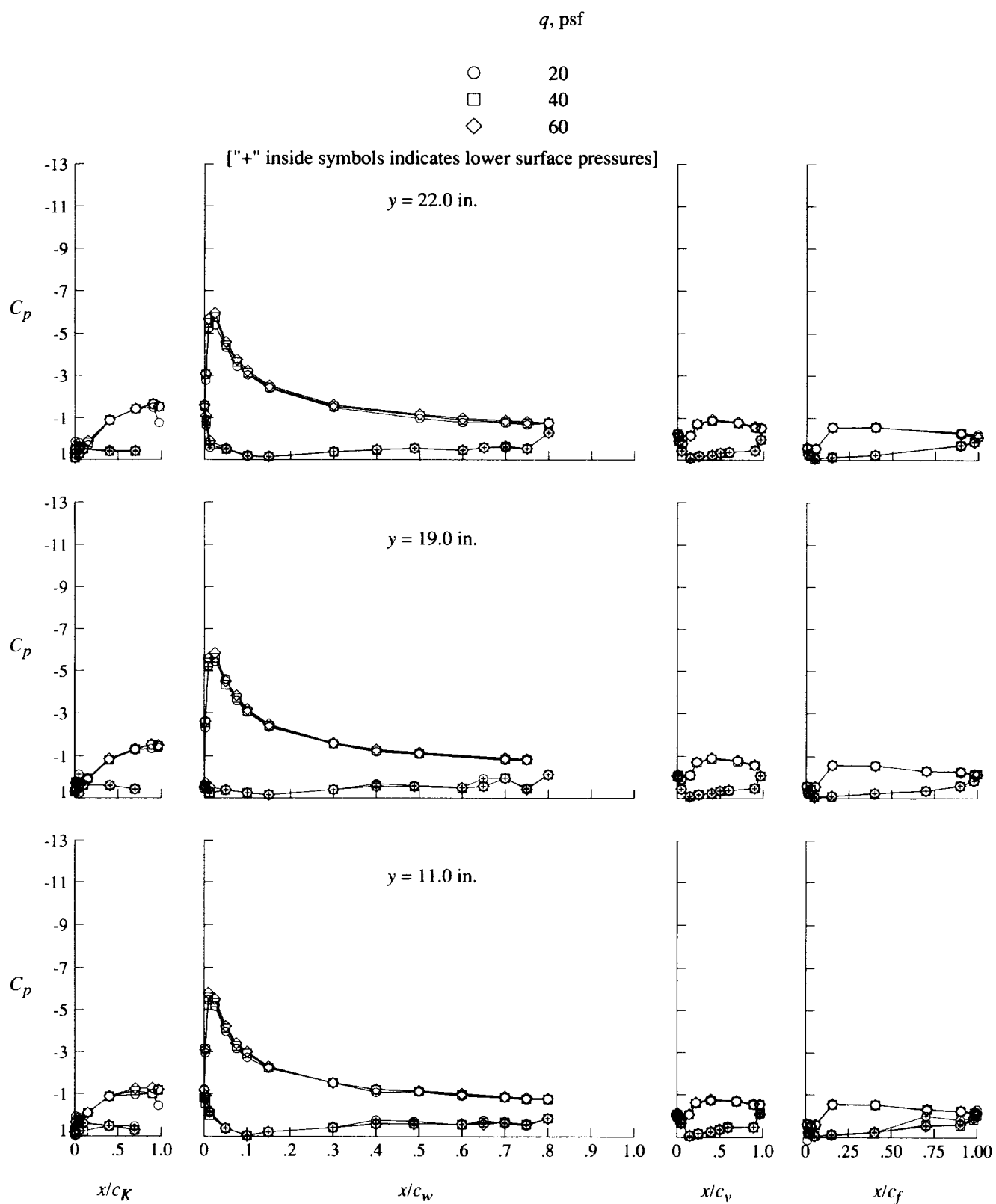
(d) $\alpha = 12^\circ$.

Figure 18. Continued.



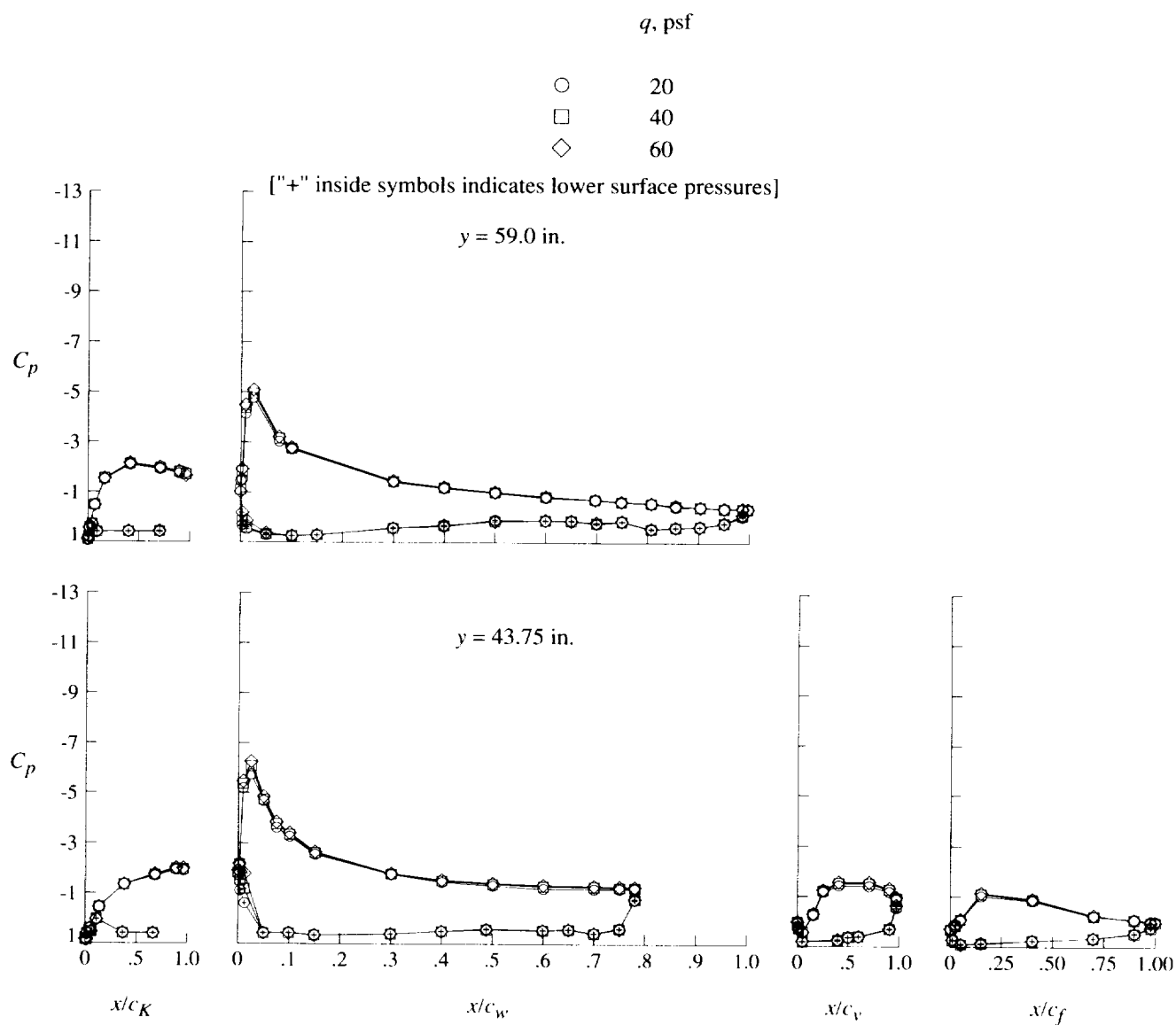
(d) Concluded.

Figure 18. Continued.



(e) $\alpha = 16^\circ$.

Figure 18. Continued.



(e) Concluded.

Figure 18. Continued.

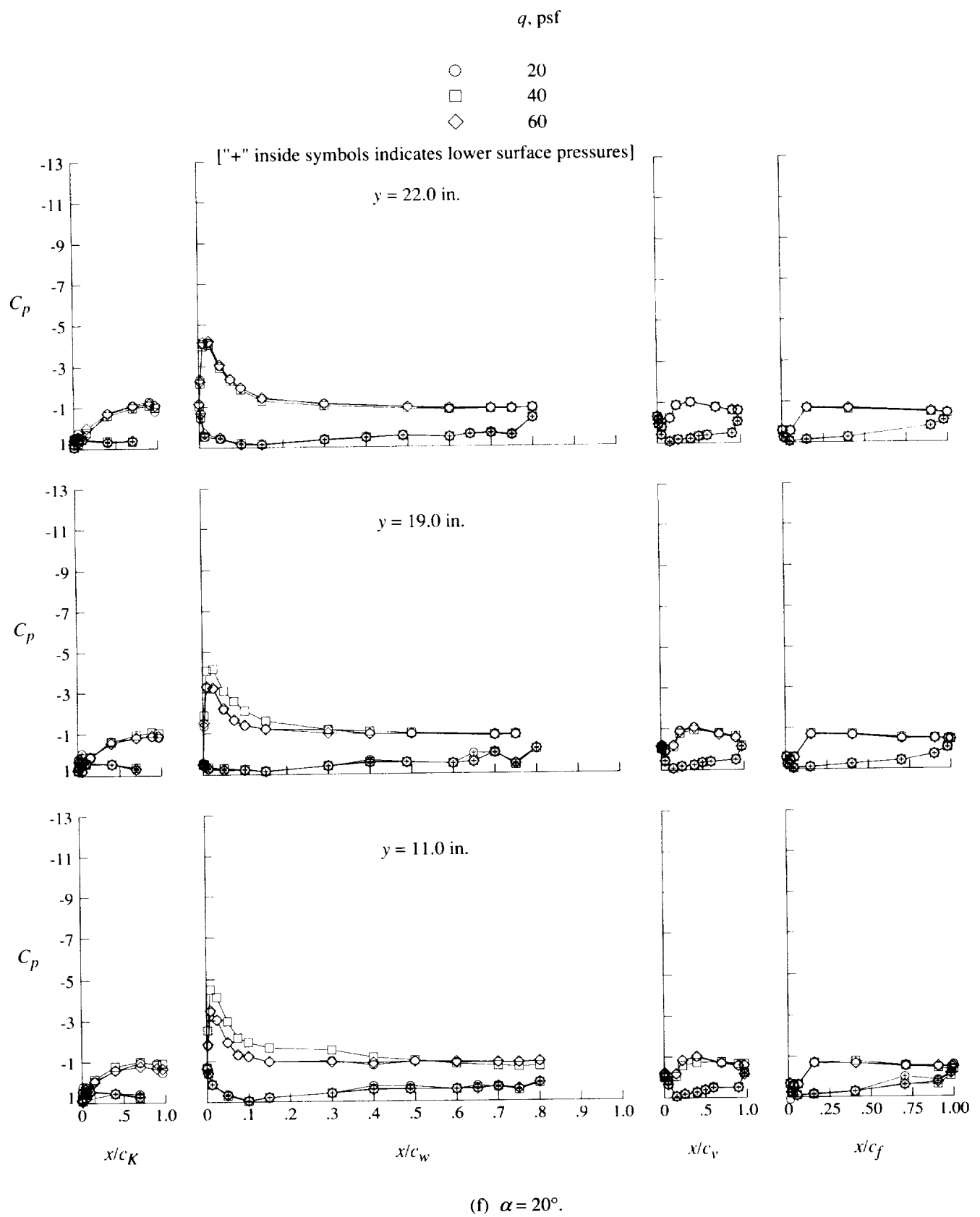
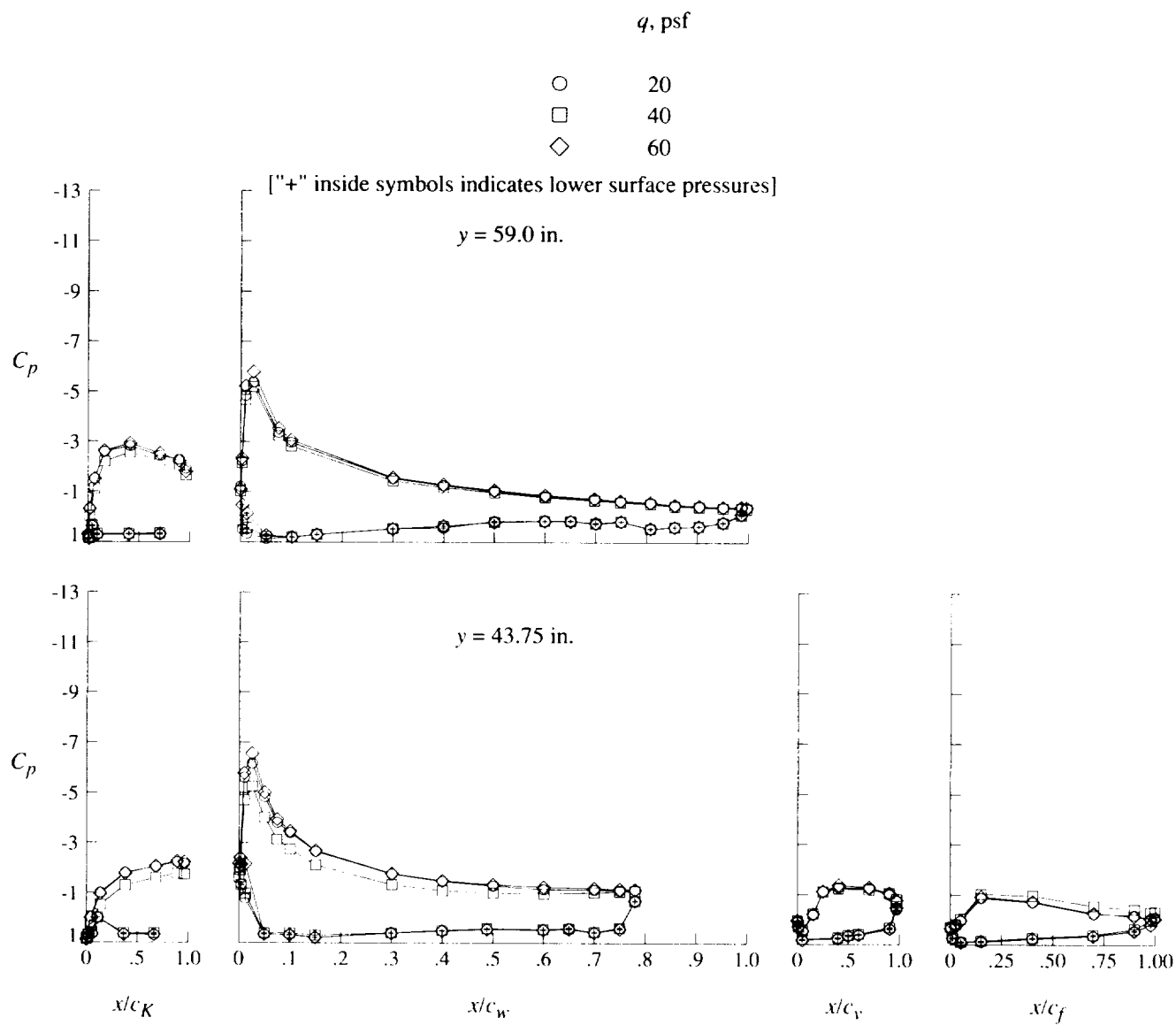


Figure 18. Continued.



(f) Concluded.

Figure 18. Concluded.

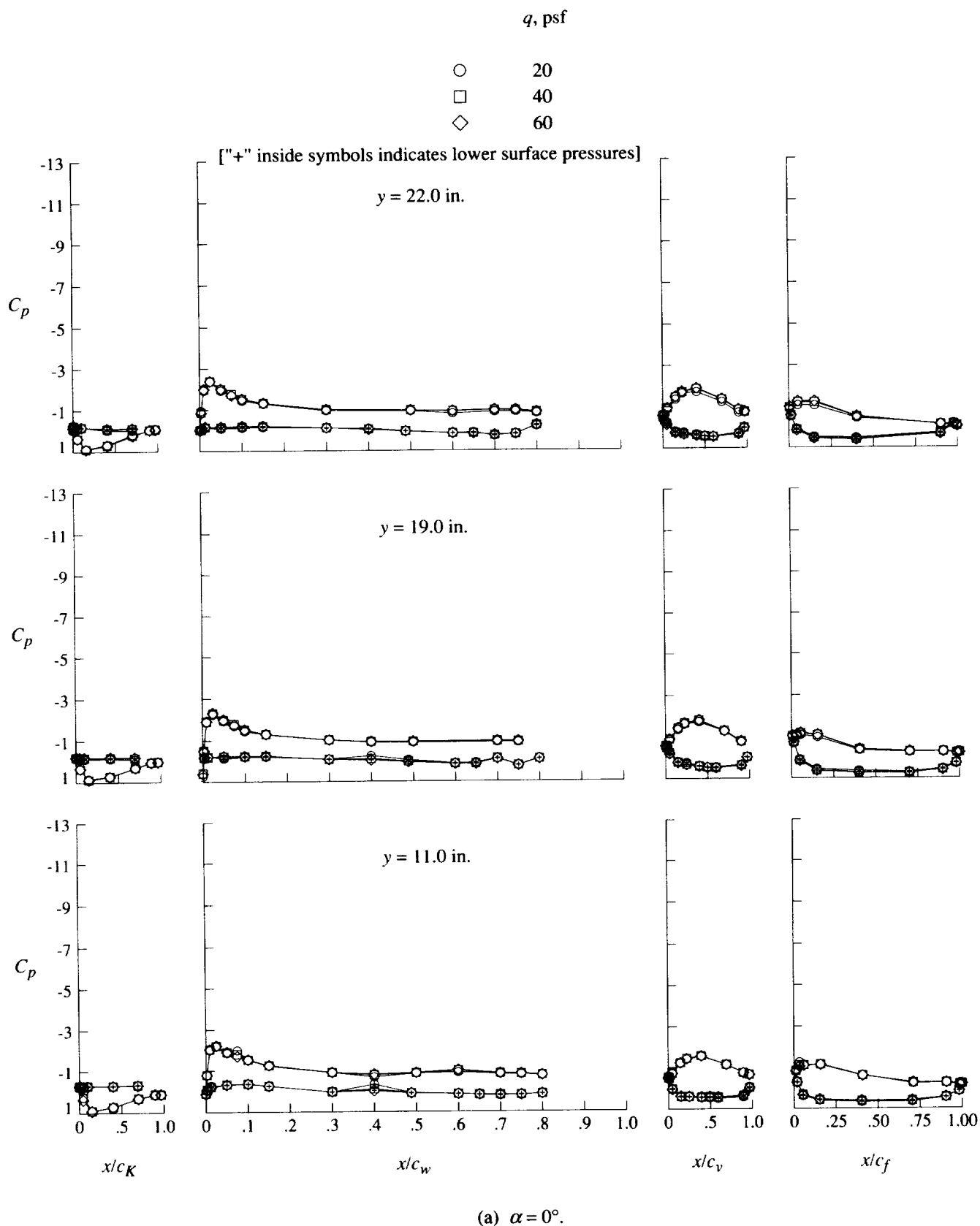
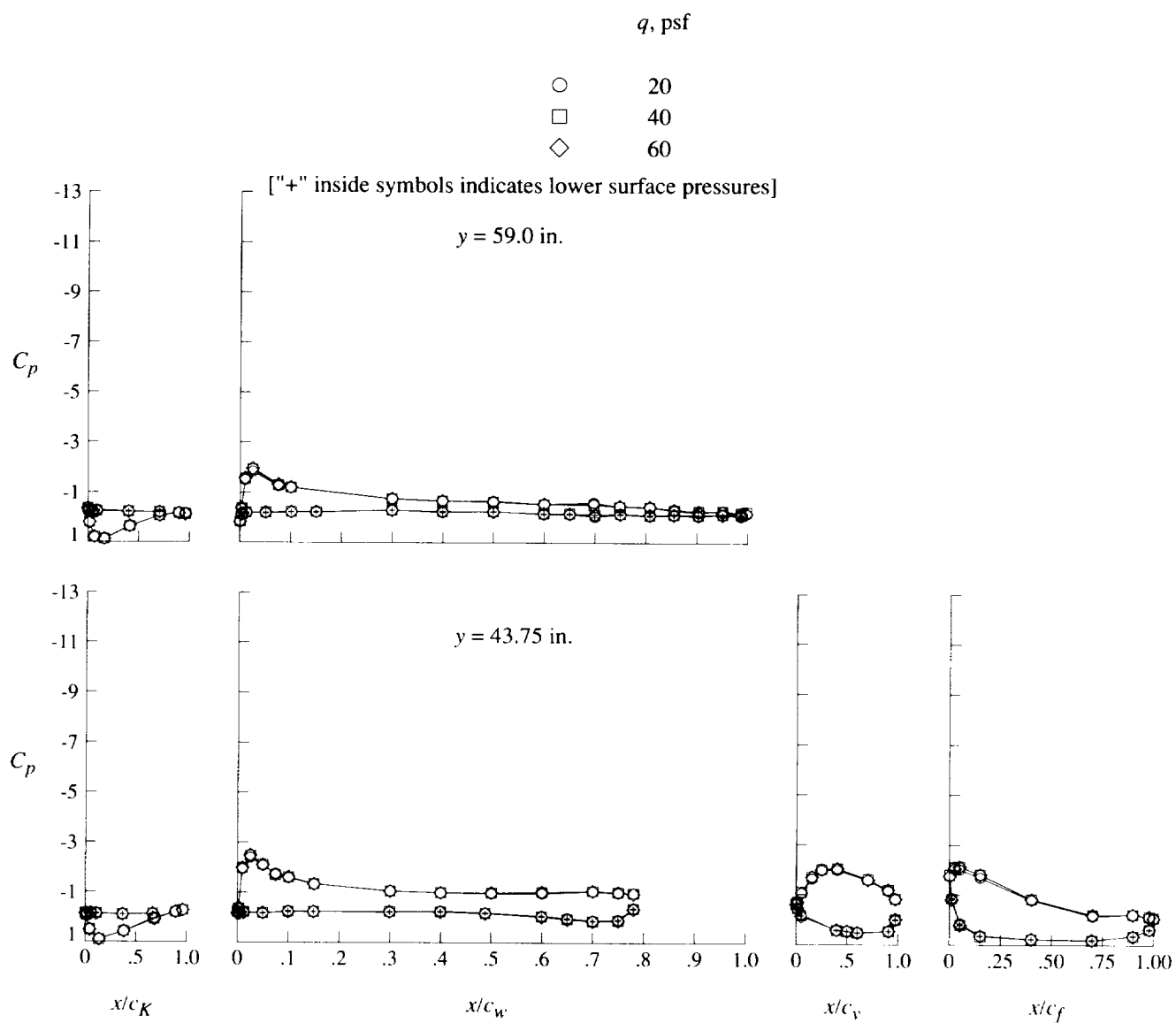
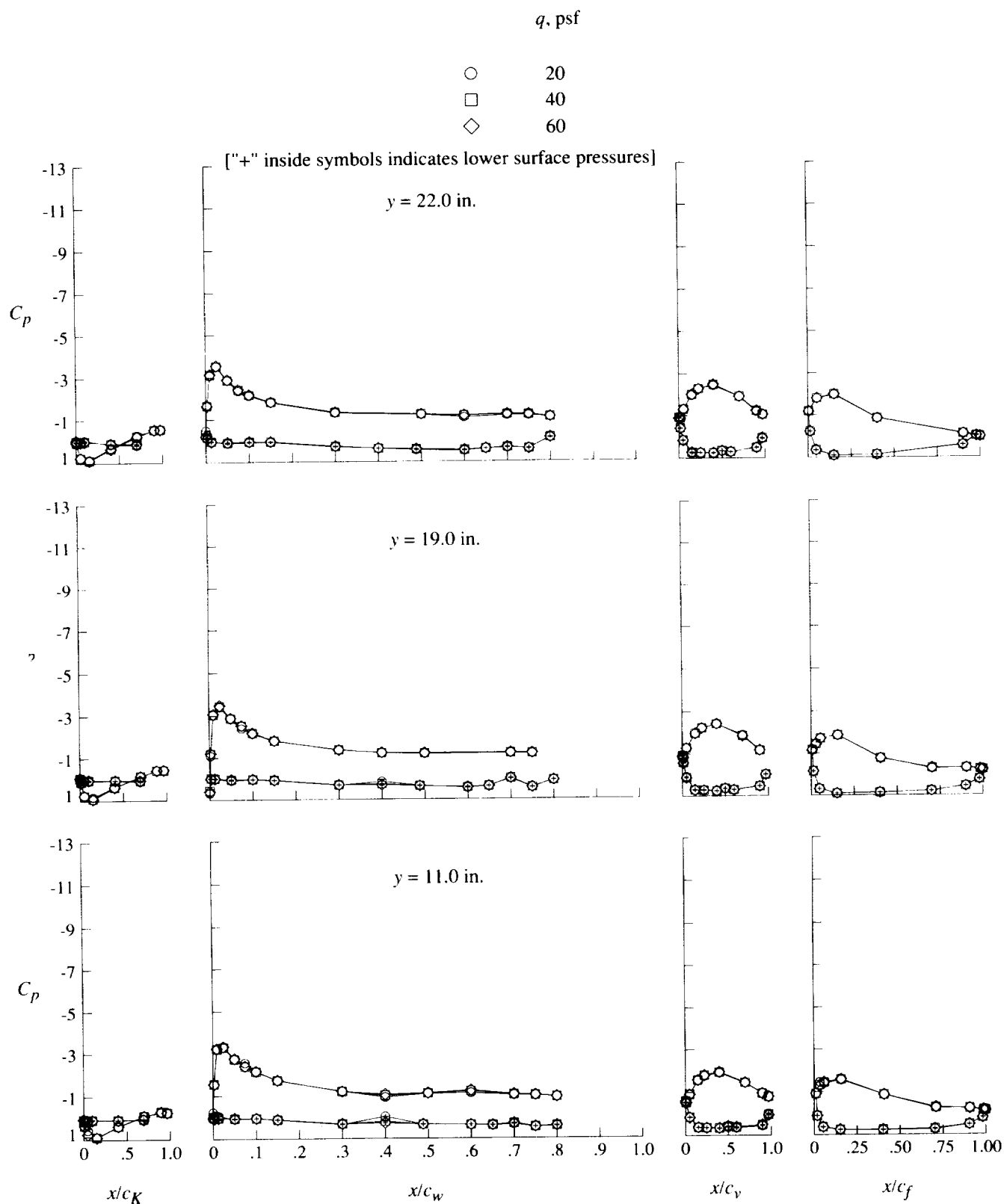


Figure 19. Effect of free-stream speed on pressure distributions for high-lift configuration at $\delta_f = 60^\circ$.



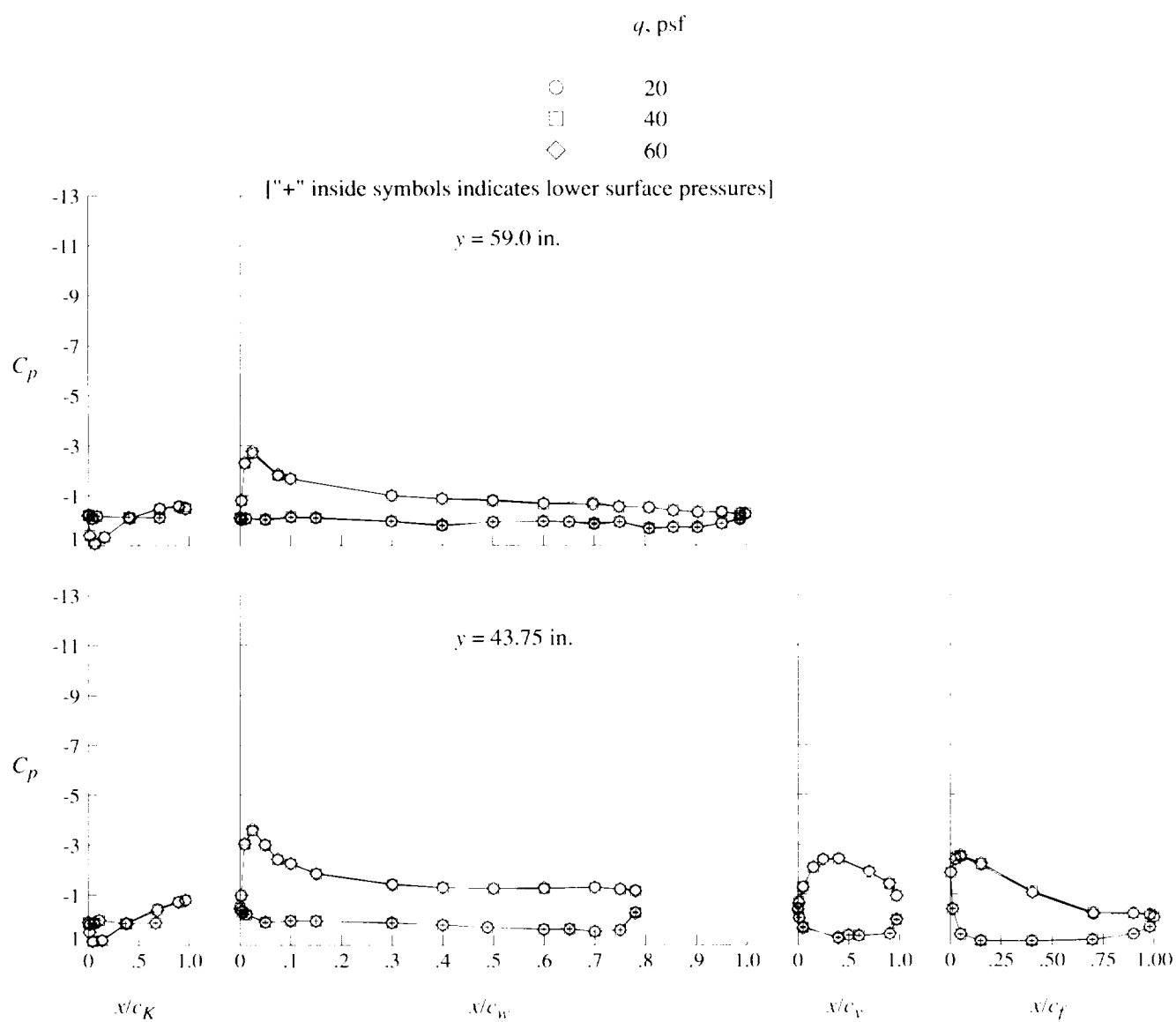
(a) Concluded.

Figure 19. Continued.



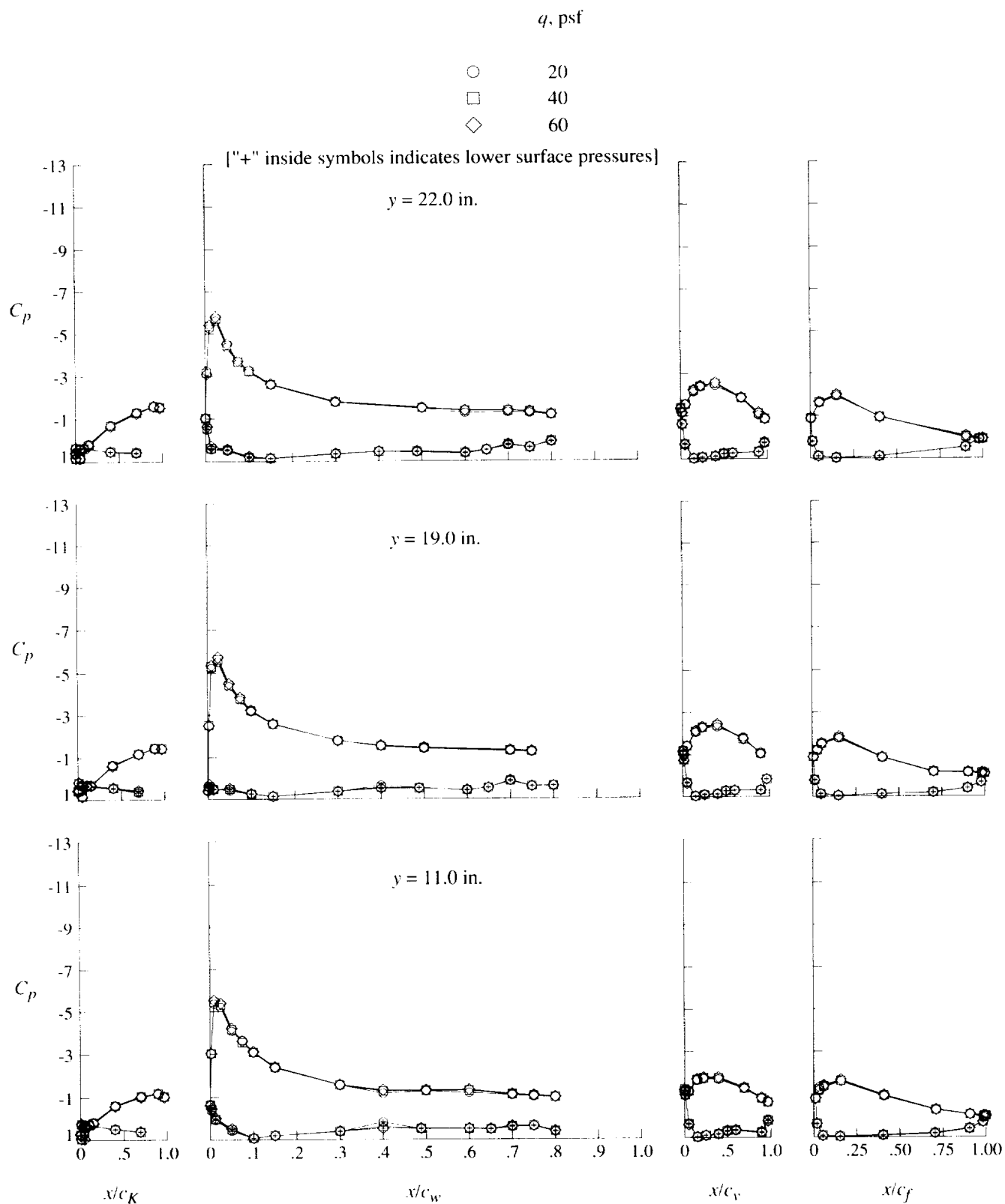
(b) $\alpha = 4^\circ$.

Figure 19. Continued.



(b) Concluded.

Figure 19. Continued.



(c) $\alpha = 8^\circ$.

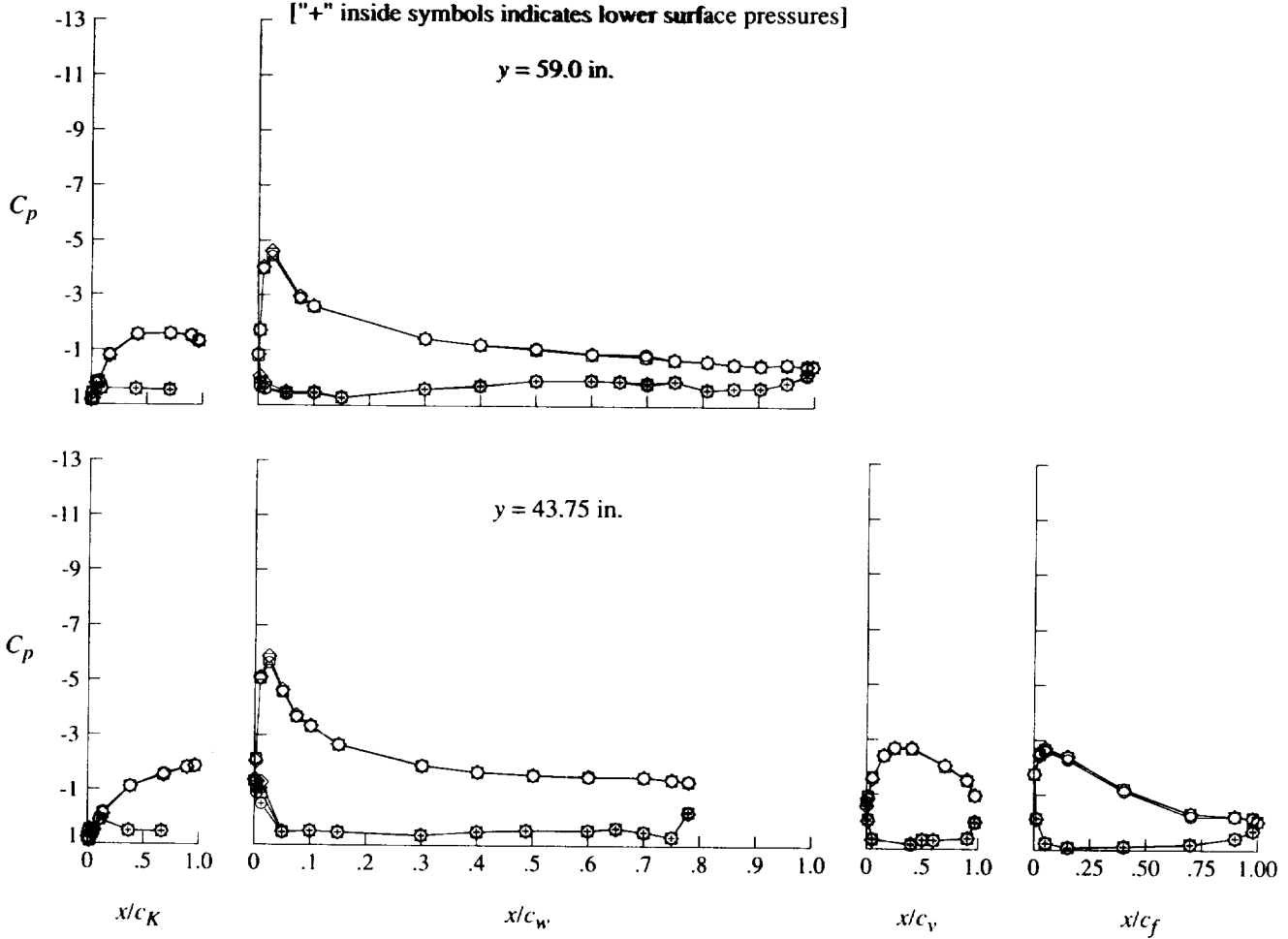
Figure 19. Continued.

q , psf

- 20
- 40
- ◇ 60

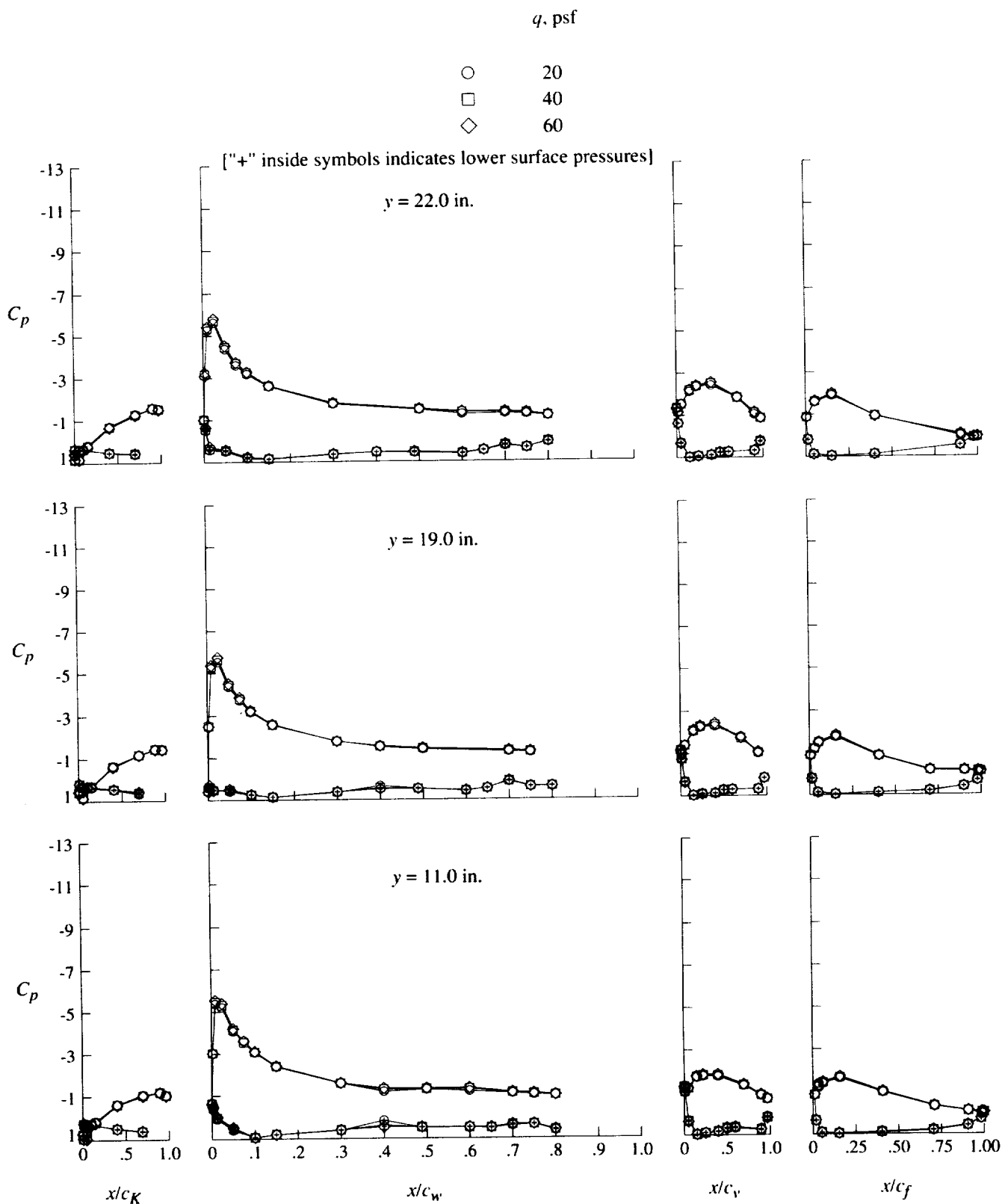
["+" inside symbols indicates lower surface pressures]

$y = 59.0$ in.



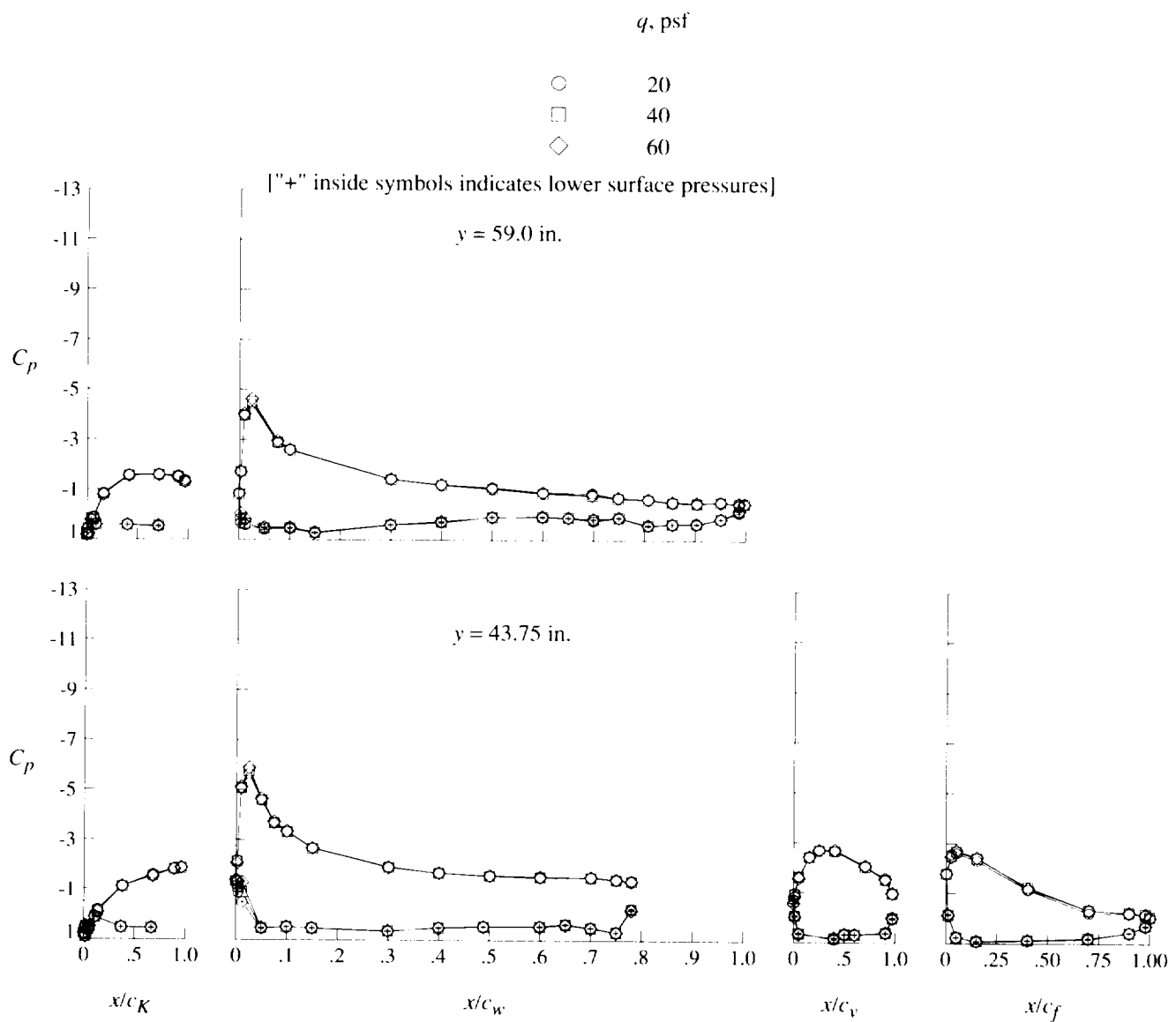
(c) Concluded.

Figure 19. Continued.



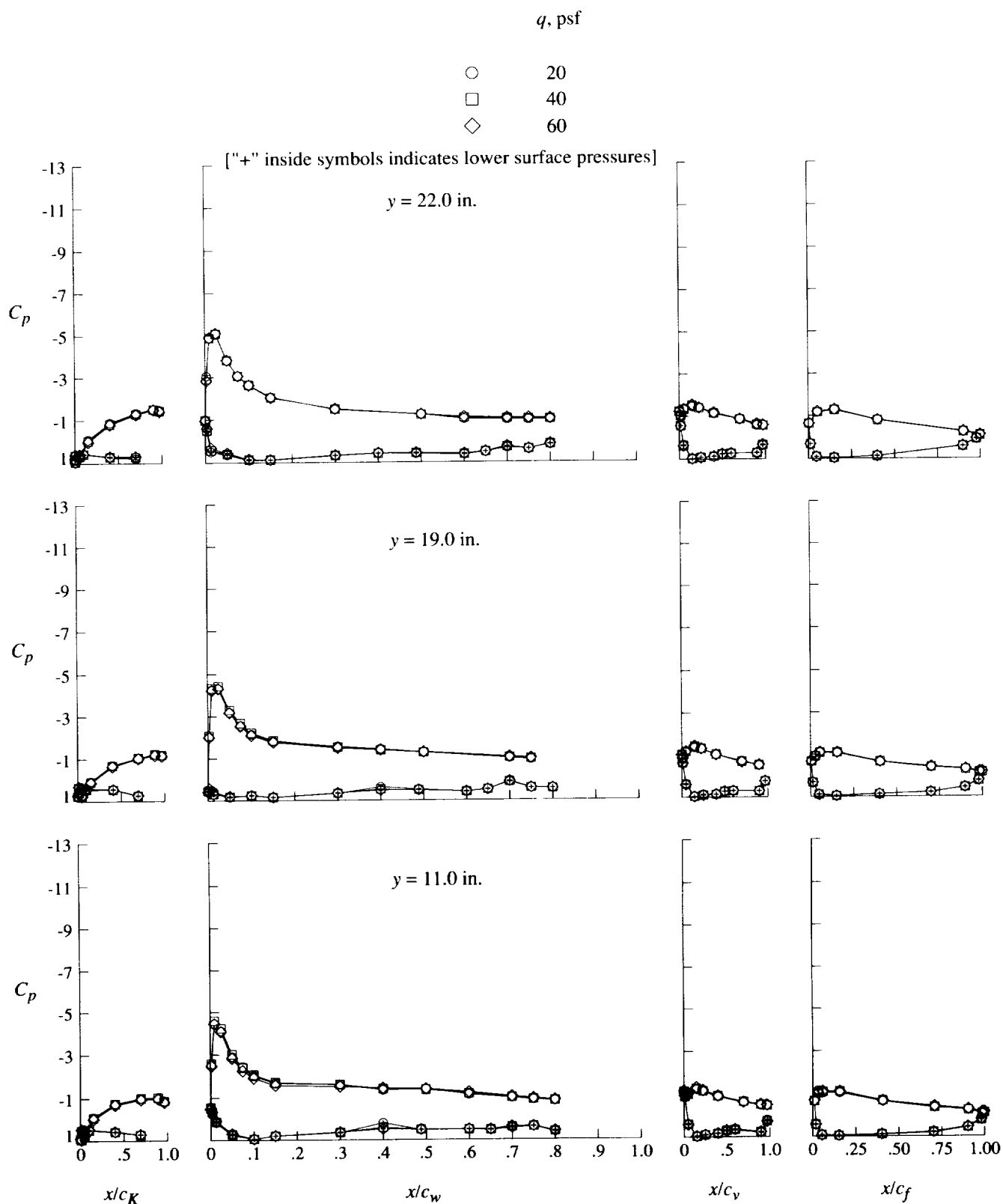
(d) $\alpha = 12^\circ$.

Figure 19. Continued.



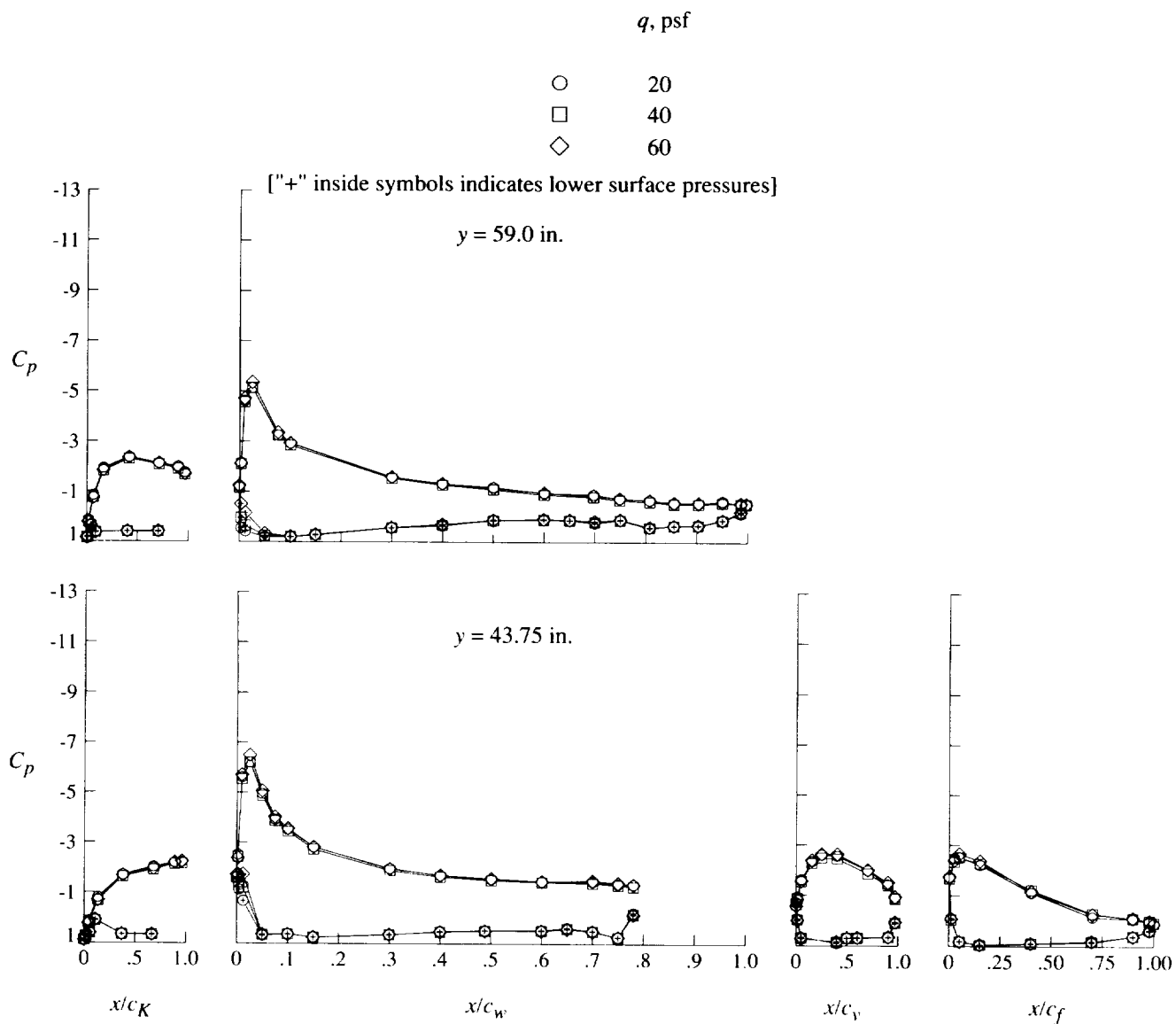
(d) Concluded.

Figure 19. Continued.



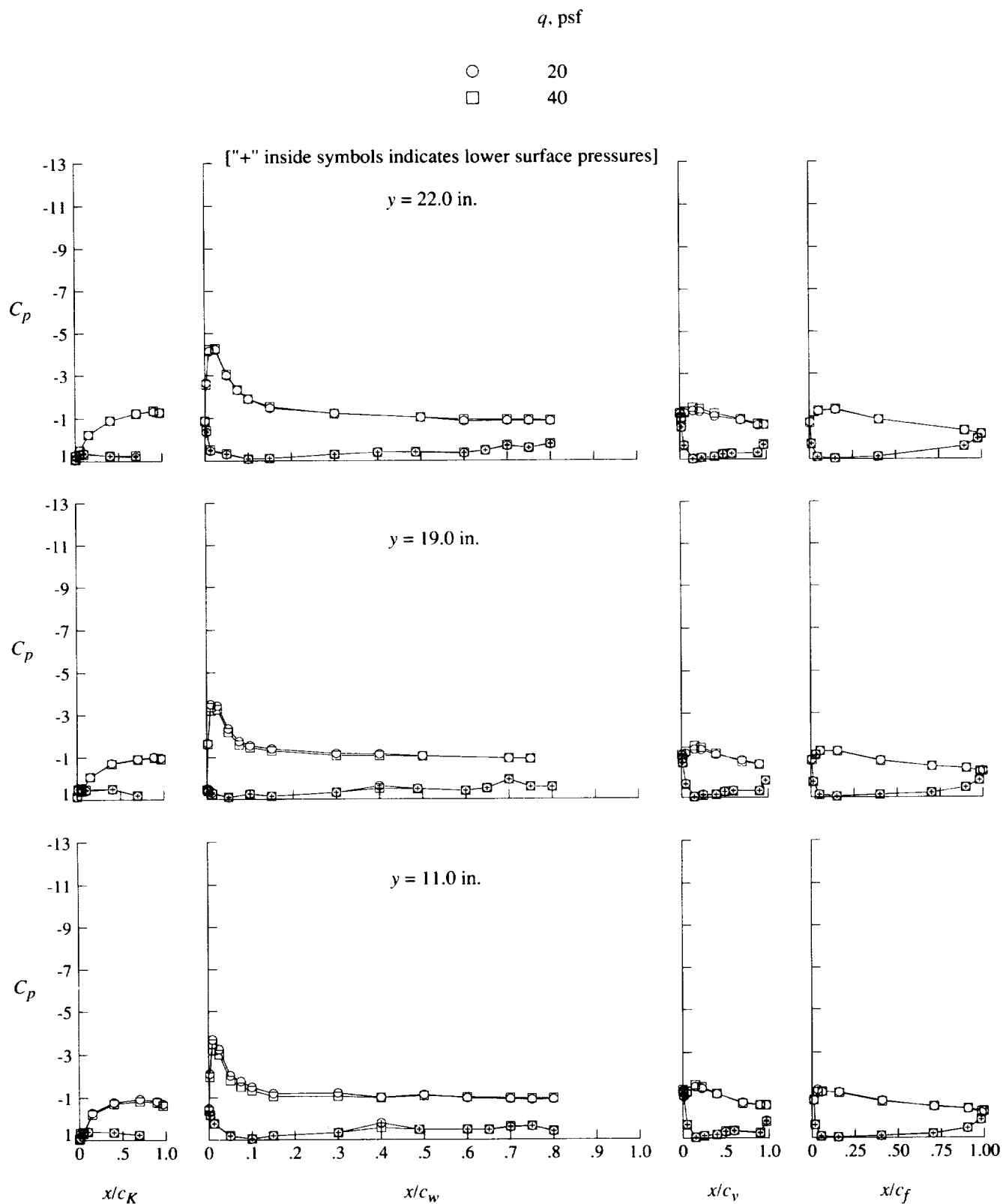
(e) $\alpha = 16^\circ$.

Figure 19. Continued.



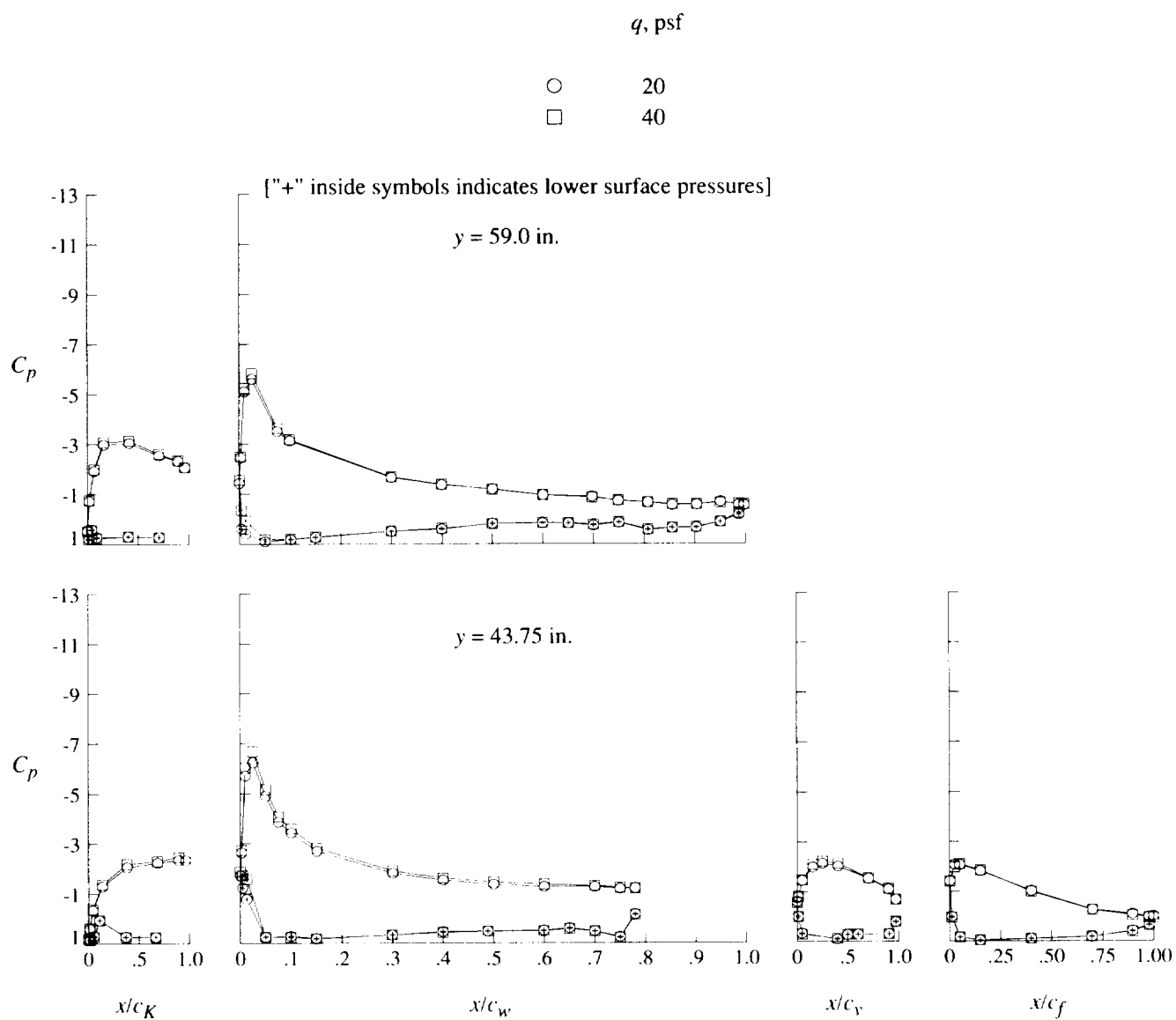
(e) Concluded.

Figure 19. Continued.



(f) $\alpha = 20^\circ$.

Figure 19. Continued.



(f) Concluded.

Figure 19. Concluded.

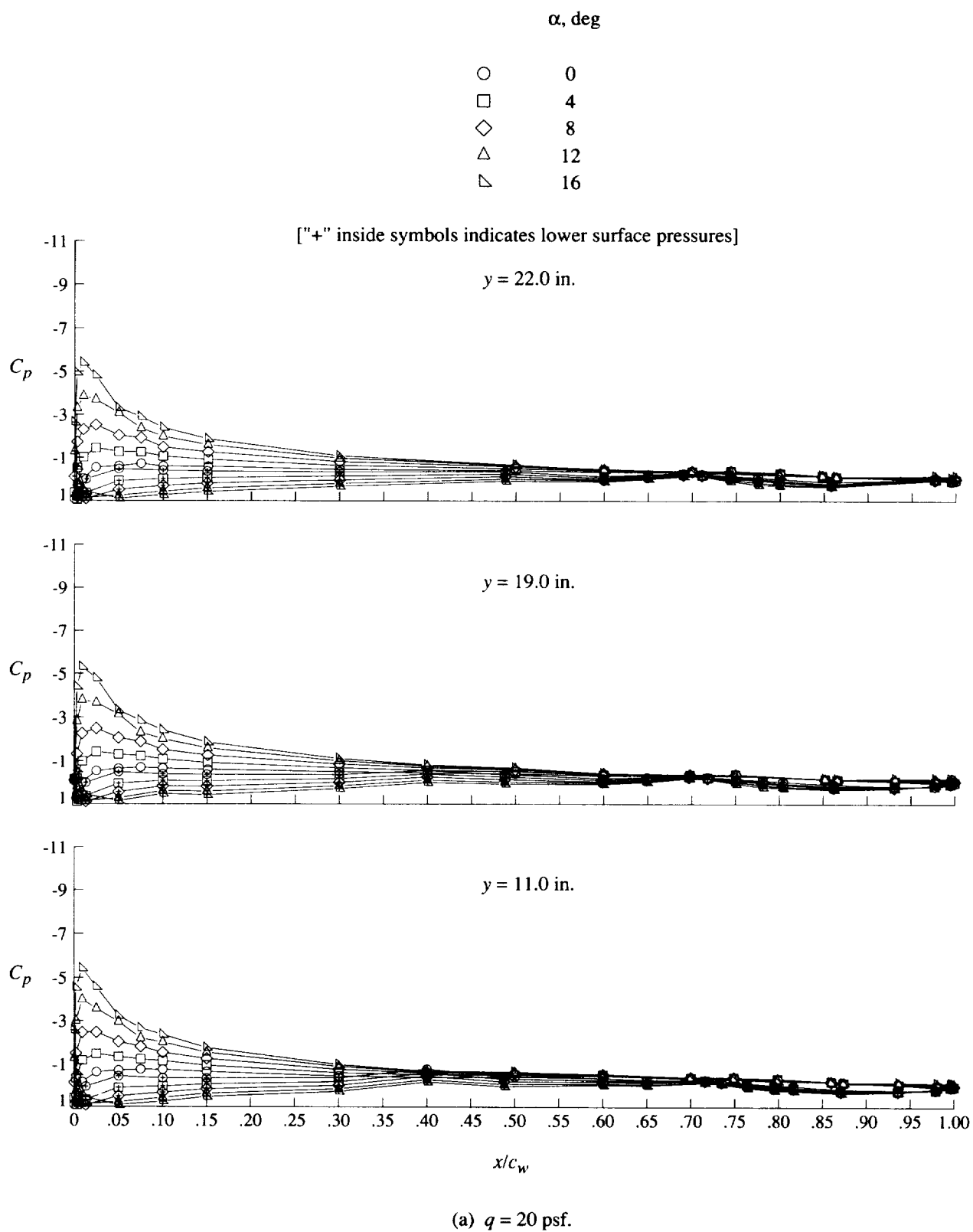
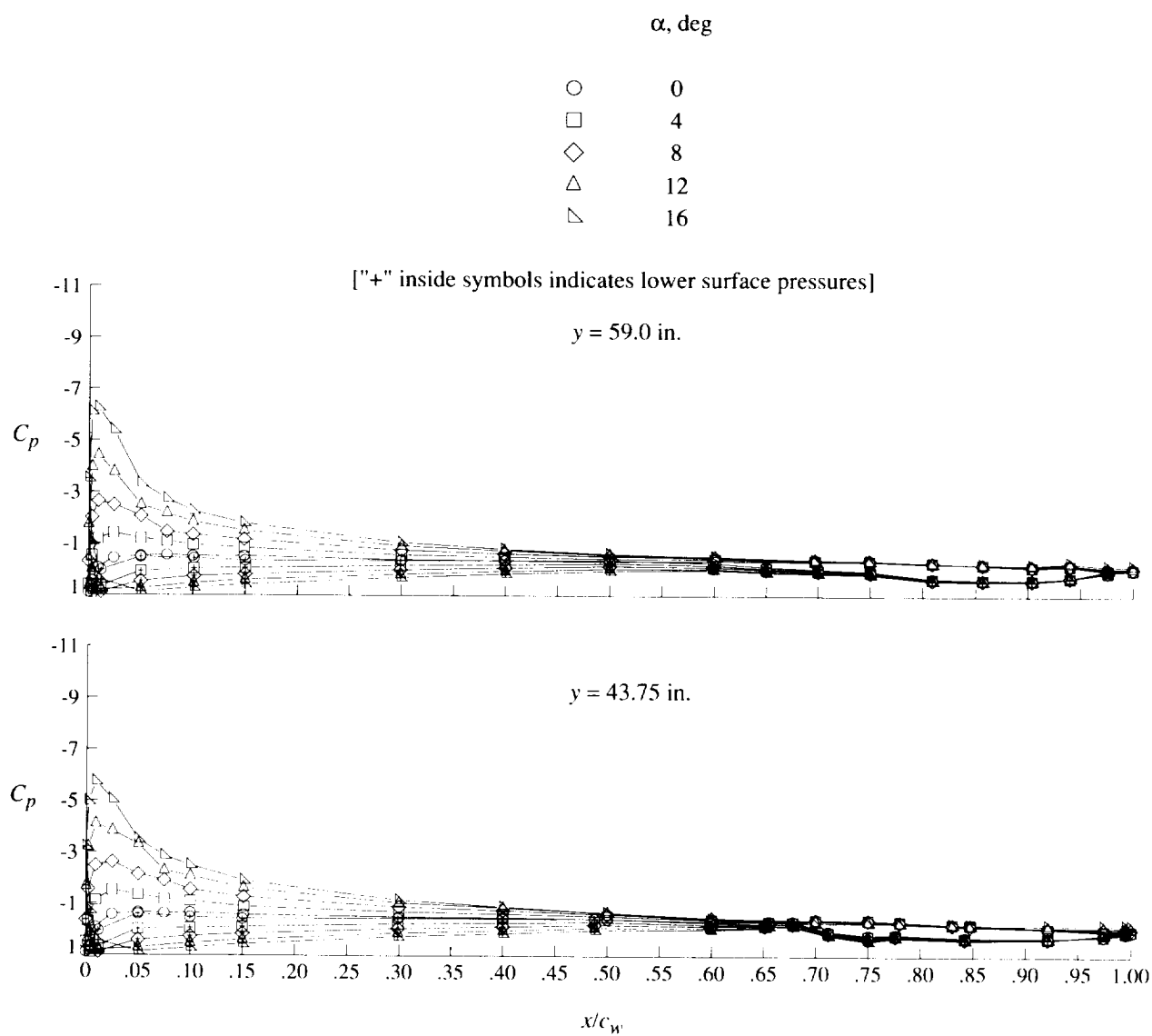


Figure 20. Effect of angle of attack on pressure distributions for cruise configuration.



(a) Concluded.

Figure 20. Continued.

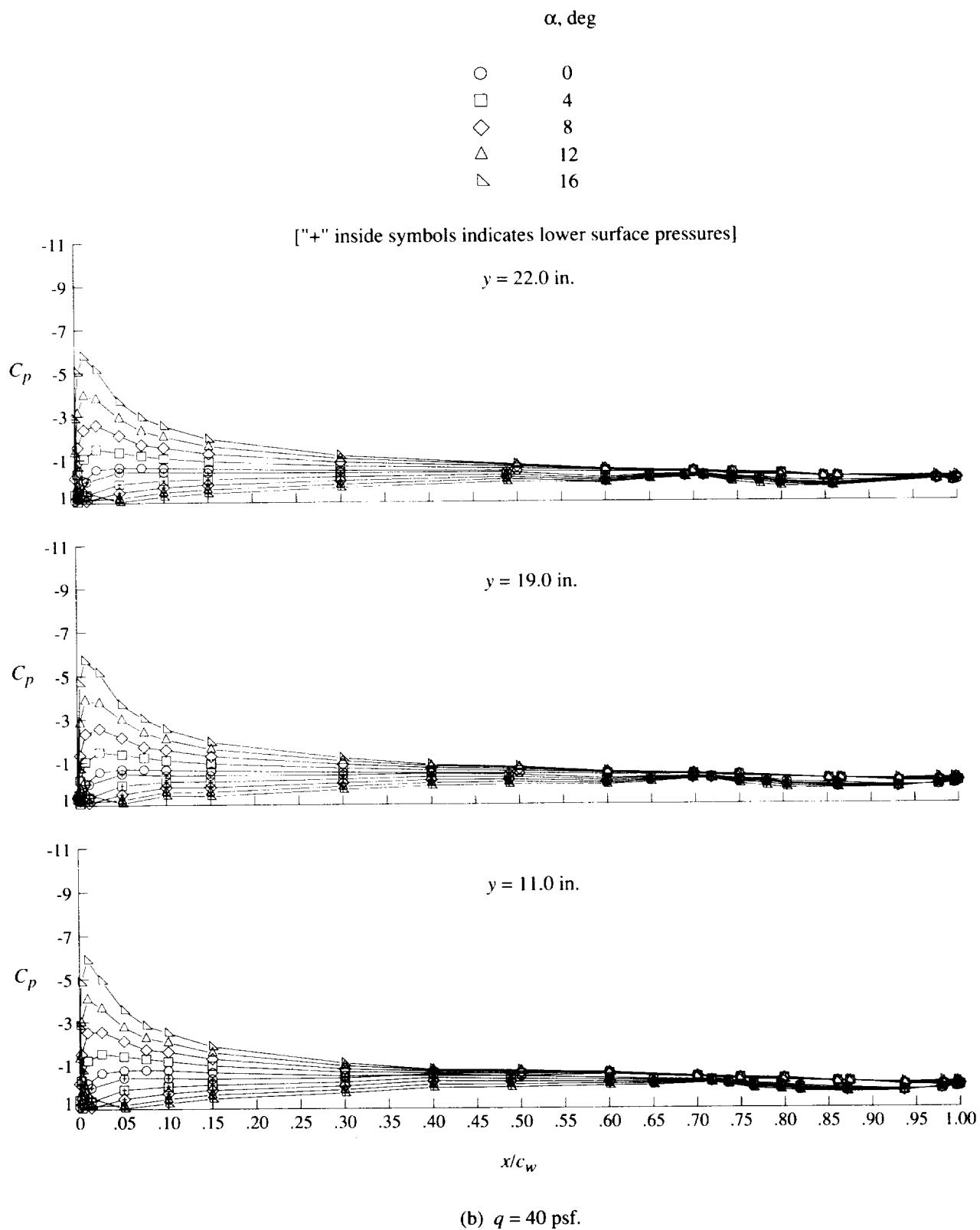


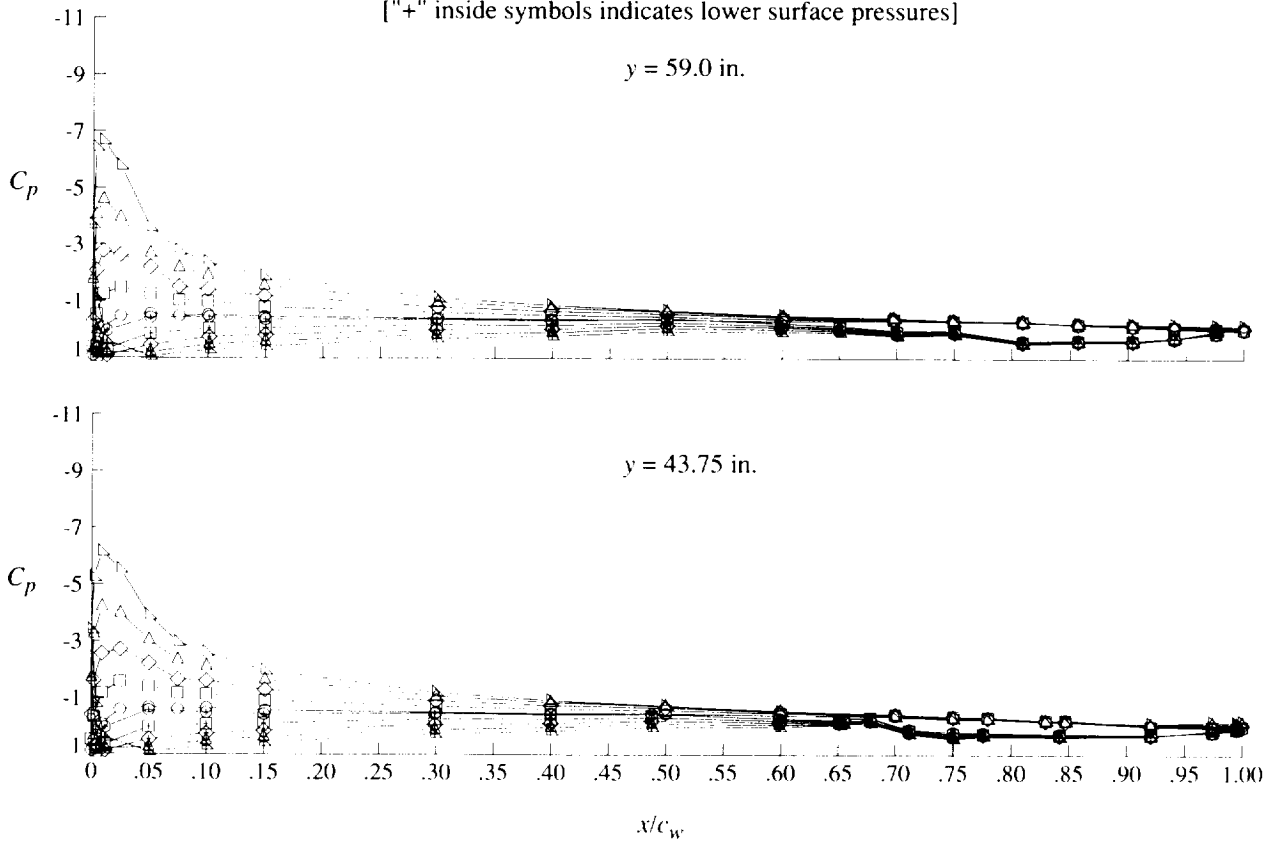
Figure 20. Continued.

α , deg

○	0
□	4
◇	8
△	12
▽	16

["+" inside symbols indicates lower surface pressures]

$y = 59.0$ in.



(b) Concluded.

Figure 20. Continued.

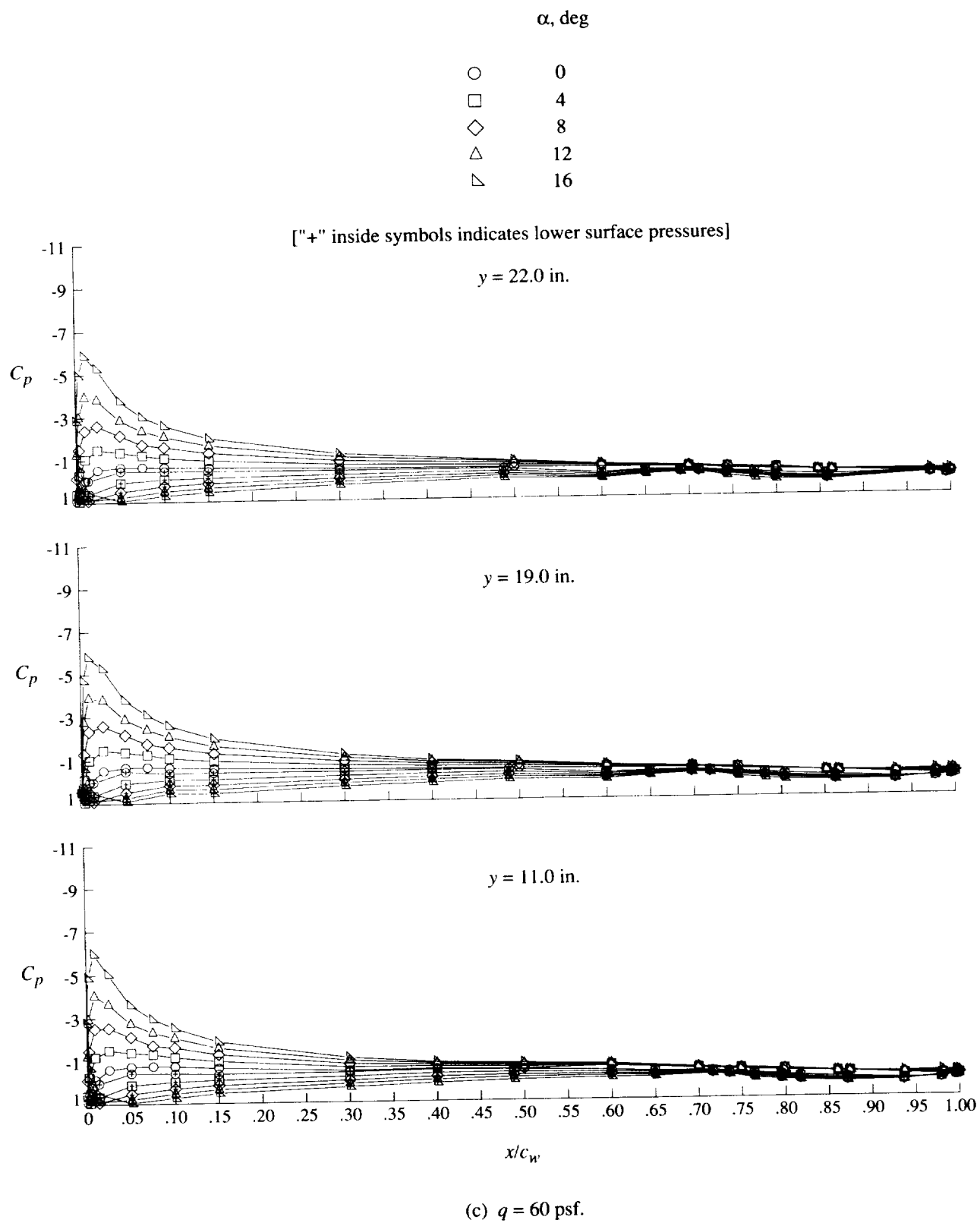
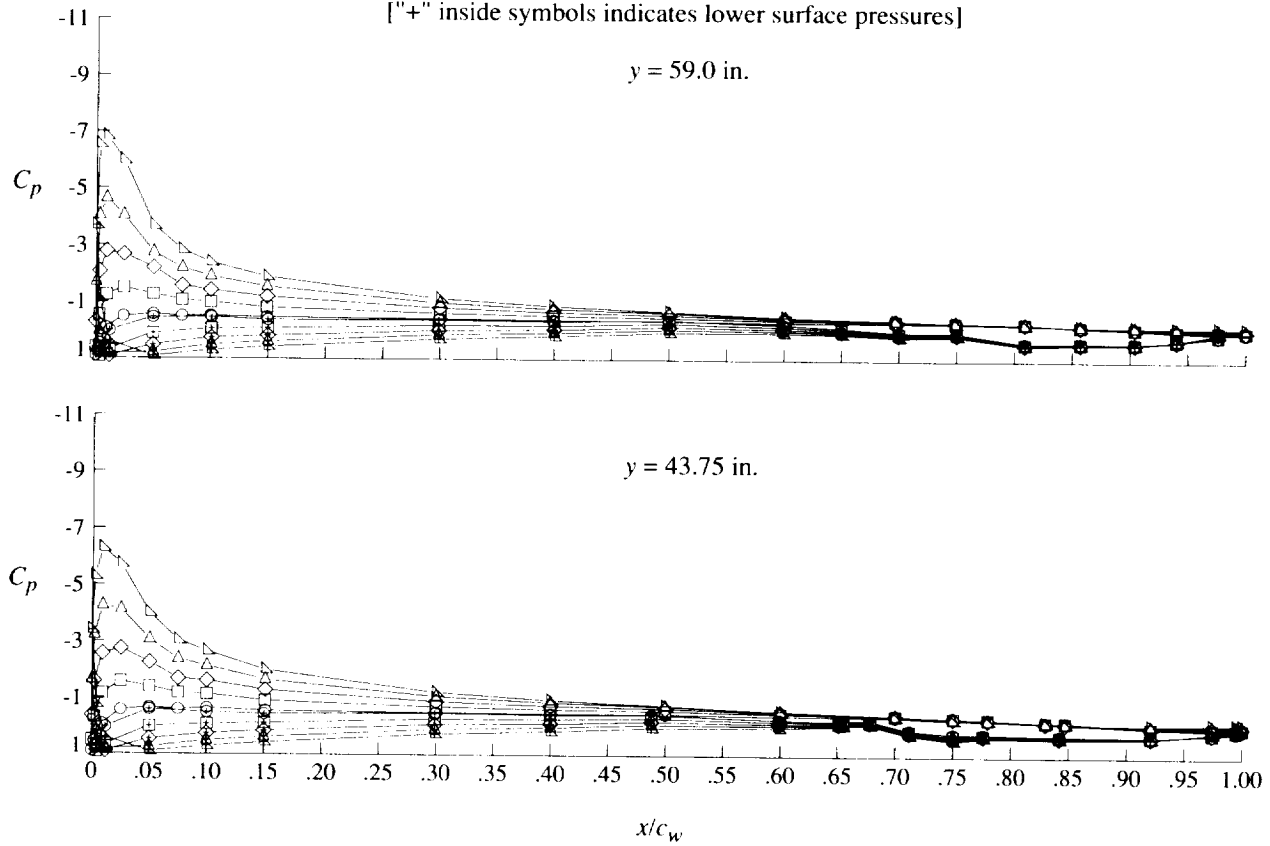


Figure 20. Continued.

α , deg

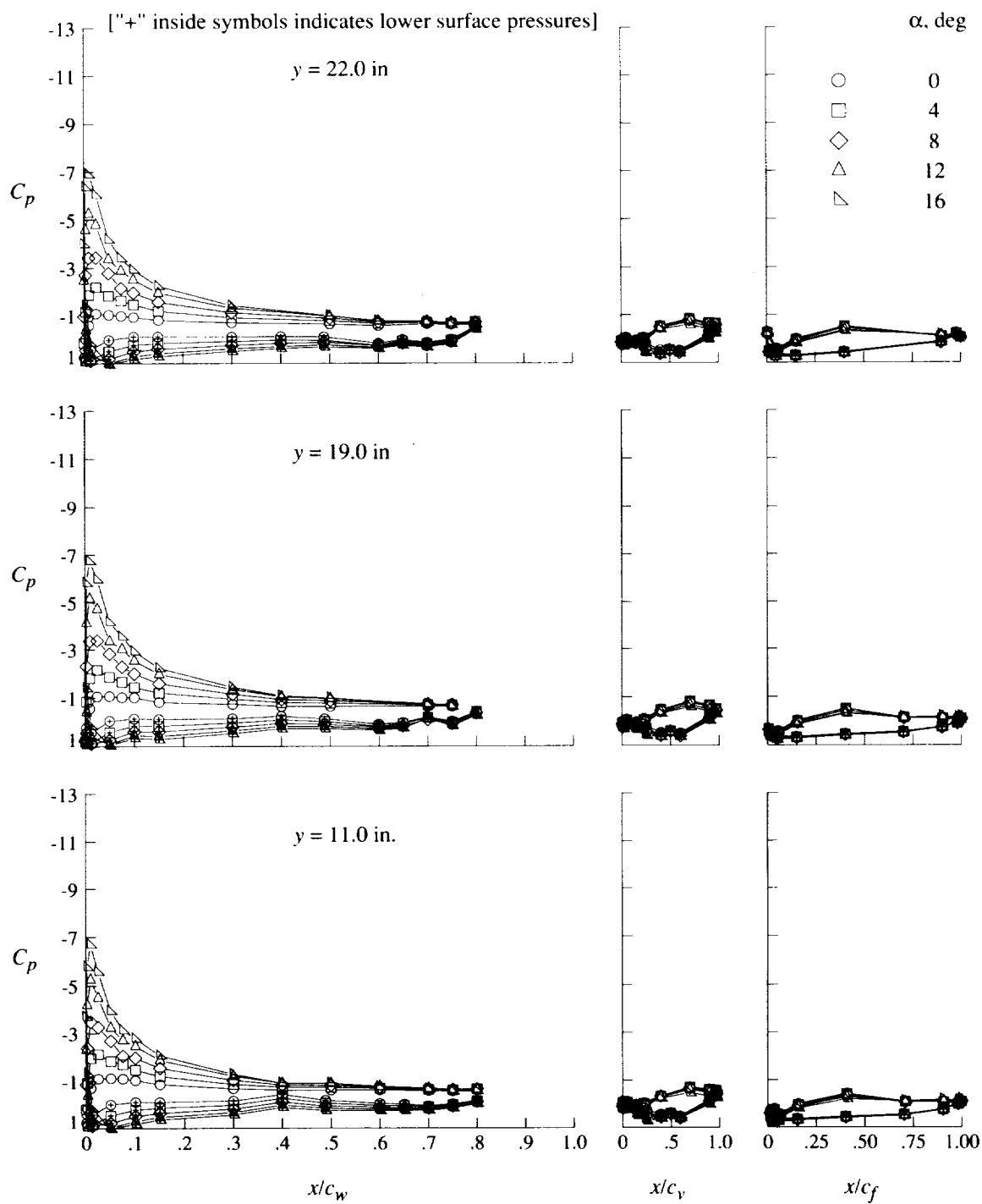
○	0
□	4
◇	8
△	12
▽	16

["+" inside symbols indicates lower surface pressures]



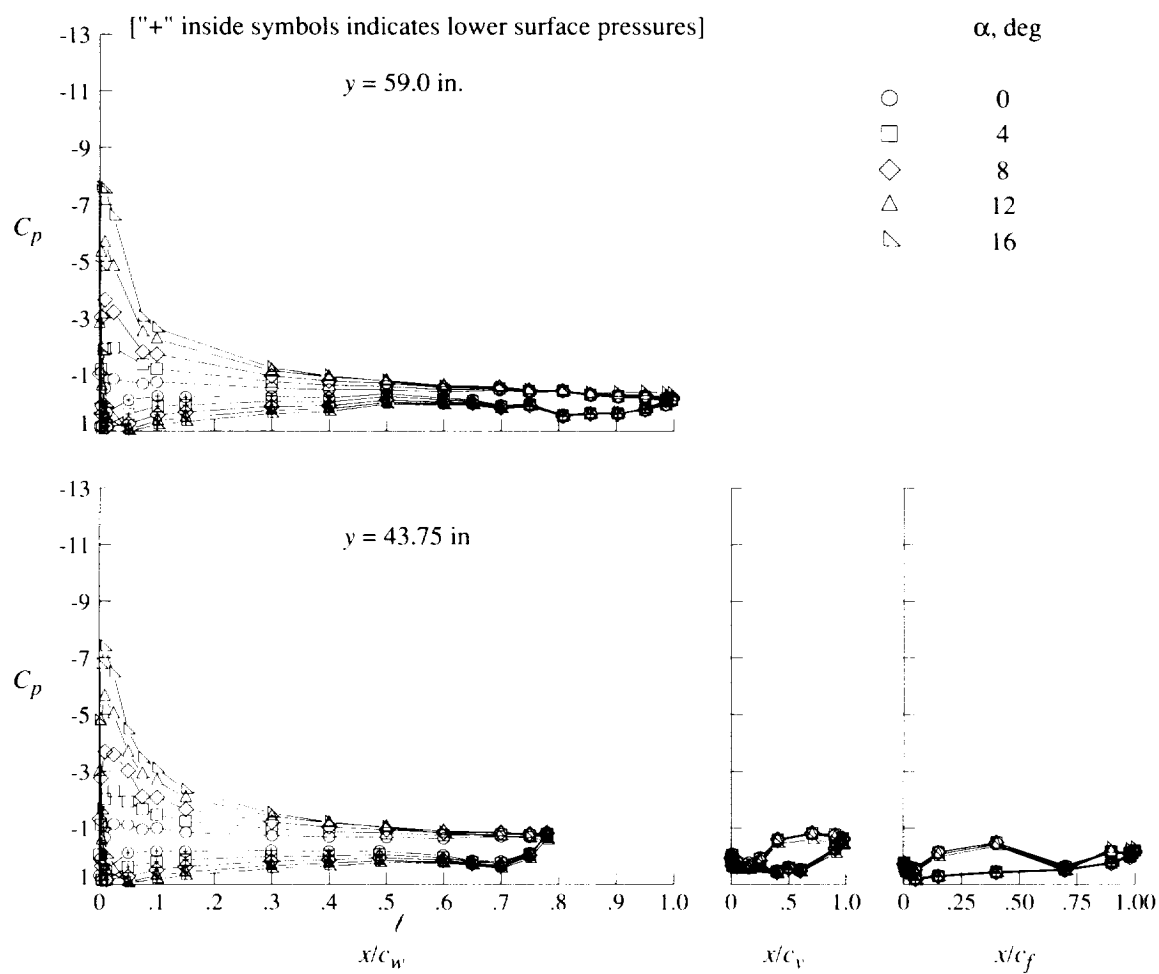
(c) Concluded.

Figure 20. Concluded.



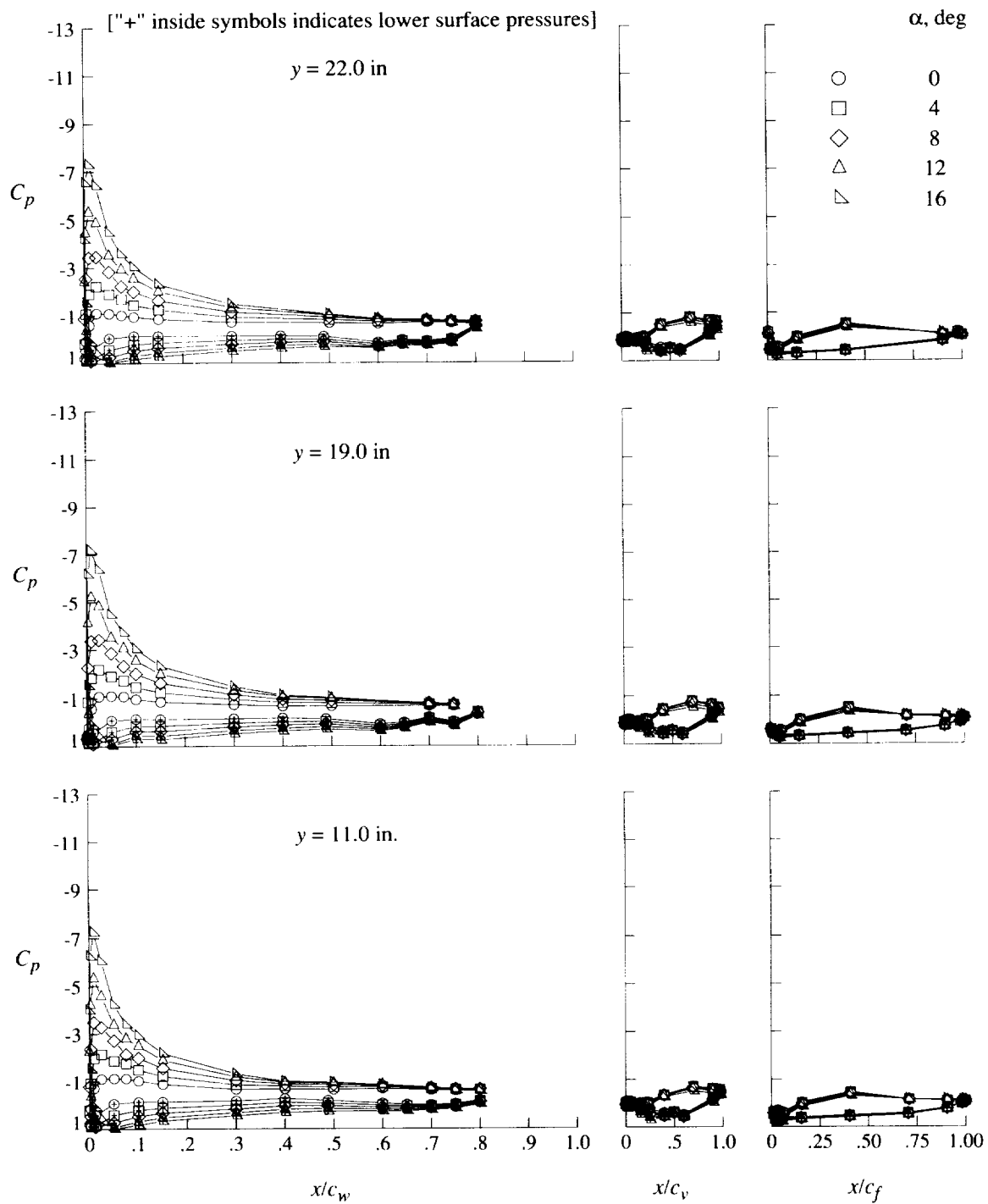
(a) $q = 20$ psf.

Figure 21. Effect of angle of attack on pressure distributions for flaps-only configuration at $\delta_f = 20^\circ$.



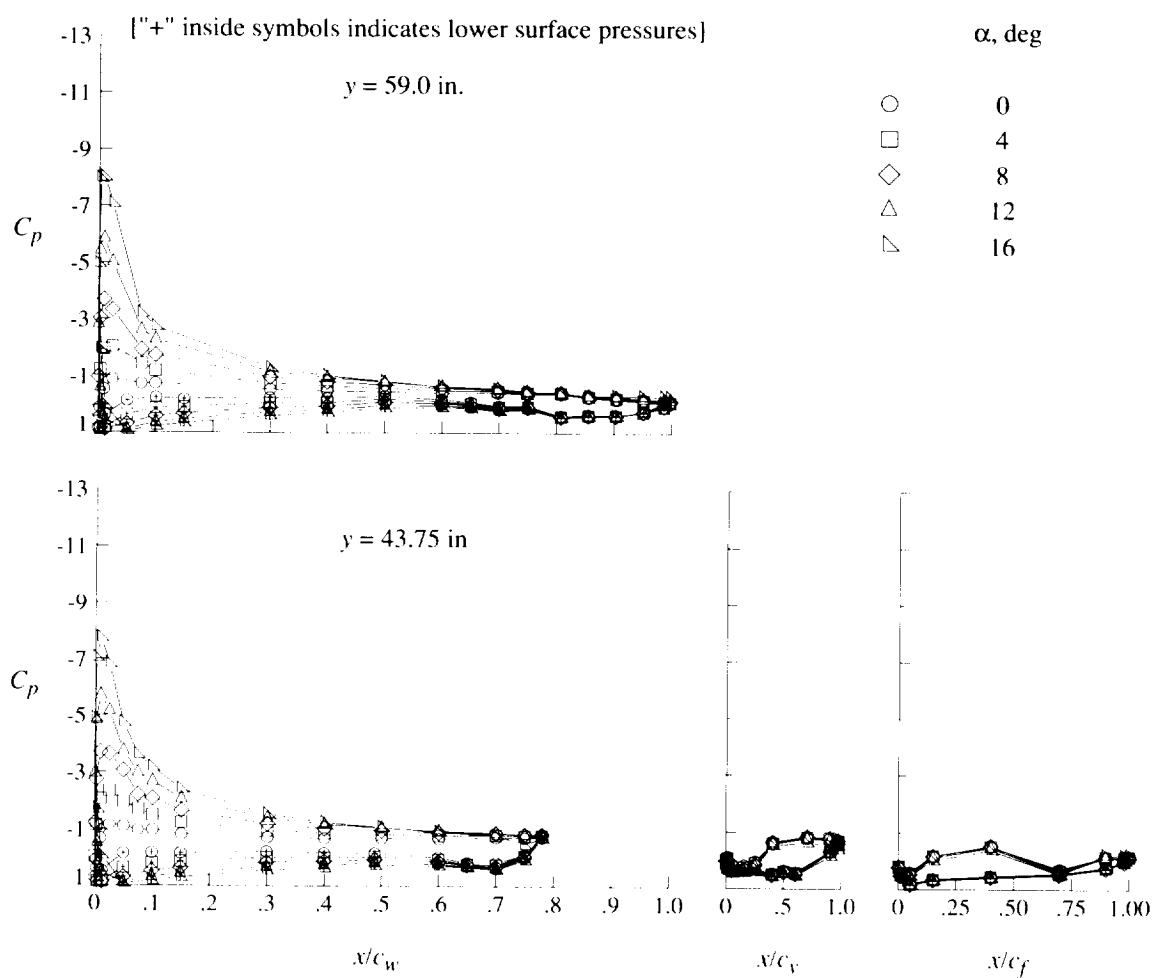
(a) Concluded.

Figure 21. Continued.



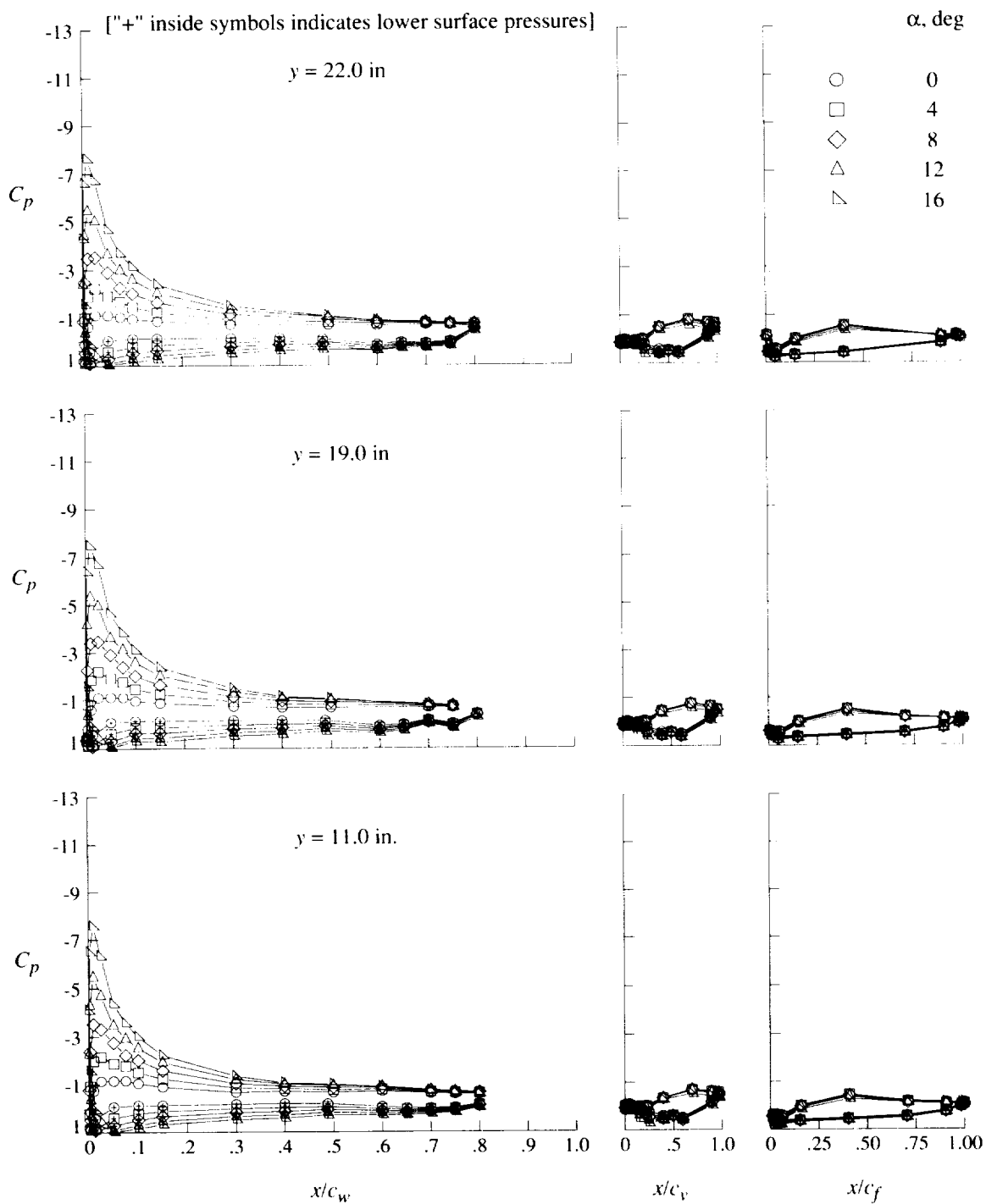
(b) $q = 40$ psf.

Figure 21. Continued.



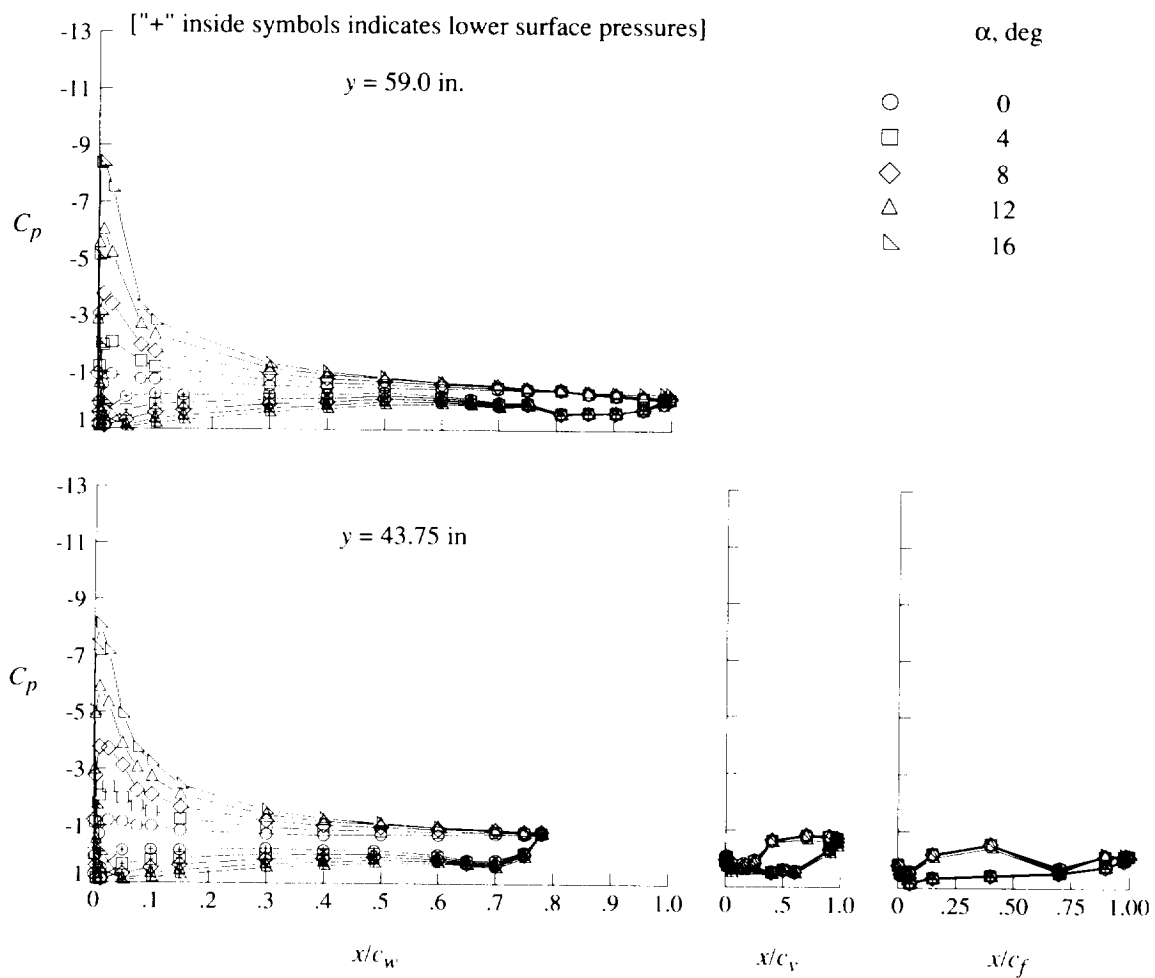
(b) Concluded.

Figure 21. Continued.



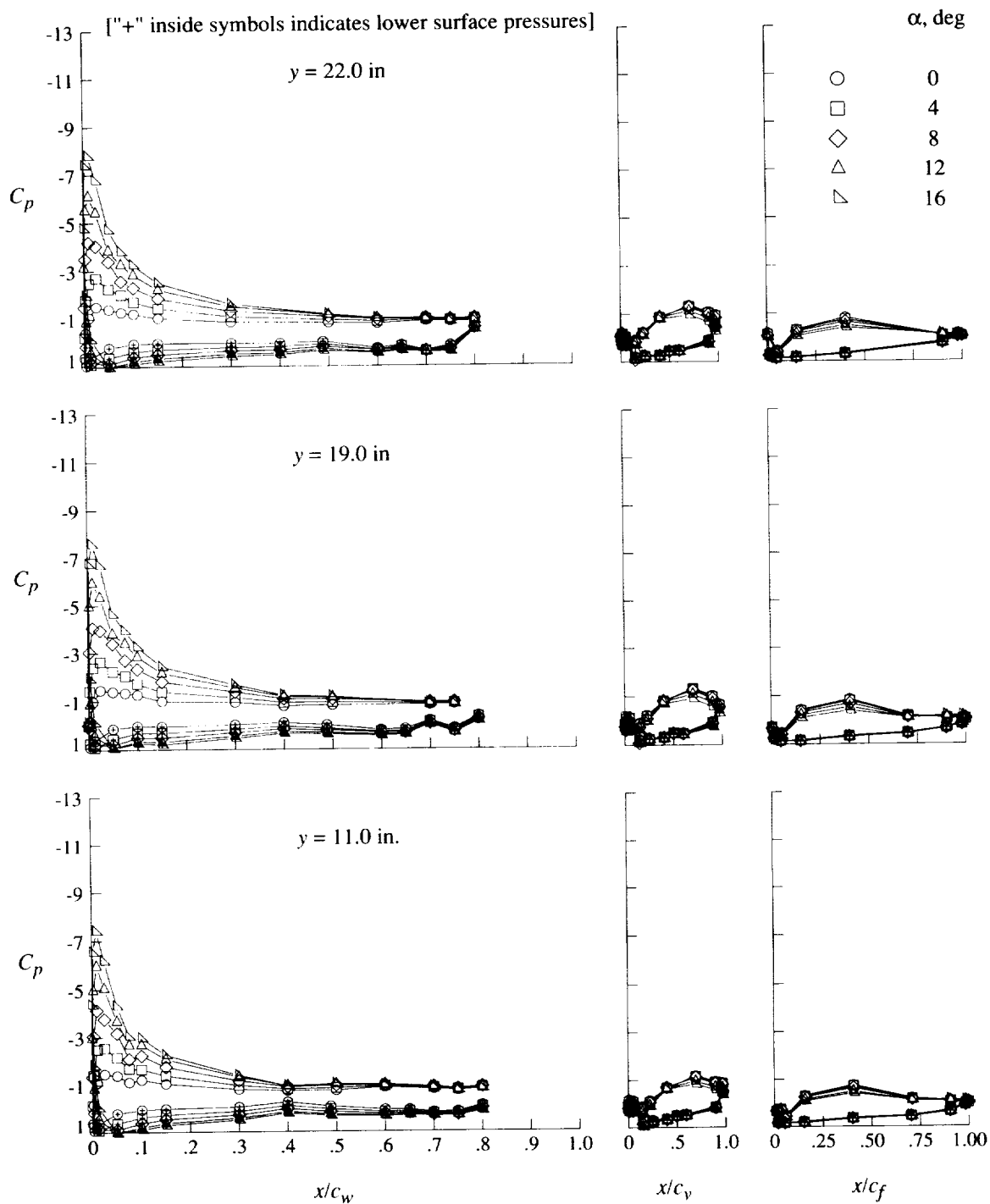
(c) $q = 60$ psf.

Figure 21. Continued.



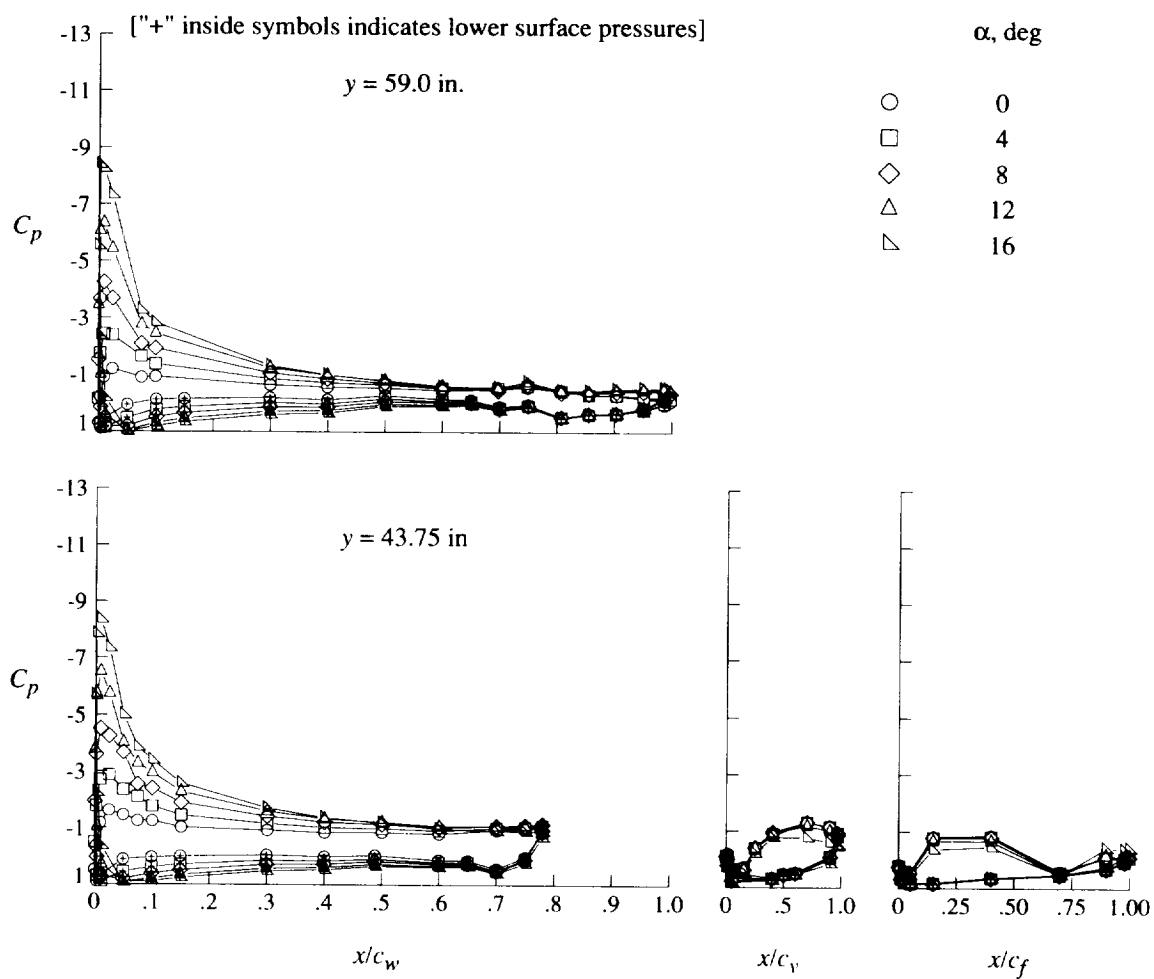
(c) Concluded.

Figure 21. Concluded.



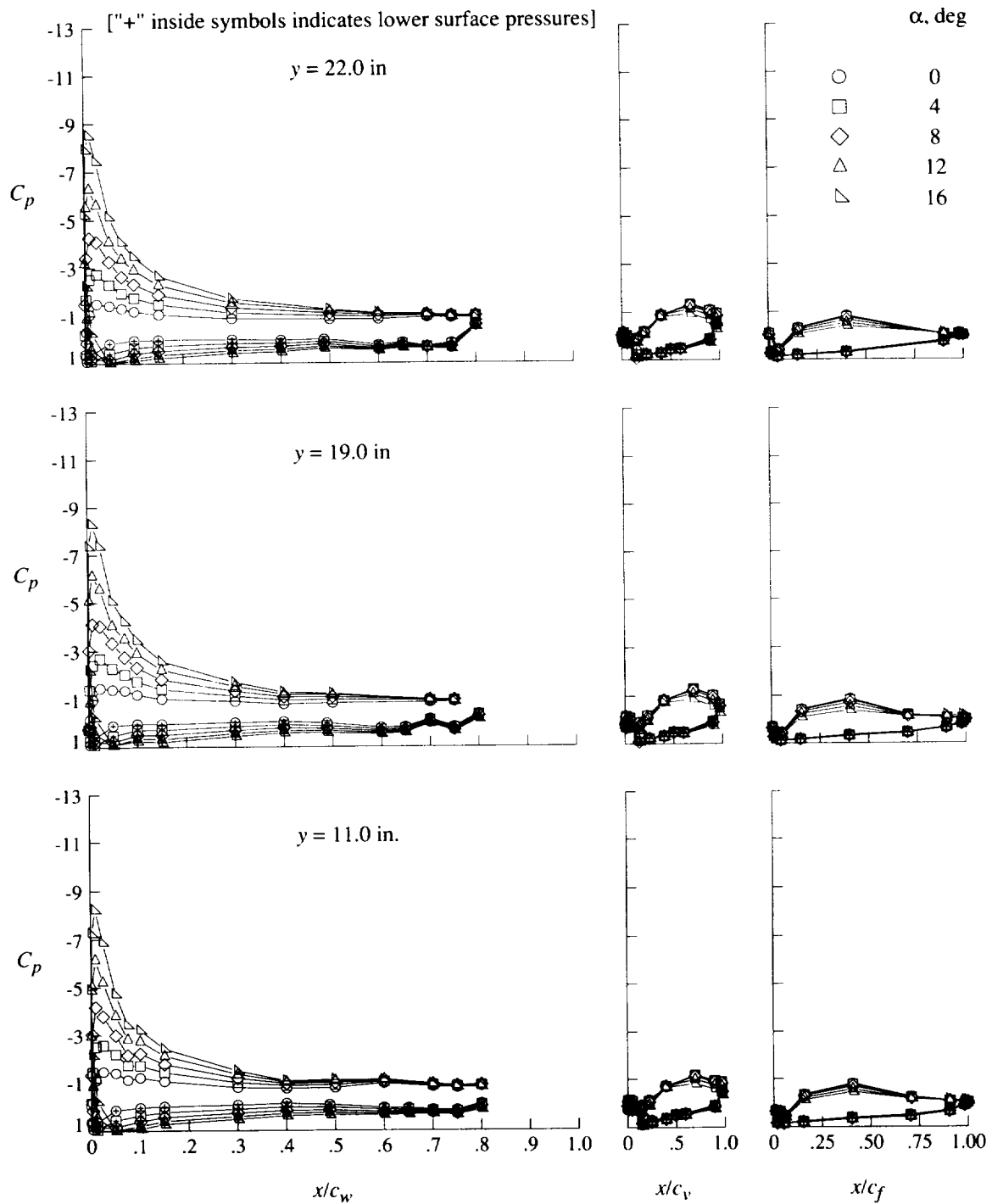
(a) $q = 20$ psf.

Figure 22. Effect of angle of attack on pressure distributions for flaps-only configuration at $\delta_f = 30^\circ$.



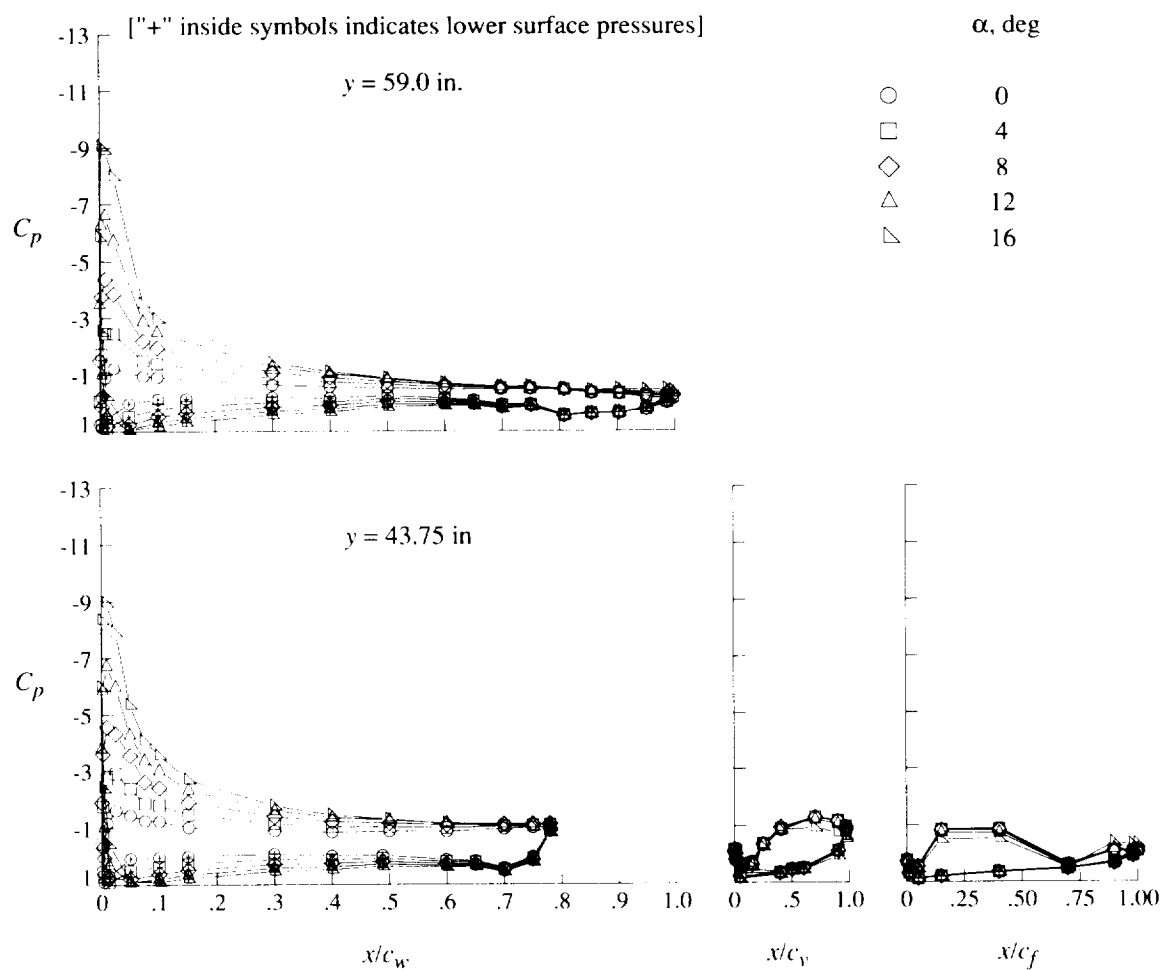
(a) Concluded.

Figure 22. Continued.



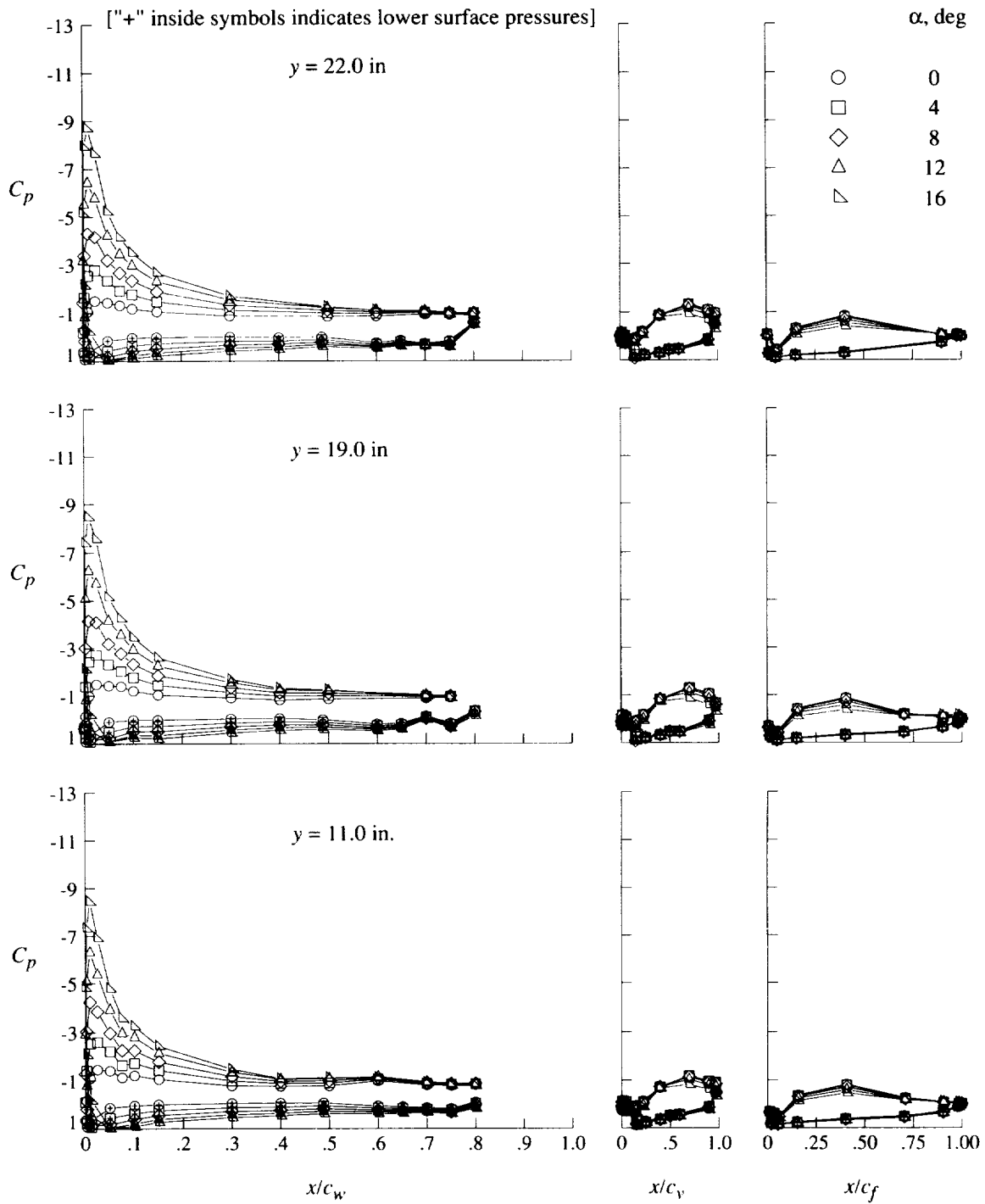
(b) $q = 40$ psf.

Figure 22. Continued.



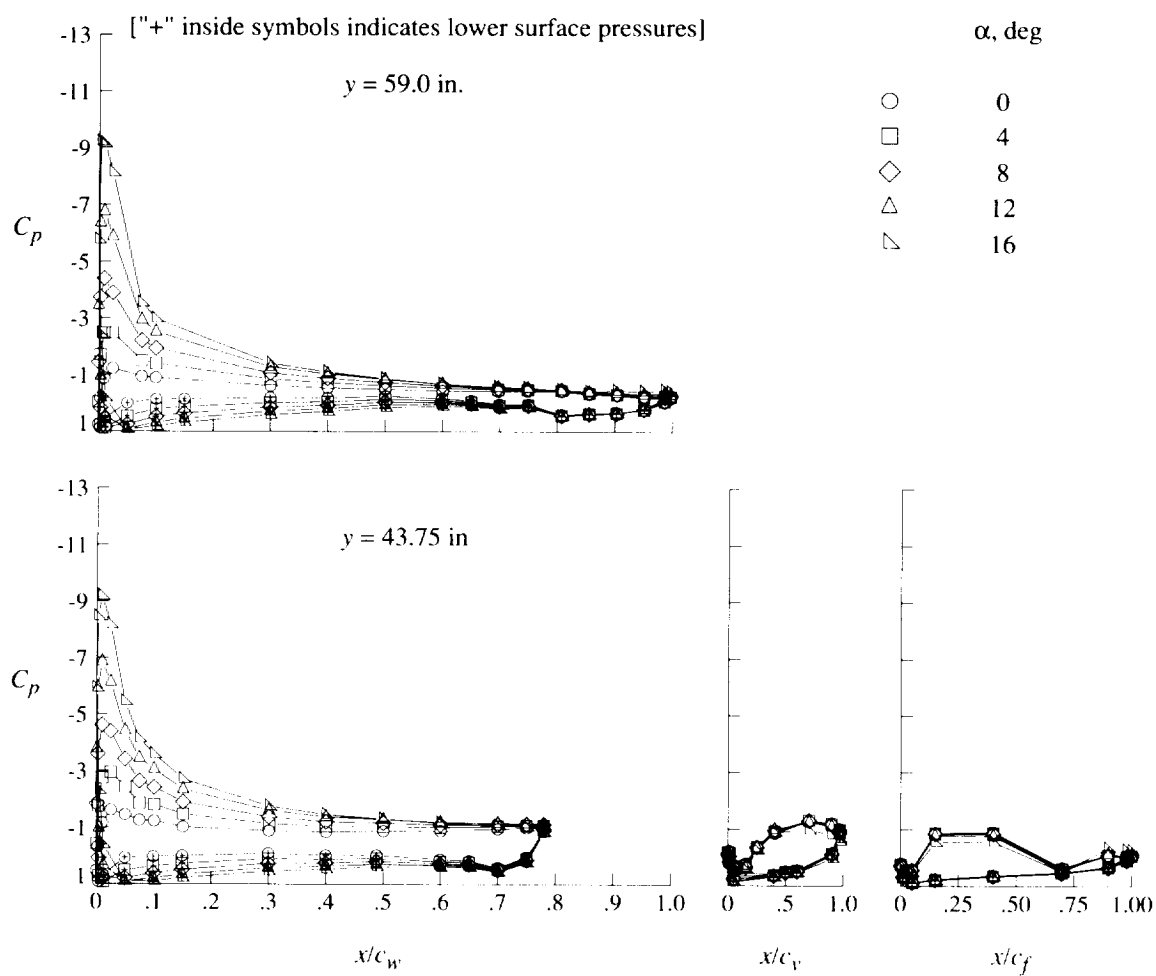
(b) Concluded.

Figure 22. Continued.



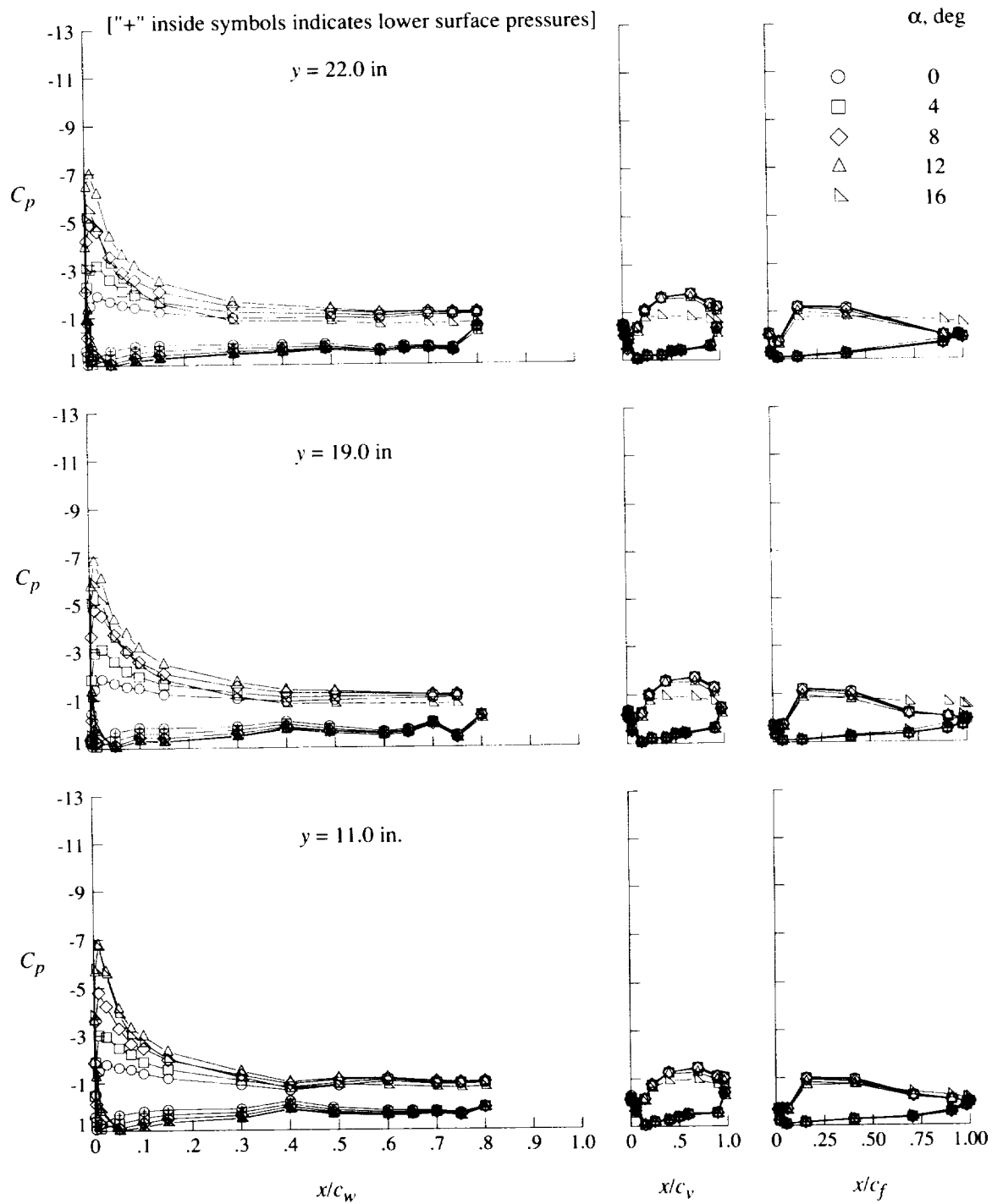
(c) $q = 60$ psf.

Figure 22. Continued.



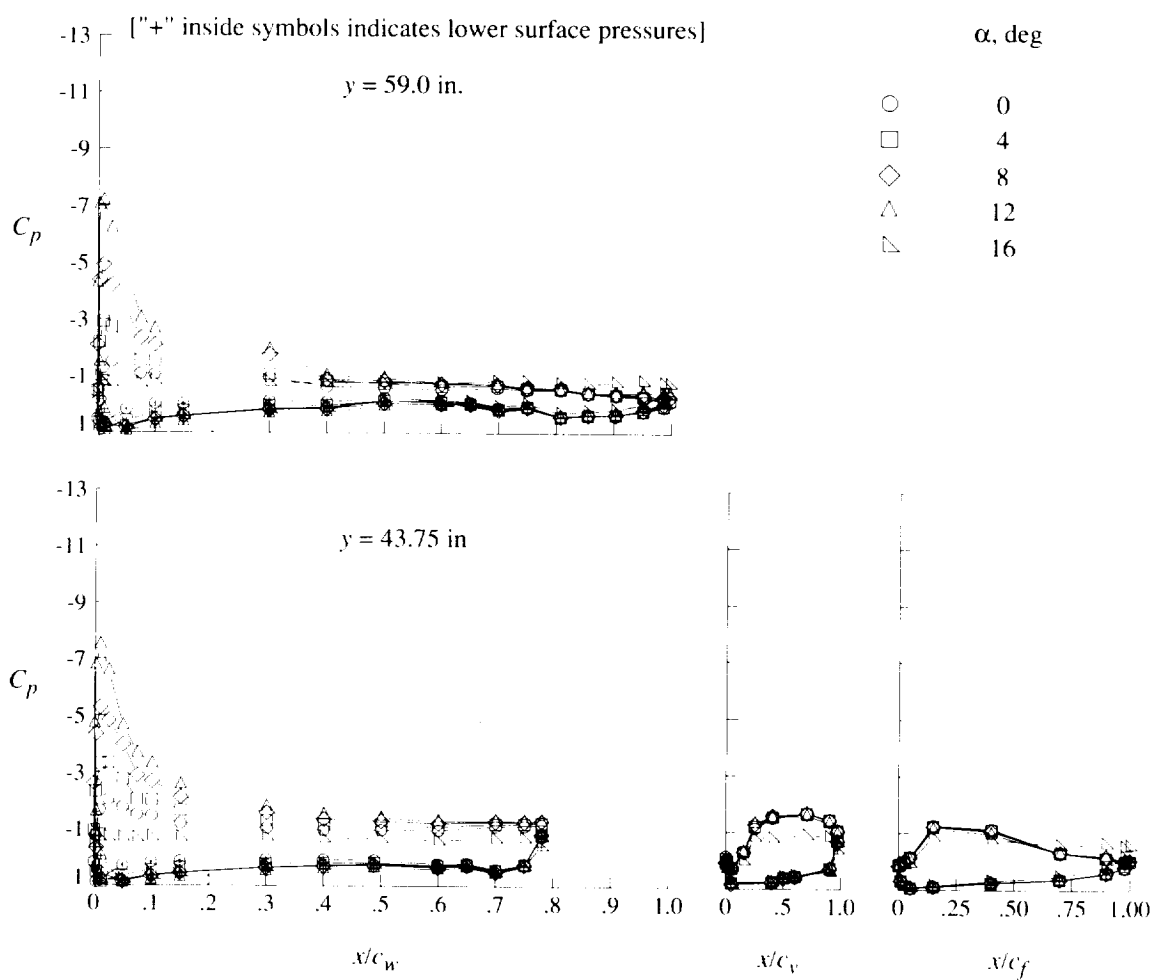
(c) Concluded.

Figure 22. Concluded.



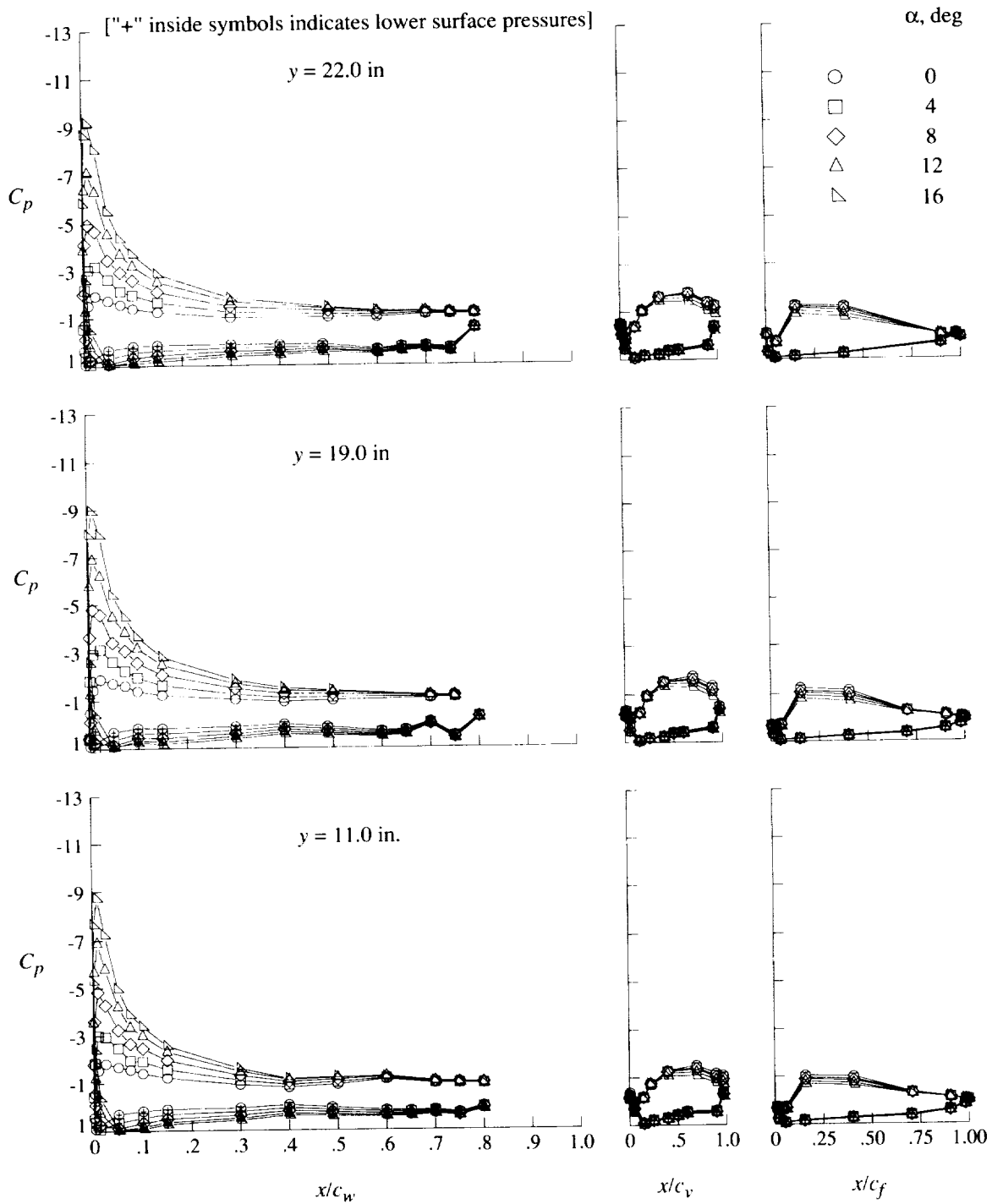
(a) $q = 20$ psf.

Figure 23. Effect of angle of attack on pressure distributions for flaps-only configuration at $\delta_f = 40^\circ$.



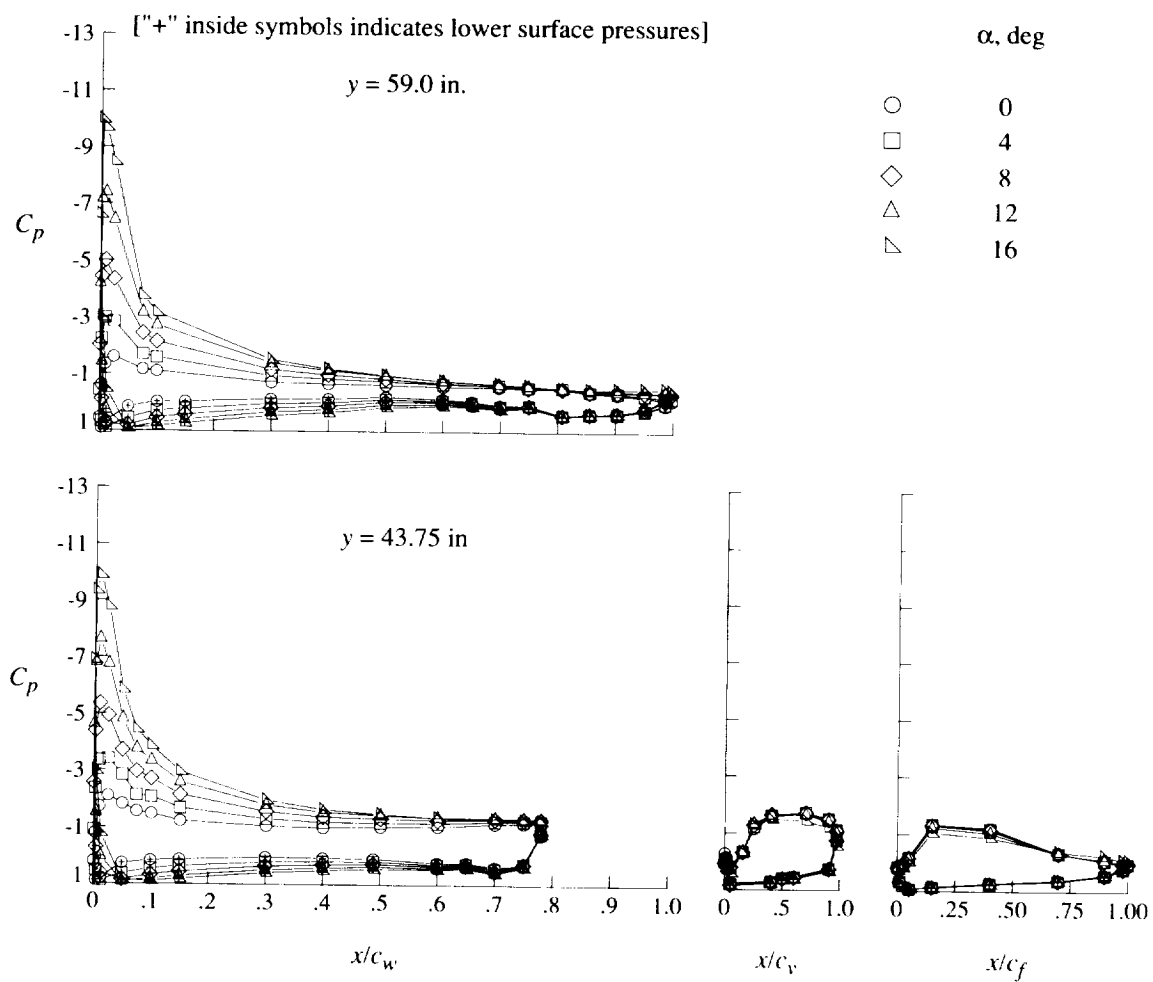
(a) Concluded.

Figure 23. Continued.



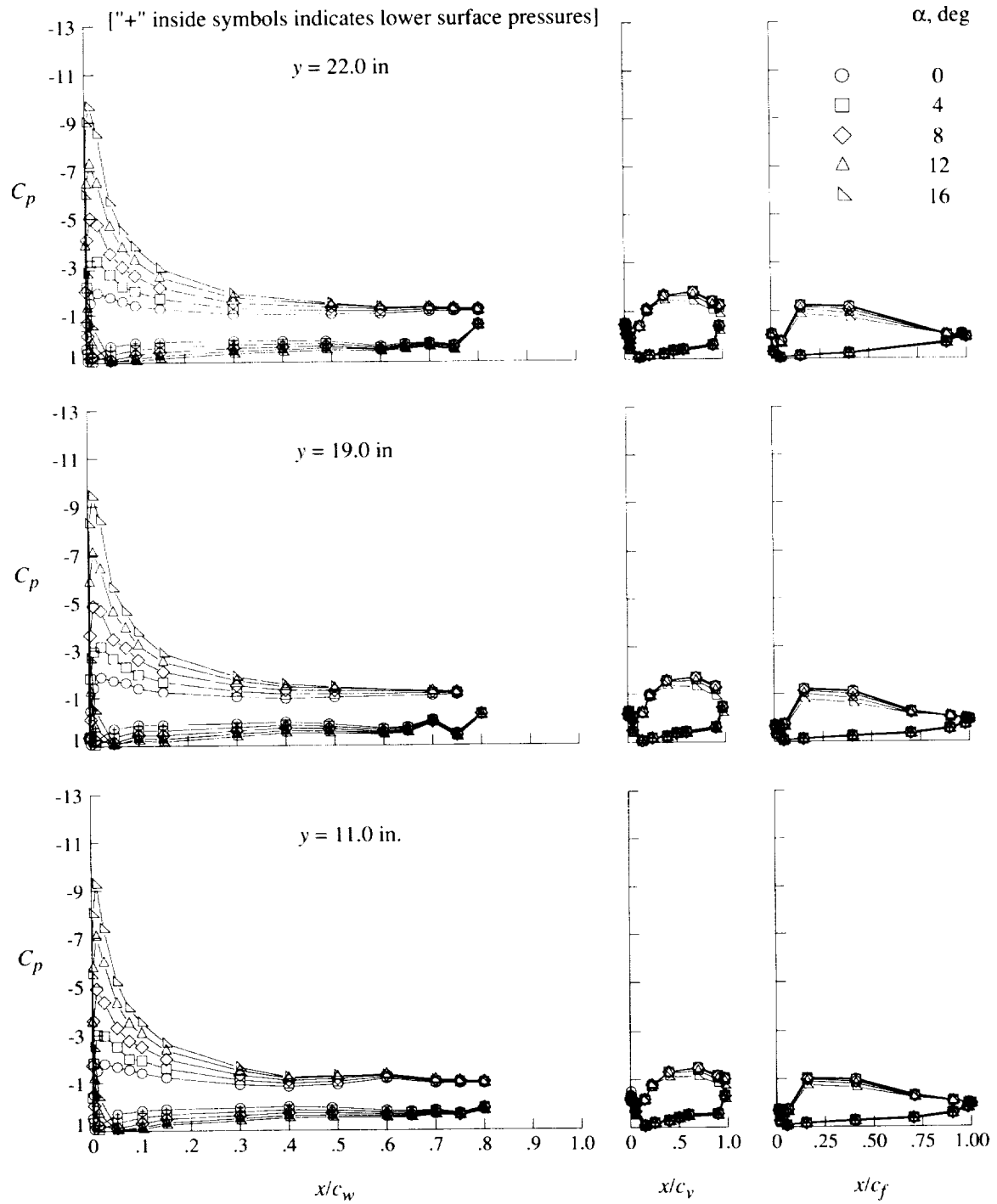
(b) $q = 40$ psf.

Figure 23. Continued.



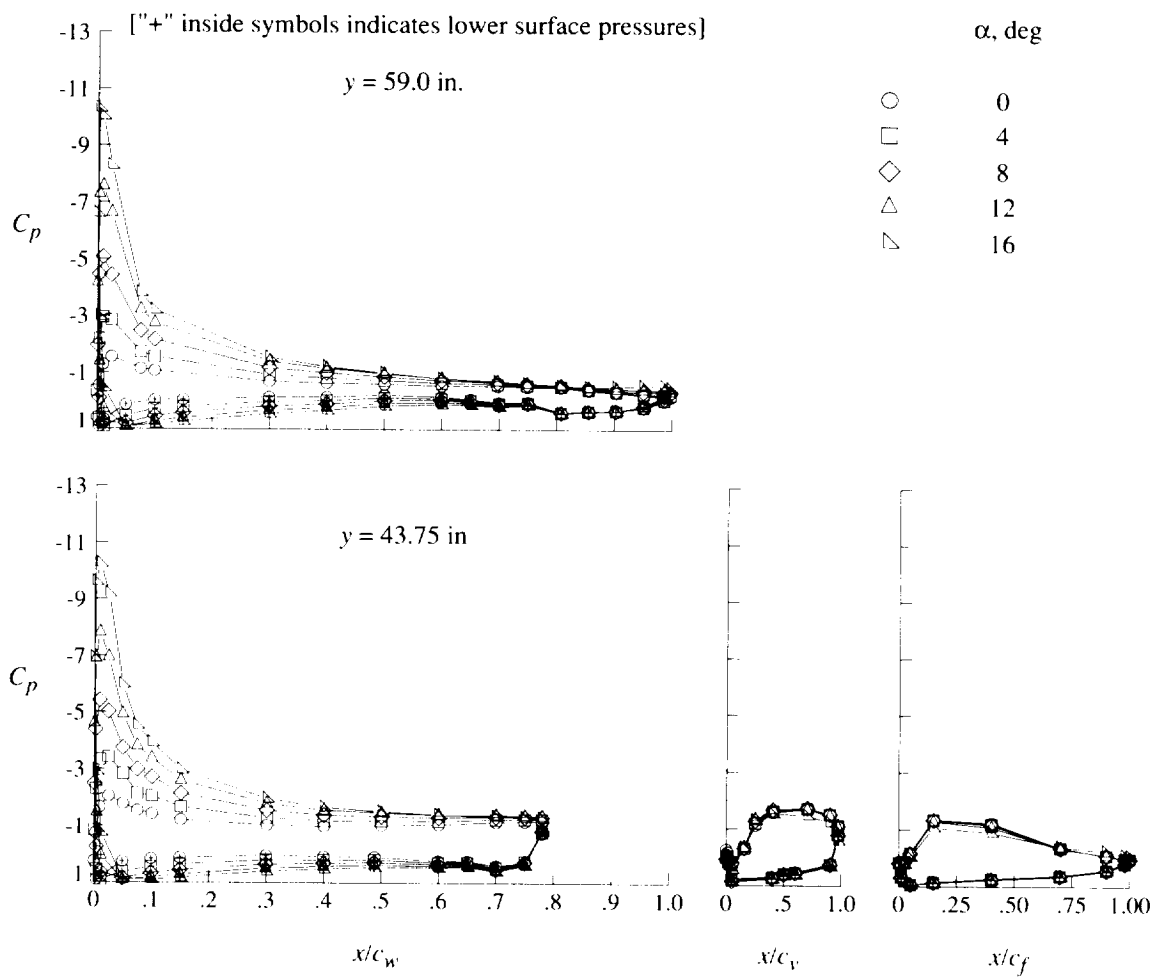
(b) Concluded.

Figure 23. Continued.



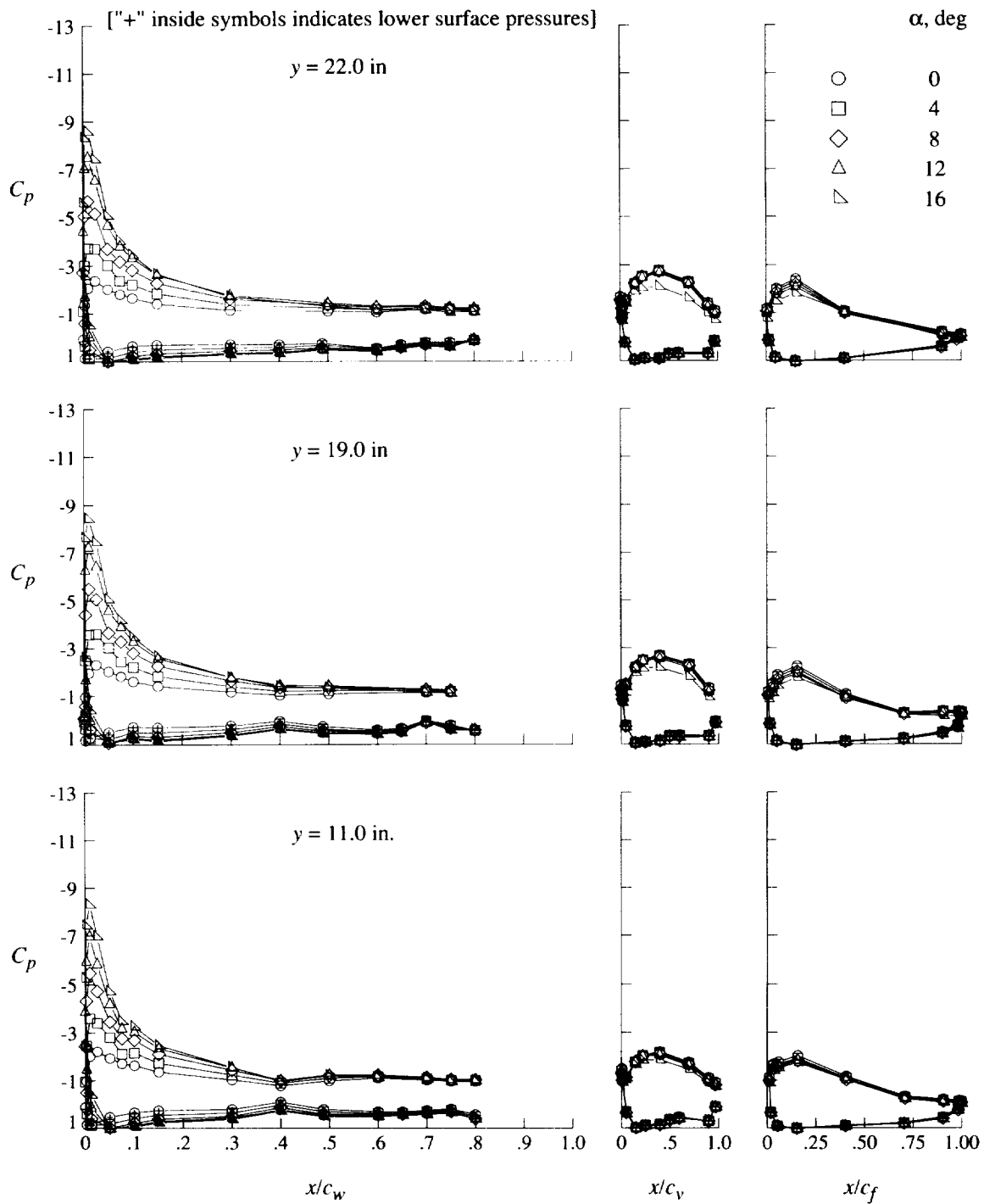
(c) $q = 60$ psf.

Figure 23. Continued.



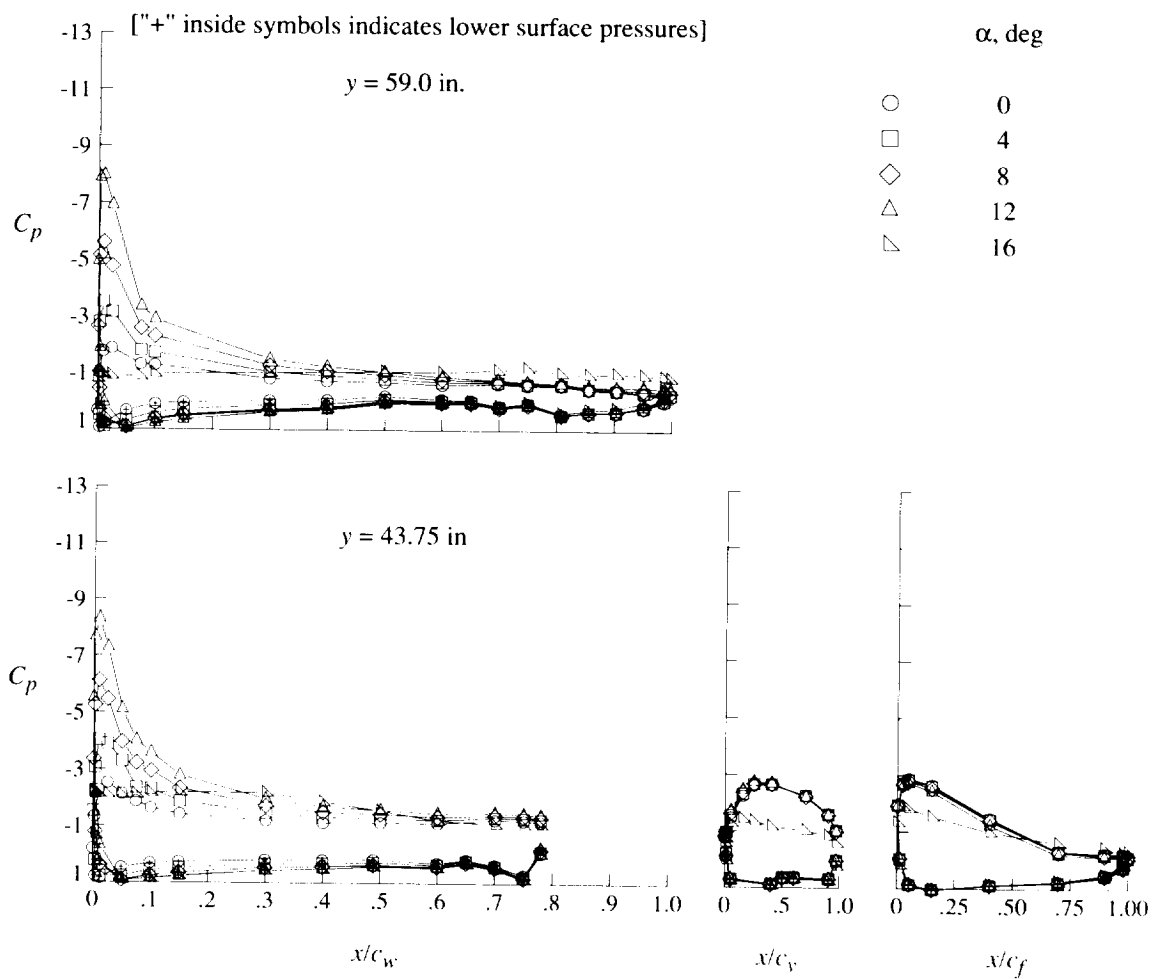
(c) Concluded.

Figure 23. Concluded.



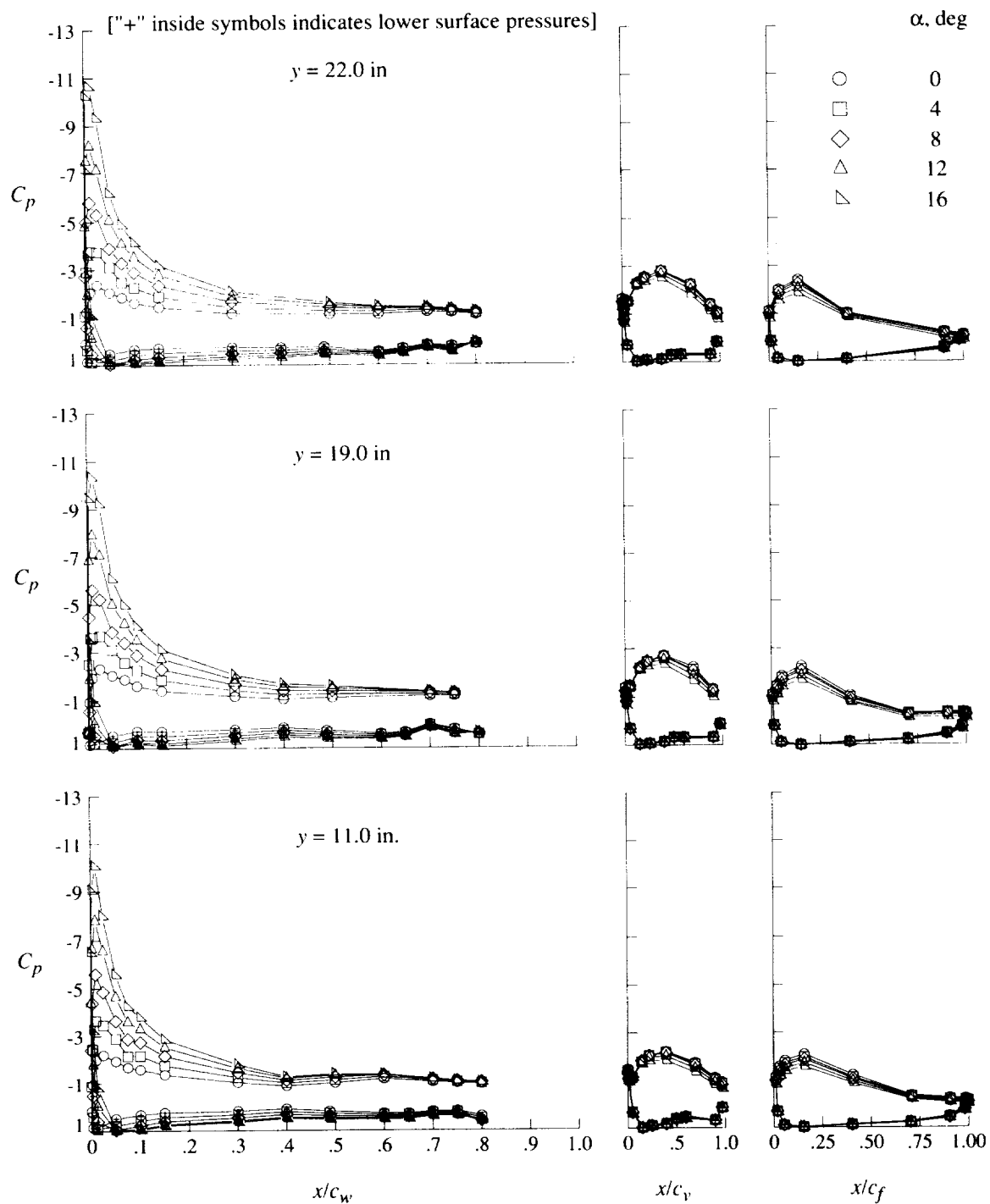
(a) $q = 20$ psf.

Figure 24. Effect of angle of attack on pressure distributions for flaps-only configuration at $\delta_f = 60^\circ$.



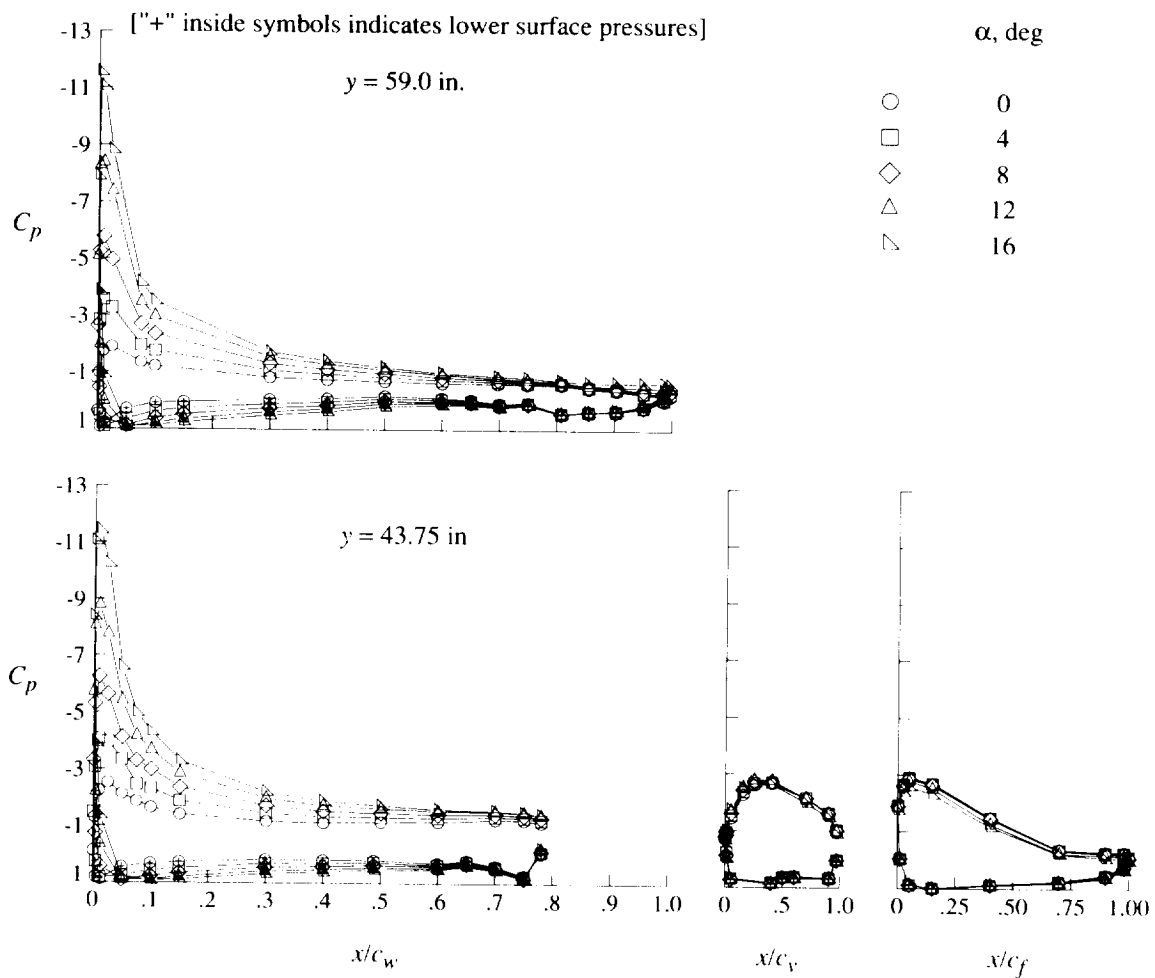
(a) Concluded.

Figure 24. Continued.



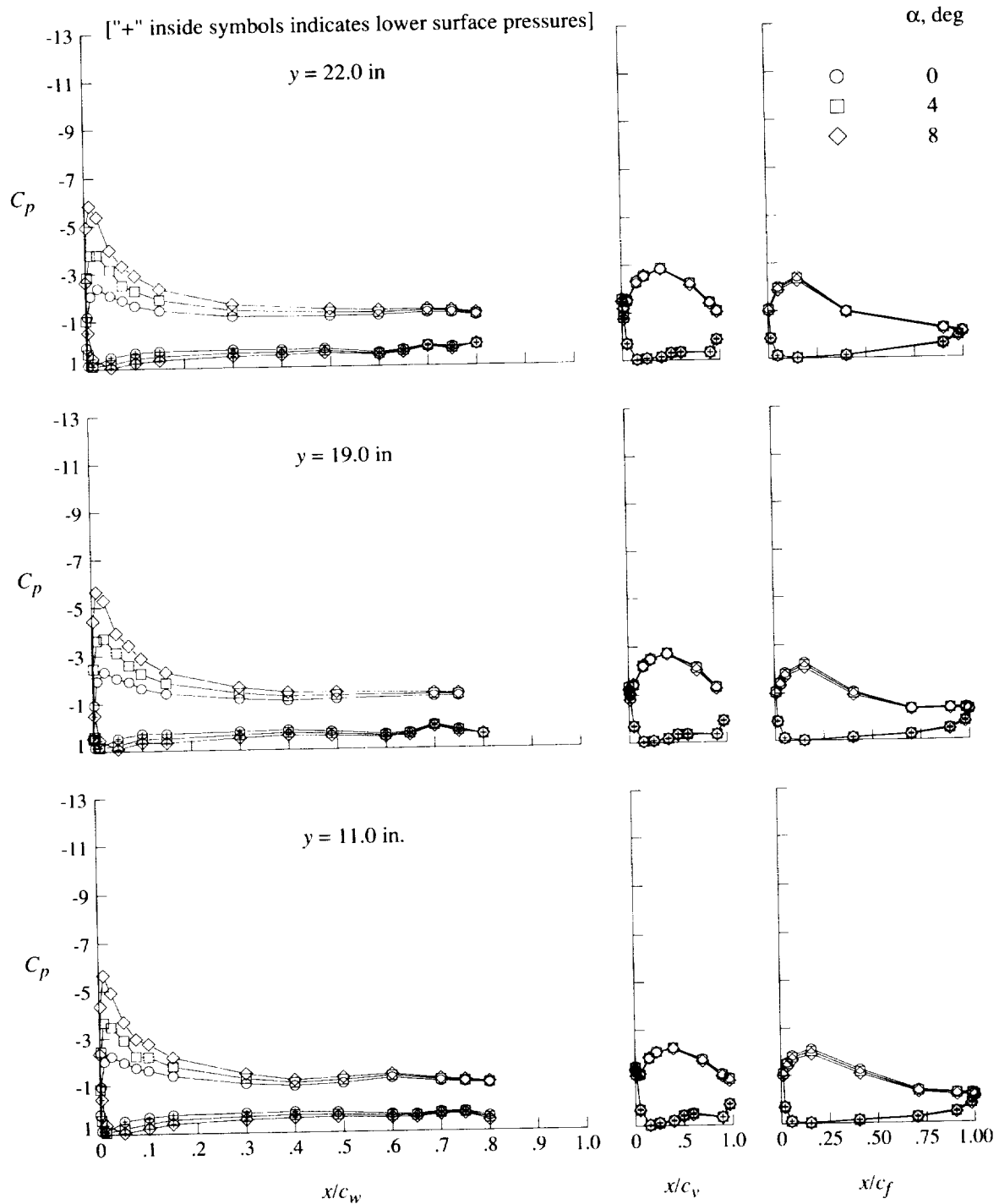
(b) $q = 40$ psf.

Figure 24. Continued.



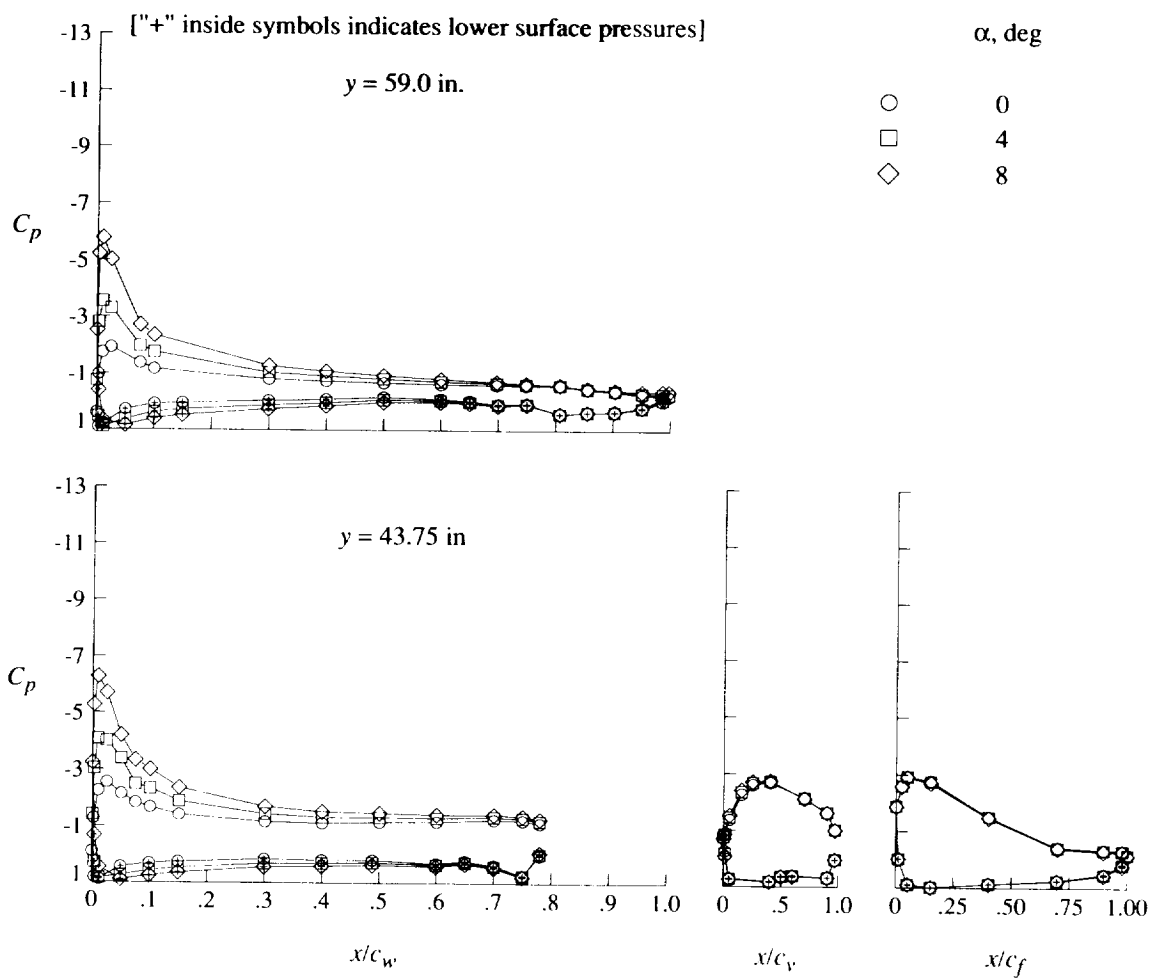
(b) Concluded.

Figure 24. Continued.



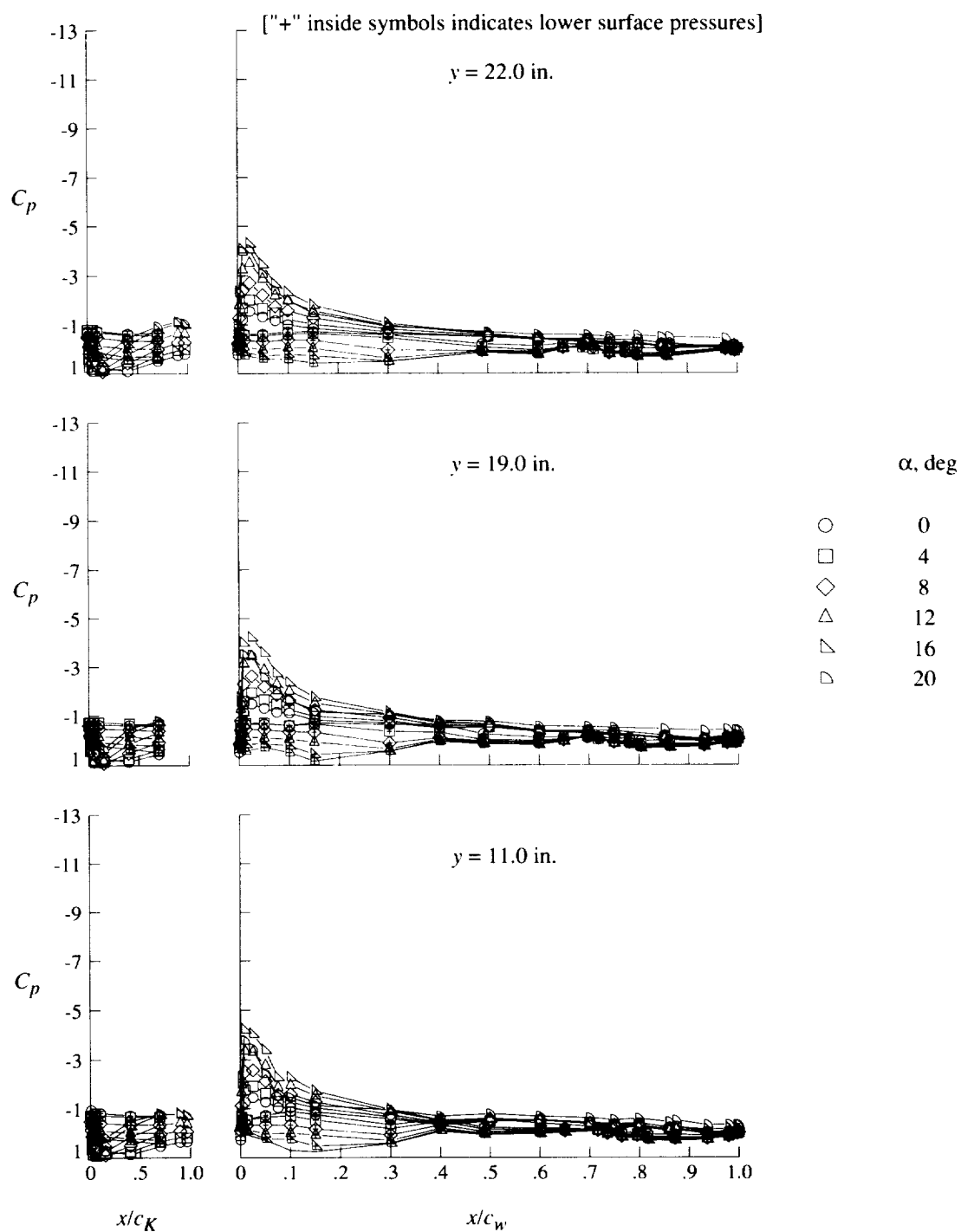
(c) $q = 60$ psf.

Figure 24. Continued.



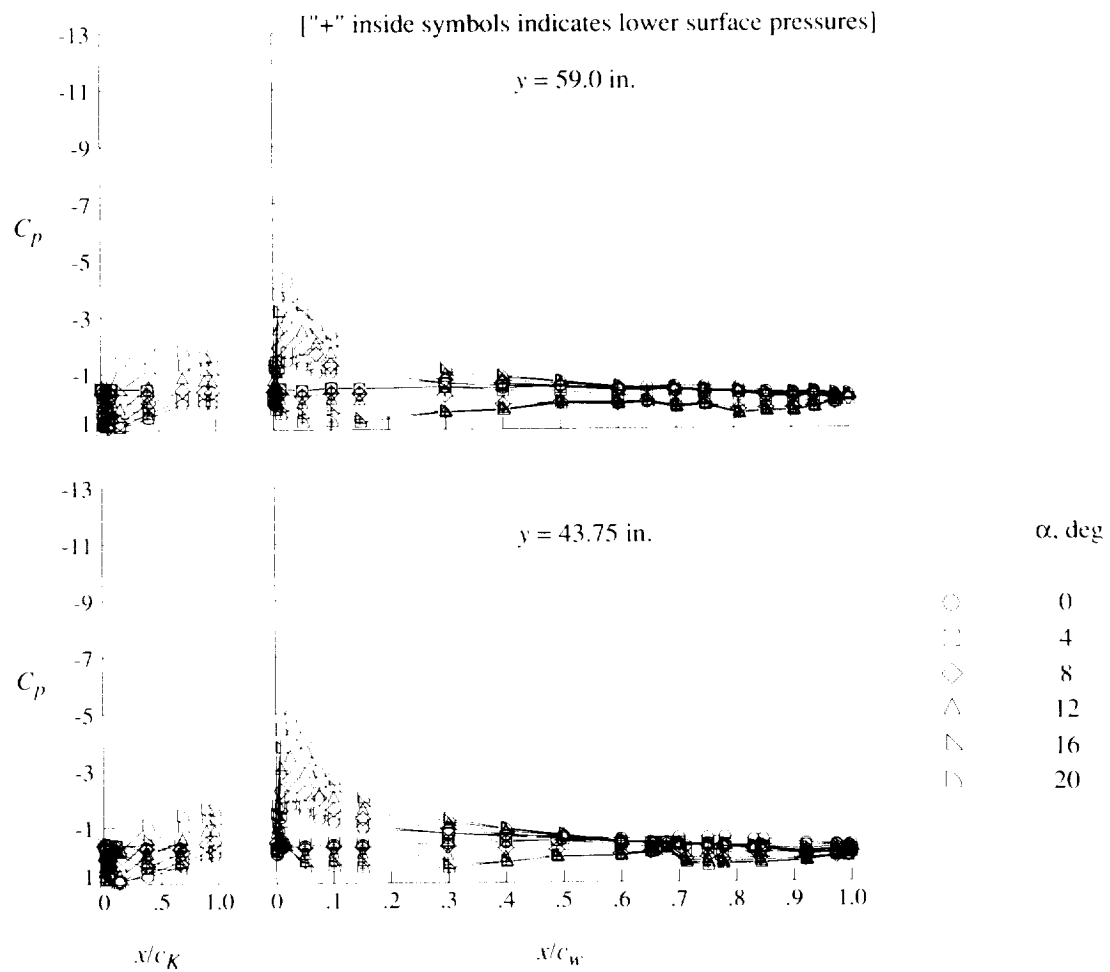
(c) Concluded.

Figure 24. Concluded.



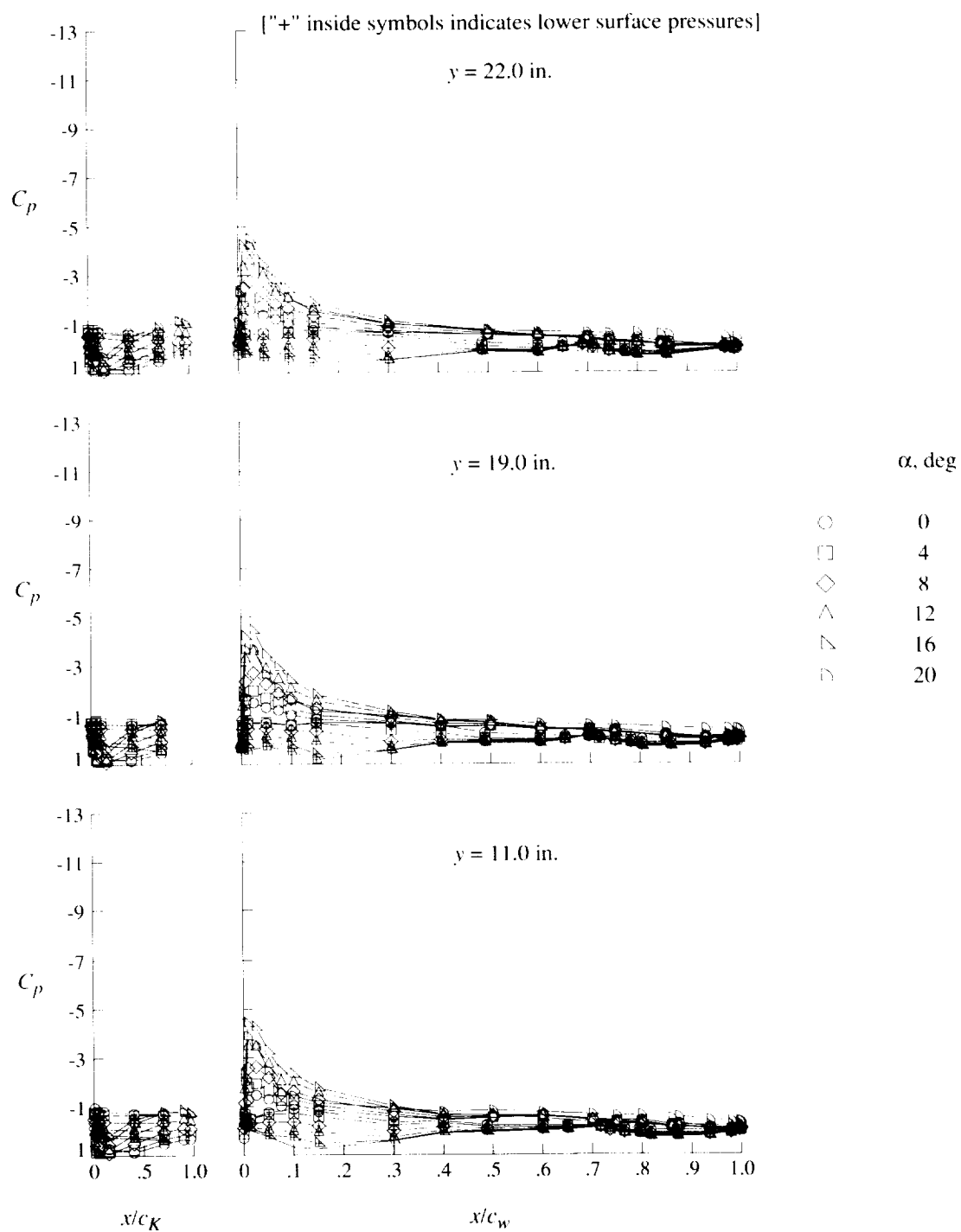
(a) $q = 20$ psf.

Figure 25. Effect of angle of attack on pressure distributions for Krueger-flap-only configuration.



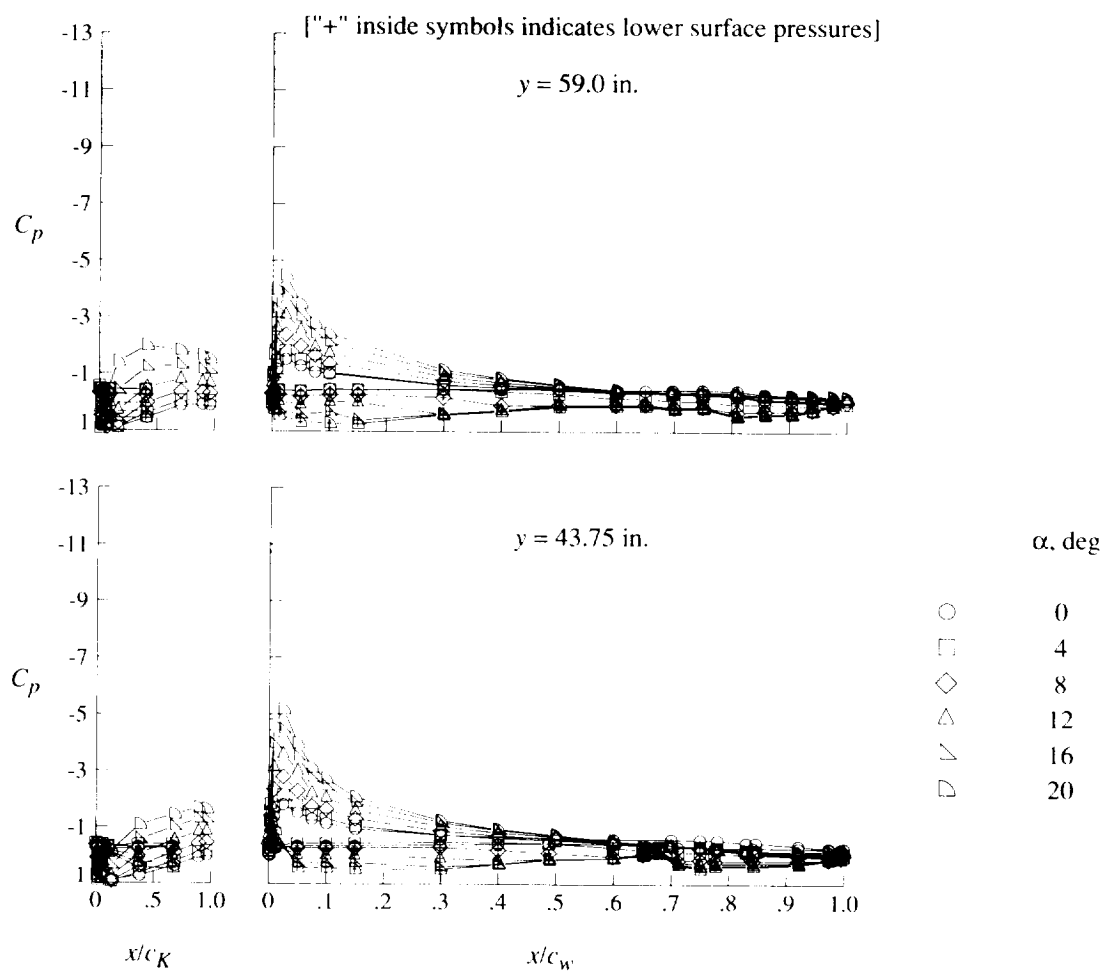
(a) Concluded.

Figure 25. Continued.



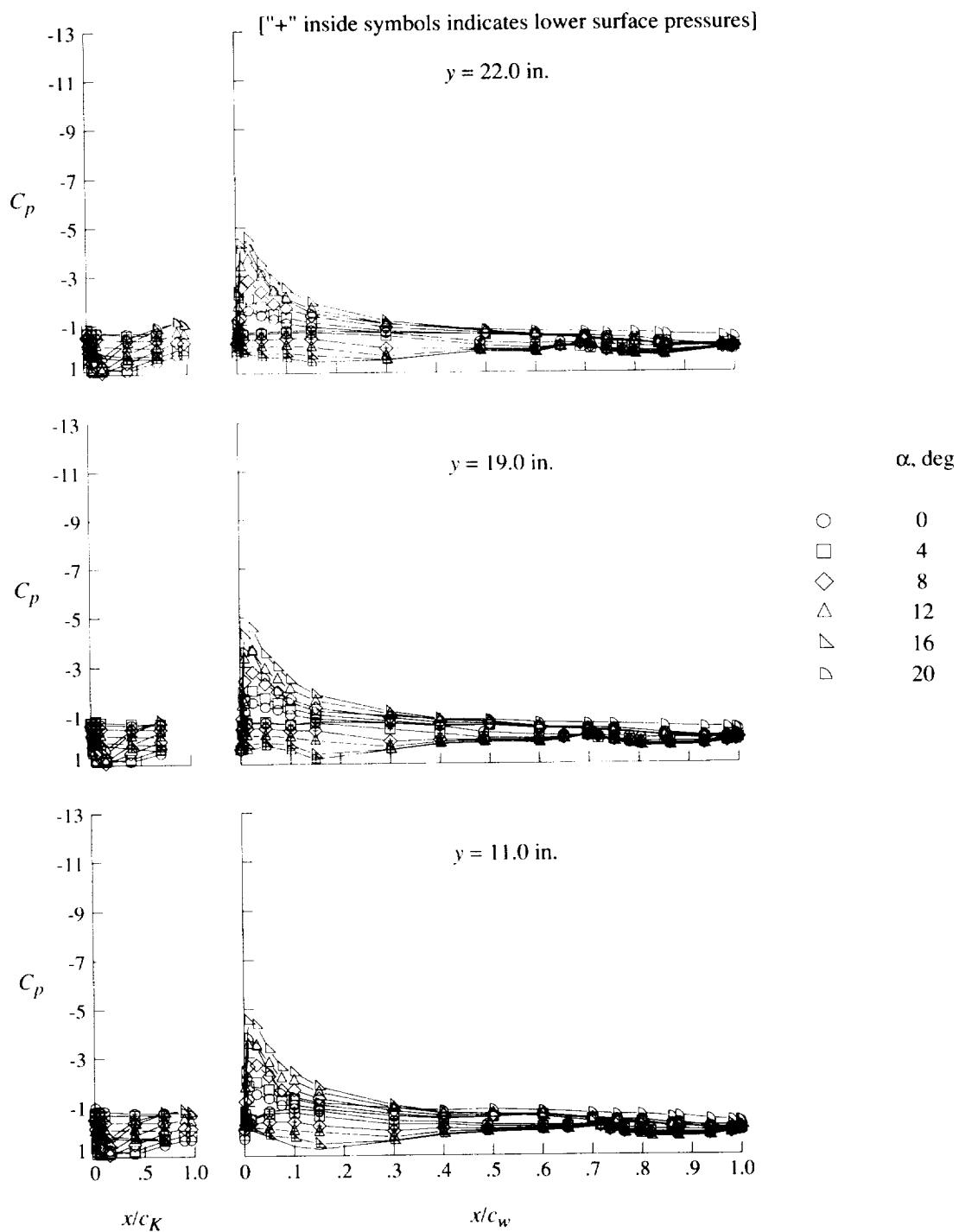
(b) $q = 40$ psf.

Figure 25. Continued.



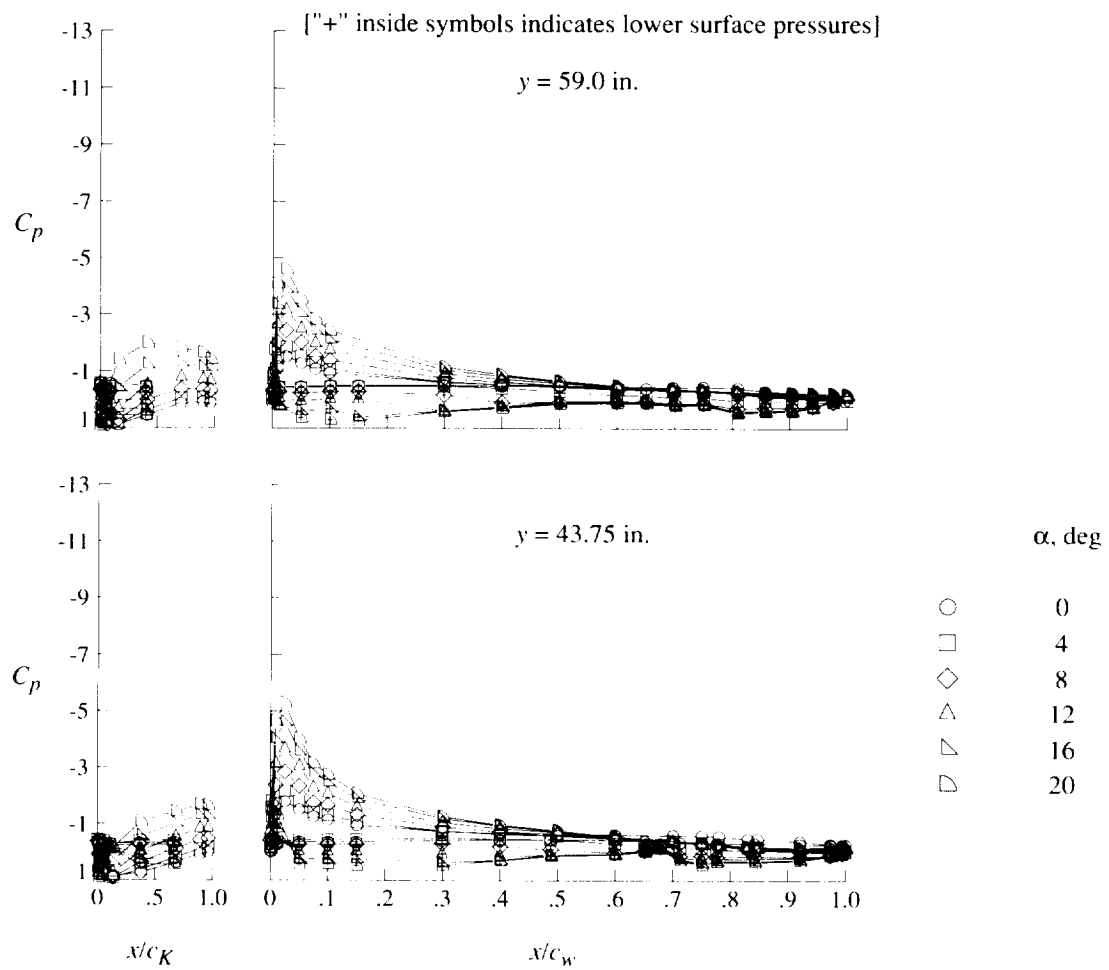
(b) Concluded.

Figure 25. Continued.



(c) $q = 60$ psf.

Figure 25. Continued.



(c) Concluded.

Figure 25. Concluded.

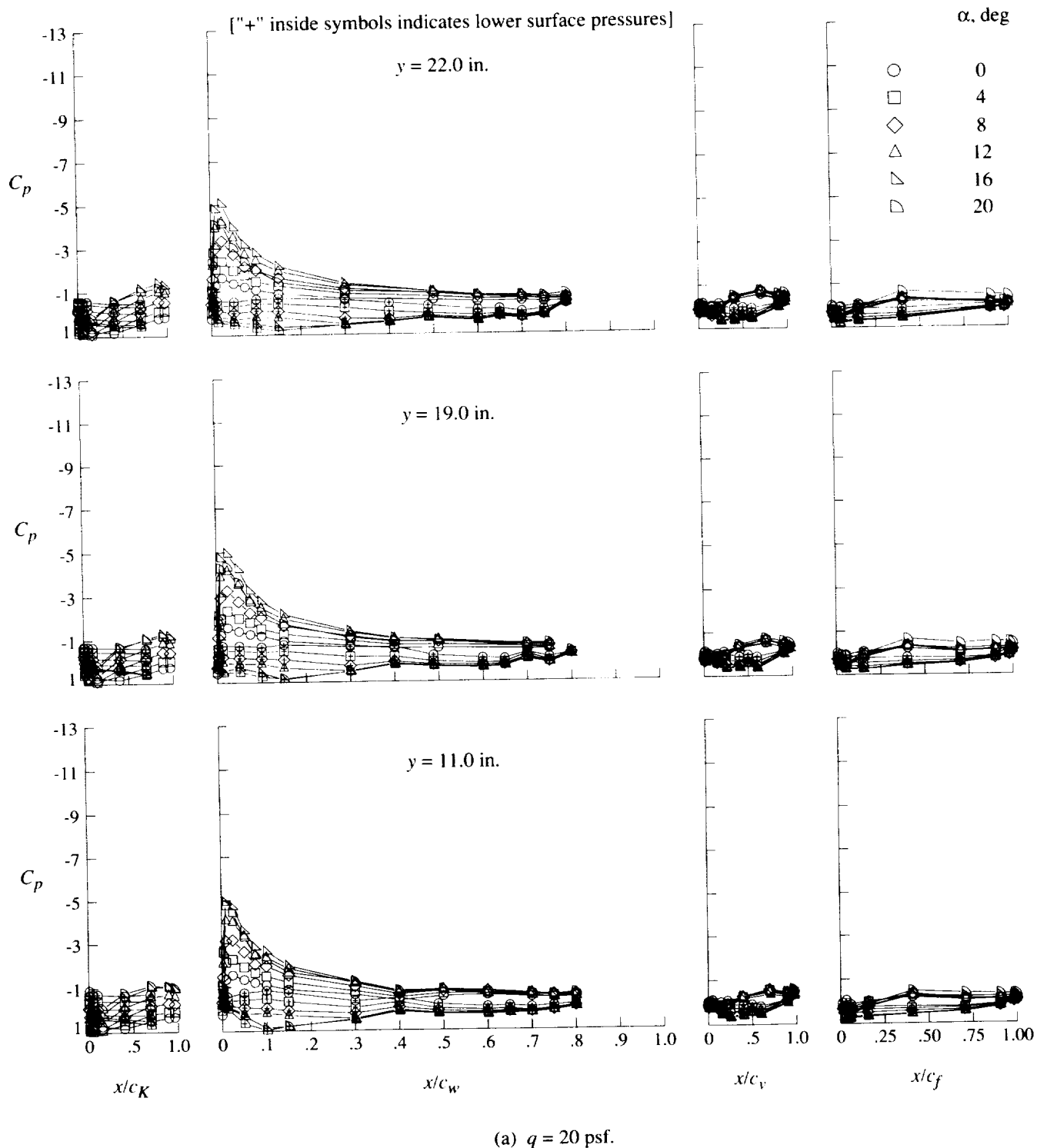
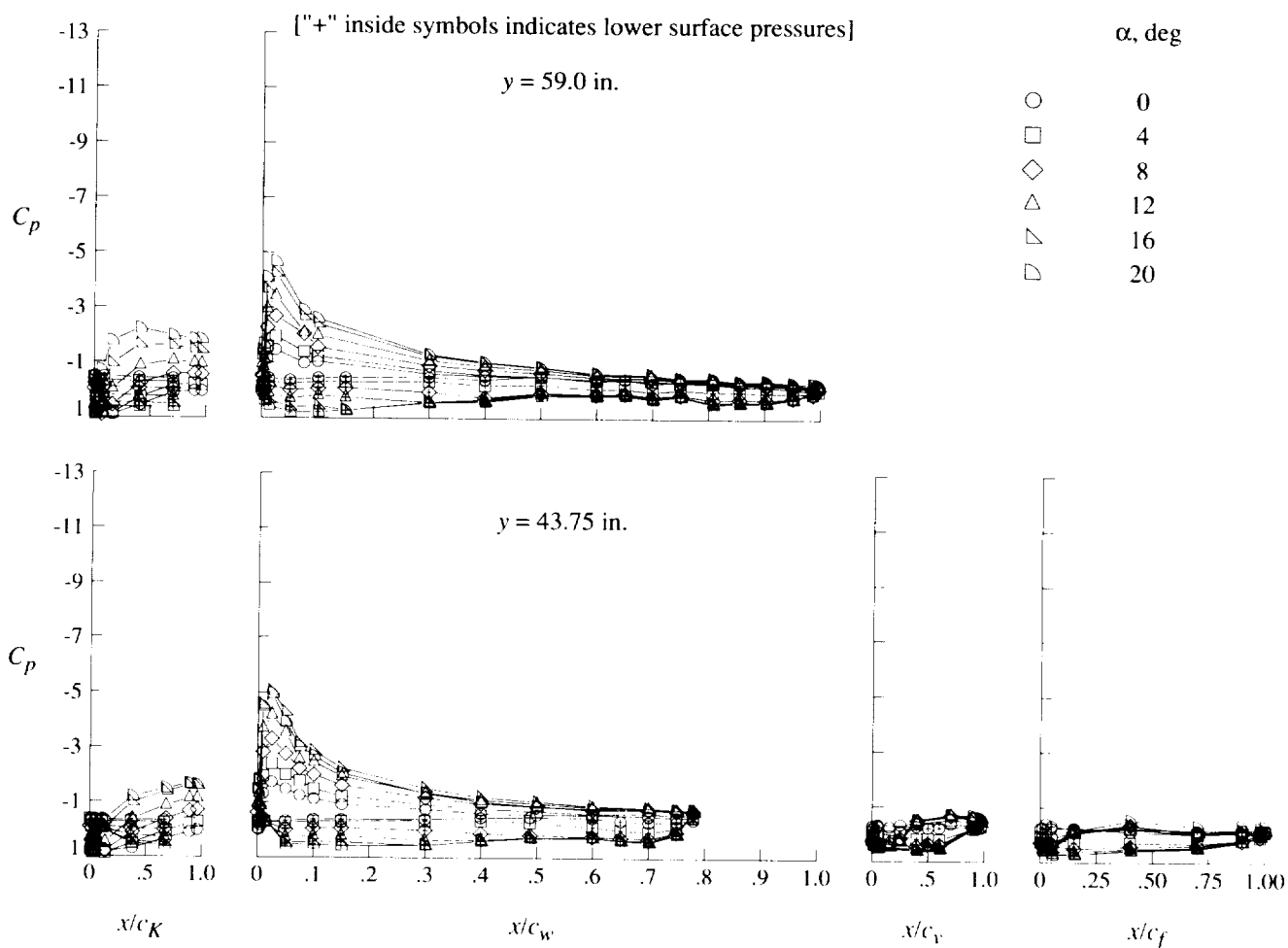
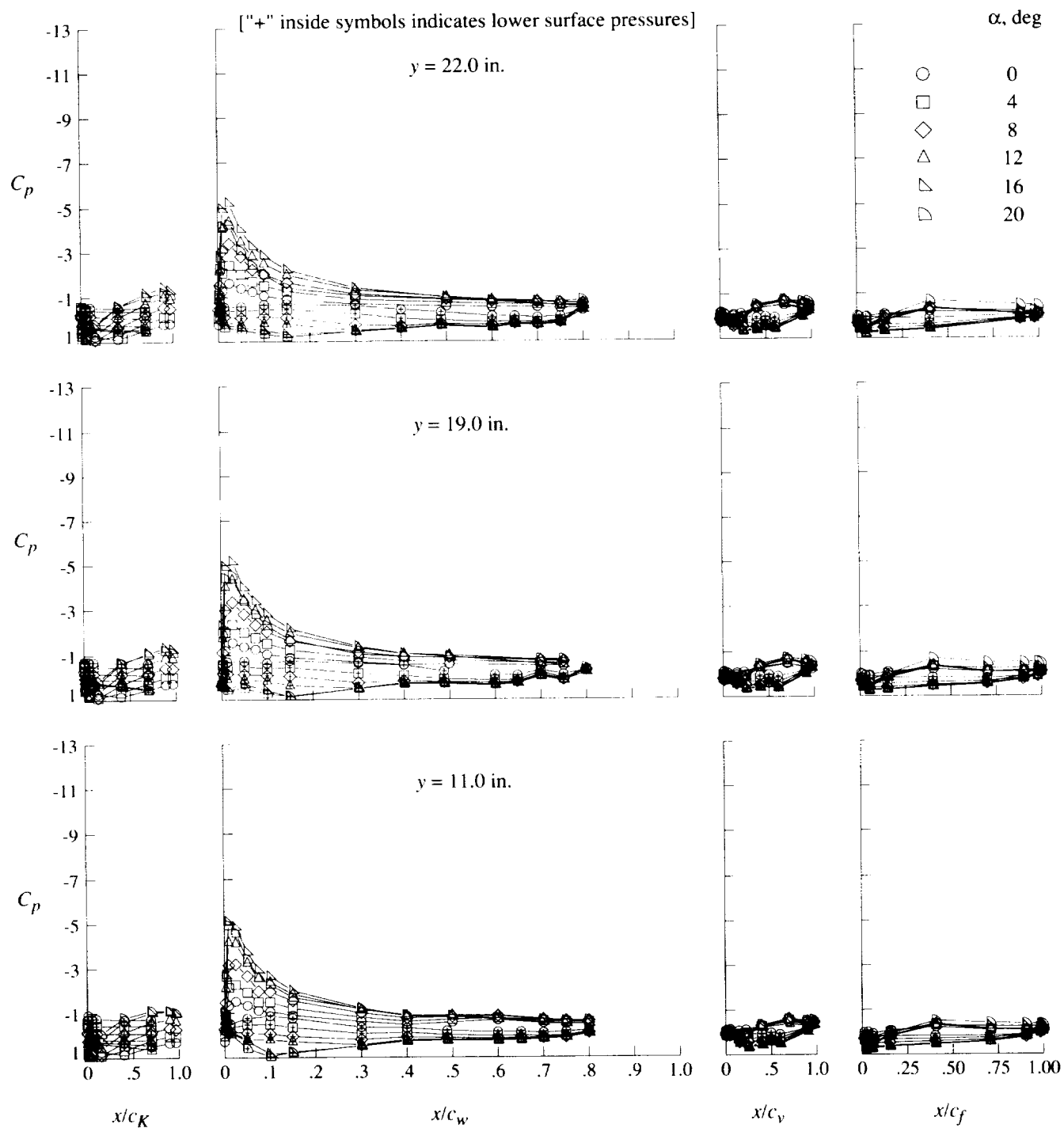


Figure 26. Effect of angle of attack on pressure distributions for high-lift configuration at $\delta_f = 20^\circ$.



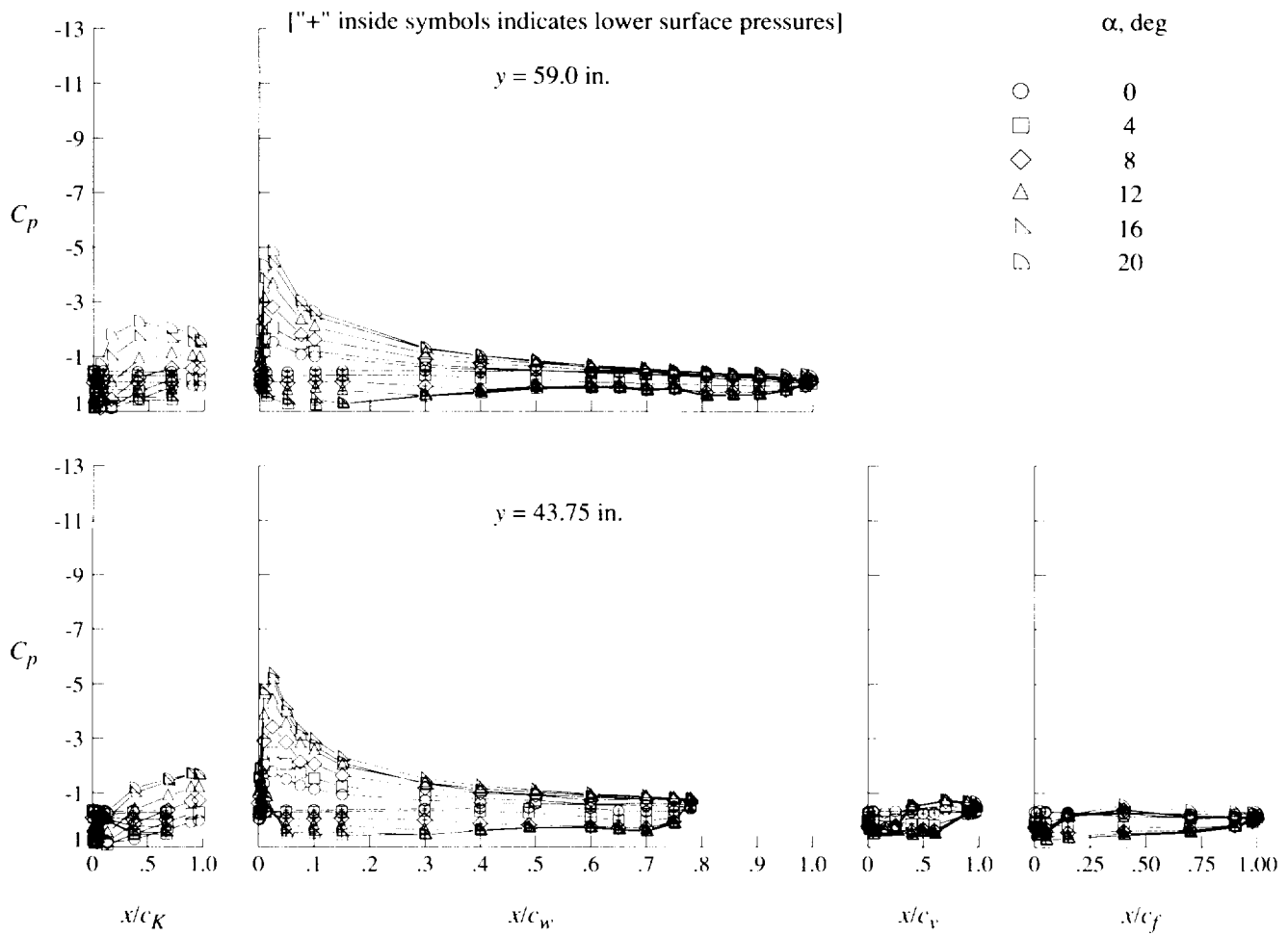
(a) Concluded.

Figure 26. Continued.



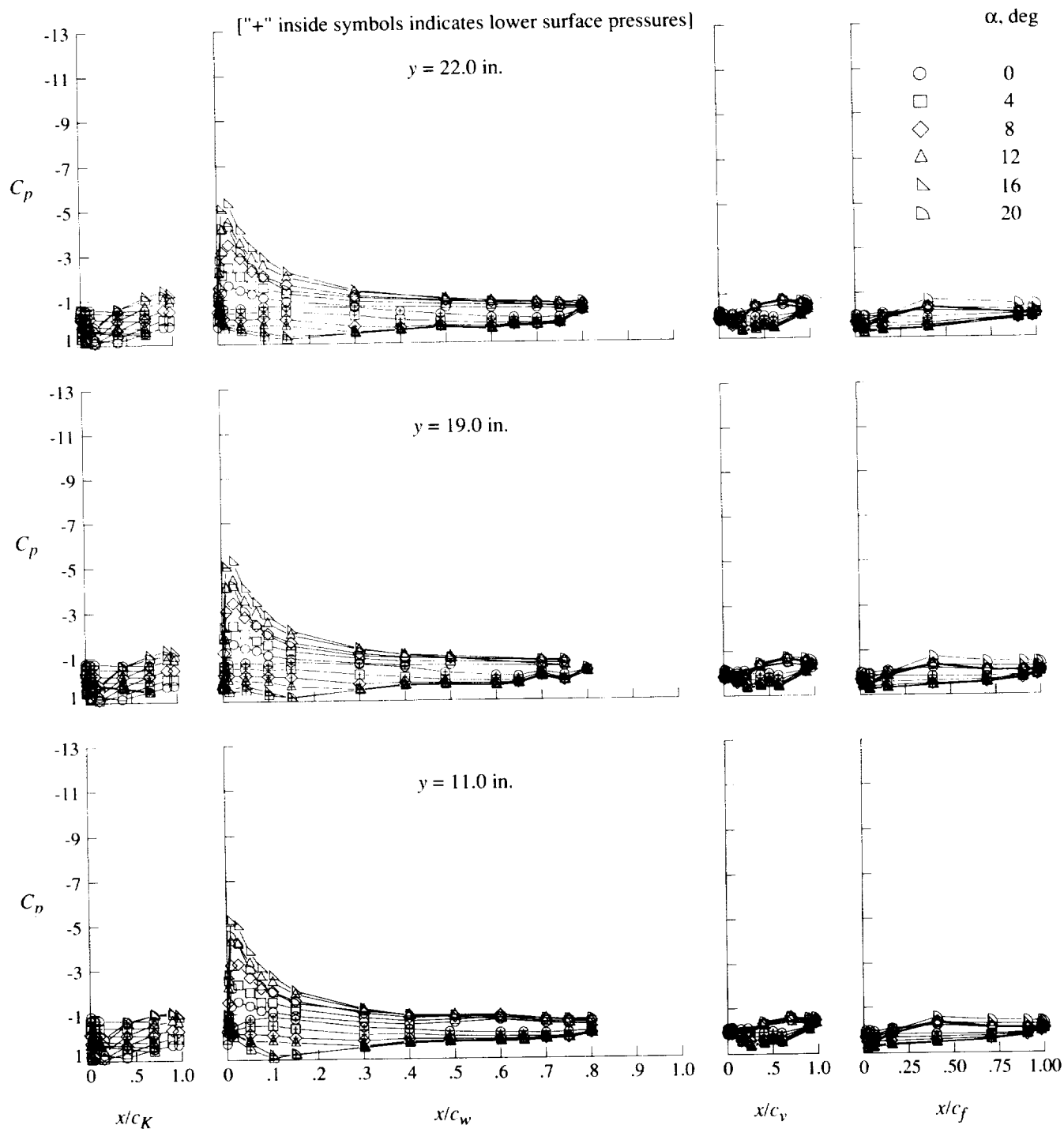
(b) $q = 40$ psf.

Figure 26. Continued.



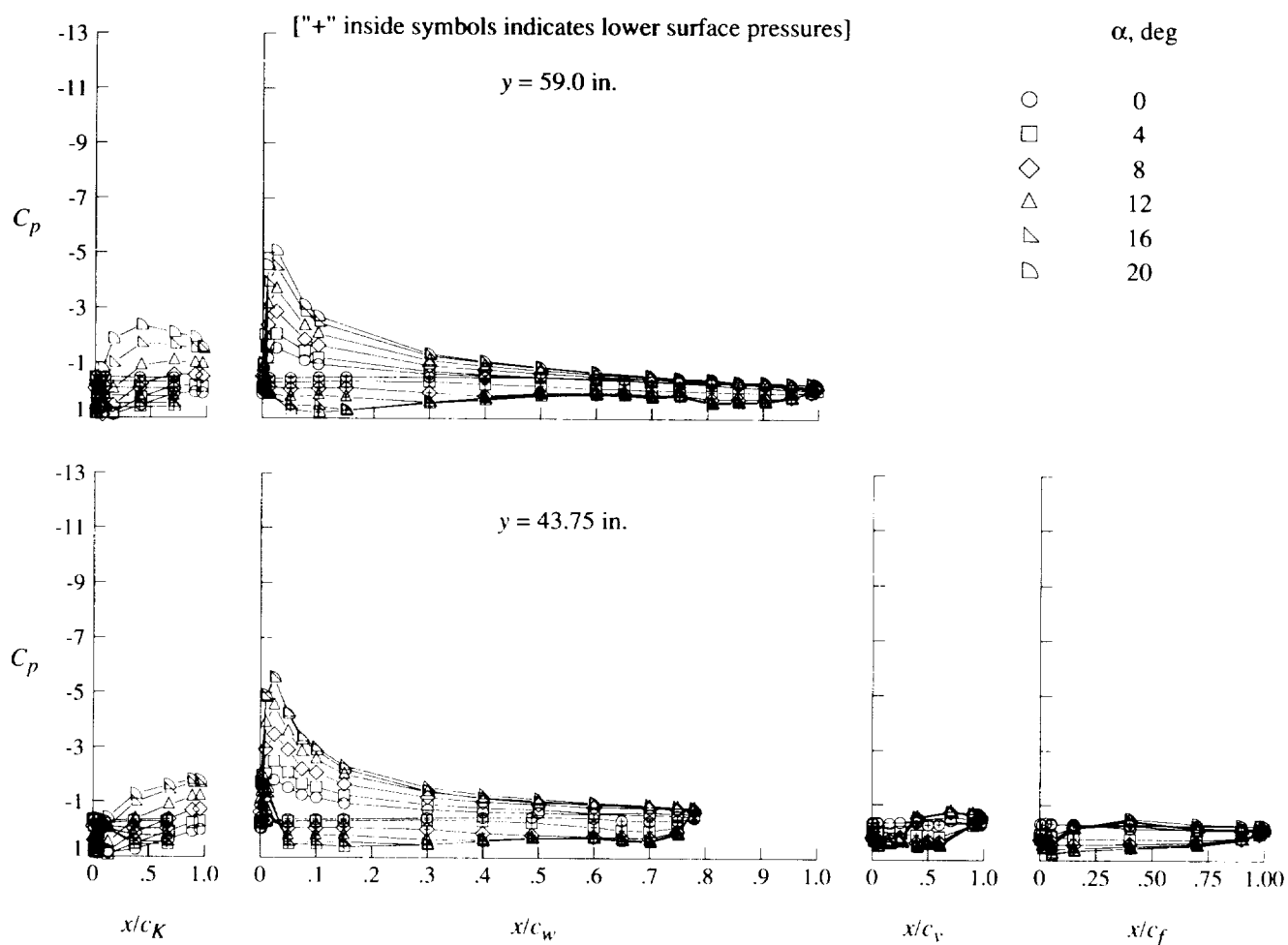
(b) Concluded.

Figure 26. Continued.



(c) $q = 60$ psf.

Figure 26. Continued.



(c) Concluded.

Figure 26. Concluded.

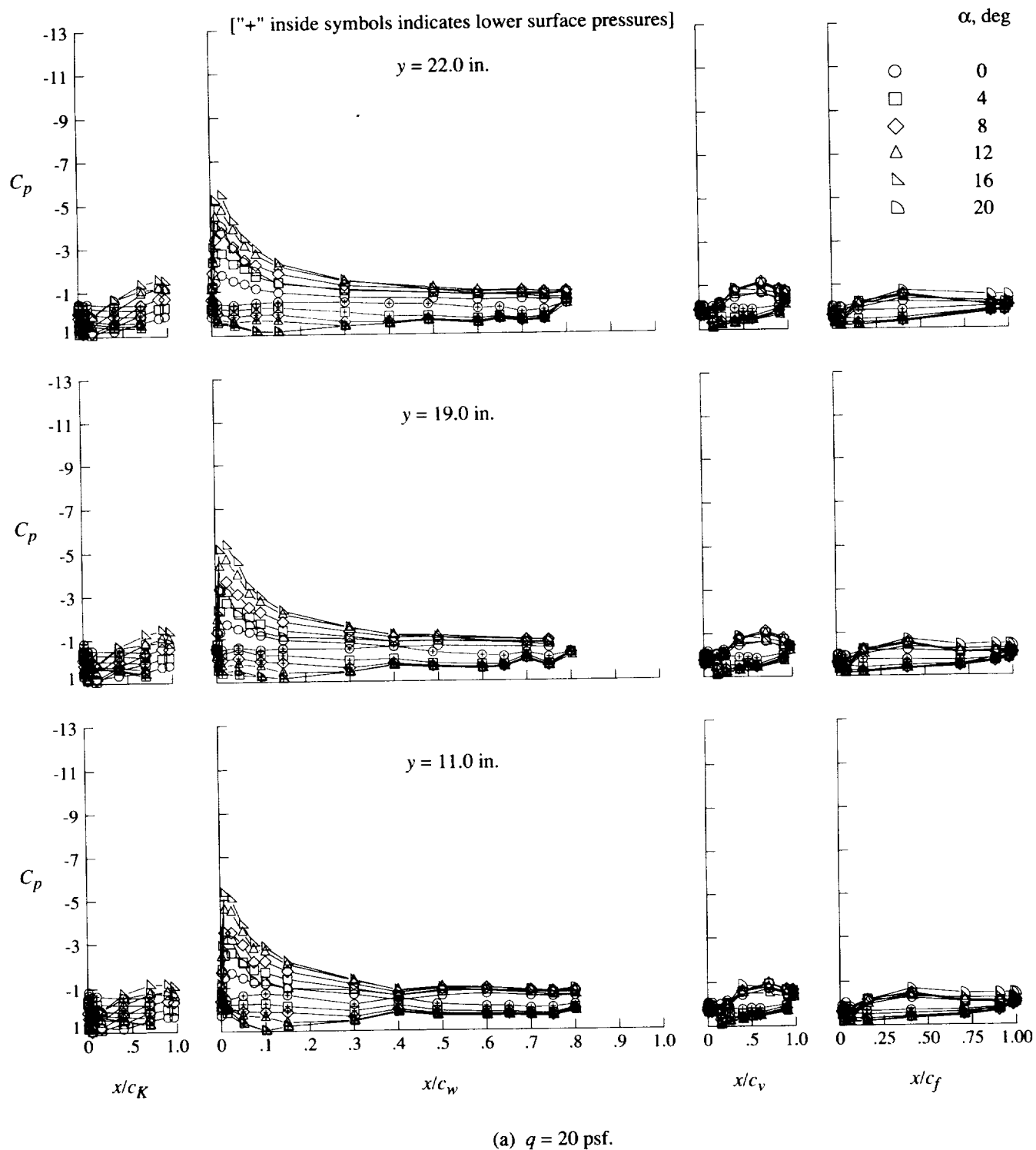
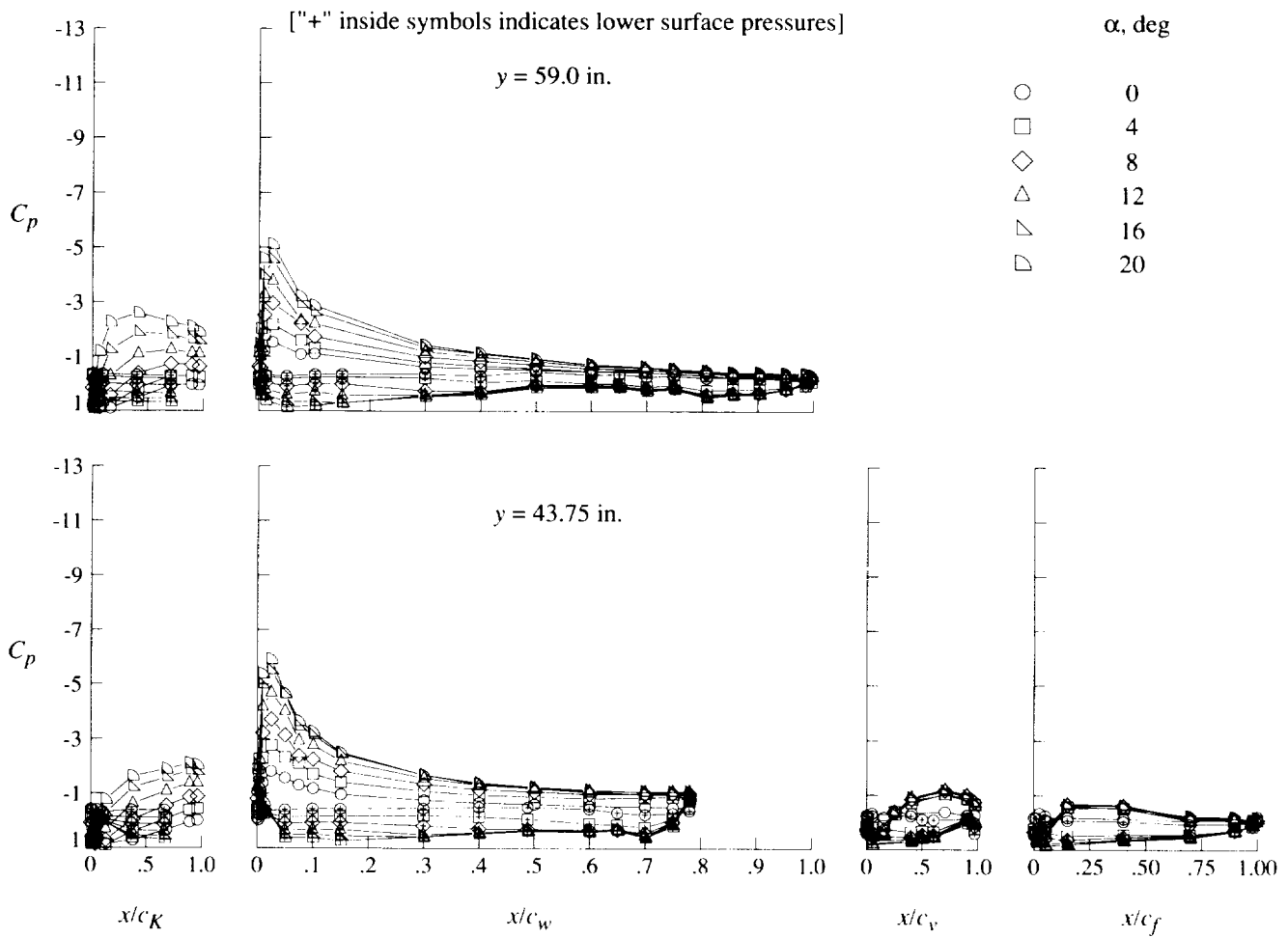
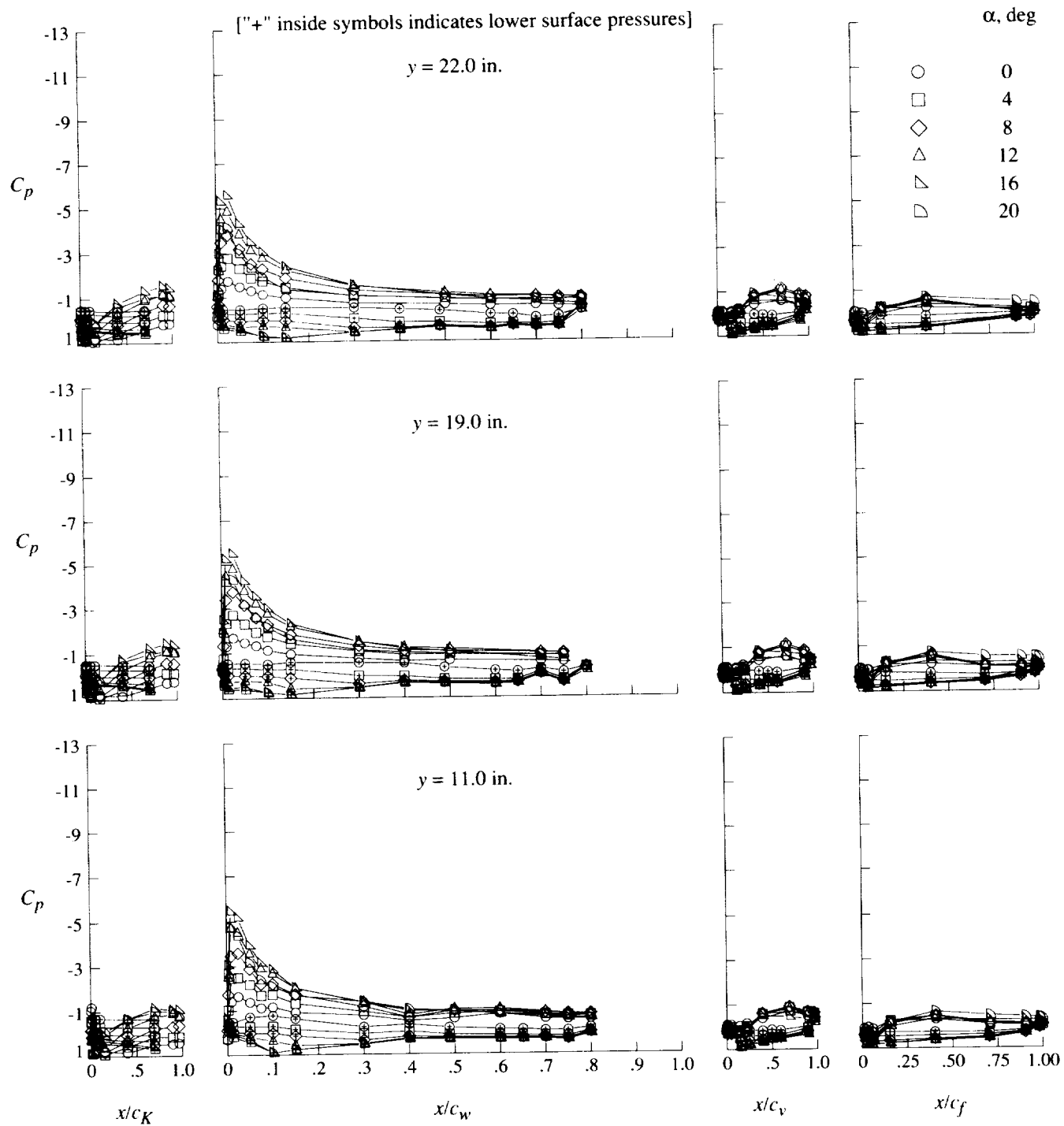


Figure 27. Effect of angle of attack on pressure distributions for high-lift configuration at $\delta_f = 30^\circ$.



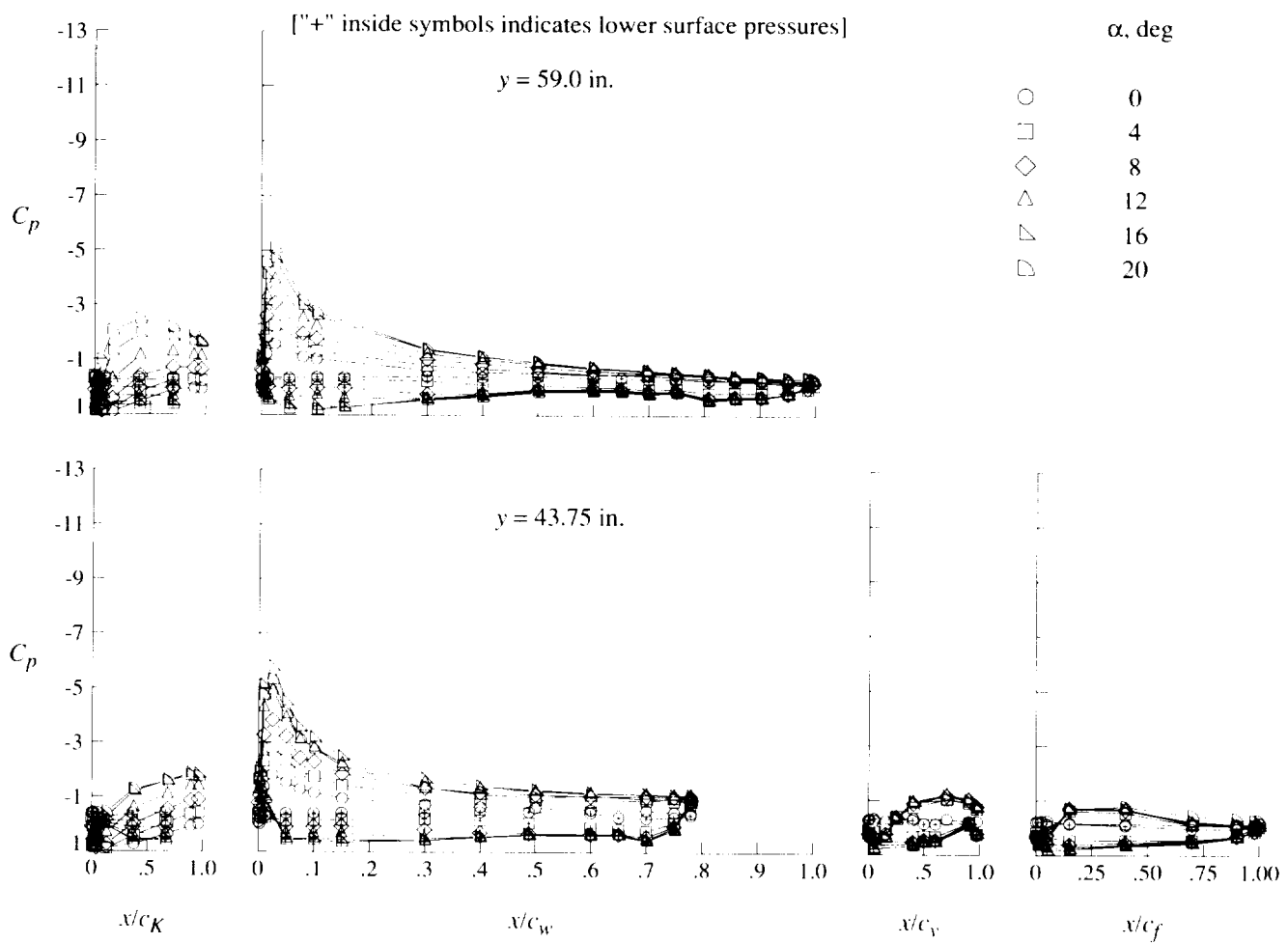
(a) Concluded.

Figure 27. Continued.



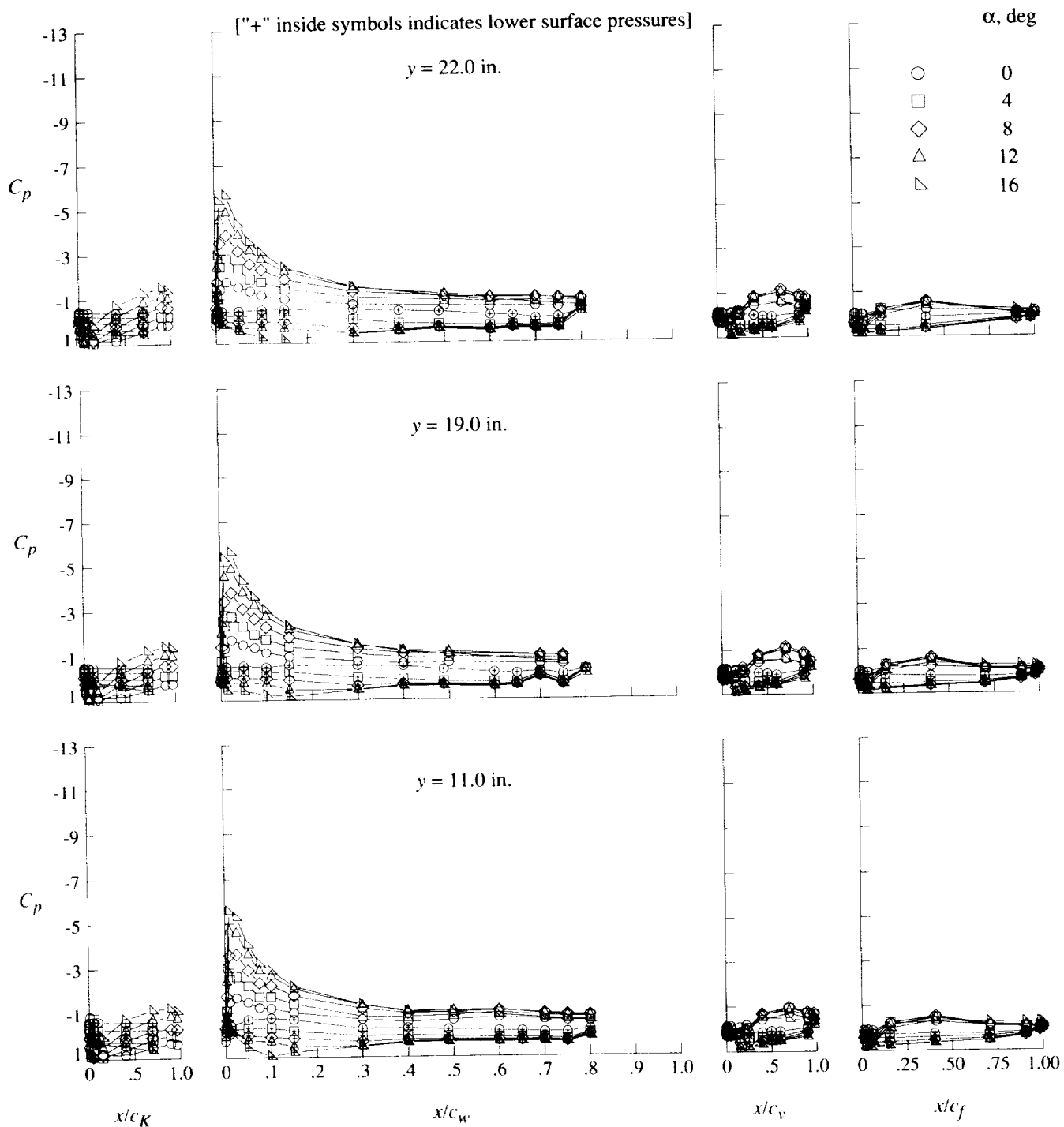
(b) $q = 40$ psf.

Figure 27. Continued.



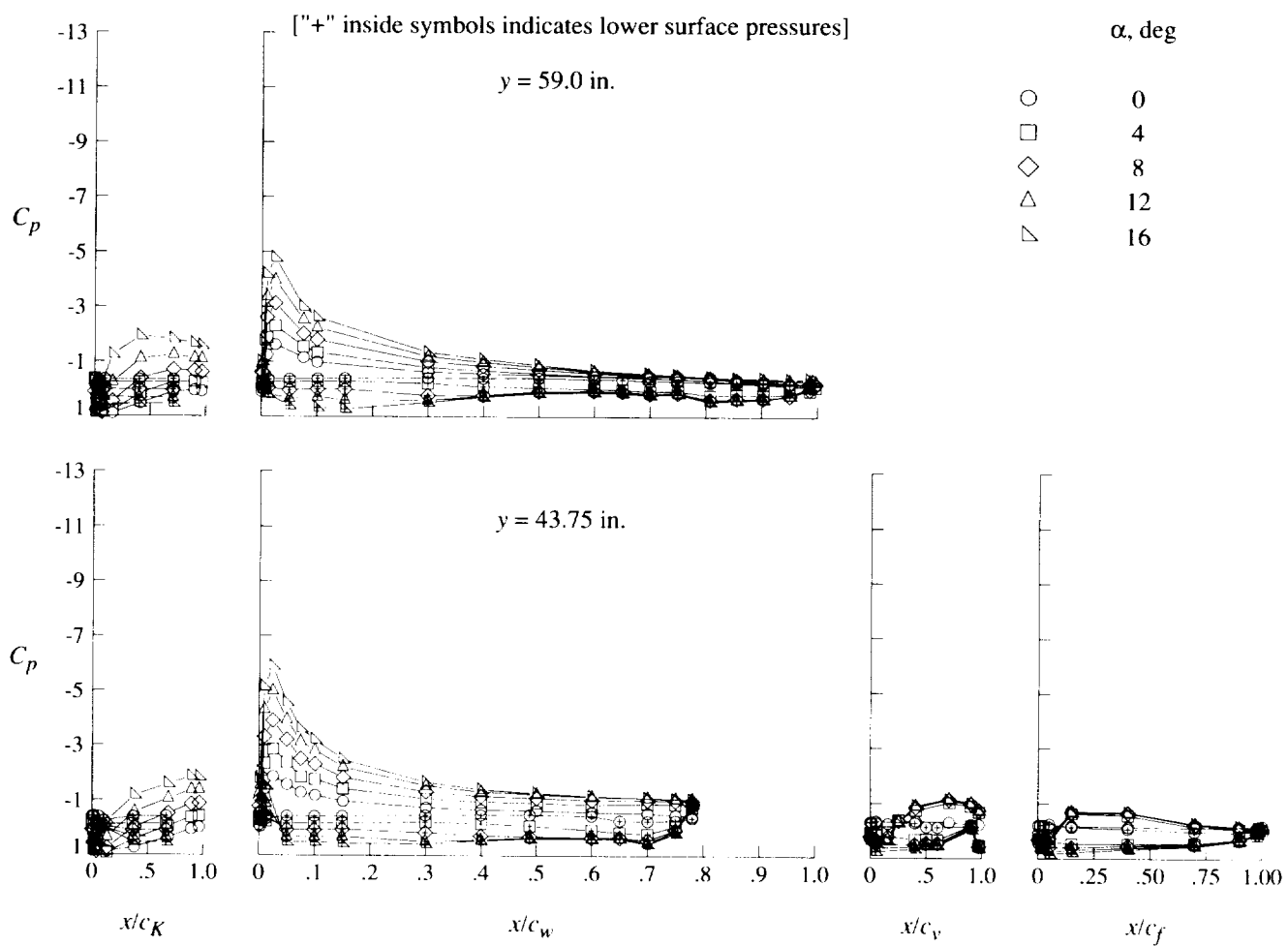
(b) Concluded.

Figure 27. Continued.



(c) $q = 60$ psf.

Figure 27. Continued.



(c) Concluded.

Figure 27. Concluded.

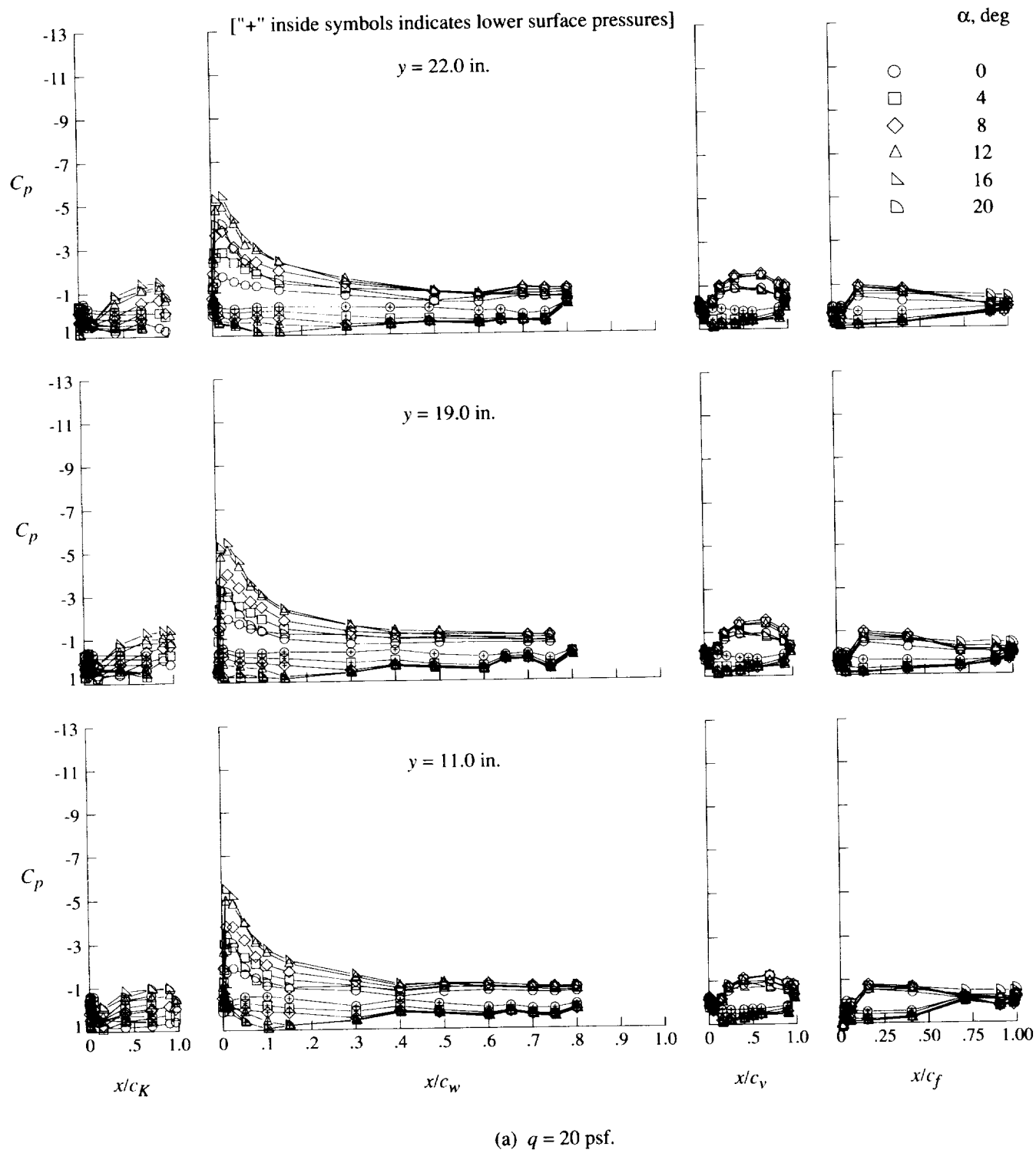
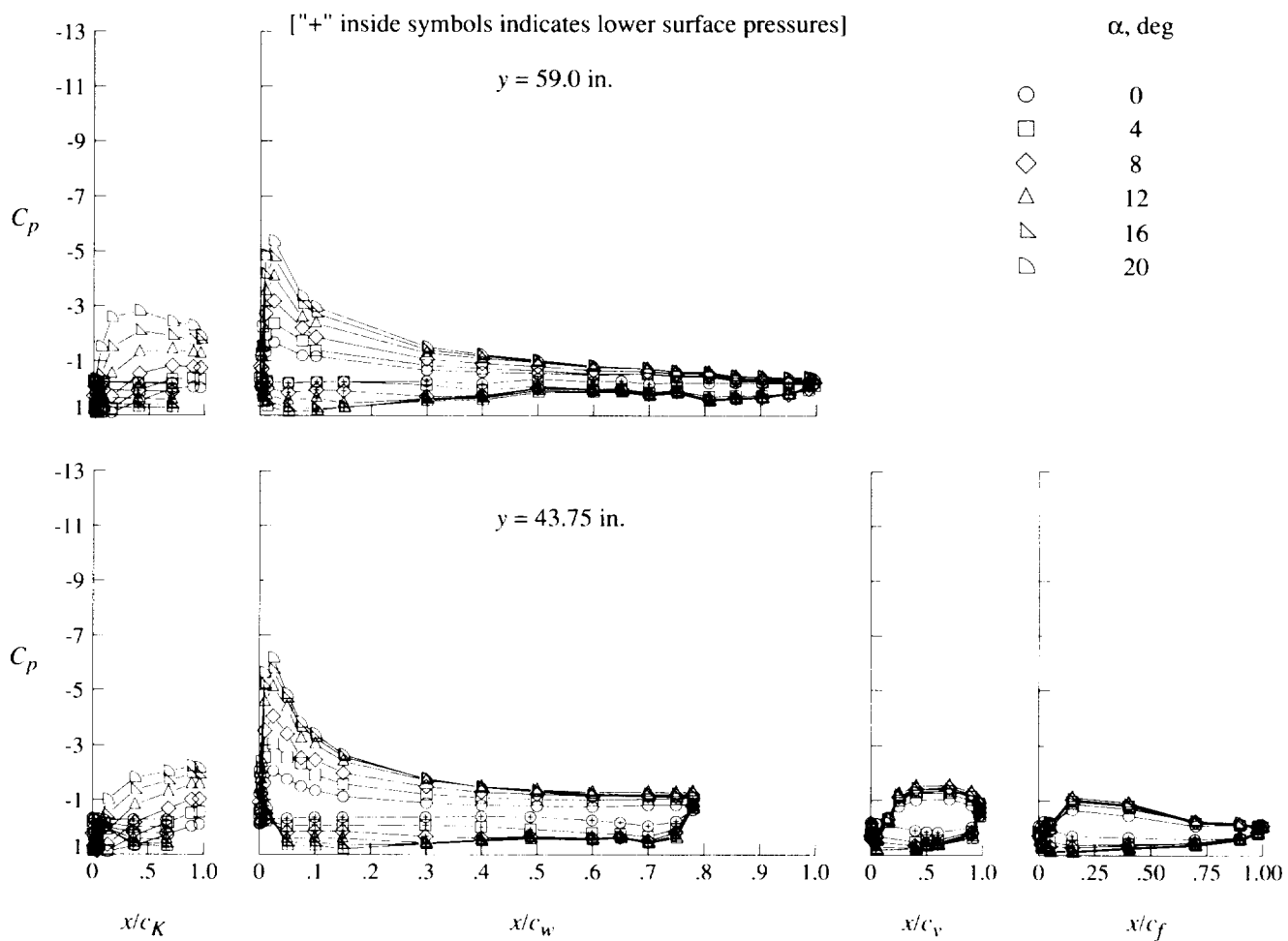
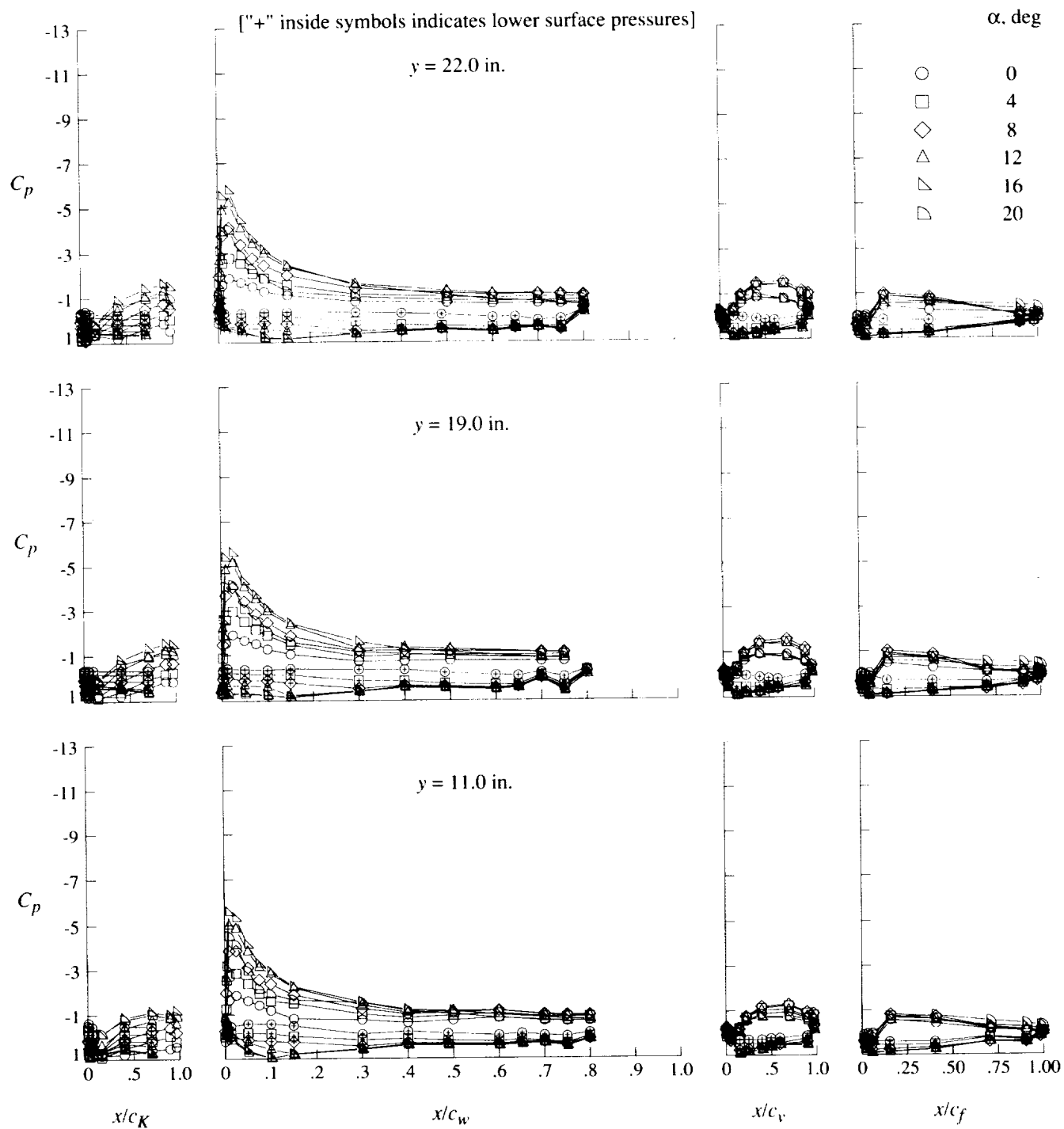


Figure 28. Effect of angle of attack on pressure distributions for high-lift configuration at $\delta_f = 40^\circ$.



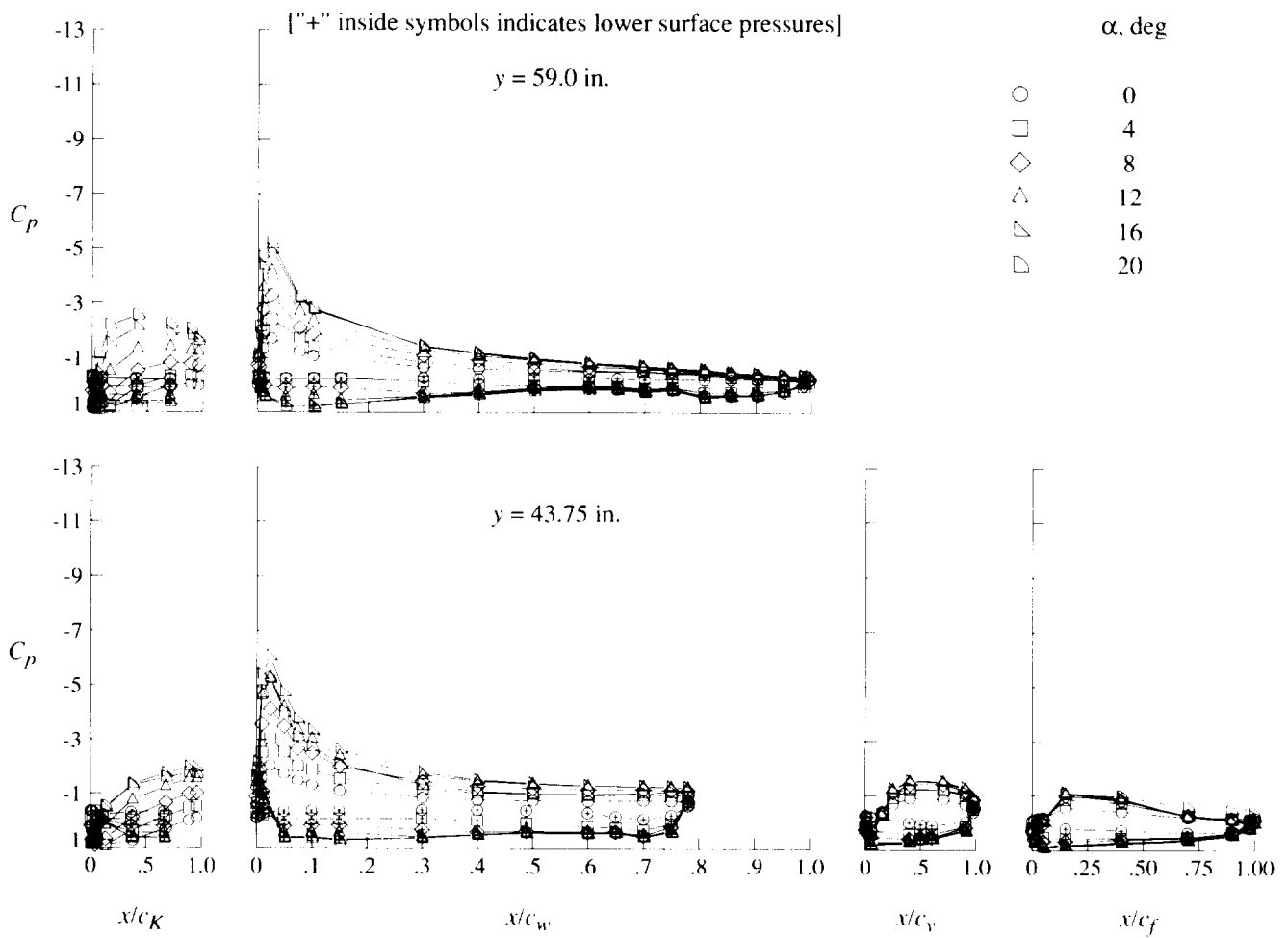
(a) Concluded.

Figure 28. Continued.



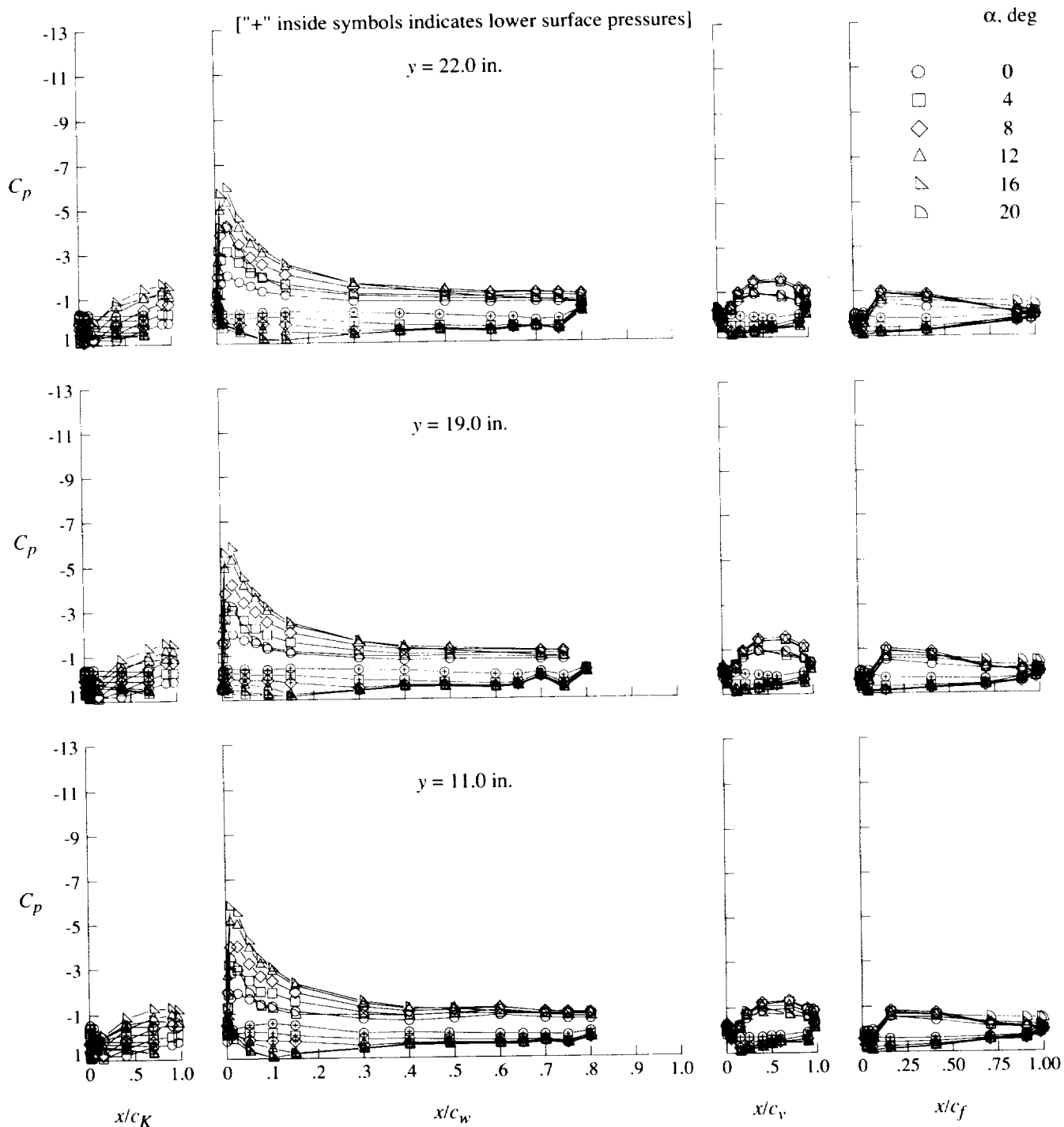
(b) $q = 40$ psf.

Figure 28. Continued.



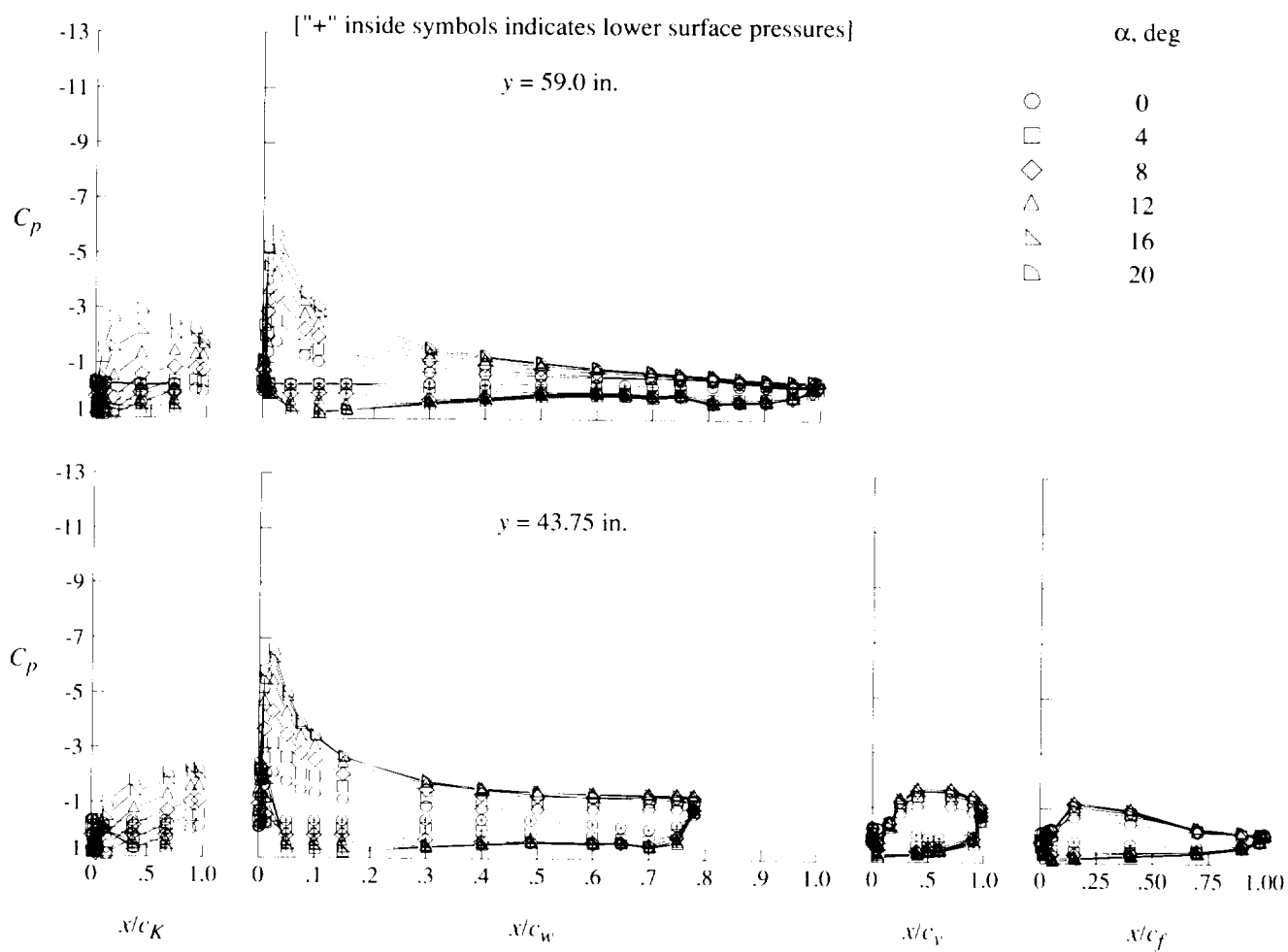
(b) Concluded.

Figure 28. Continued.



(c) $q = 60$ psf.

Figure 28. Continued.



(c) Concluded.

Figure 28. Concluded.

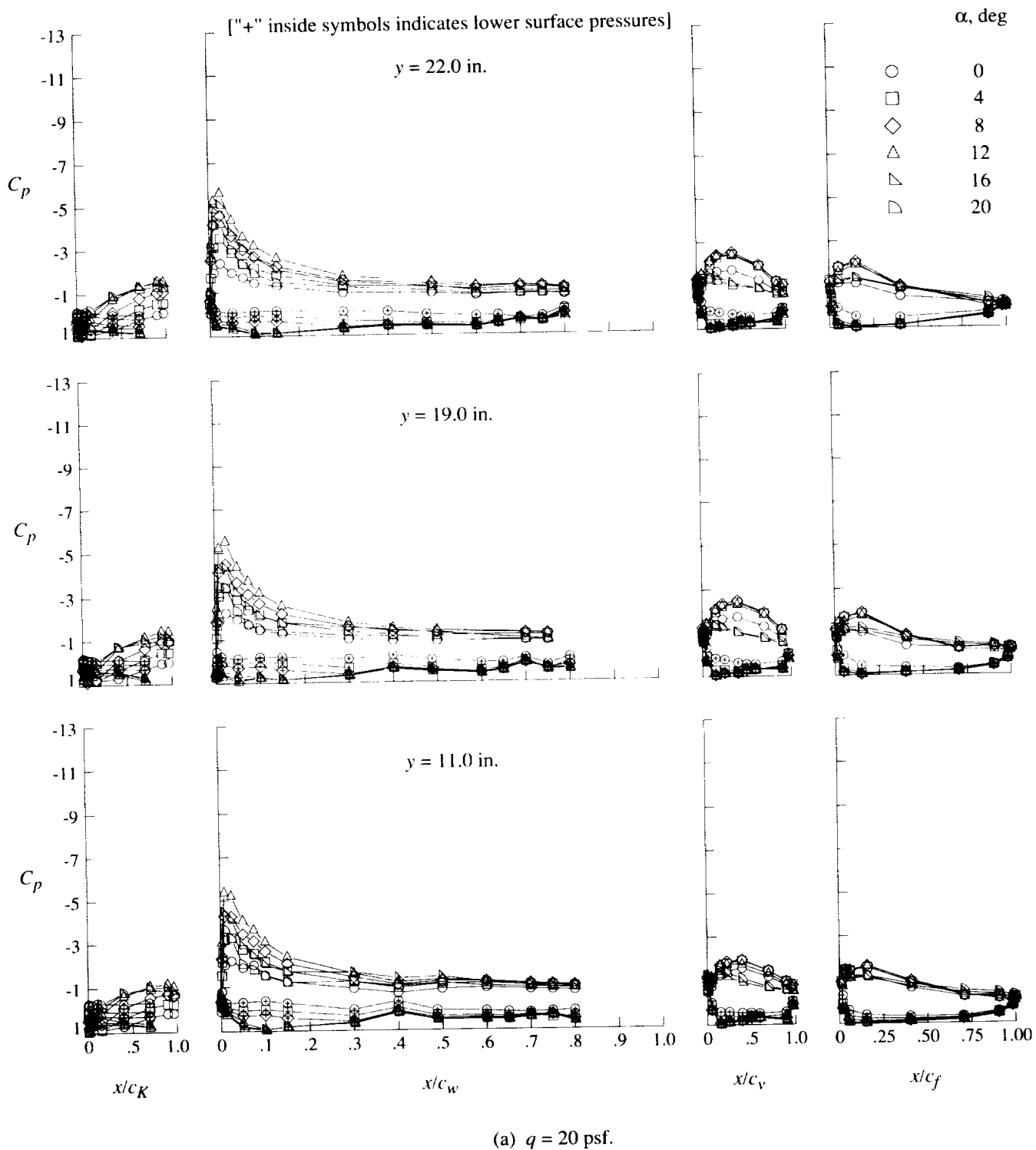
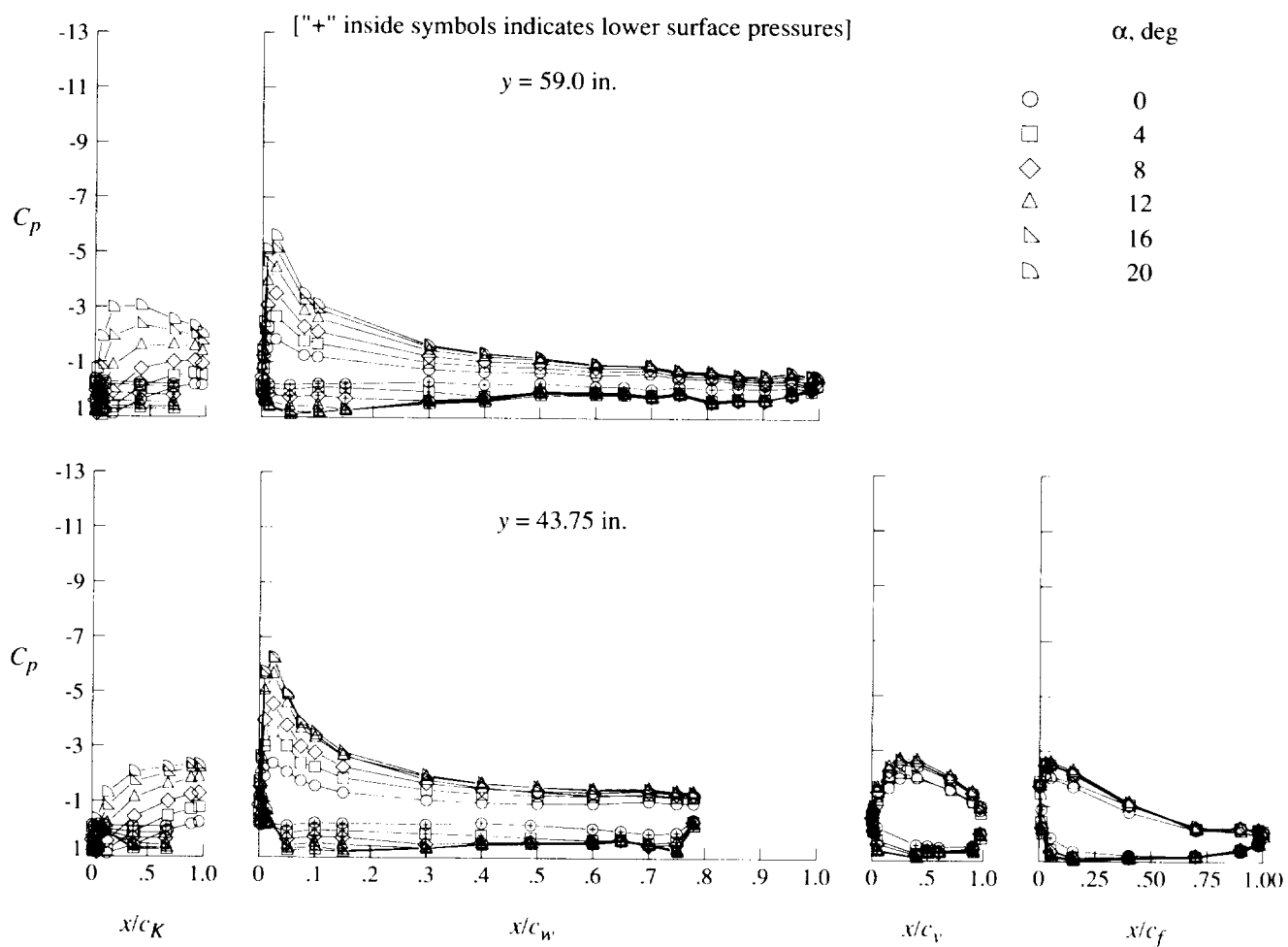
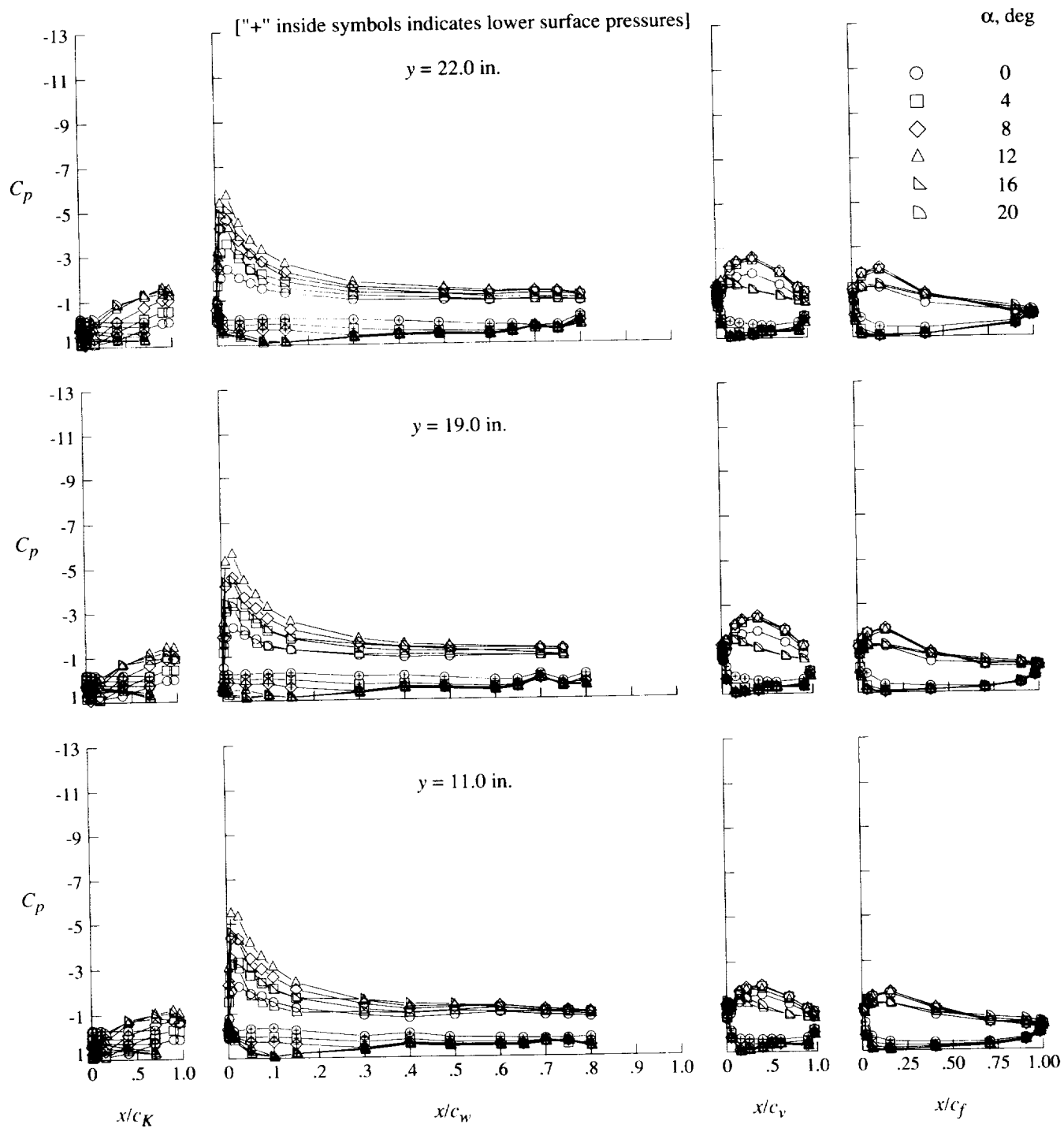


Figure 29. Effect of angle of attack on pressure distributions for high-lift configuration at $\delta_f = 60^\circ$.



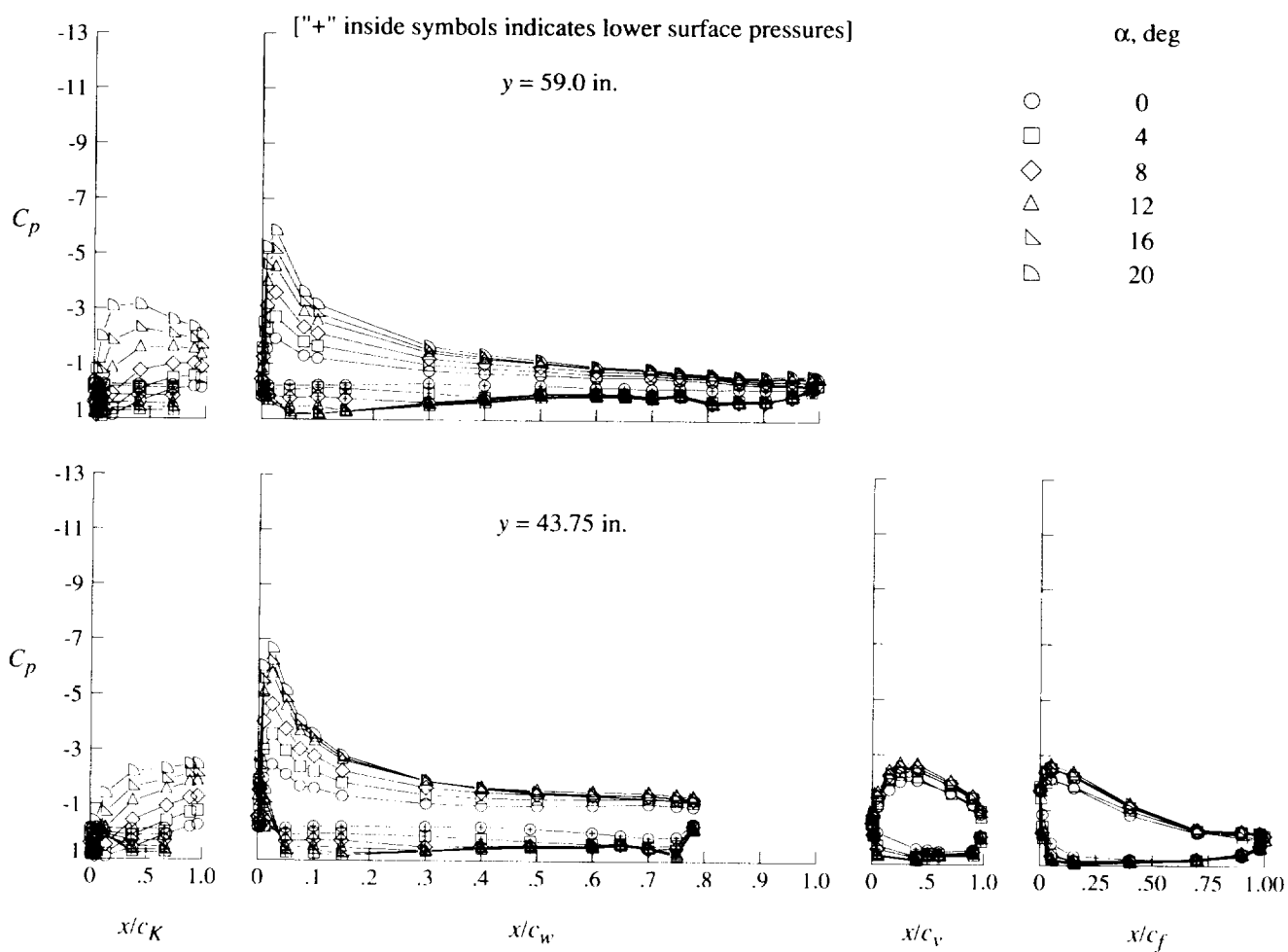
(a) Concluded.

Figure 29. Continued.



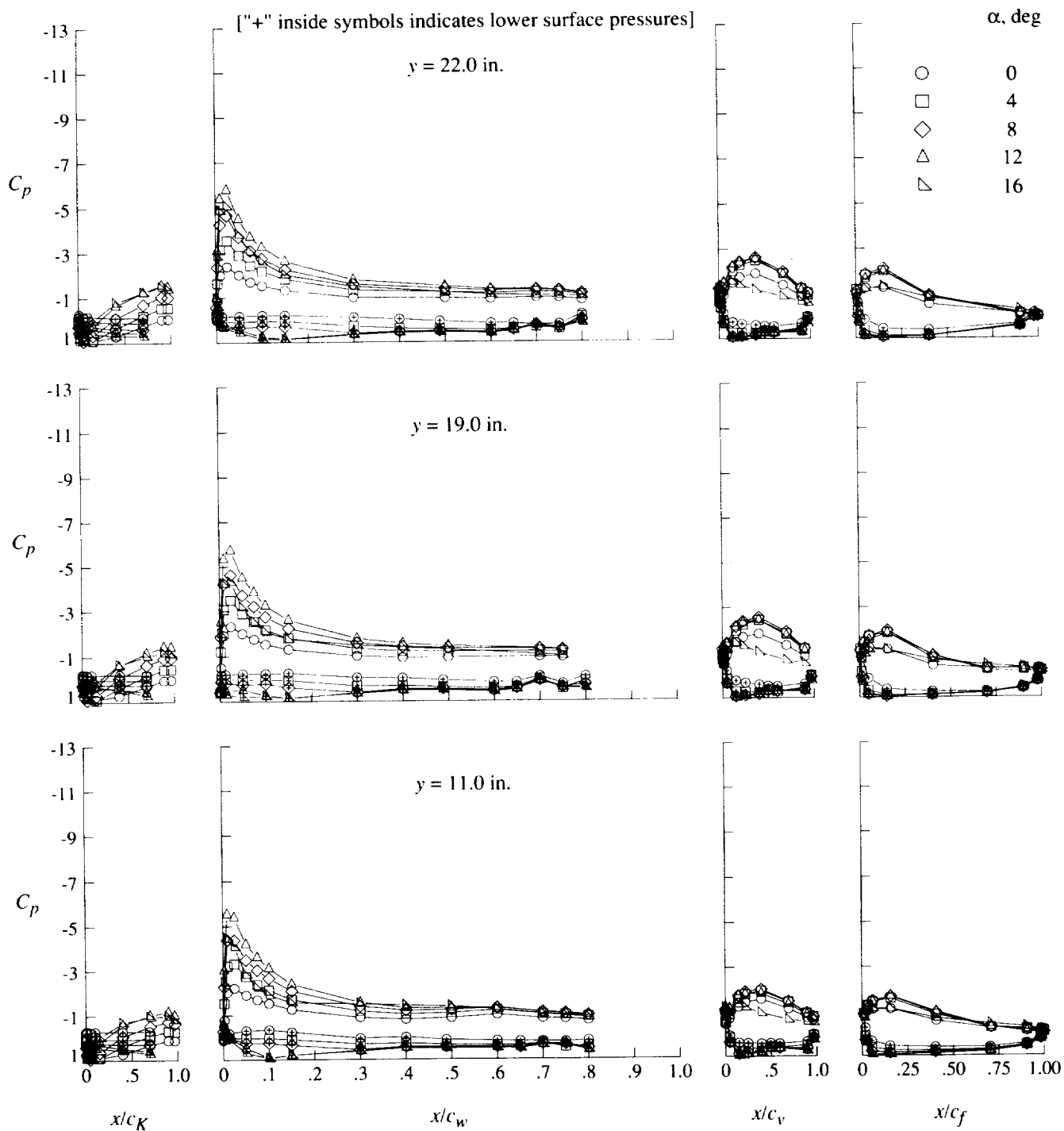
(b) $q = 40$ psf.

Figure 29. Continued.



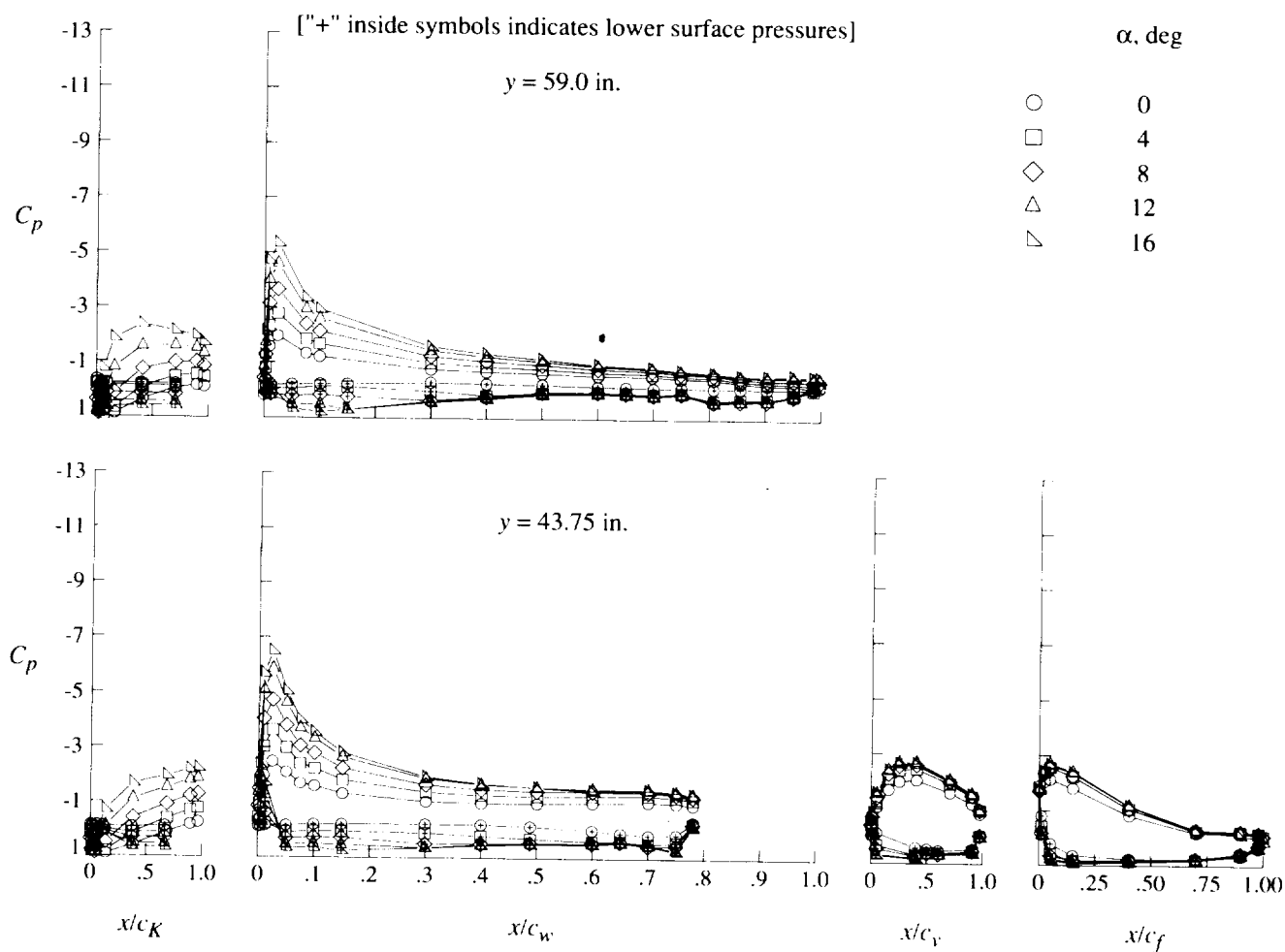
(b) Concluded.

Figure 29. Continued.



(c) $q = 60$ psf.

Figure 29. Continued.



(c) Concluded.

Figure 29. Concluded.

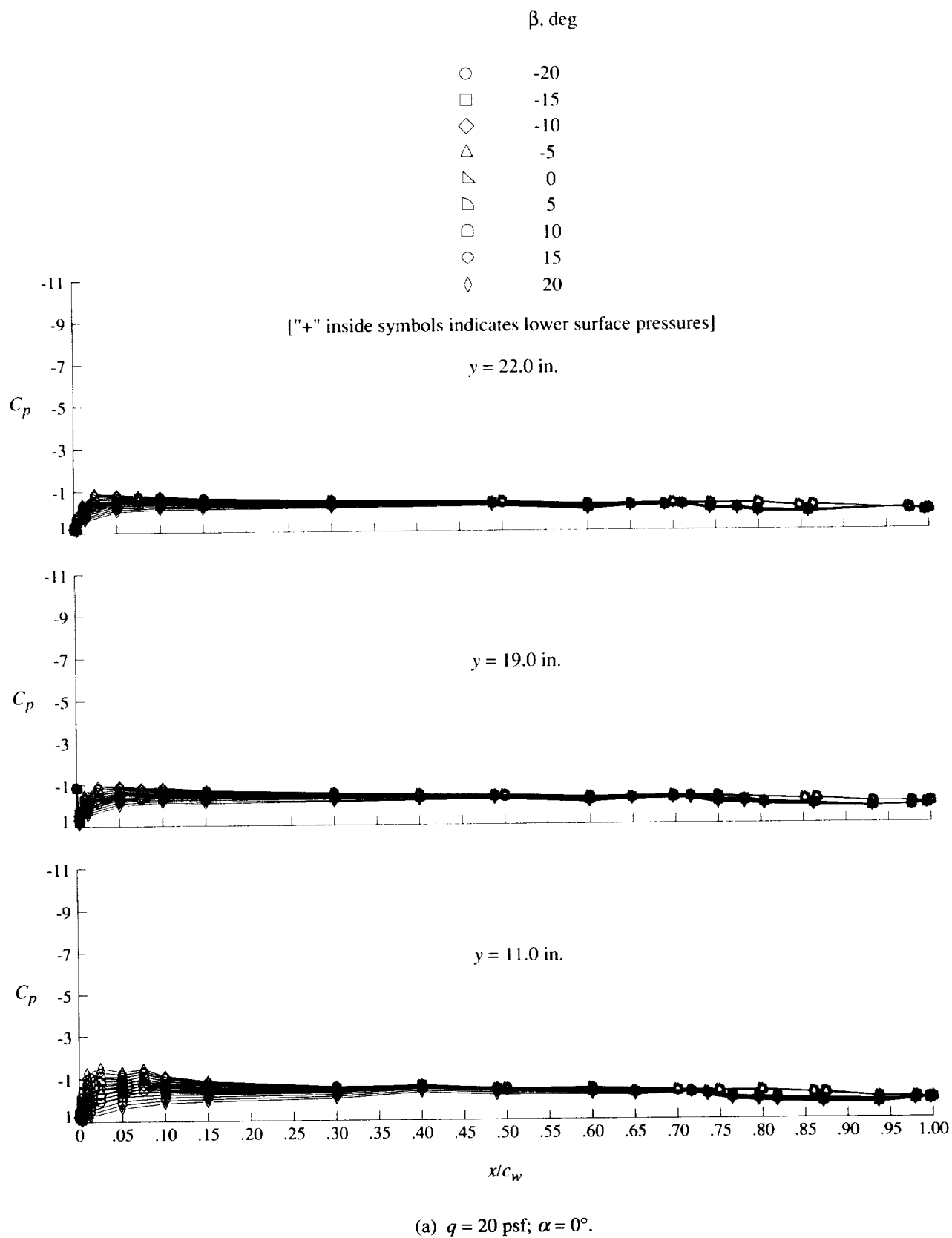
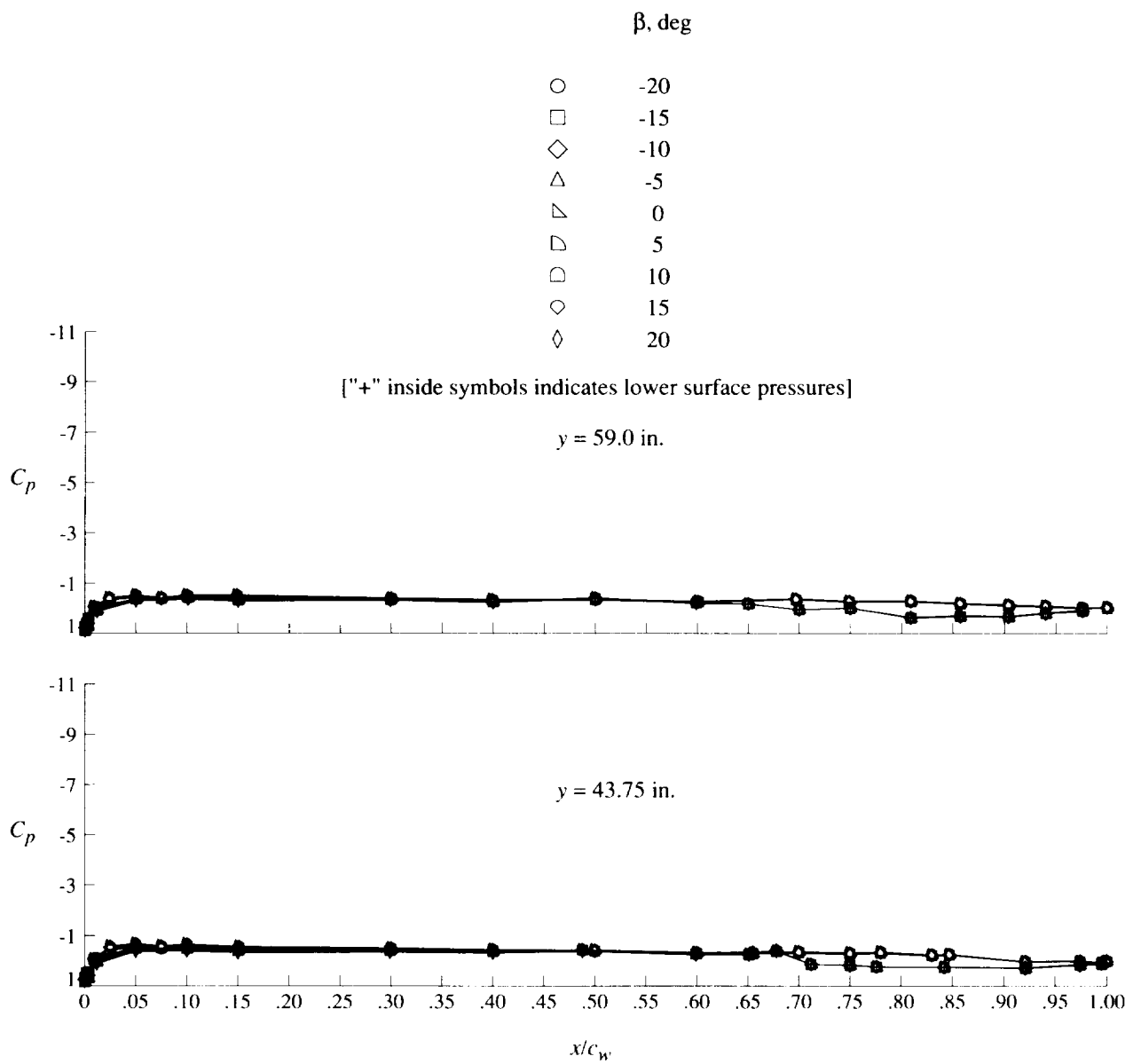
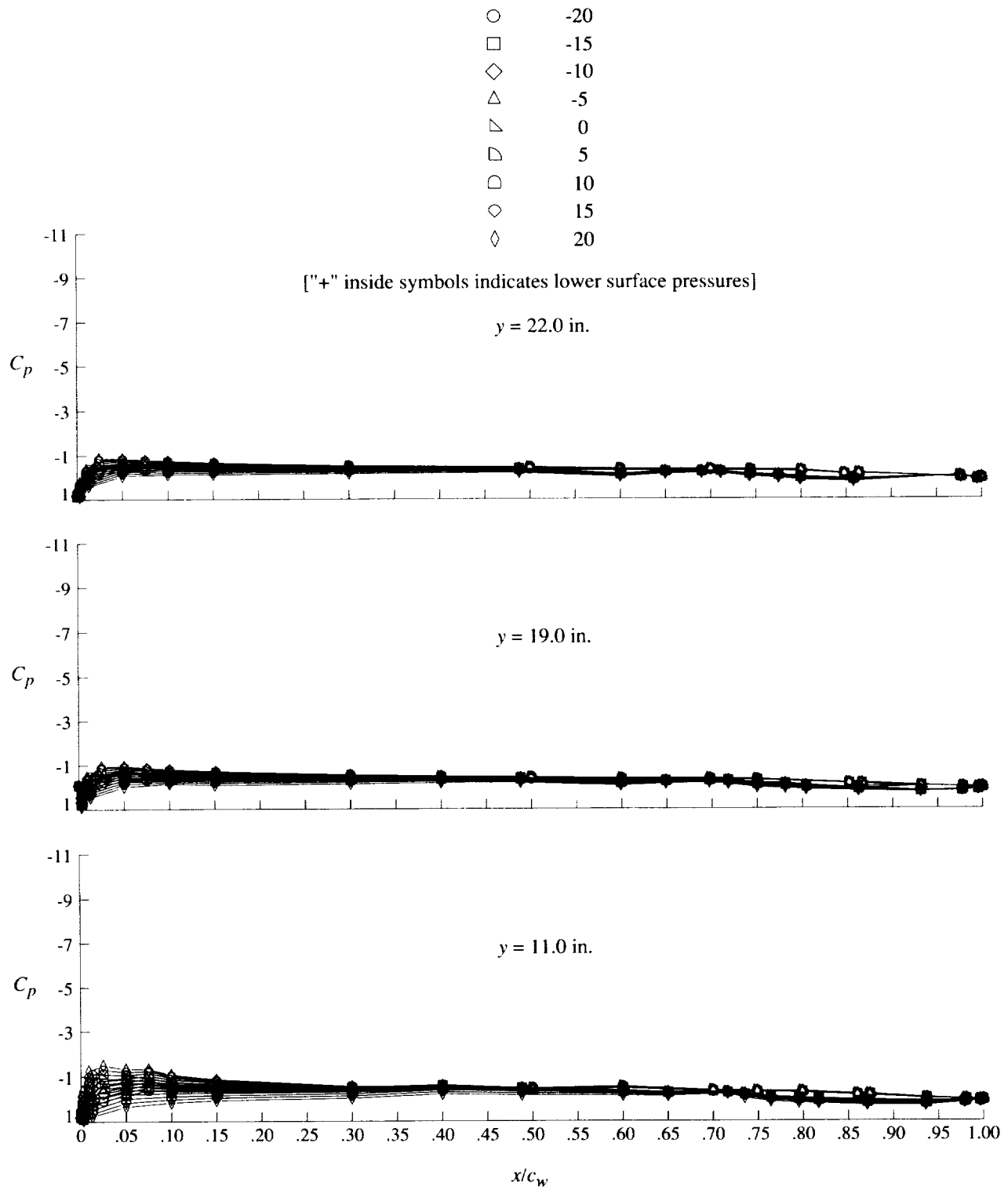


Figure 30. Effect of sideslip angle on pressure distributions. Cruise configuration.



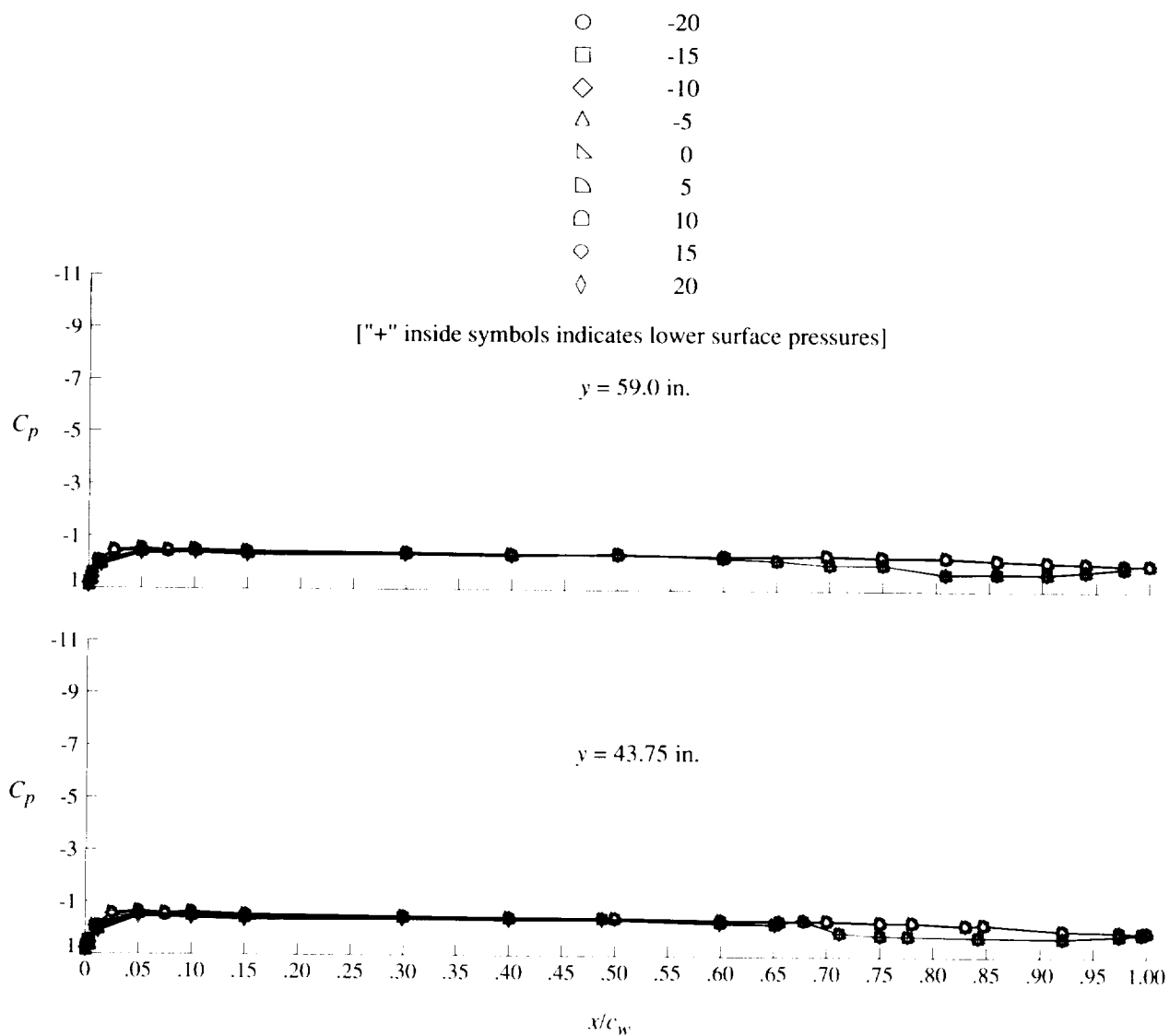
(a) Concluded.

Figure 30. Continued.



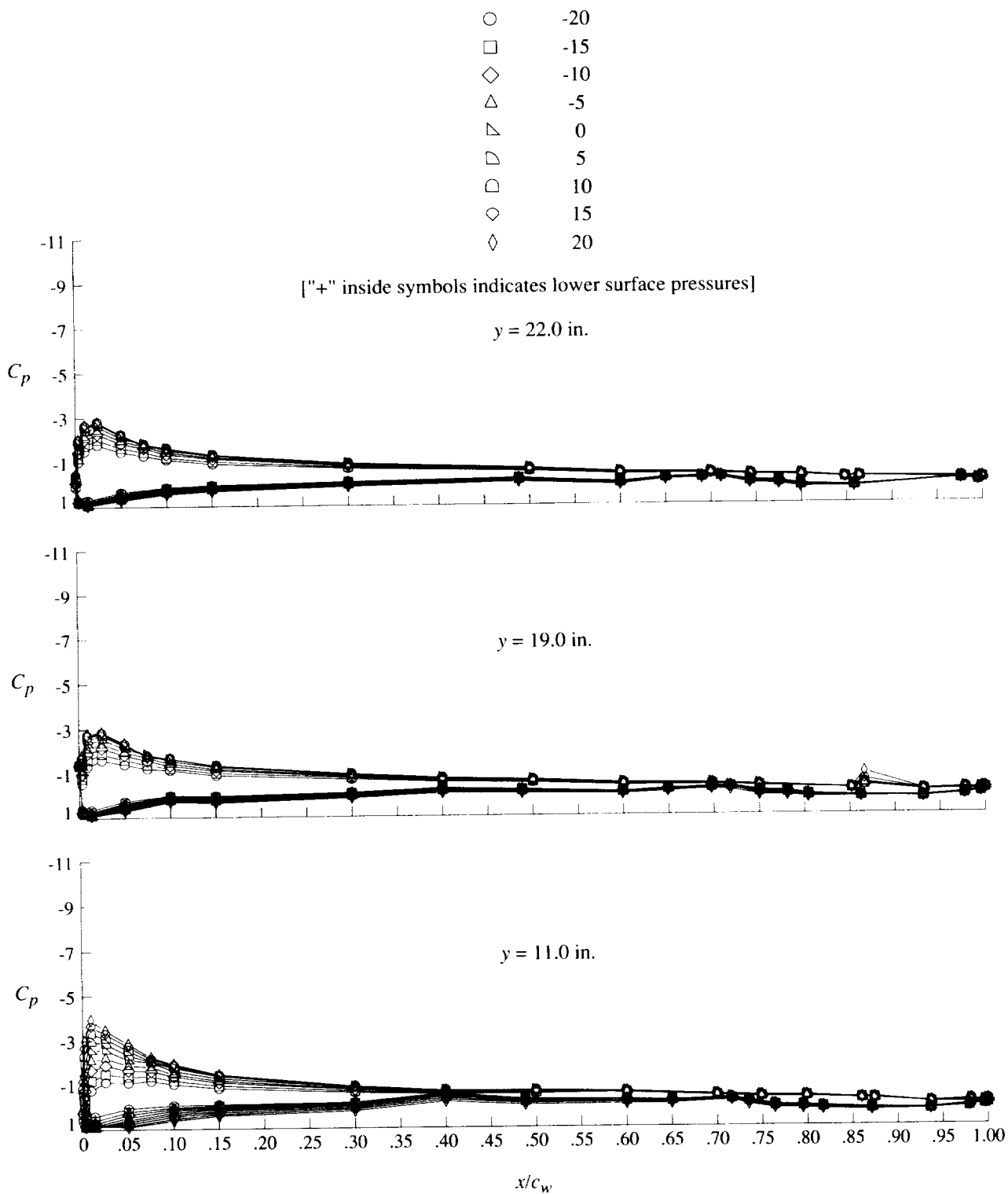
(b) $q = 40 \text{ psf}$; $\alpha = 0^\circ$.

Figure 30. Continued.



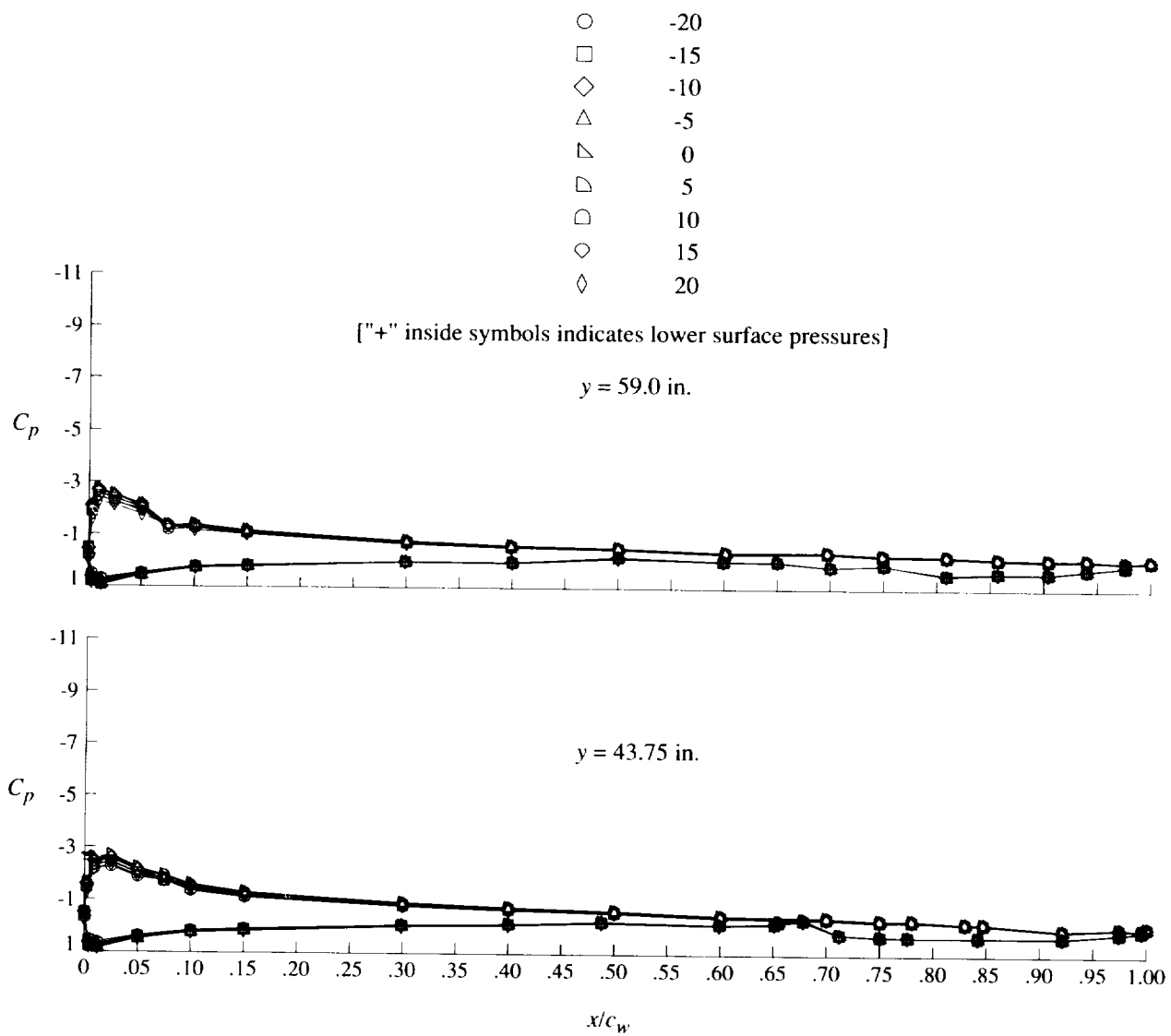
(b) Concluded.

Figure 30. Continued.



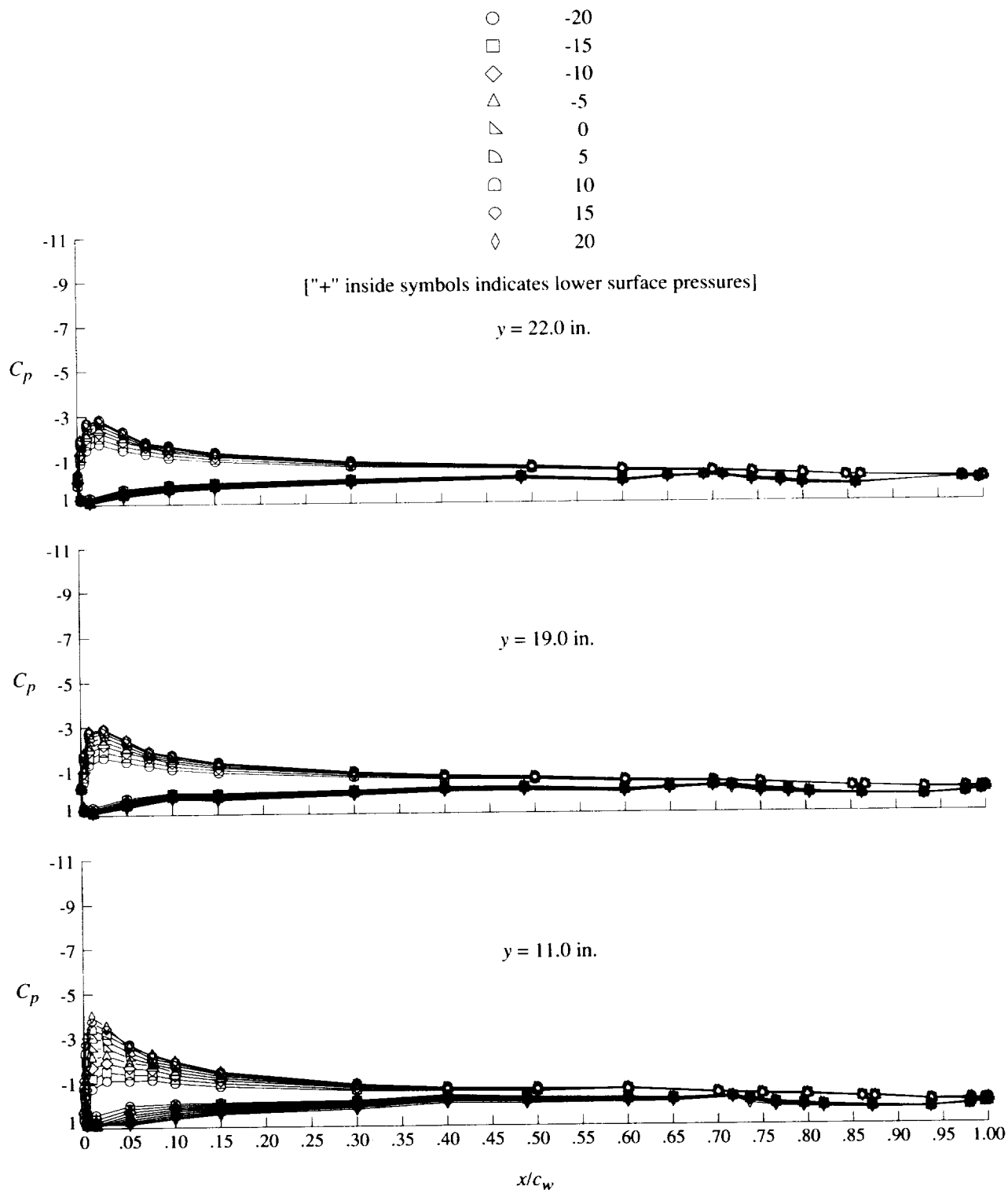
(c) $q = 20 \text{ psf}$; $\alpha = 8^\circ$.

Figure 30. Continued.



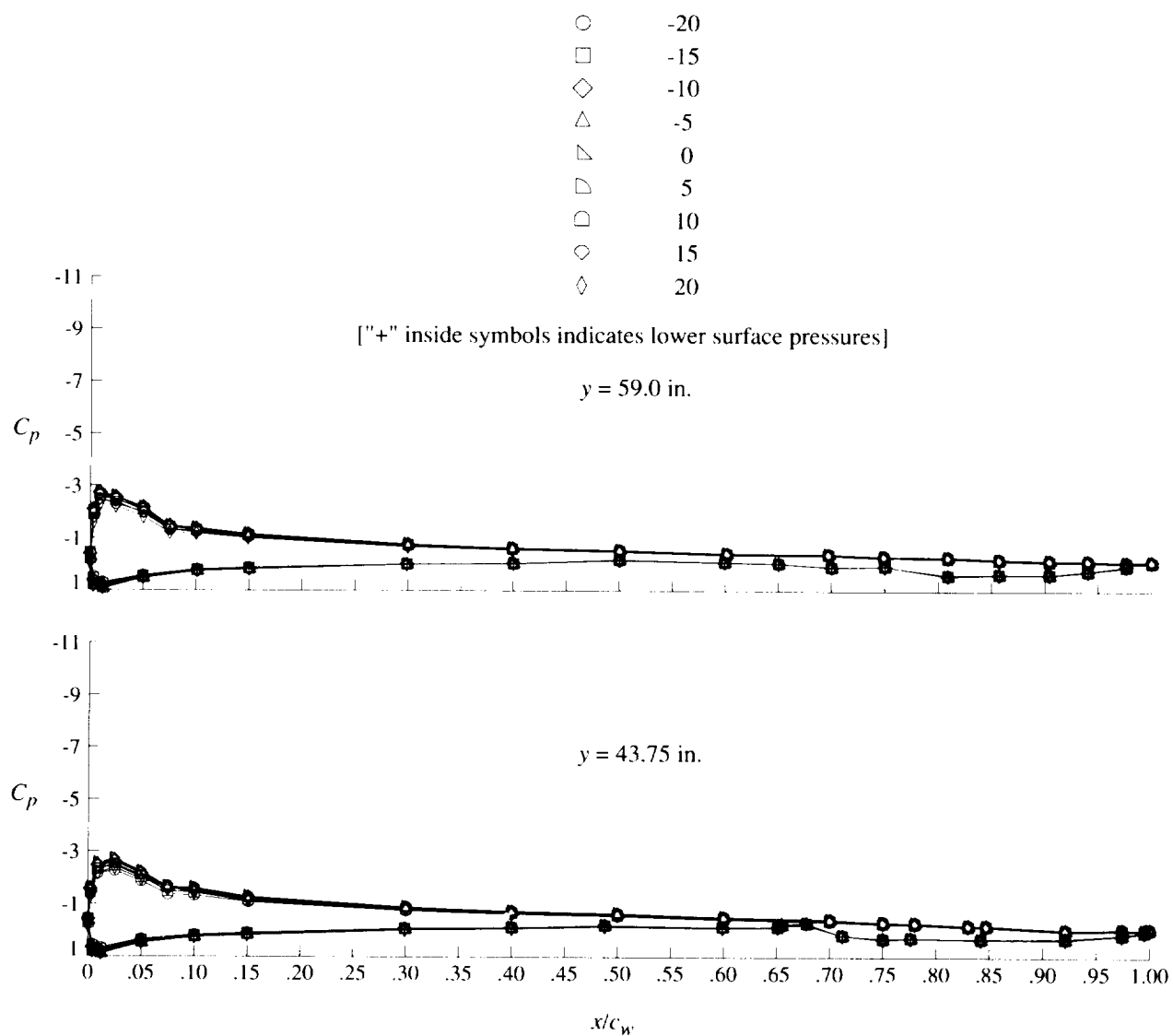
(c) Concluded.

Figure 30. Continued.



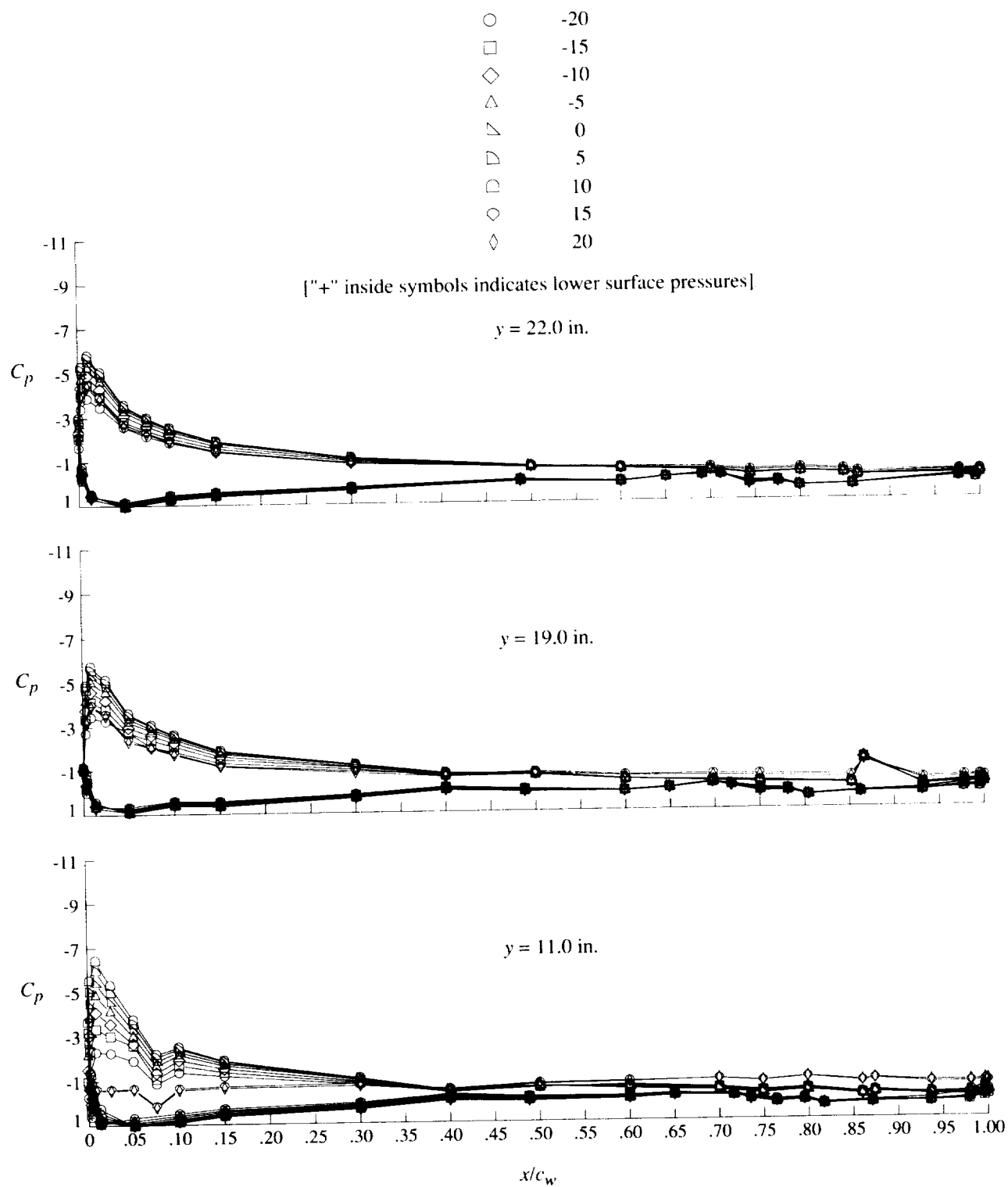
(d) $q = 40$ psf; $\alpha = 8^\circ$.

Figure 30. Continued.



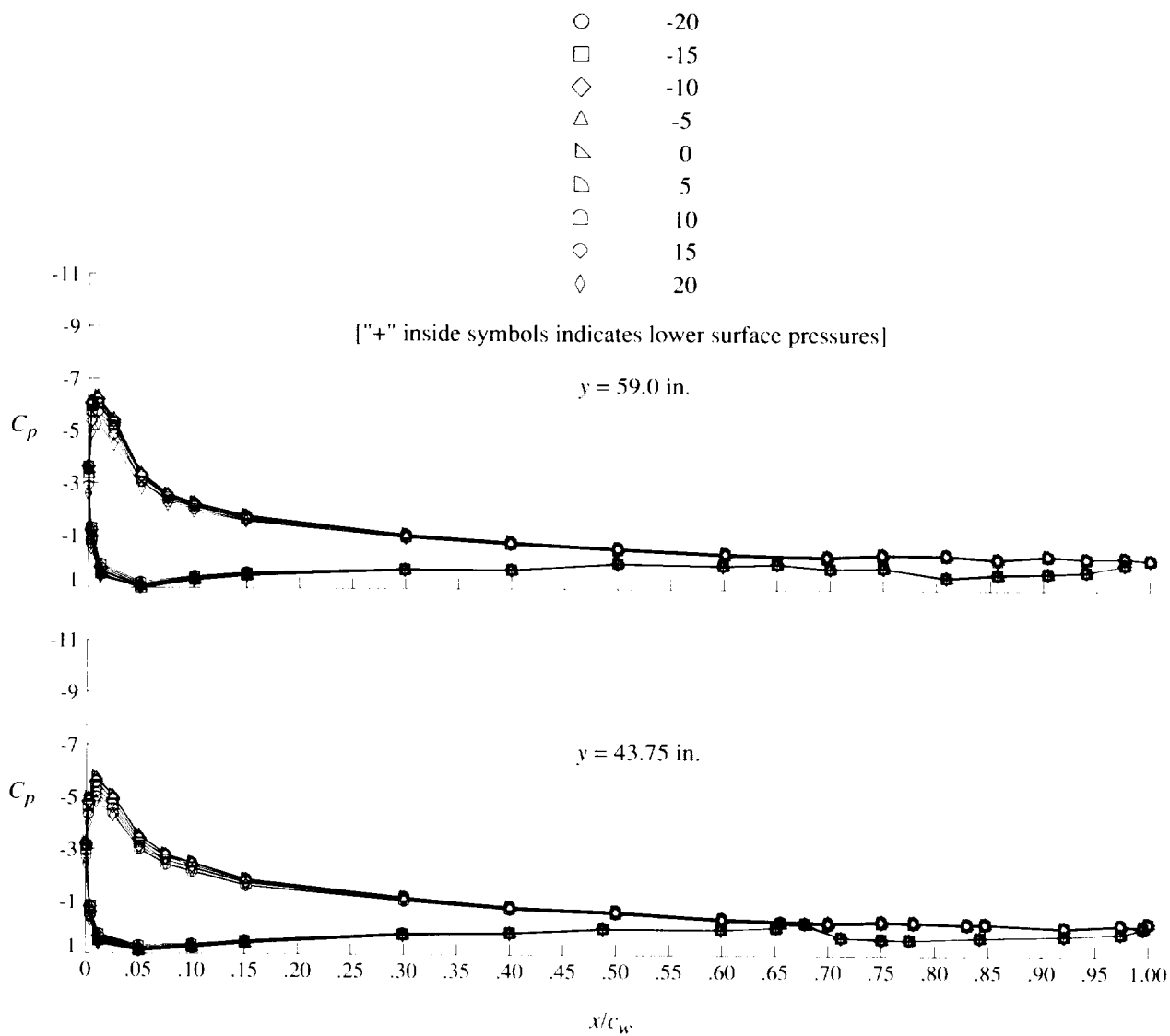
(d) Concluded.

Figure 30. Continued.



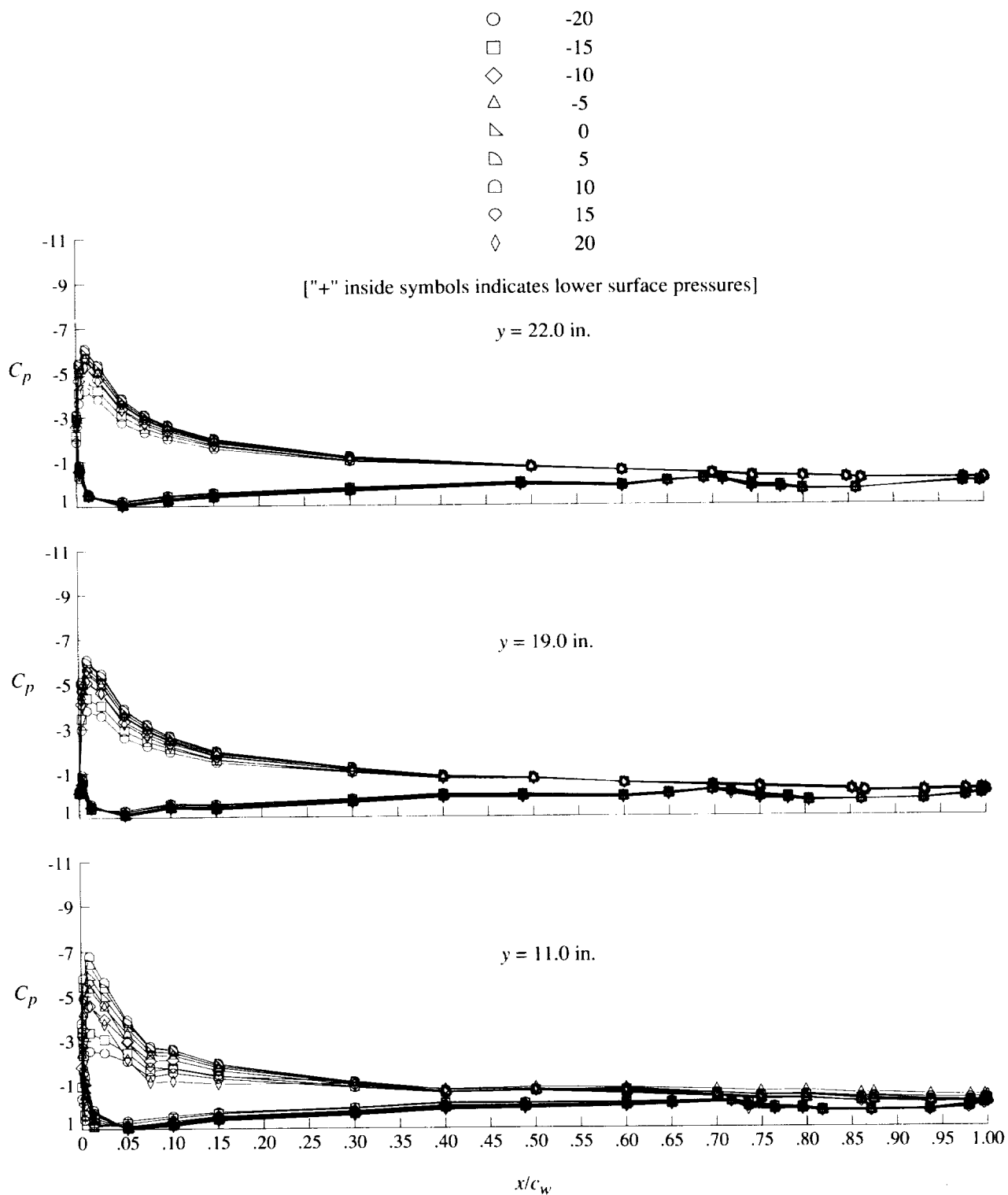
(e) $q = 20$ psf; $\alpha = 16^\circ$.

Figure 30. Continued.



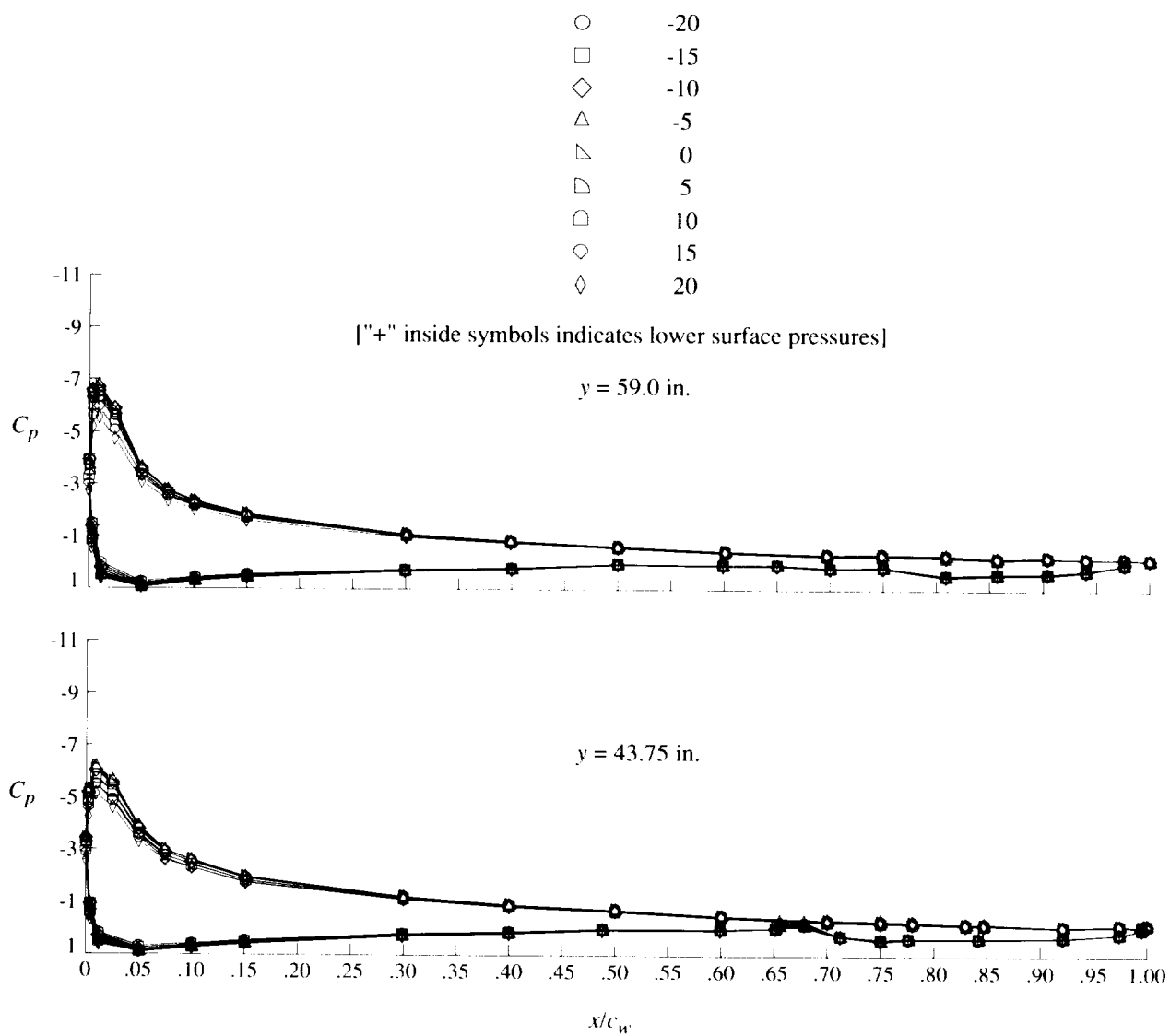
(e) Concluded.

Figure 30. Continued.



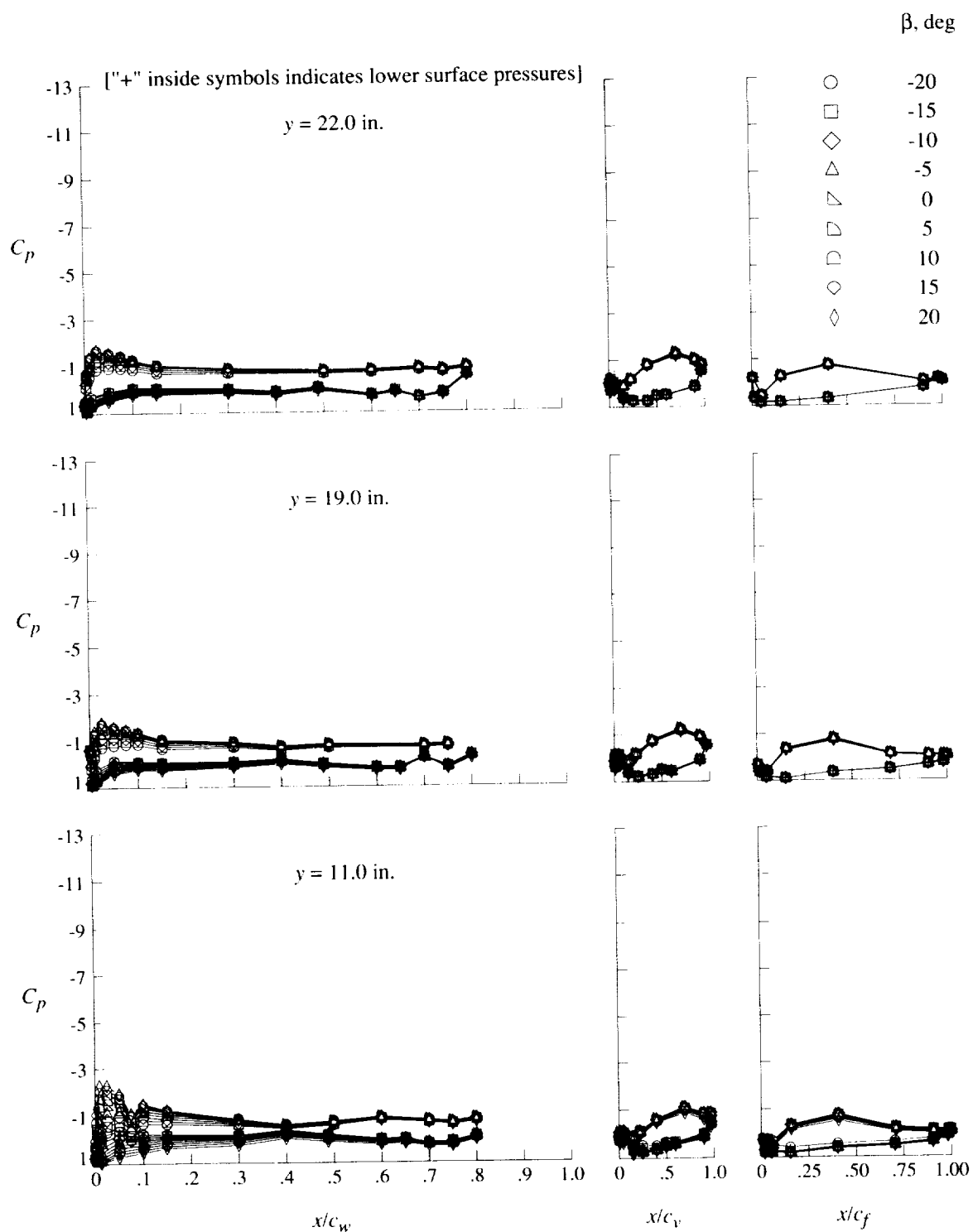
(f) $q = 40 \text{ psf}$; $\alpha = 16^\circ$.

Figure 30. Continued.



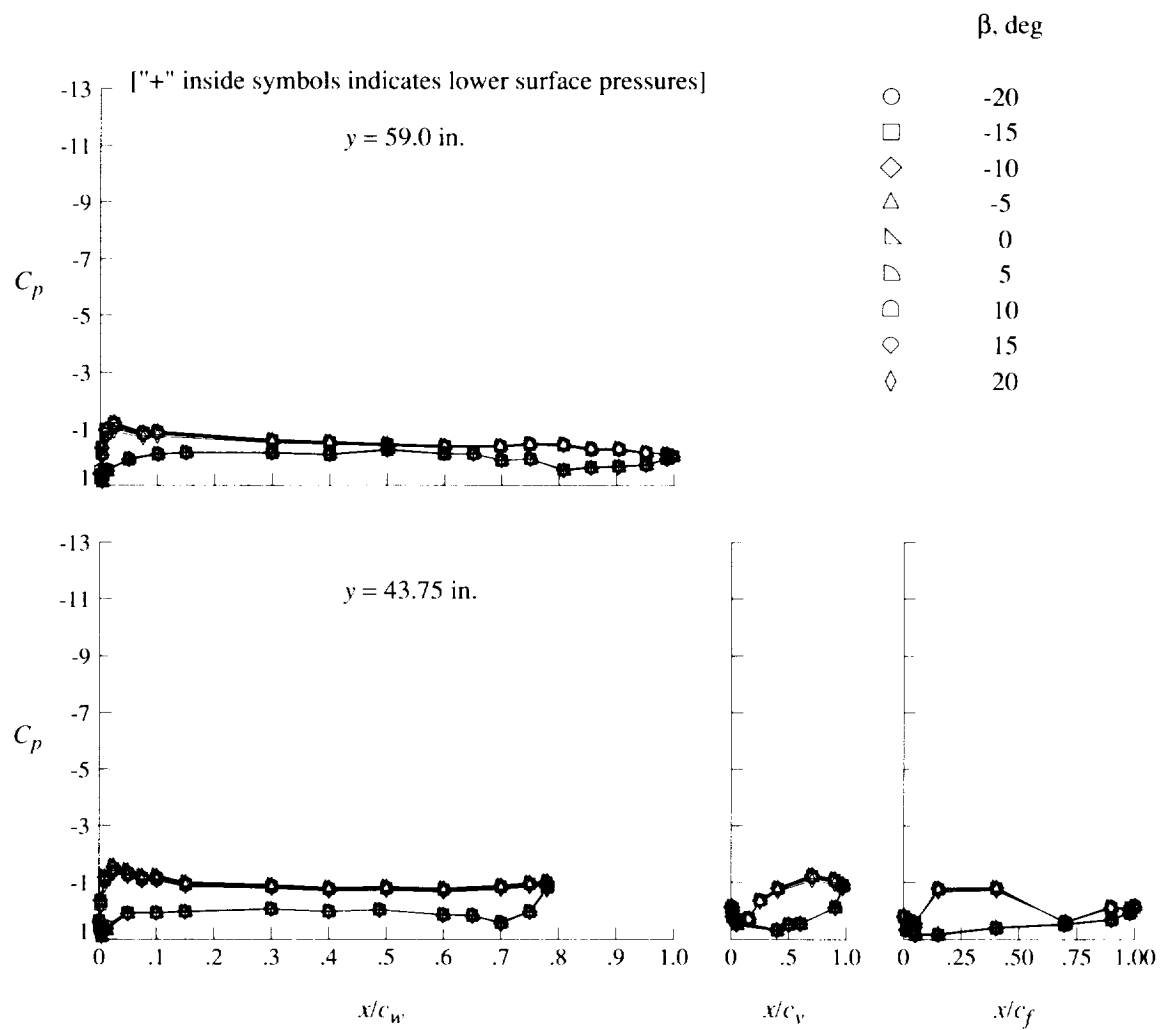
(f) Concluded.

Figure 30. Concluded.



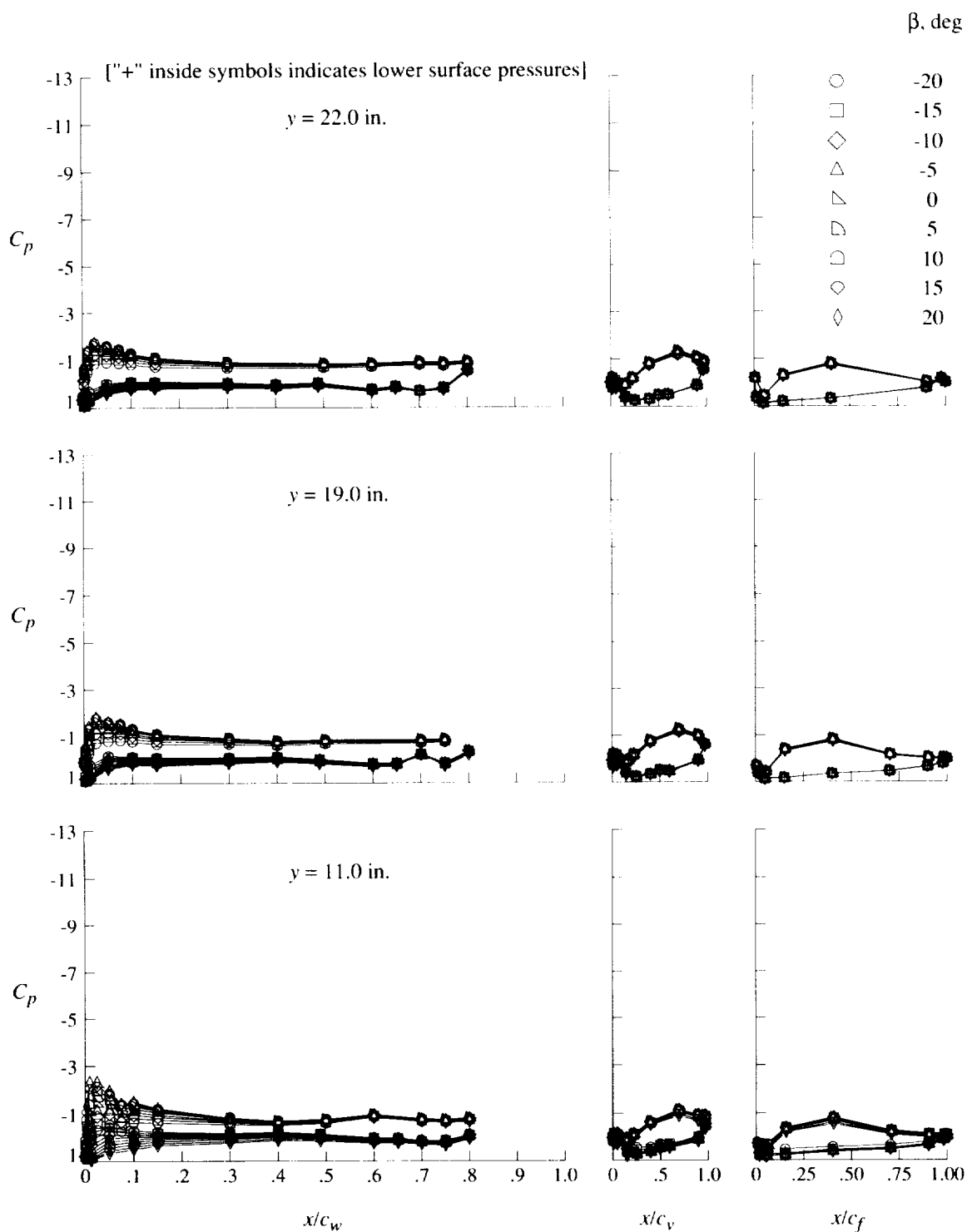
(a) $q = 20$ psf; $\alpha = 0^\circ$.

Figure 31. Effect of sideslip angle on pressure distributions for flaps-only configuration at $\delta_f = 30^\circ$.



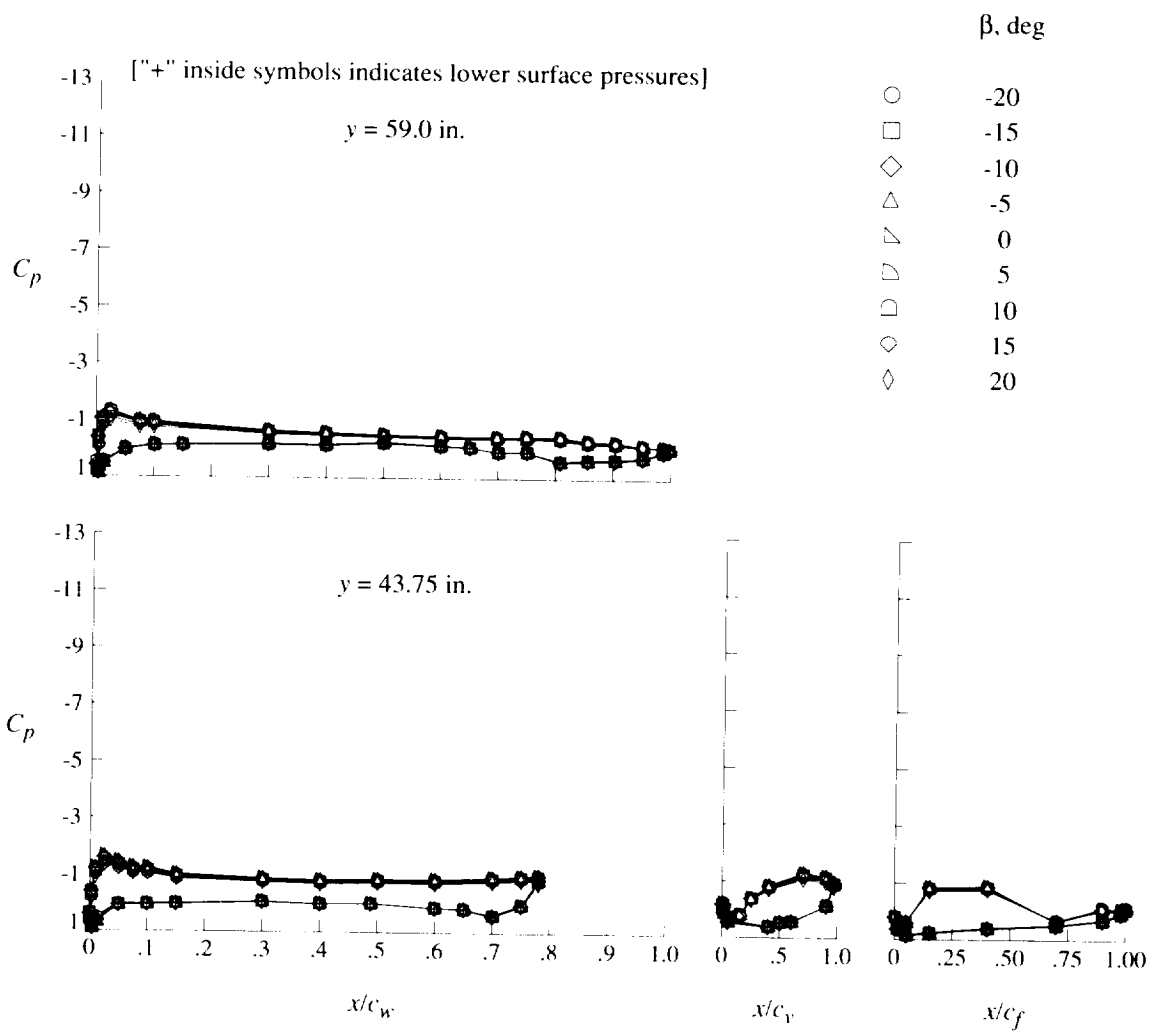
(a) Concluded.

Figure 31. Continued.



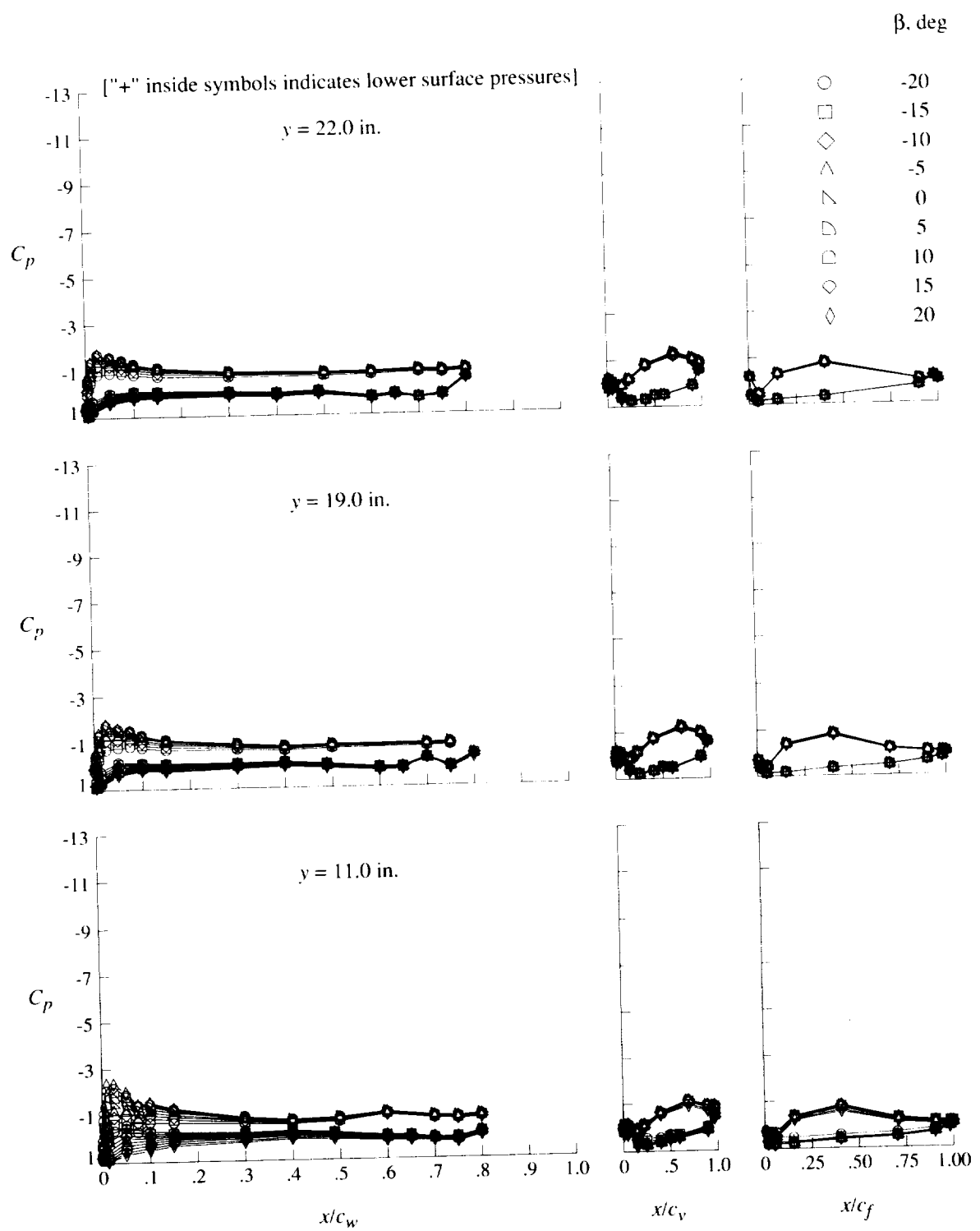
(b) $q = 40$ psf; $\alpha = 0^\circ$.

Figure 31. Continued.



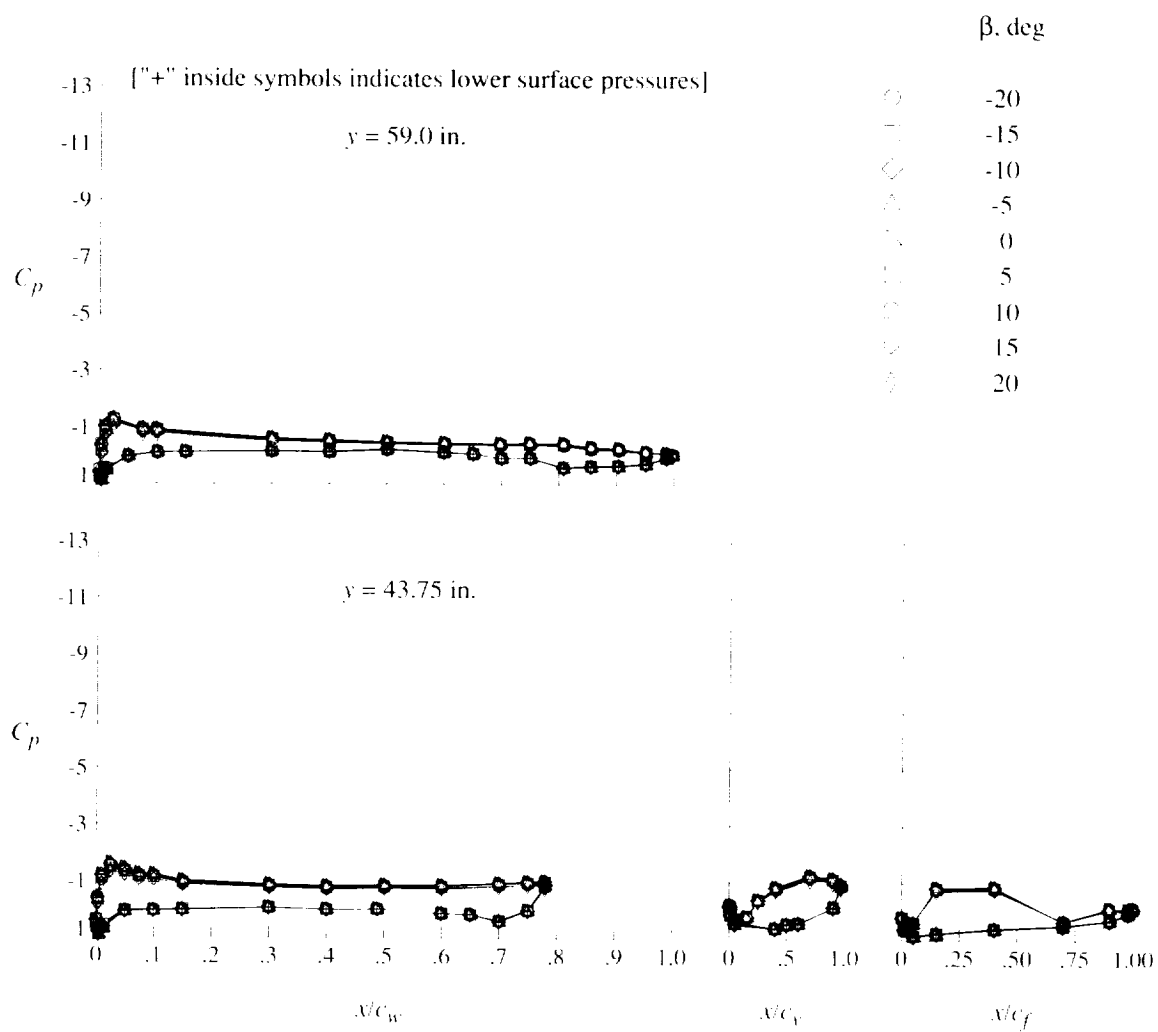
(b) Concluded.

Figure 31. Continued.



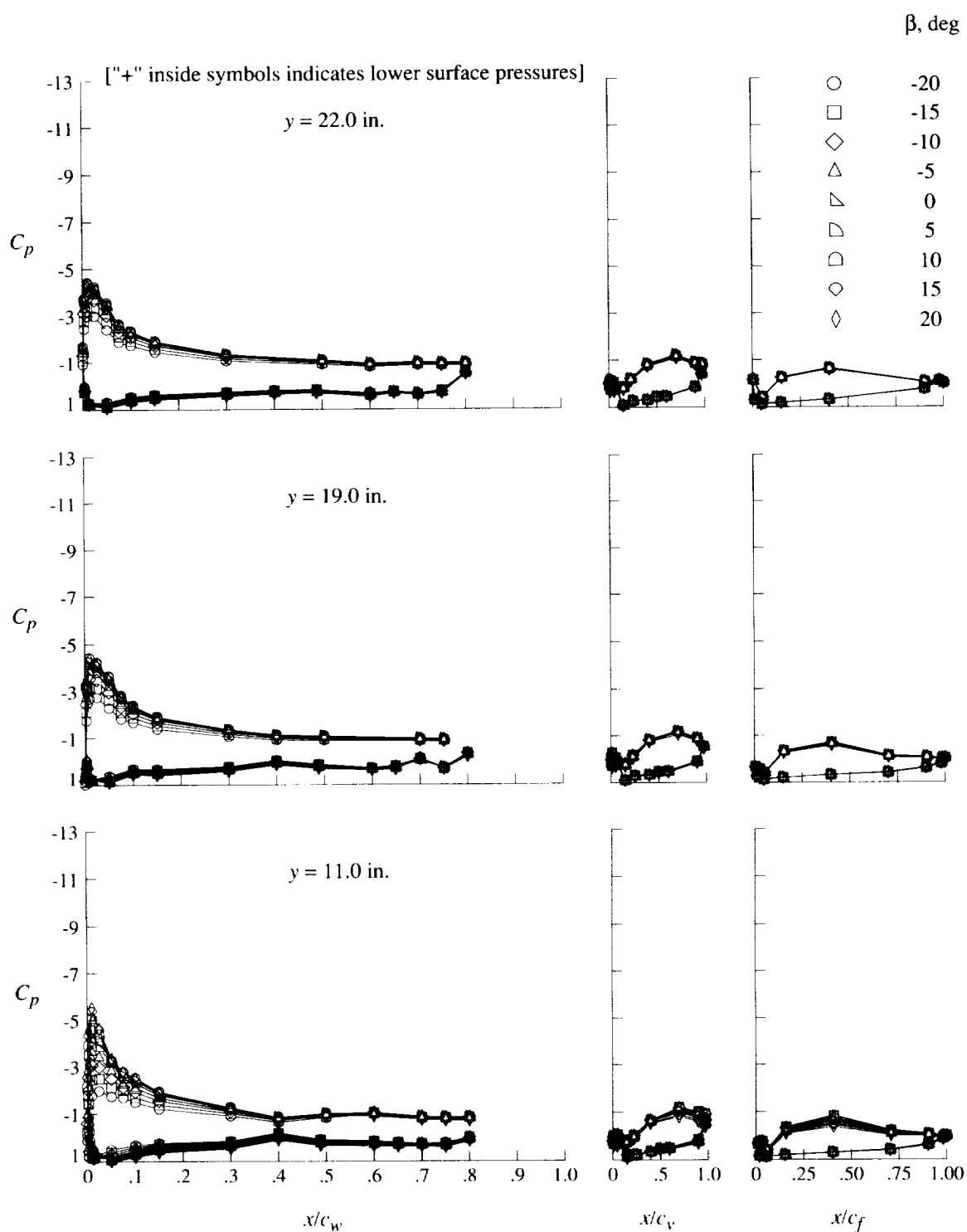
(c) $q = 20$ psf; $\alpha = 8^\circ$.

Figure 31. Continued.



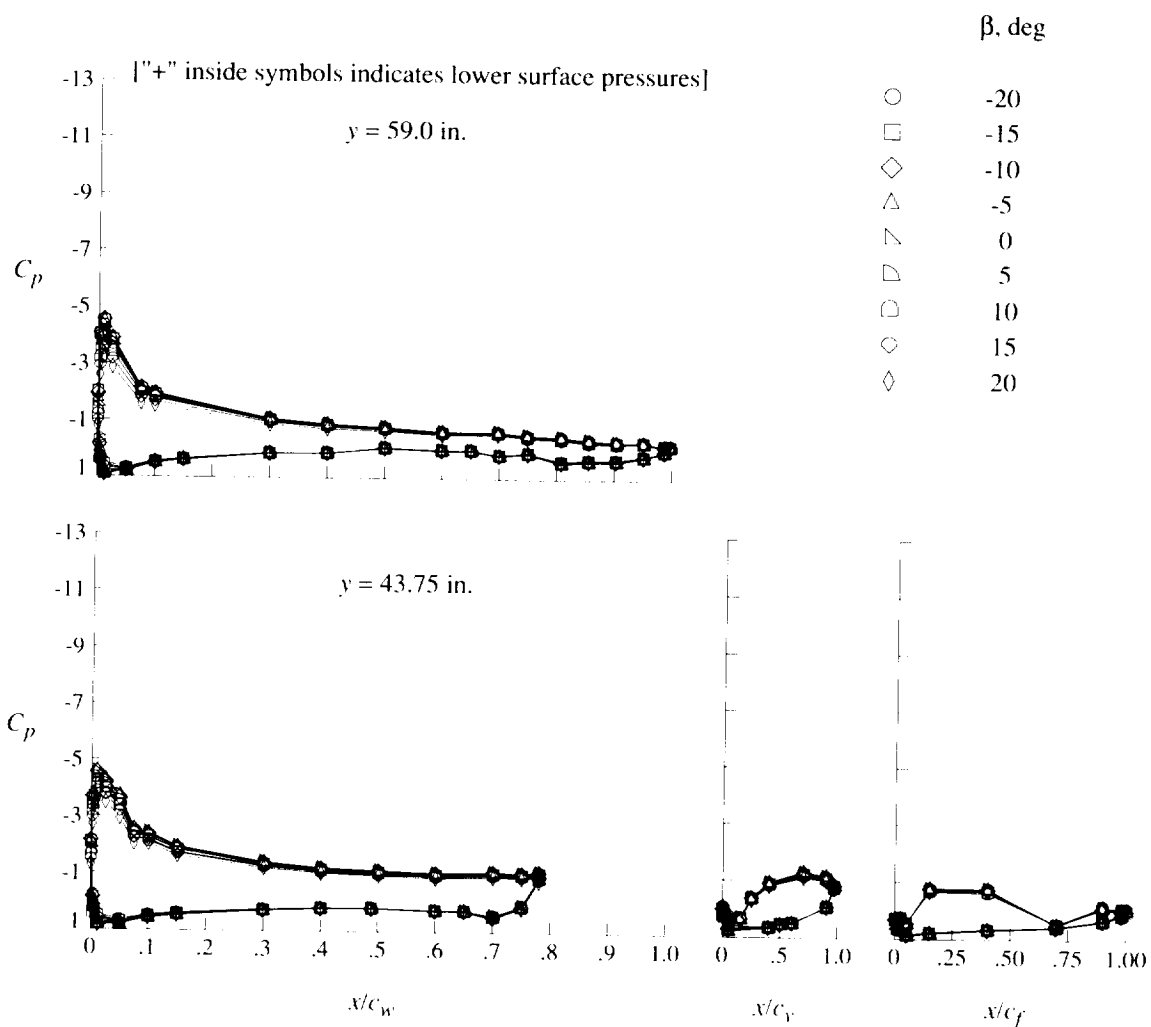
(c) Concluded.

Figure 31. Continued.



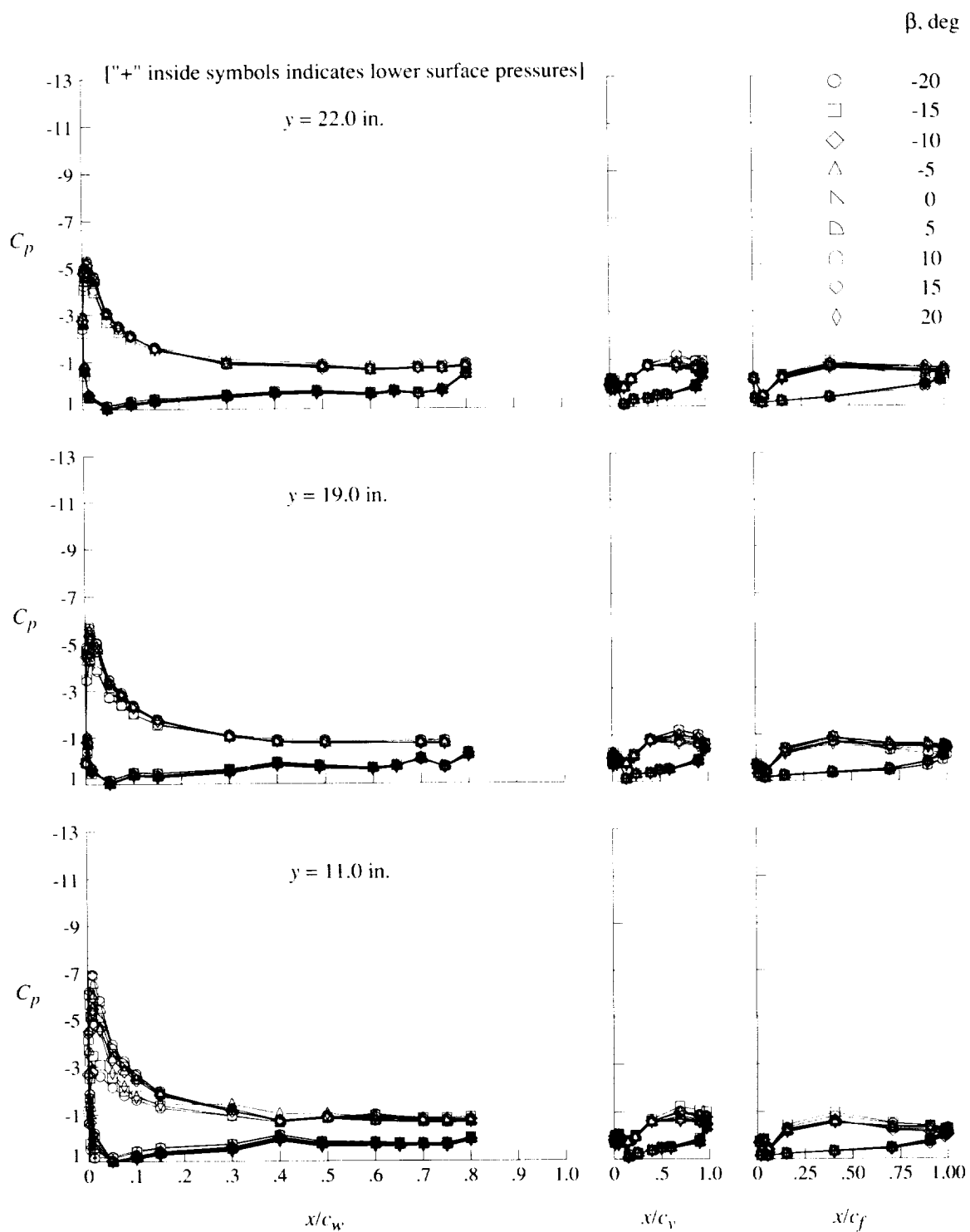
(d) $q = 40$ psf; $\alpha = 8^\circ$.

Figure 31. Continued.



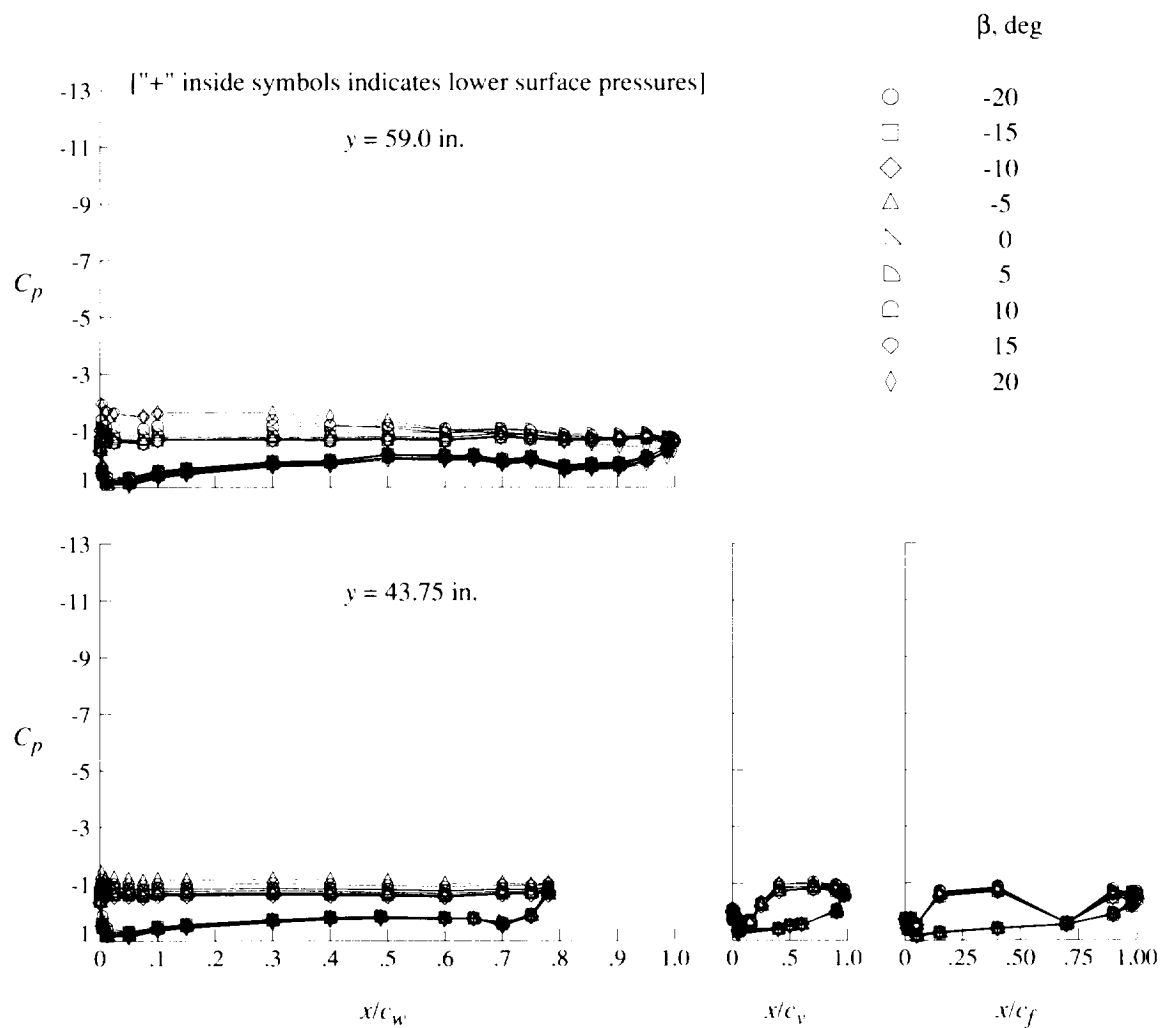
(d) Concluded.

Figure 31. Continued.



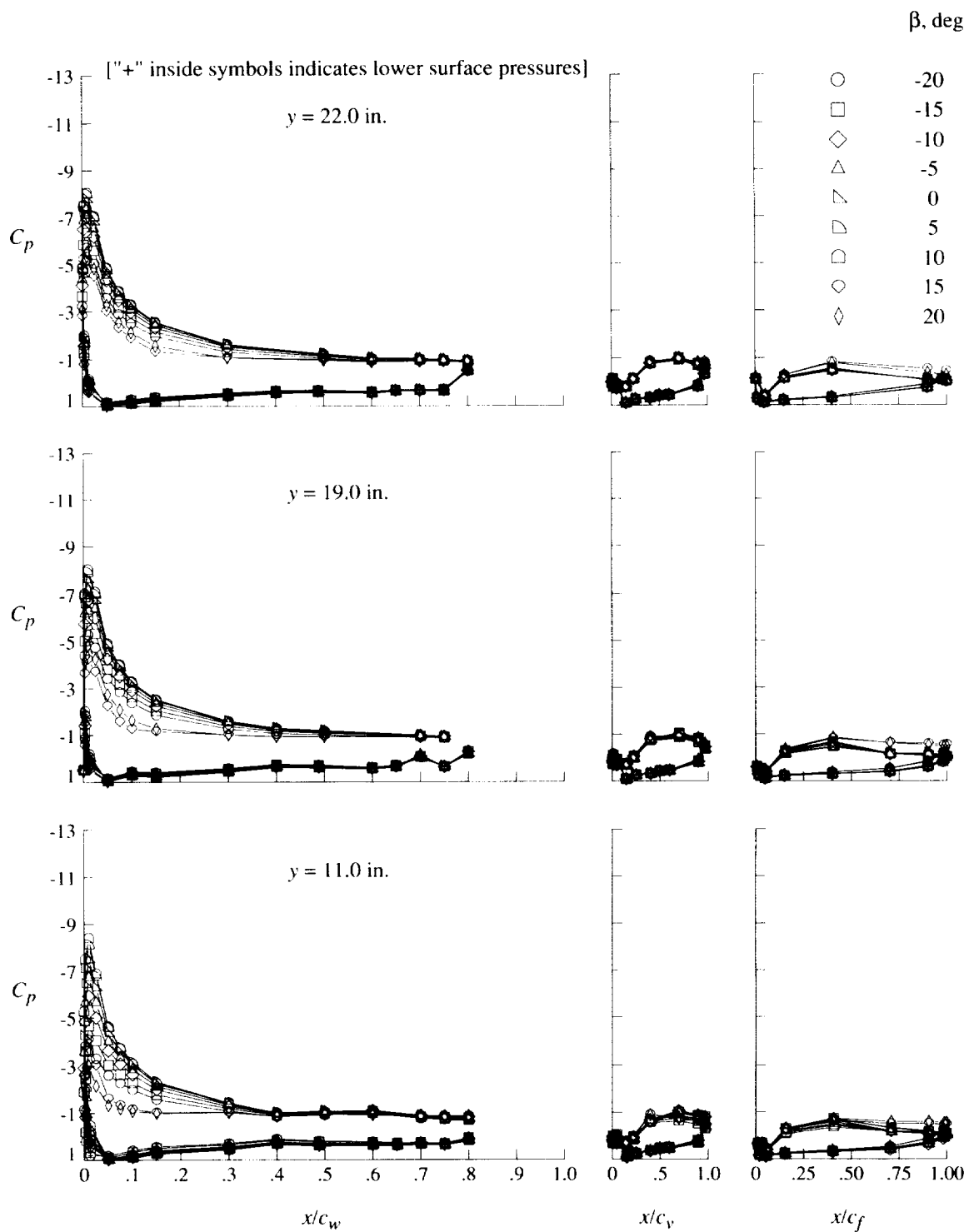
(e) $q = 20$ psf; $\alpha = 16^\circ$.

Figure 31. Continued.



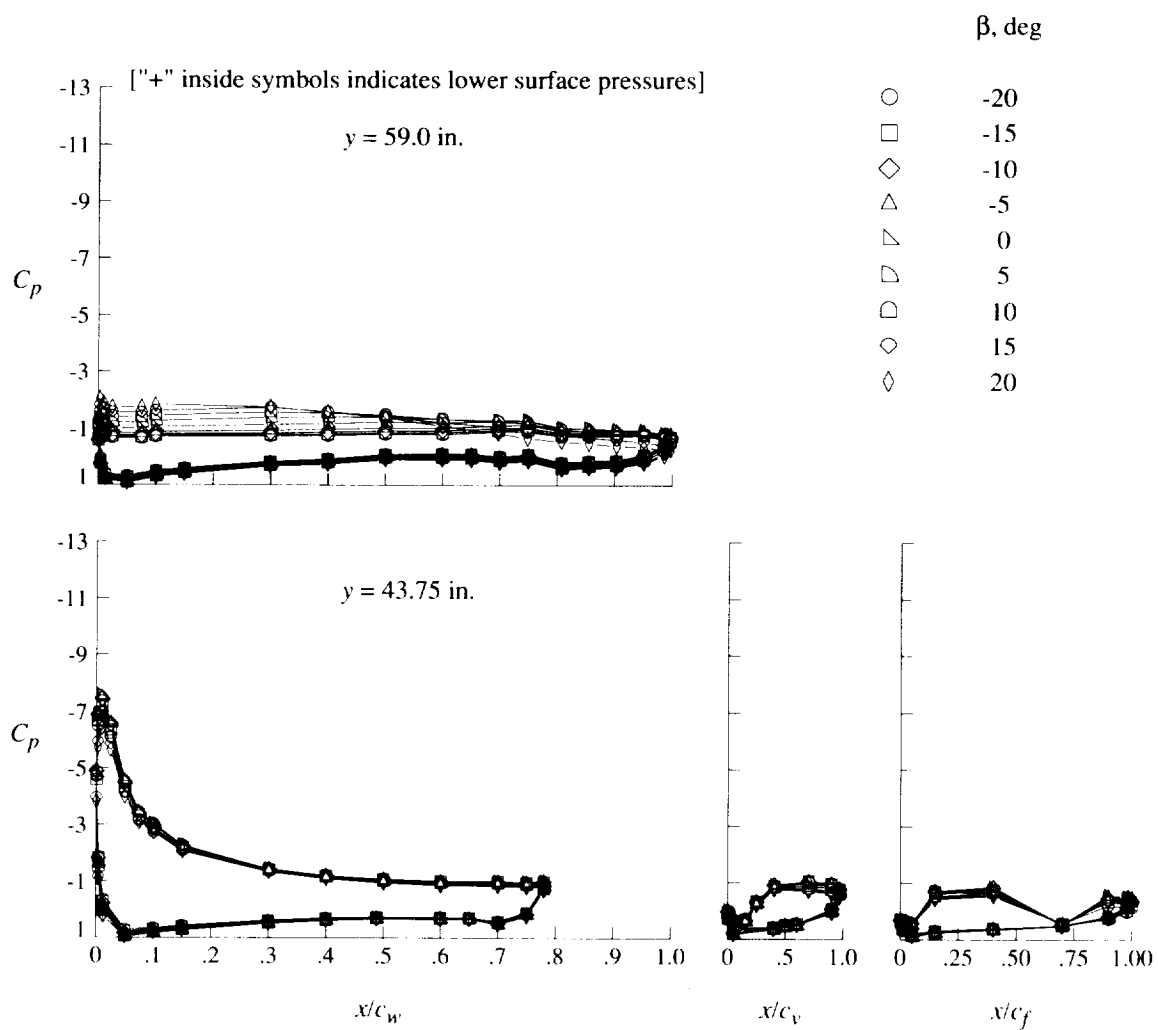
(e) Concluded.

Figure 31. Continued.



(f) $q = 40$ psf; $\alpha = 16^\circ$.

Figure 31. Continued.



(f) Concluded.

Figure 31. Concluded.

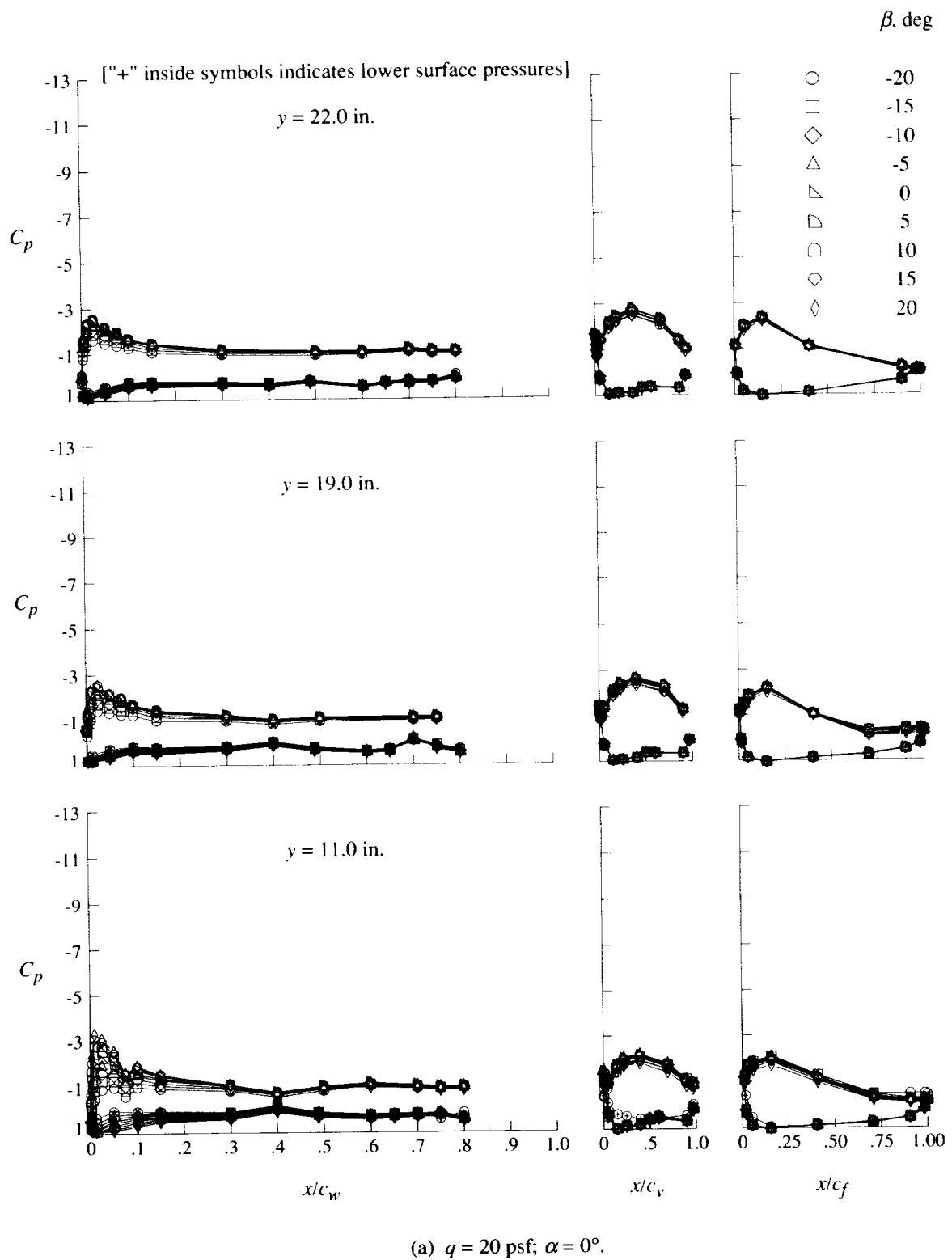


Figure 32. Effect of sideslip angle on pressure distributions for flaps-only configuration at $\delta_f = 60^\circ$.

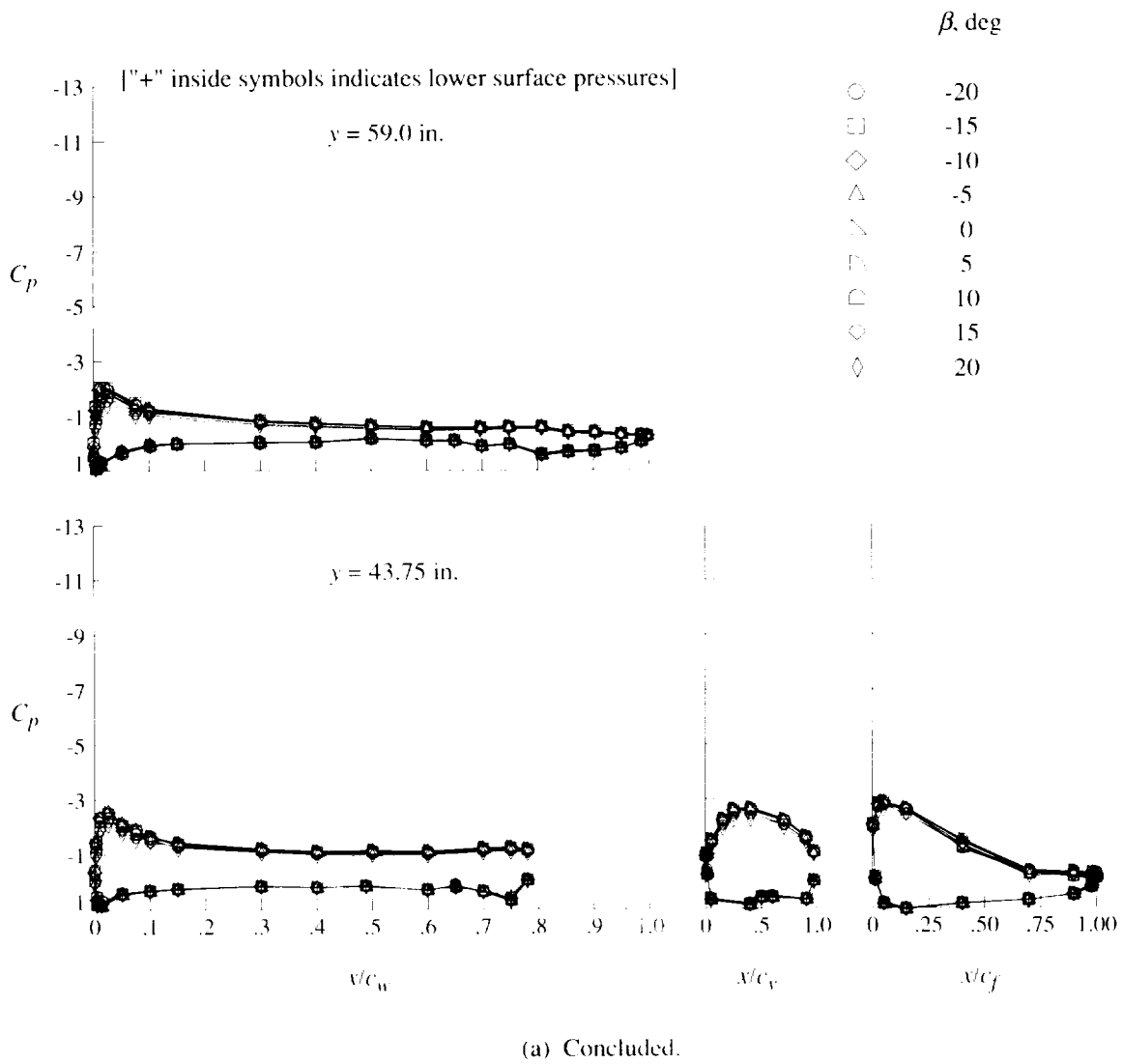
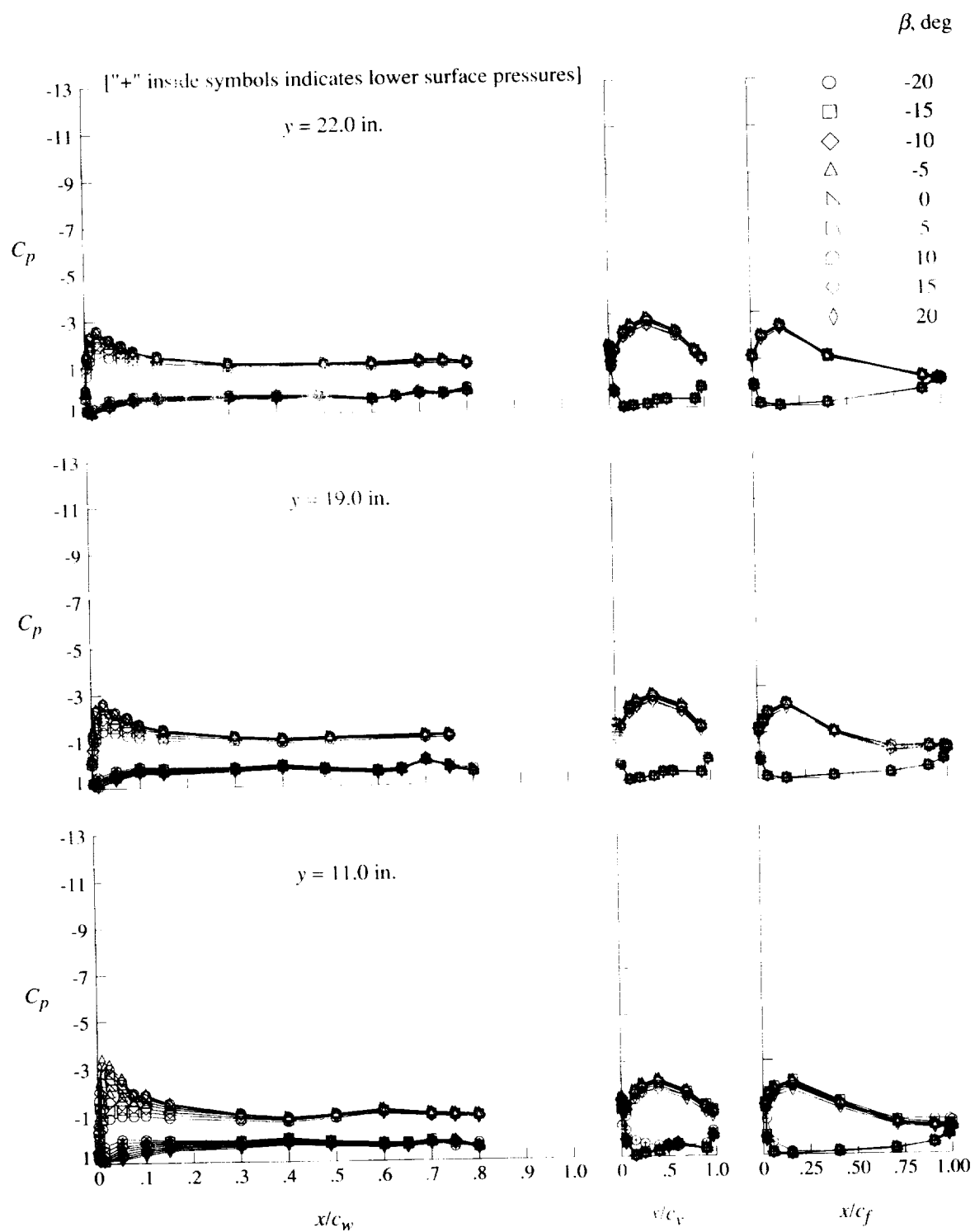
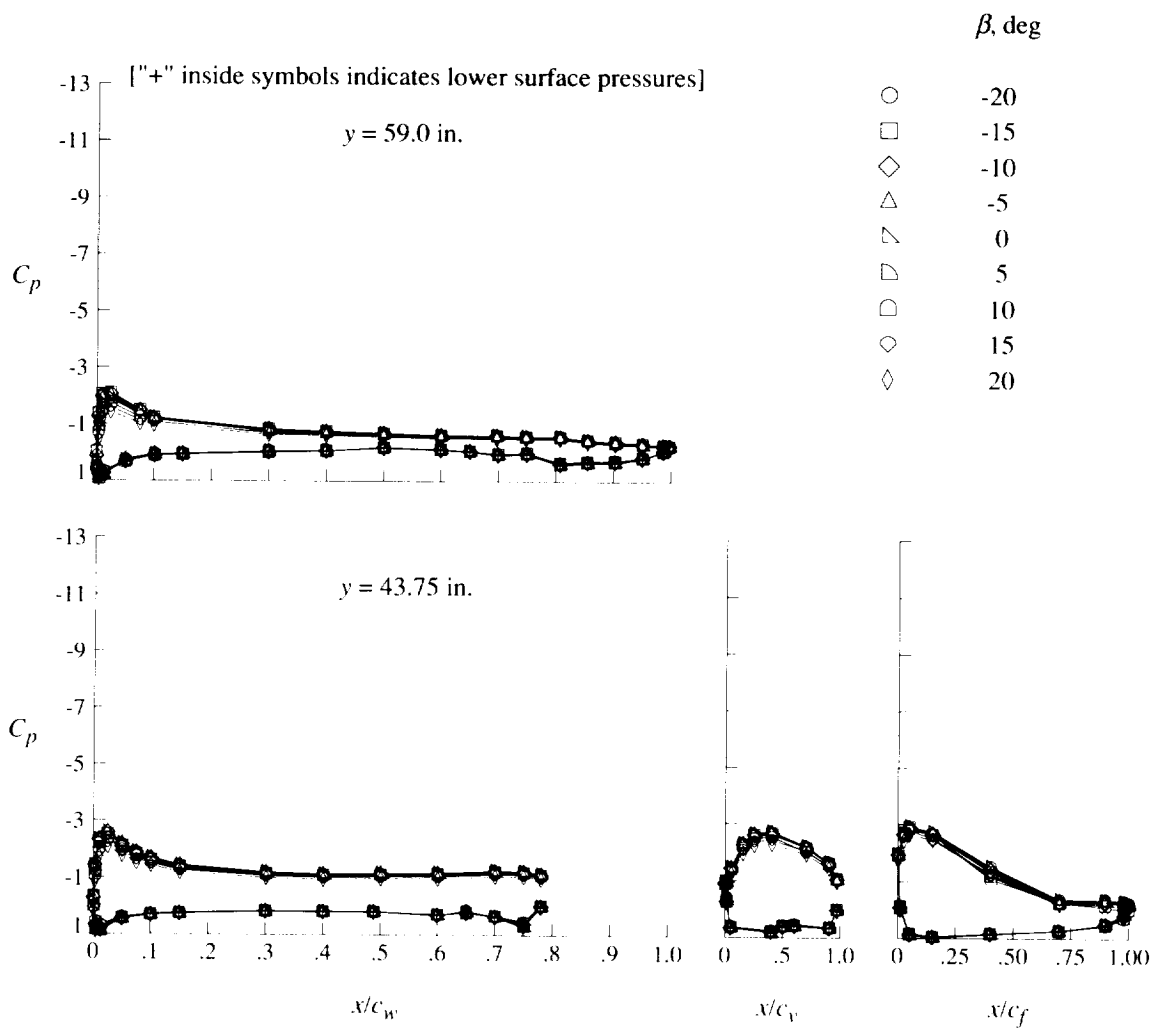


Figure 32. Continued.



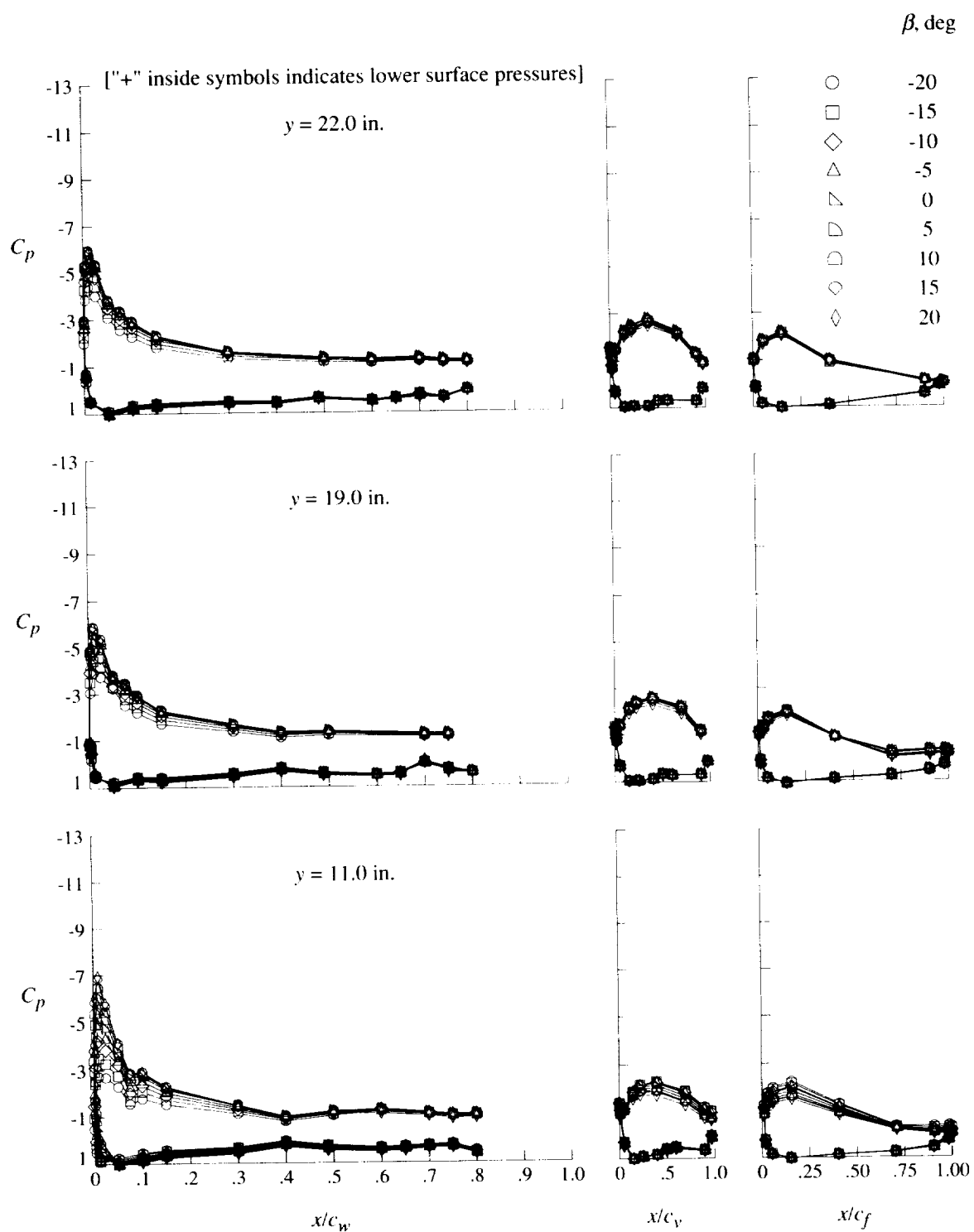
(b) $q = 40$ psf; $\alpha = 0^\circ$.

Figure 32. Continued.



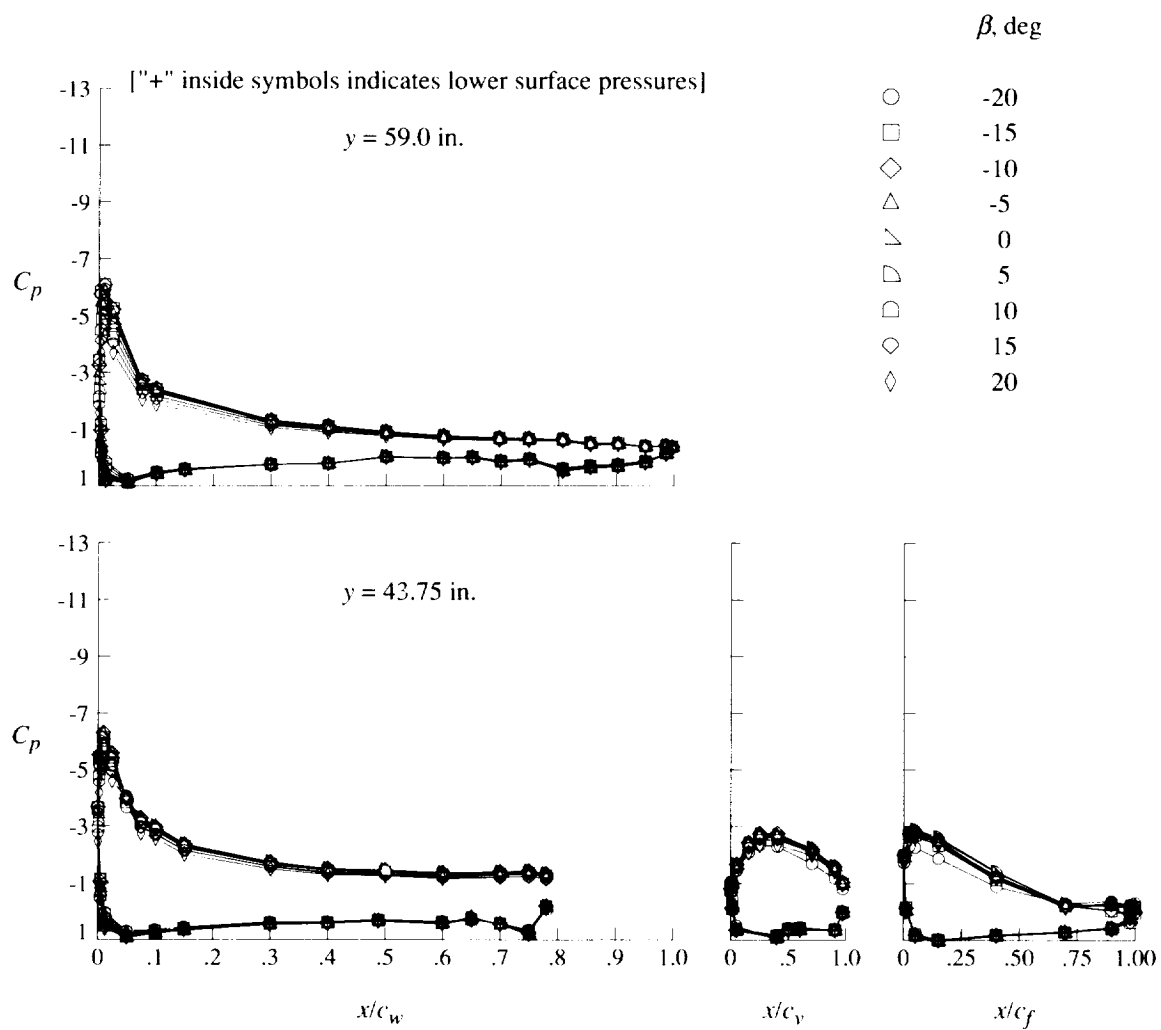
(b) Concluded.

Figure 32. Continued.



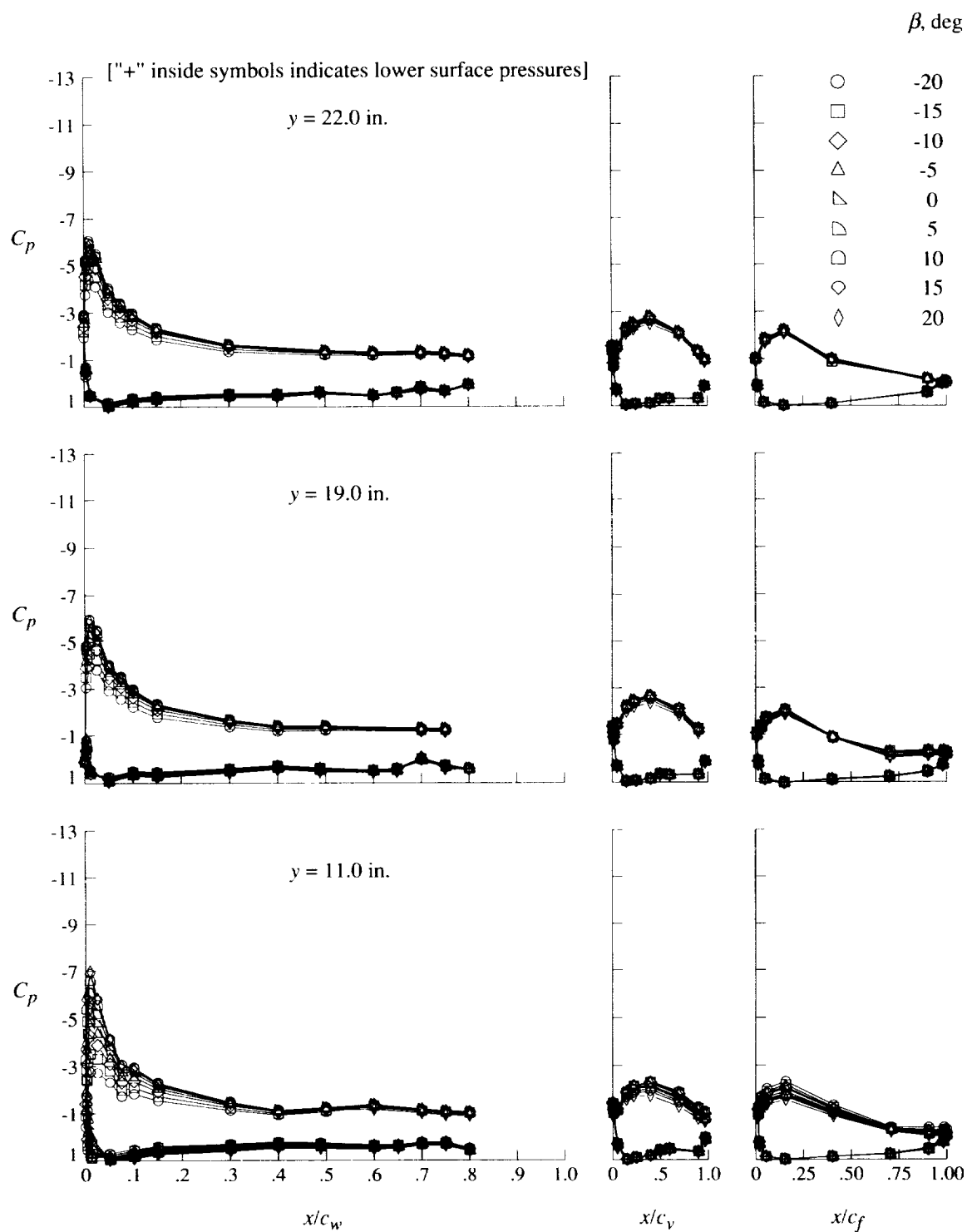
(c) $q = 20$ psf; $\alpha = 8^\circ$.

Figure 32. Continued.



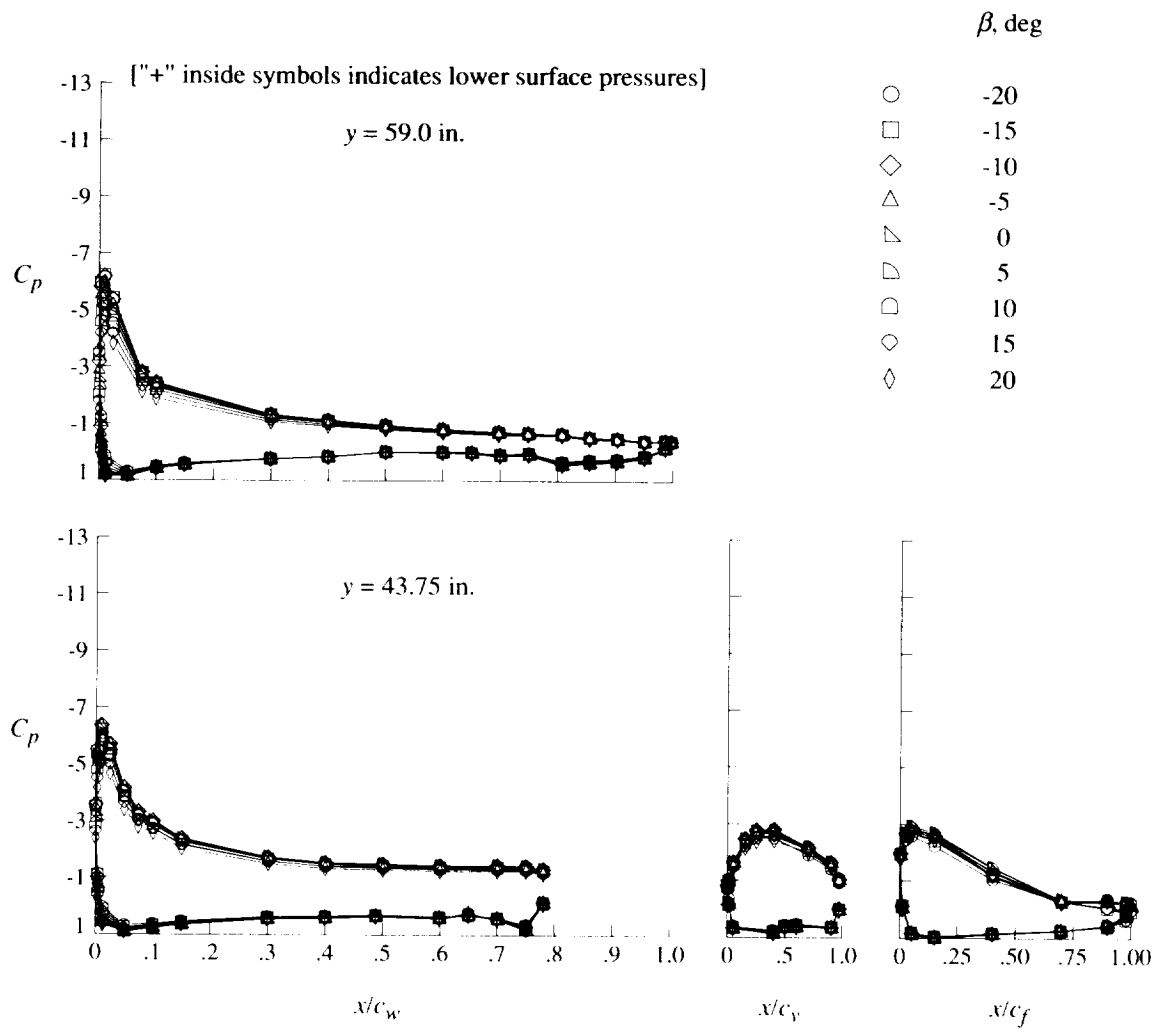
(c) Concluded.

Figure 32. Continued.



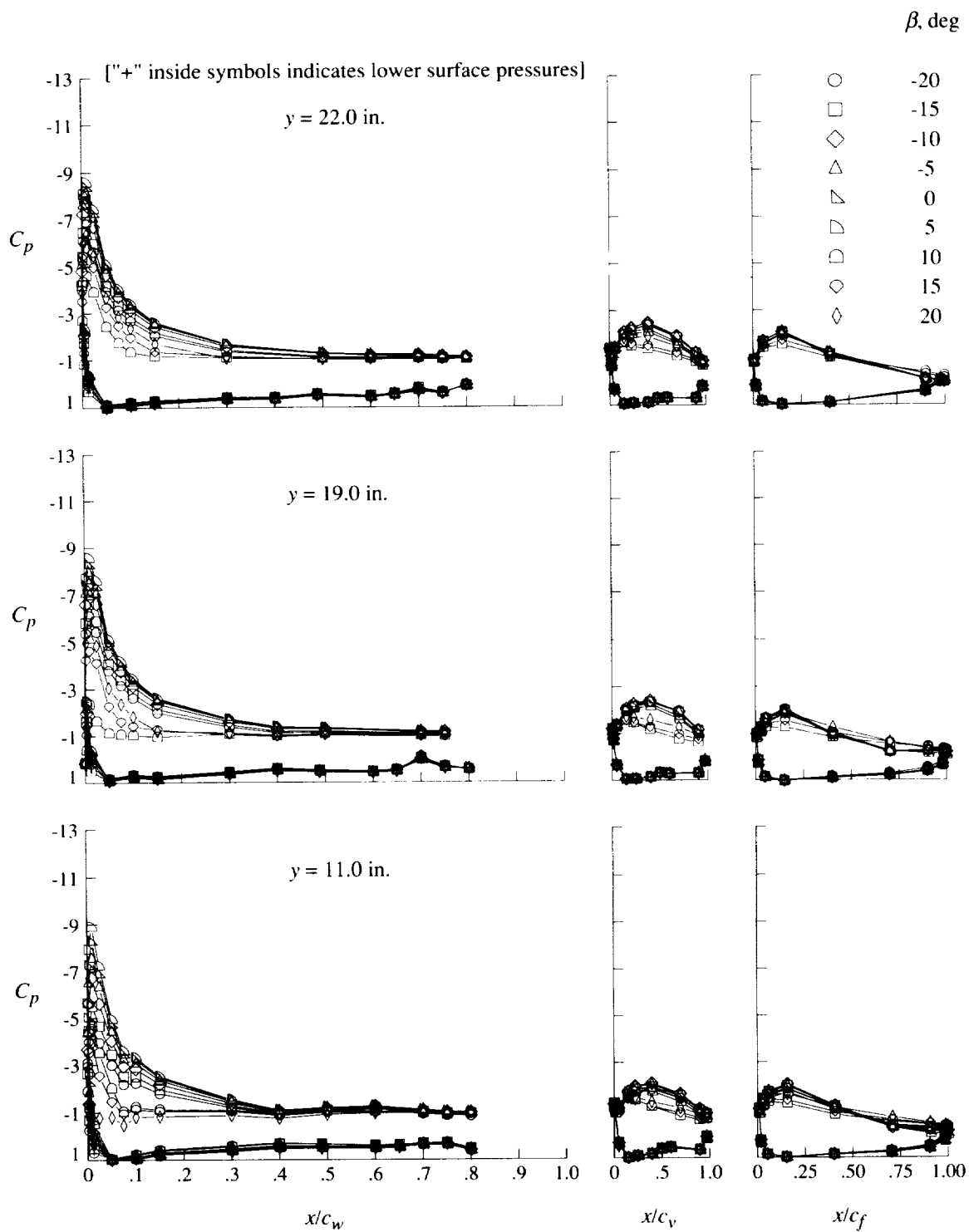
(d) $q = 40$ psf; $\alpha = 8^\circ$.

Figure 32. Continued.



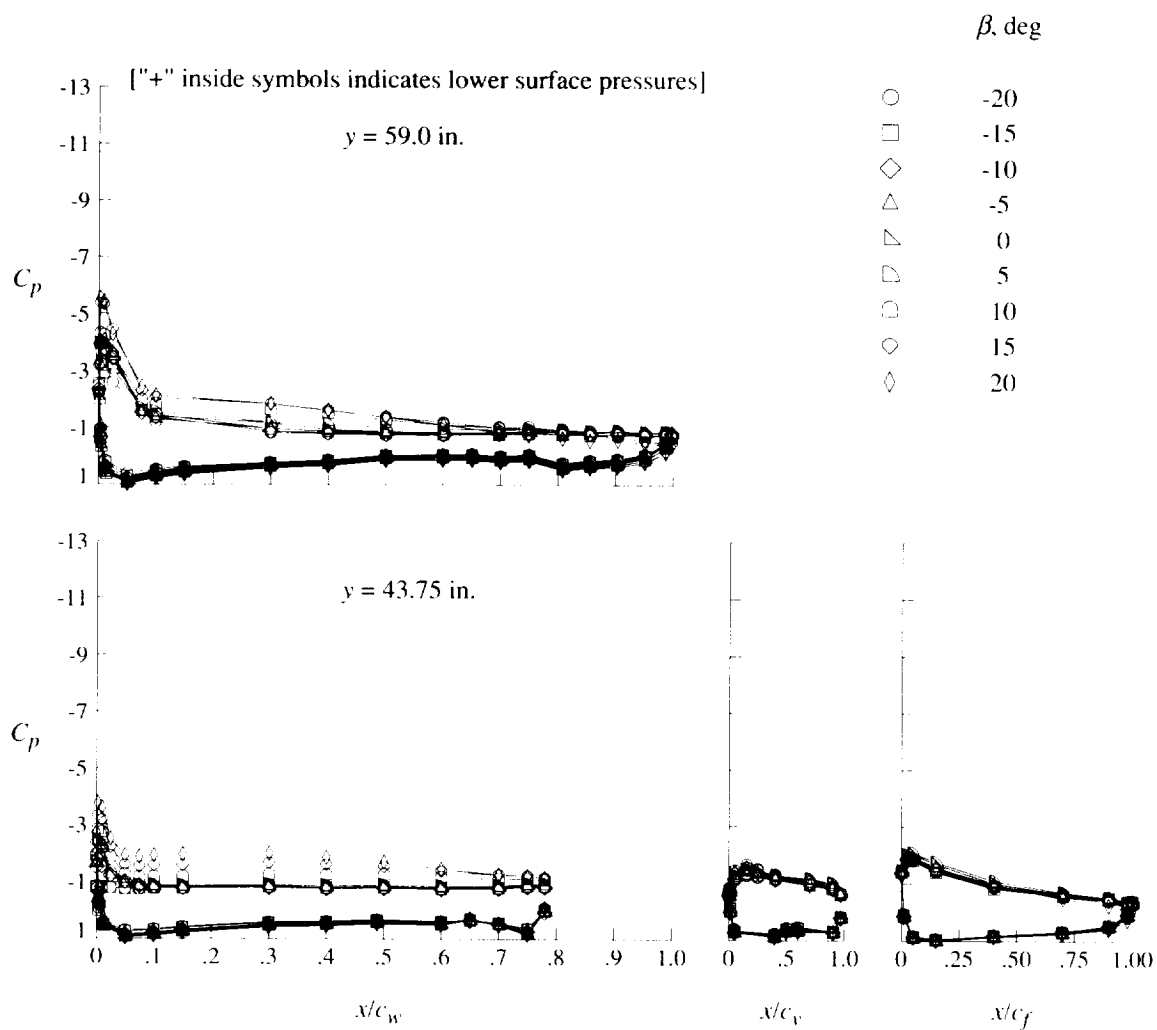
(d) Concluded.

Figure 32. Continued.



(e) $q = 20$ psf; $\alpha = 16^\circ$.

Figure 32. Continued.



(e) Concluded.

Figure 32. Concluded.

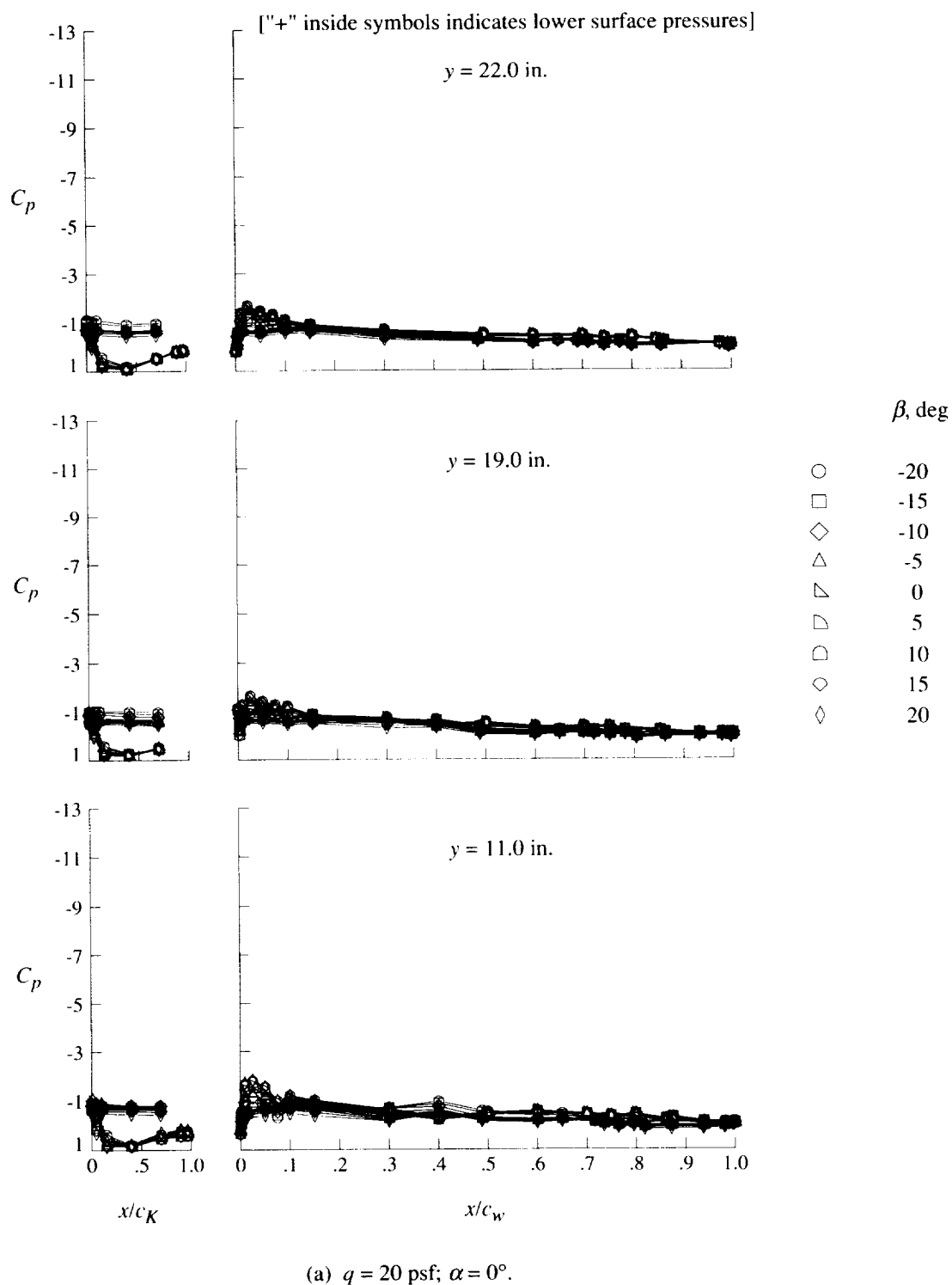
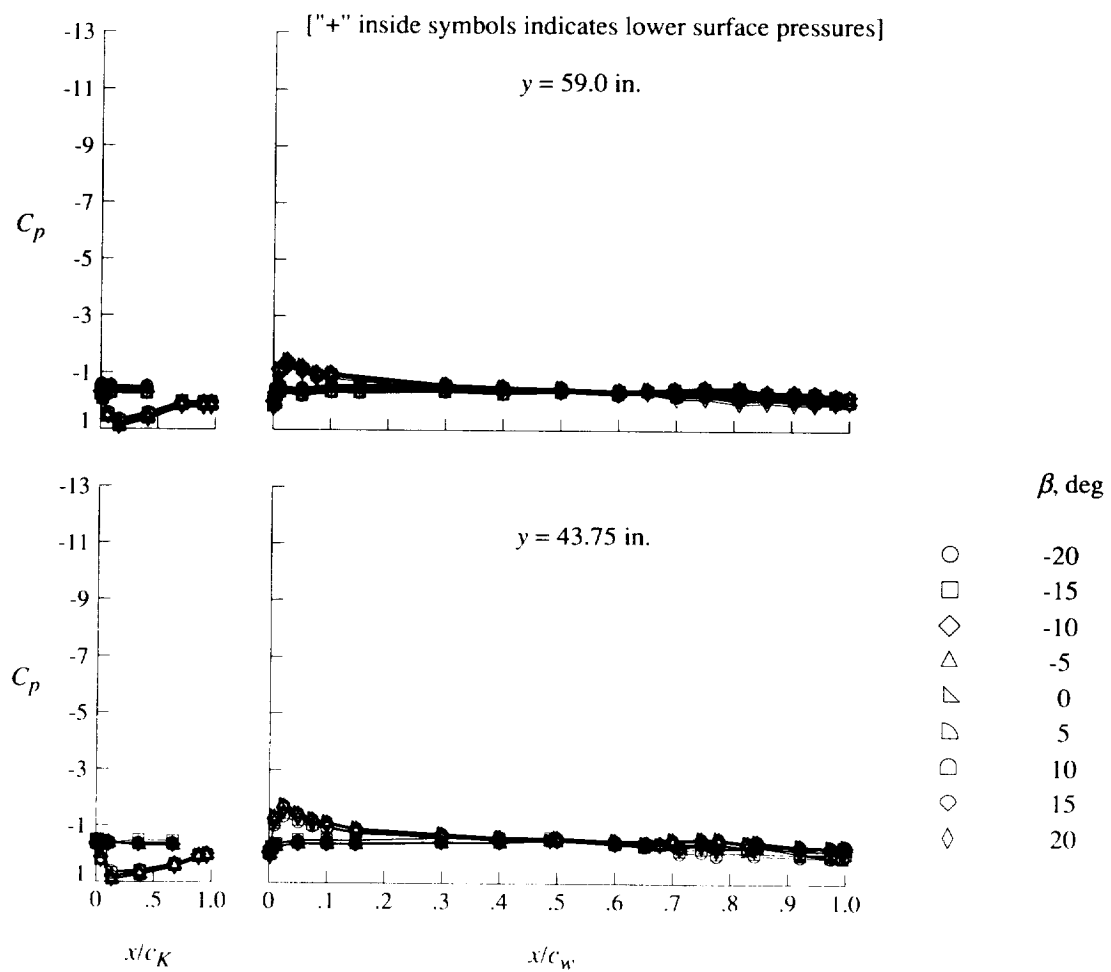
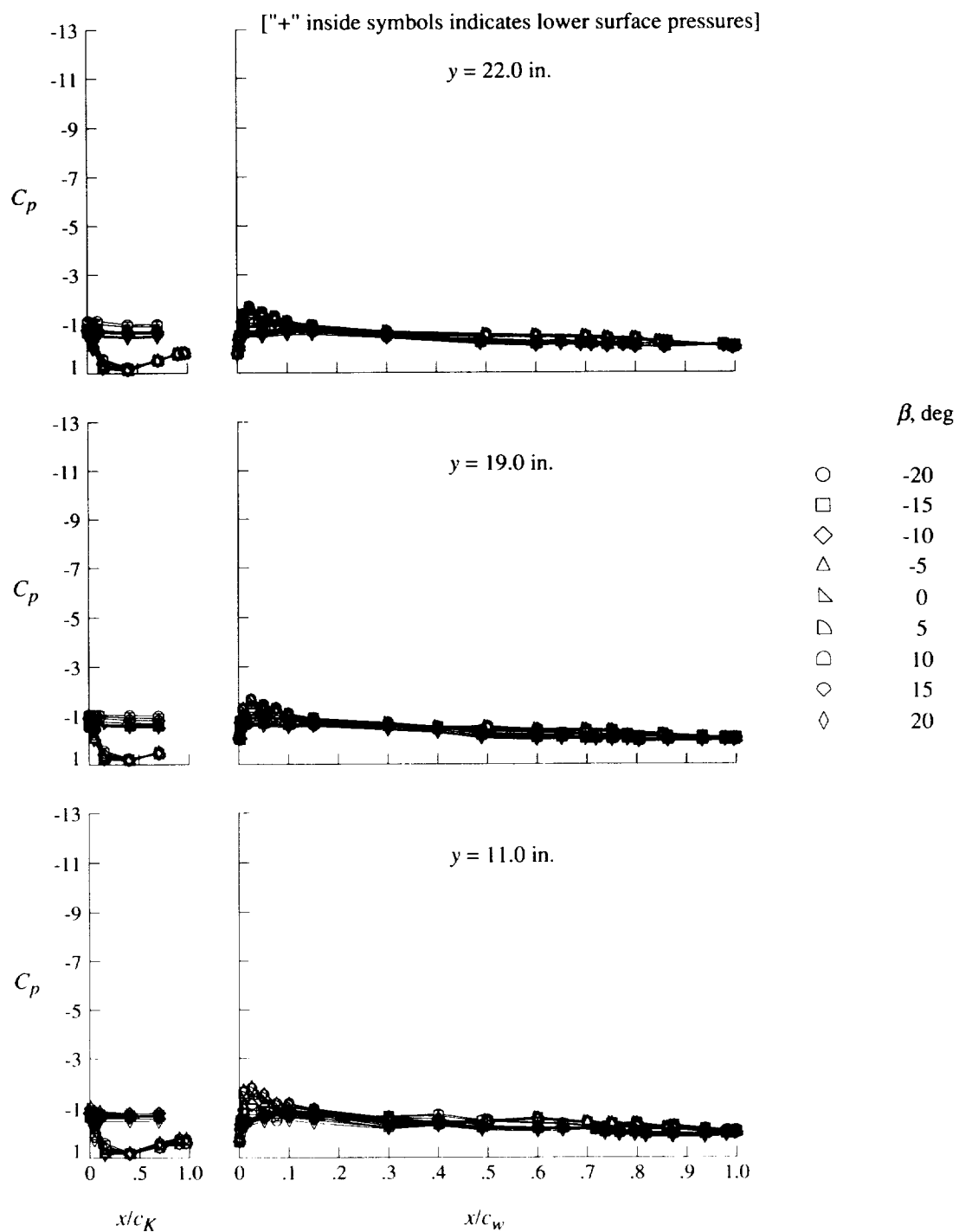


Figure 33. Effect of sideslip angle on pressure distributions for Krueger-flap-only configuration.



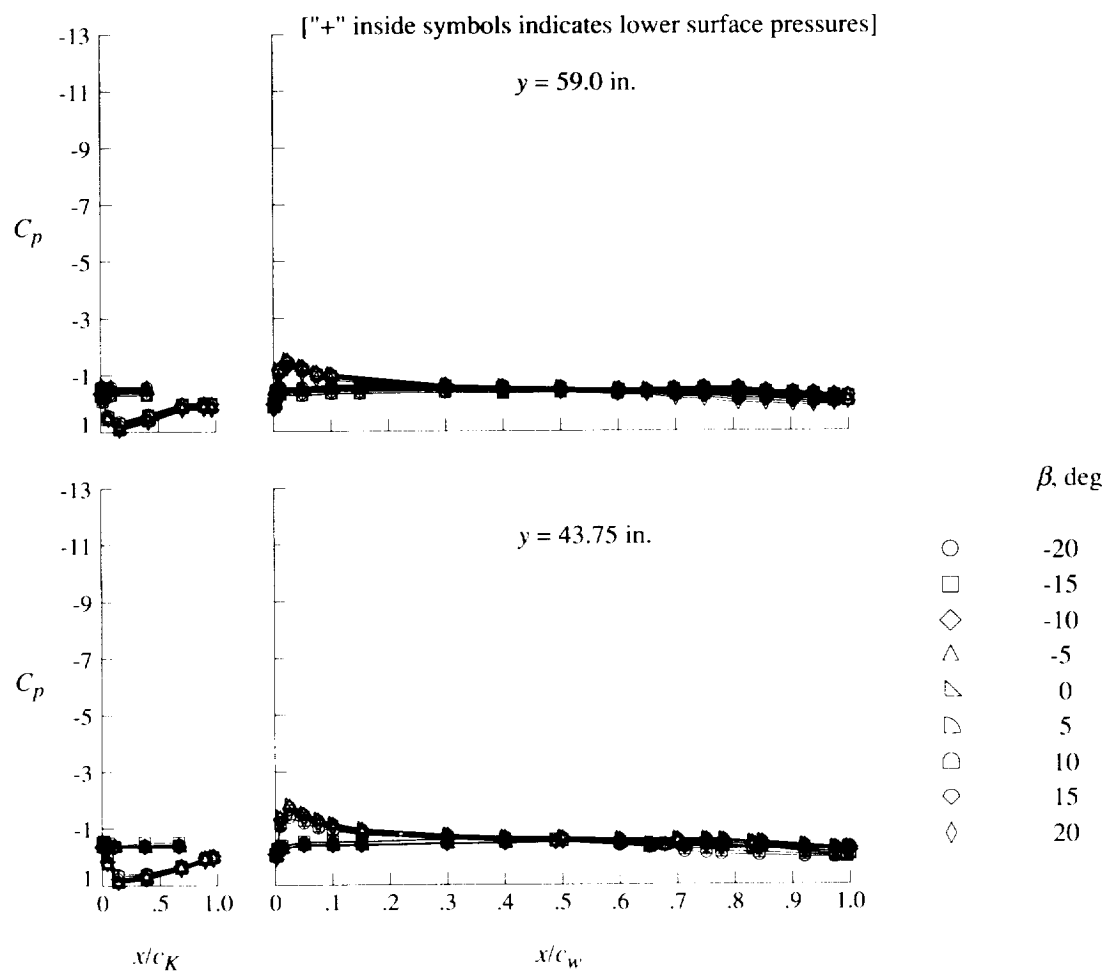
(a) Concluded.

Figure 33. Continued.



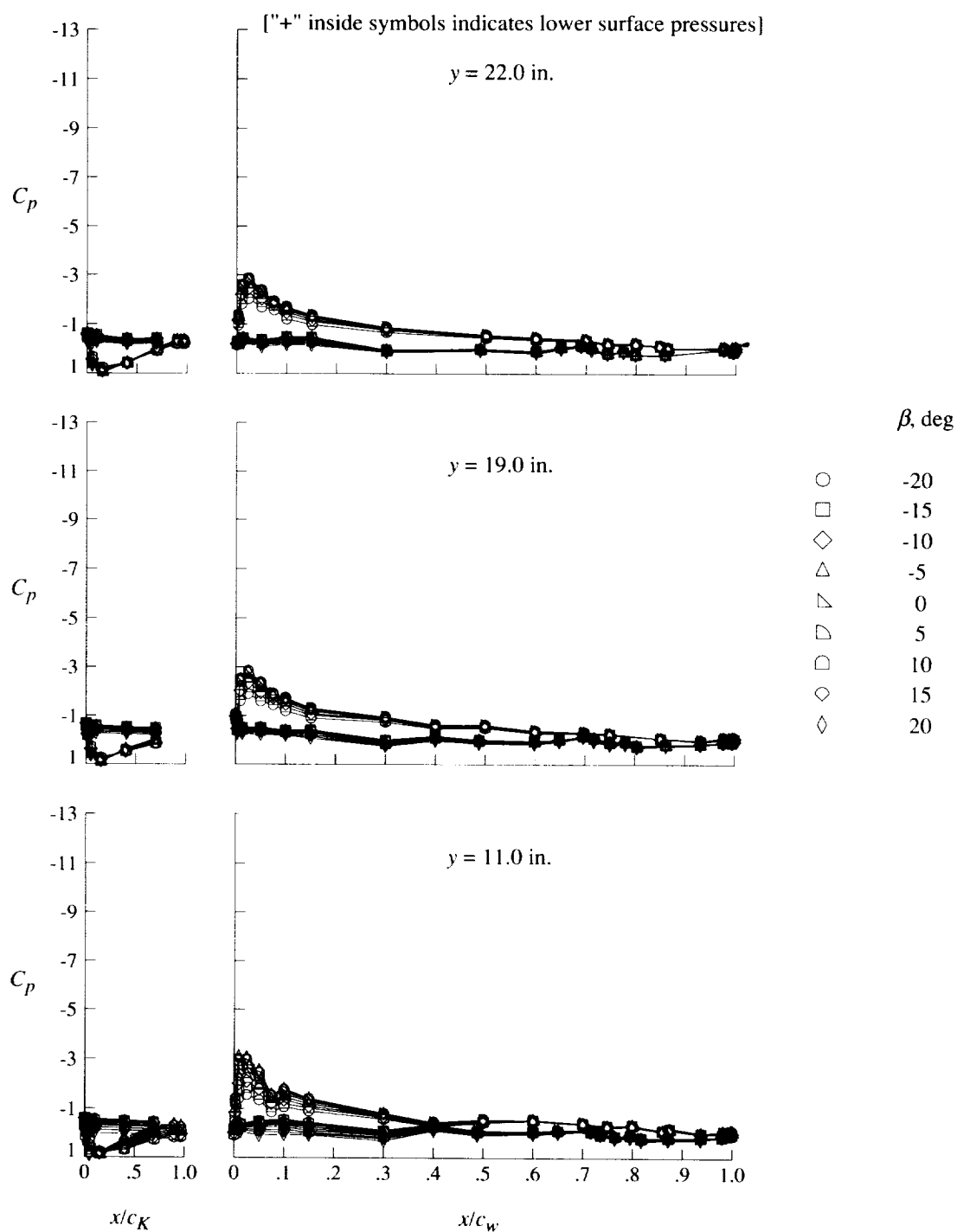
(b) $q = 40$ psf; $\alpha = 0^\circ$.

Figure 33. Continued.



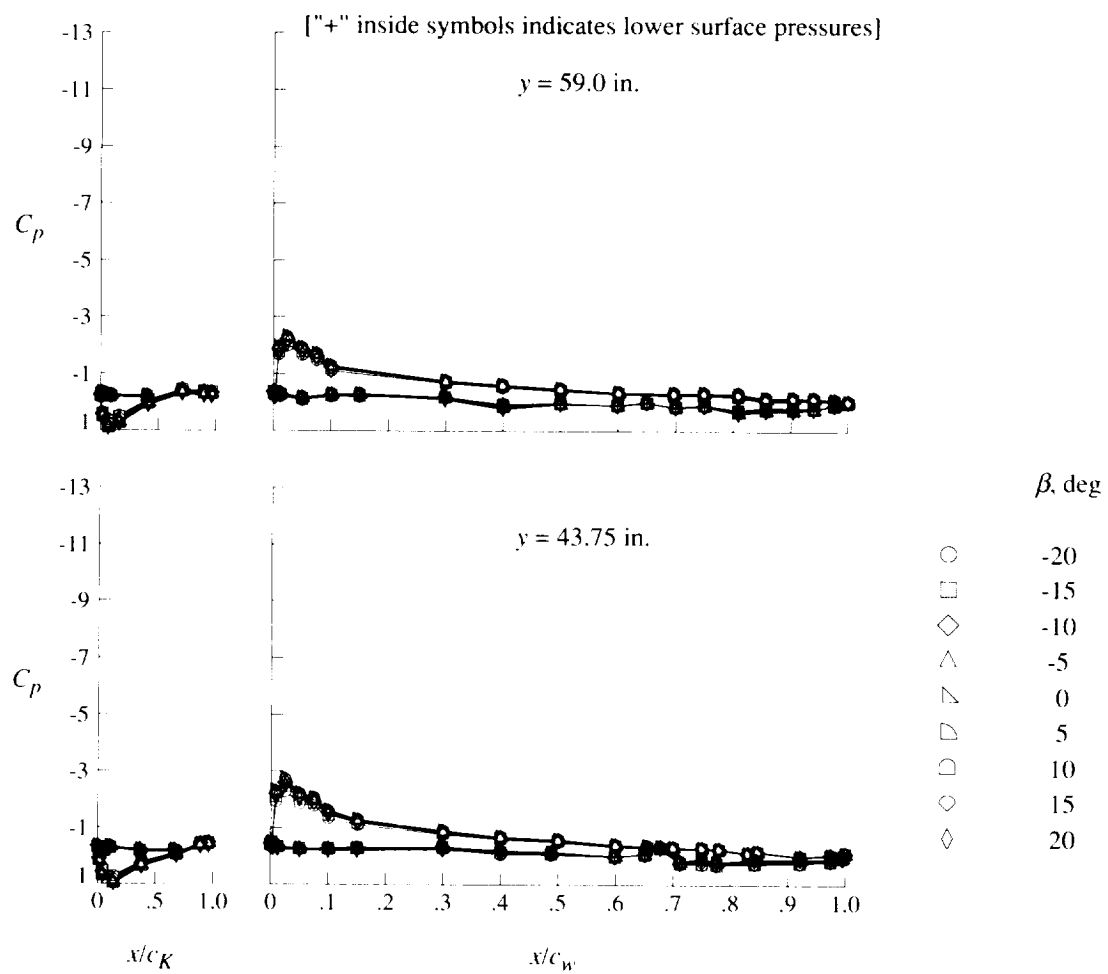
(b) Concluded.

Figure 33. Continued.



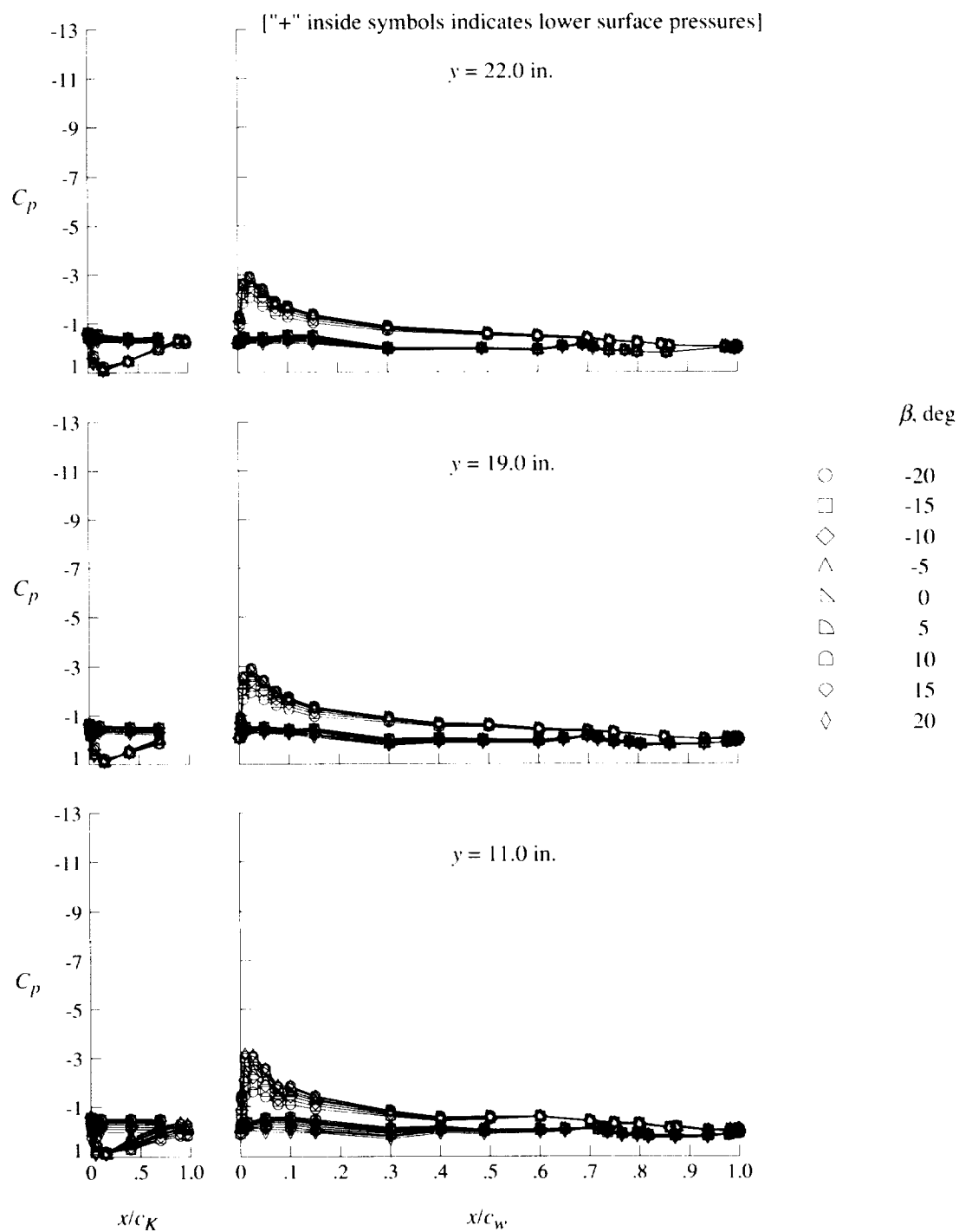
(c) $q = 20$ psf; $\alpha = 8^\circ$.

Figure 33. Continued.



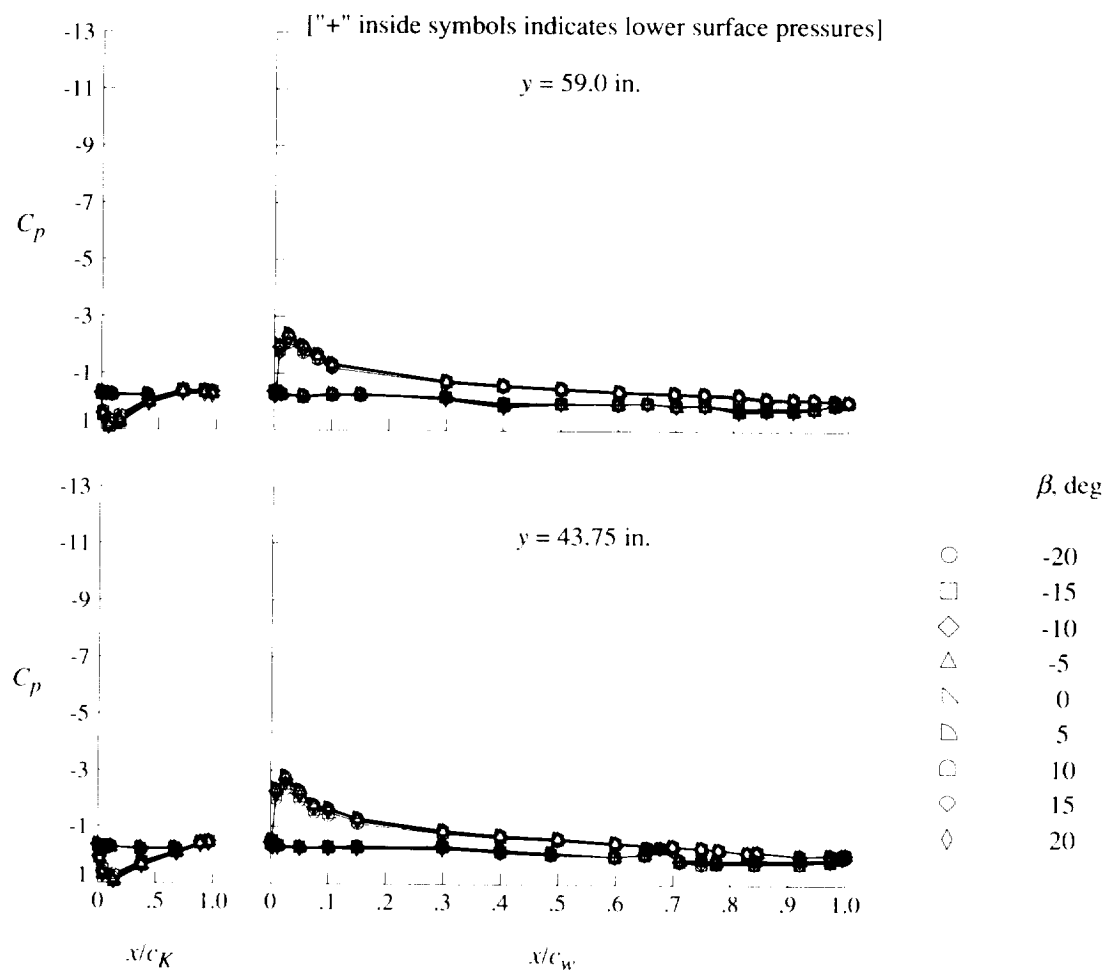
(c) Concluded.

Figure 33. Continued.



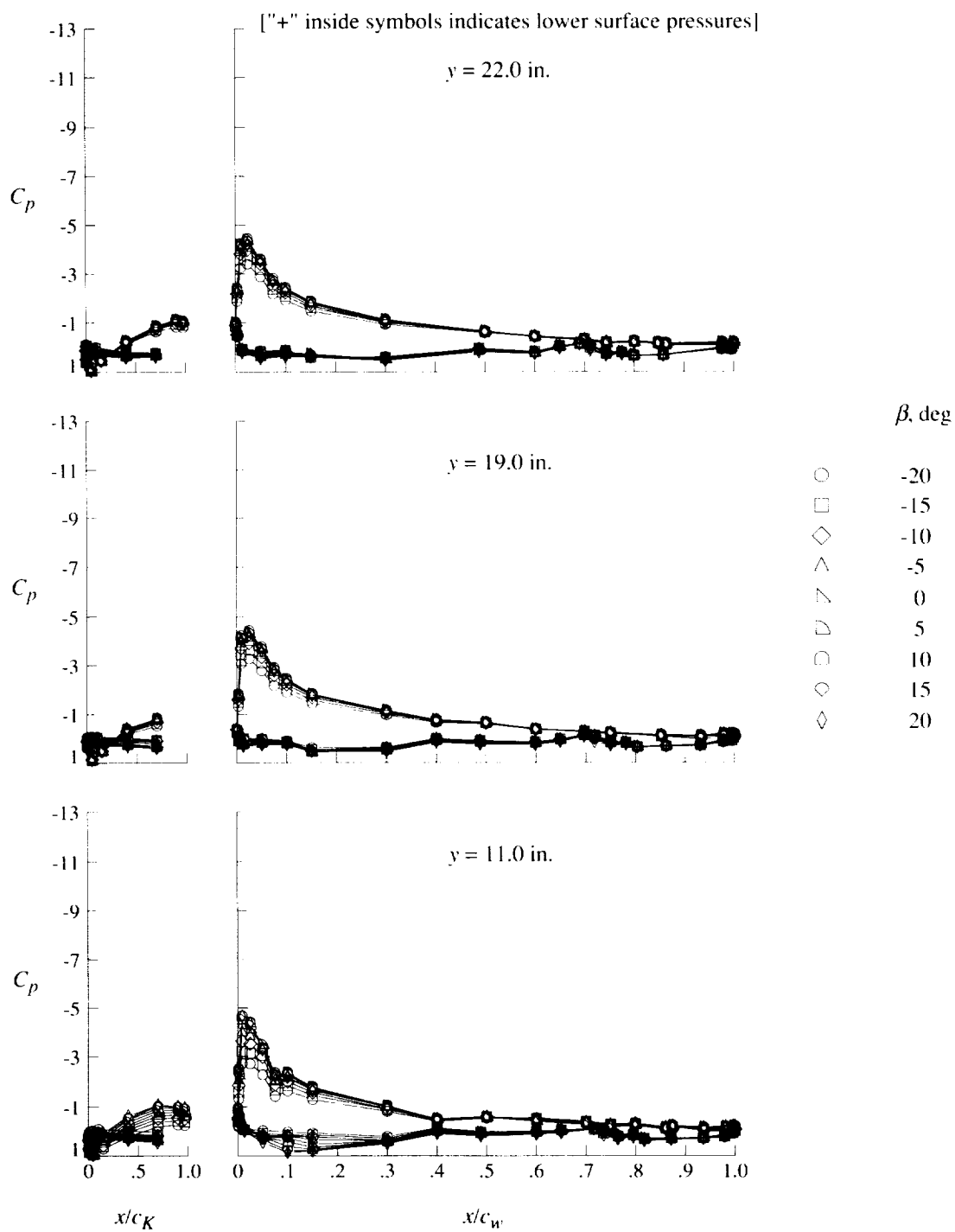
(d) $q = 40$ psf; $\alpha = 8^\circ$.

Figure 33. Continued.



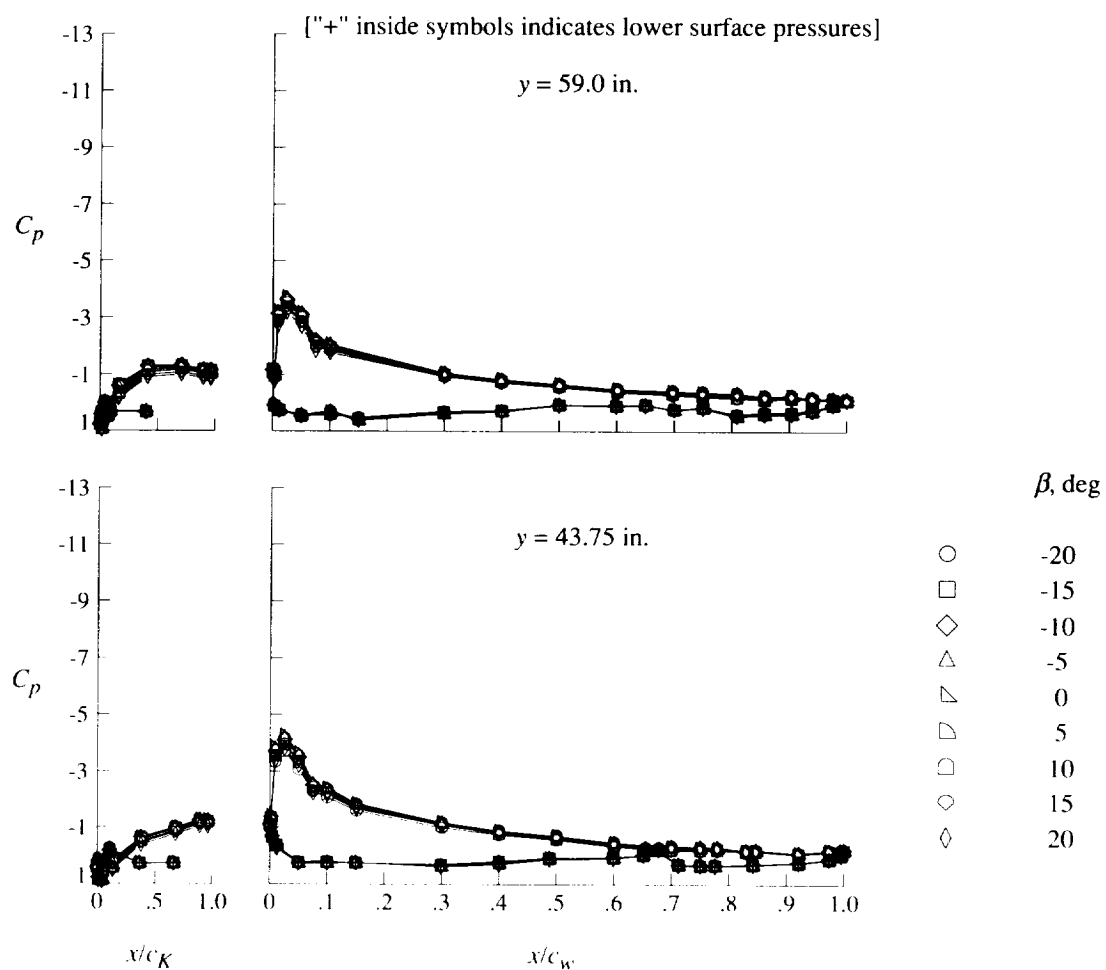
(d) Concluded.

Figure 33. Continued.



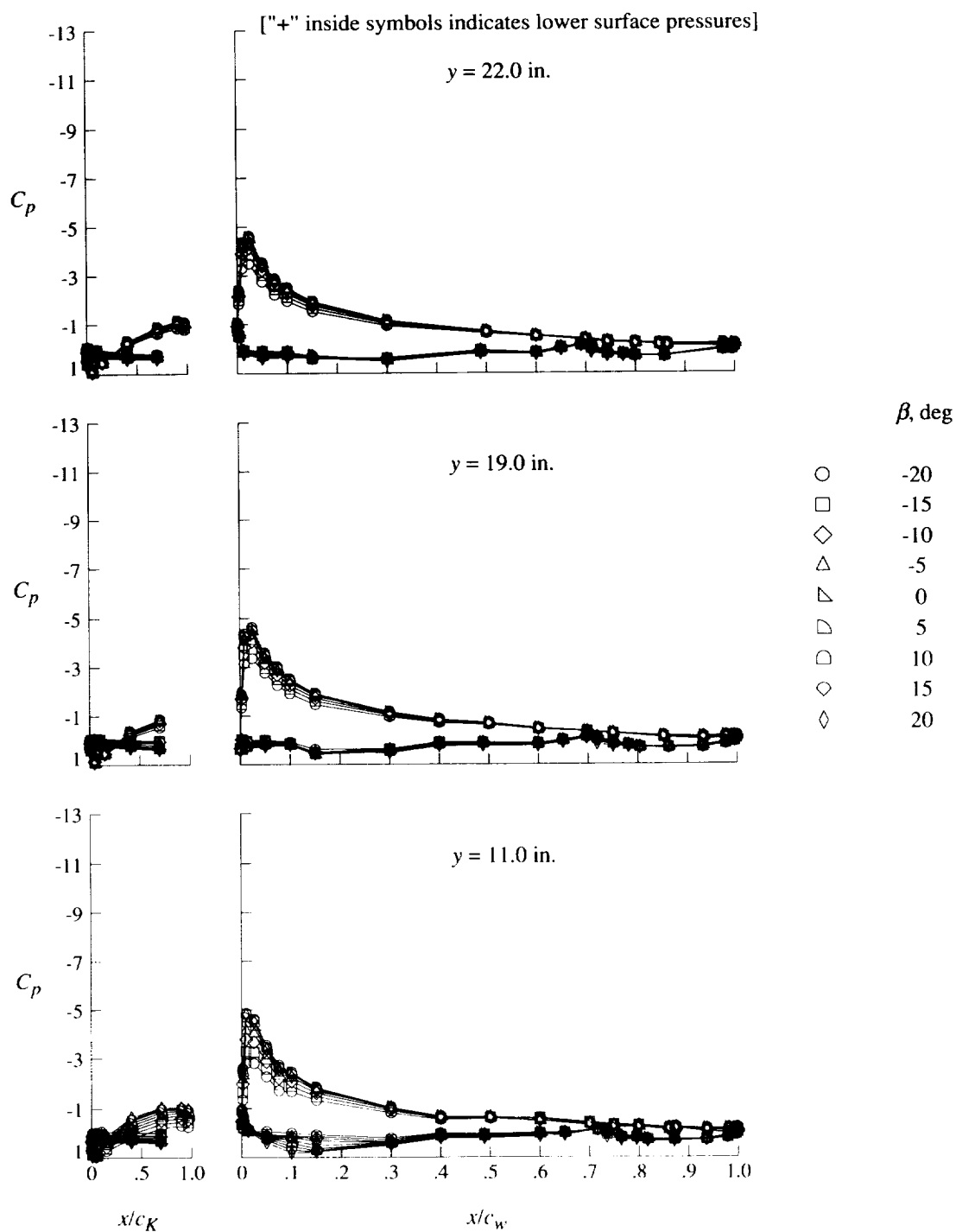
(e) $q = 20$ psf; $\alpha = 16^\circ$.

Figure 33. Continued.



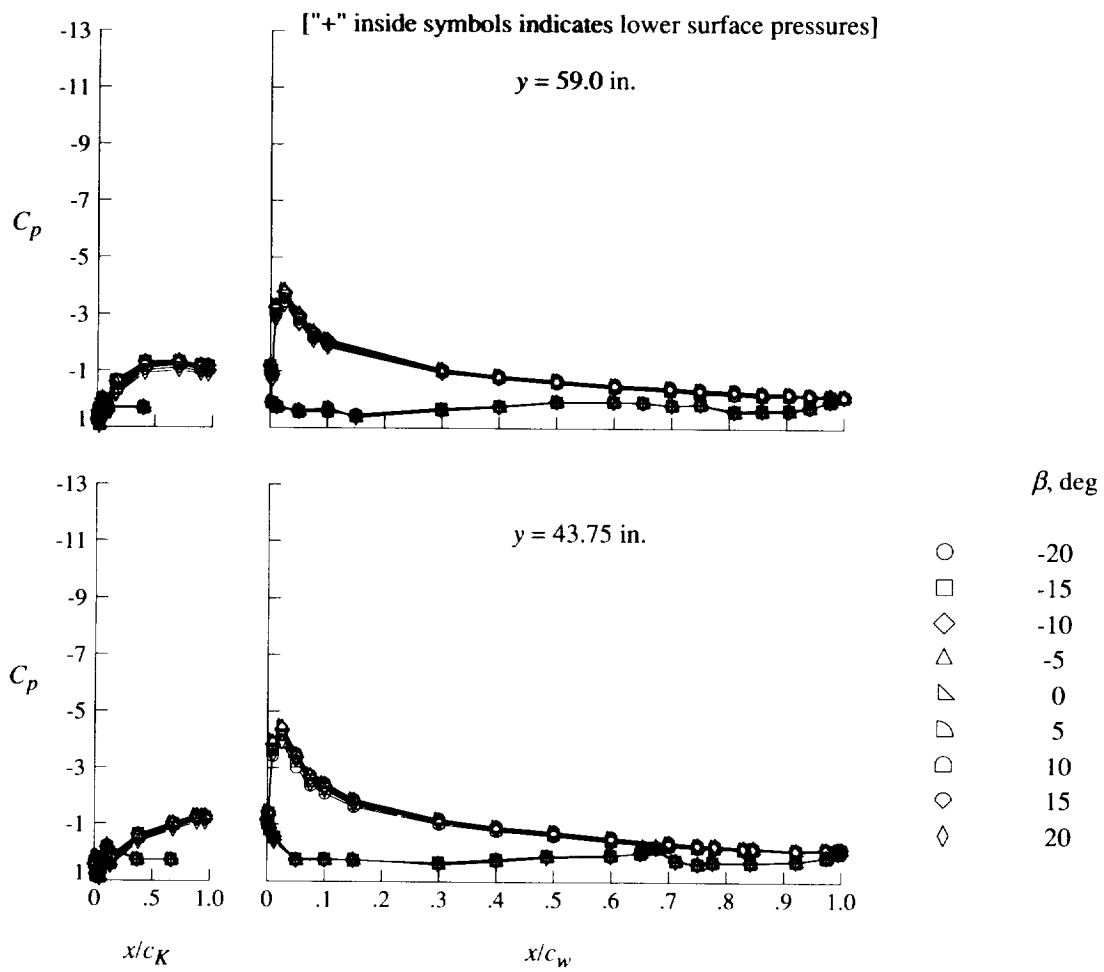
(e) Concluded.

Figure 33. Continued.



(f) $q = 40$ psf; $\alpha = 16^\circ$.

Figure 33. Continued.



(f) Concluded.

Figure 33. Concluded.

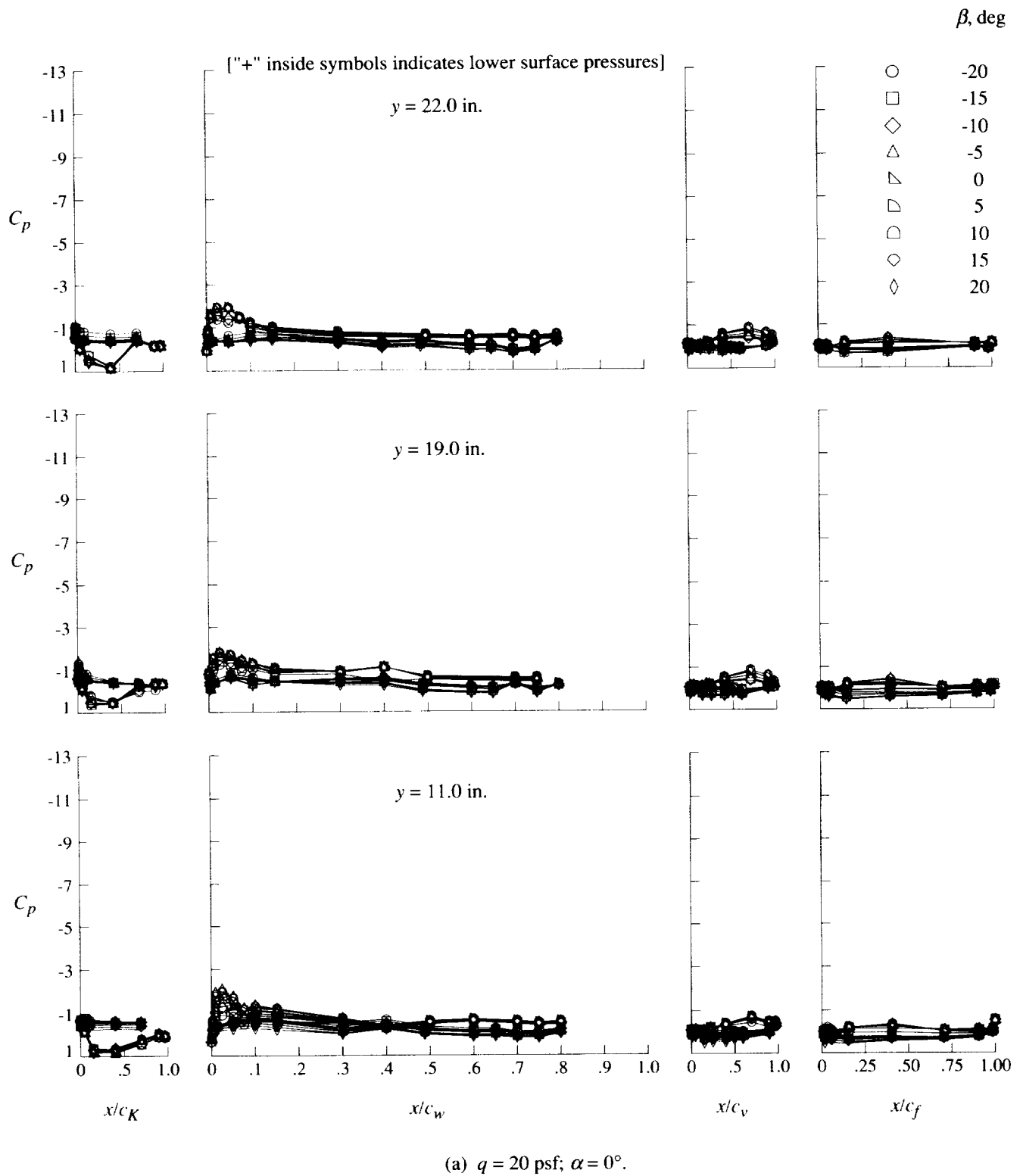
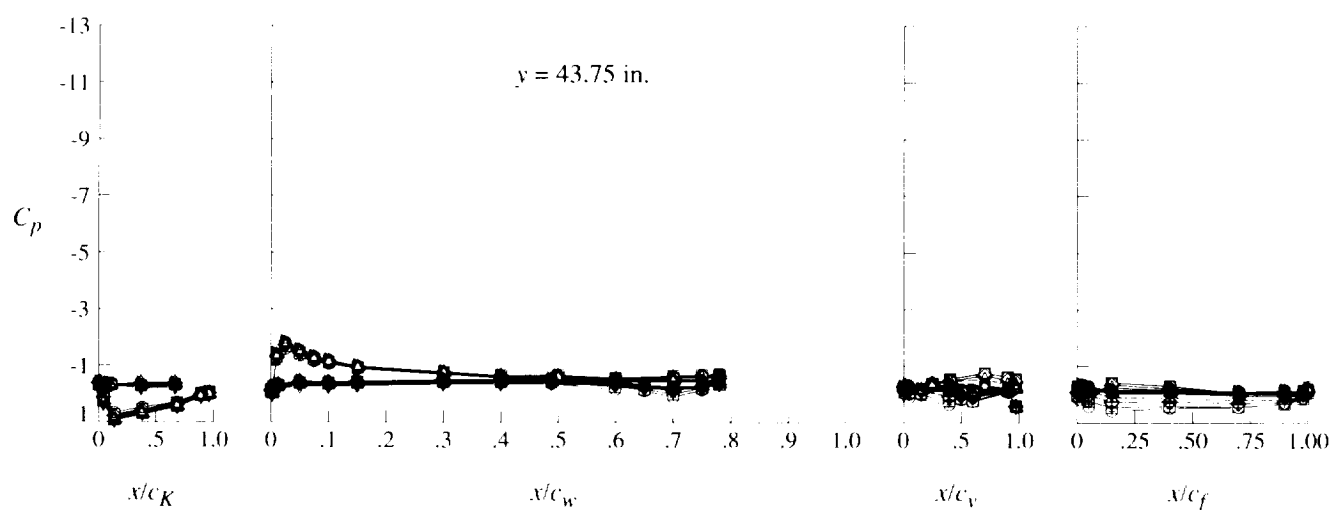
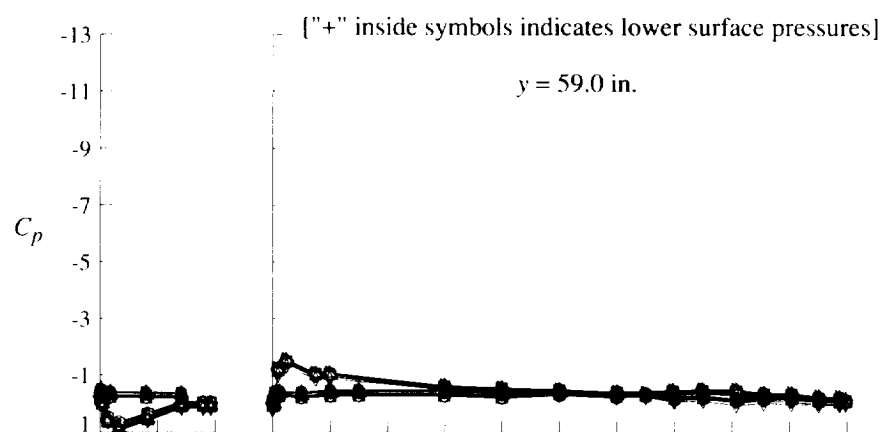


Figure 34. Effect of sideslip angle on pressure distributions for high-lift configuration at $\delta_f = 30^\circ$.

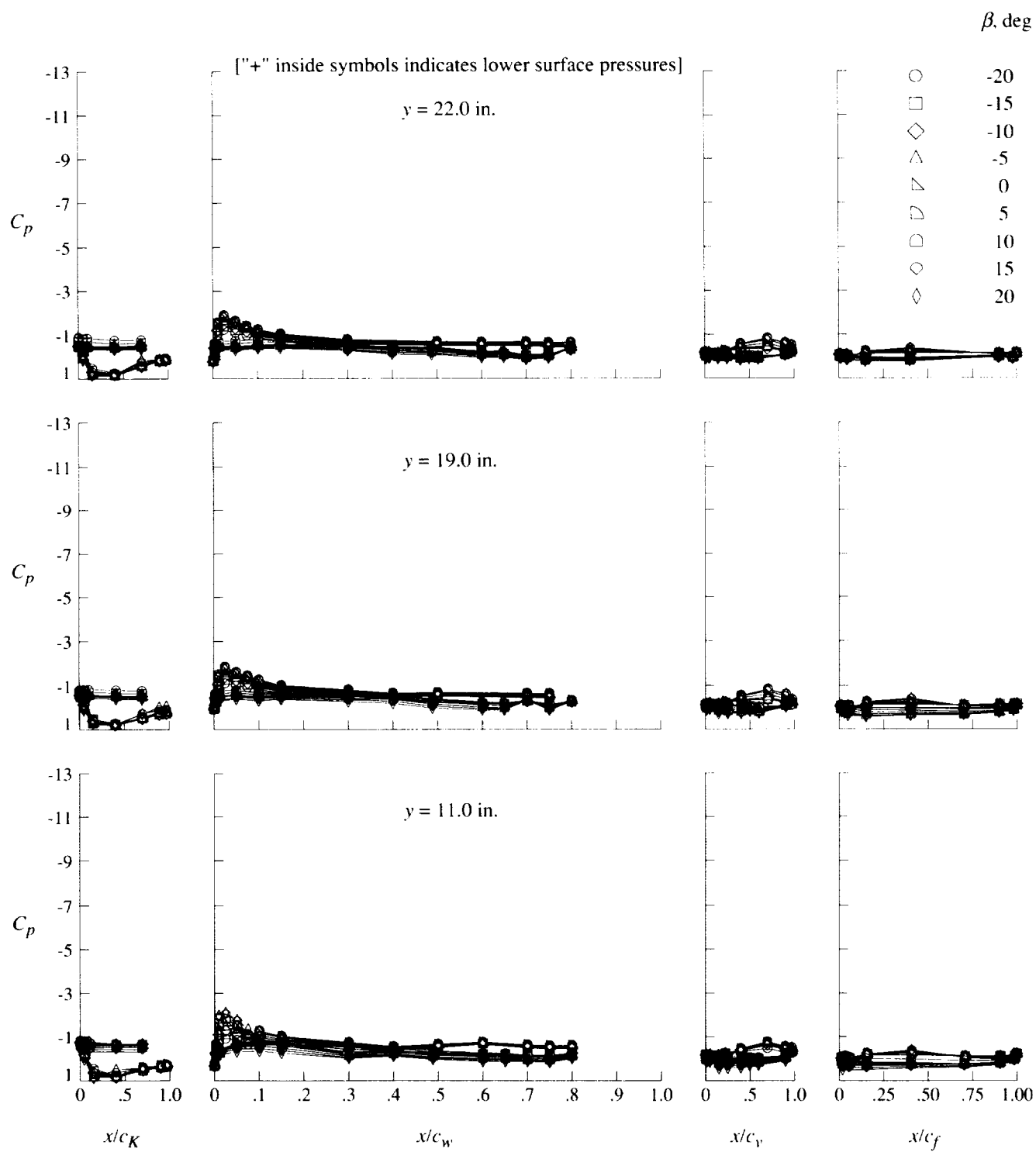
β , deg

- -20
- -15
- ◇ -10
- △ -5
- ▽ 0
- ▴ 5
- ◐ 10
- ◑ 15
- ◒ 20



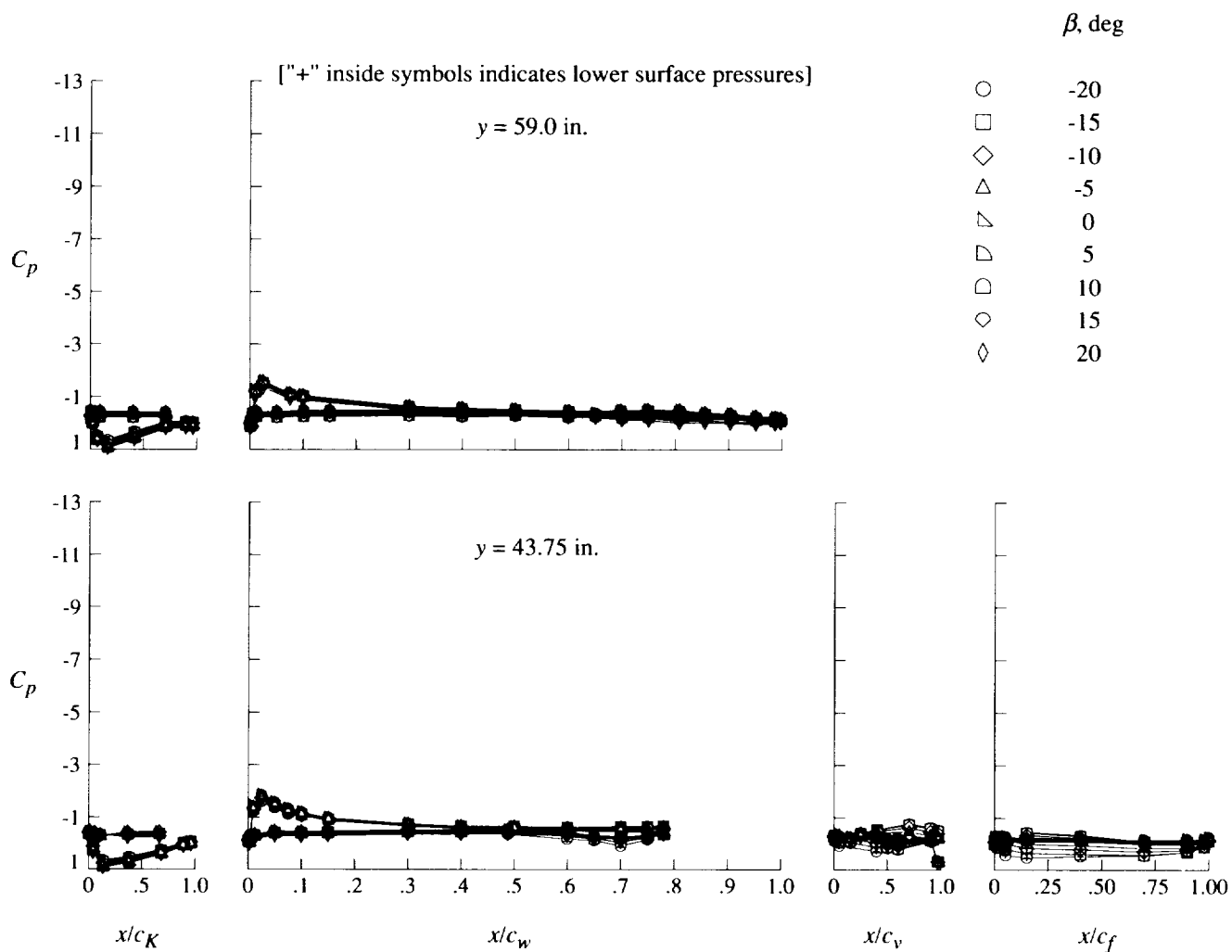
(a) Concluded.

Figure 34. Continued.



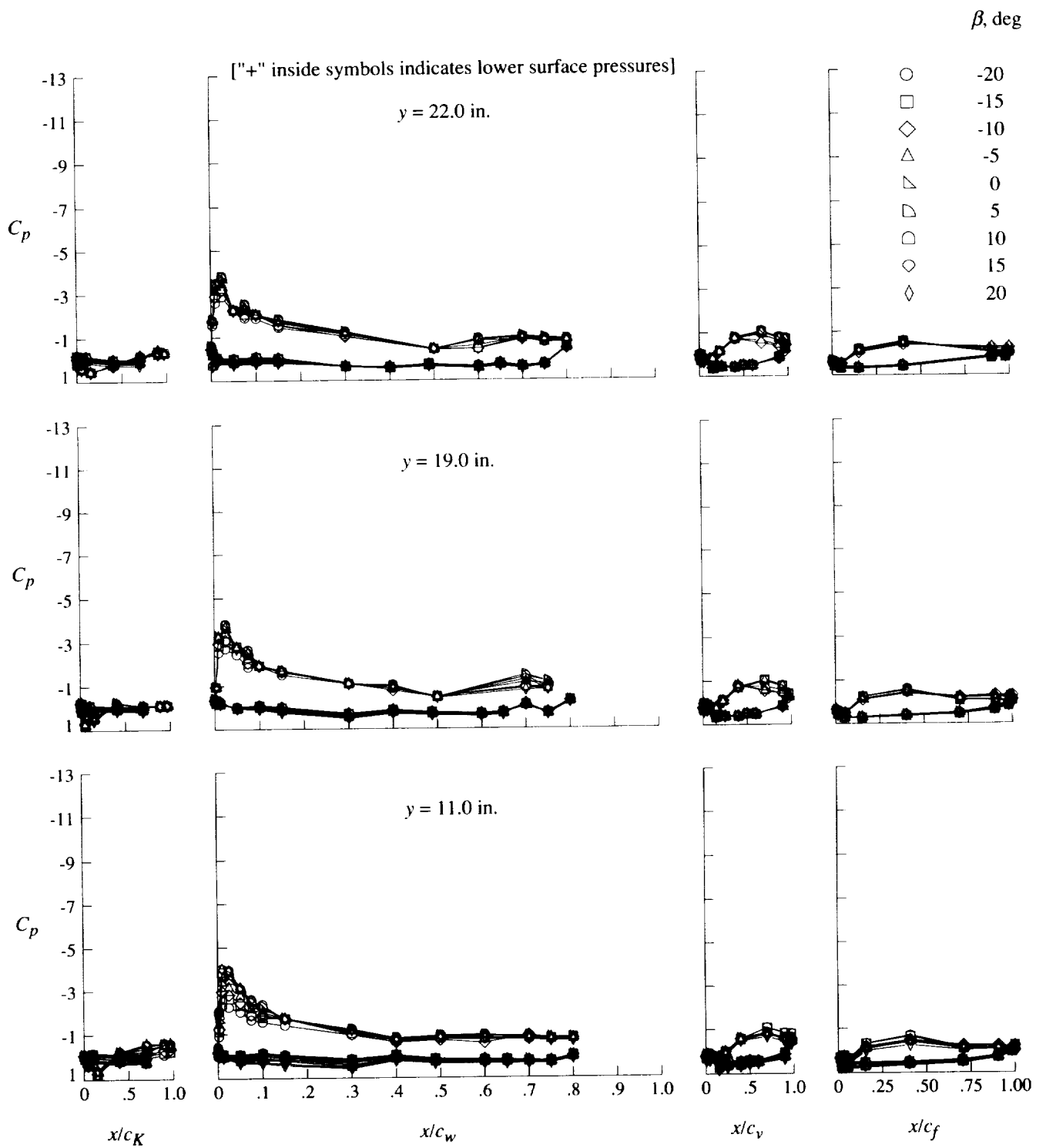
(b) $q = 40$ psf; $\alpha = 0^\circ$.

Figure 34. Continued.



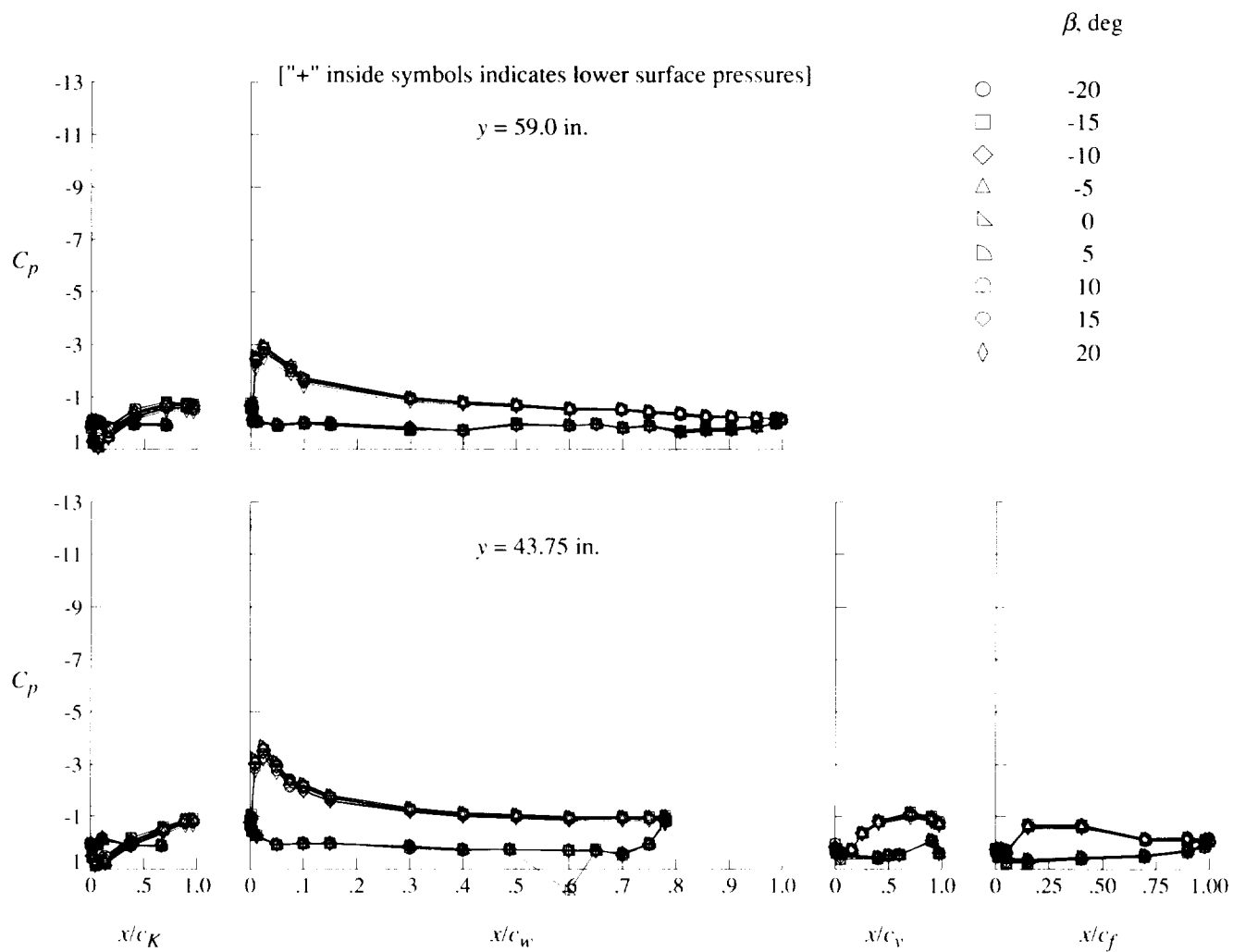
(b) Concluded.

Figure 34. Continued.



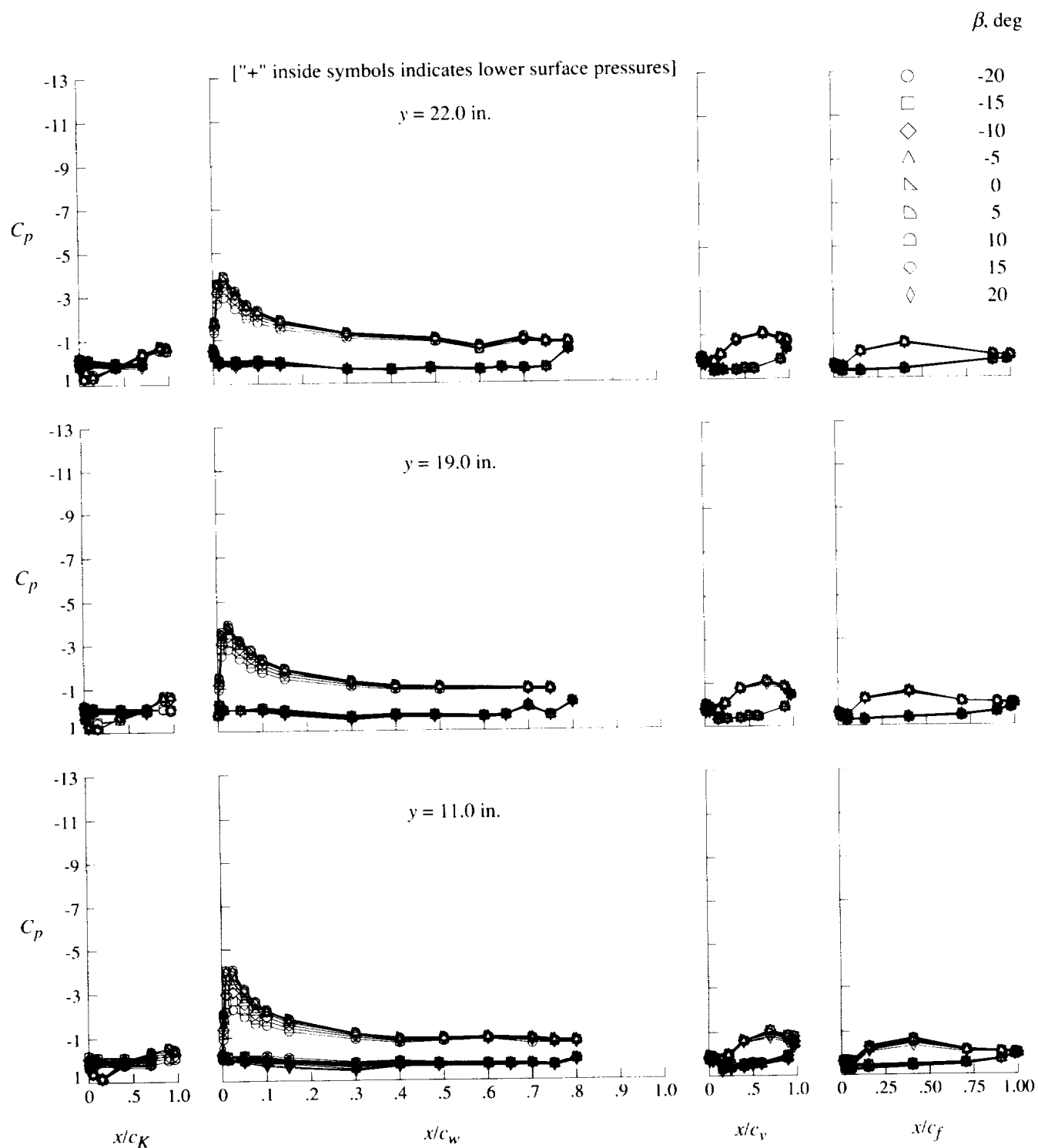
(c) $q = 20$ psf; $\alpha = 8^\circ$.

Figure 34. Continued.



(c) Concluded.

Figure 34. Continued.



(d) $q = 40$ psf; $\alpha = 8^\circ$.

Figure 34. Continued.

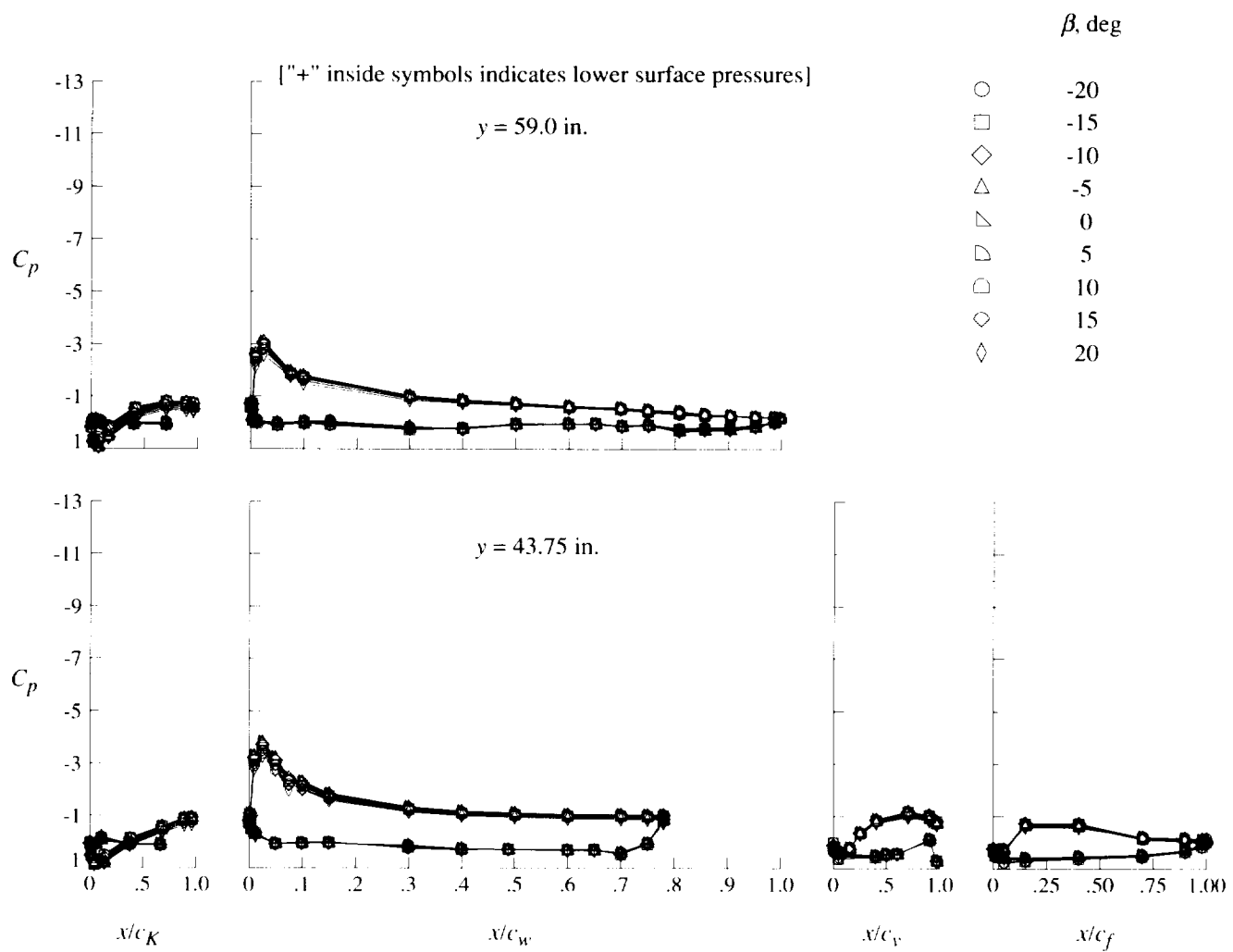
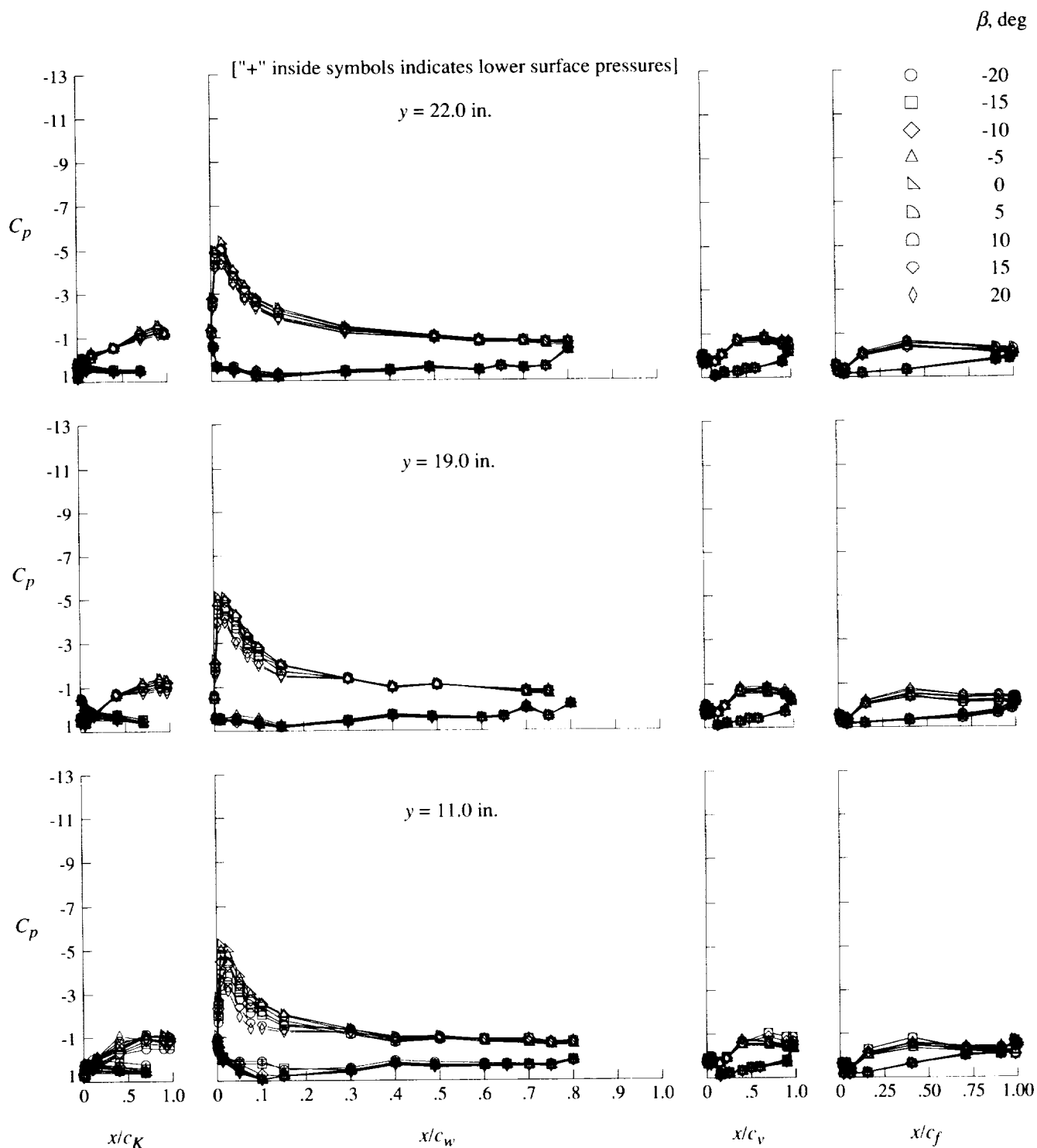


Figure 34. Continued.



(e) $q = 20$ psf; $\alpha = 16^\circ$.

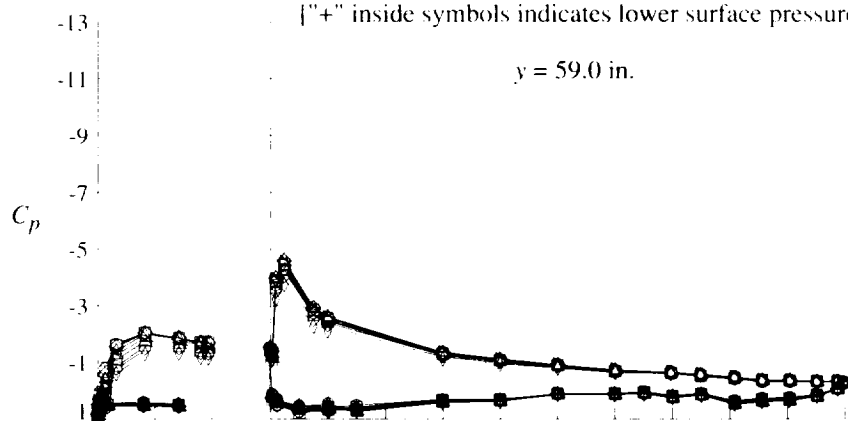
Figure 34. Continued.

β , deg

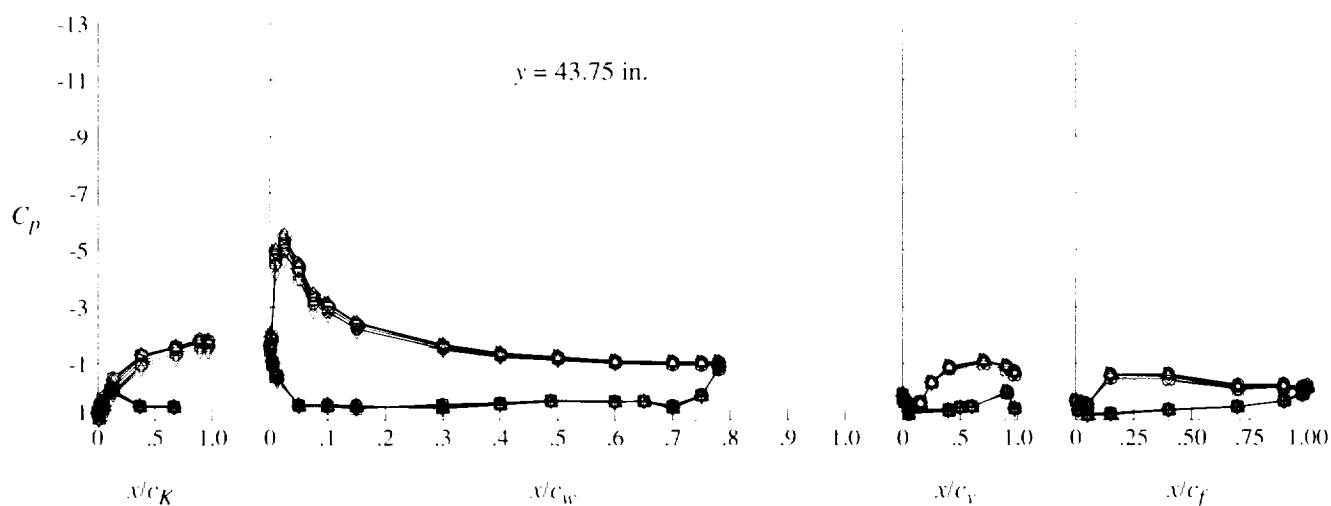
- \circ -20
- \square -15
- \diamond -10
- \triangle -5
- ∇ 0
- \square 5
- \triangle 10
- \diamond 15
- \circ 20

["+" inside symbols indicates lower surface pressures]

$y = 59.0$ in.

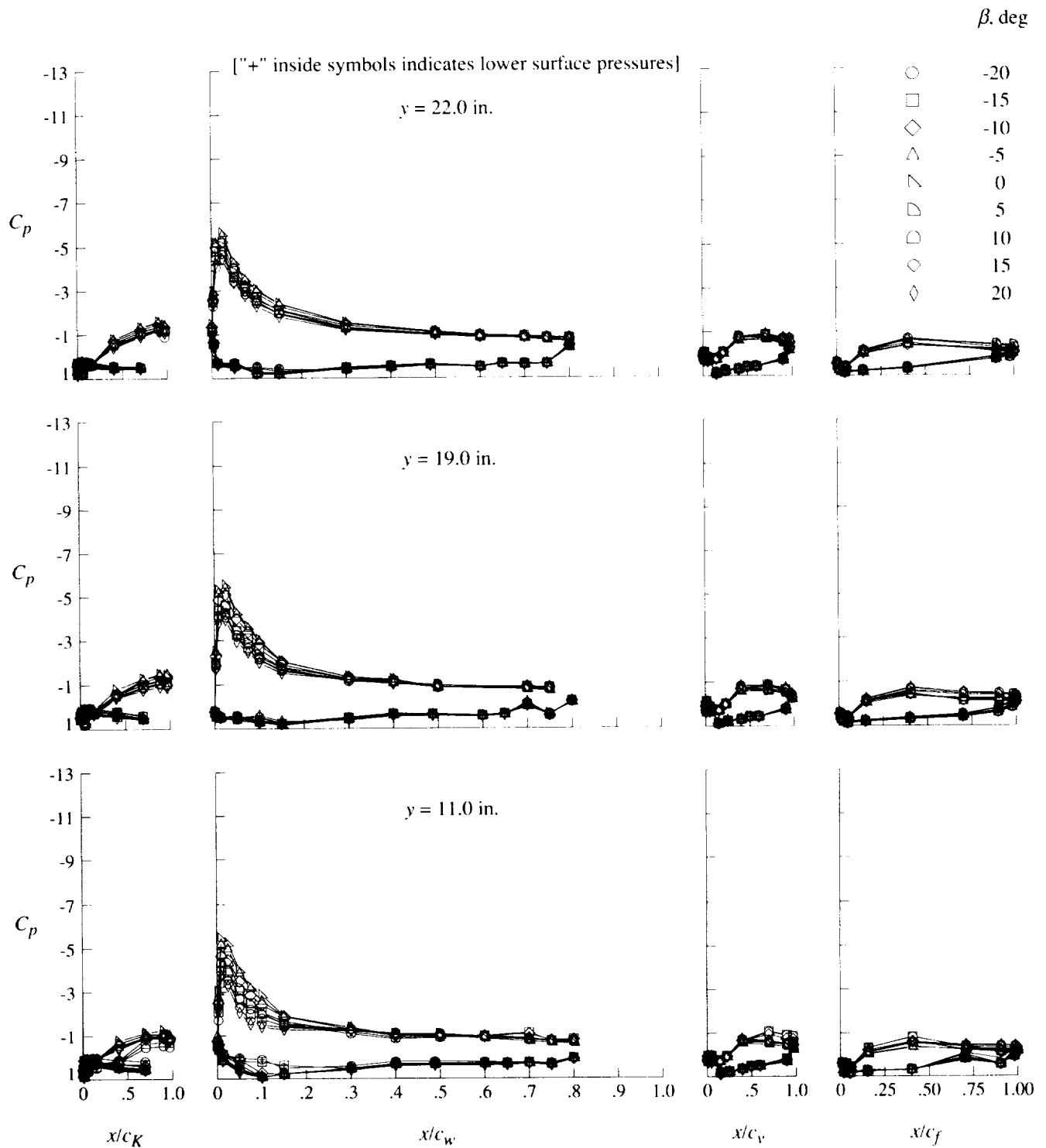


$y = 43.75$ in.



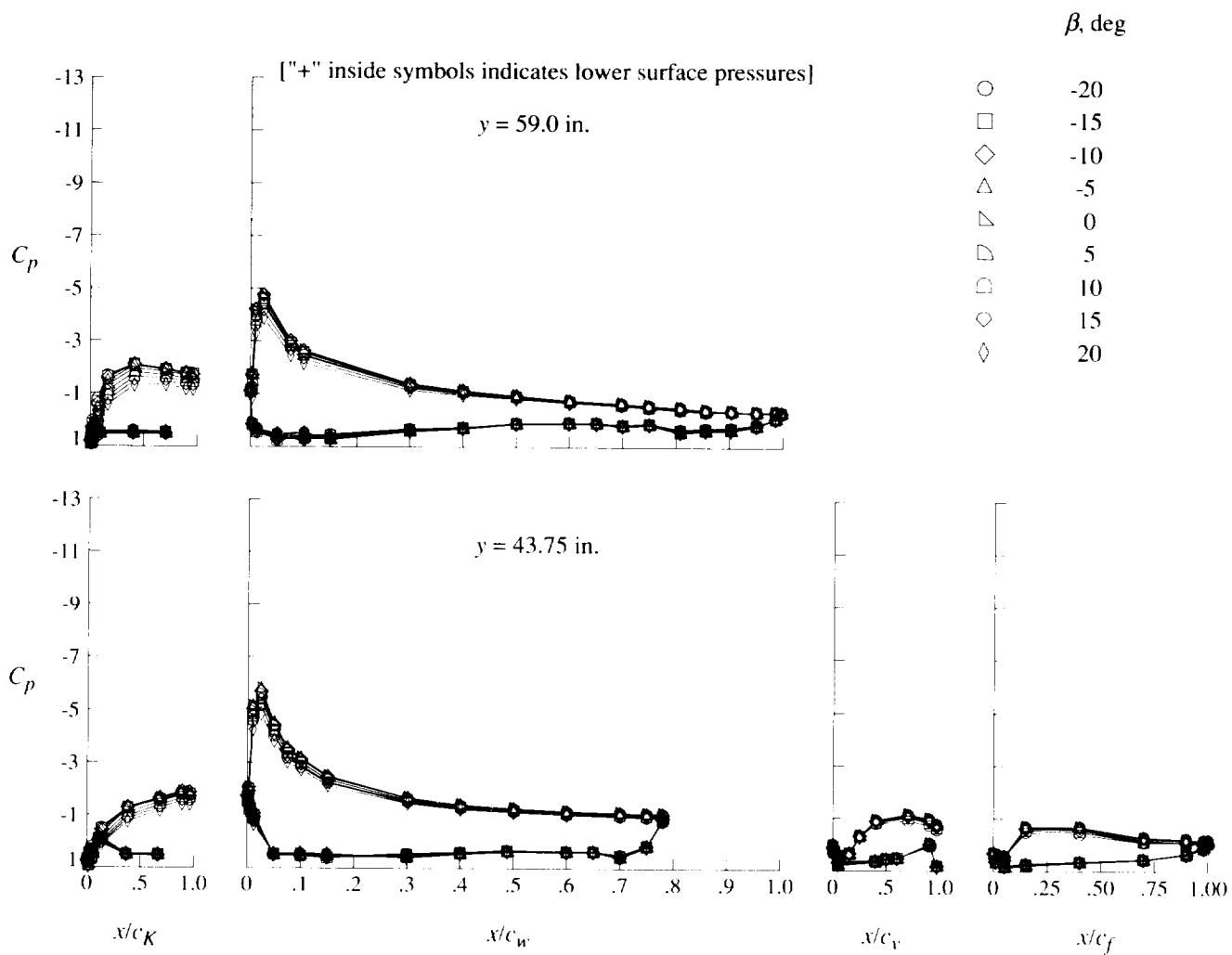
(e) Concluded.

Figure 34. Continued.



(f) $q = 40$ psf; $\alpha = 16^\circ$.

Figure 34. Continued.



(f) Concluded.

Figure 34. Concluded.

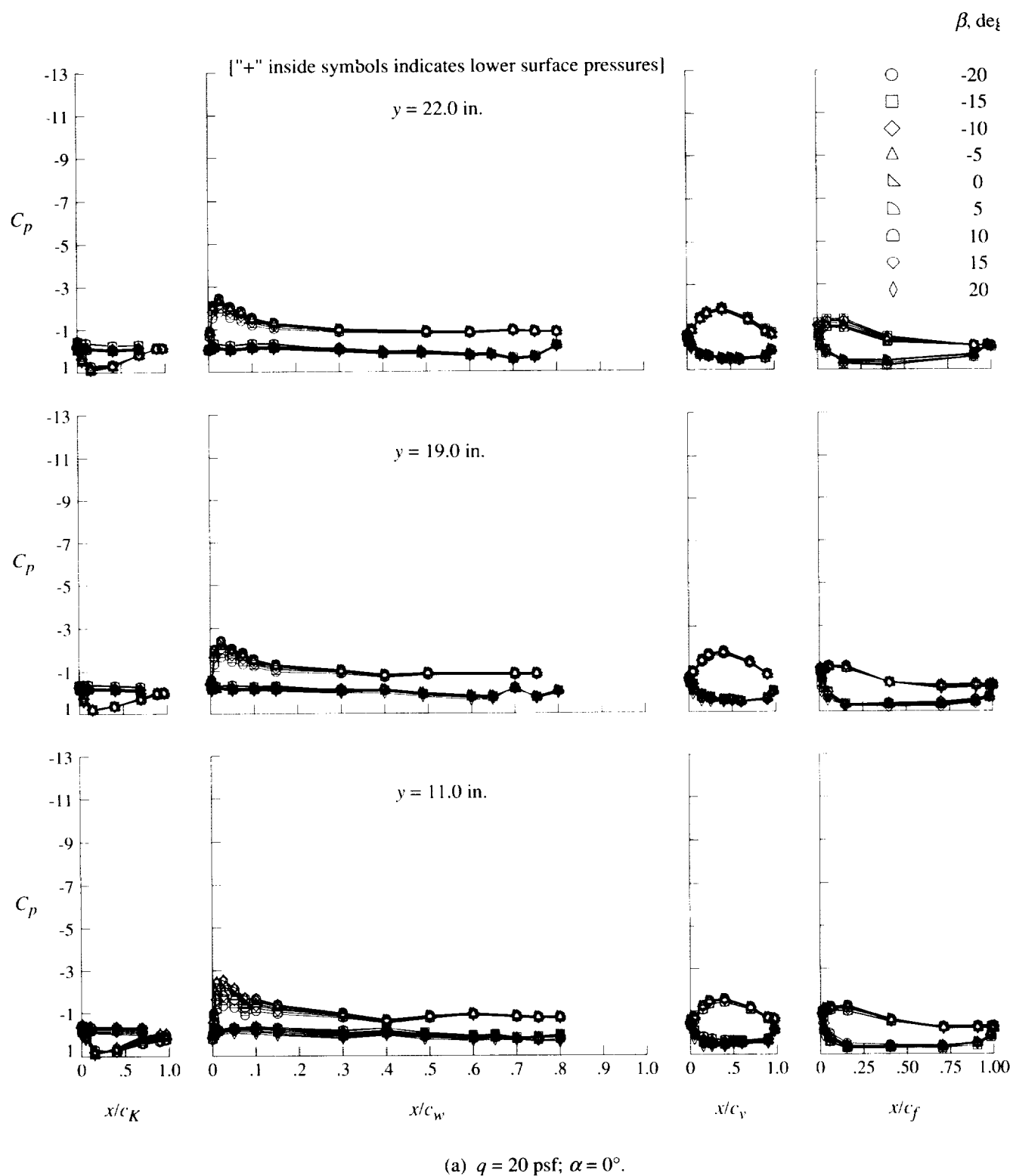
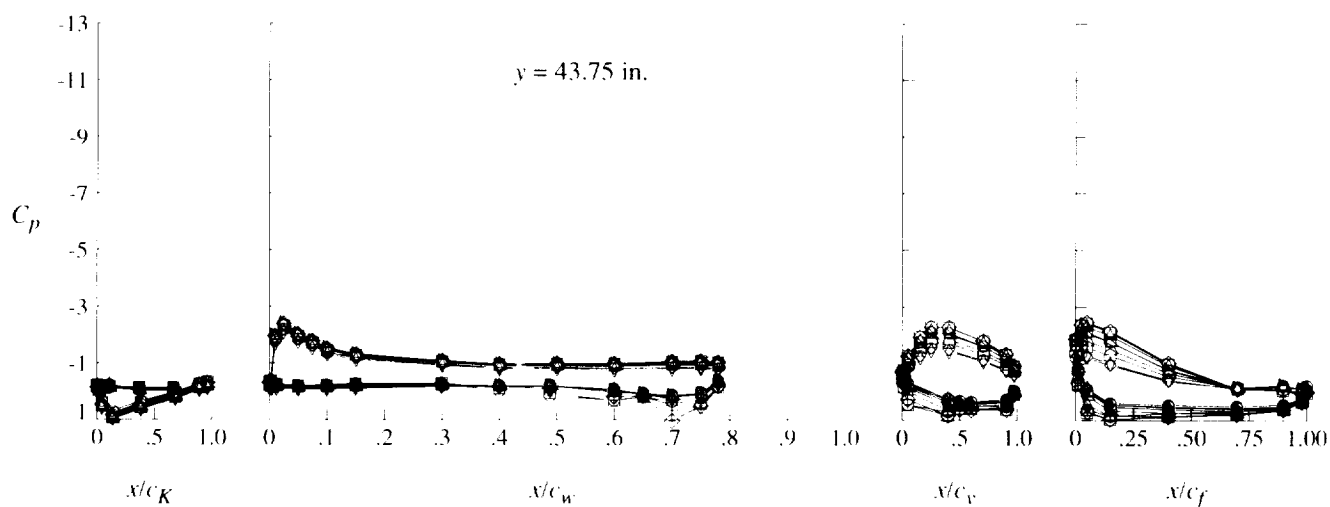
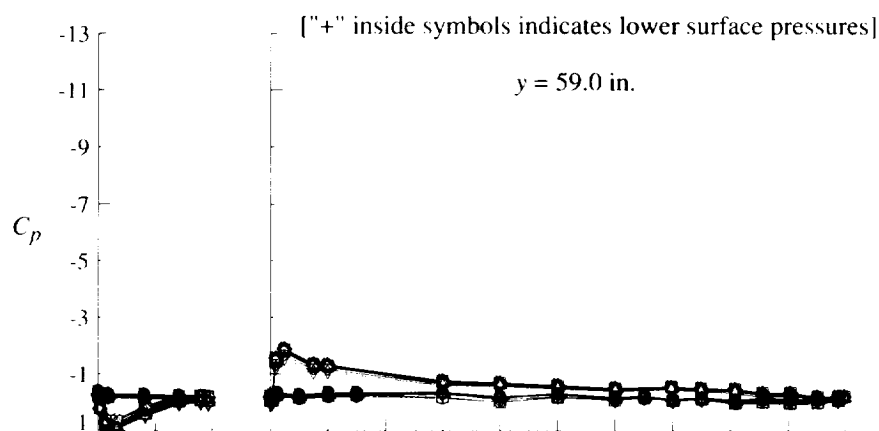


Figure 35. Effect of sideslip angle on pressure distributions for high-lift configuration at $\delta_f = 60^\circ$.

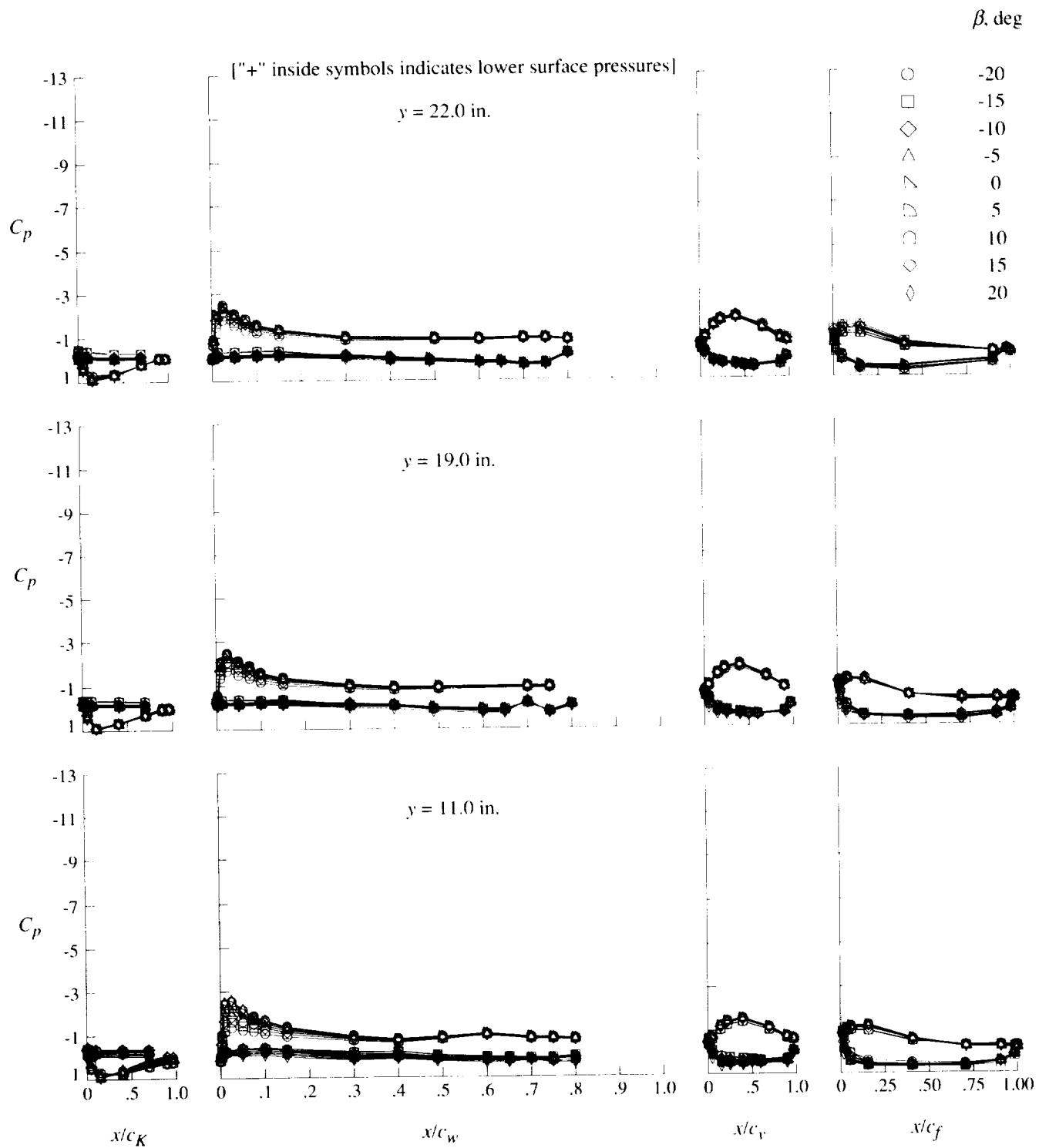
β , deg

- -20
- -15
- ◇ -10
- △ -5
- ▽ 0
- ◁ 5
- ◊ 10
- ◈ 15
- ◉ 20



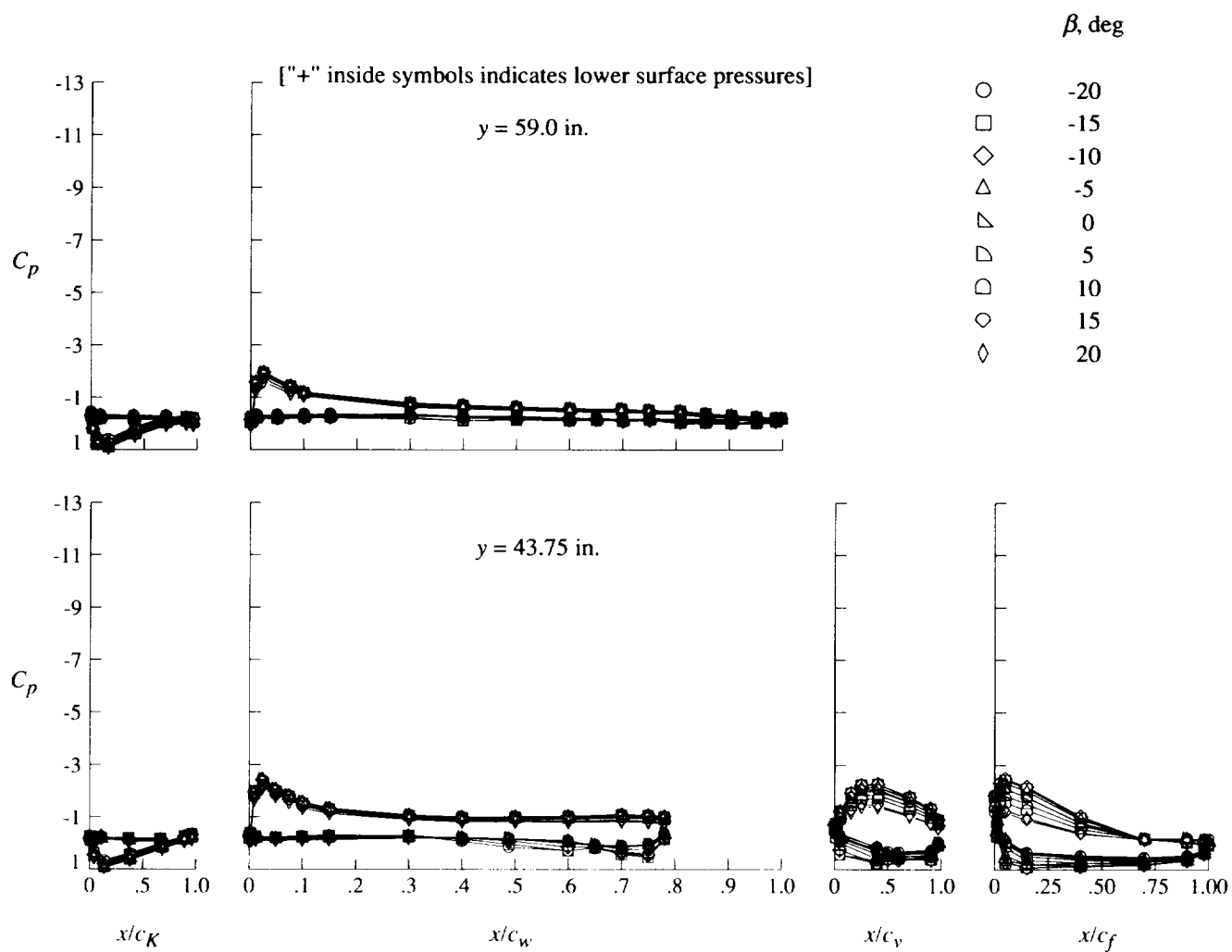
(a) Concluded.

Figure 35. Continued.



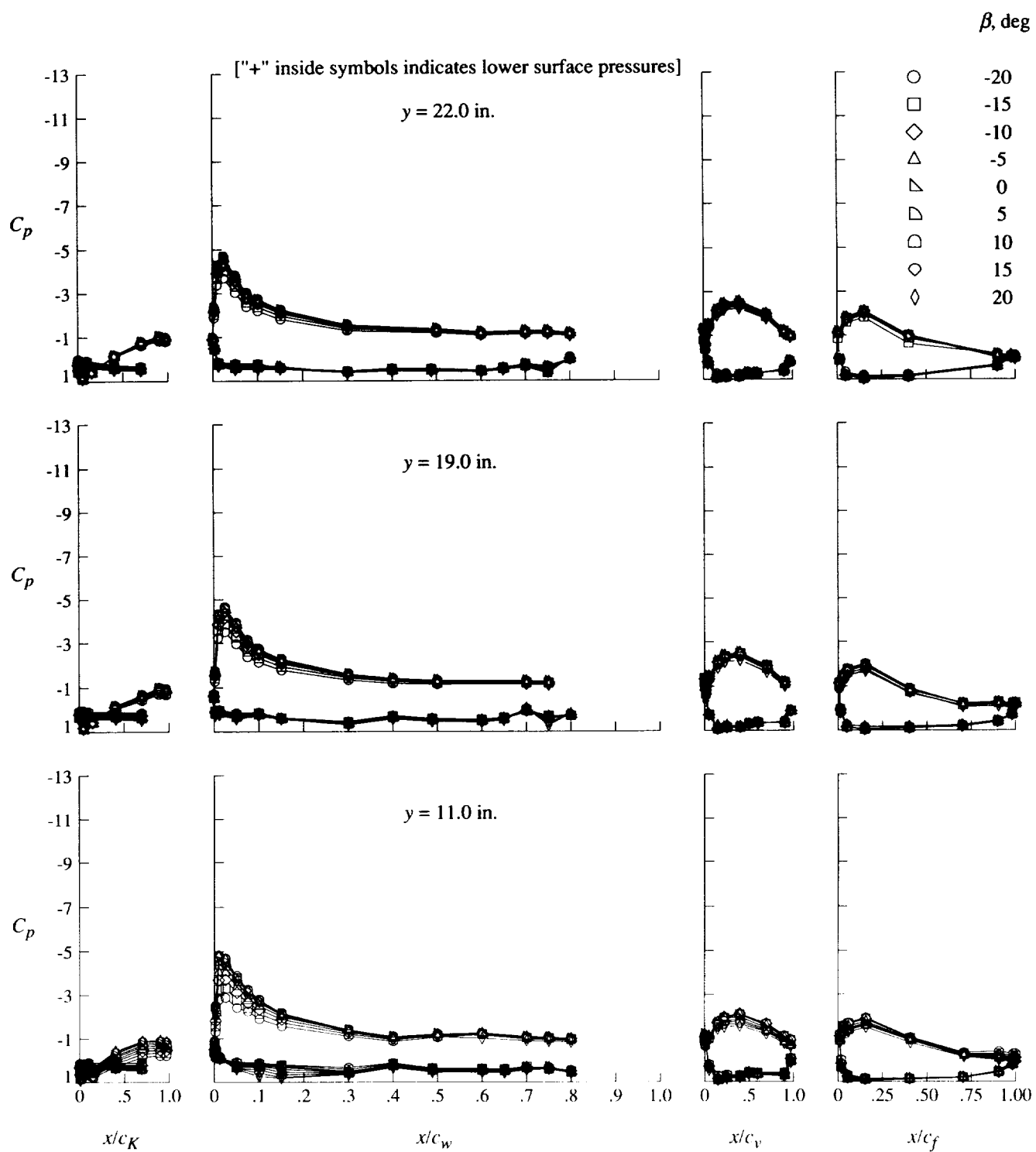
(b) $q = 40$ psf; $\alpha = 0^\circ$.

Figure 35. Continued.



(b) Concluded.

Figure 35. Continued.

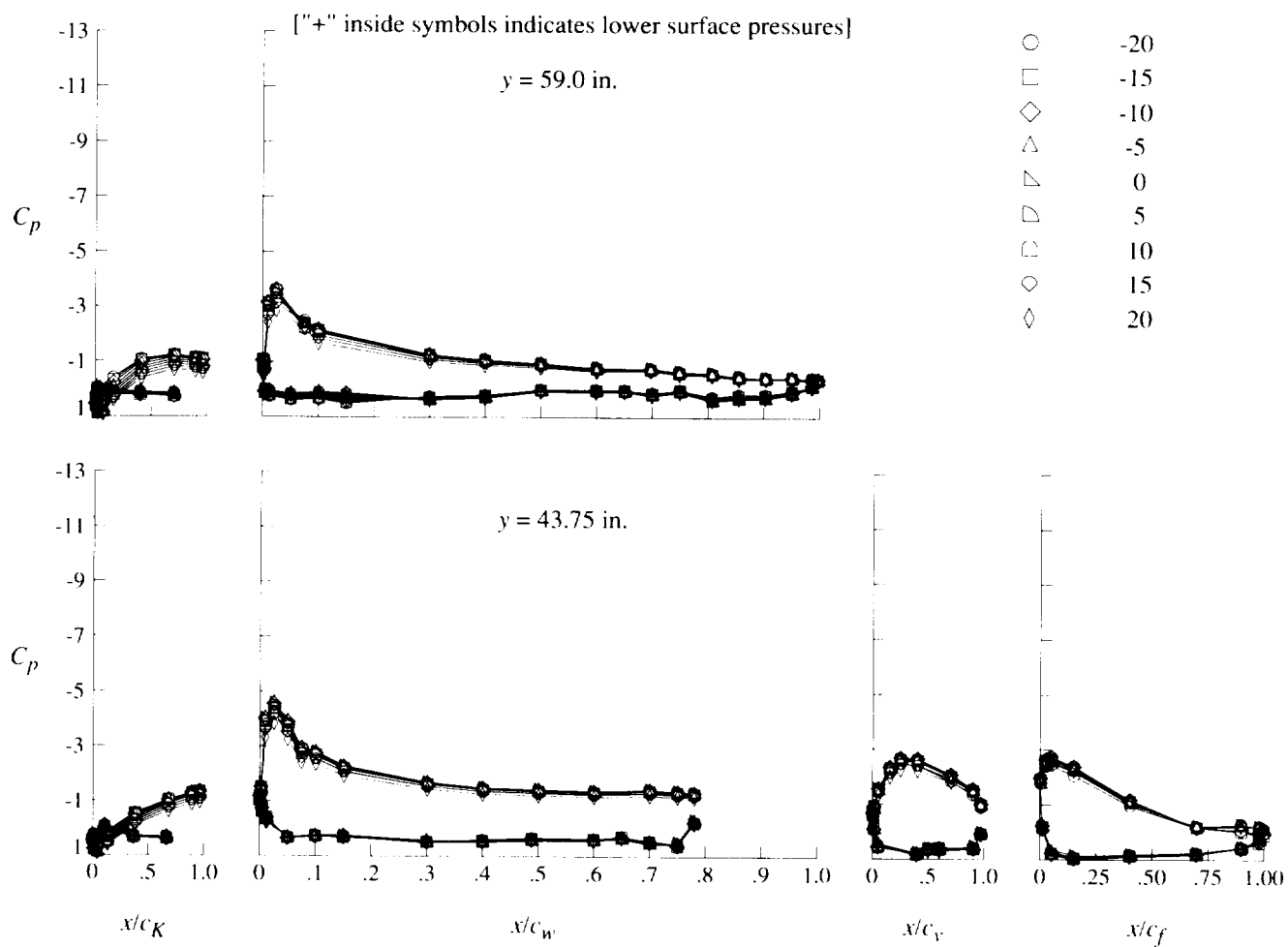


(c) $q = 20$ psf; $\alpha = 8^\circ$.

Figure 35. Continued.

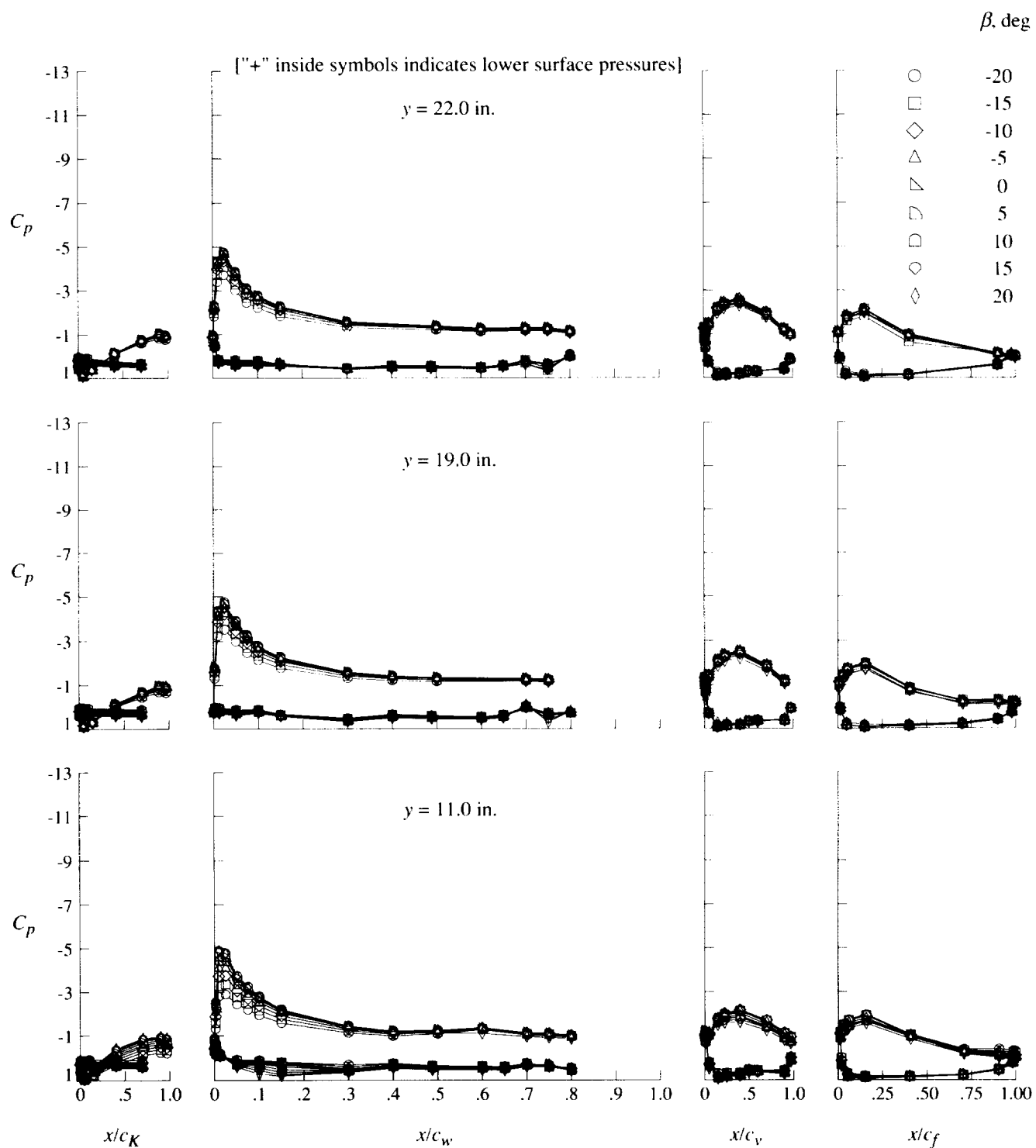
β , deg

- -20
- -15
- ◇ -10
- △ -5
- ▽ 0
- ◐ 5
- ◑ 10
- ◒ 15
- ◓ 20



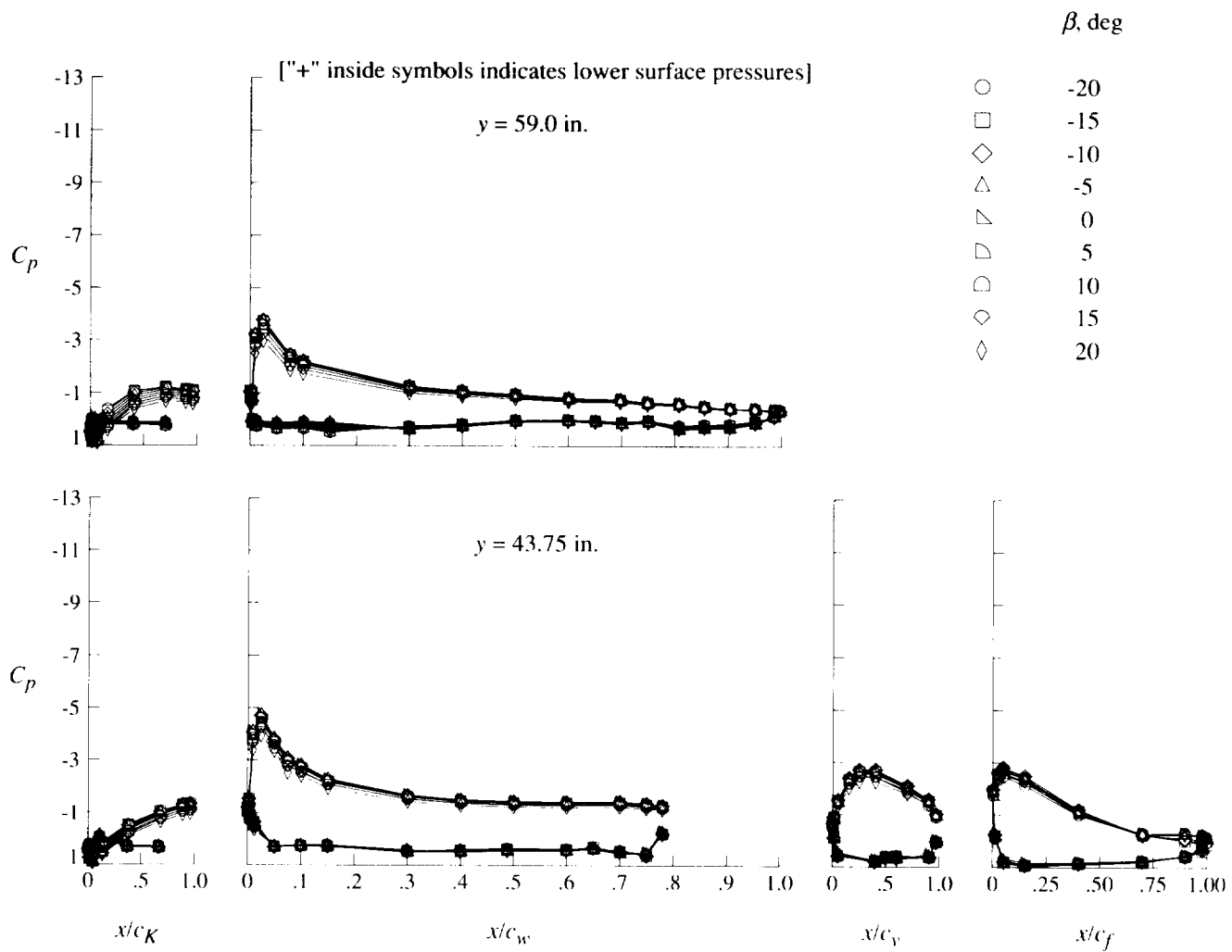
(c) Concluded.

Figure 35. Continued.



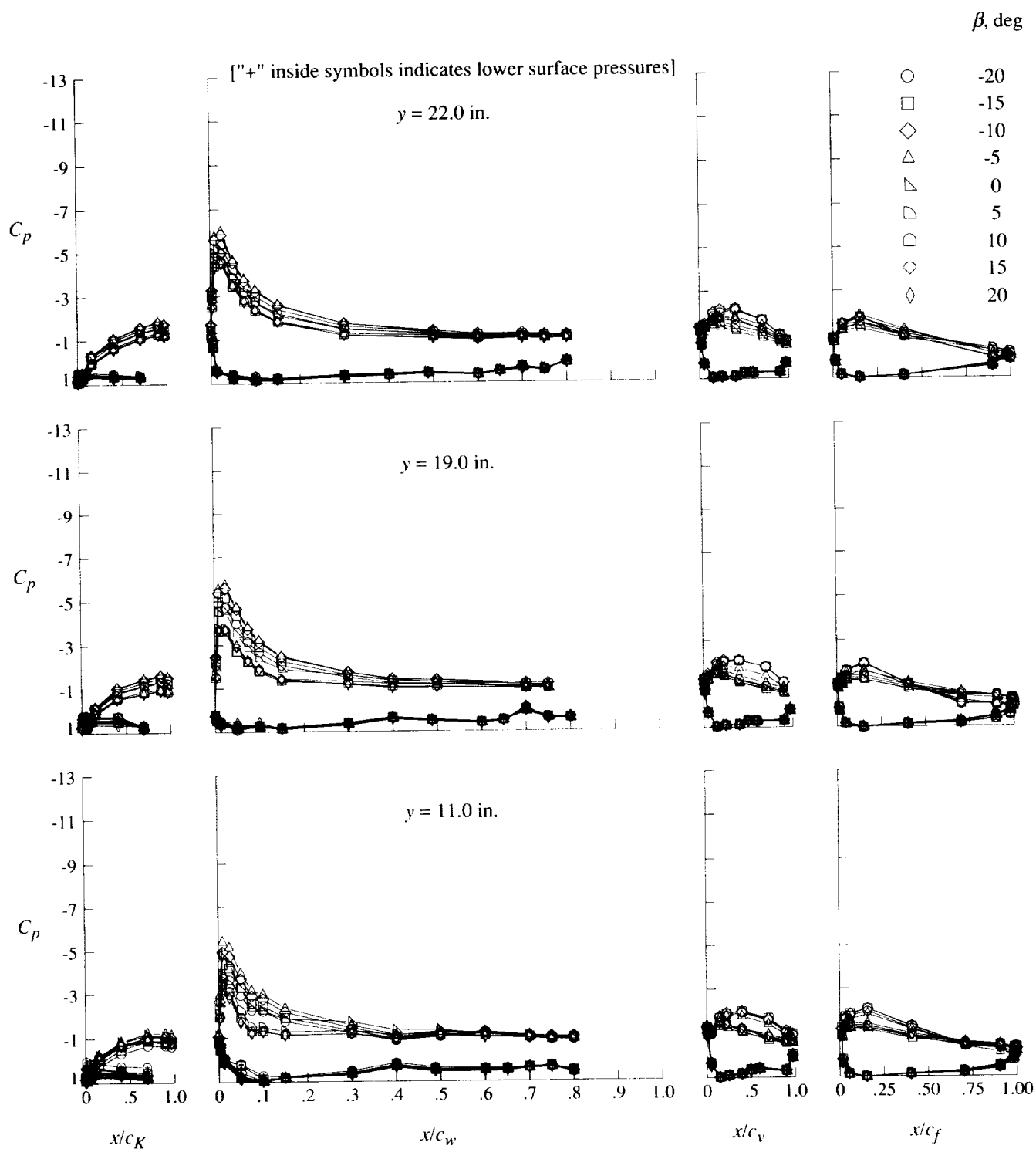
(d) $q = 40$ psf; $\alpha = 8^\circ$.

Figure 35. Continued.



(d) Concluded.

Figure 35. Continued.

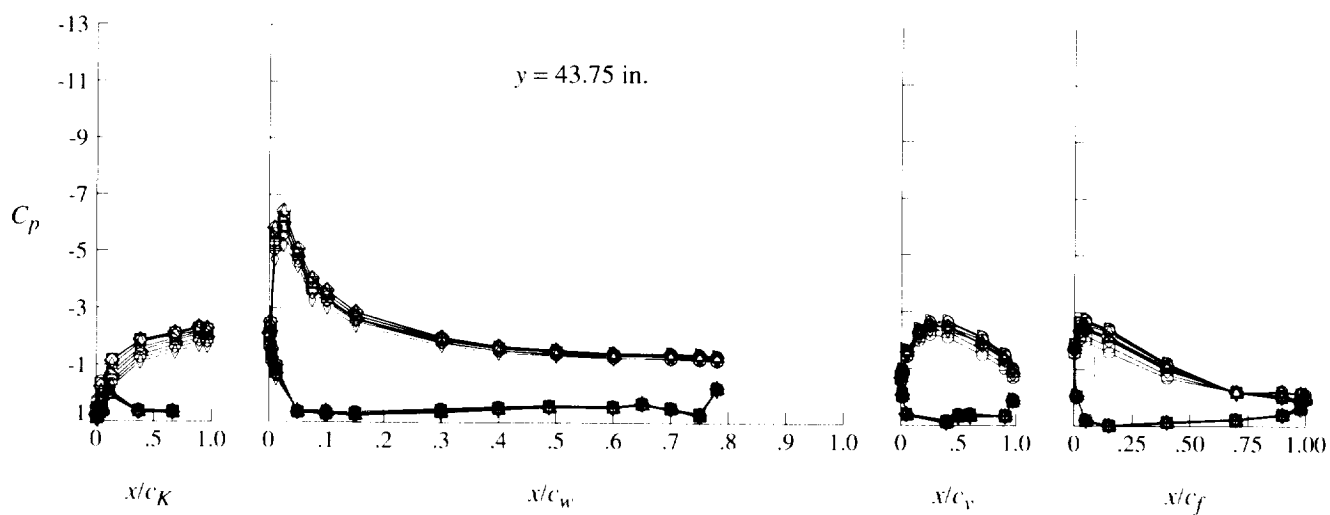
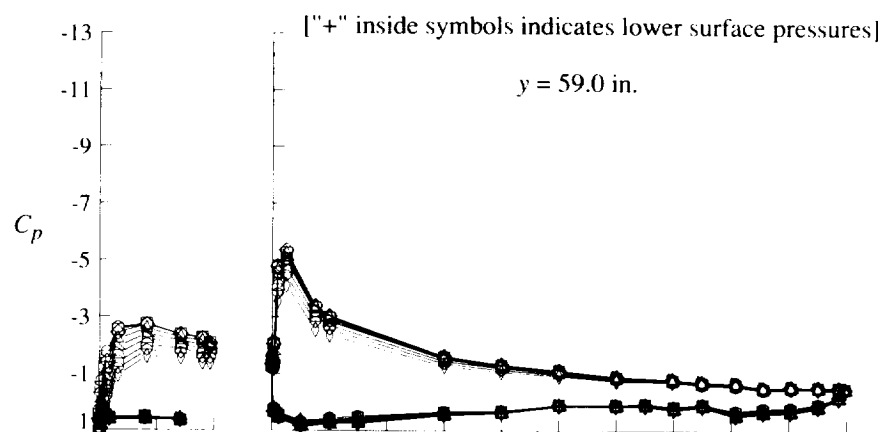


(e) $q = 20$ psf; $\alpha = 16^\circ$.

Figure 35. Continued.

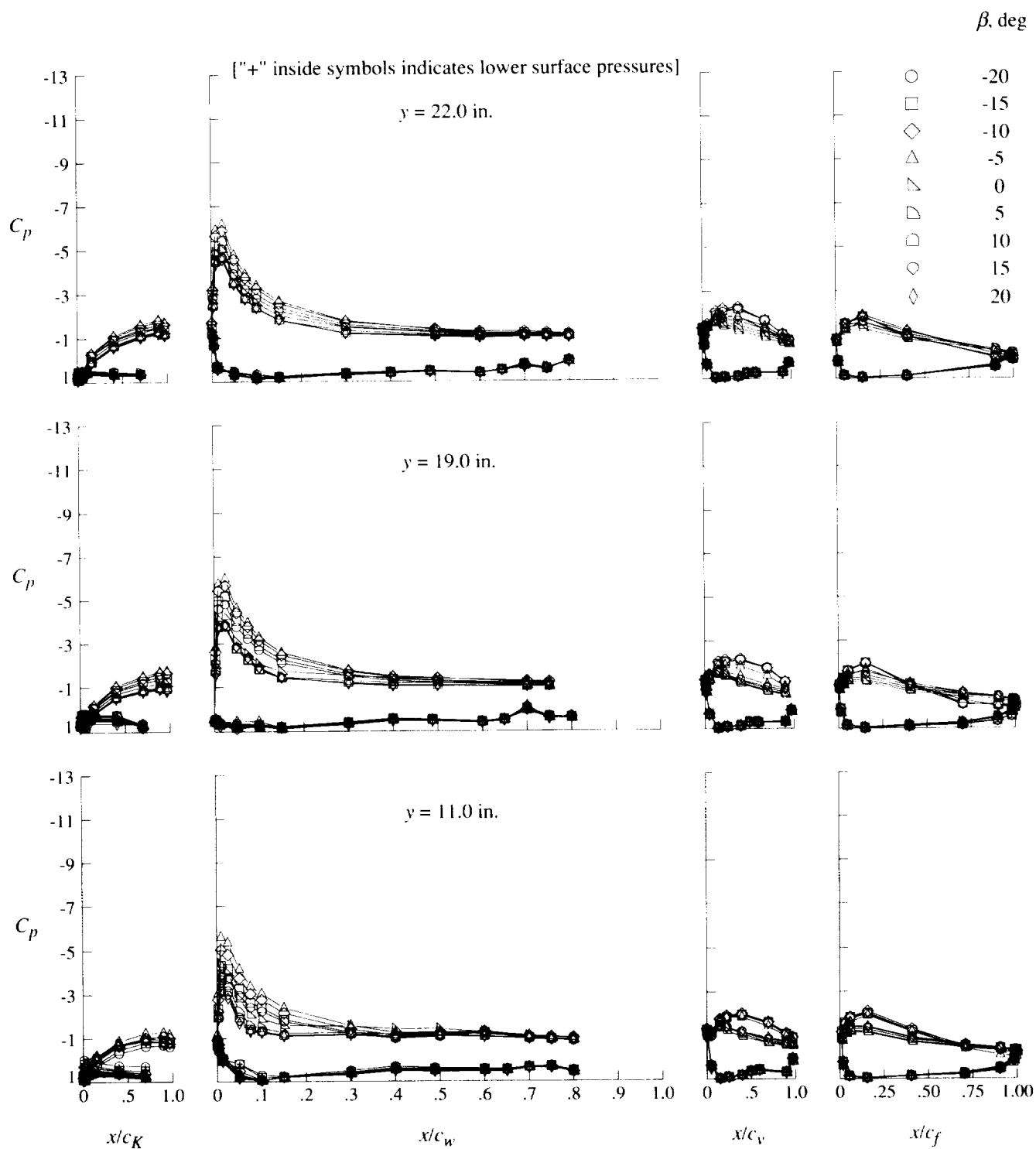
β , deg

- -20
- -15
- ◇ -10
- △ -5
- ▽ 0
- ◐ 5
- ◑ 10
- ◒ 15
- ◓ 20



(e) Concluded.

Figure 35. Continued.

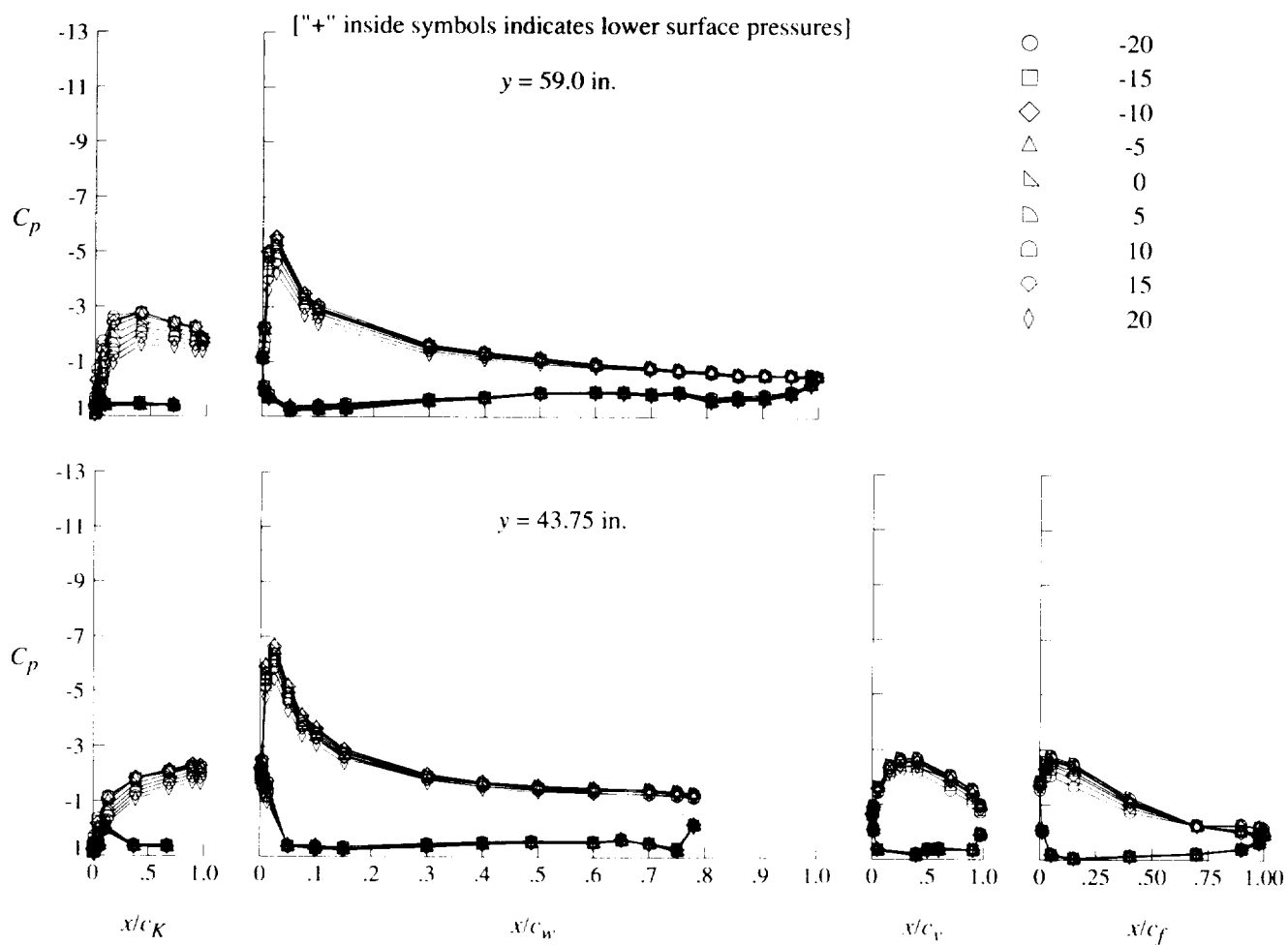


(f) $q = 40$ psf; $\alpha = 16^\circ$.

Figure 35. Continued.

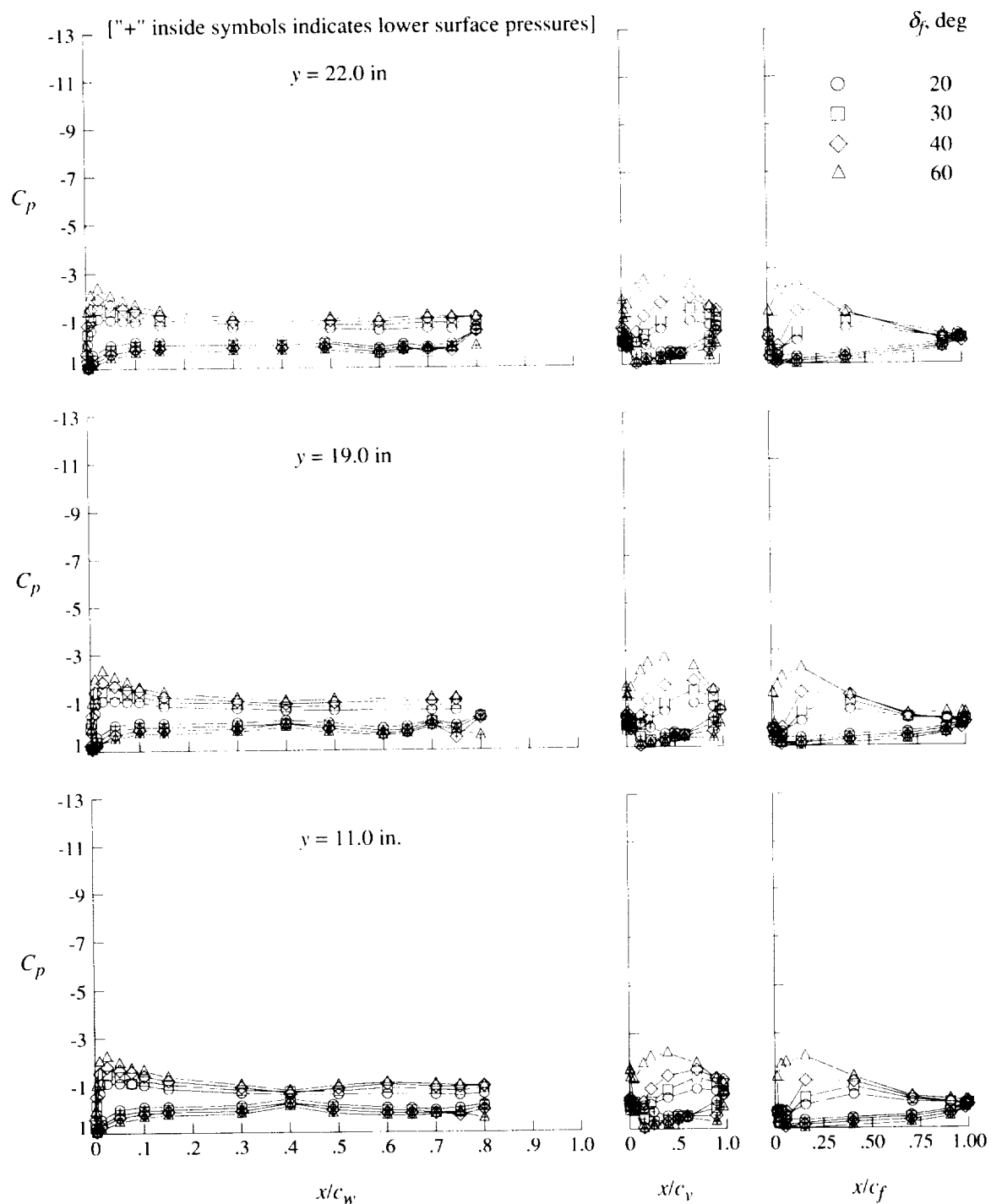
β , deg

- -20
- -15
- ◇ -10
- △ -5
- ▽ 0
- ◐ 5
- ◑ 10
- ◒ 15
- ◓ 20



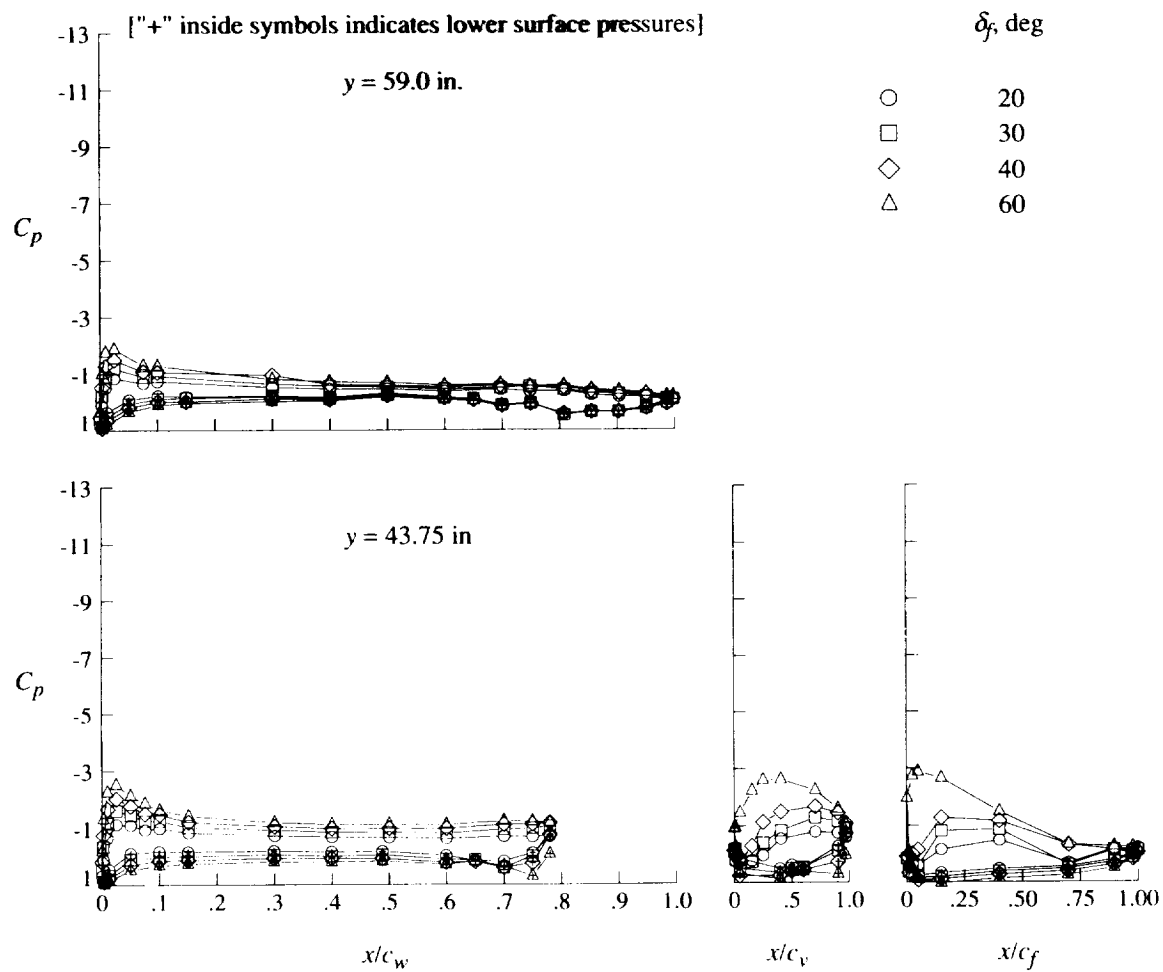
(f) Concluded.

Figure 35. Concluded.



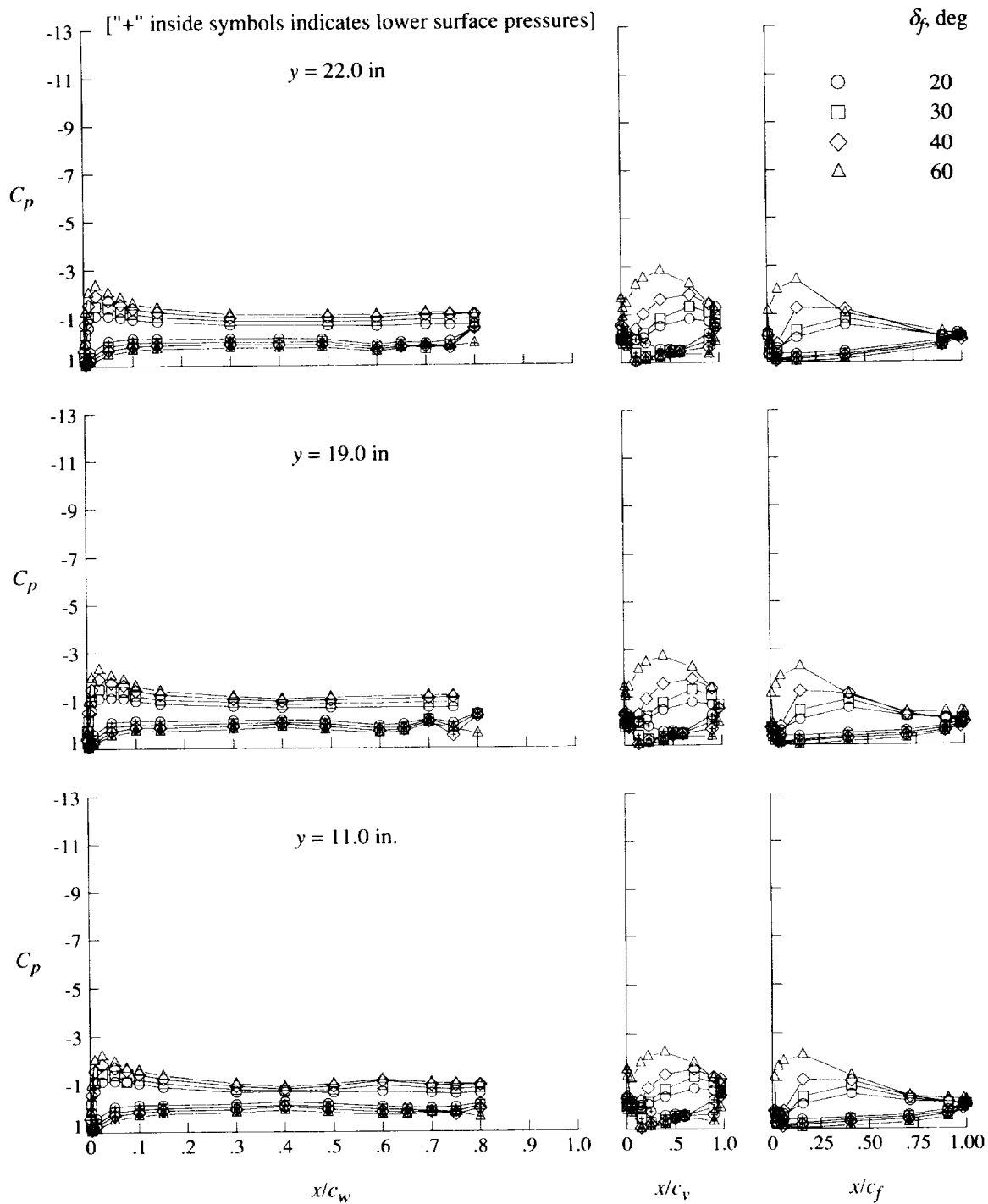
(a) $q = 20$ psf; $\alpha = 0^\circ$.

Figure 36. Effect of angle of attack on pressure distributions for flaps-only configuration.



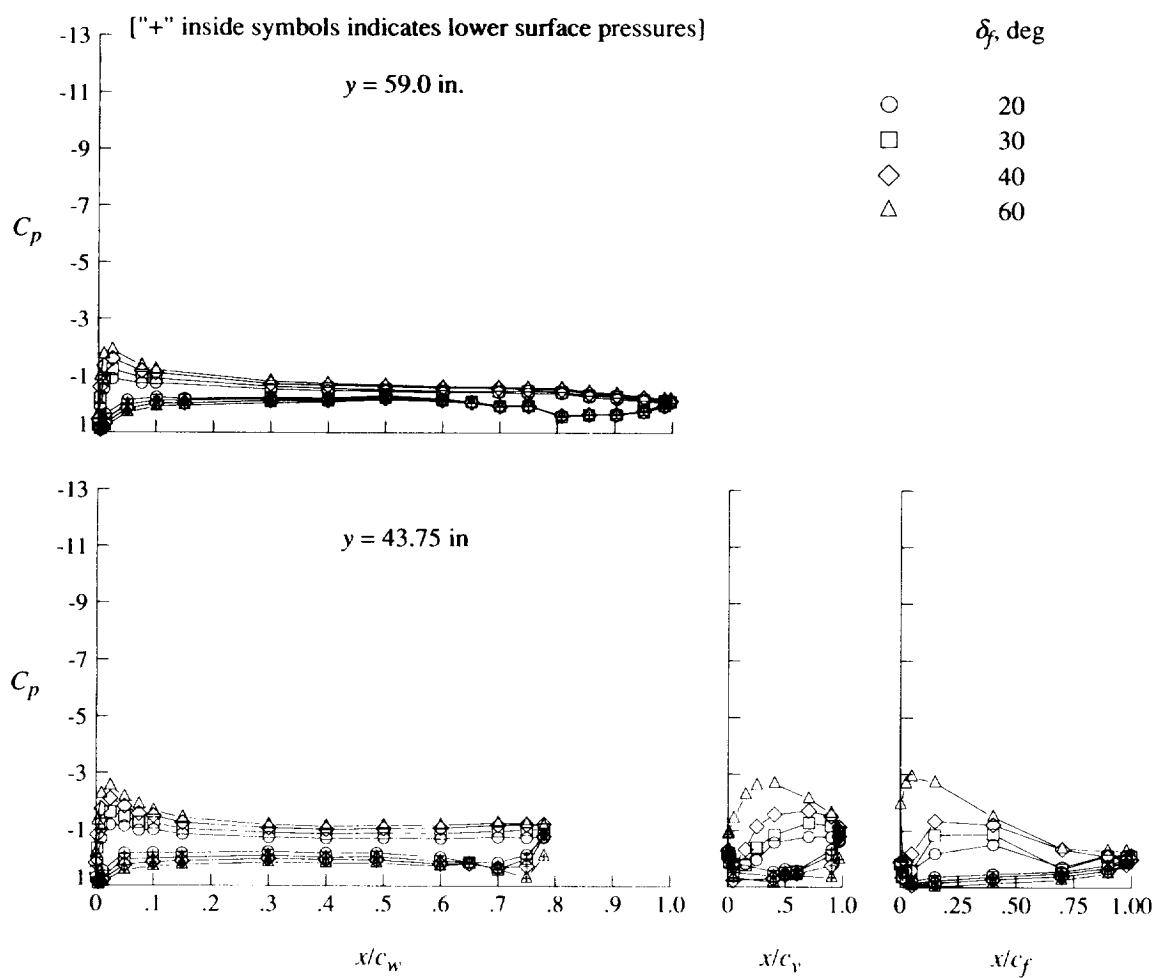
(a) Concluded.

Figure 36. Continued.



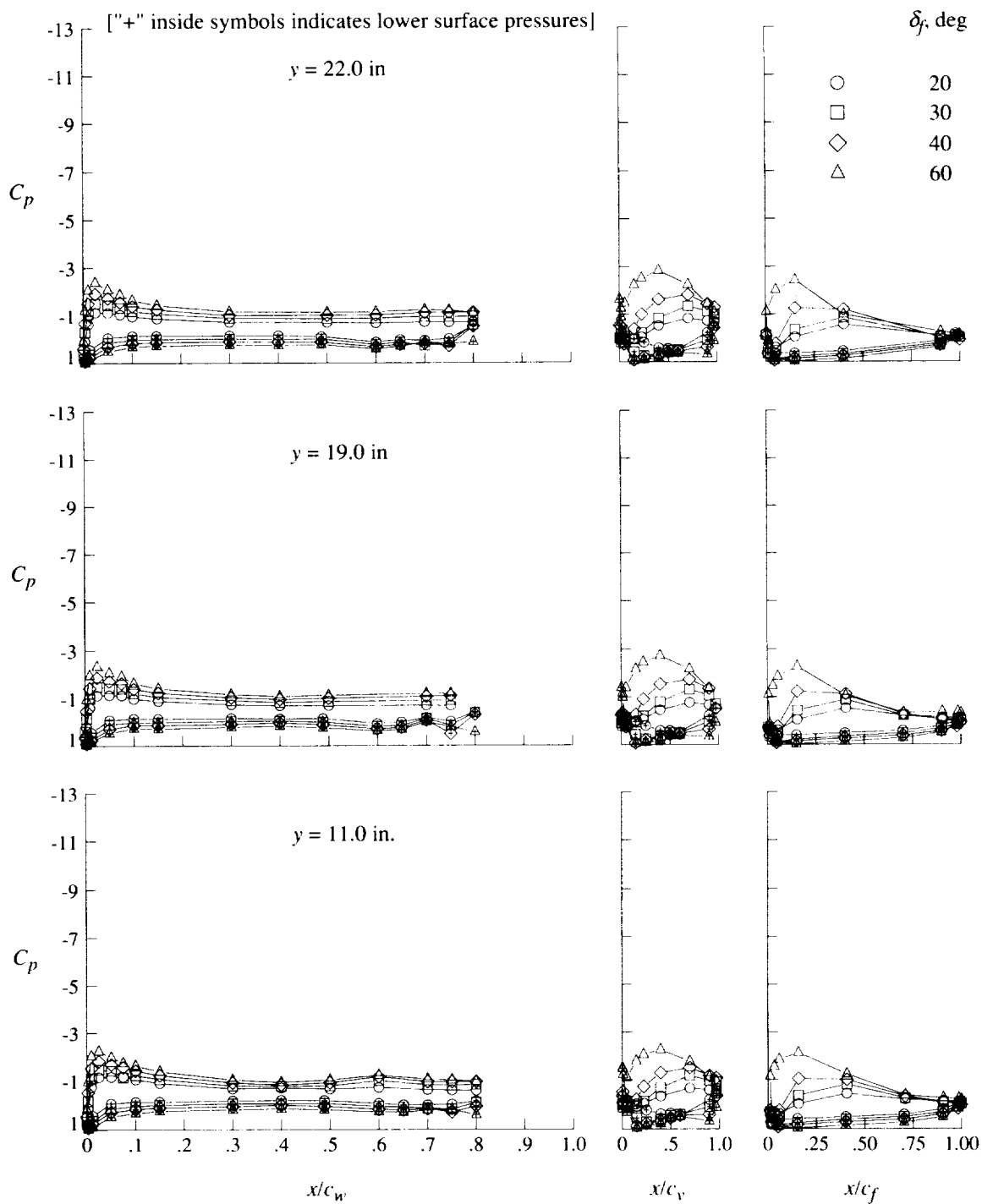
(b) $q = 40$ psf; $\alpha = 0^\circ$.

Figure 36. Continued.



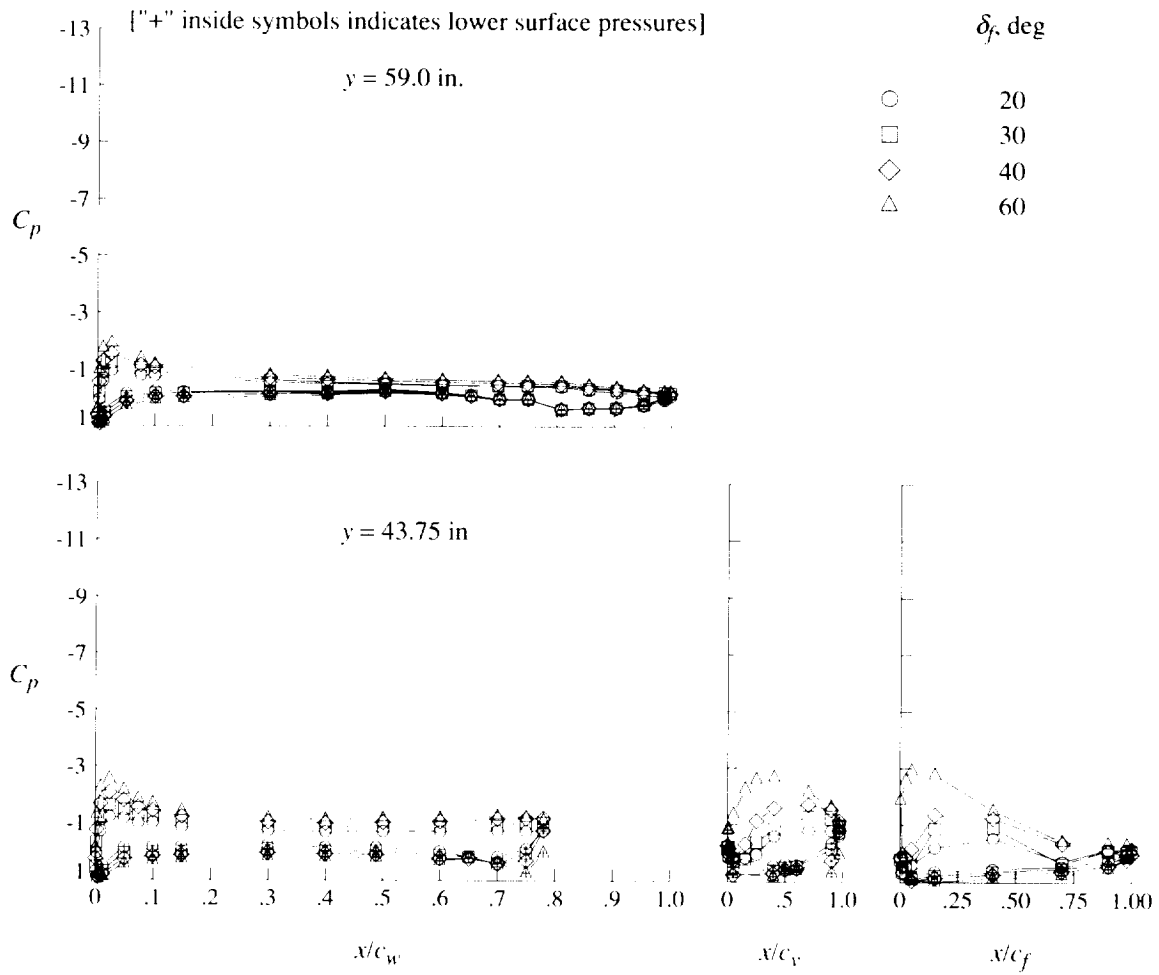
(b) Concluded.

Figure 36. Continued.



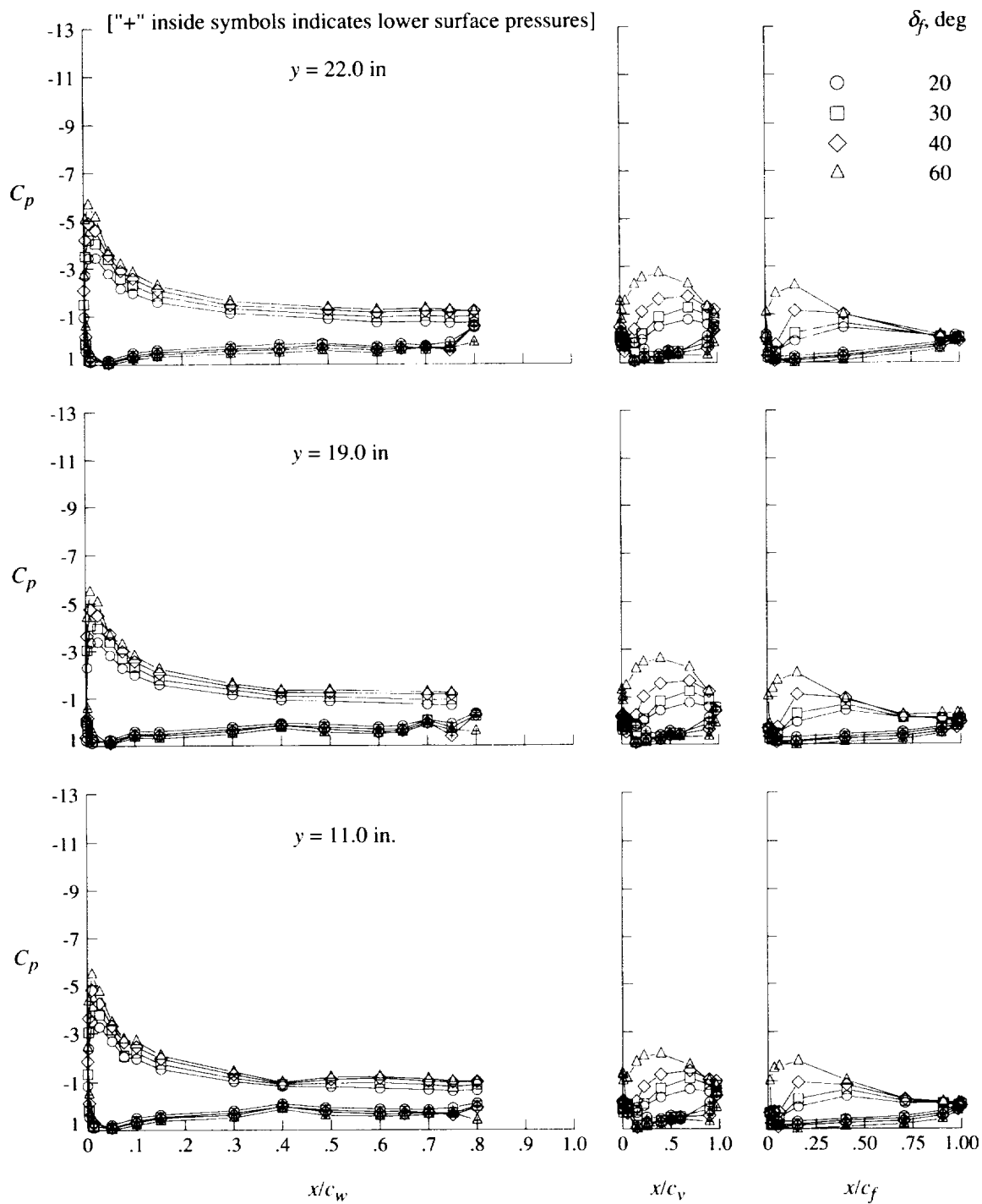
(c) $q = 60$ psf; $\alpha = 0^\circ$.

Figure 36. Continued.



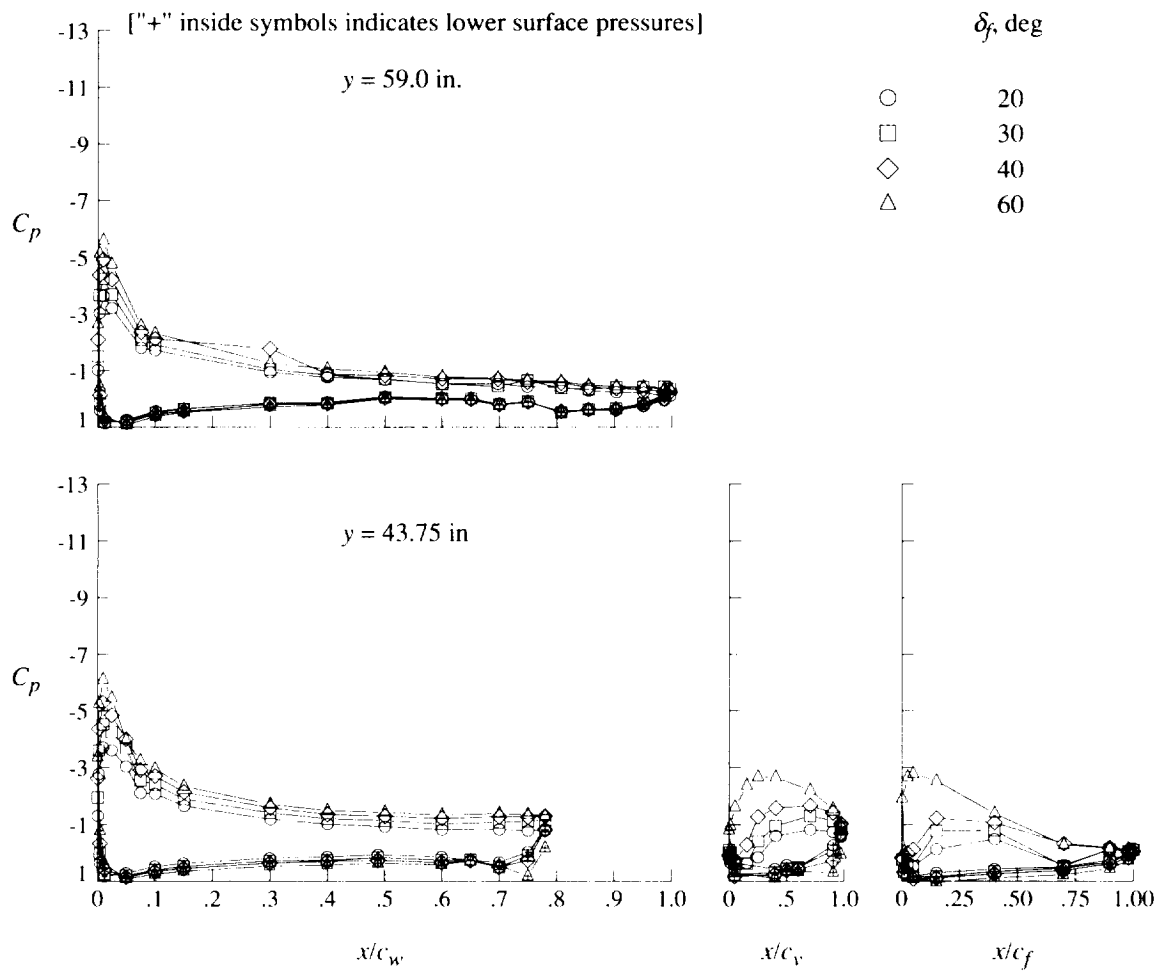
(c) Concluded.

Figure 36. Continued.



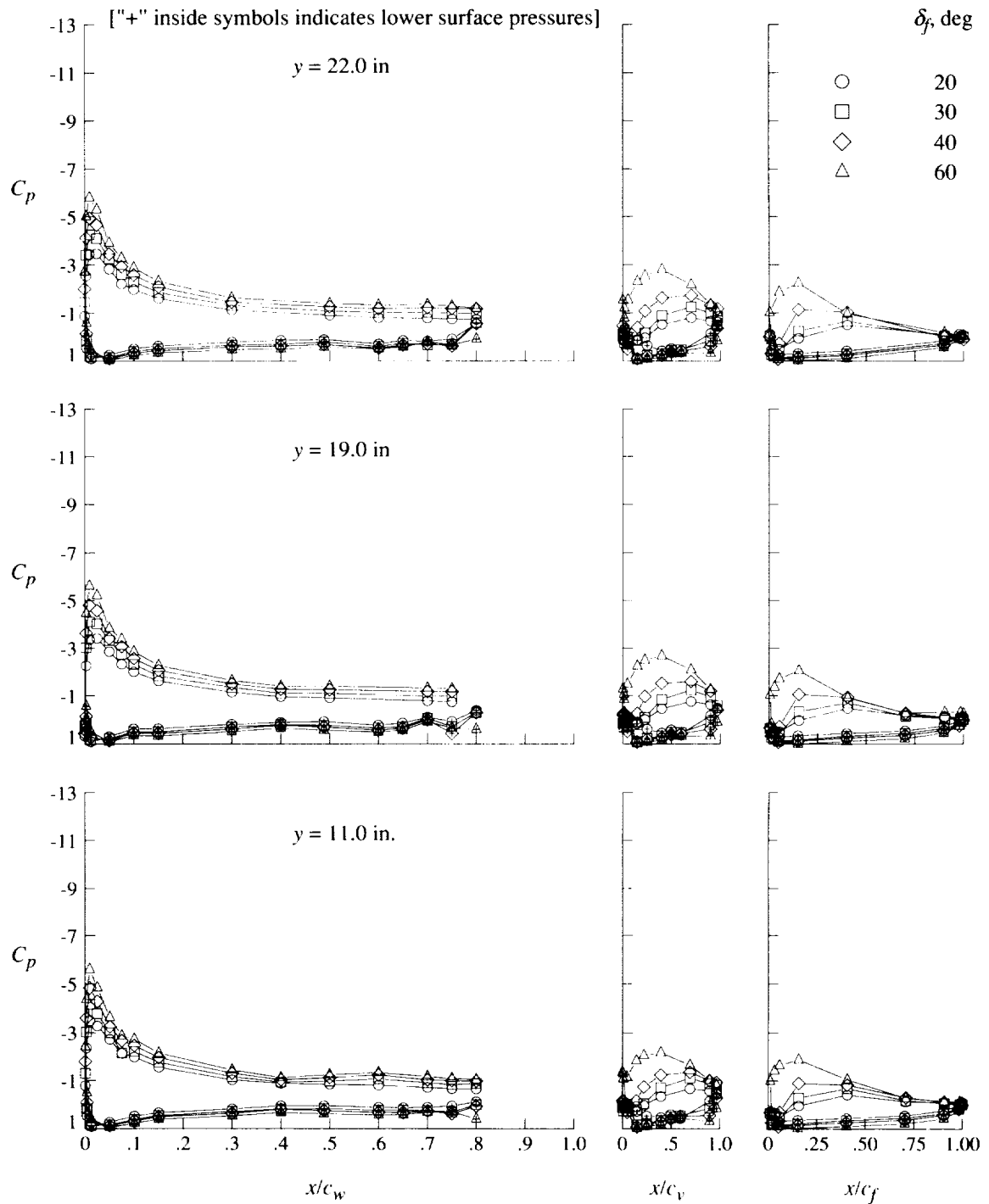
(d) $q = 20$ psf; $\alpha = 8^\circ$.

Figure 36. Continued.



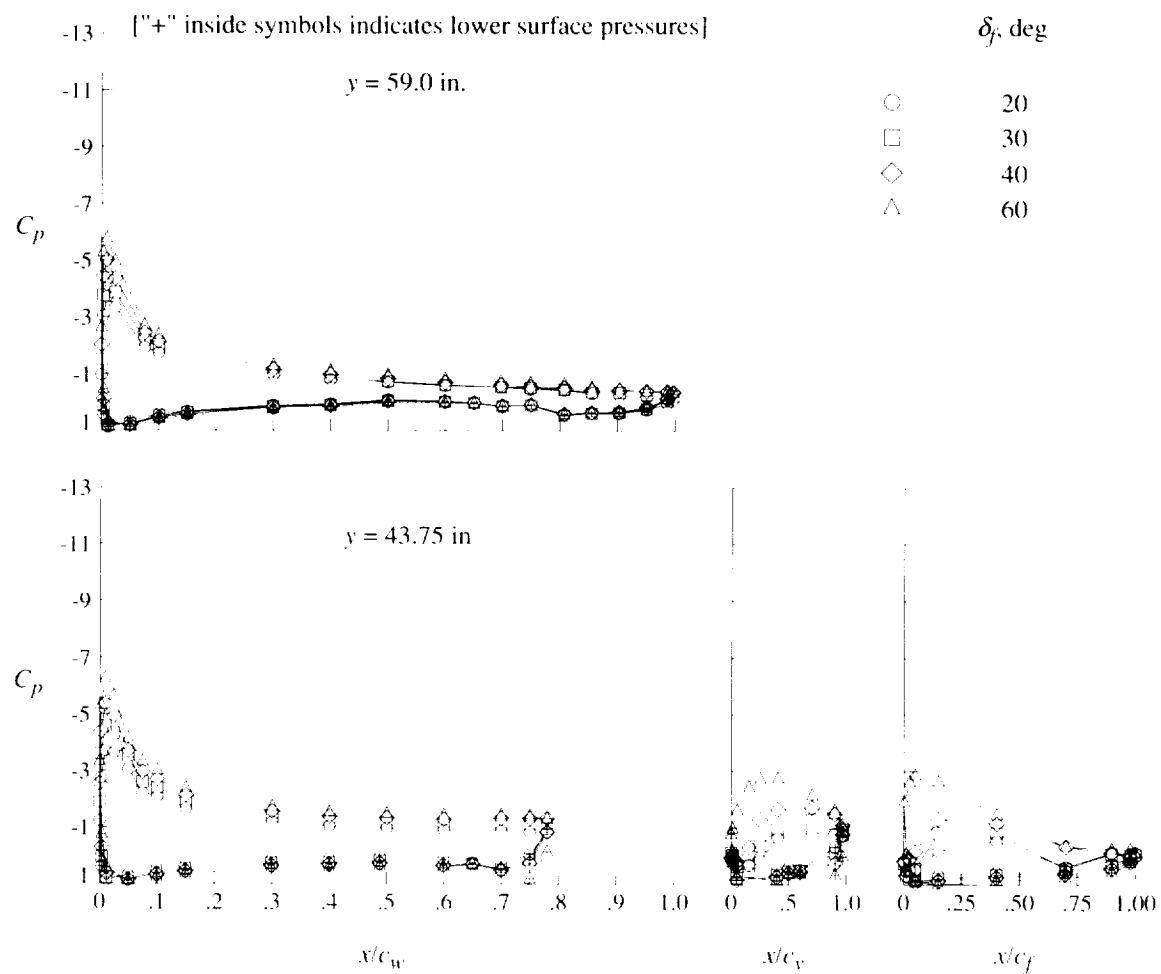
(d) Concluded.

Figure 36. Continued.



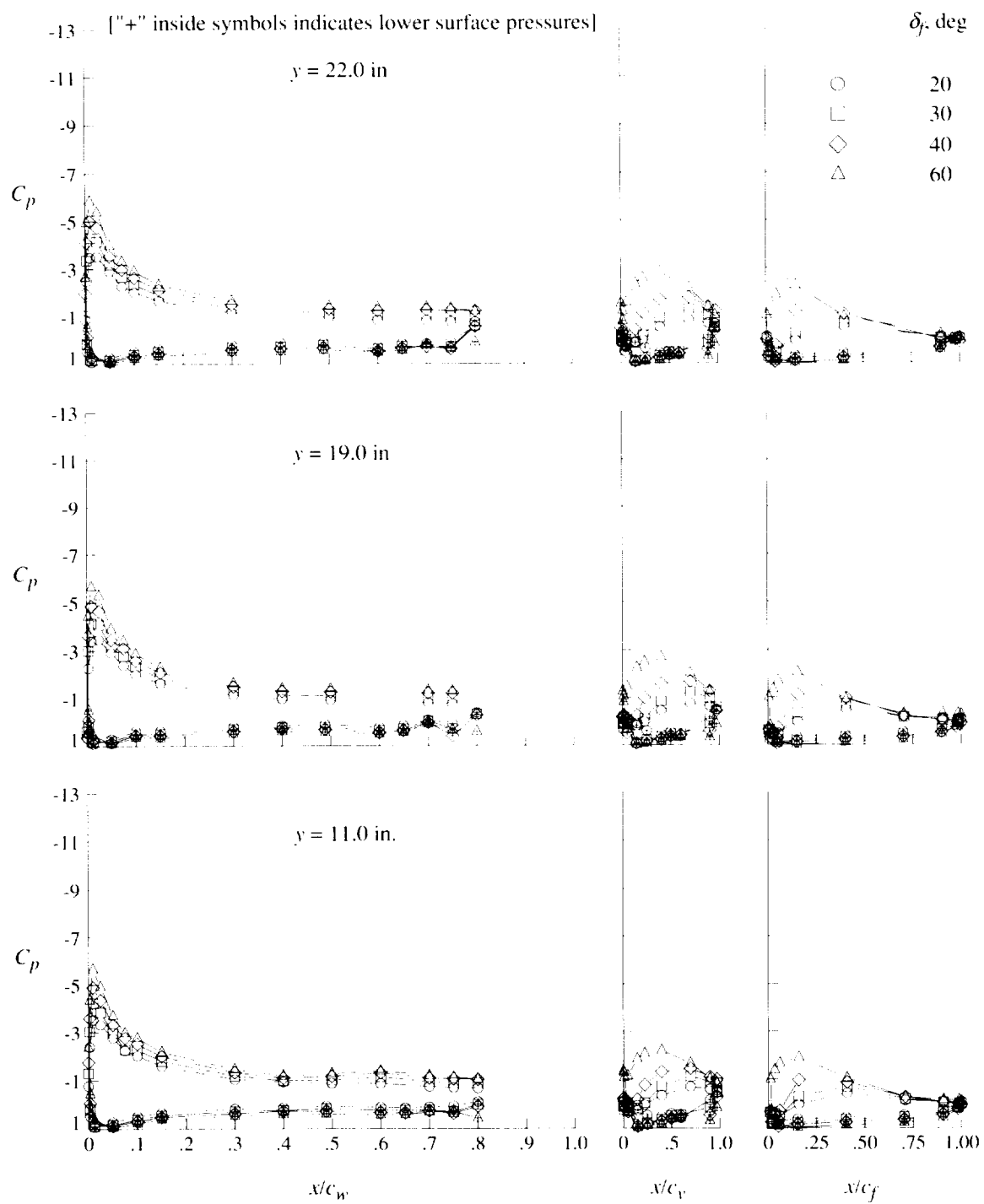
(e) $q = 40$ psf; $\alpha = 8^\circ$.

Figure 36. Continued.



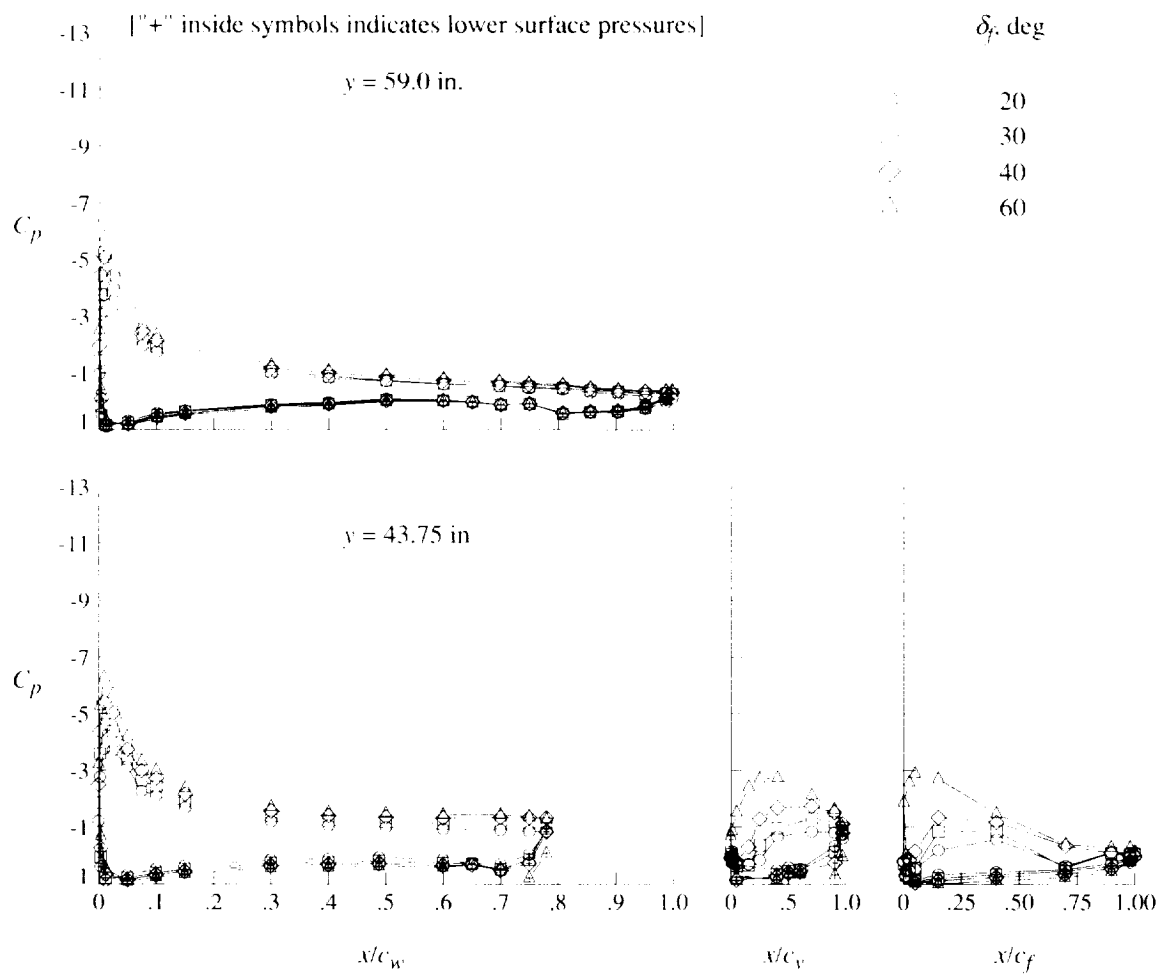
(e) Concluded.

Figure 36. Continued.



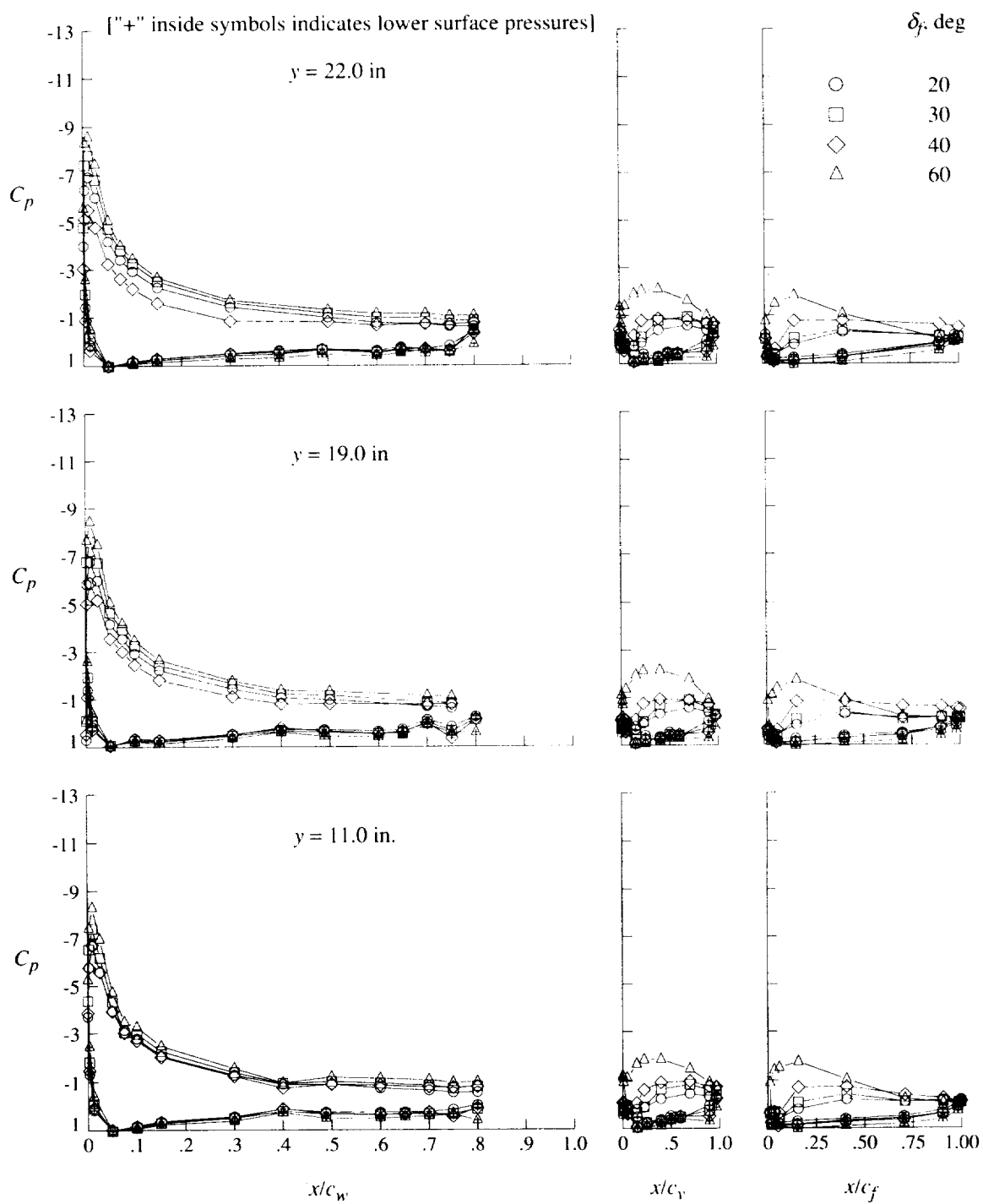
(f) $q = 60$ psf; $\alpha = 8^\circ$.

Figure 36. Continued.



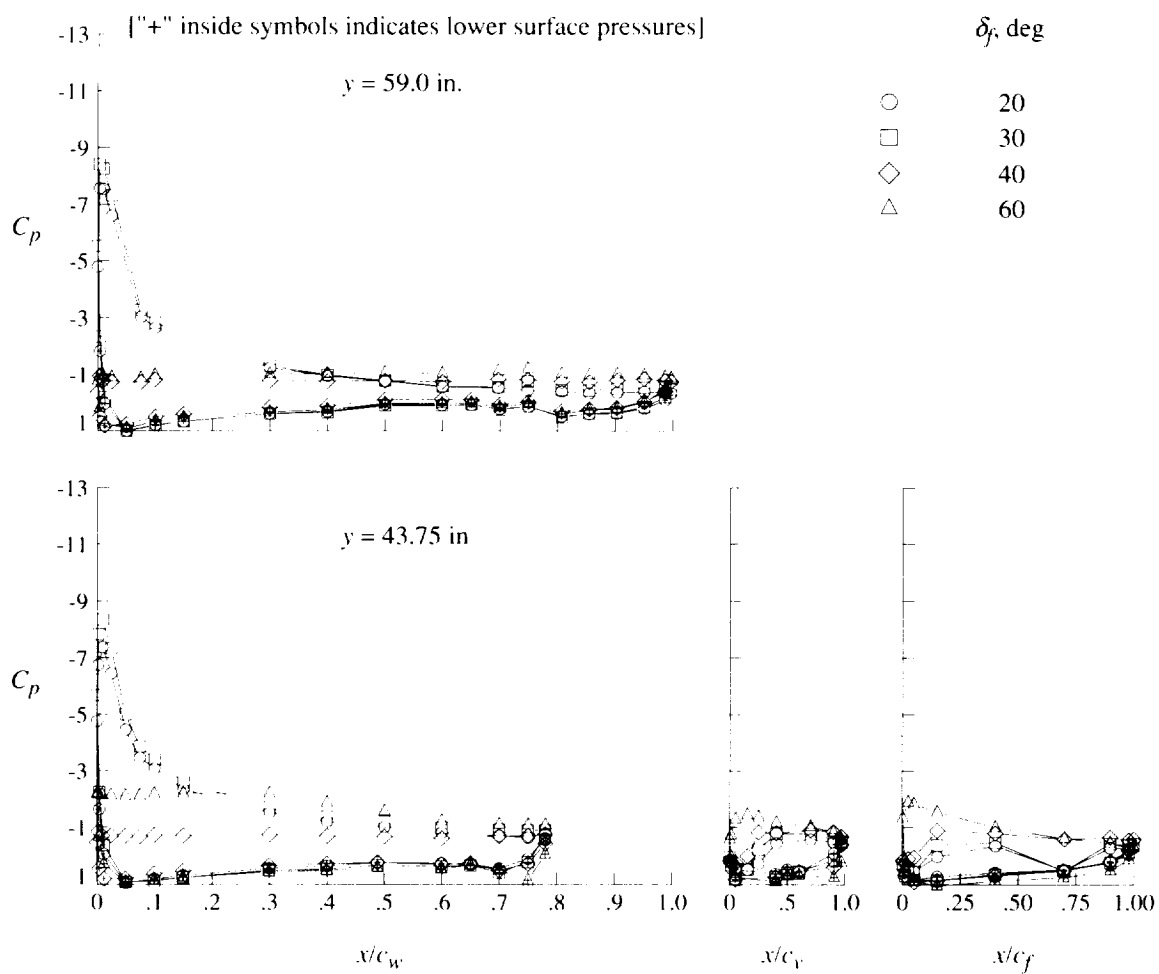
(f) Concluded.

Figure 36. Continued.



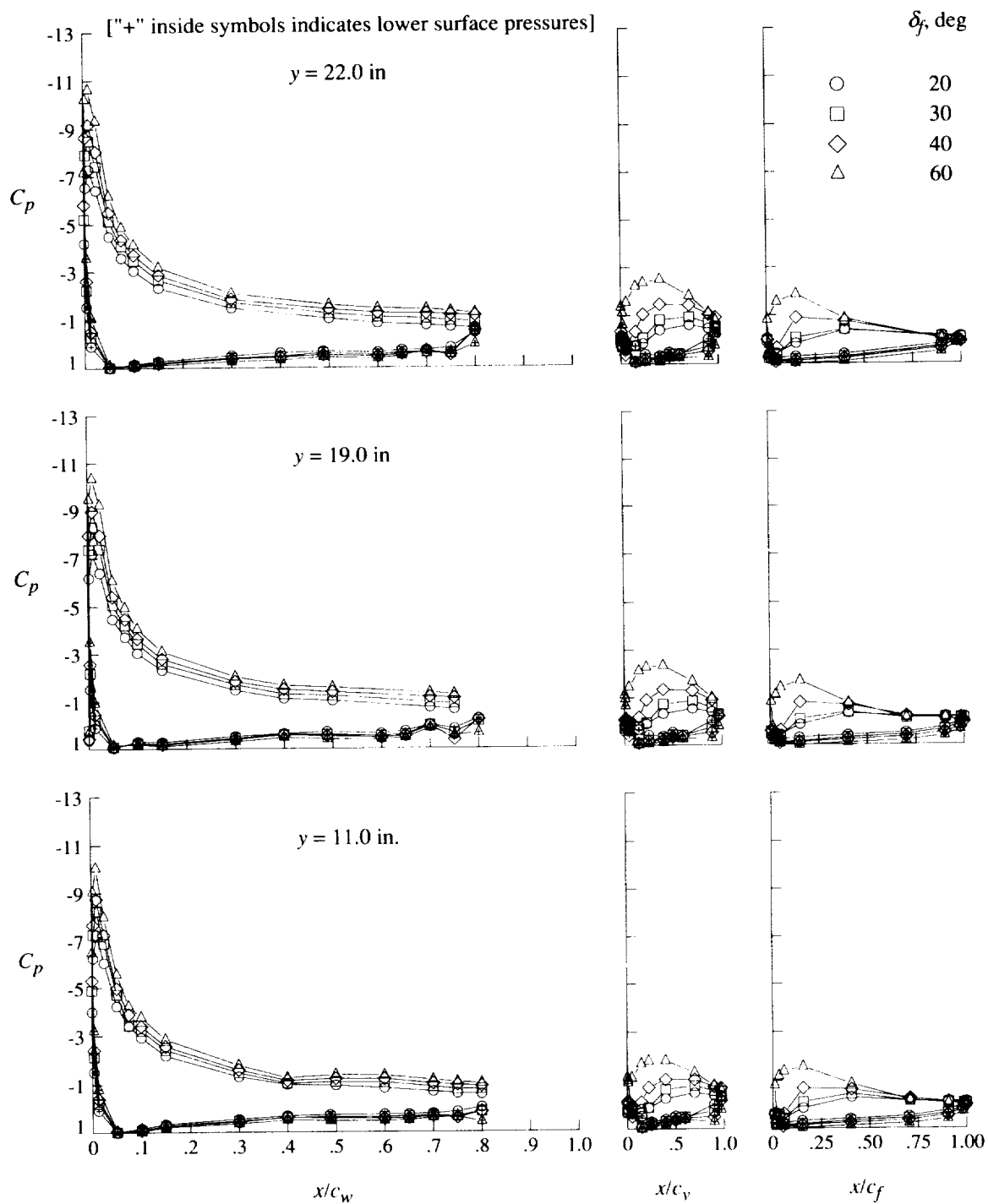
(g) $q = 20$ psf; $\alpha = 16^\circ$.

Figure 36. Continued.



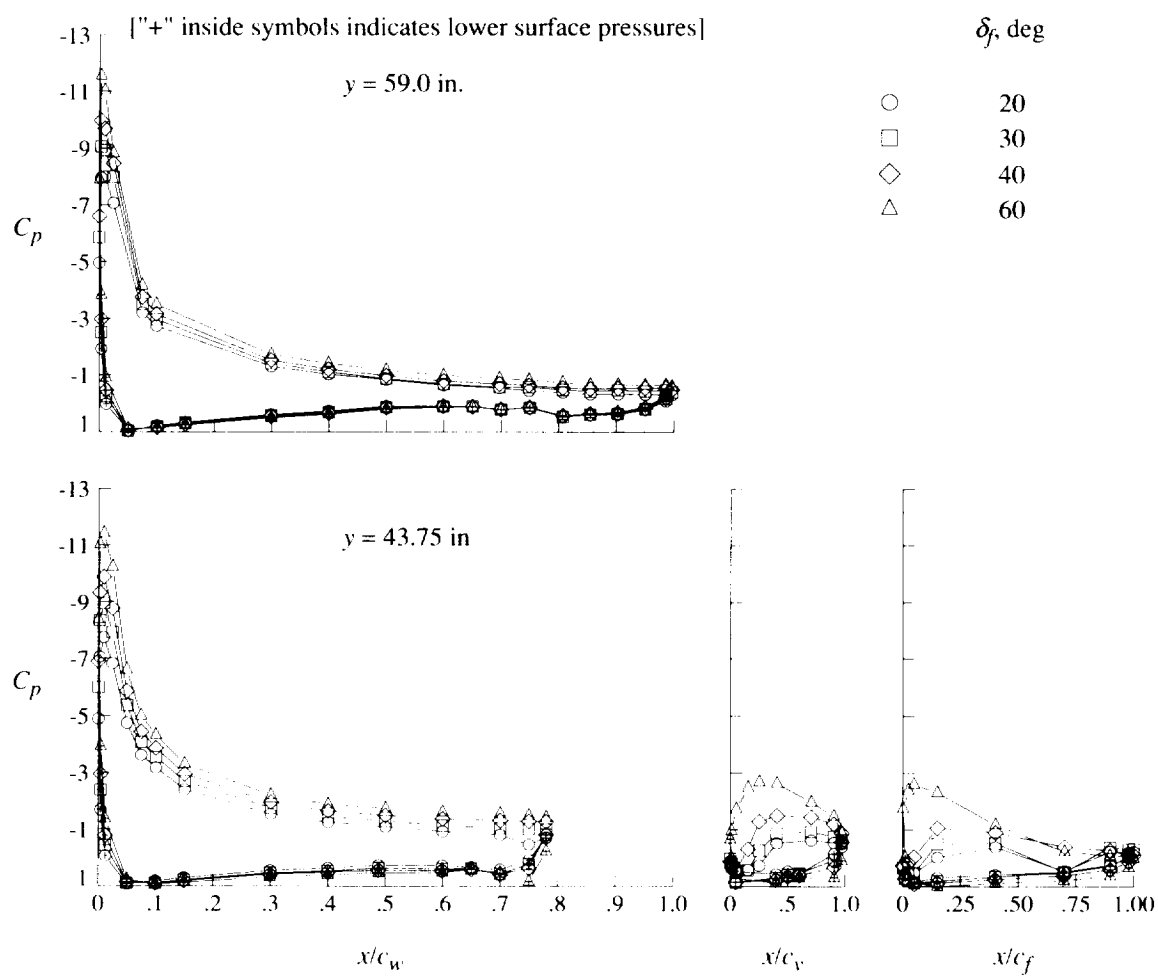
(g) Concluded.

Figure 36. Continued.



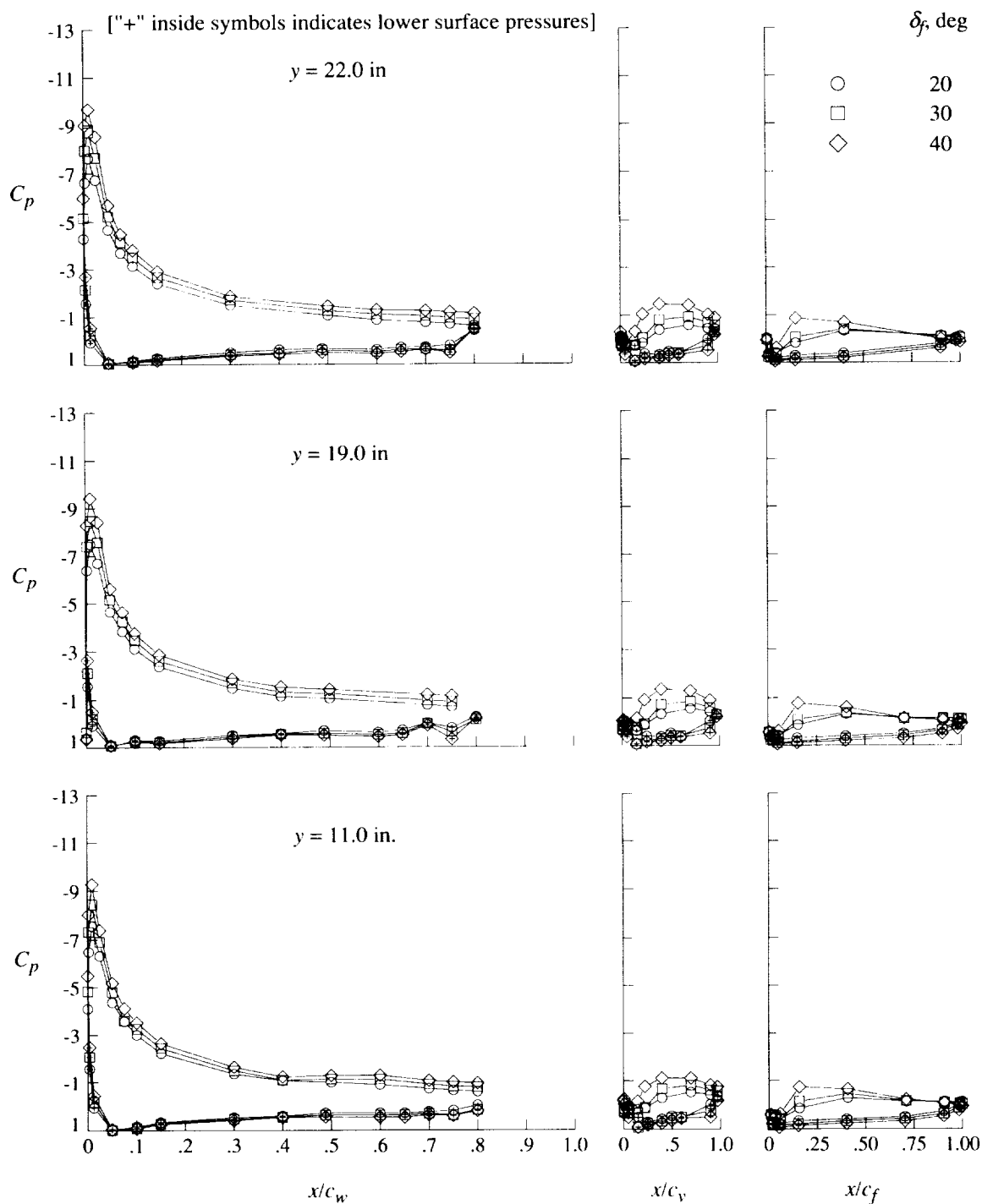
(h) $q = 40$ psf; $\alpha = 16^\circ$.

Figure 36. Continued.



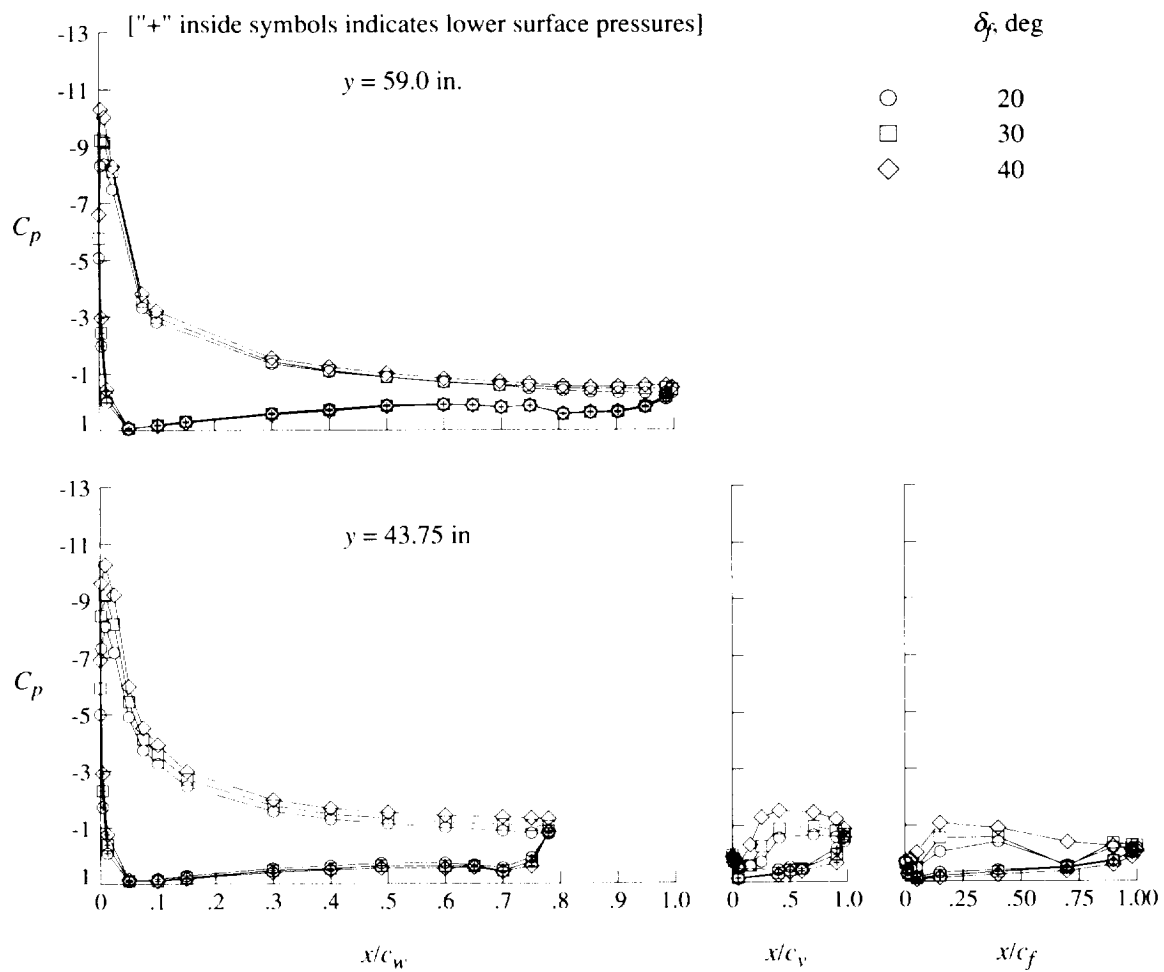
(h) Concluded.

Figure 36. Continued.



(i) $q = 60$ psf; $\alpha = 16^\circ$.

Figure 36. Continued.



(i) Concluded.

Figure 36. Concluded.

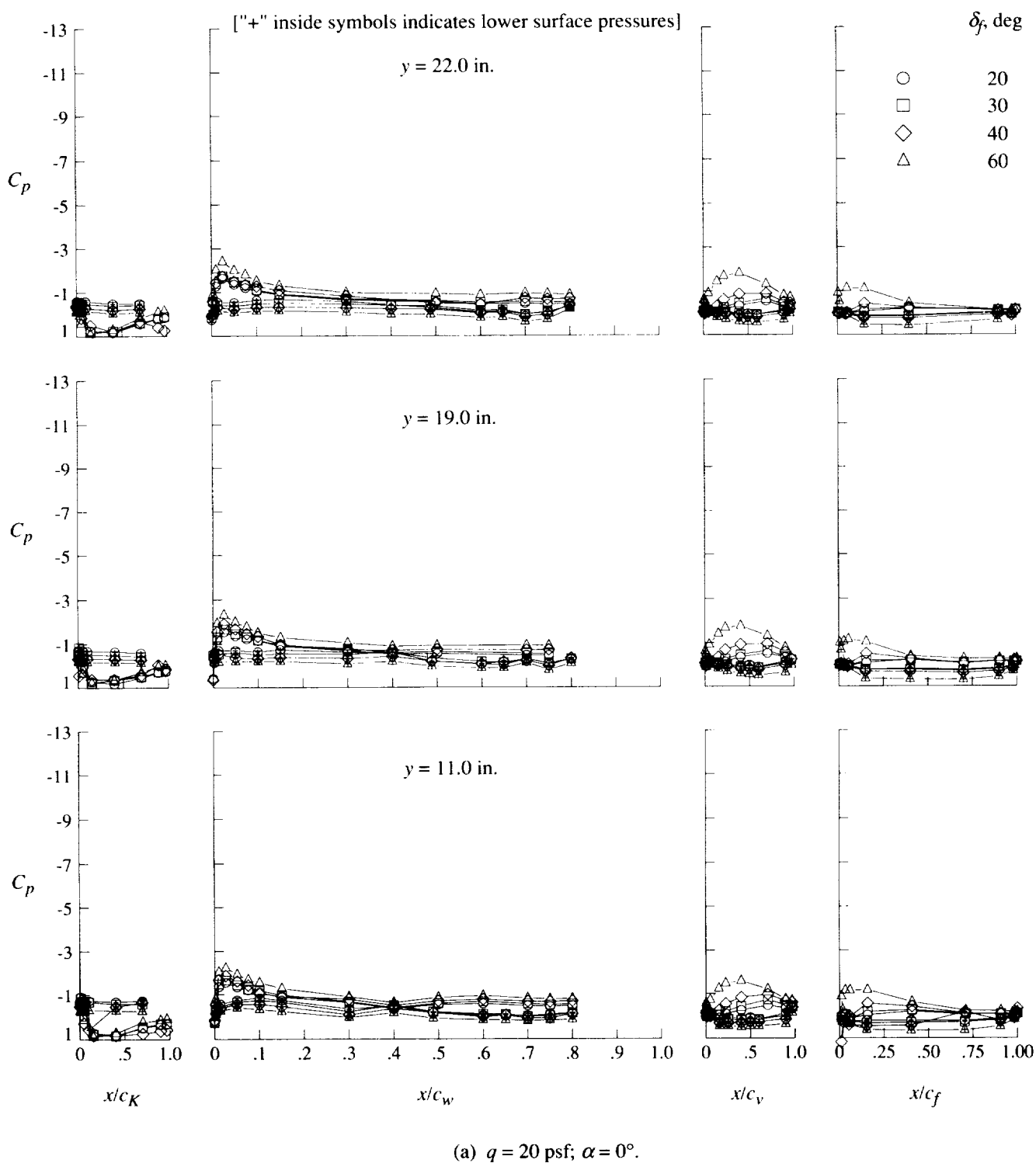
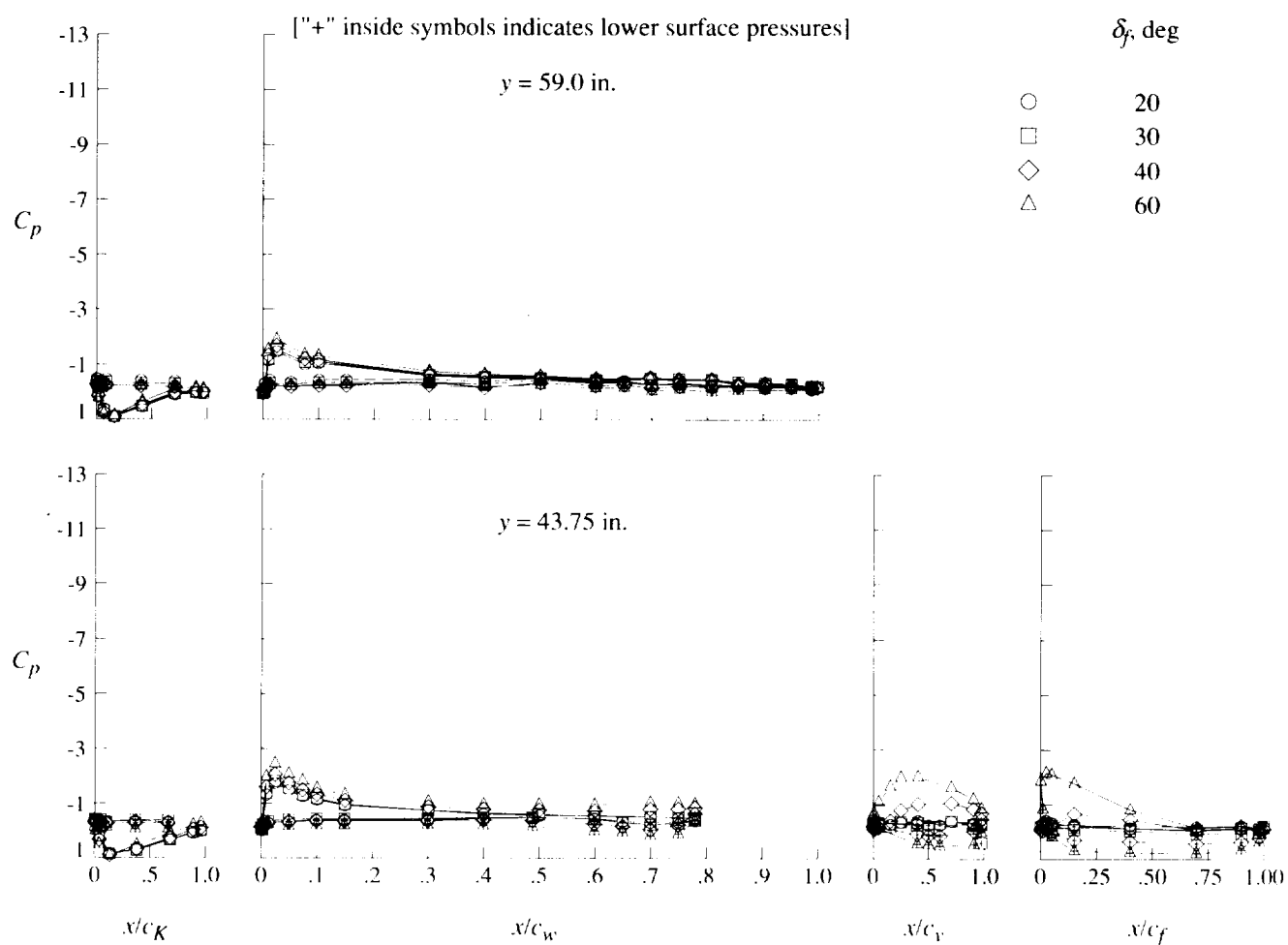
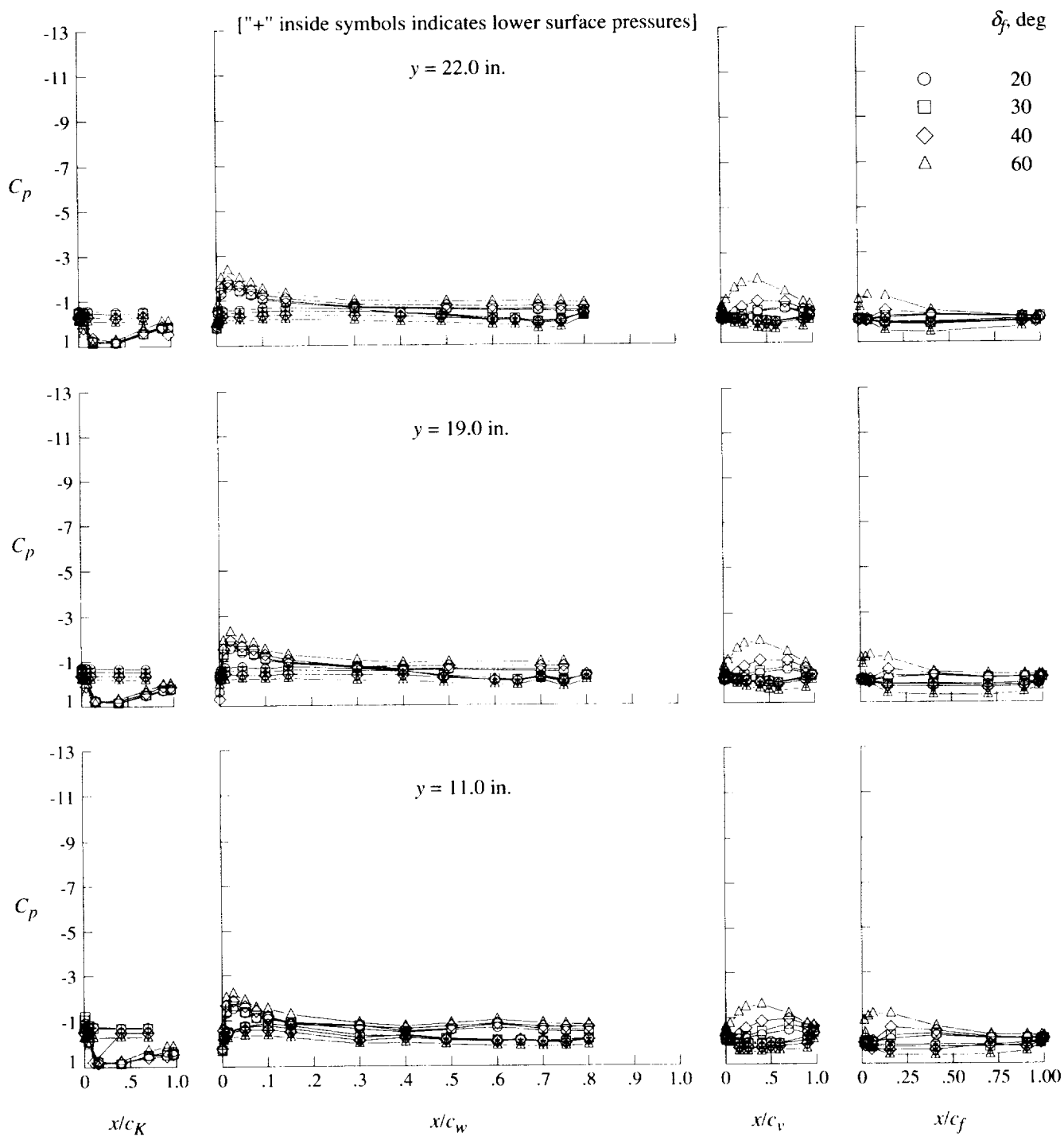


Figure 37. Effect of angle of attack on pressure distributions for high-lift configuration.



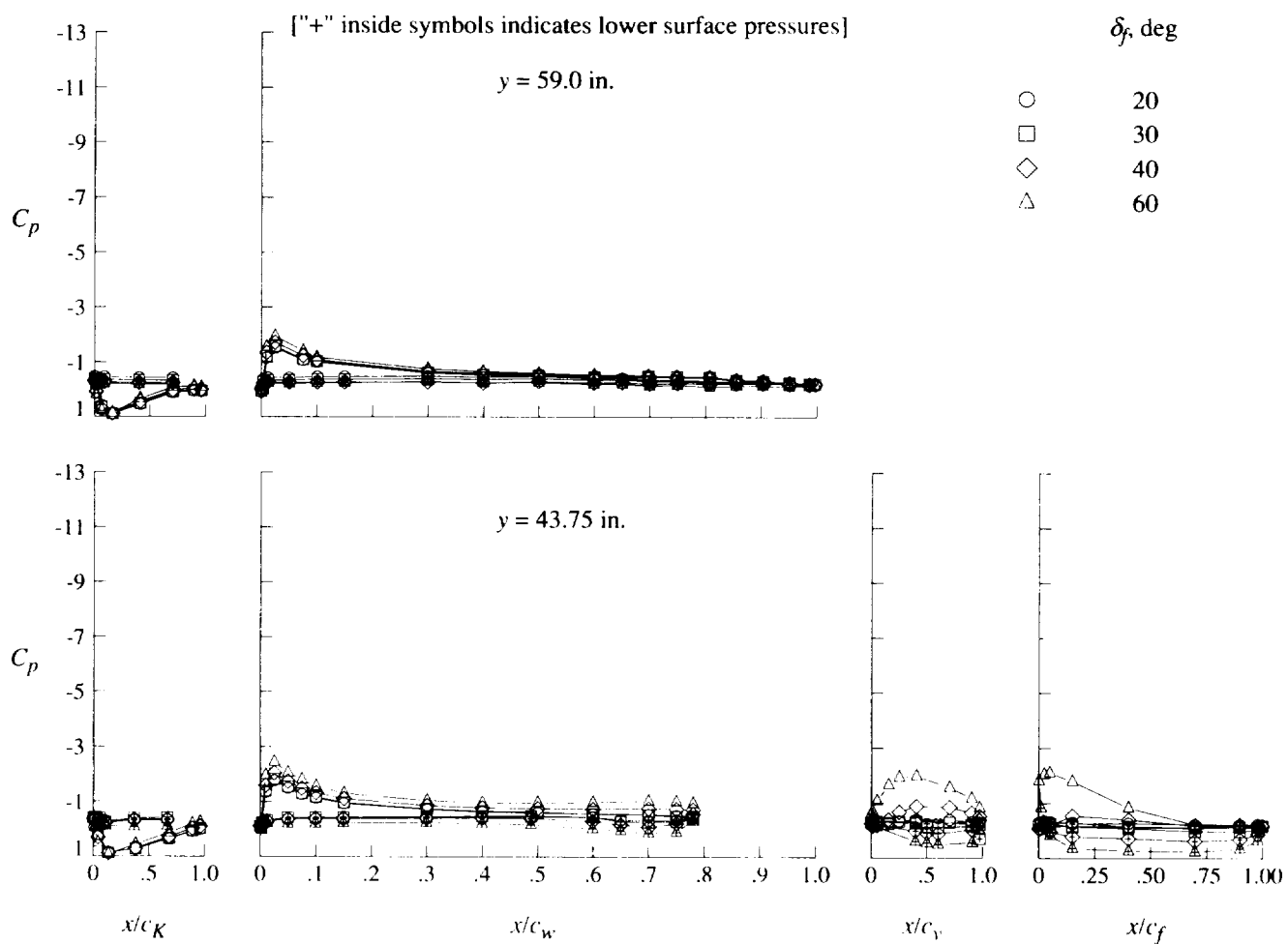
(a) Concluded.

Figure 37. Continued.



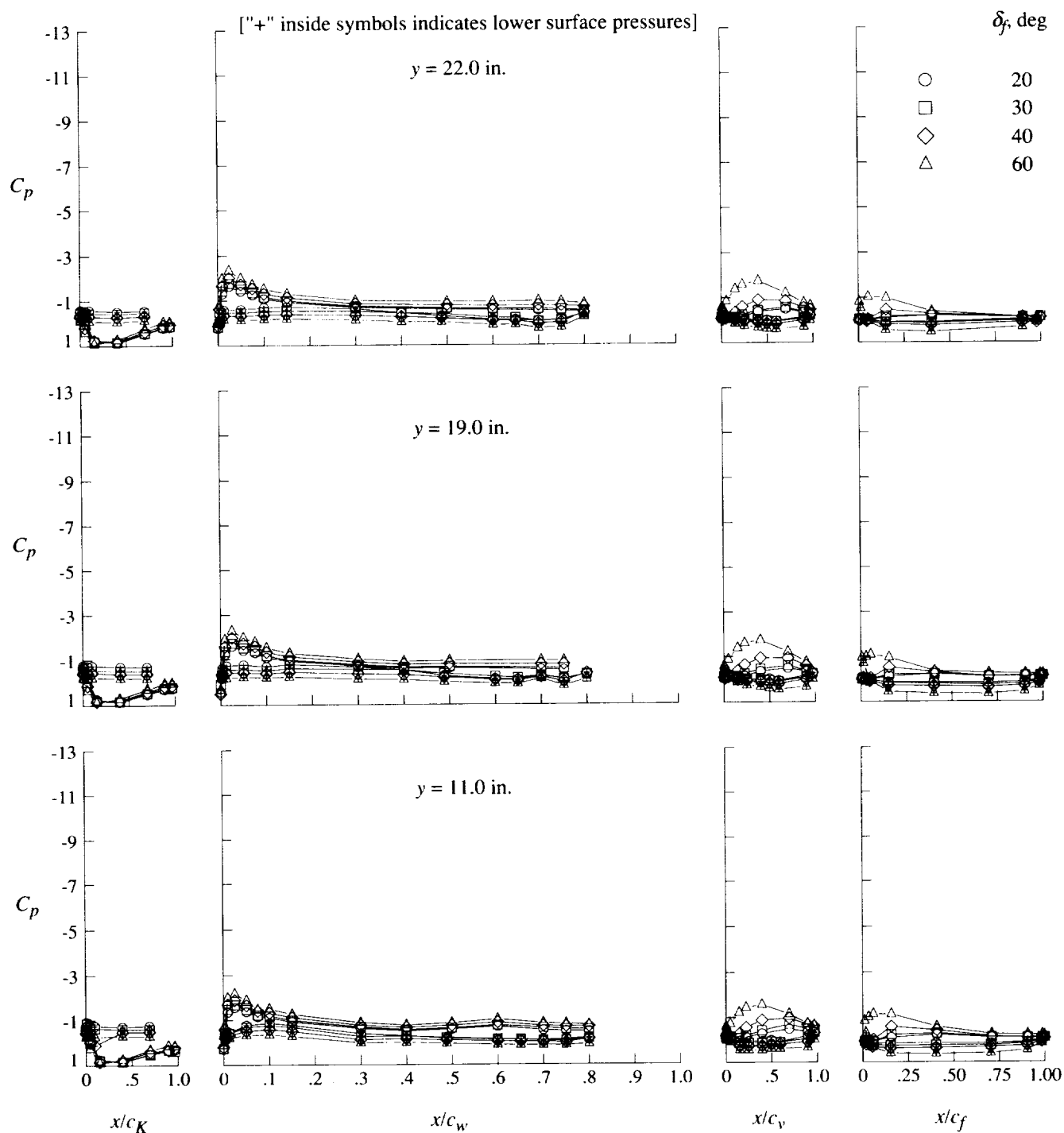
(b) $q = 40$ psf; $\alpha = 0^\circ$.

Figure 37. Continued.



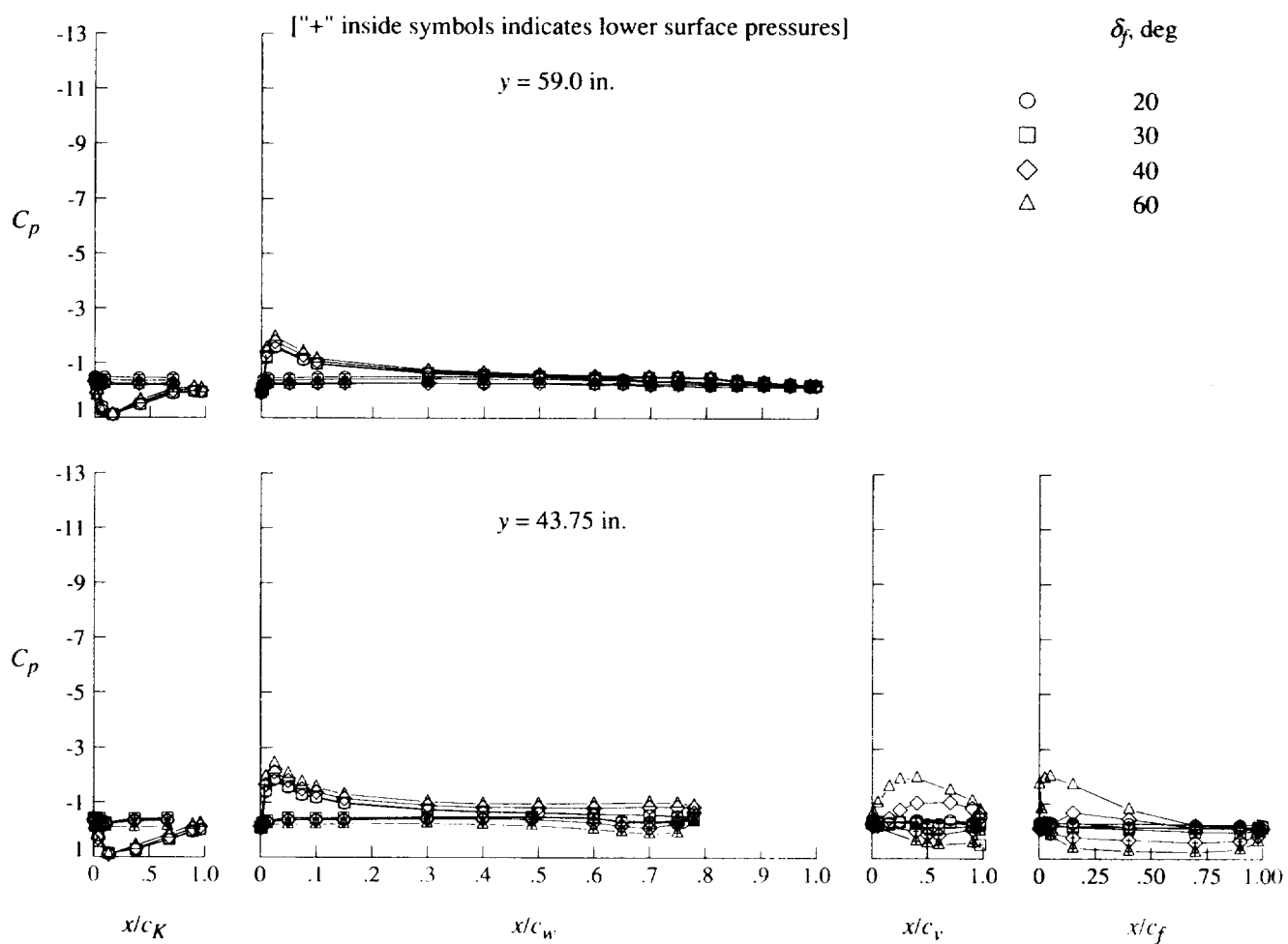
(b) Concluded.

Figure 37. Continued.



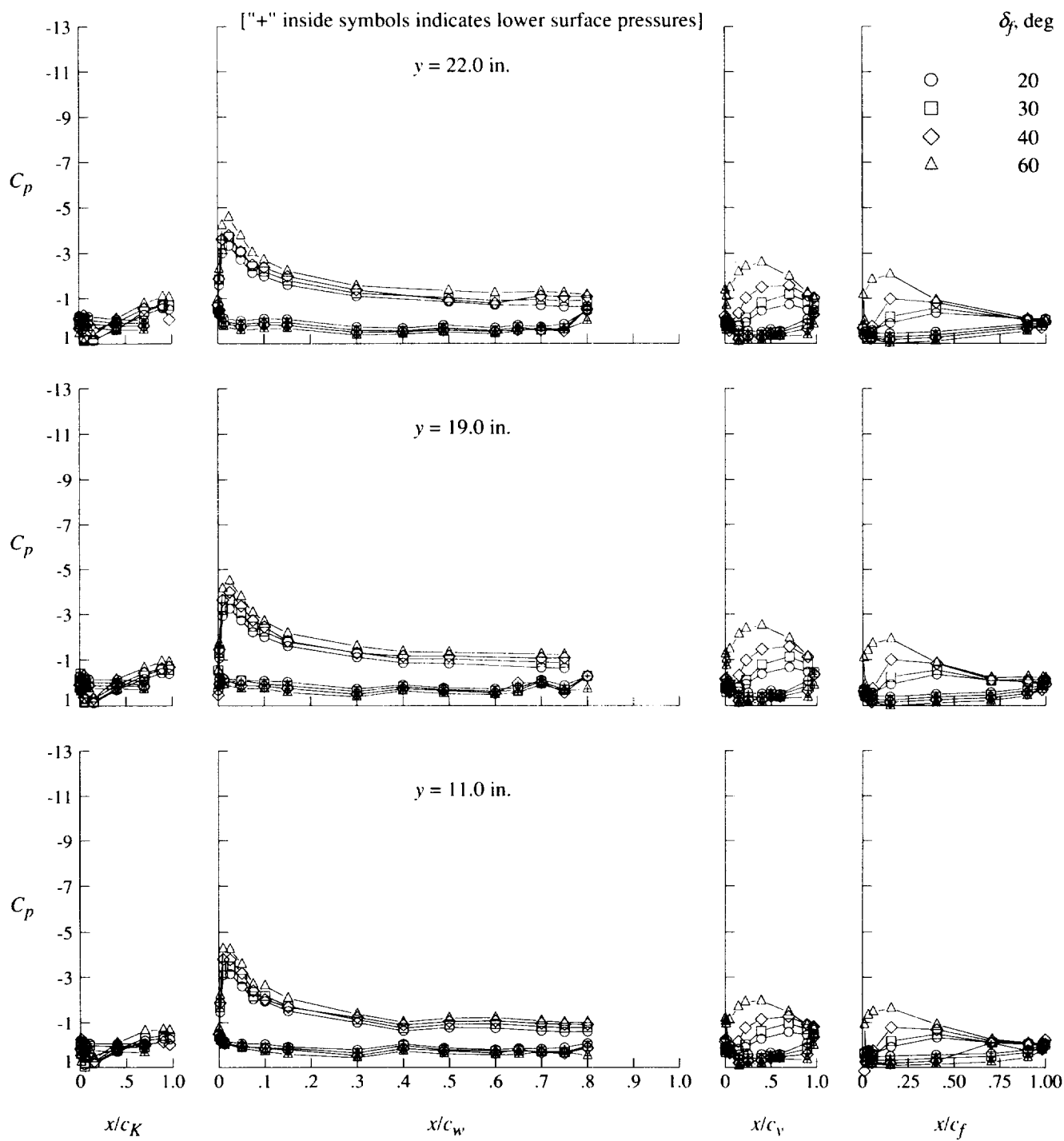
(c) $q = 60$ psf; $\alpha = 0^\circ$.

Figure 37. Continued.



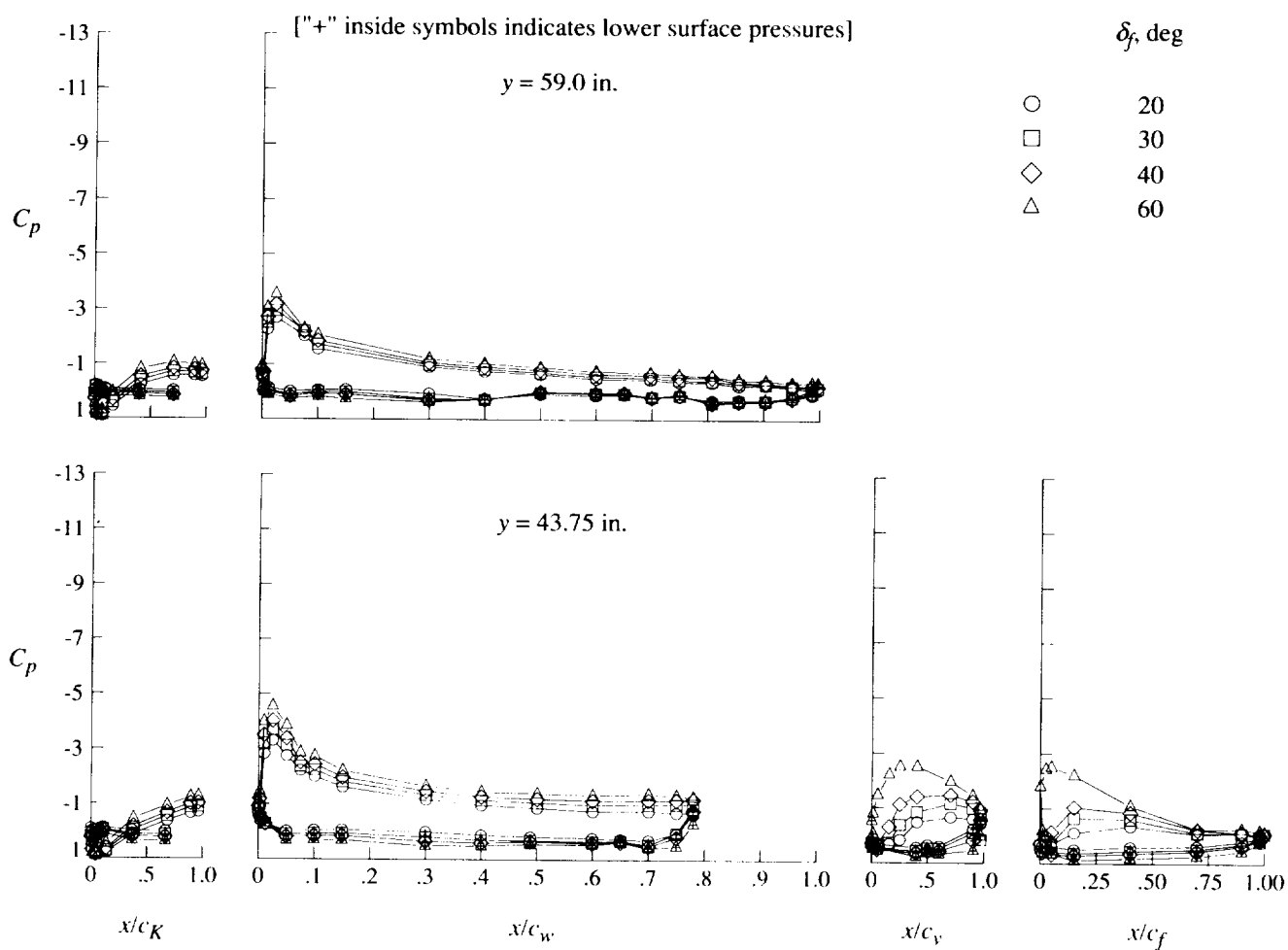
(c) Concluded.

Figure 37. Continued.



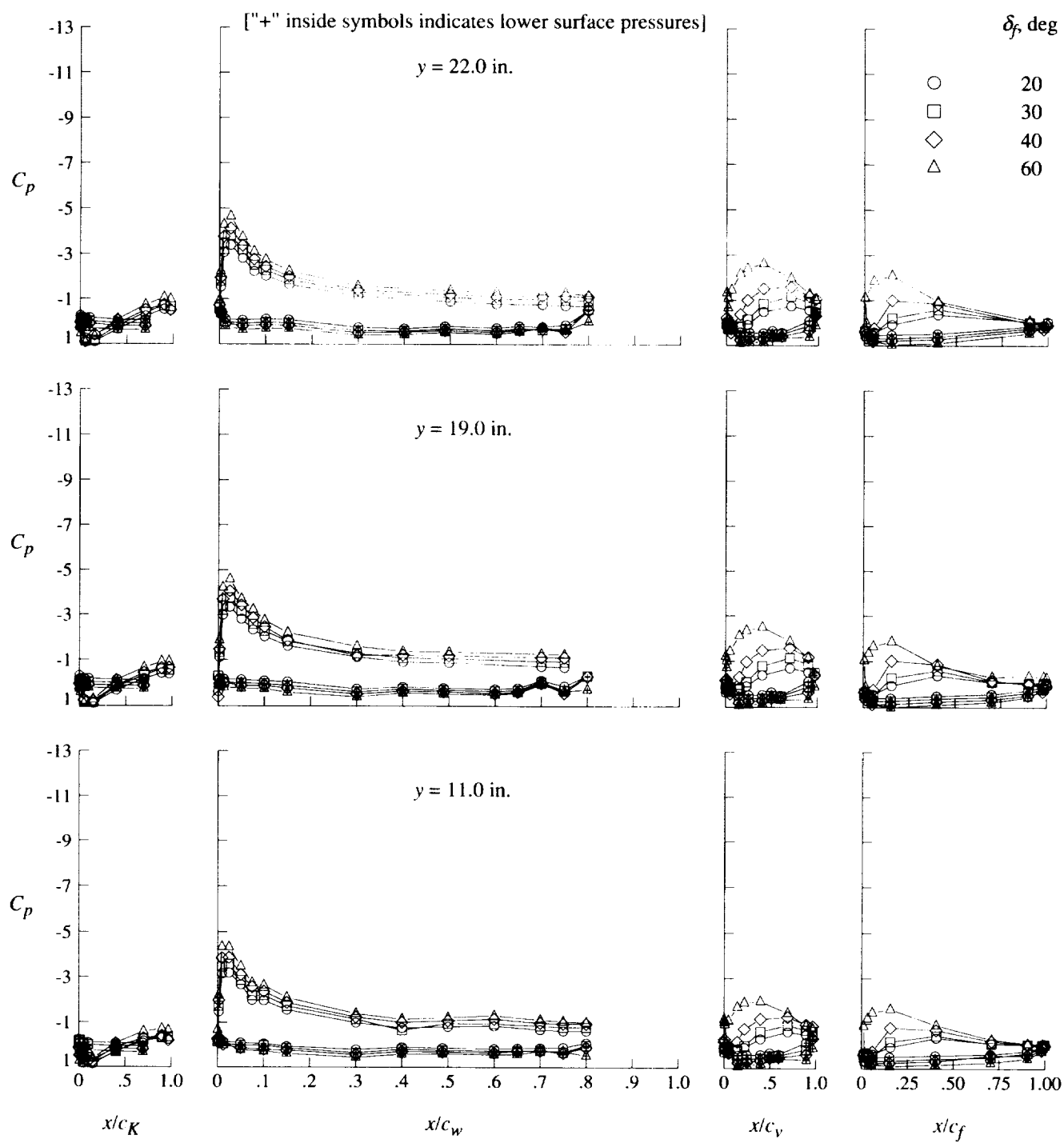
(d) $q = 20$ psf; $\alpha = 8^\circ$.

Figure 37. Continued.



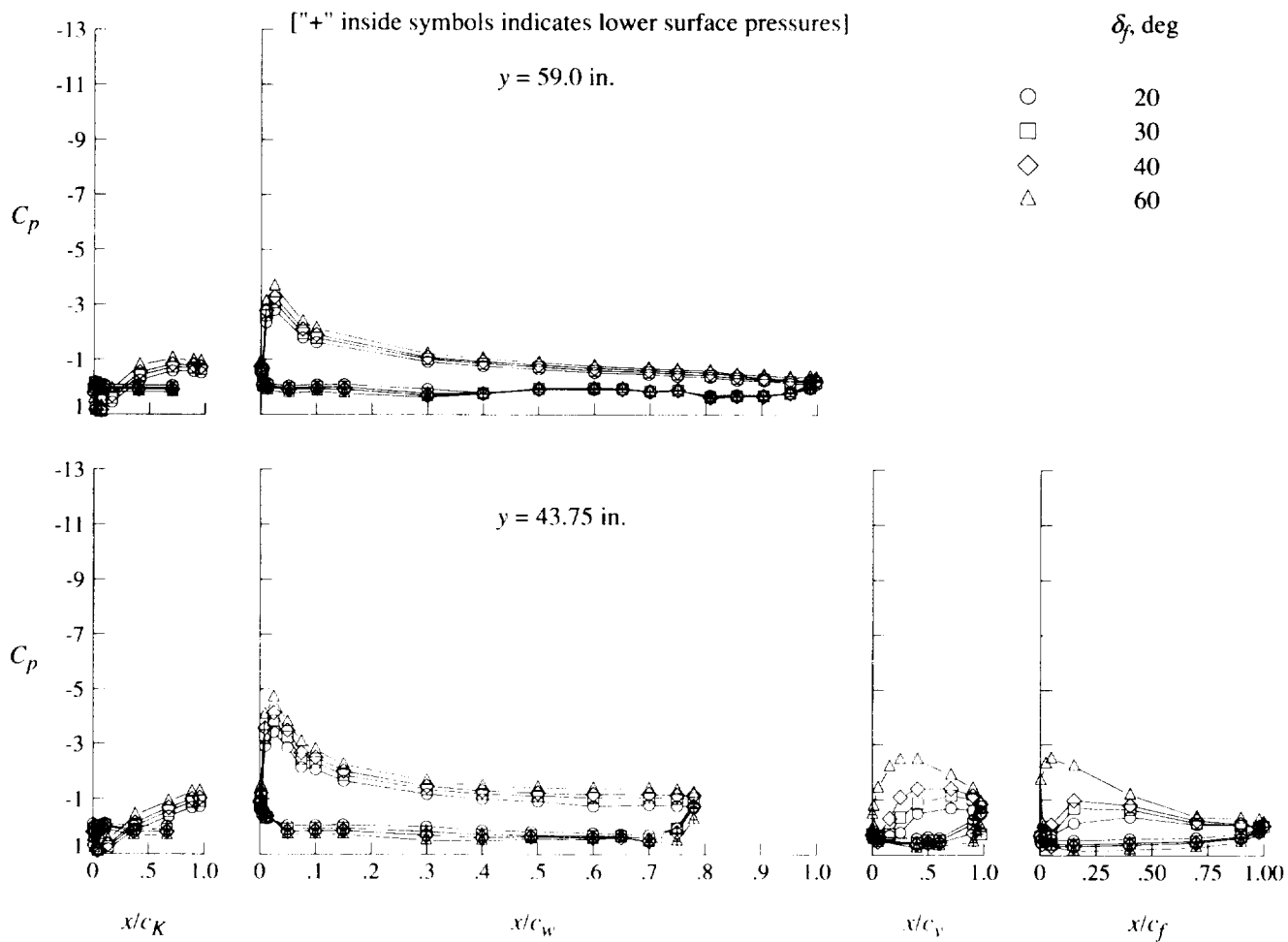
(d) Concluded.

Figure 37. Continued.



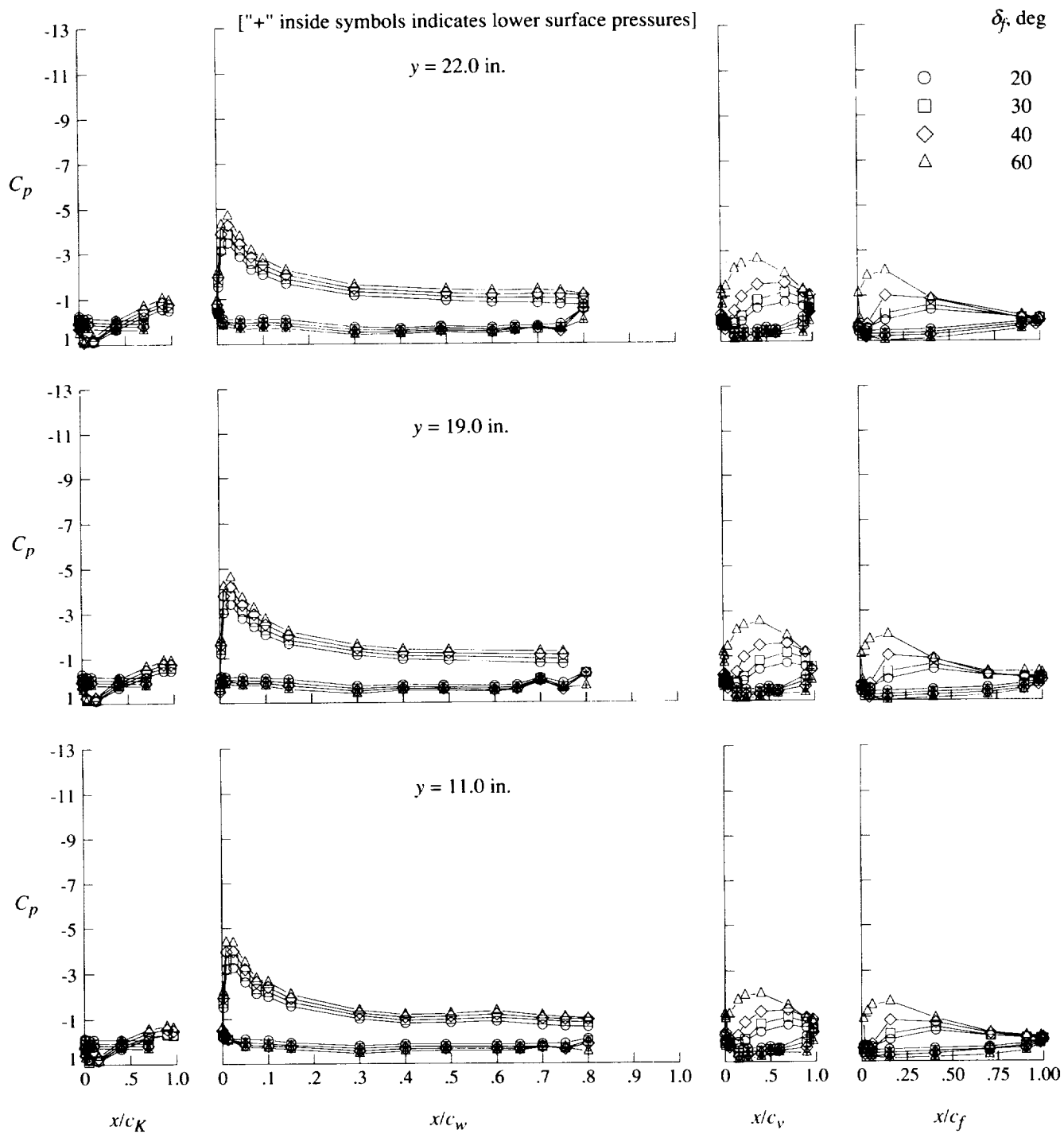
(e) $q = 40$ psf; $\alpha = 8^\circ$.

Figure 37. Continued.



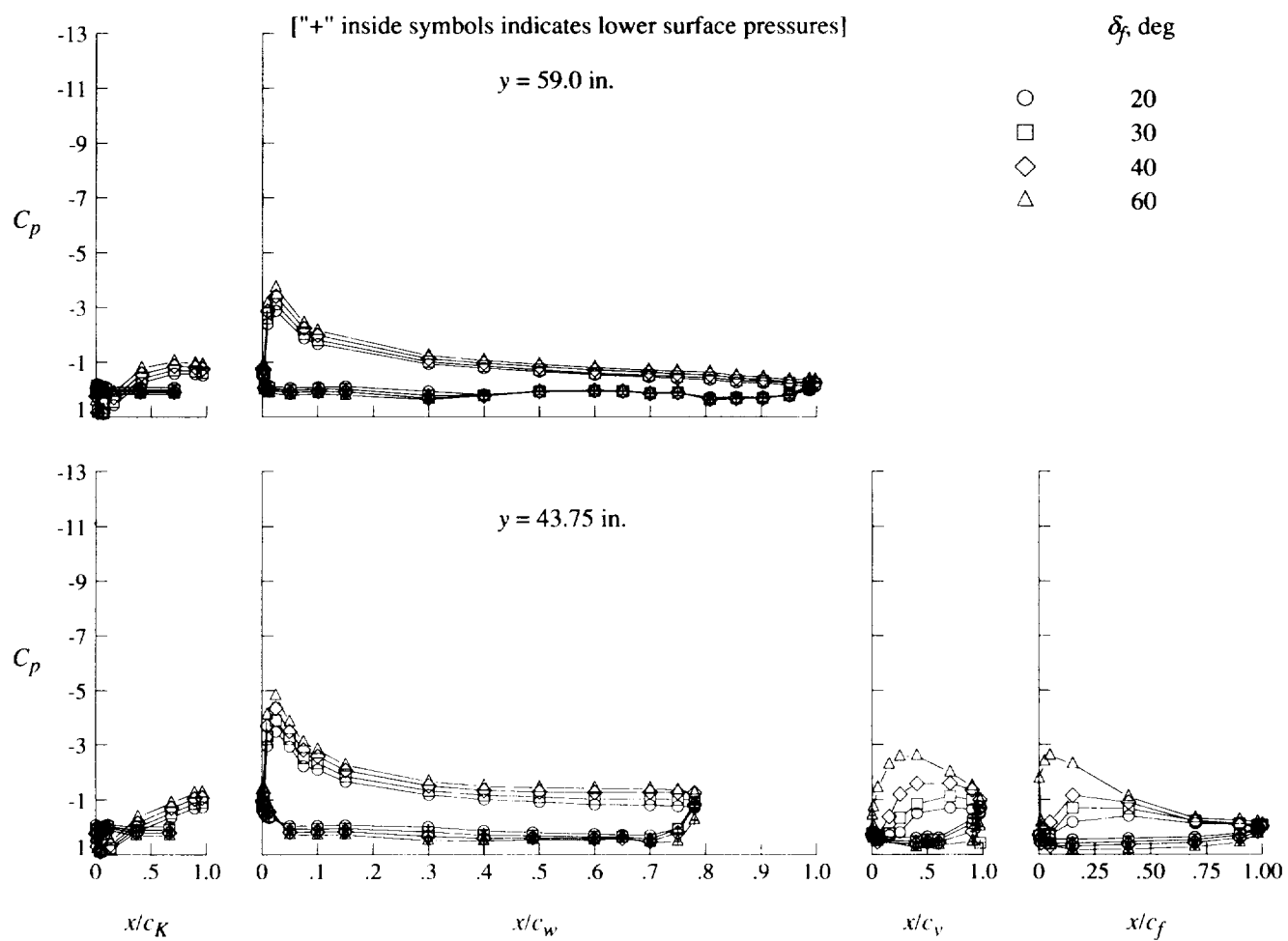
(e) Concluded.

Figure 37. Continued.



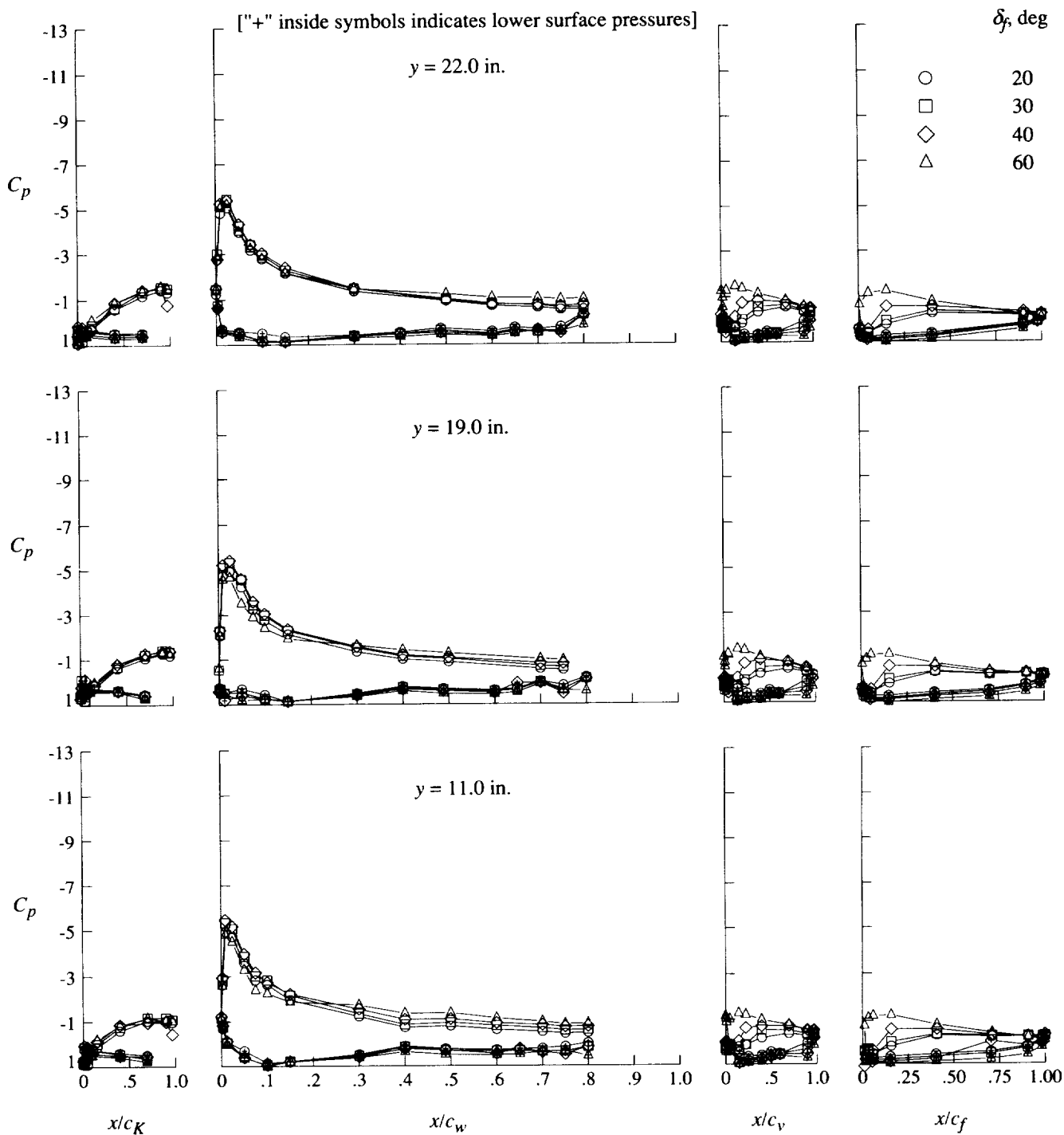
(f) $q = 60$ psf; $\alpha = 8^\circ$.

Figure 37. Continued.



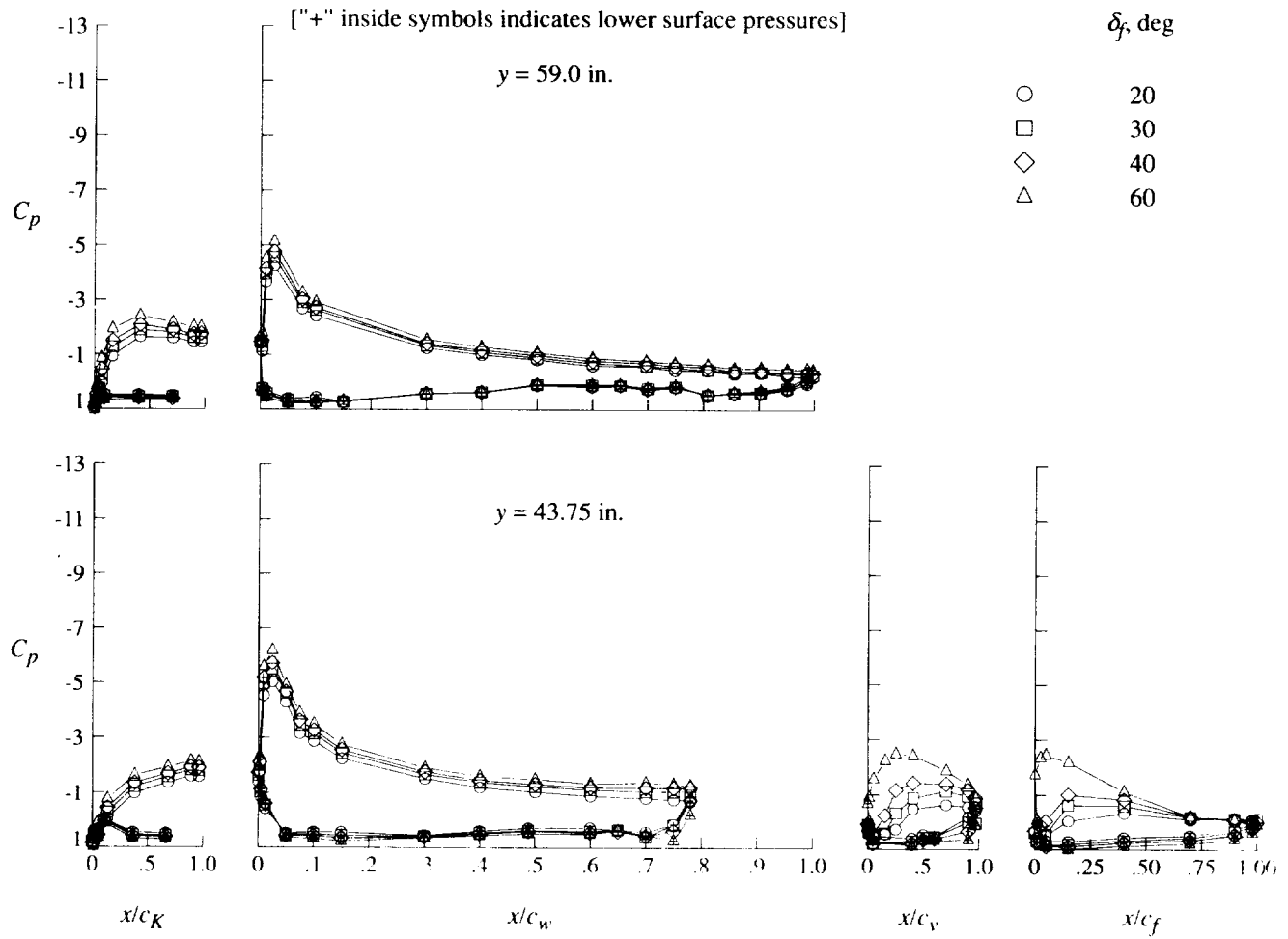
(f) Concluded.

Figure 37. Continued.



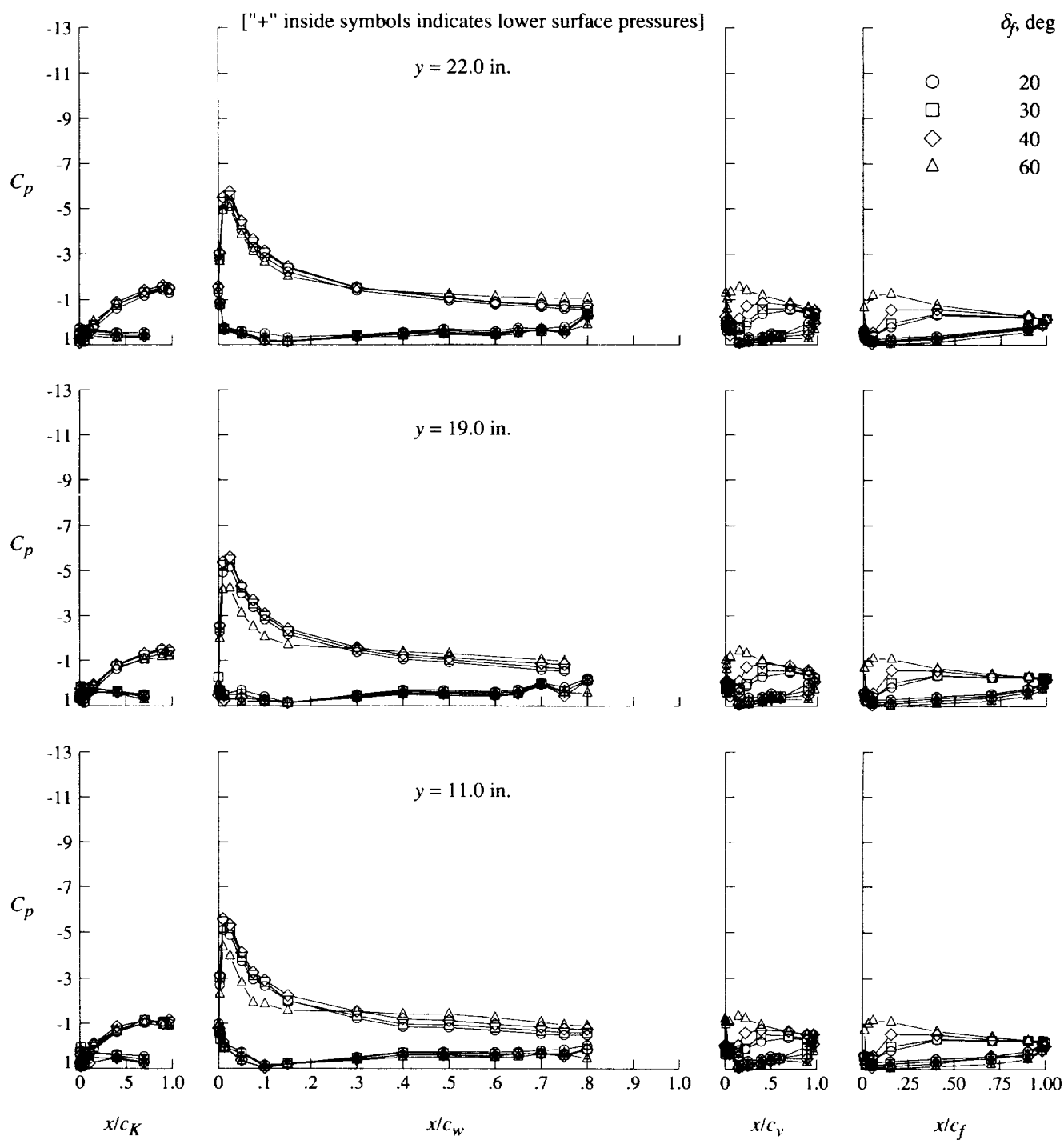
(g) $q = 20$ psf; $\alpha = 16^\circ$.

Figure 37. Continued.



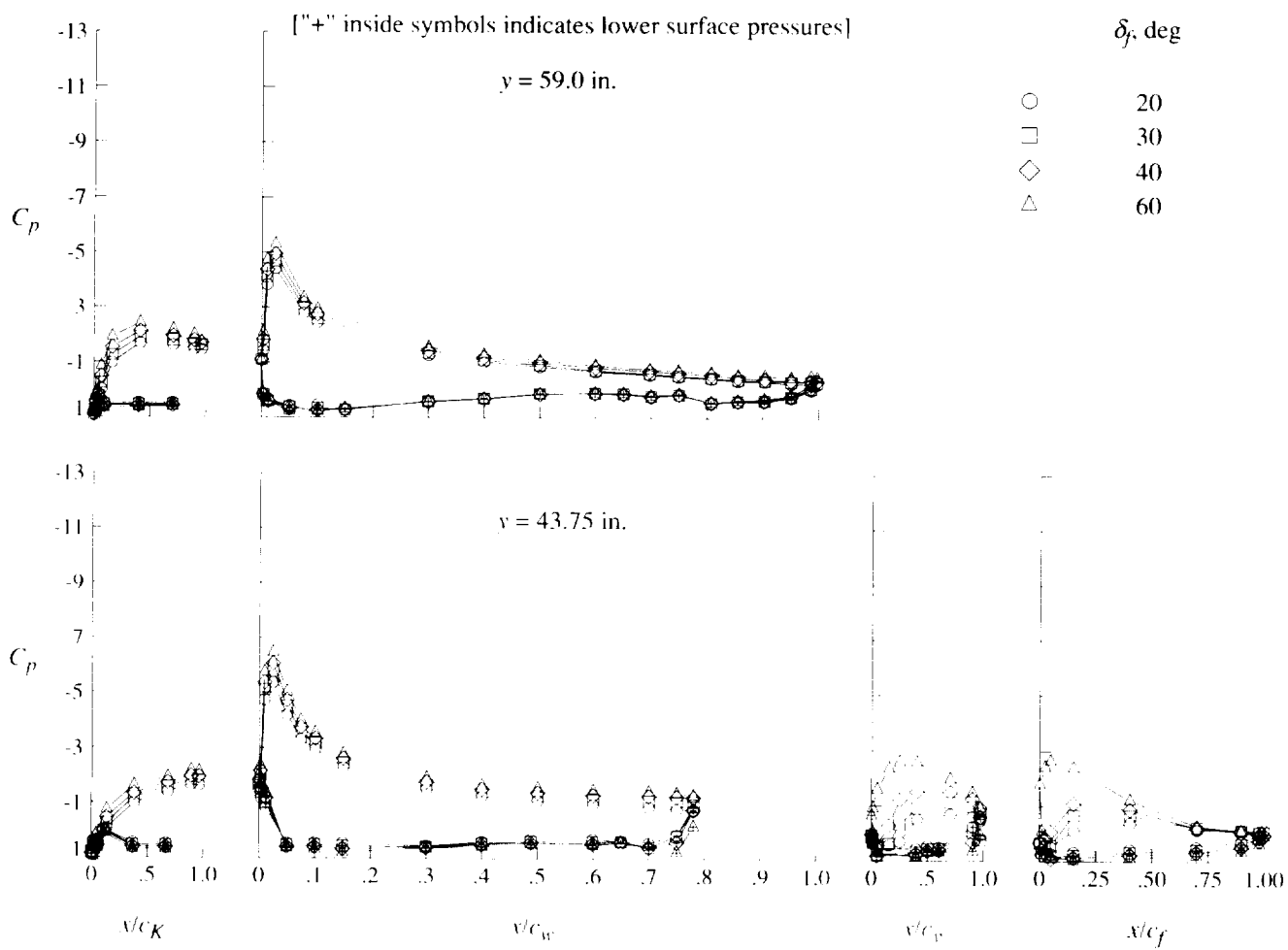
(g) Concluded.

Figure 37. Continued.



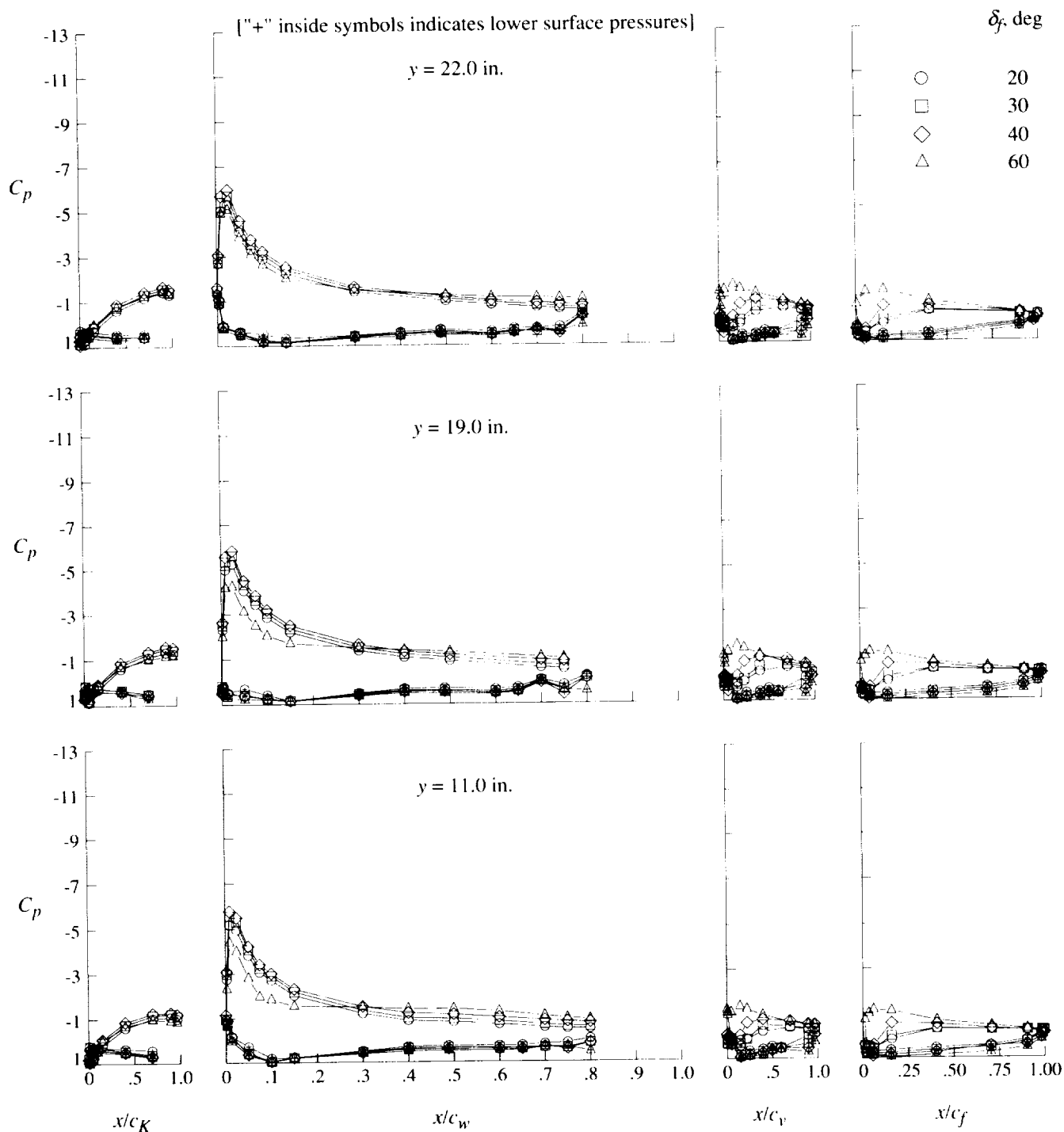
(h) $q = 40$ psf; $\alpha = 16^\circ$.

Figure 37. Continued.



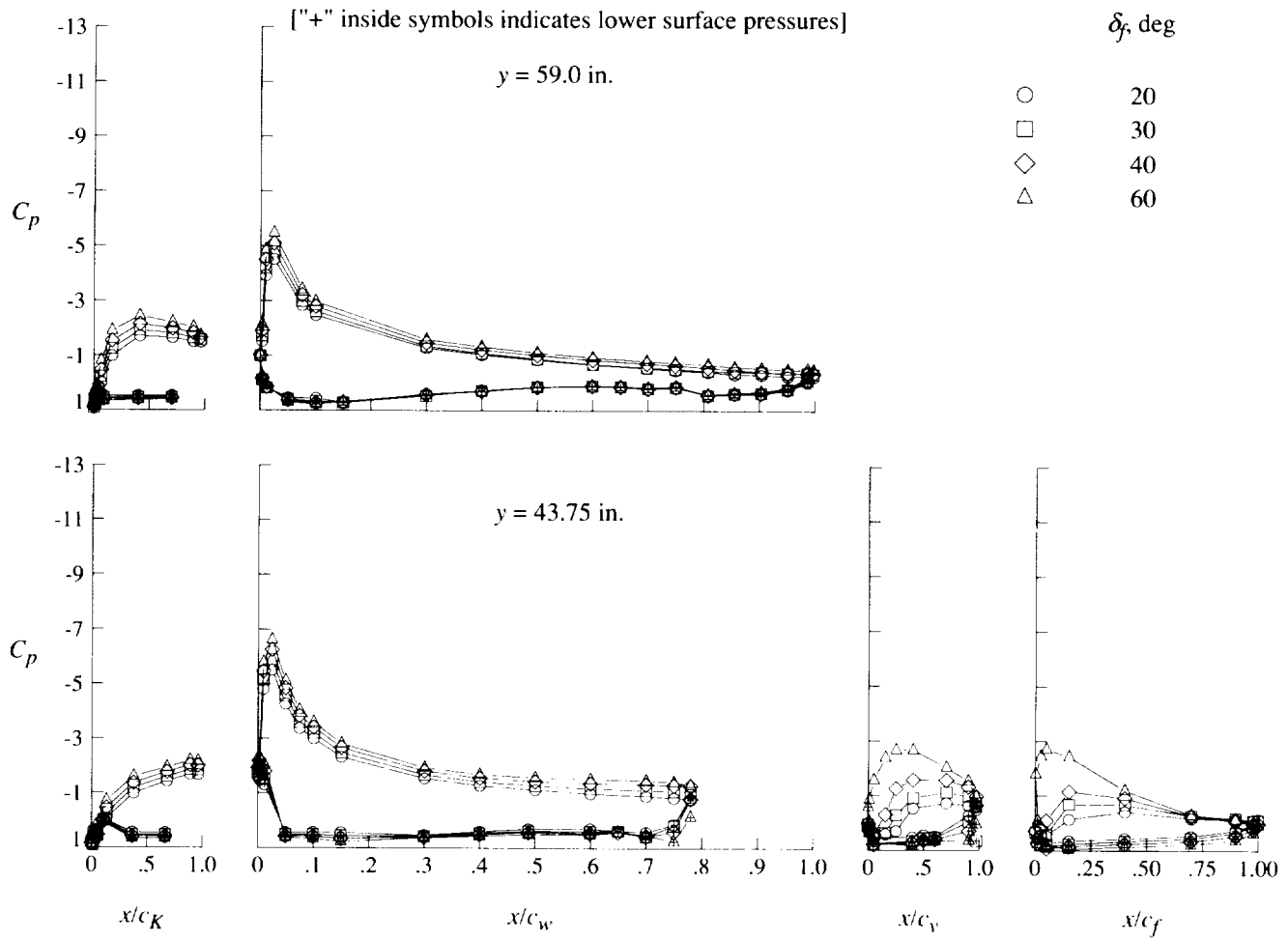
(h) Concluded.

Figure 37. Continued.



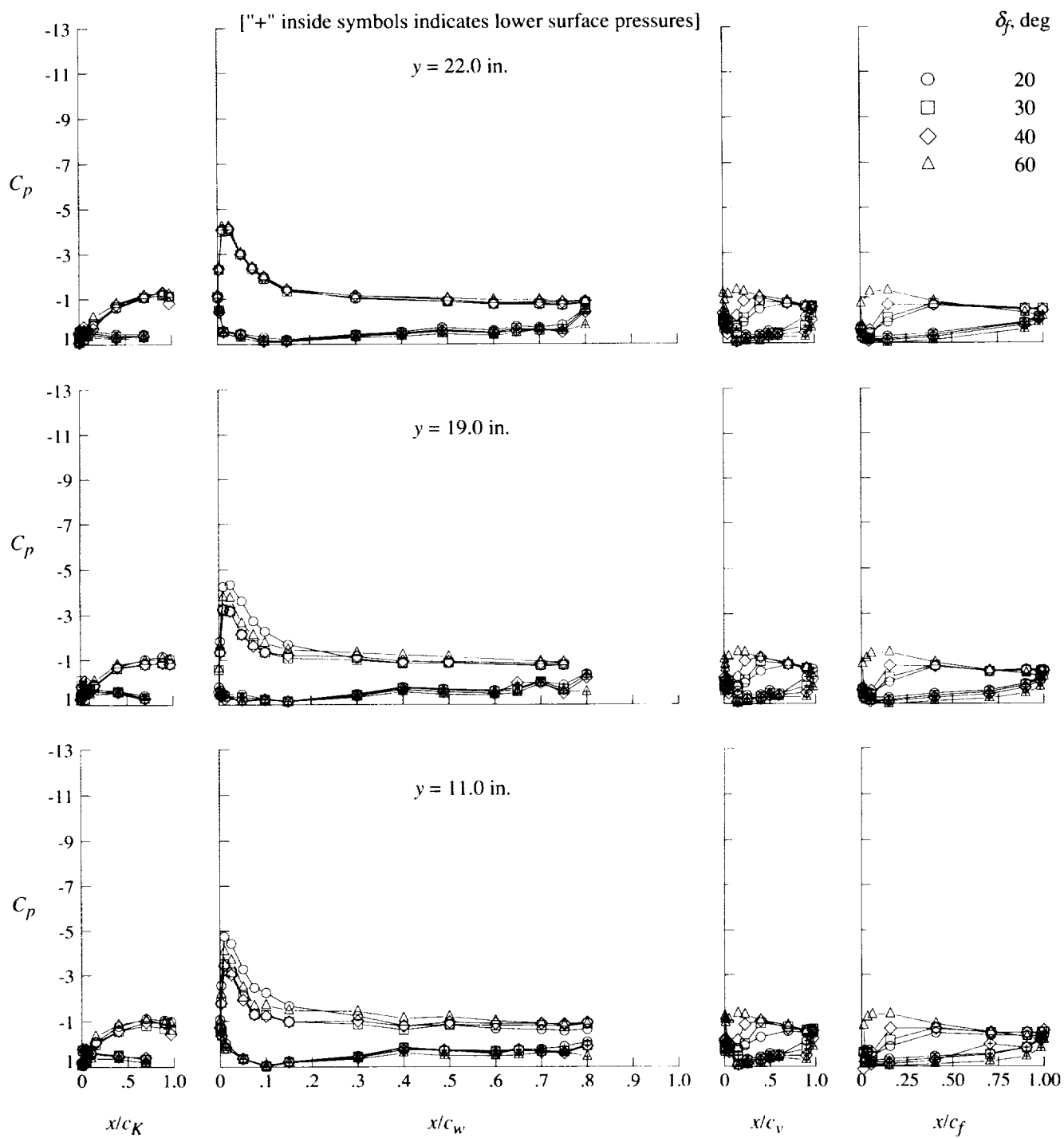
(i) $q = 60$ psf; $\alpha = 16^\circ$.

Figure 37. Continued.



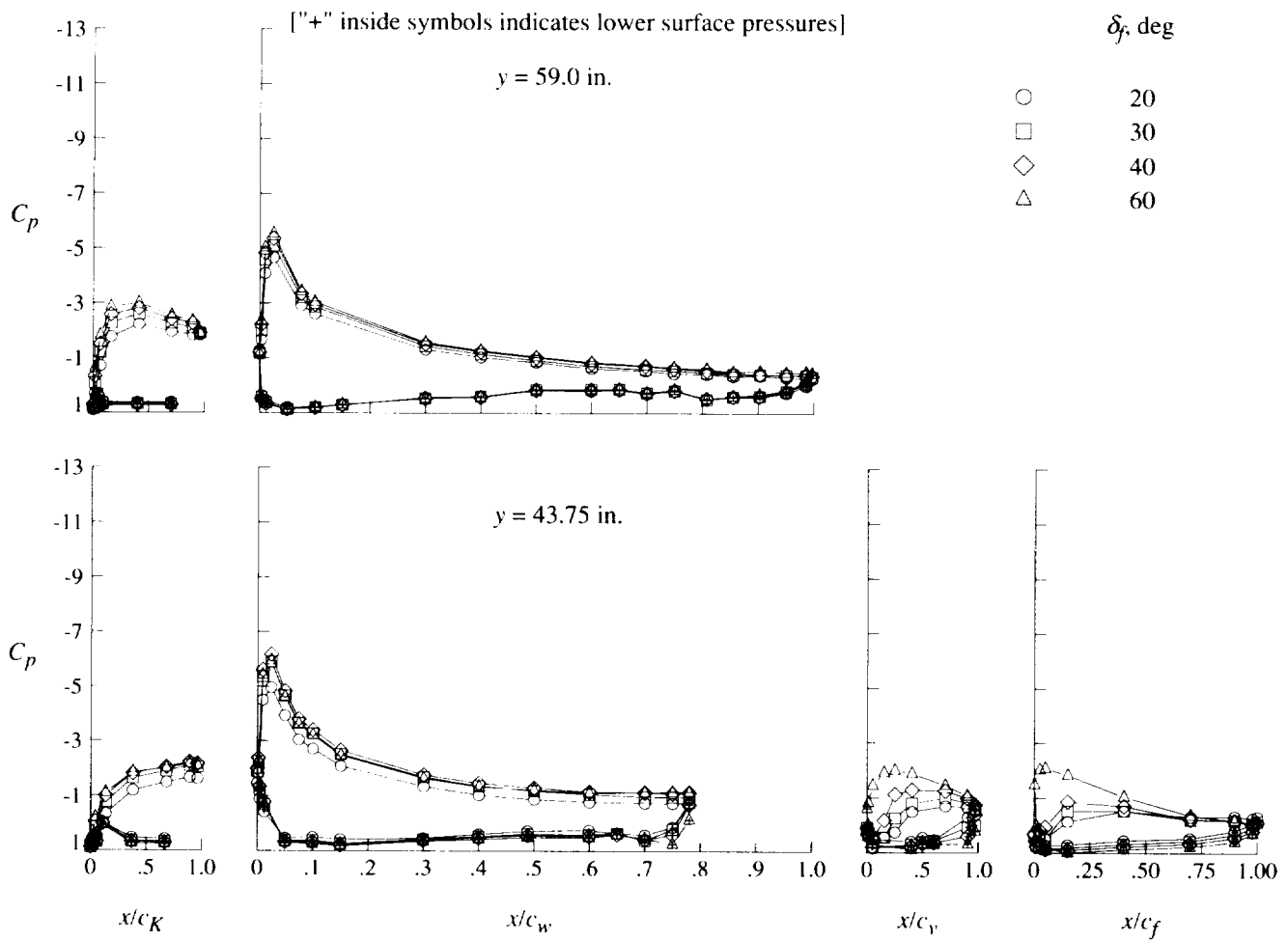
(i) Concluded.

Figure 37. Continued.



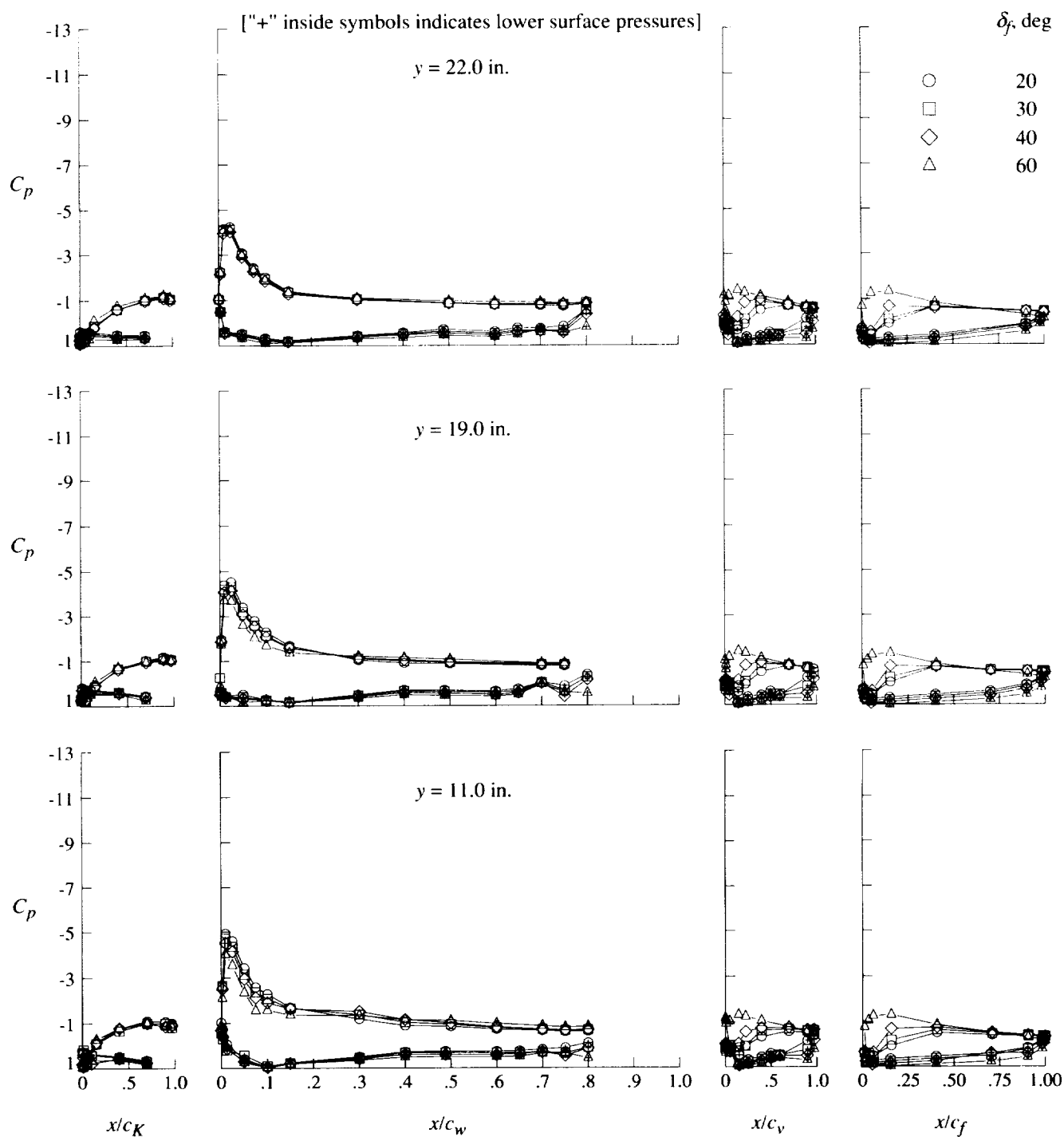
(j) $q = 20$ psf; $\alpha = 20^\circ$.

Figure 37. Continued.



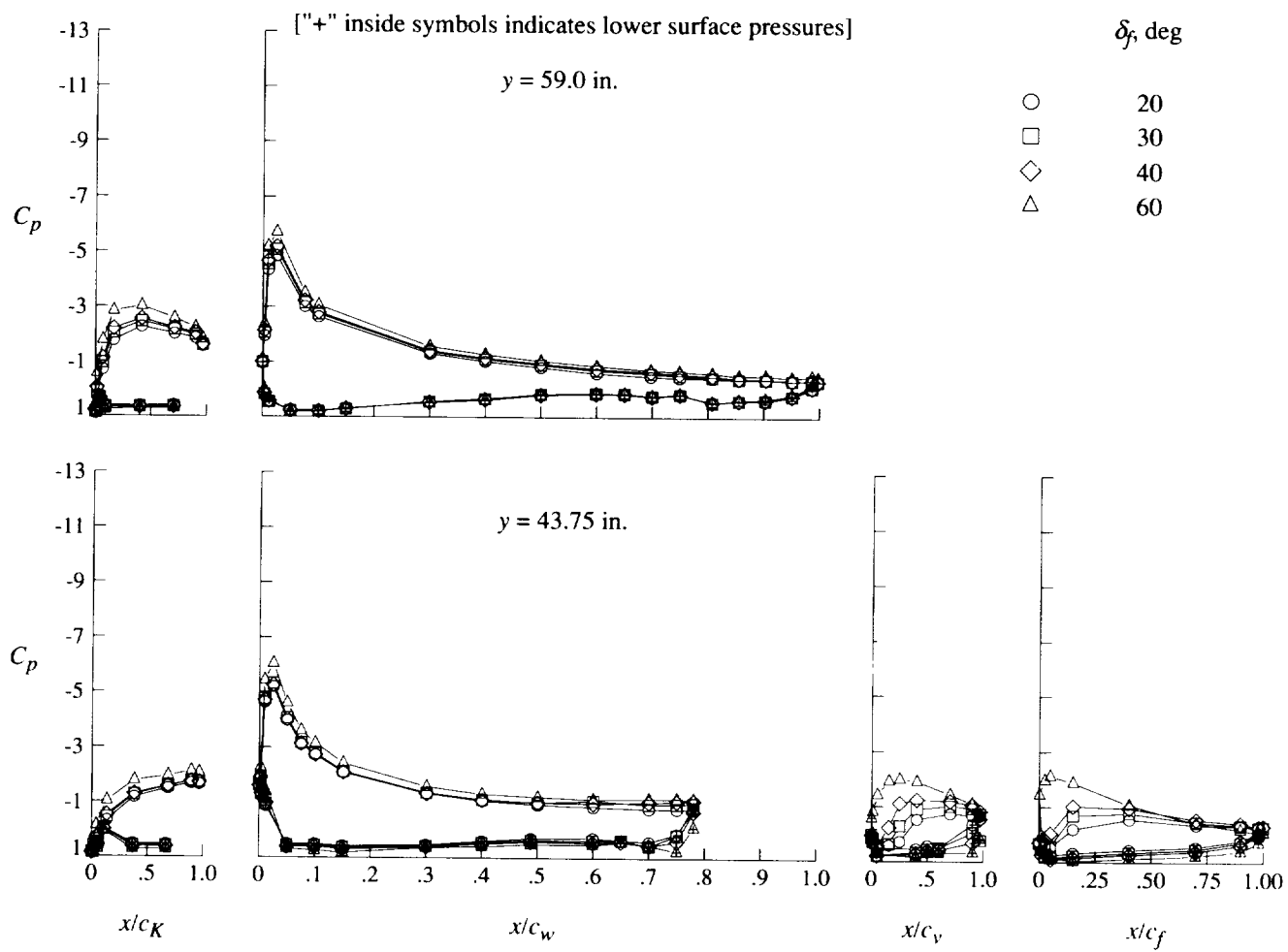
(j) Concluded.

Figure 37. Continued.



(k) $q = 40$ psf; $\alpha = 20^\circ$.

Figure 37. Continued.



(k) Concluded.

Figure 37. Concluded.

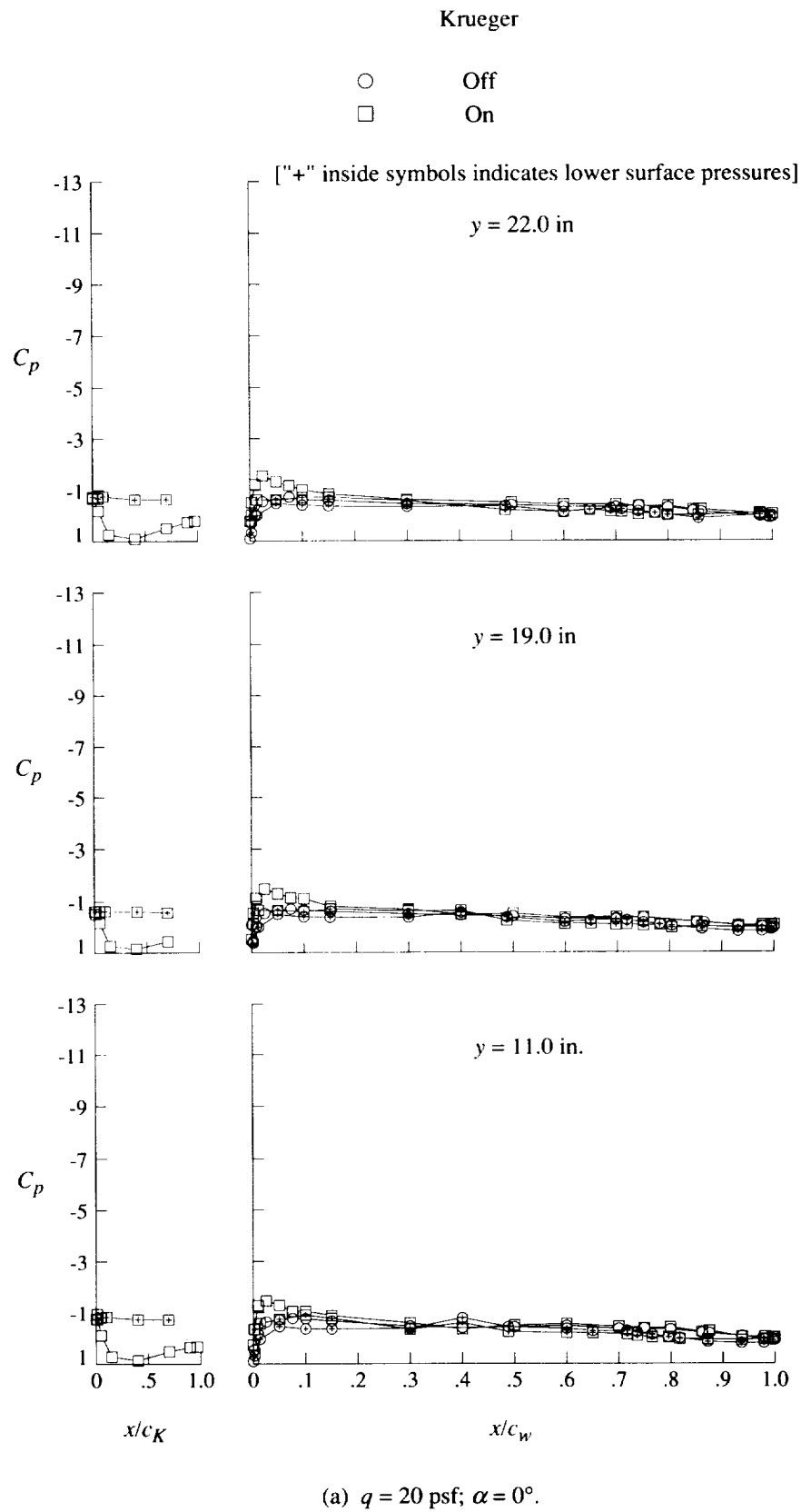
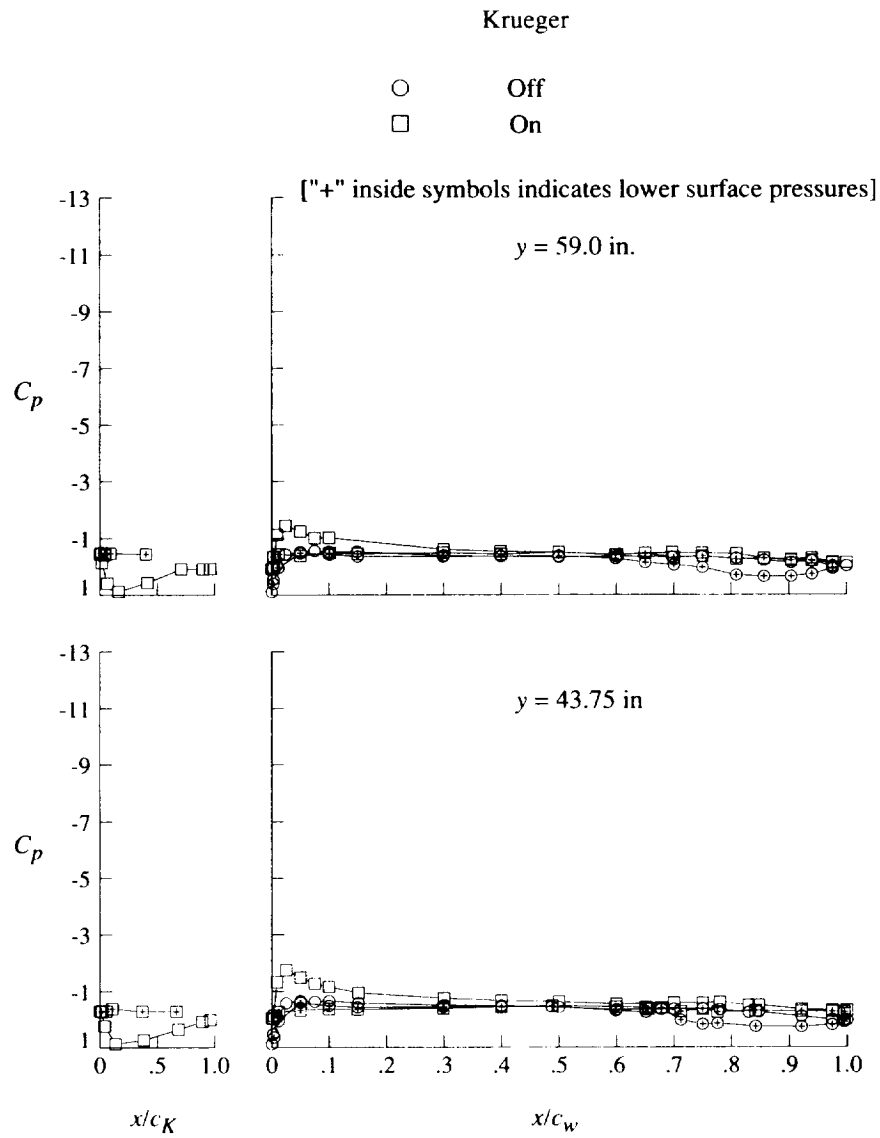
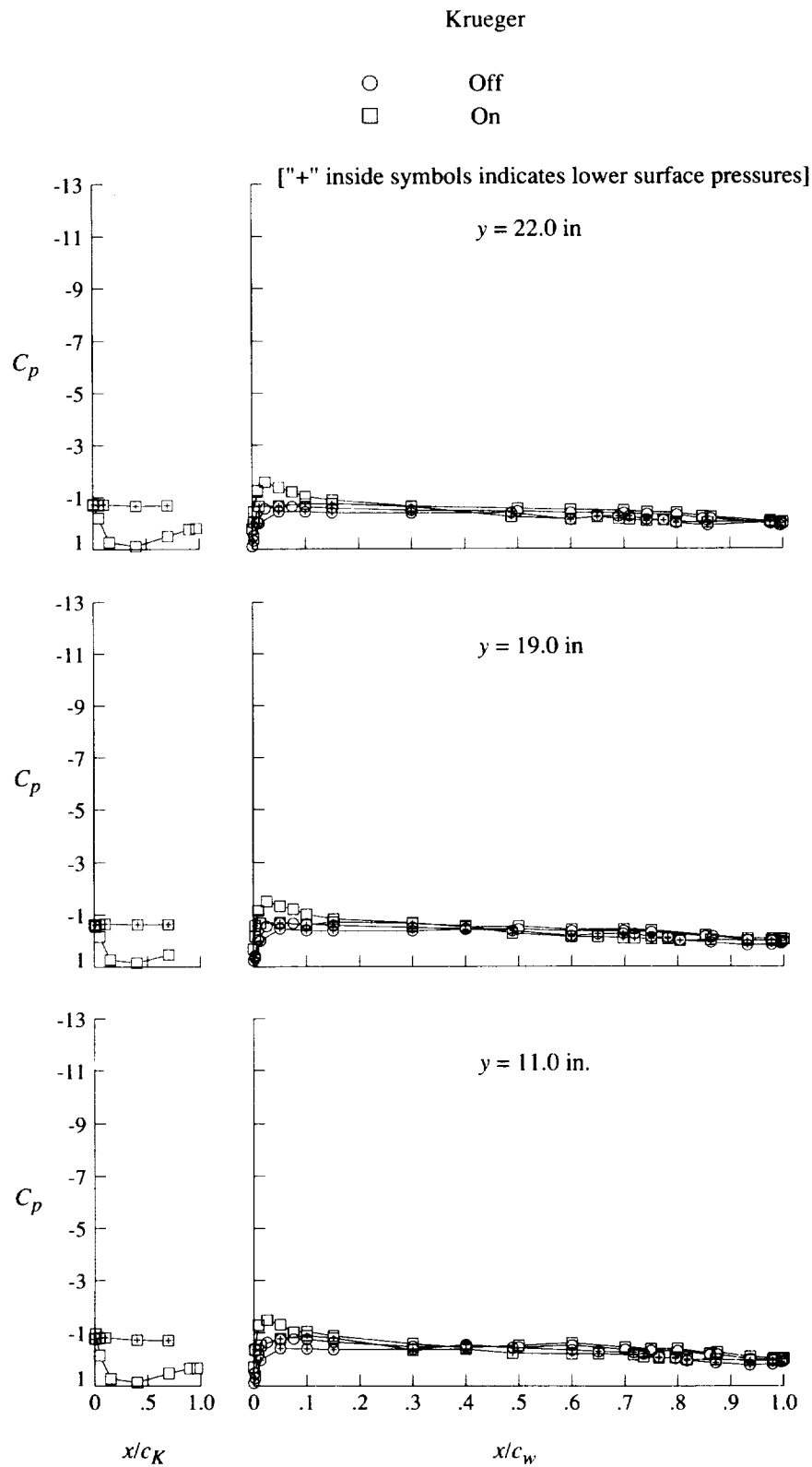


Figure 38. Effect of leading-edge Krueger flap on pressure distributions.



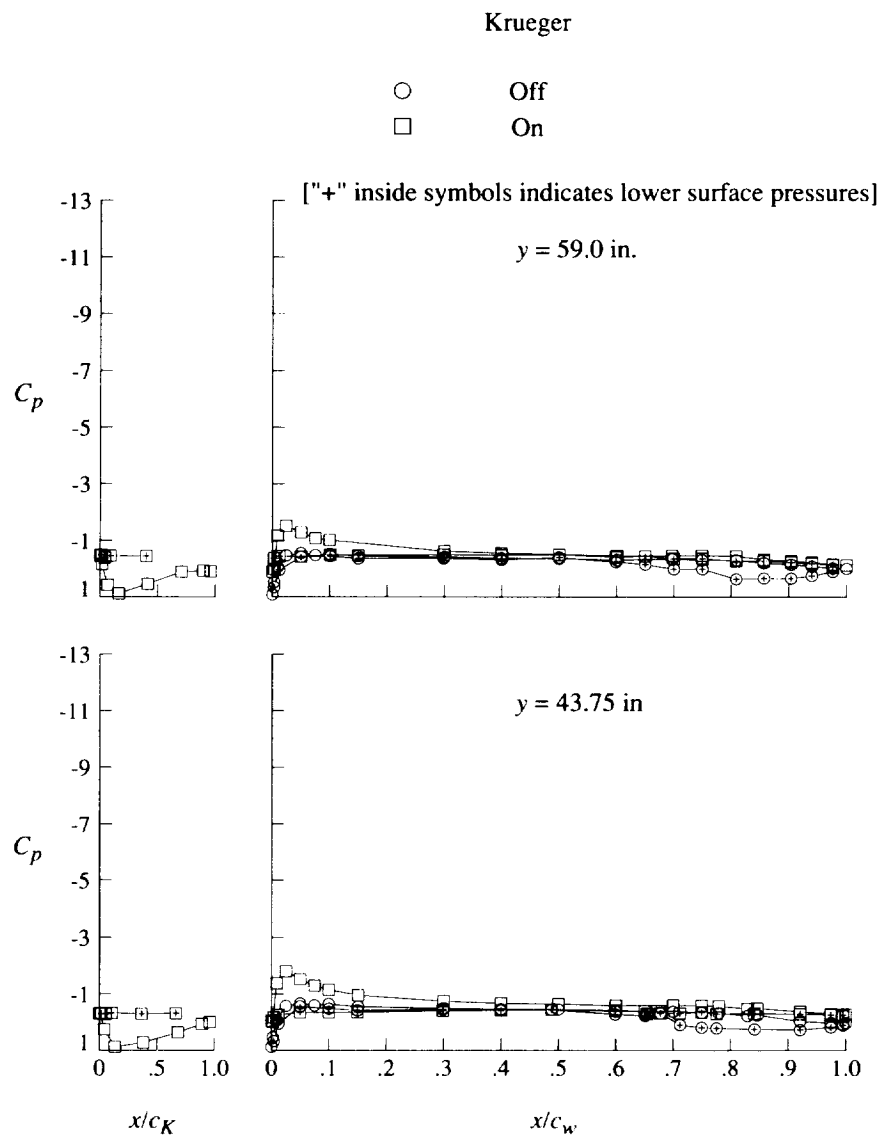
(a) Concluded.

Figure 38. Continued.



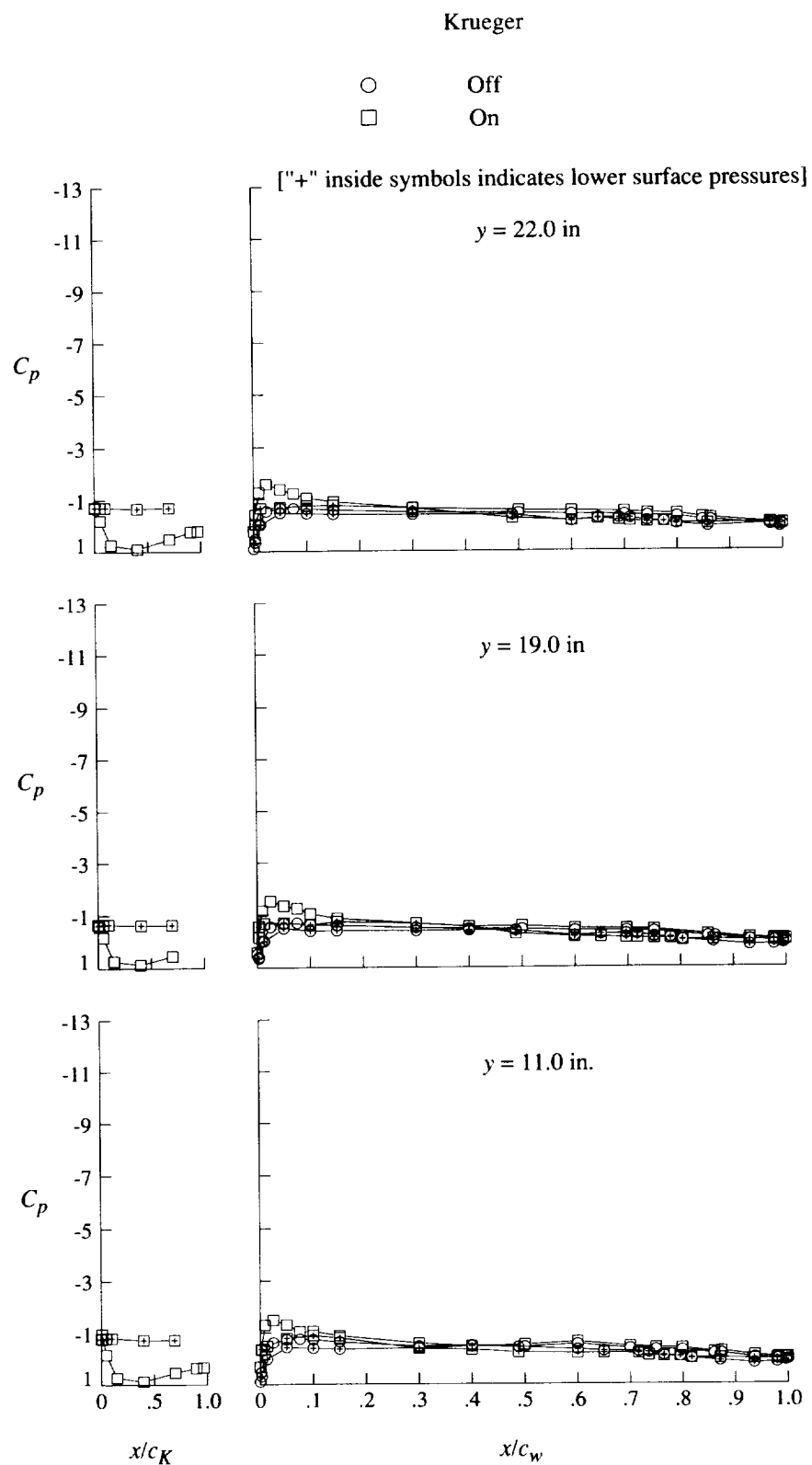
(b) $q = 40$ psf; $\alpha = 0^\circ$.

Figure 38. Continued.



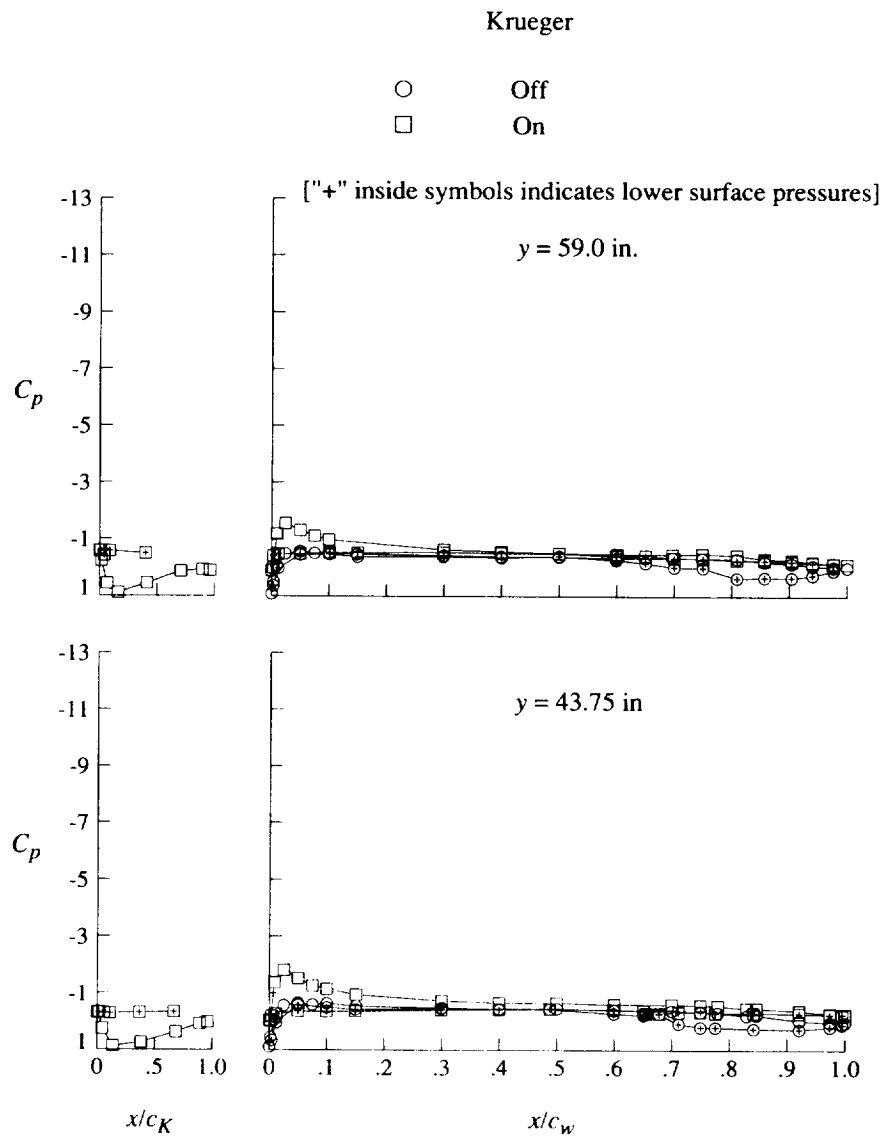
(b) Concluded.

Figure 38. Continued.



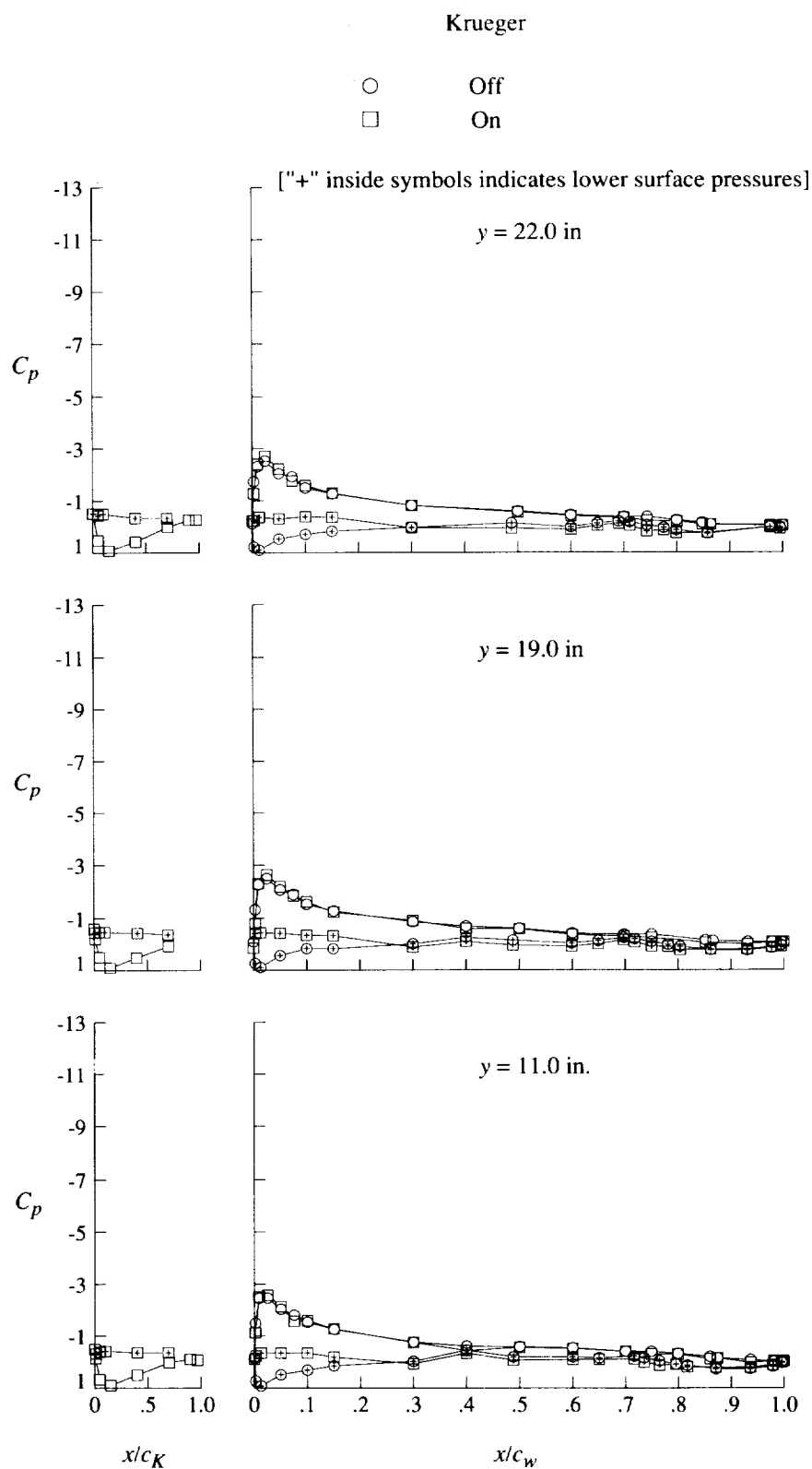
(c) $q = 60$ psf; $\alpha = 0^\circ$.

Figure 38. Continued.



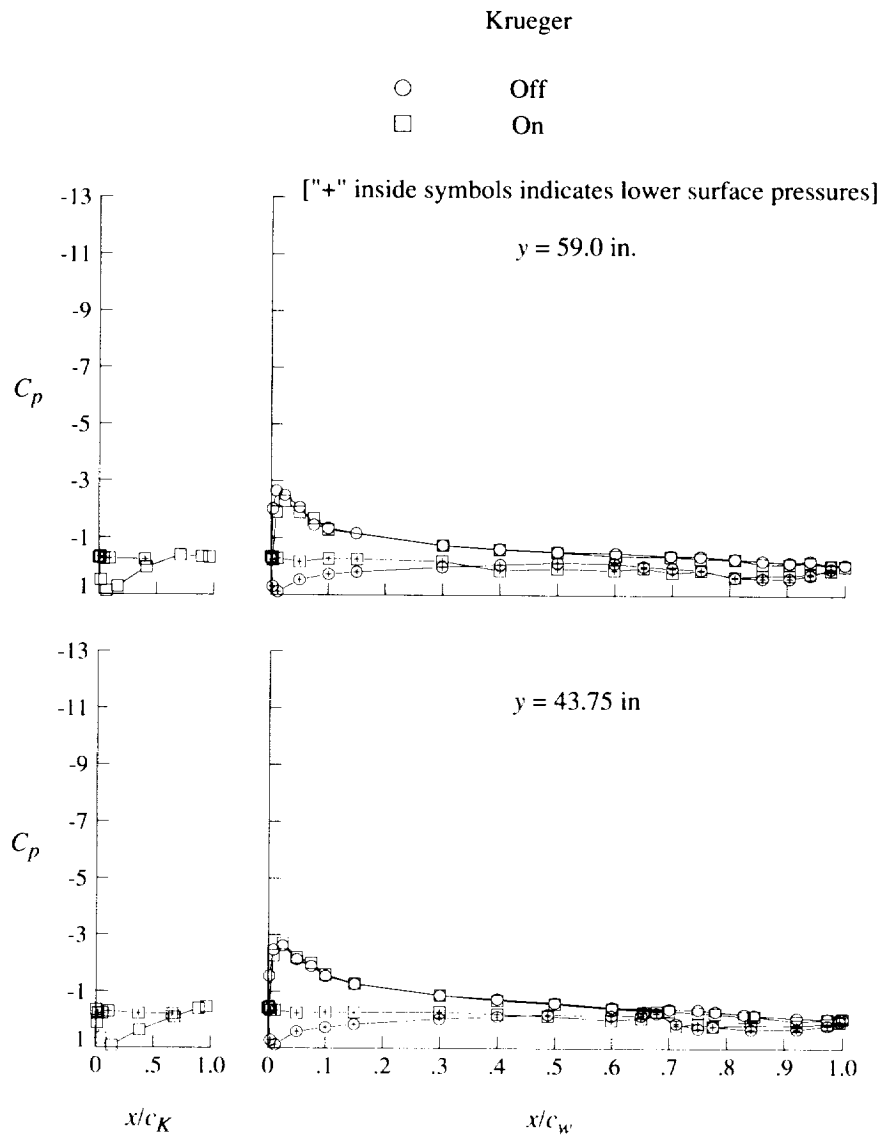
(c) Concluded.

Figure 38. Continued.



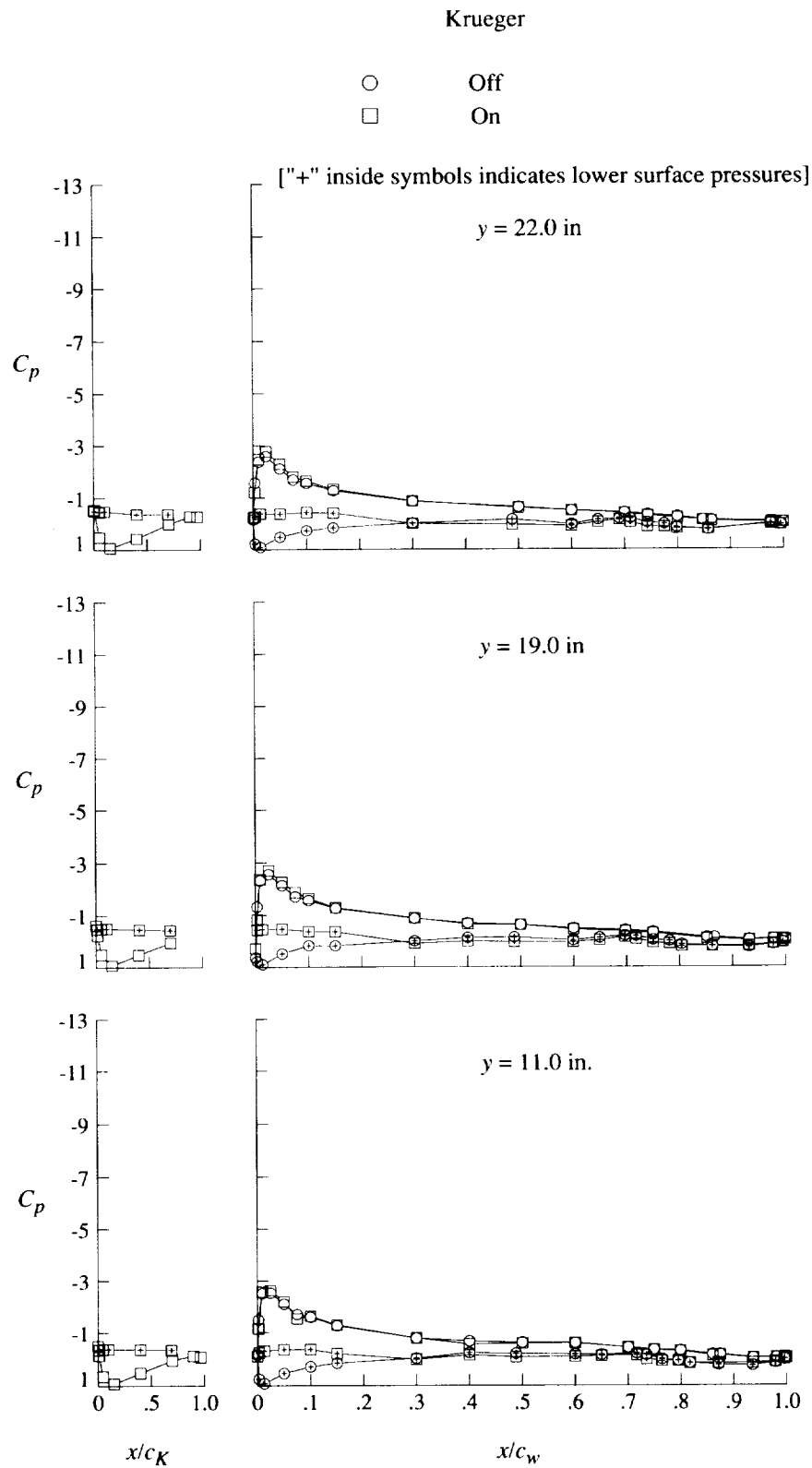
(d) $q = 20$ psf; $\alpha = 8^\circ$.

Figure 38. Continued.



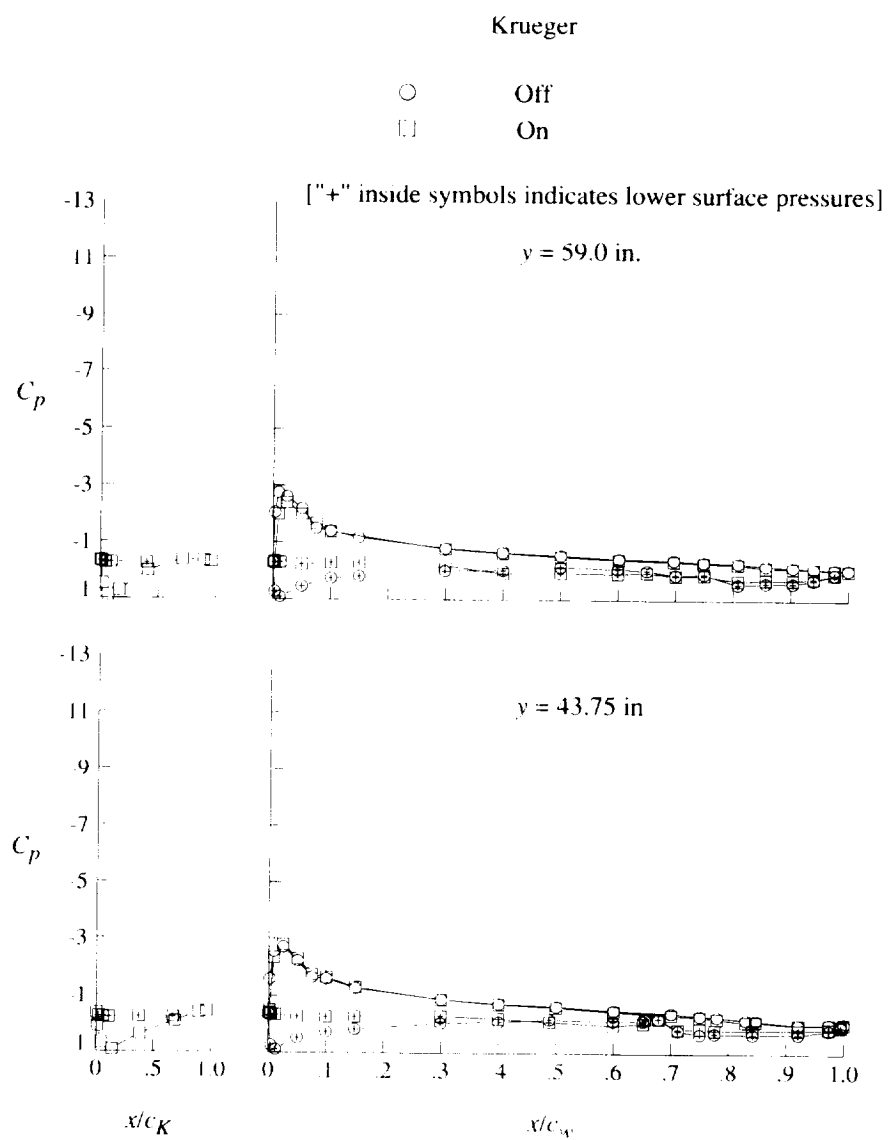
(d) Concluded.

Figure 38. Continued.



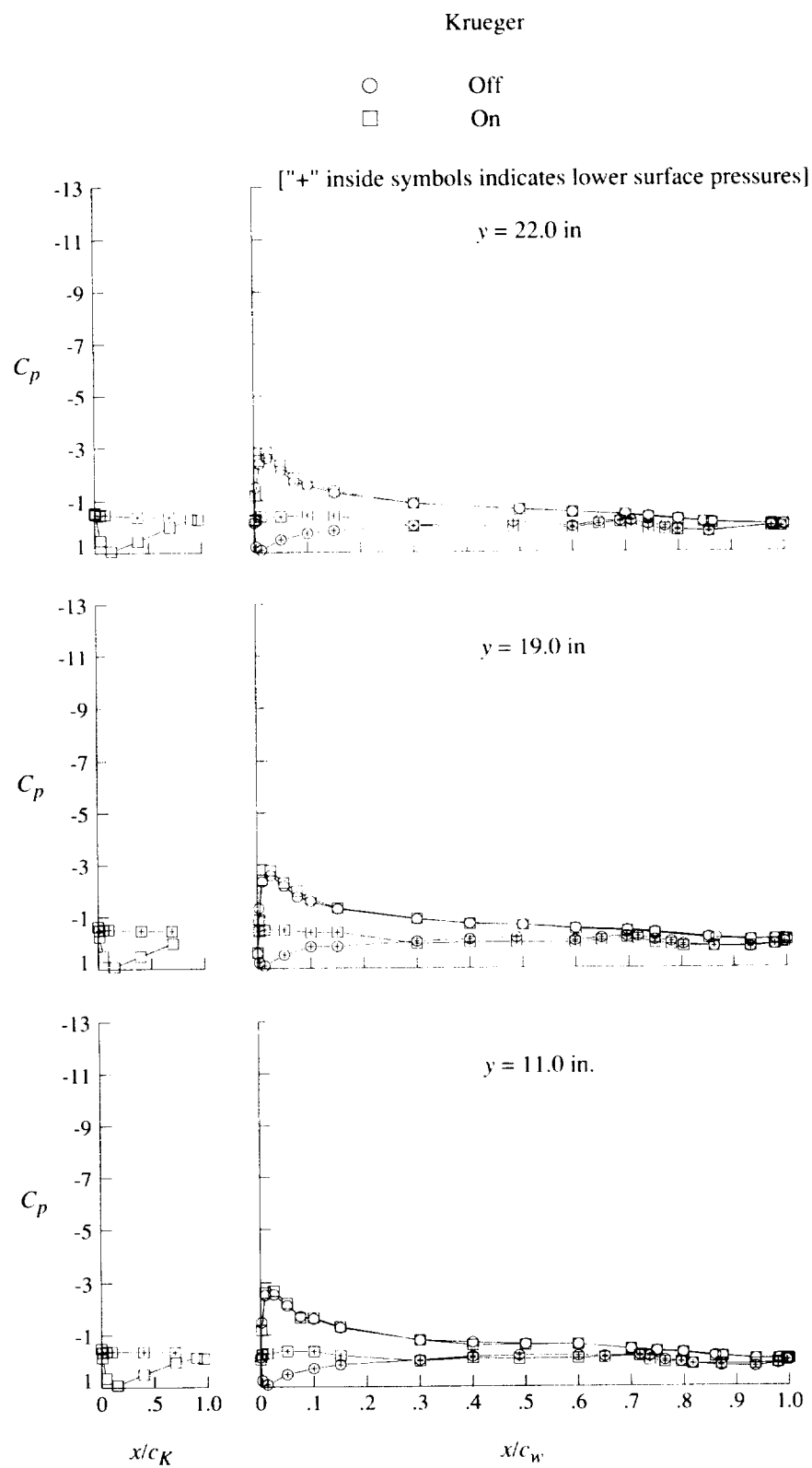
(e) $q = 40$ psf; $\alpha = 8^\circ$.

Figure 38. Continued.



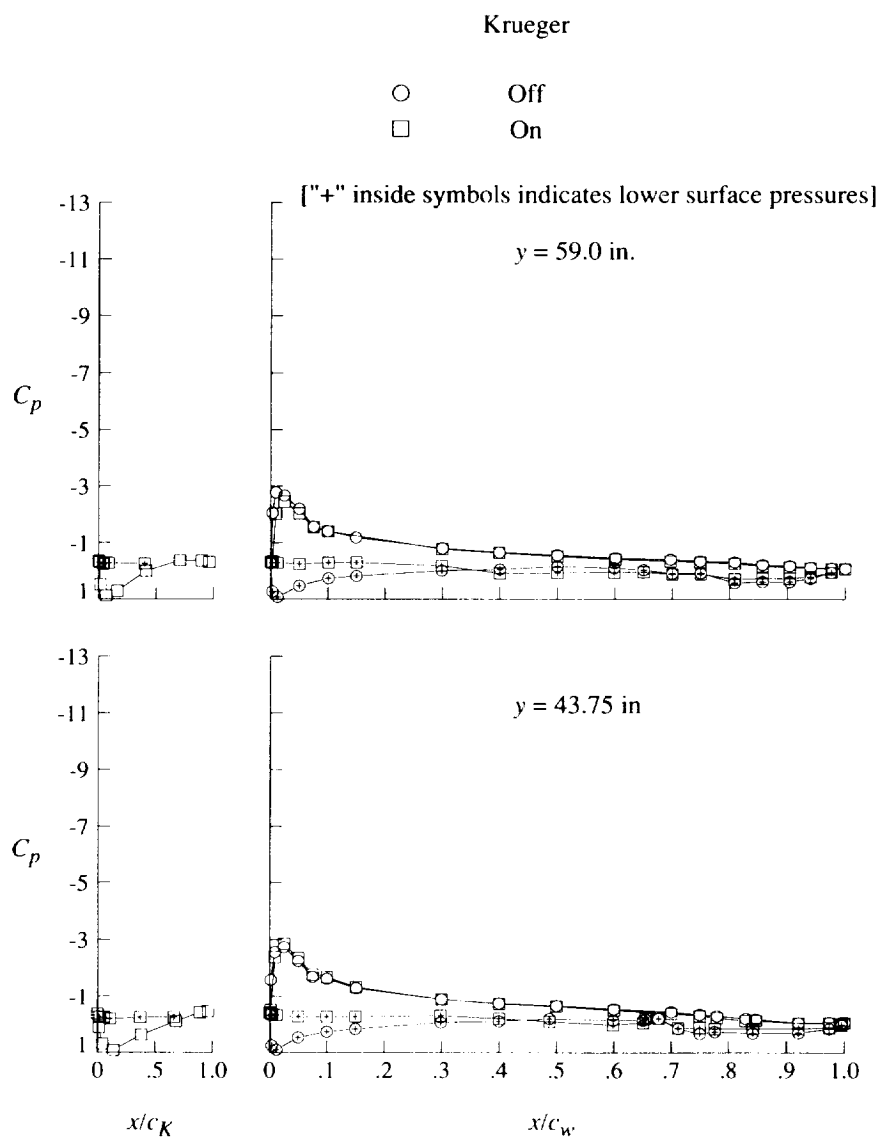
(e) Concluded.

Figure 38. Continued.



(f) $q = 60$ psf; $\alpha = 8^\circ$.

Figure 38. Continued.



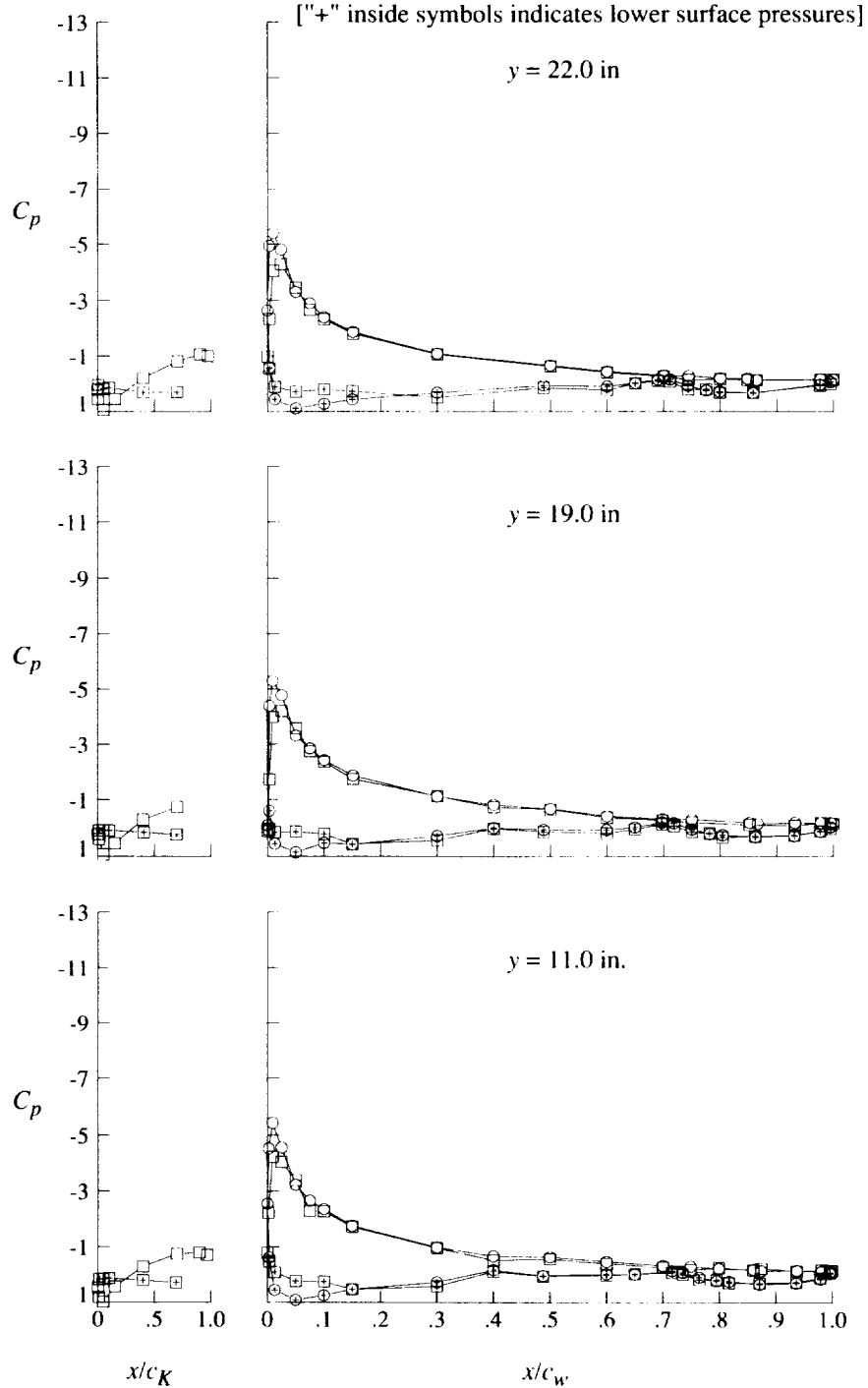
(f) Concluded.

Figure 38. Continued.

Krueger

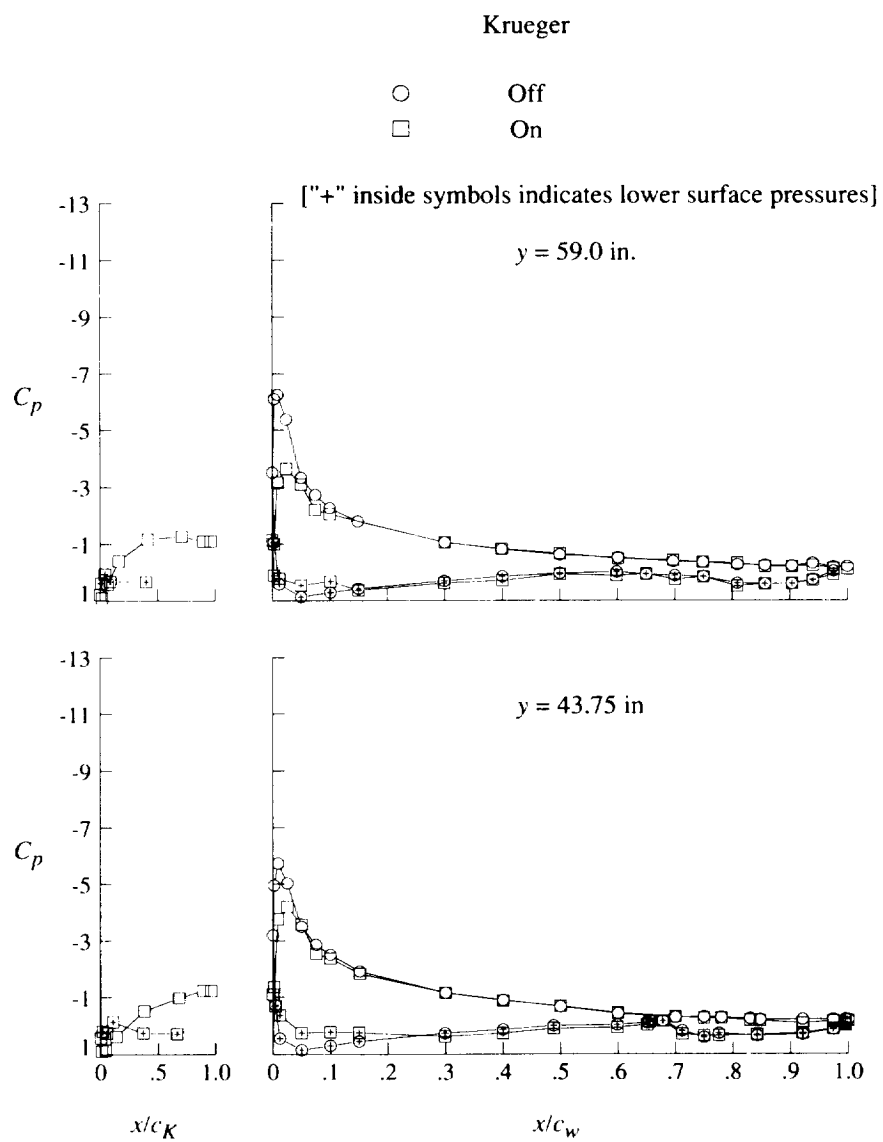
○ Off
□ On

["+" inside symbols indicates lower surface pressures]



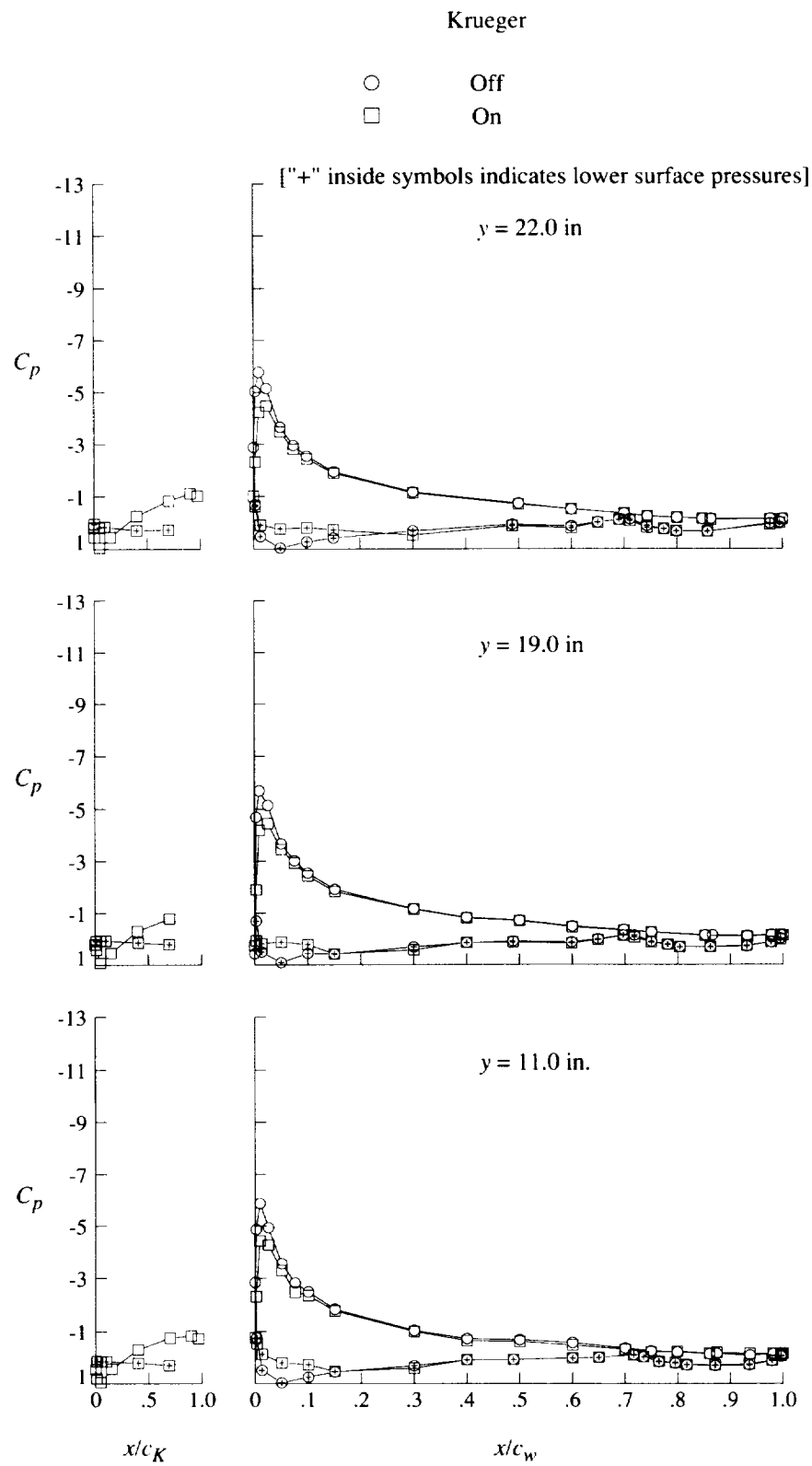
(g) $q = 20$ psf; $\alpha = 16^\circ$.

Figure 38. Continued.



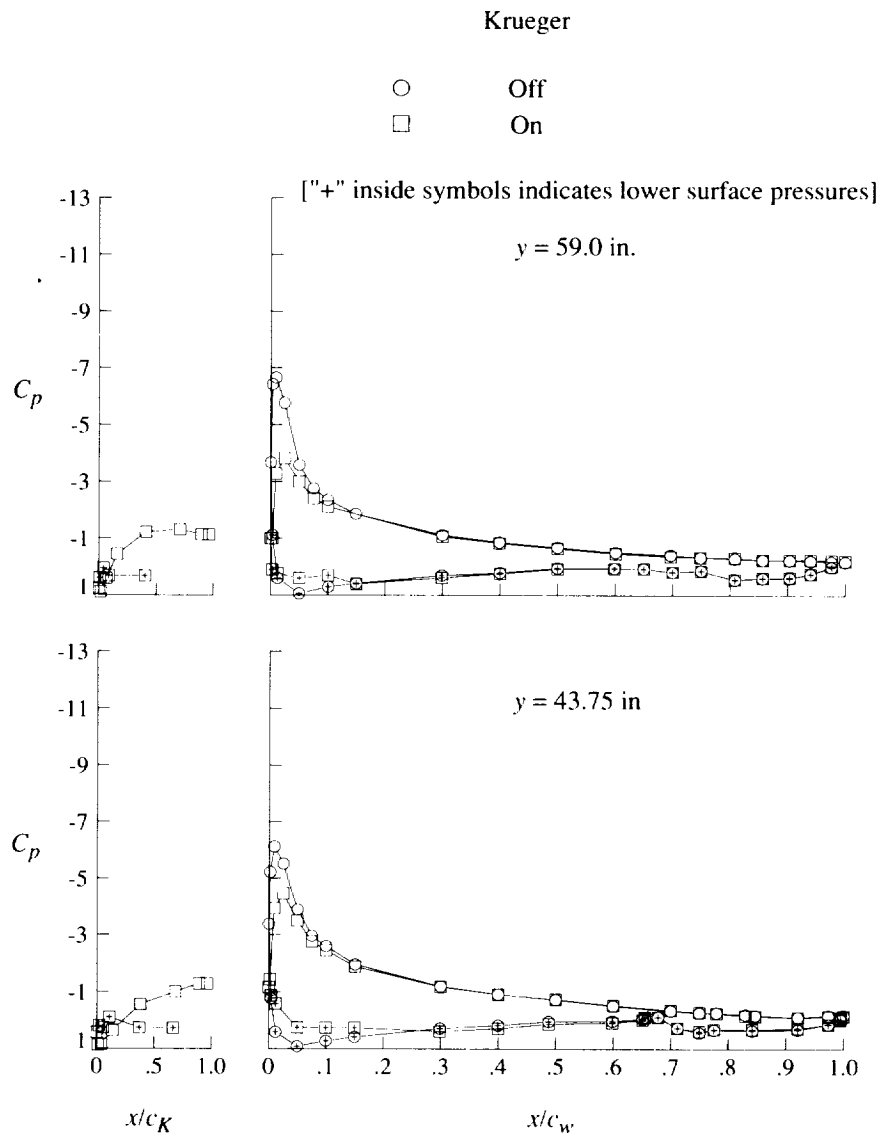
(g) Concluded.

Figure 38. Continued.



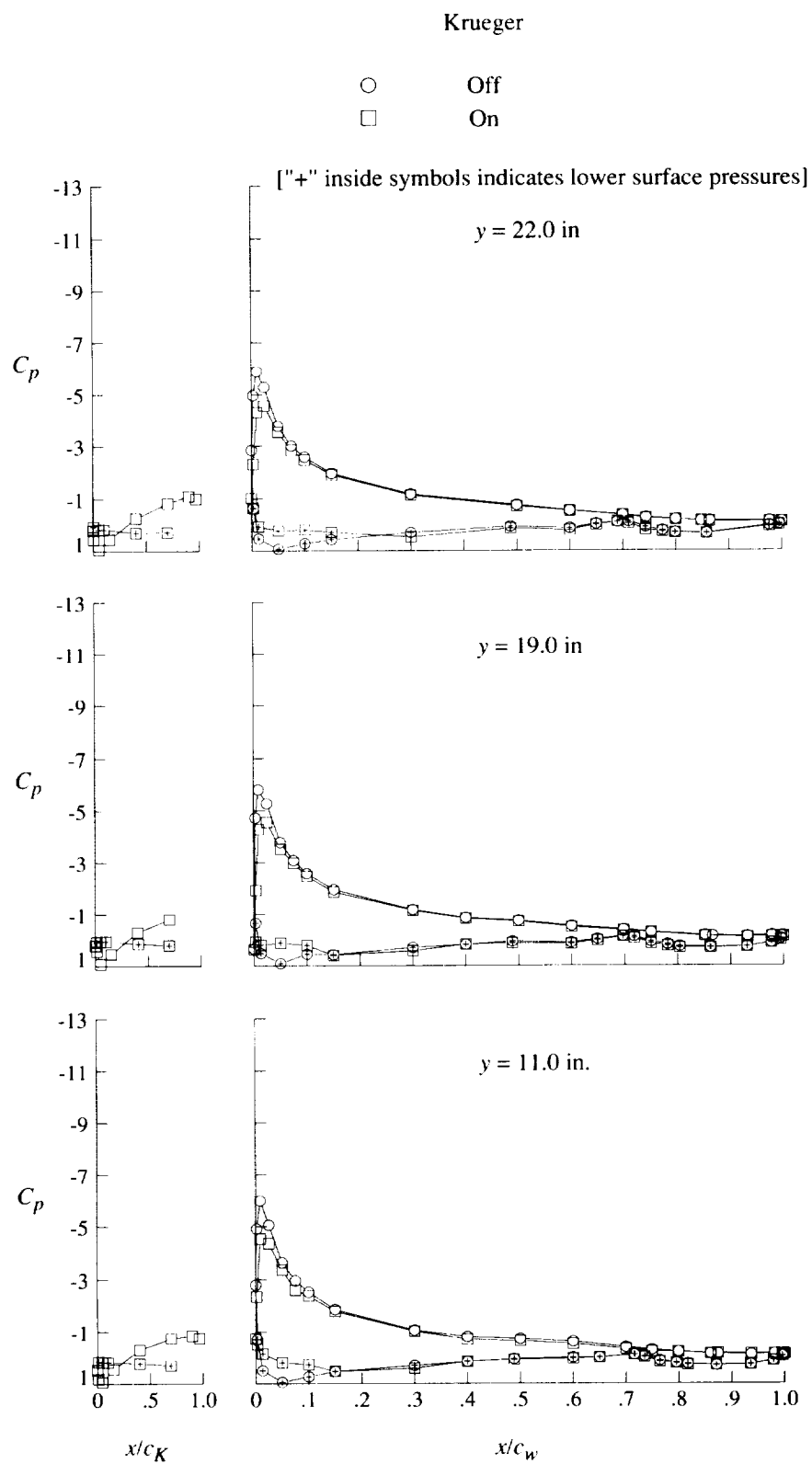
(h) $q = 40$ psf; $\alpha = 16^\circ$.

Figure 38. Continued.



(h) Concluded.

Figure 38. Continued.

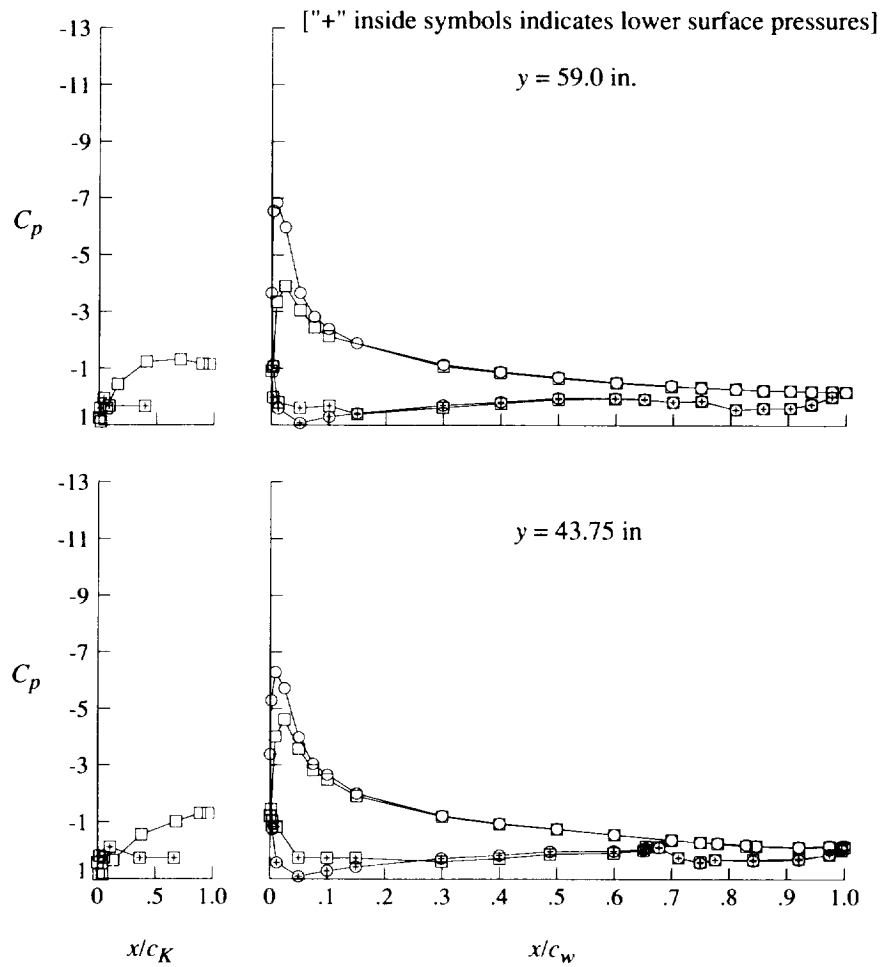


(i) $q = 60$ psf; $\alpha = 16^\circ$.

Figure 38. Continued.

Krueger

○ Off
□ On



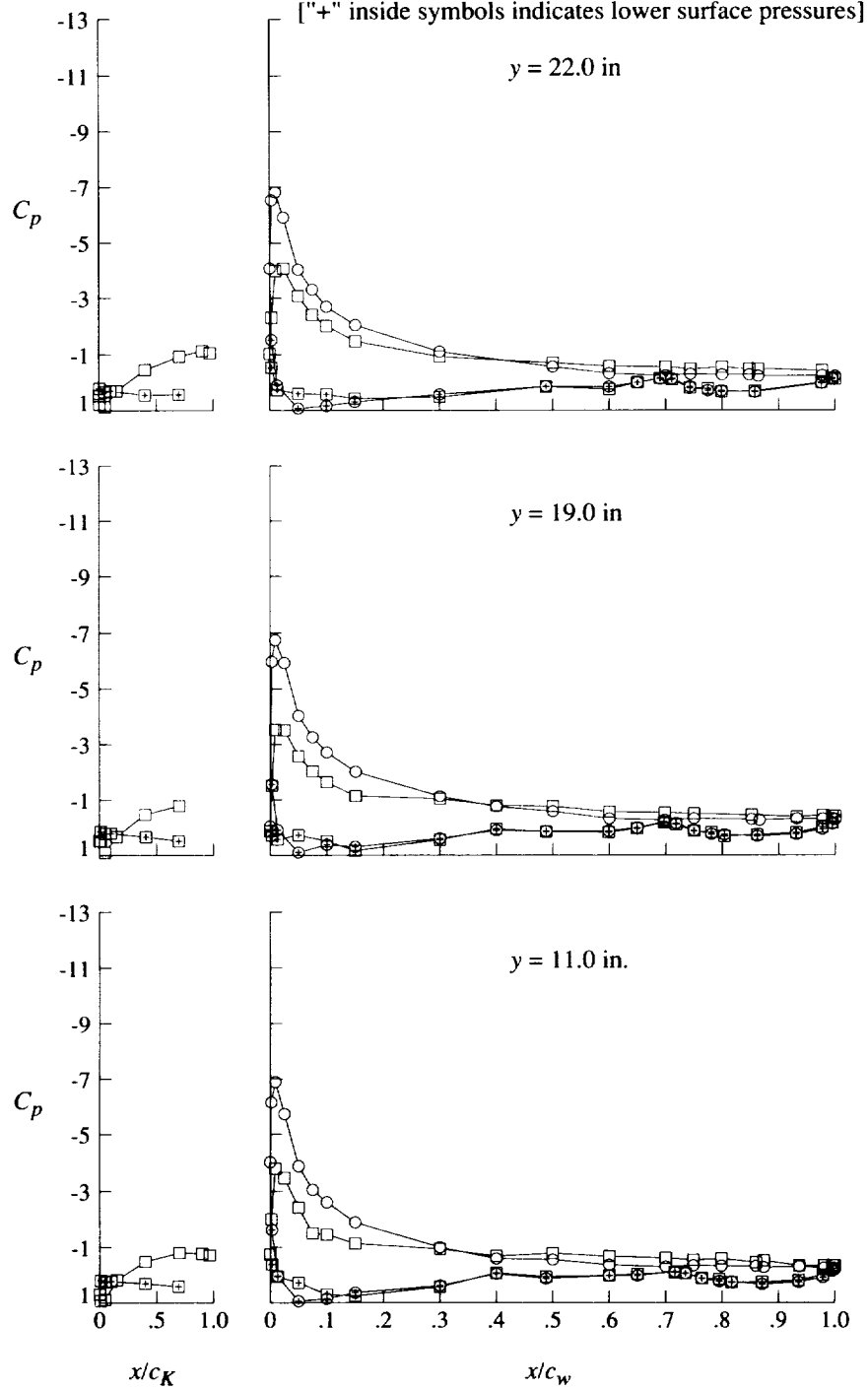
(i) Concluded.

Figure 38. Continued.

Krueger

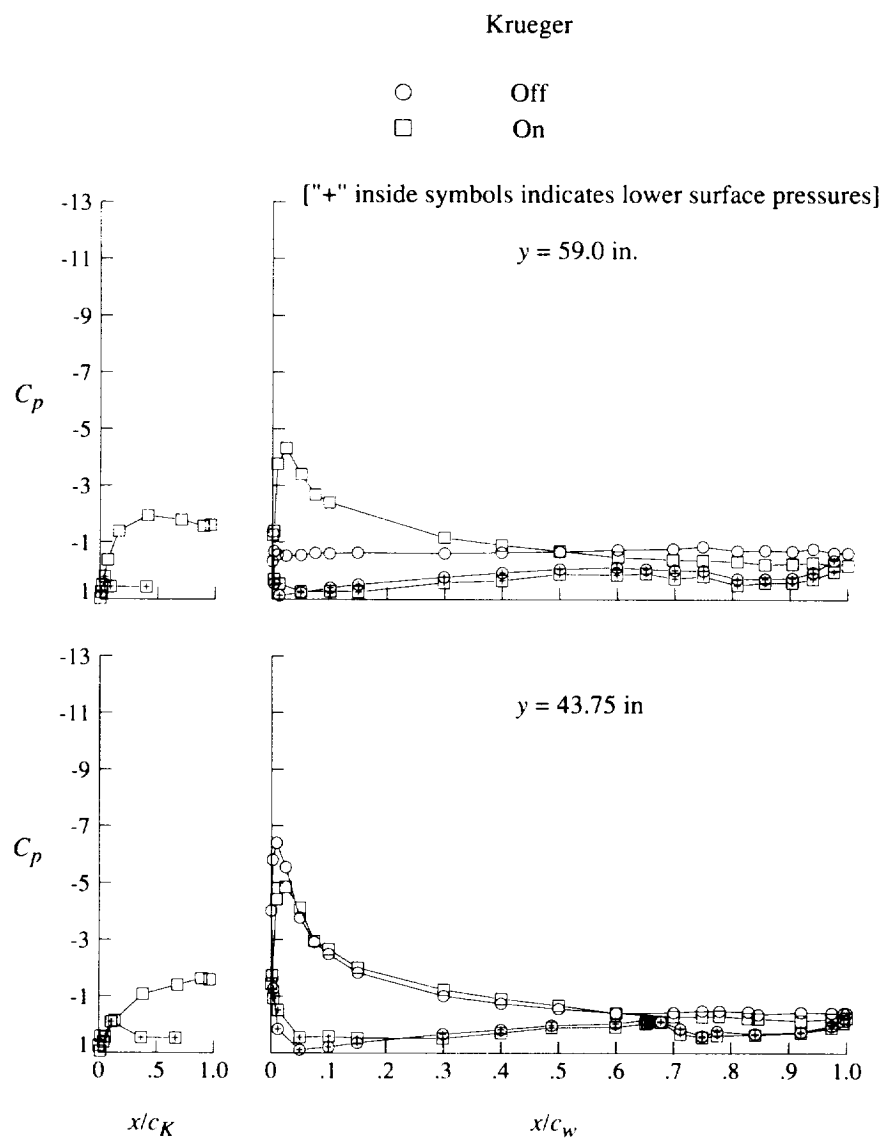
○ Off
□ On

["+" inside symbols indicates lower surface pressures]



(j) $q = 20$ psf; $\alpha = 20^\circ$.

Figure 38. Continued.

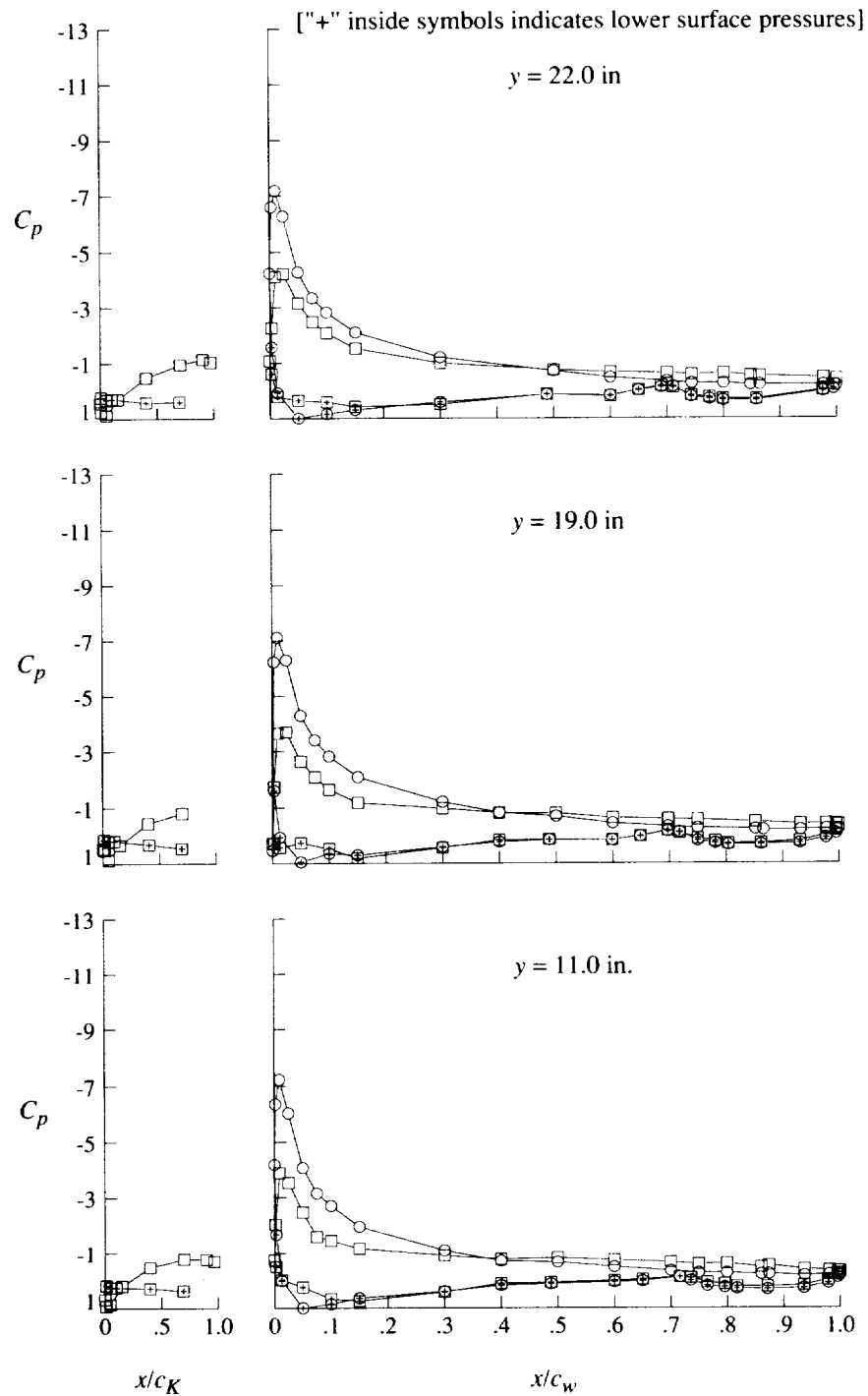


(j) Concluded.

Figure 38. Continued.

Krueger

○ Off
□ On

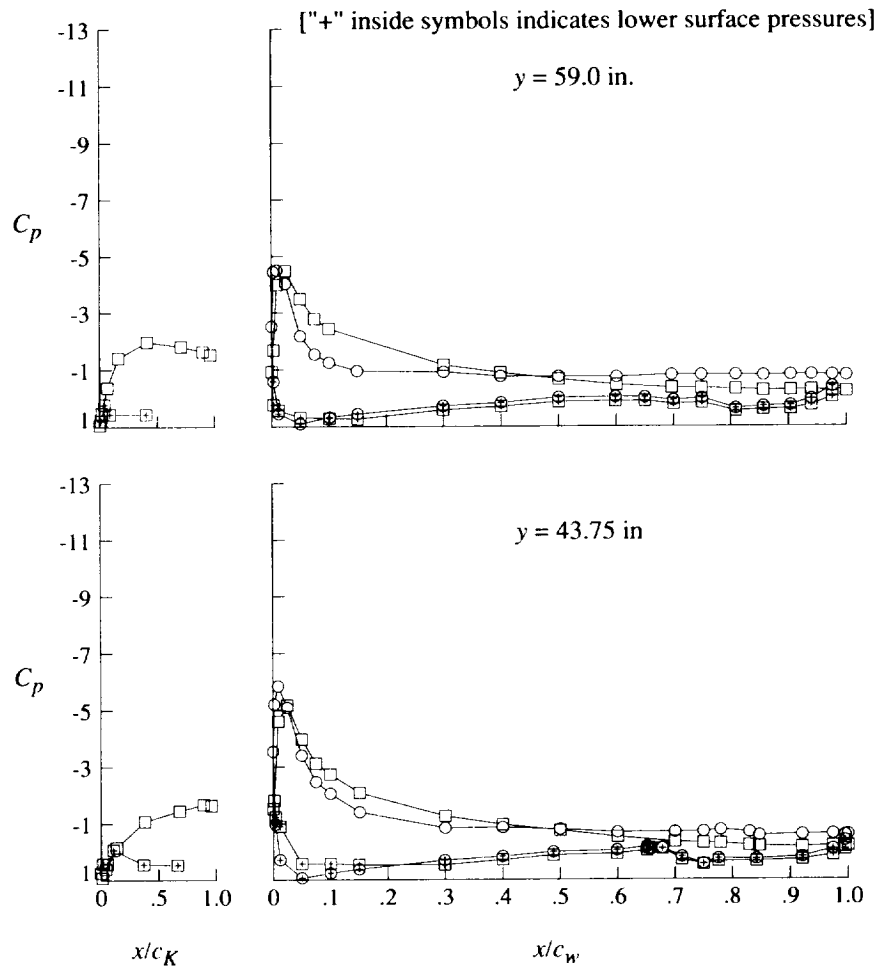


(k) $q = 40$ psf; $\alpha = 20^\circ$.

Figure 38. Continued.

Krueger

○ Off
□ On

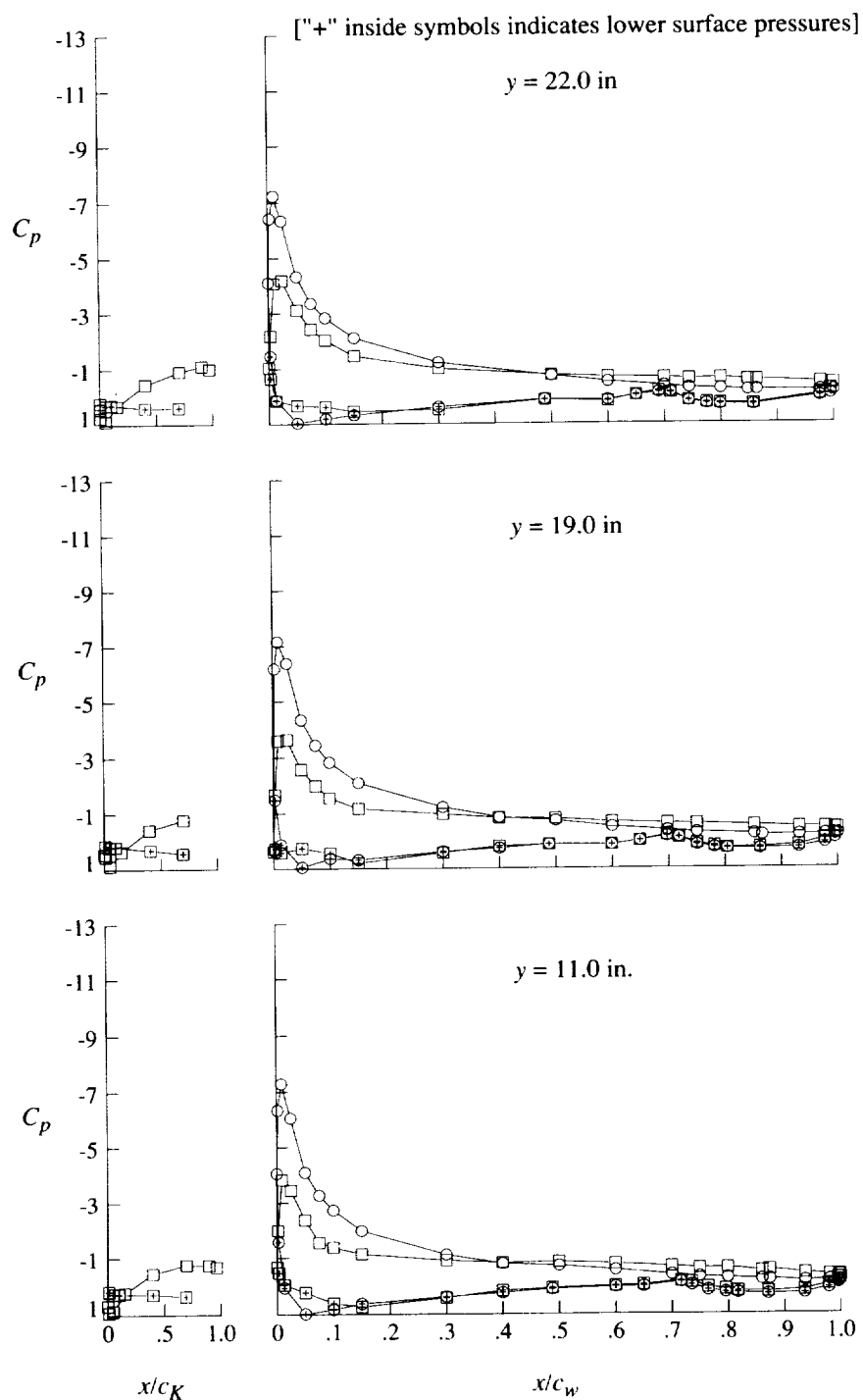


(k) Concluded.

Figure 38. Continued.

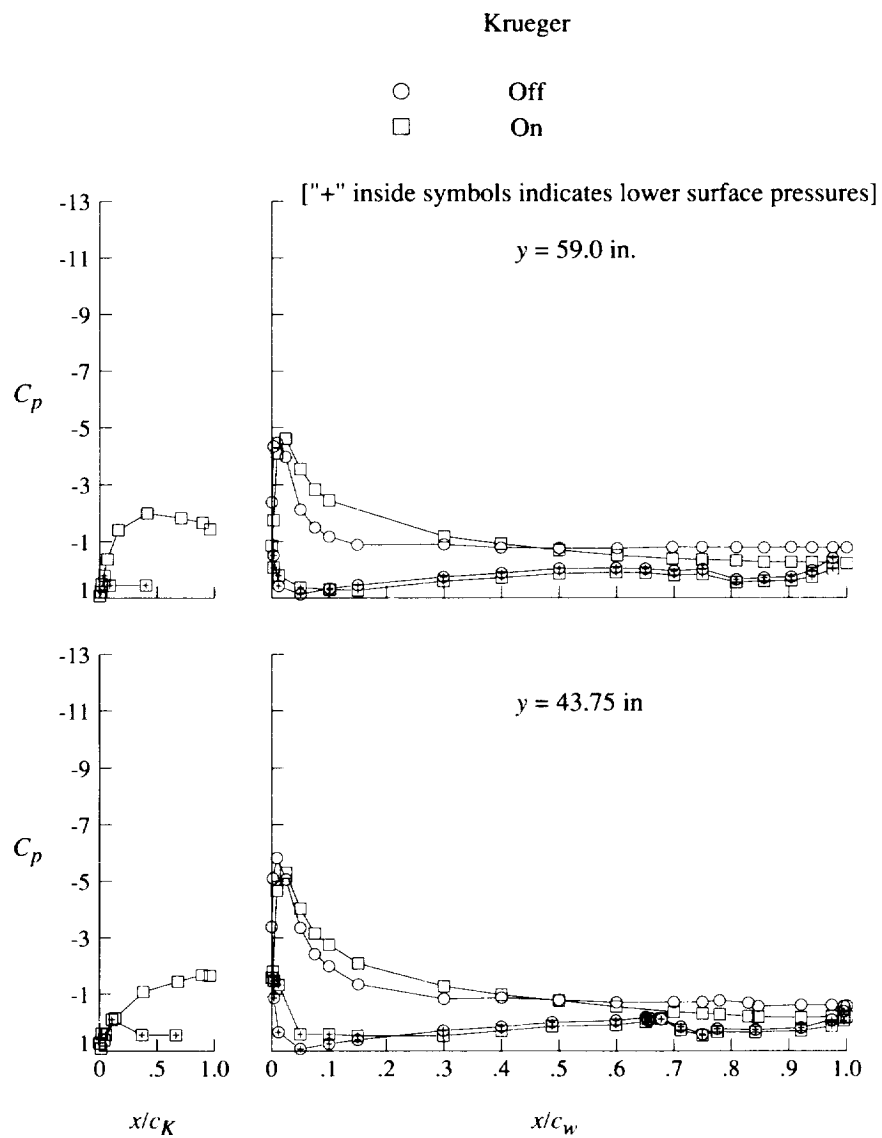
Krueger

○ Off
□ On



(1) $q = 60$ psf; $\alpha = 20^\circ$.

Figure 38. Continued.



(I) Concluded.

Figure 38. Concluded.

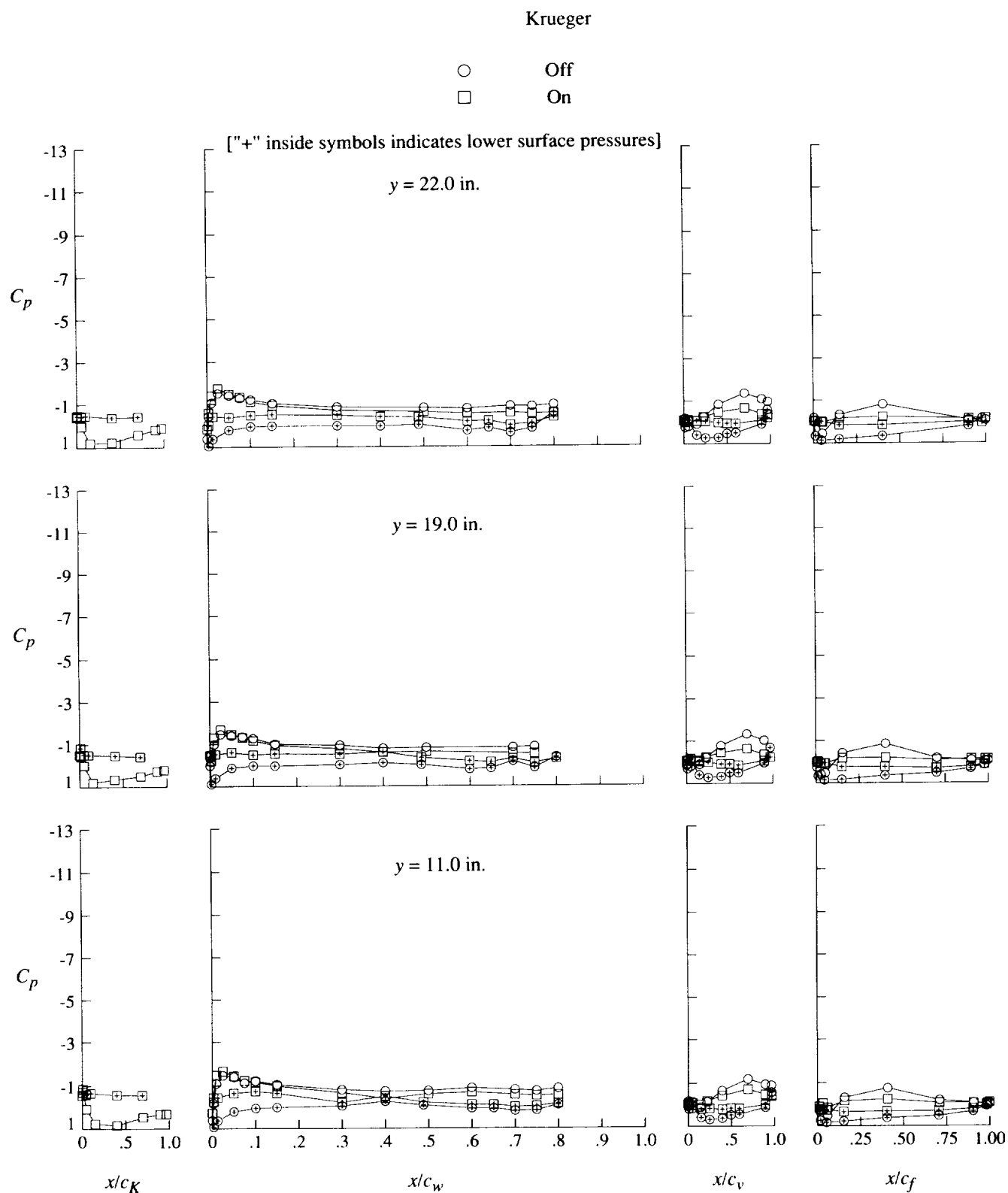


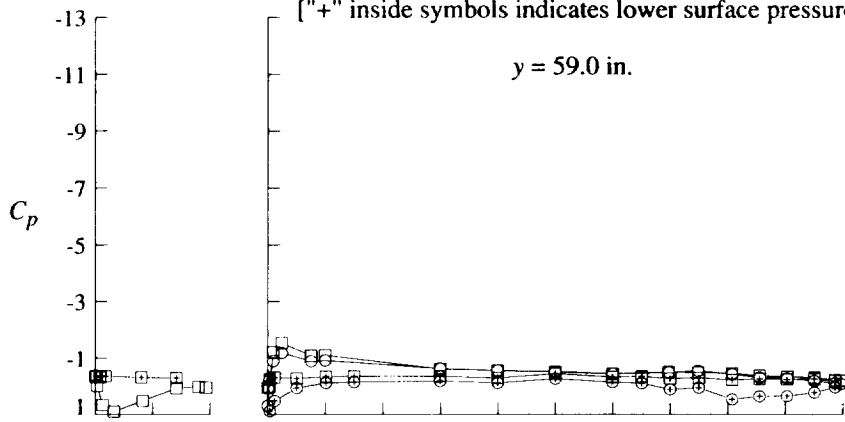
Figure 39. Effect of leading-edge Krueger flap on pressure distributions for high-lift configuration at $\delta_f = 30^\circ$.

Krueger

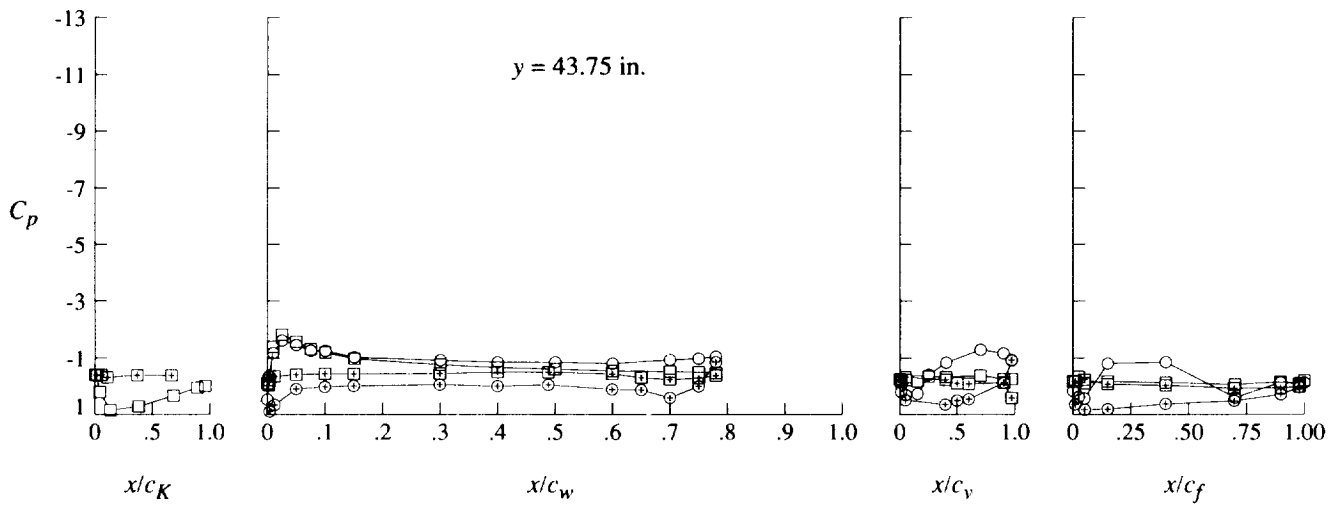
○ Off
□ On

["+" inside symbols indicates lower surface pressures]

$y = 59.0$ in.



$y = 43.75$ in.



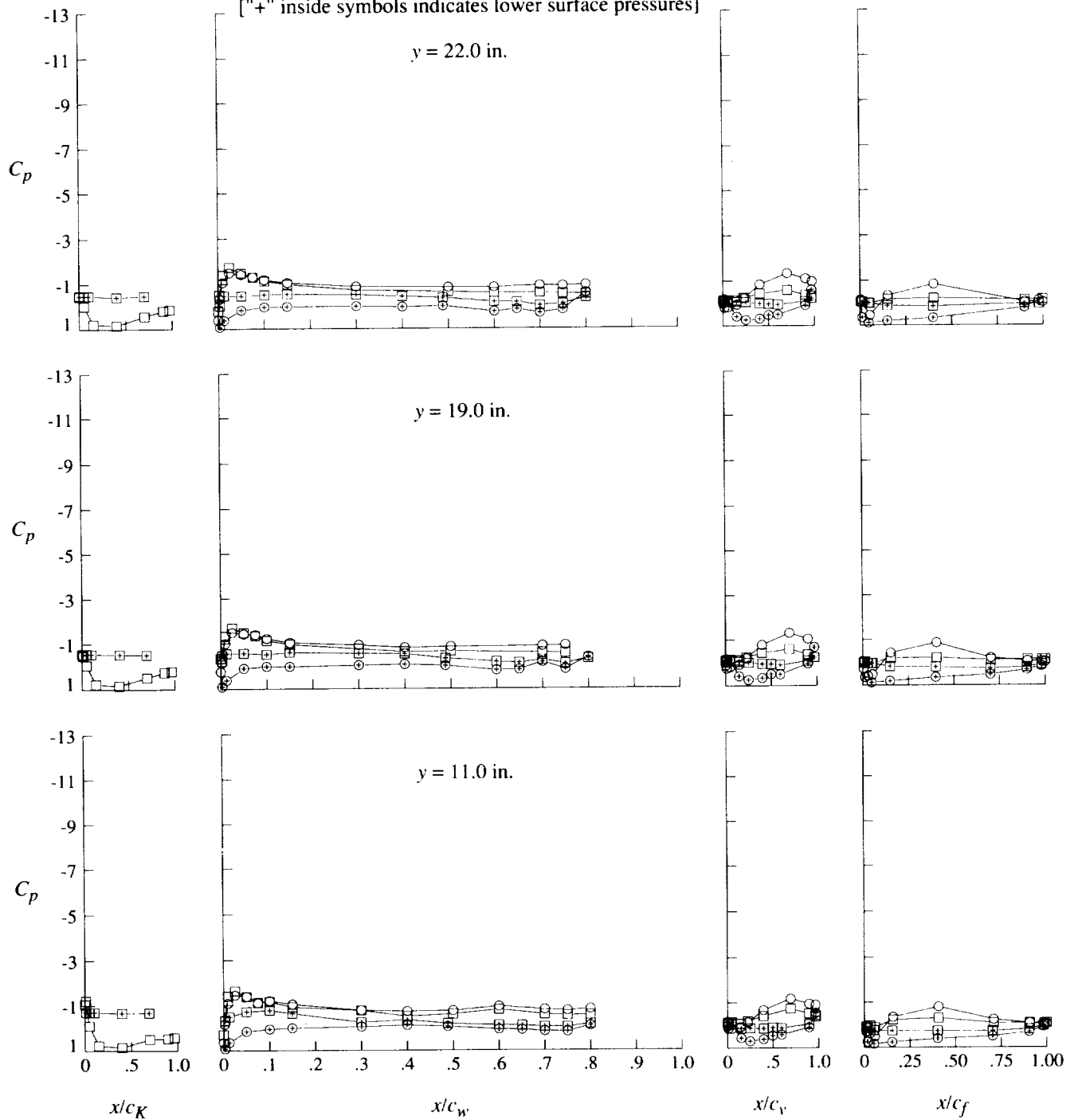
(a) Concluded.

Figure 39. Continued.

Krueger

○ Off
□ On

["+" inside symbols indicates lower surface pressures]



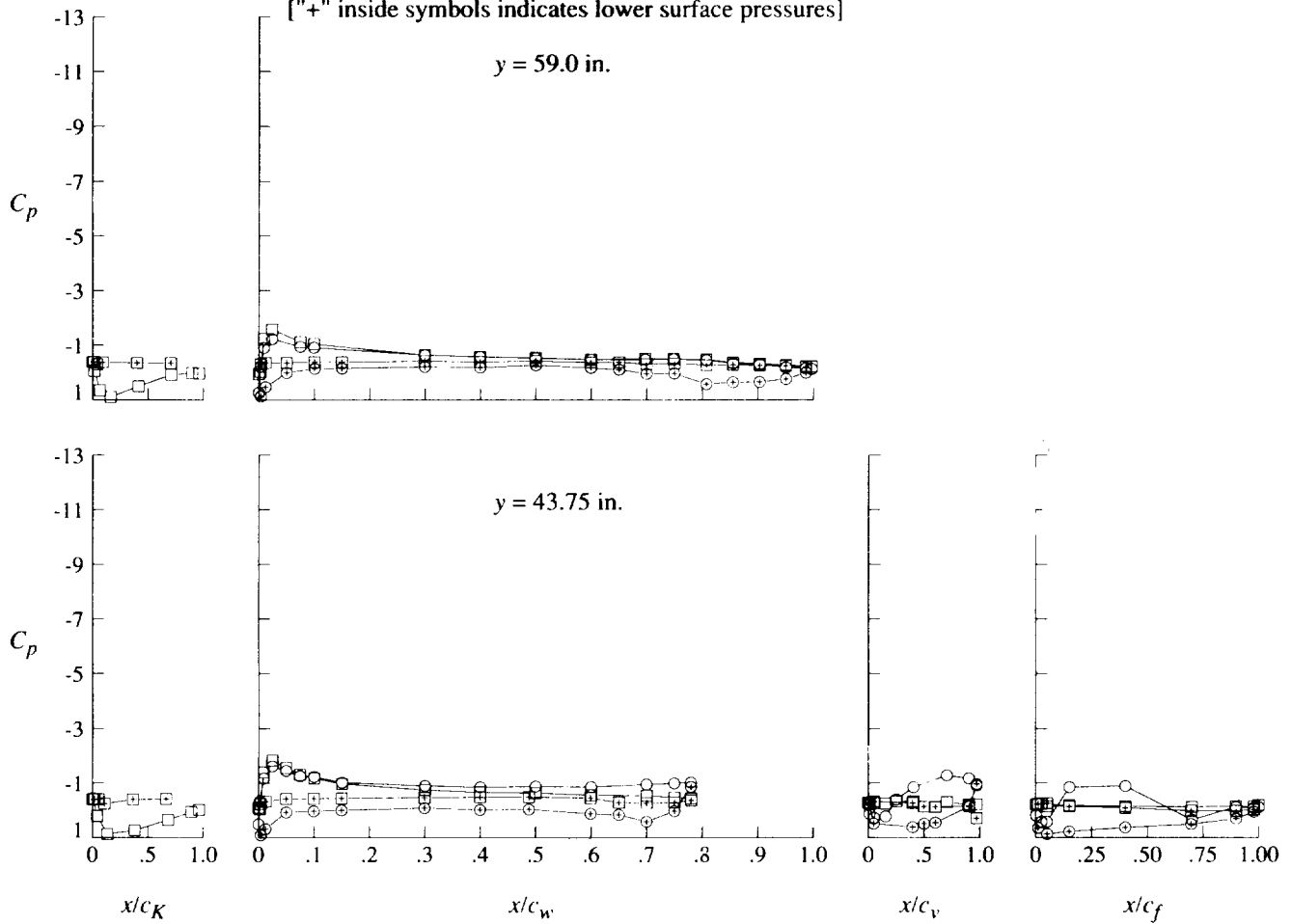
(b) $q = 40$ psf; $\alpha = 0^\circ$.

Figure 39. Continued.

Krueger

○ Off
□ On

["+" inside symbols indicates lower surface pressures]

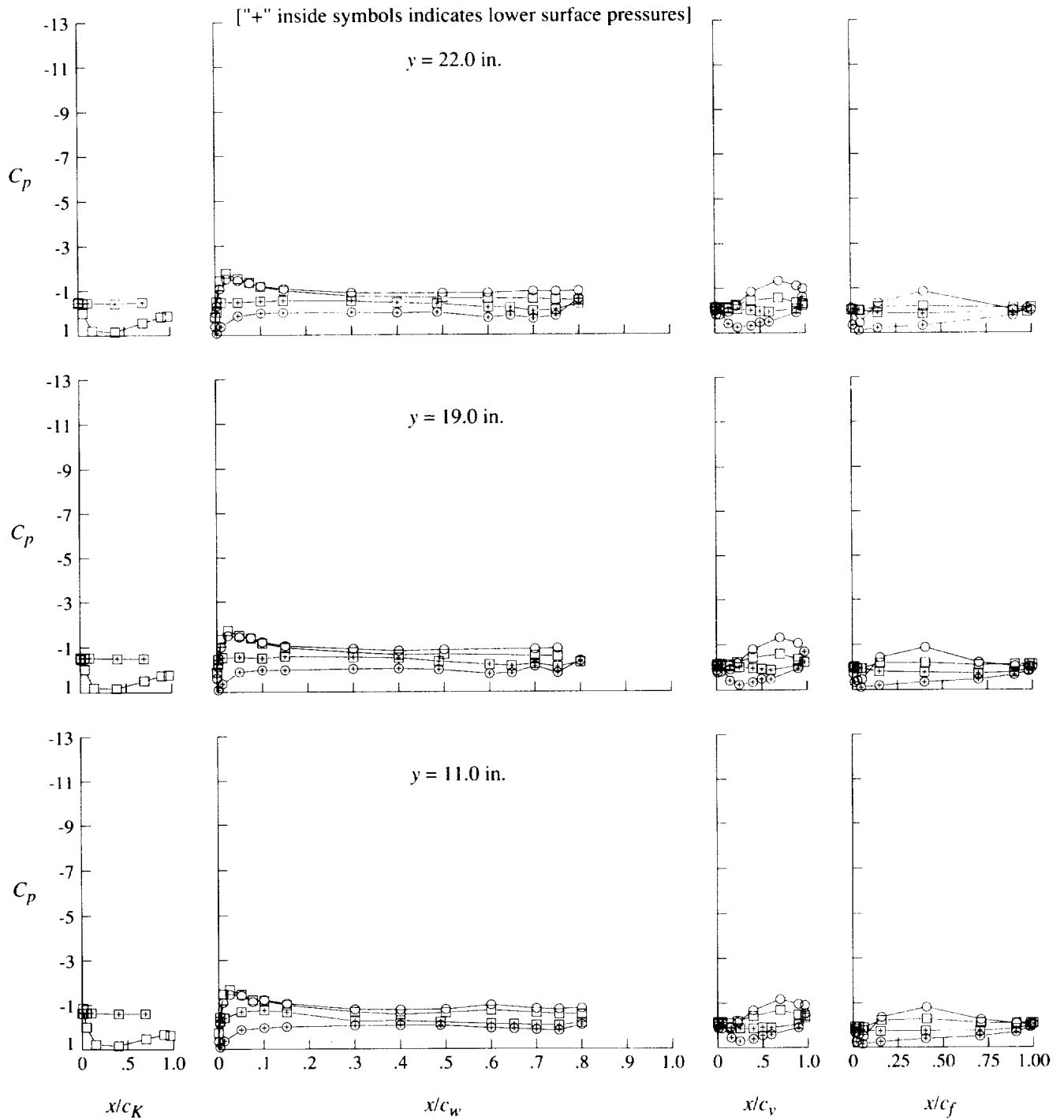


(b) Concluded.

Figure 39. Continued.

Krueger

○ Off
□ On

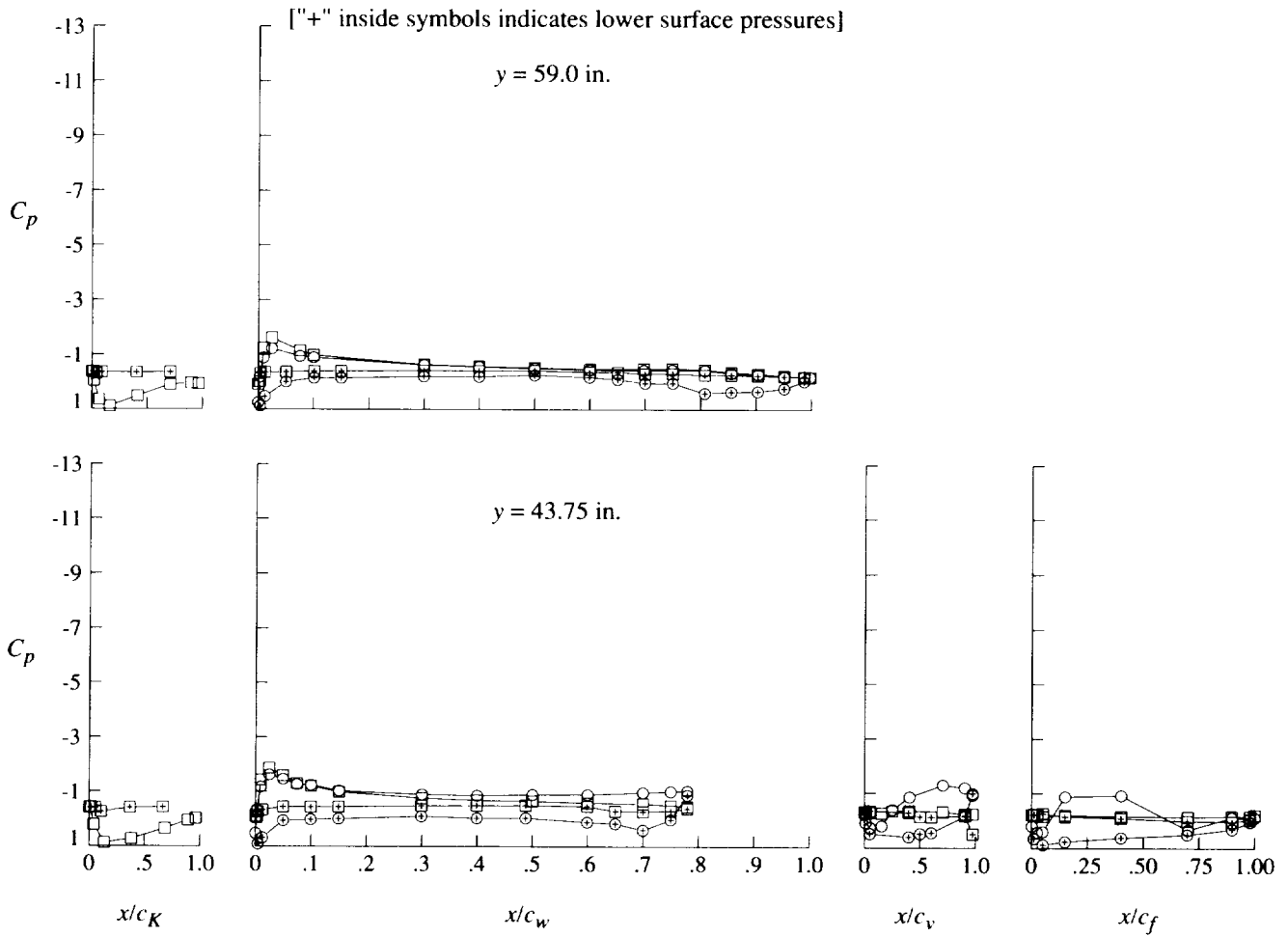


(c) $q = 60$ psf; $\alpha = 0^\circ$.

Figure 39. Continued.

Krueger

○ Off
□ On

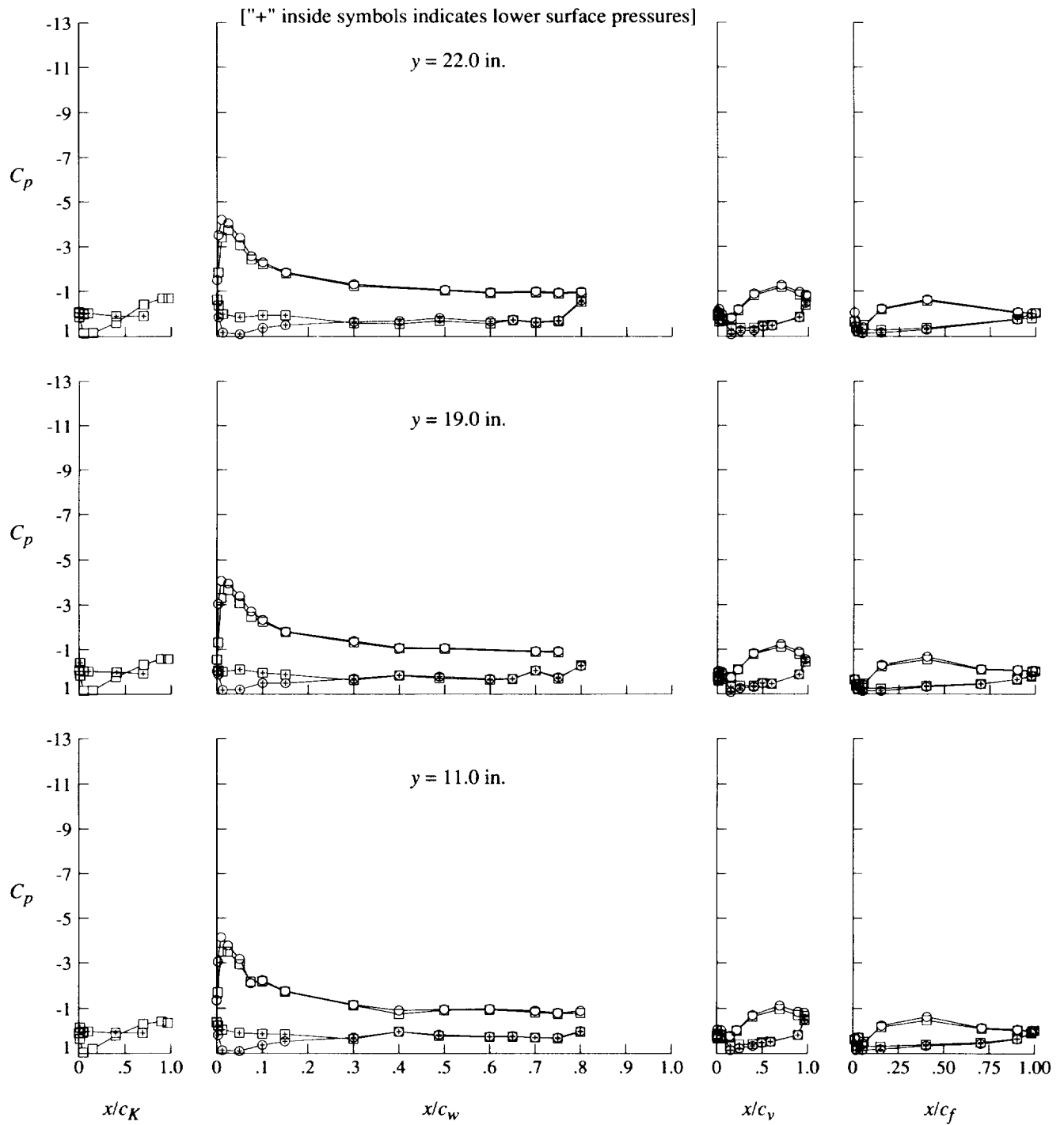


(c) Concluded.

Figure 39. Continued.

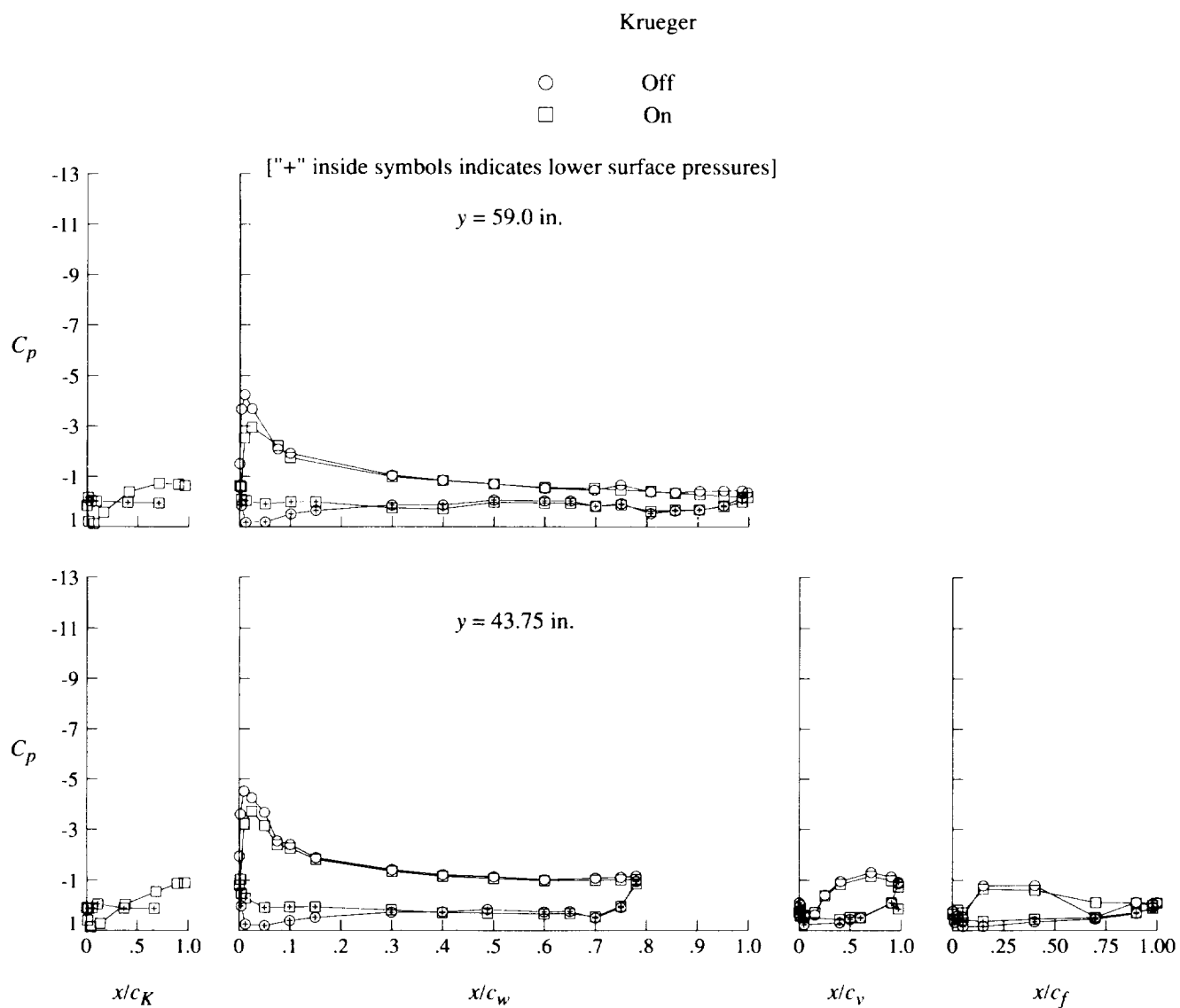
Krueger

○ Off
□ On



(d) $q = 20$ psf; $\alpha = 8^\circ$.

Figure 39. Continued.

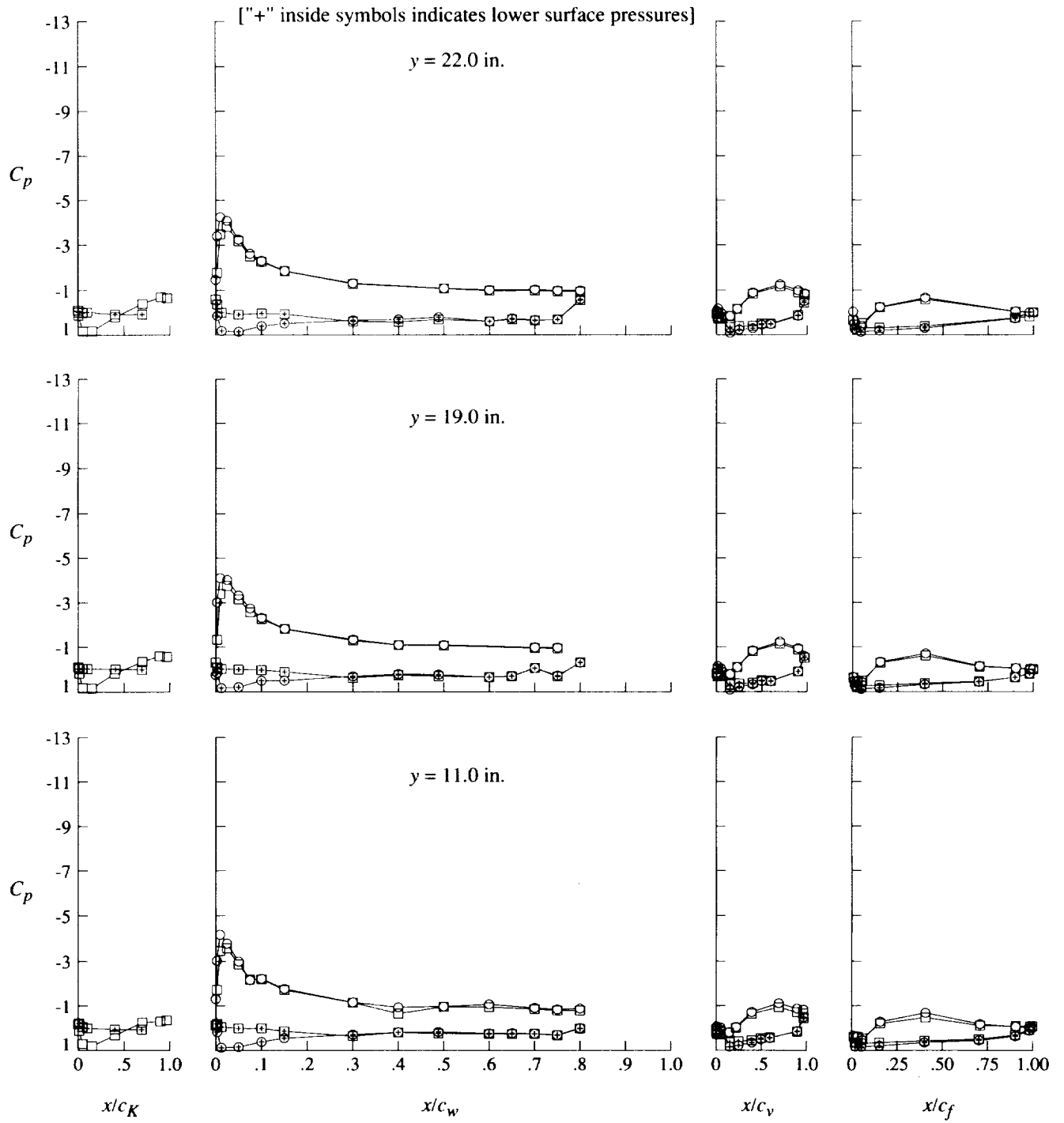


(d) Concluded.

Figure 39. Continued.

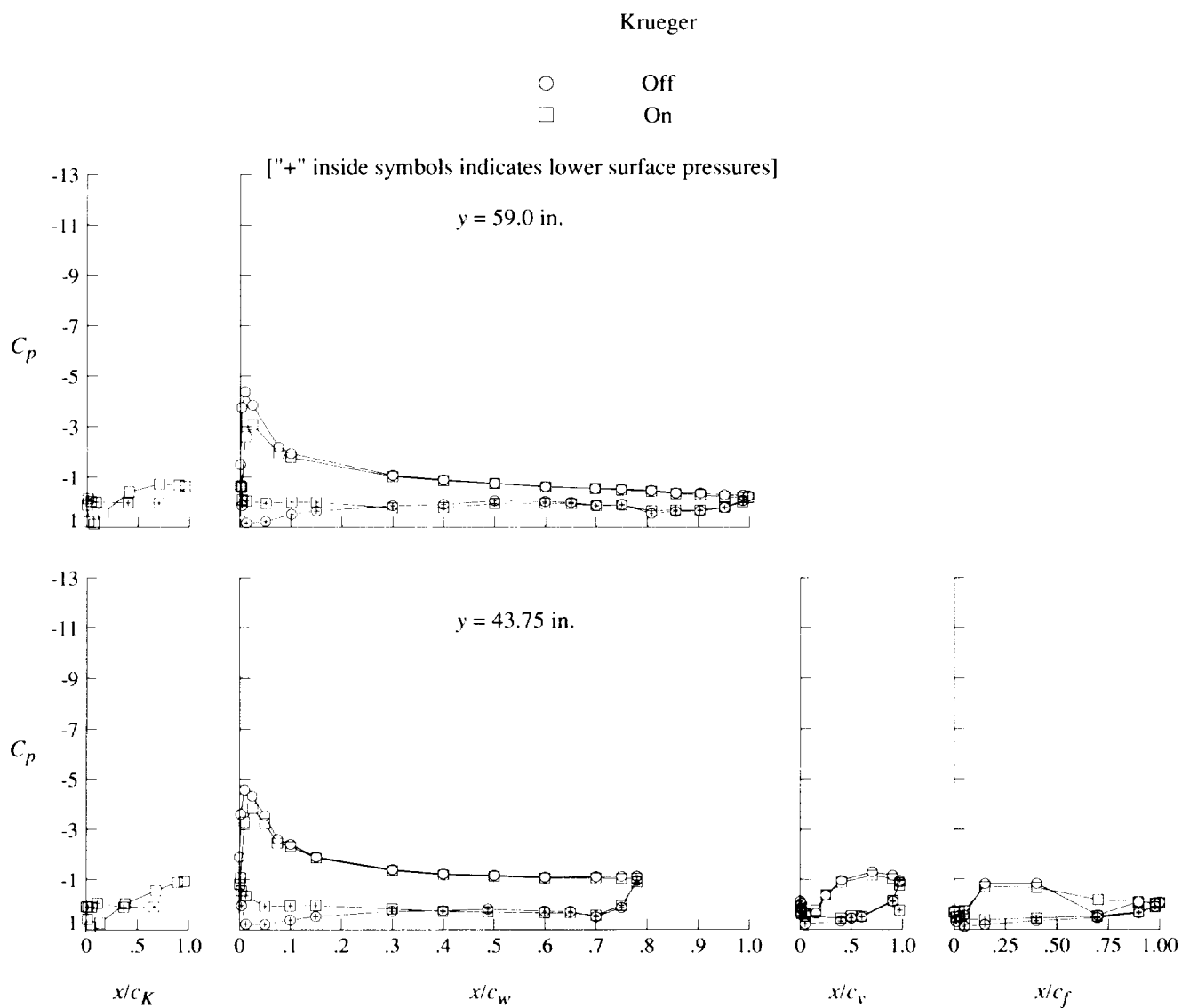
Krueger

○ Off
□ On



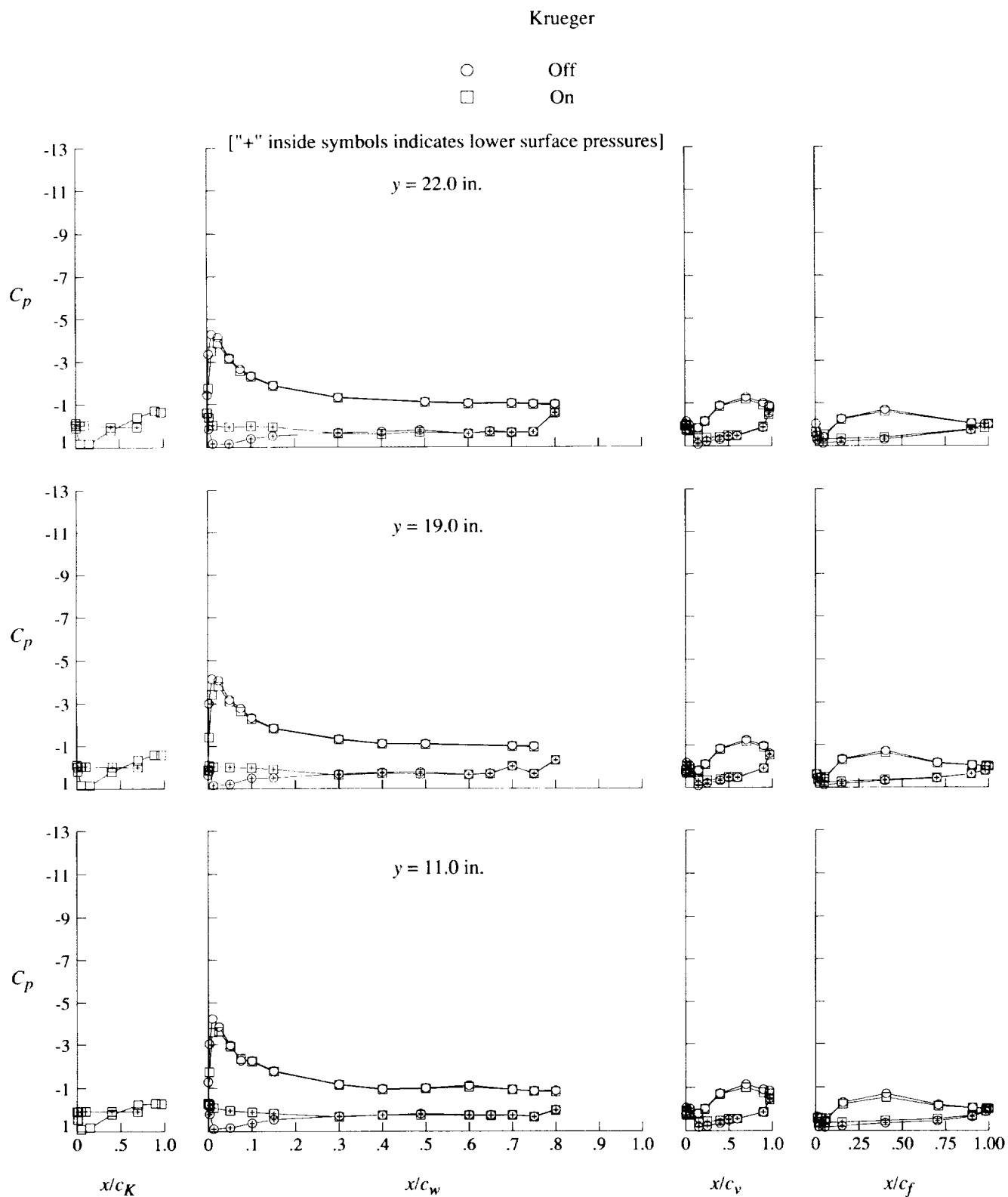
(e) $q = 40$ psf; $\alpha = 8^\circ$.

Figure 39. Continued.



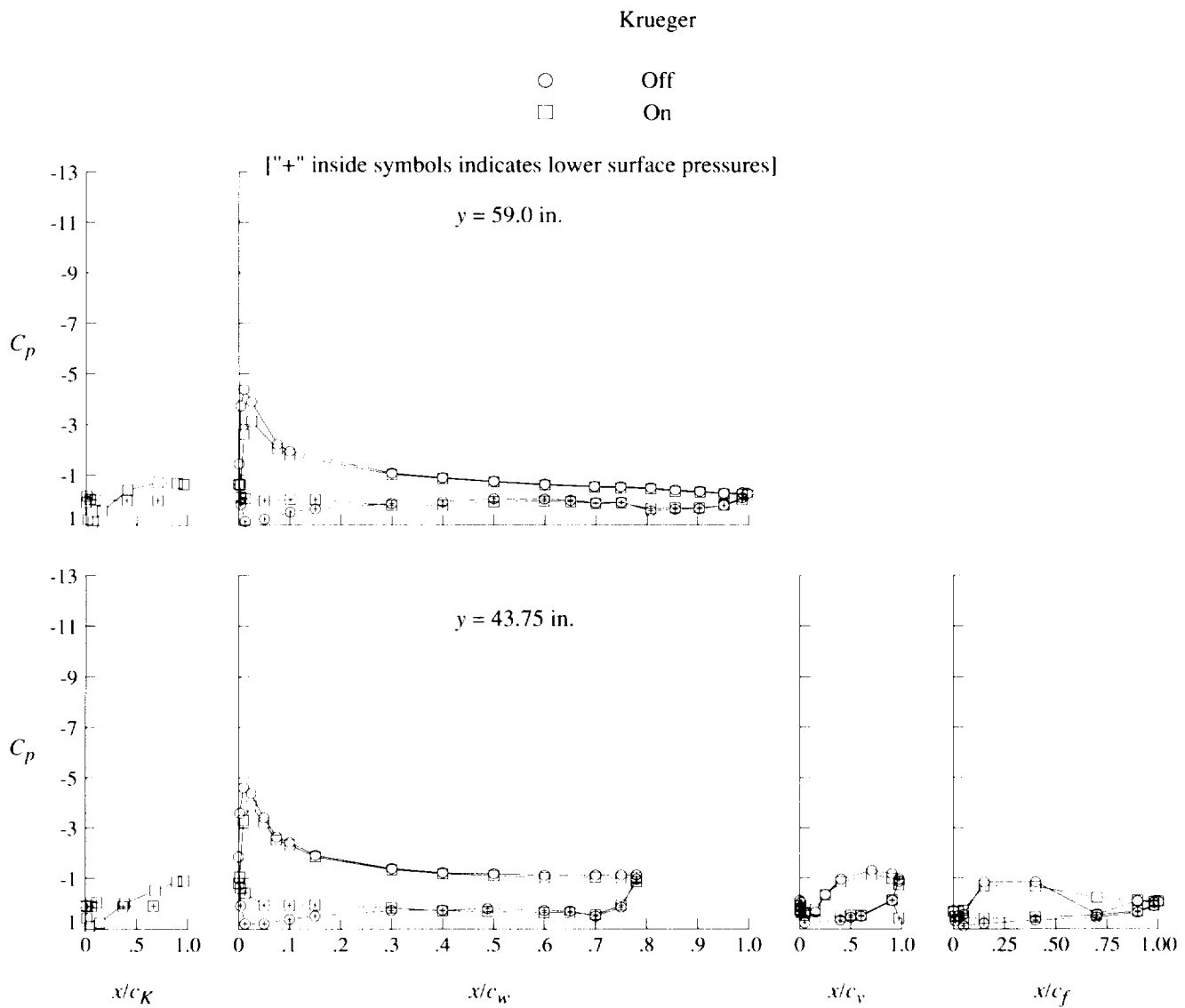
(e) Concluded.

Figure 39. Continued.



(f) $q = 60$ psf; $\alpha = 8^\circ$.

Figure 39. Continued.

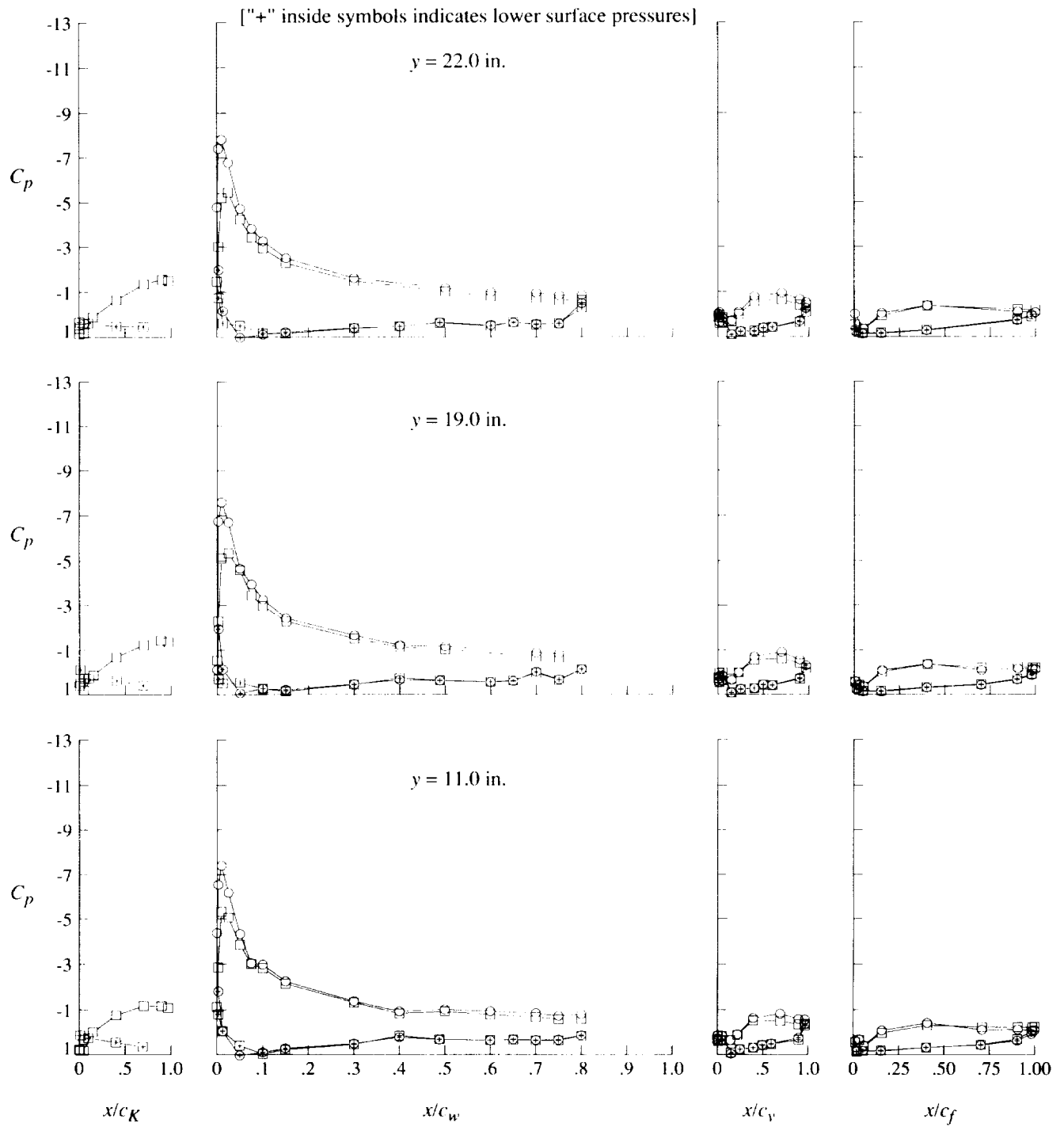


(f) Concluded.

Figure 39. Continued.

Krueger

○ Off
□ On

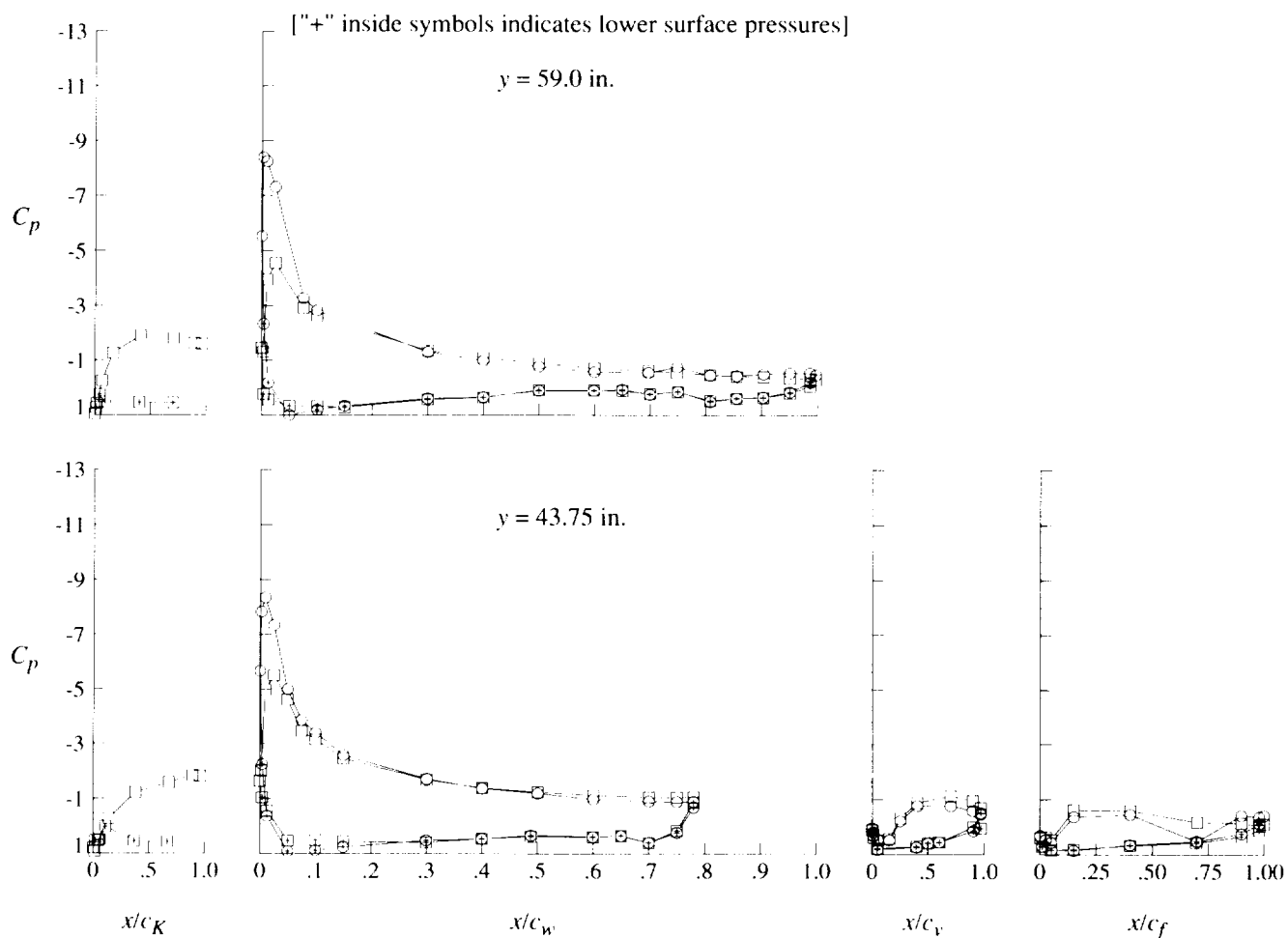


(g) $q = 20$ psf; $\alpha = 16^\circ$.

Figure 39. Continued.

Krueger

- Off
- On

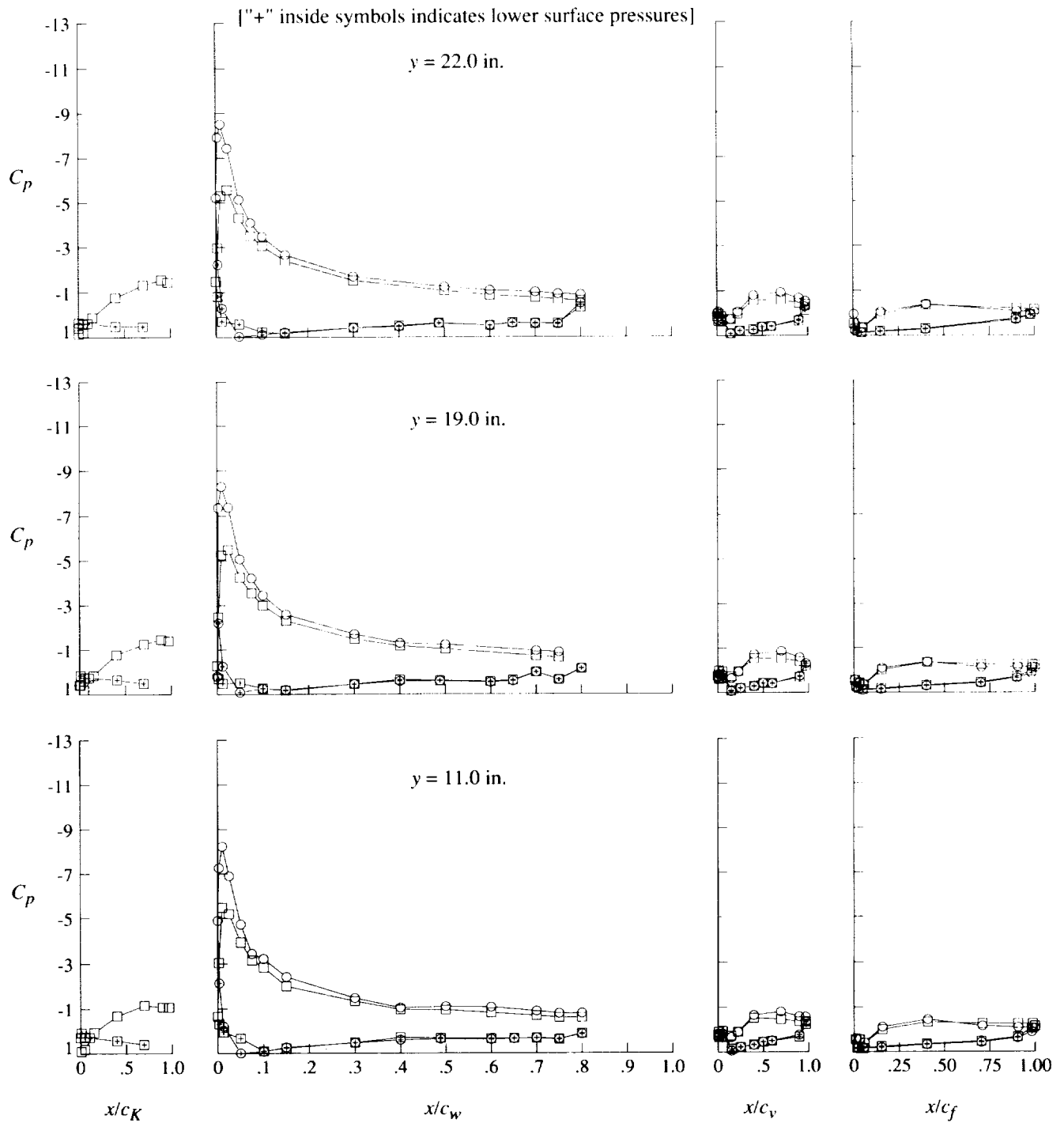


(g) Concluded.

Figure 39. Continued.

Krueger

○ Off
□ On



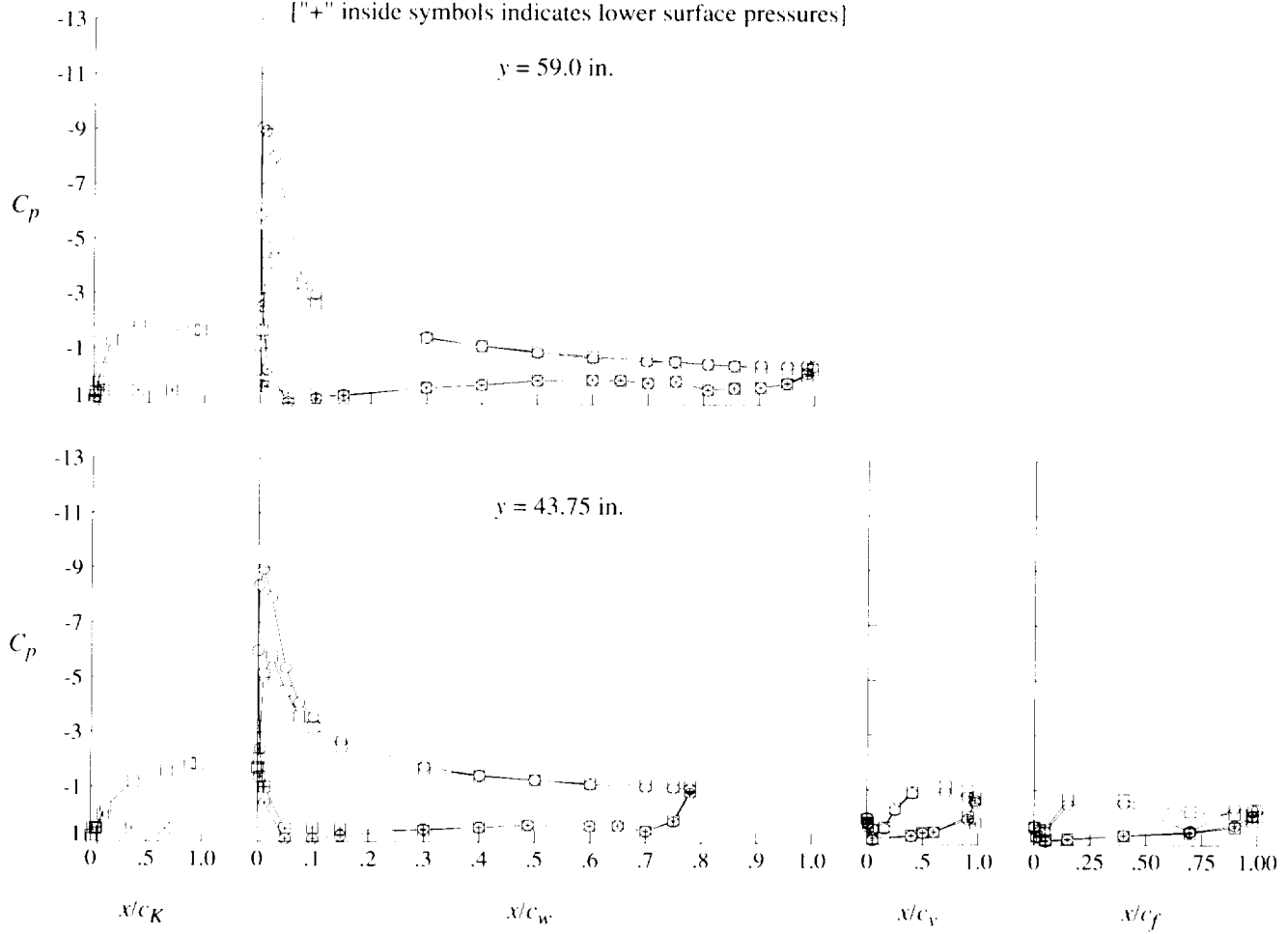
(h) $q = 40$ psf; $\alpha = 16^\circ$.

Figure 39. Continued.

Krueger

○ Off
□ On

["+" inside symbols indicates lower surface pressures]

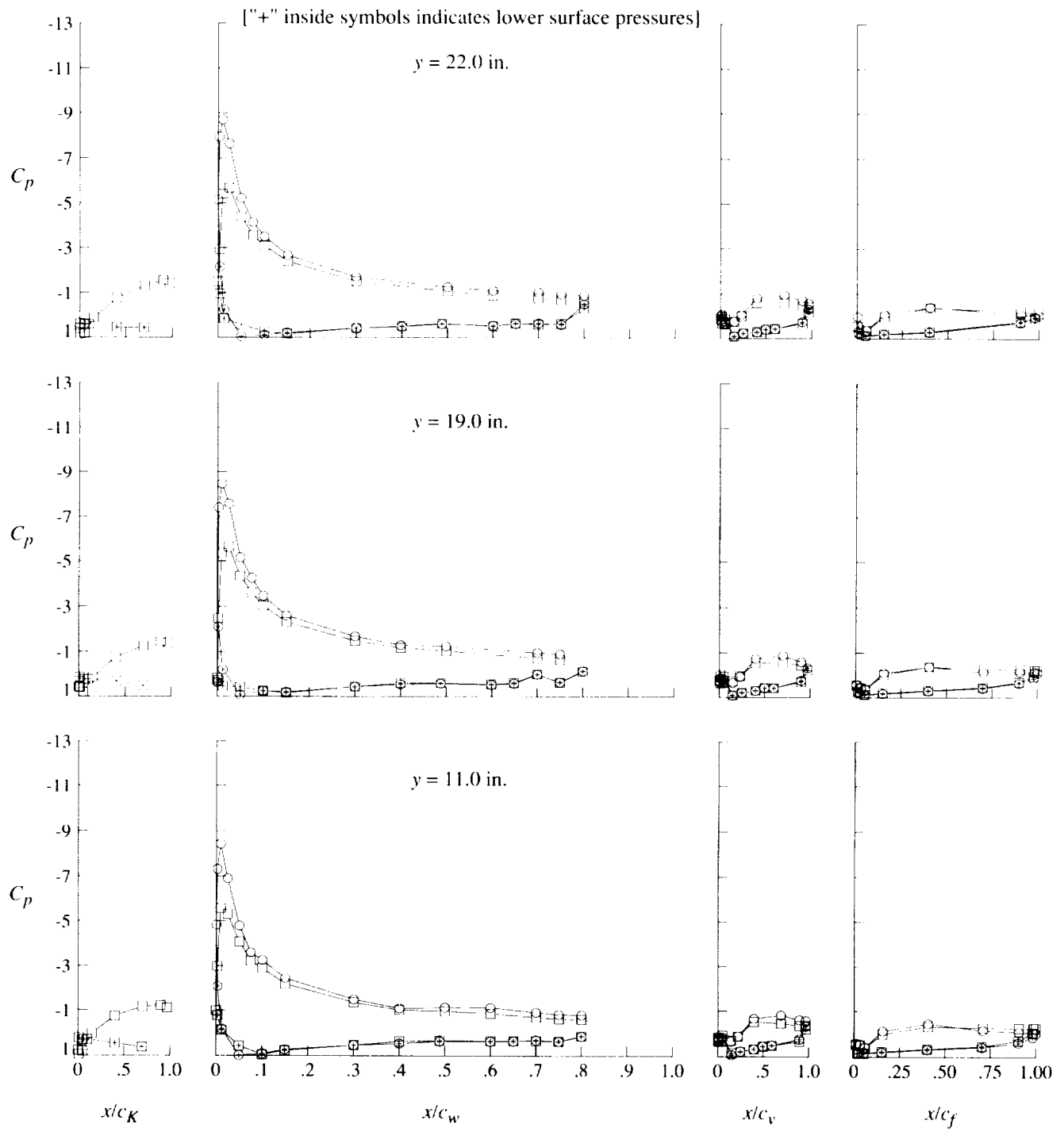


(h) Concluded.

Figure 39. Continued.

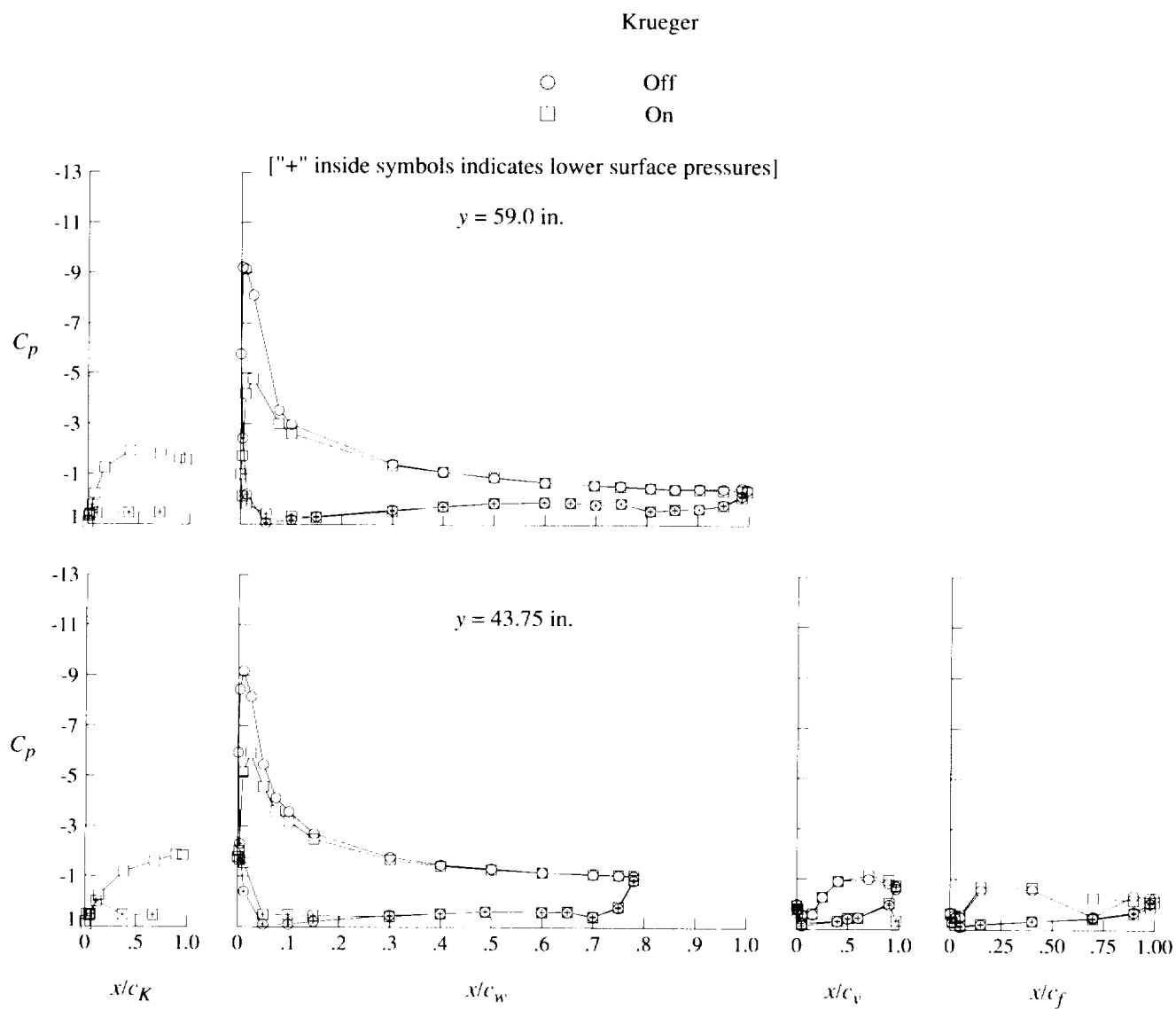
Krueger

○ Off
□ On



(i) $q = 60$ psf; $\alpha = 16^\circ$.

Figure 39. Continued.

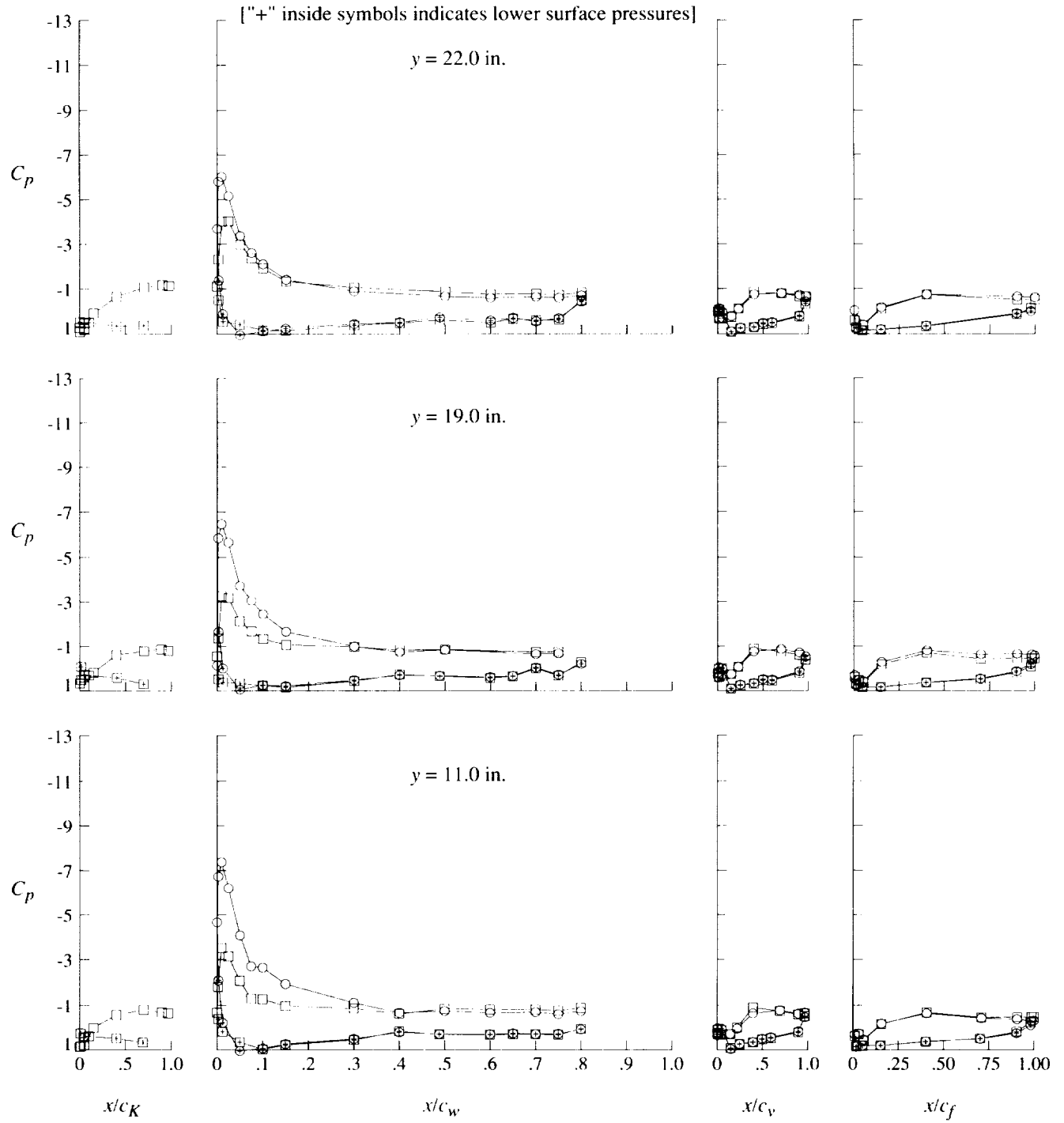


(i) Concluded.

Figure 39. Continued.

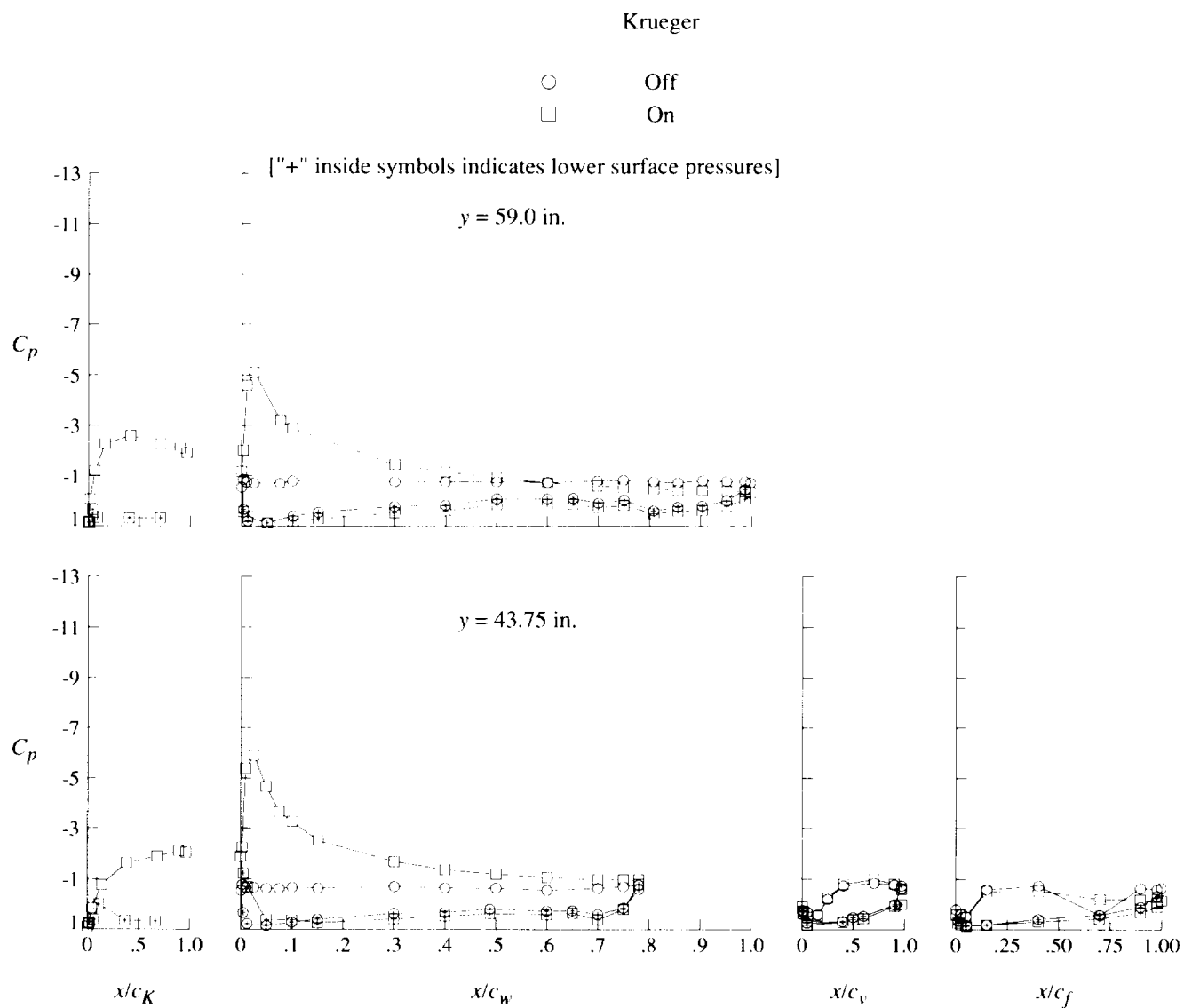
Krueger

○ Off
□ On



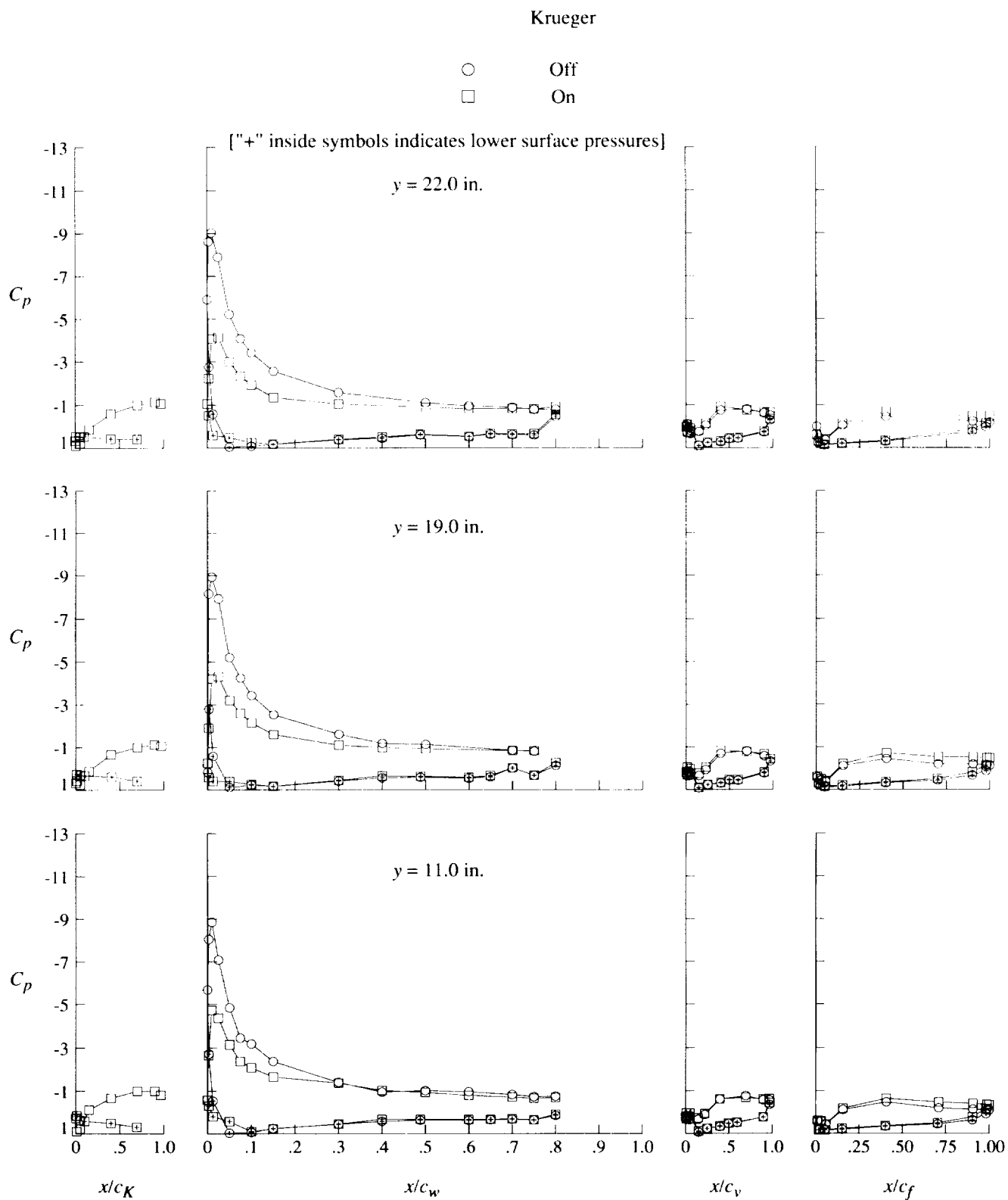
(j) $q = 20$ psf; $\alpha = 20^\circ$.

Figure 39. Continued.



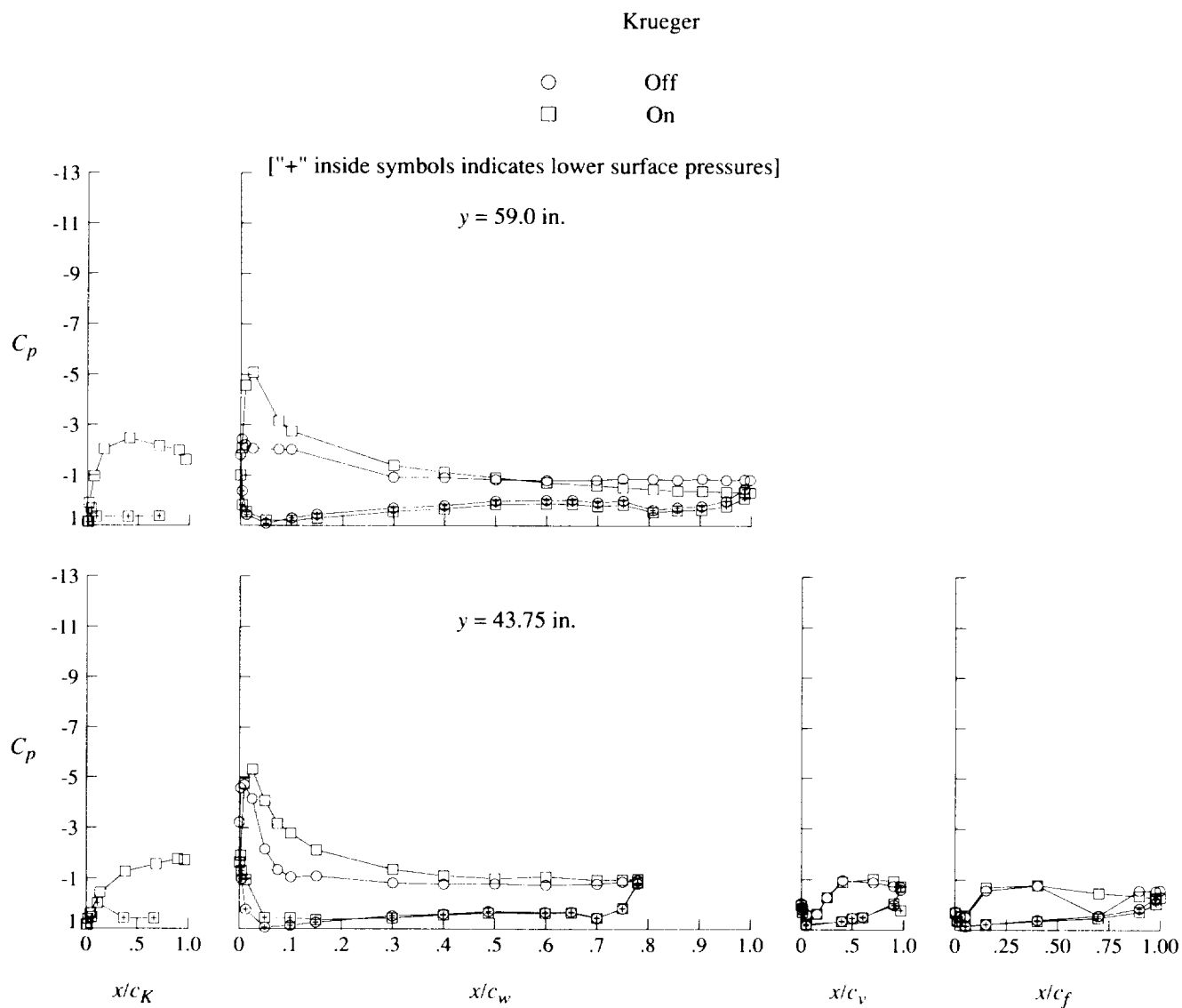
(j) Concluded.

Figure 39. Continued.



(k) $q = 40$ psf; $\alpha = 20^\circ$.

Figure 39. Continued.



(k) Concluded.

Figure 39. Concluded.

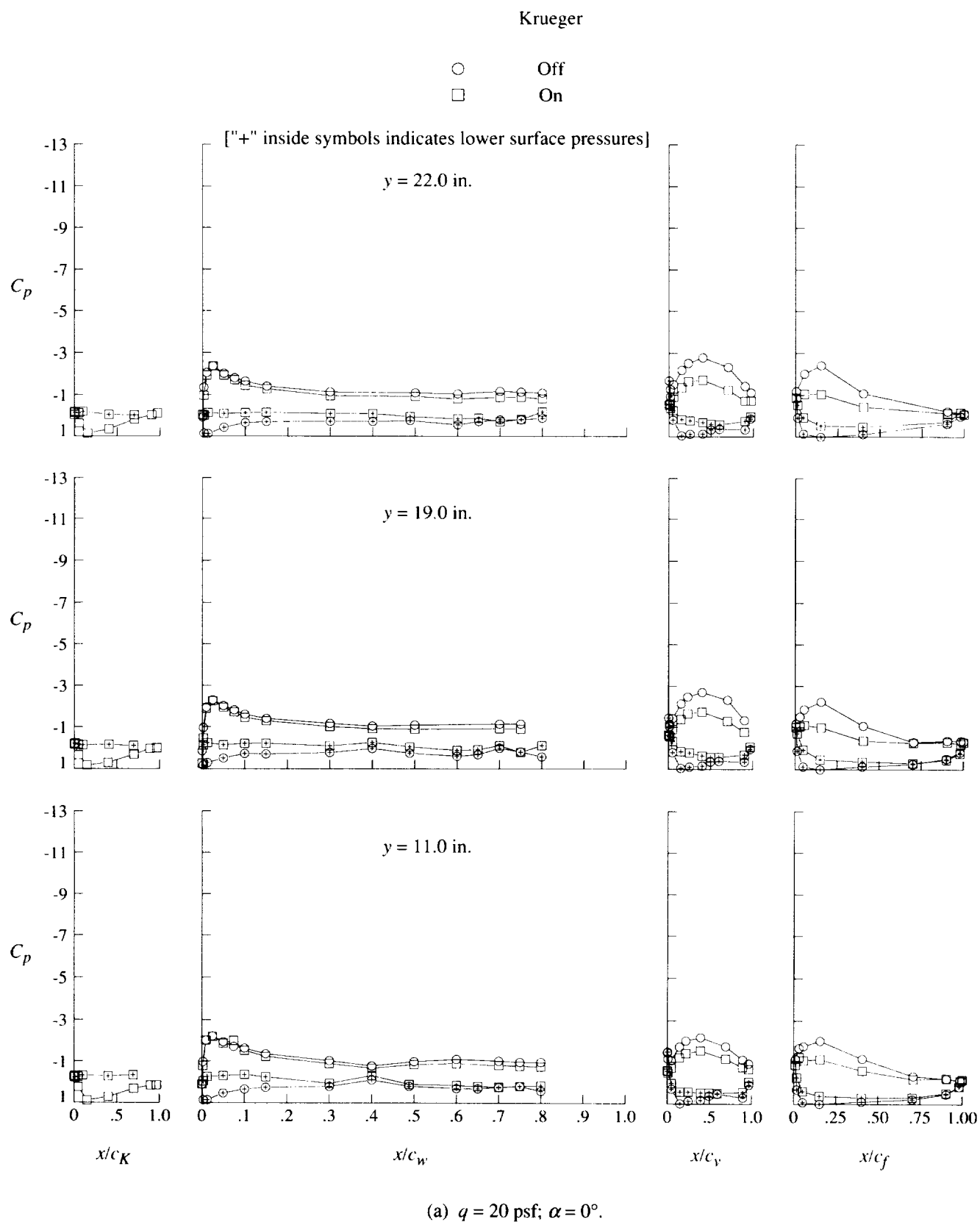


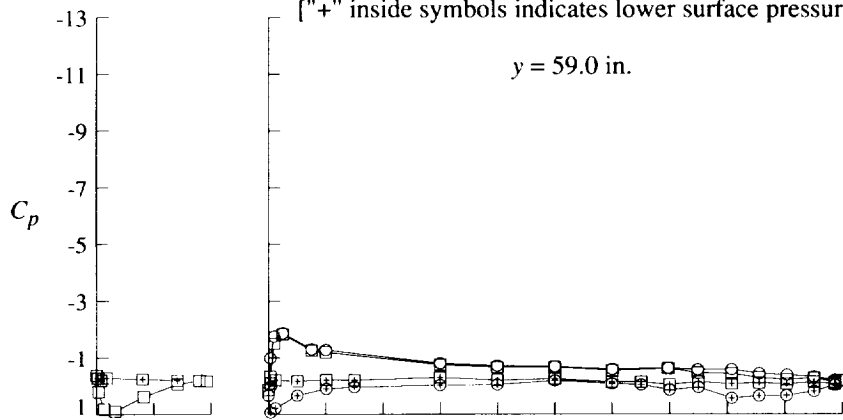
Figure 40. Effect of leading-edge Krueger flap on pressure distributions for high-lift configuration at $\delta_f = 60^\circ$.

Krueger

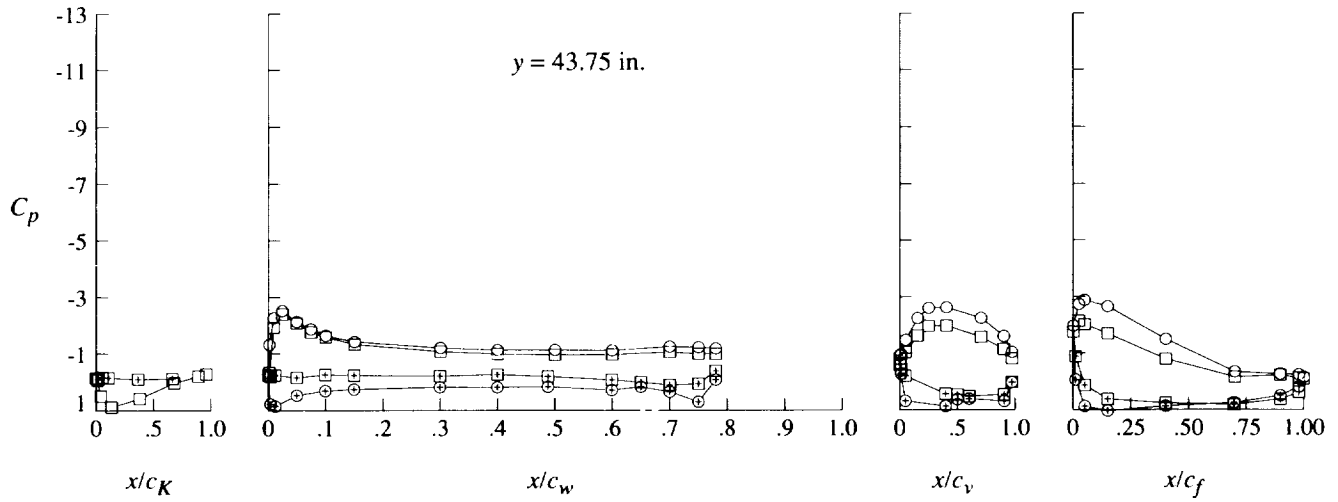
○ Off
□ On

["+" inside symbols indicates lower surface pressures]

$y = 59.0$ in.

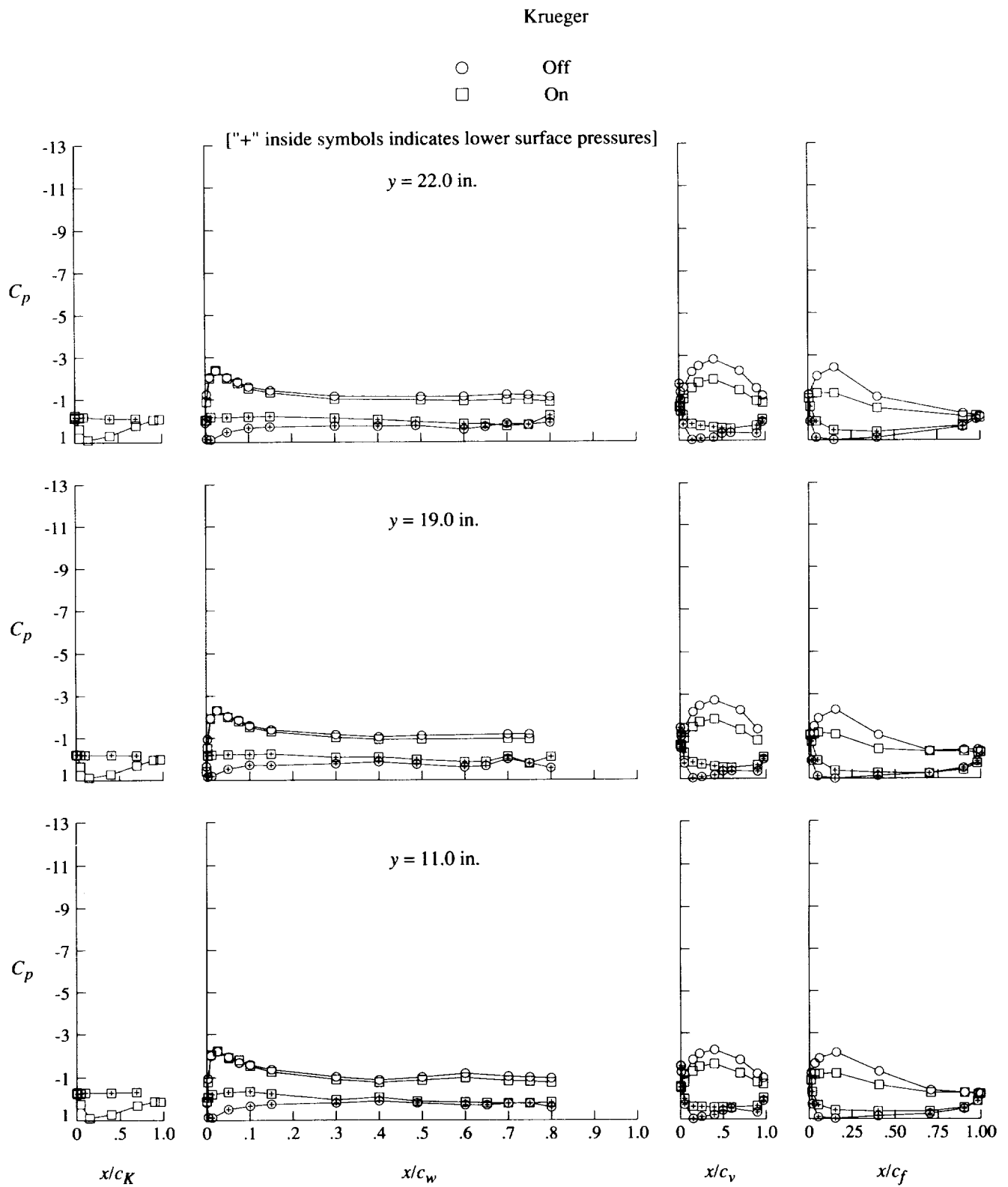


$y = 43.75$ in.



(a) Concluded.

Figure 40. Continued.



(b) $q = 40 \text{ psf}$; $\alpha = 0^\circ$.

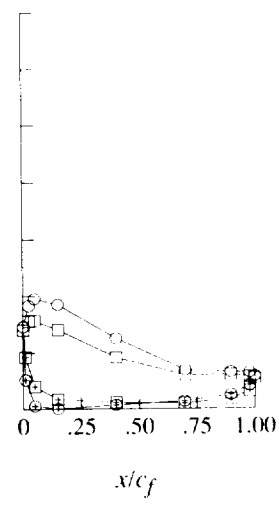
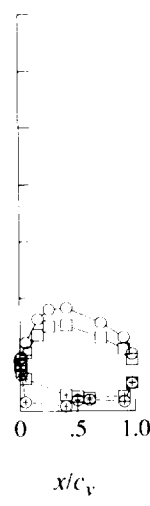
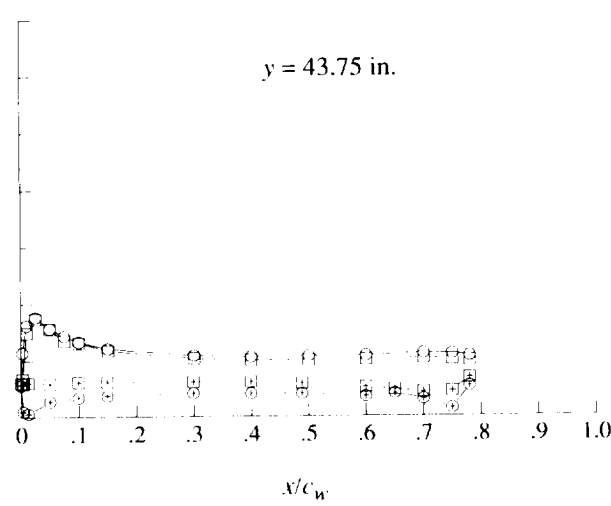
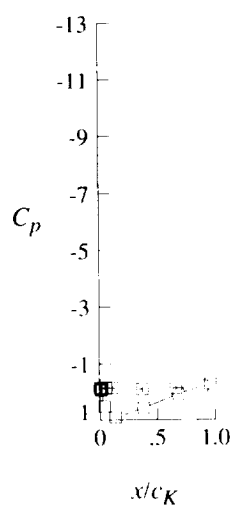
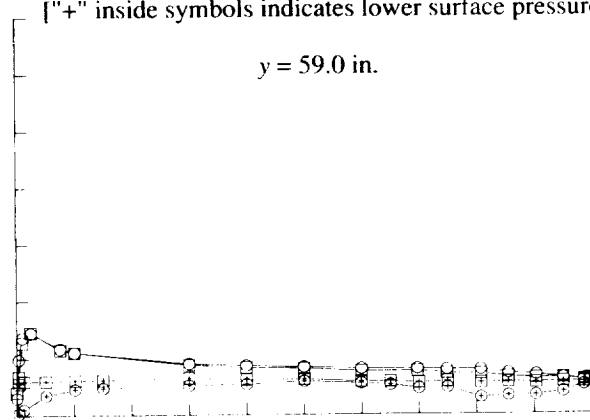
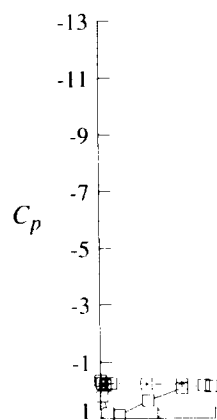
Figure 40. Continued.

Krueger

○ Off
□ On

["+" inside symbols indicates lower surface pressures]

$y = 59.0$ in.



(b) Concluded.

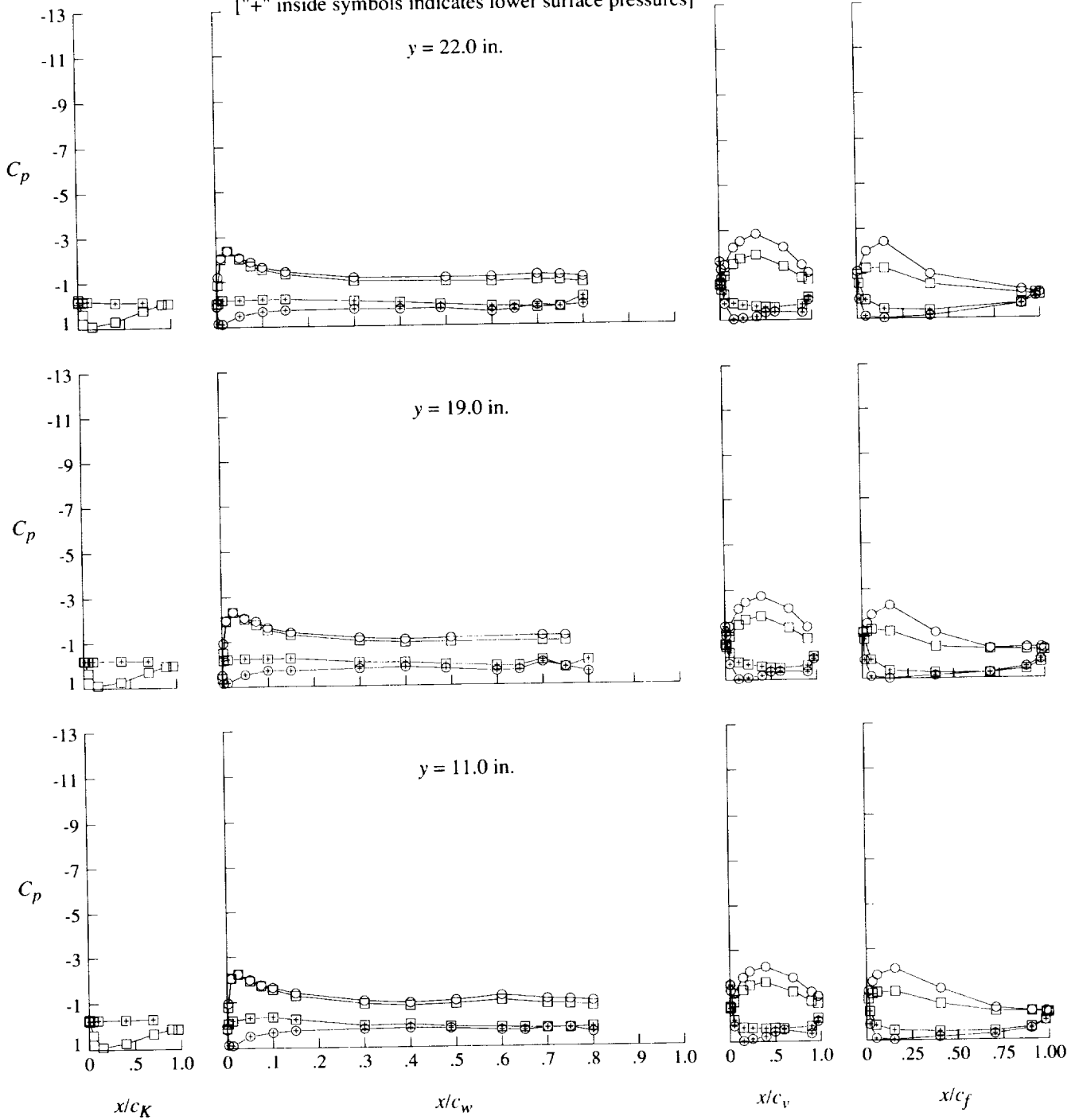
Figure 40. Continued.

Krueger

○ Off
□ On

["+" inside symbols indicates lower surface pressures]

$y = 22.0$ in.



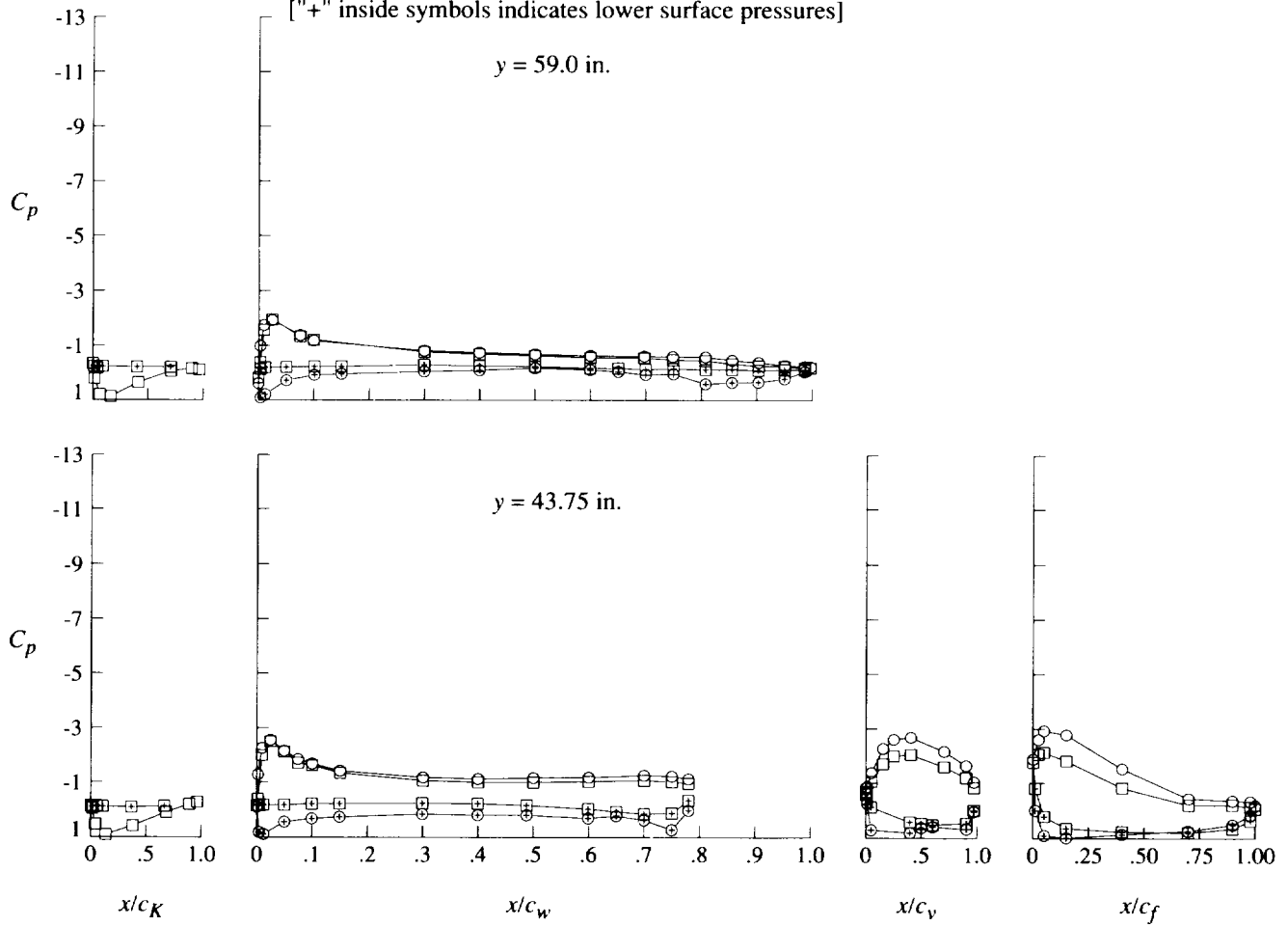
(c) $q = 60$ psf; $\alpha = 0^\circ$.

Figure 40. Continued.

Krueger

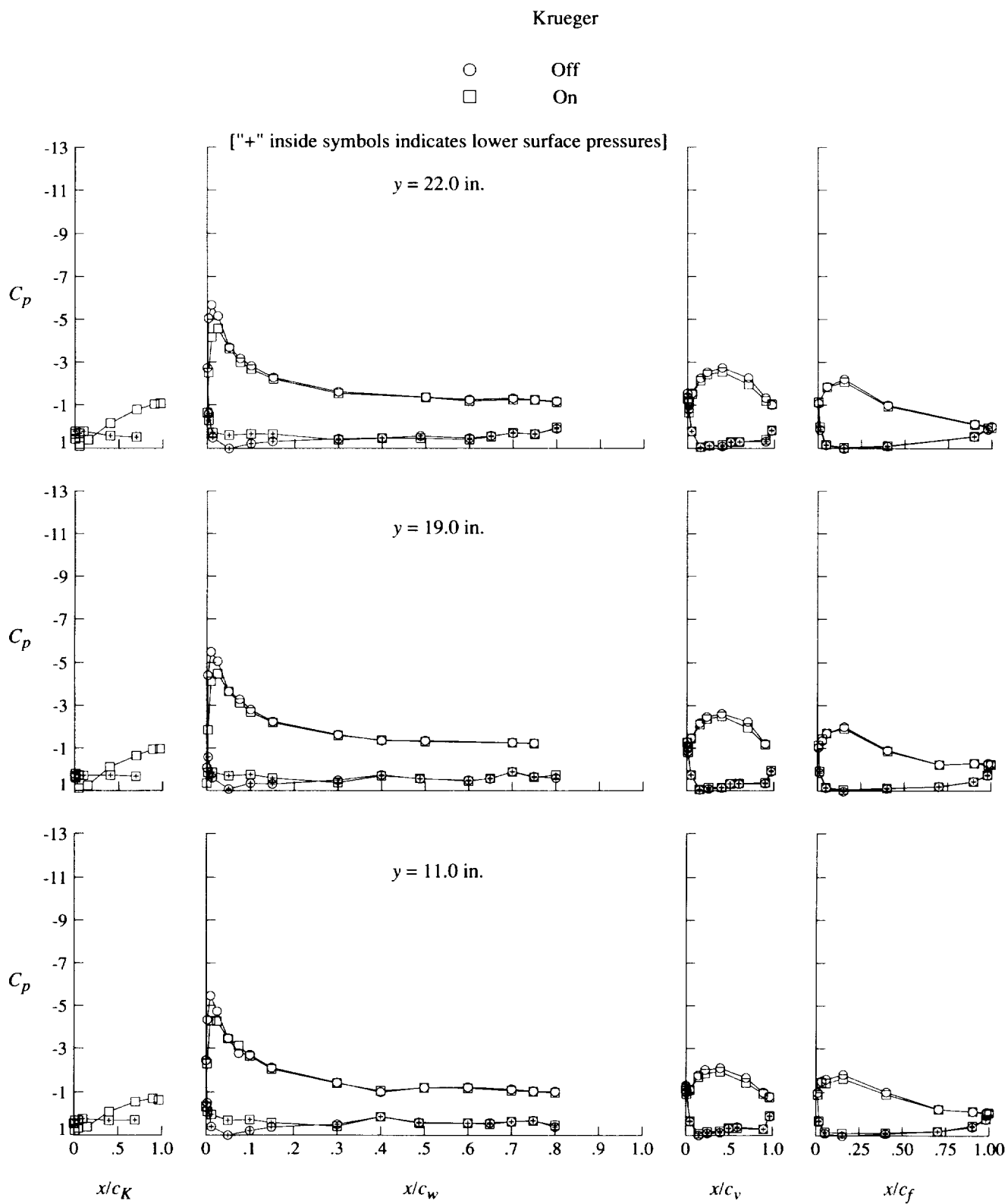
○ Off
□ On

["+" inside symbols indicates lower surface pressures]



(c) Concluded.

Figure 40. Continued.



(d) $q = 20$ psf; $\alpha = 8^\circ$.

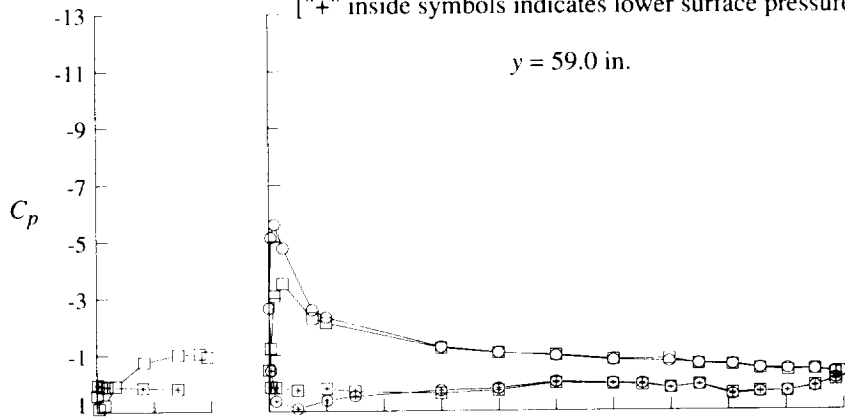
Figure 40. Continued.

Krueger

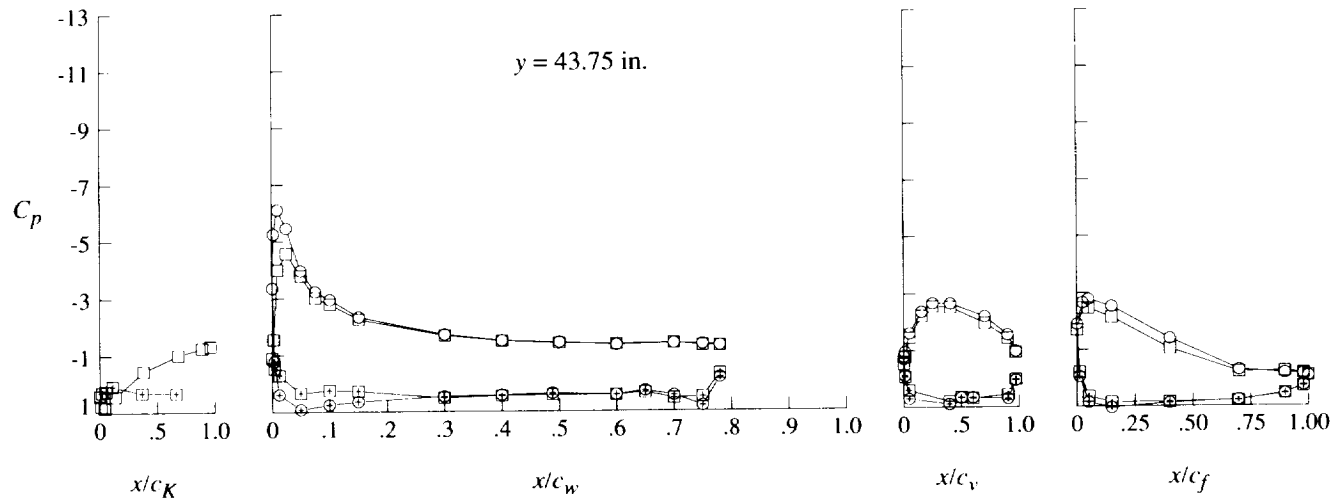
○ Off
□ On

["+" inside symbols indicates lower surface pressures]

$y = 59.0$ in.



$y = 43.75$ in.



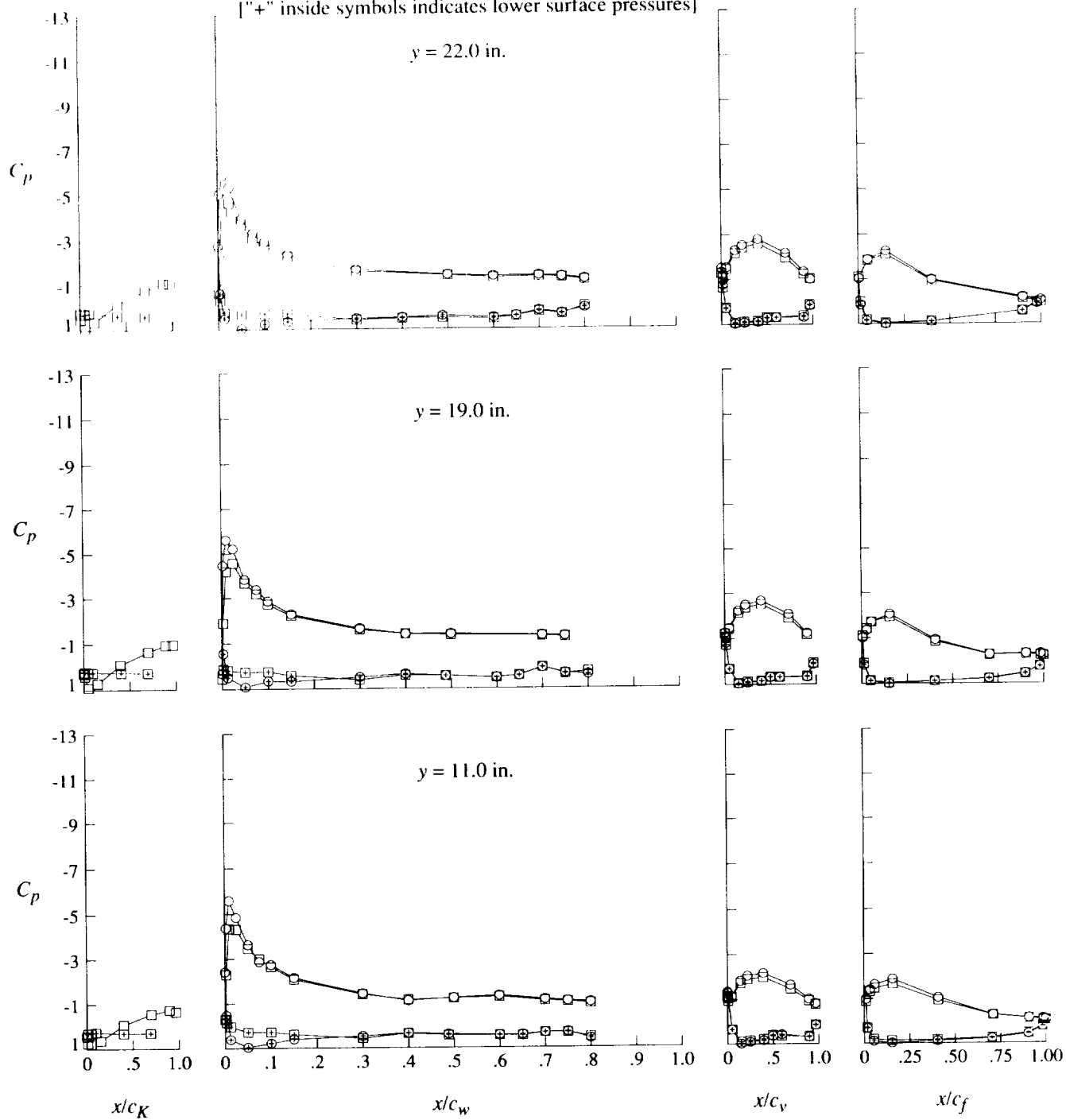
(d) Concluded.

Figure 40. Continued.

Krueger

○ Off
□ On

["+" inside symbols indicates lower surface pressures]



(e) $q = 40$ psf; $\alpha = 8^\circ$.

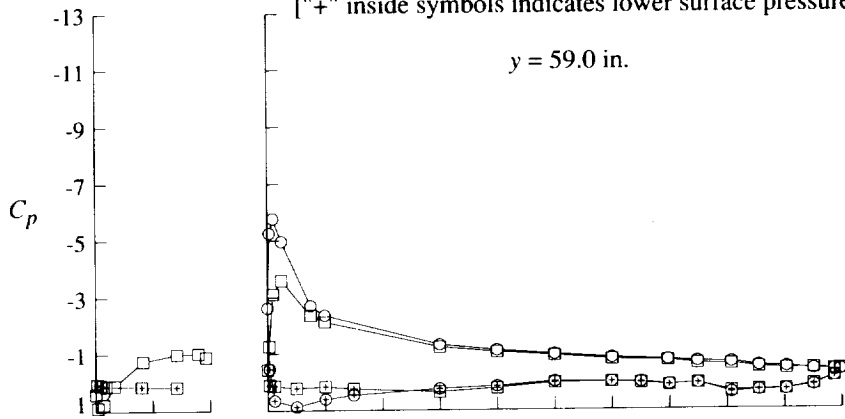
Figure 40. Continued.

Krueger

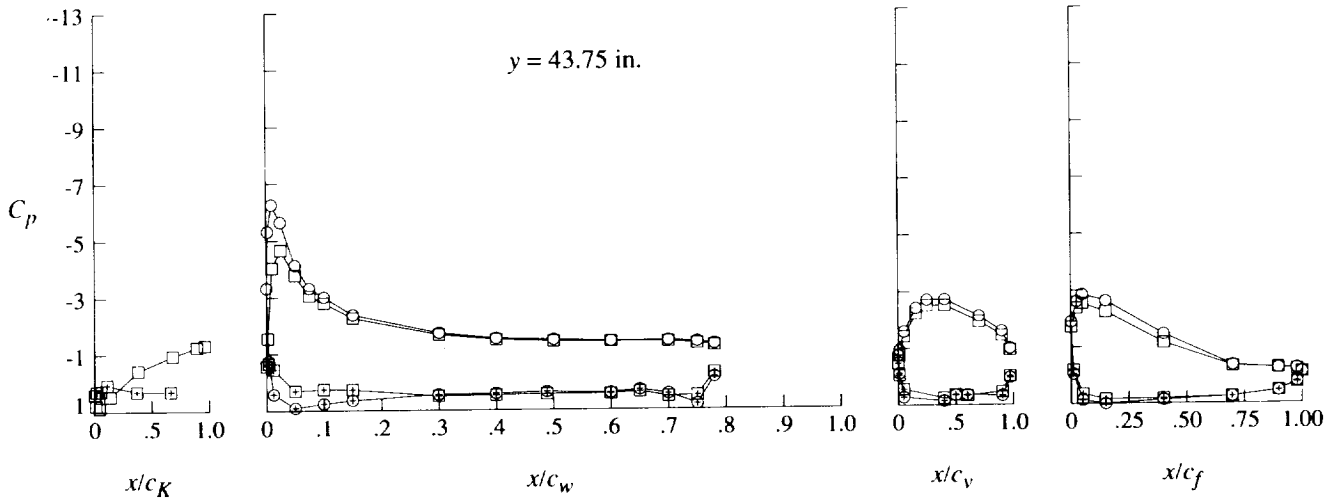
○ Off
□ On

["+" inside symbols indicates lower surface pressures]

$y = 59.0$ in.

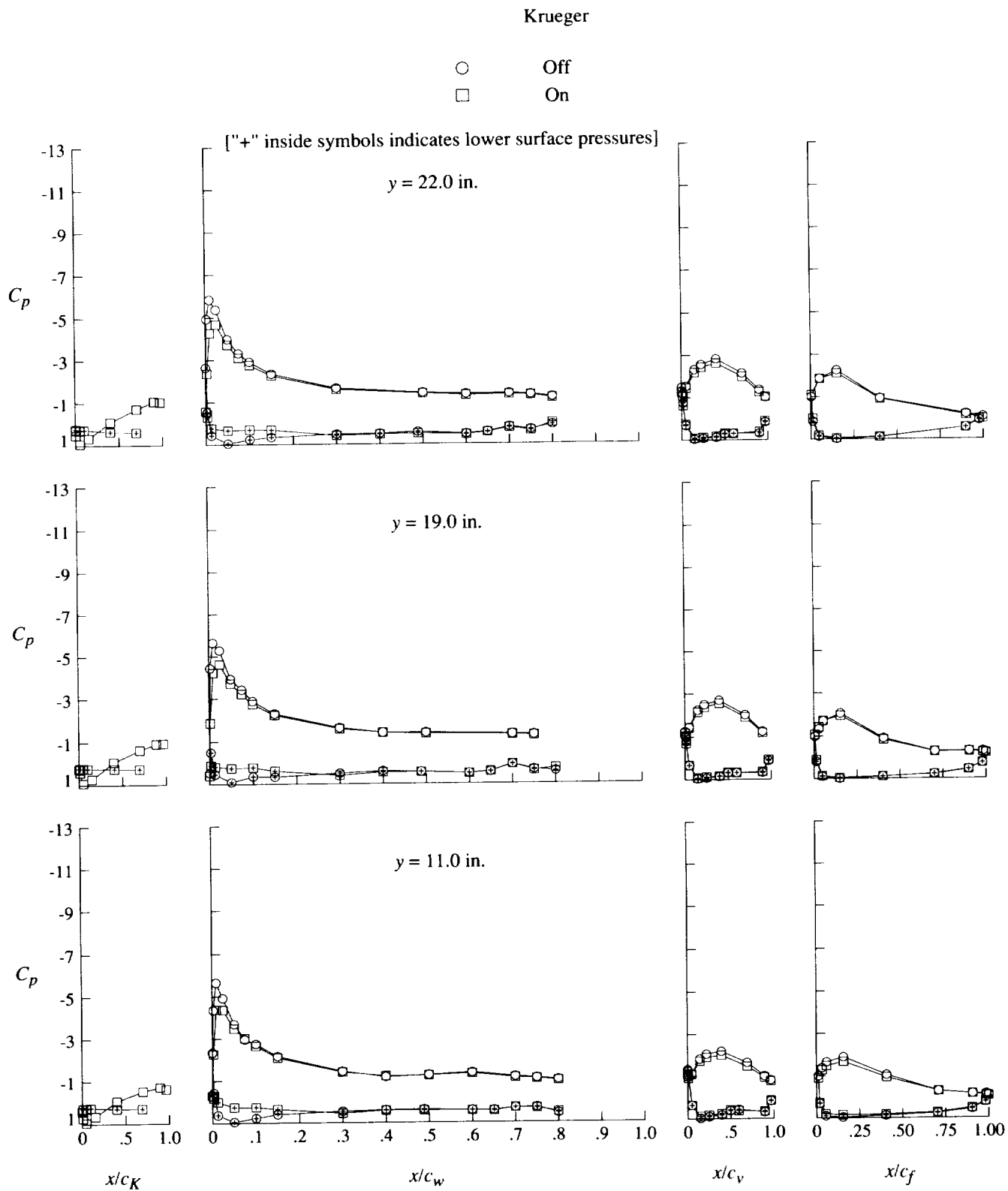


$y = 43.75$ in.



(e) Concluded.

Figure 40. Continued.



(f) $q = 60$ psf; $\alpha = 8^\circ$.

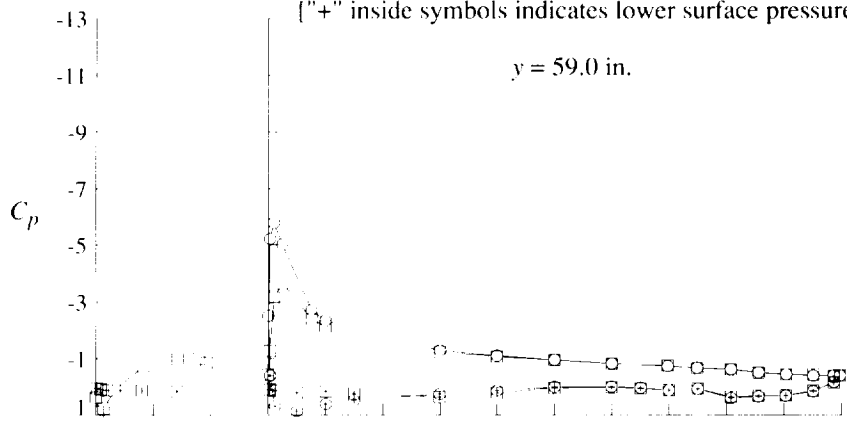
Figure 40. Continued.

Krueger

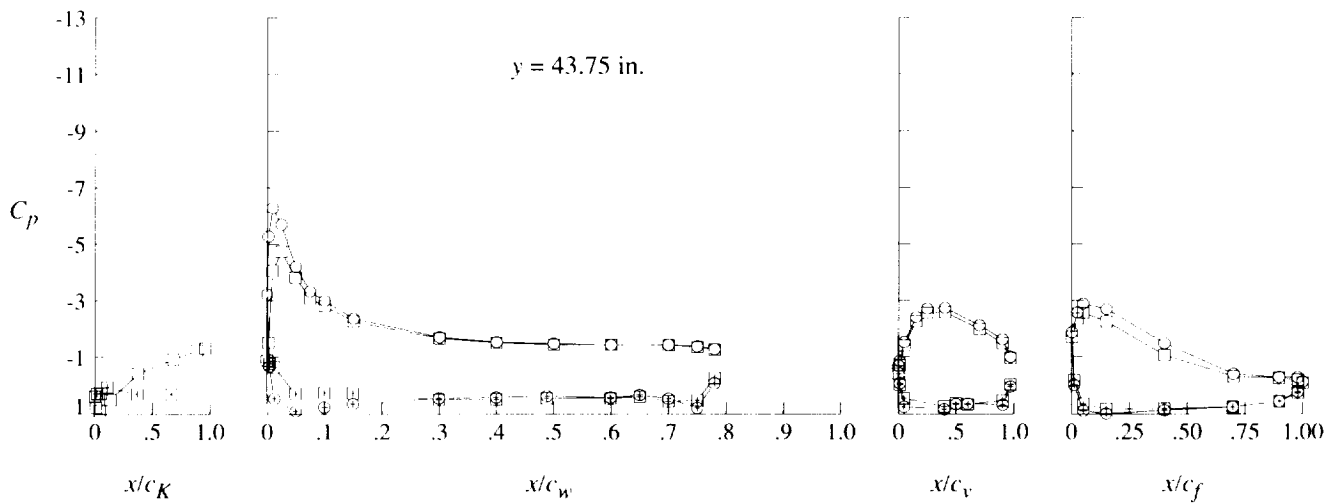
○ Off
□ On

["+ " inside symbols indicates lower surface pressures]

$y = 59.0$ in.



$y = 43.75$ in.



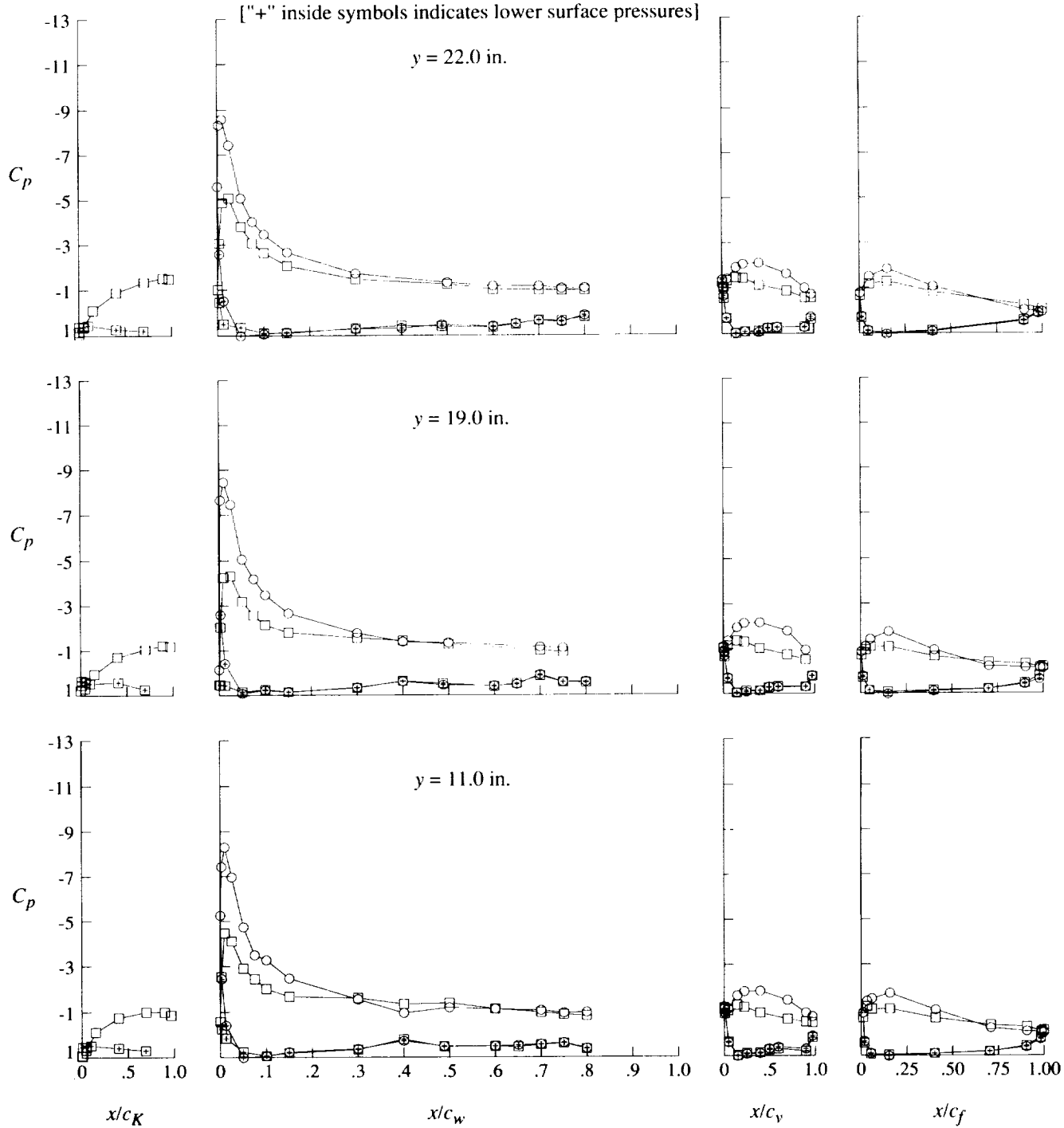
(f) Concluded.

Figure 40. Continued.

Krueger

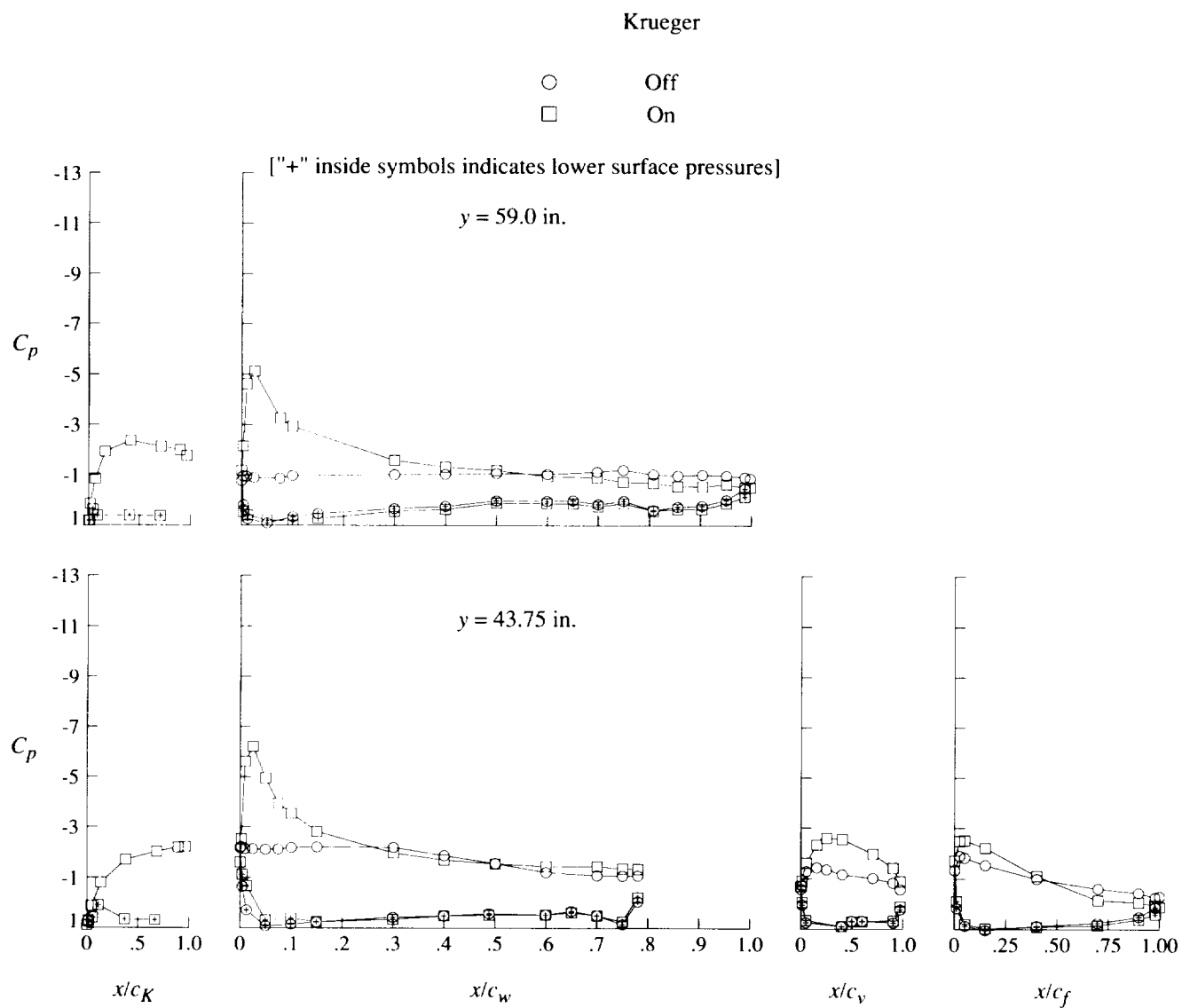
○ Off
□ On

["+" inside symbols indicates lower surface pressures]



(g) $q = 20 \text{ psf}$; $\alpha = 16^\circ$.

Figure 40. Continued.

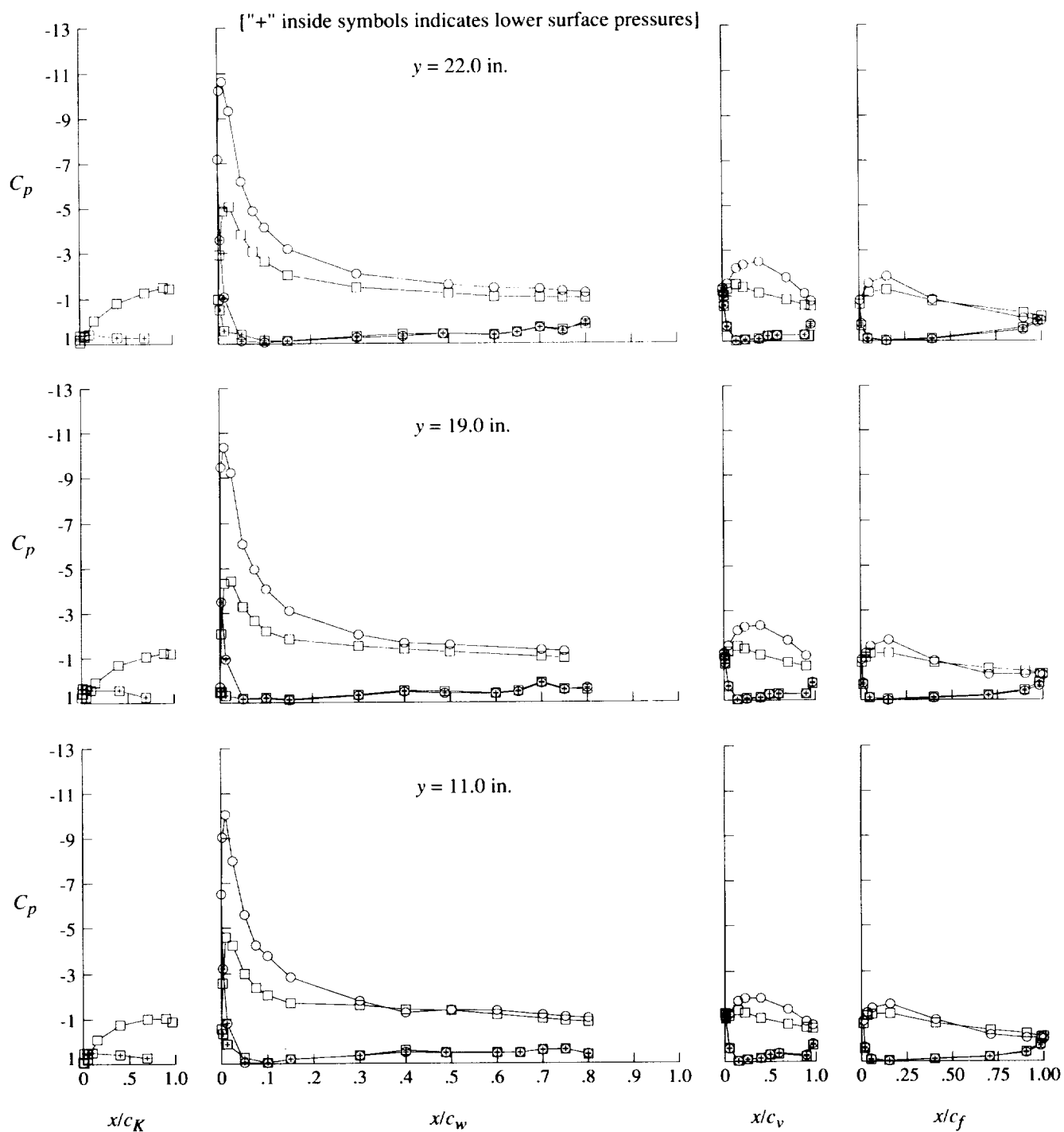


(g) Concluded.

Figure 40. Continued.

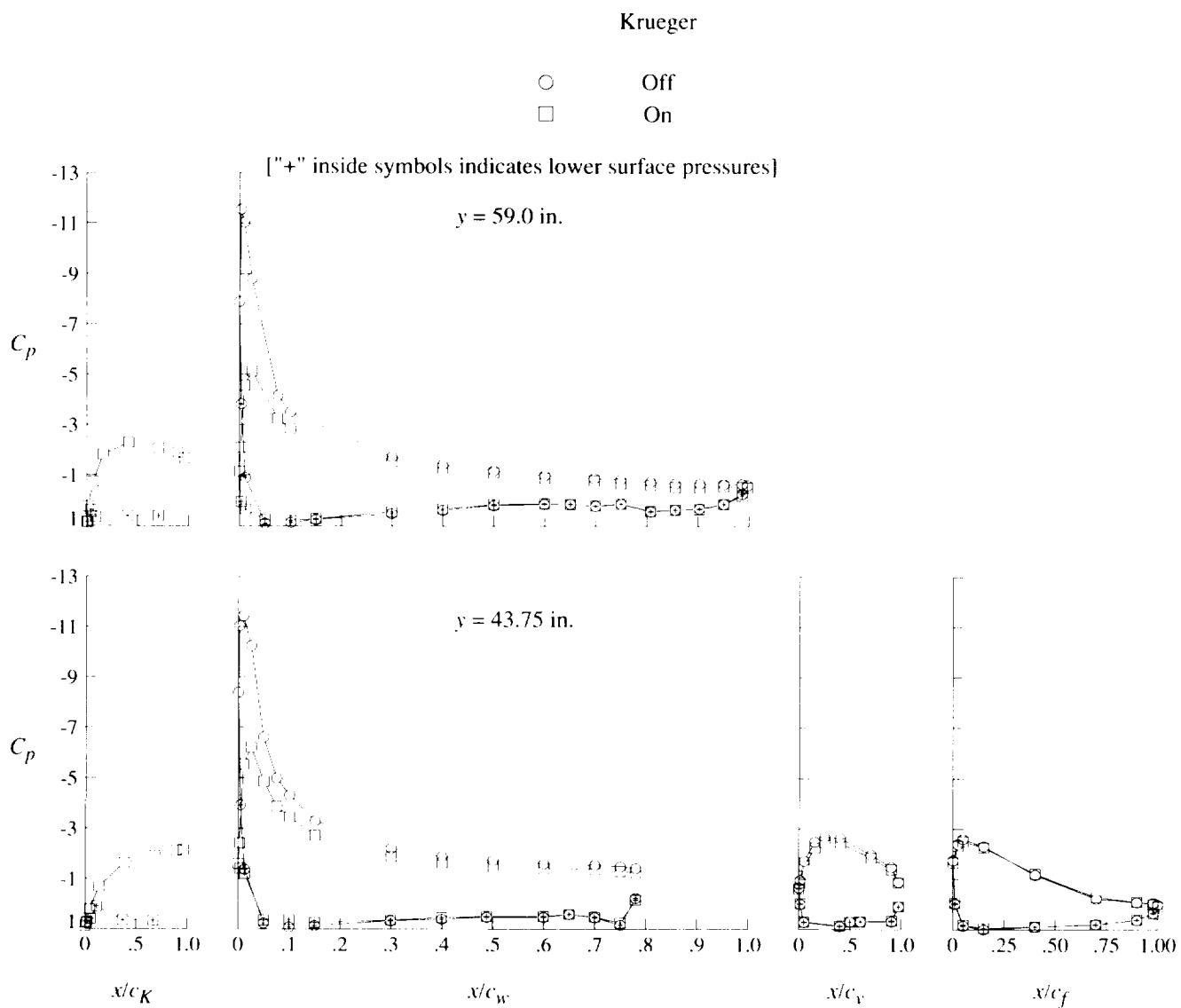
Krueger

○ Off
□ On



(h) $q = 40$ psf; $\alpha = 16^\circ$.

Figure 40. Continued.

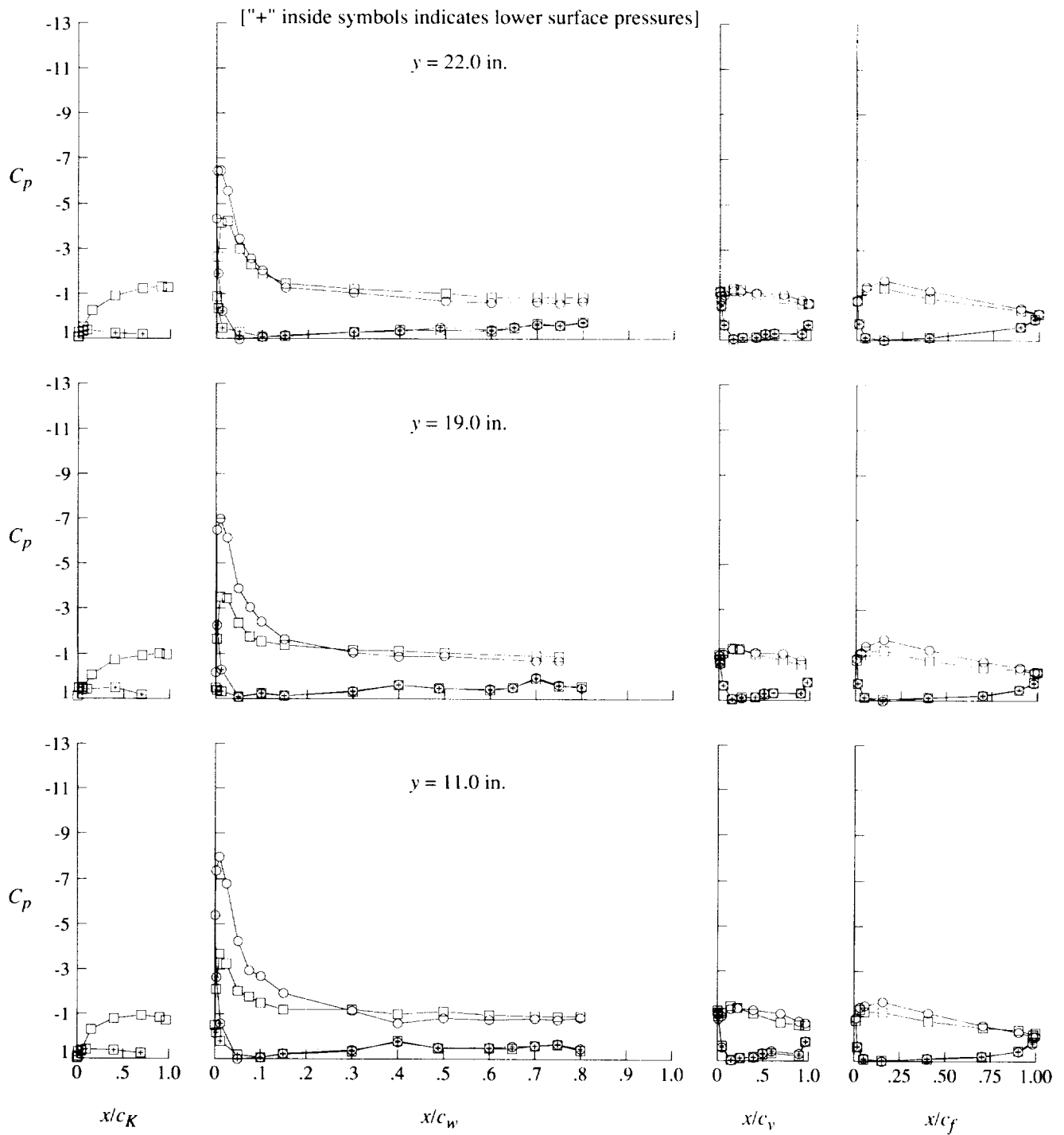


(h) Concluded.

Figure 40. Continued.

Krueger

○ Off
□ On



(i) $q = 20$ psf; $\alpha = 20^\circ$.

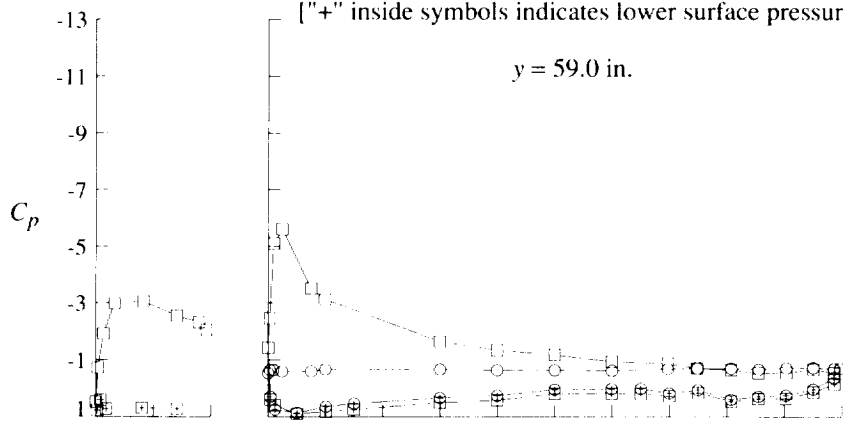
Figure 40. Continued.

Krueger

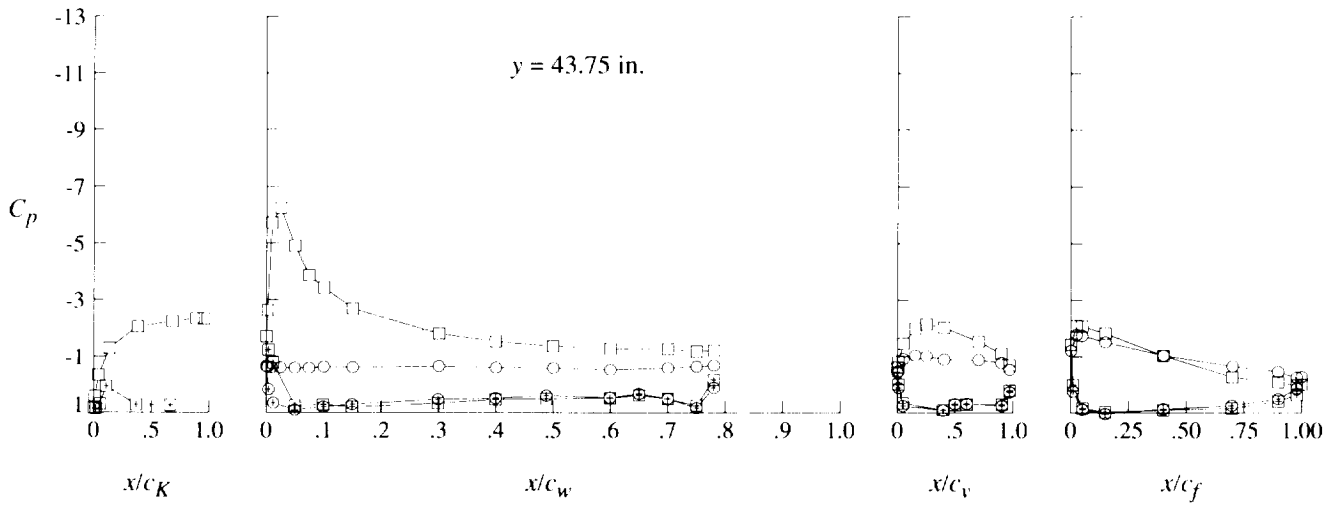
○ Off
□ On

["+ " inside symbols indicates lower surface pressures]

$y = 59.0$ in.



$y = 43.75$ in.



(i) Concluded.

Figure 40. Concluded.

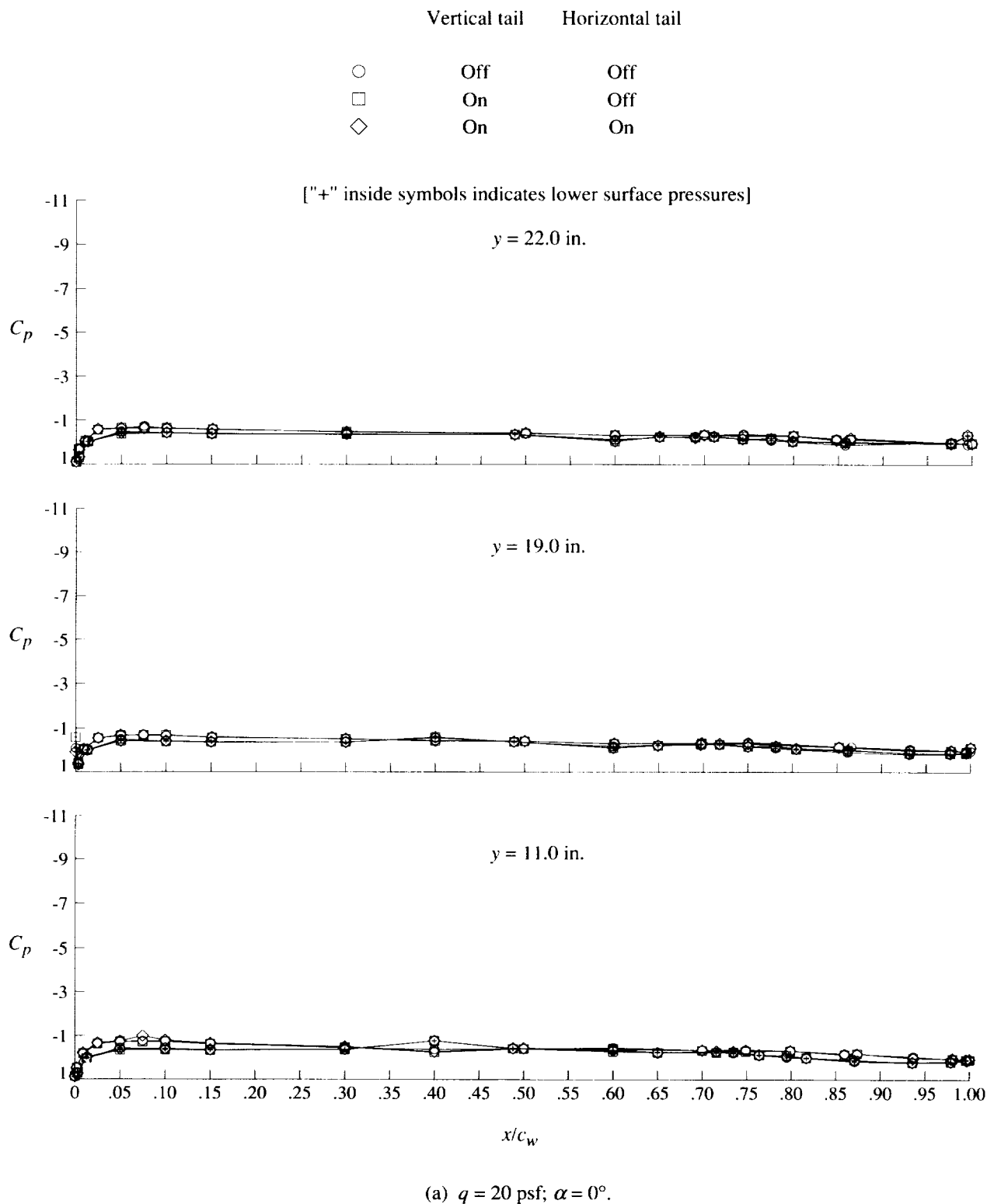
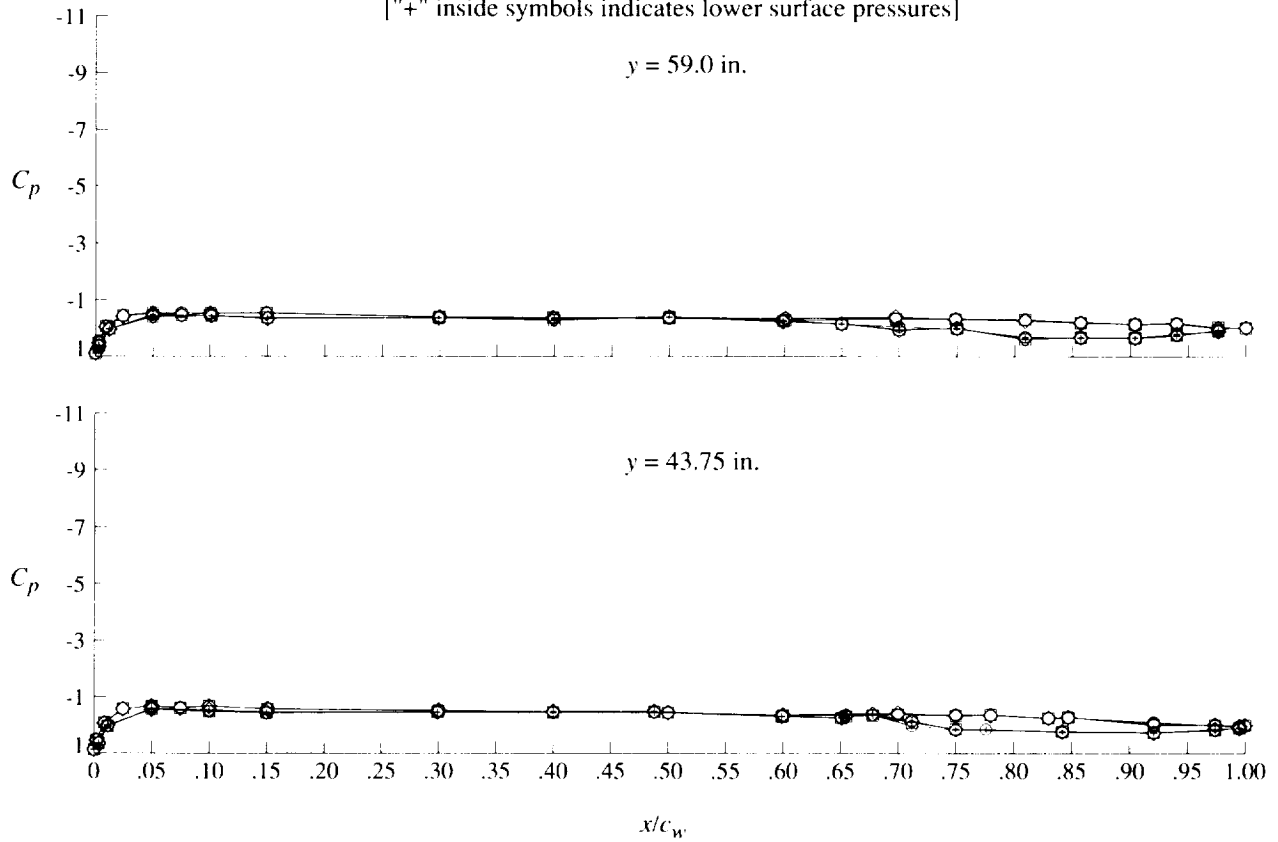


Figure 41. Effect of empennage on pressure distributions for cruise configuration.

Vertical tail Horizontal tail

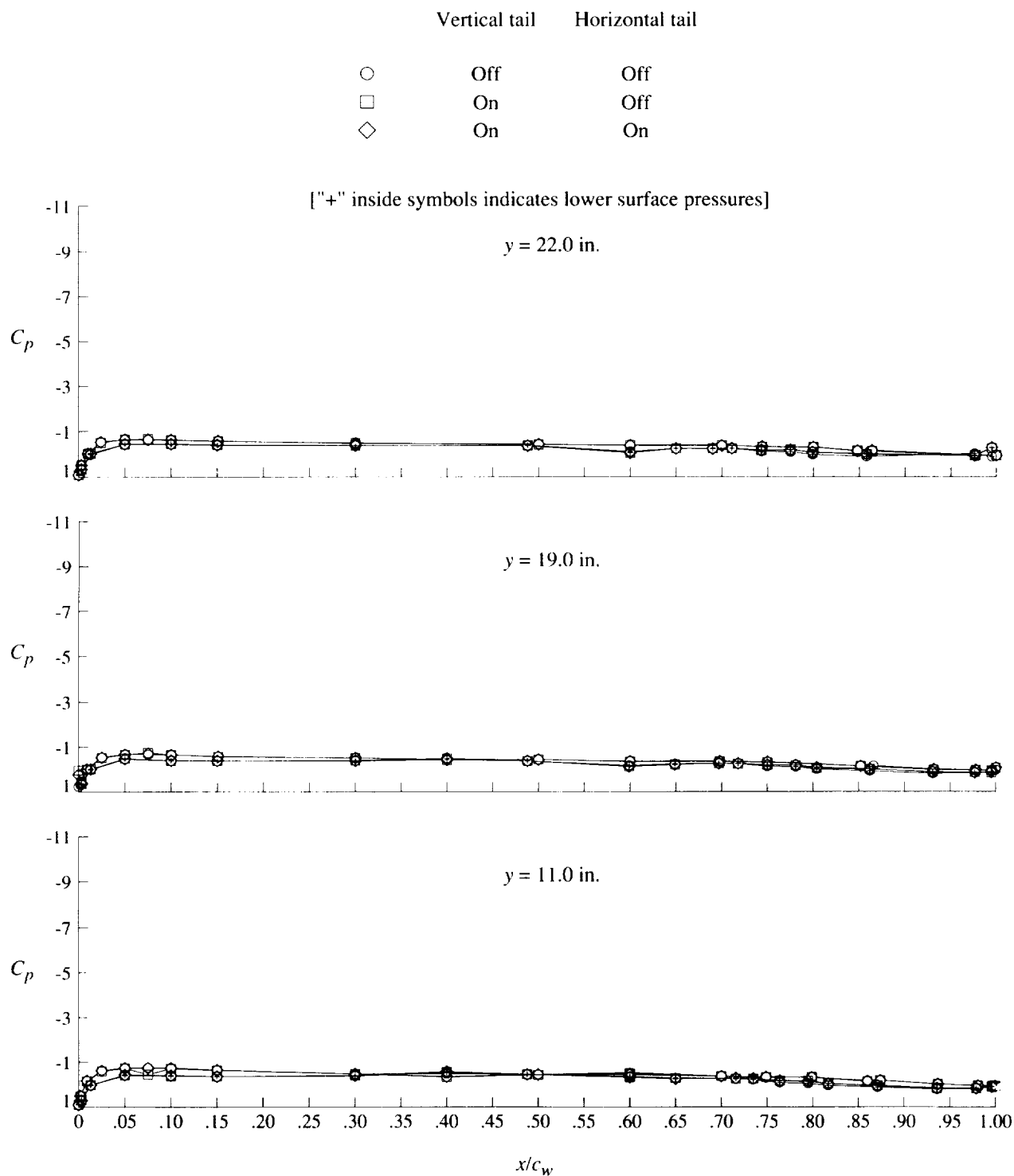
○	Off	Off
□	On	Off
◇	On	On

["+" inside symbols indicates lower surface pressures]



(a) Concluded.

Figure 41. Continued.



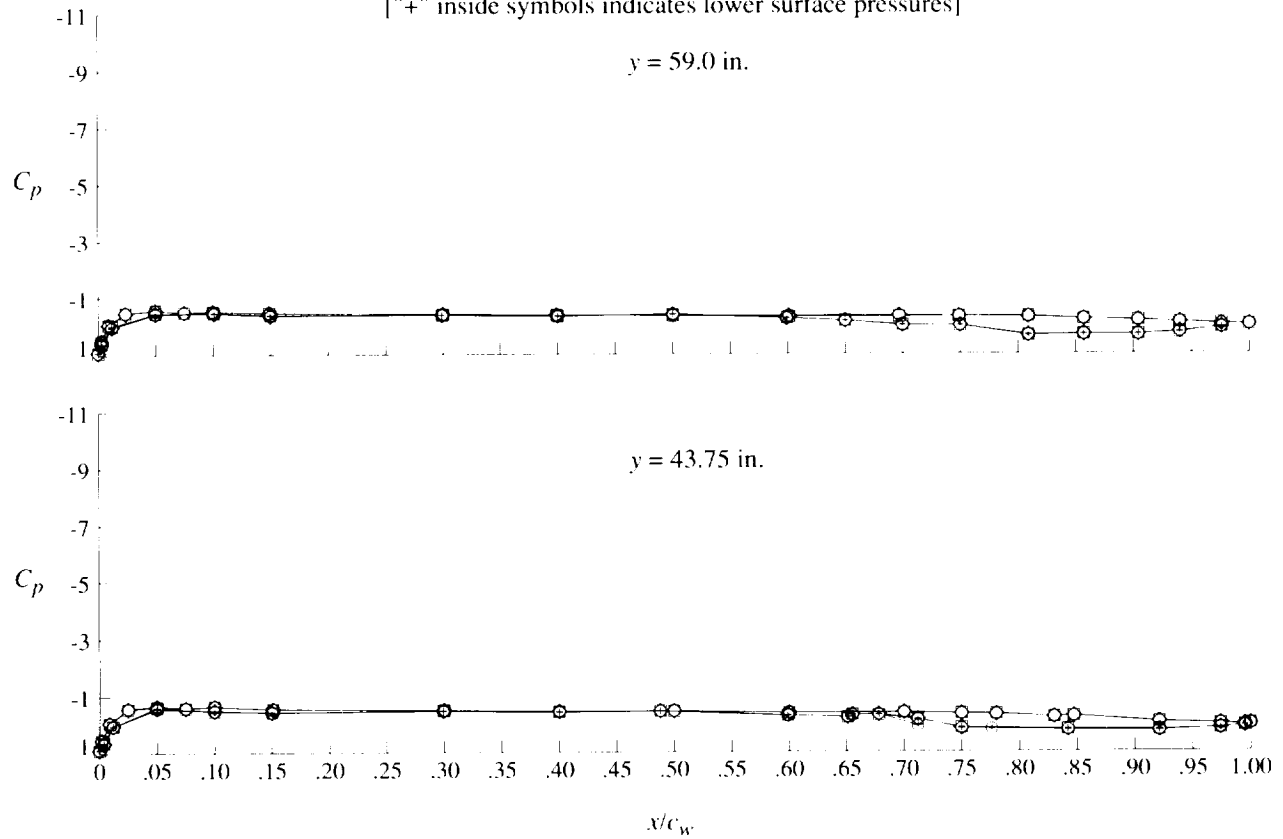
(b) $q = 40 \text{ psf}$; $\alpha = 0^\circ$.

Figure 41. Continued.

Vertical tail Horizontal tail

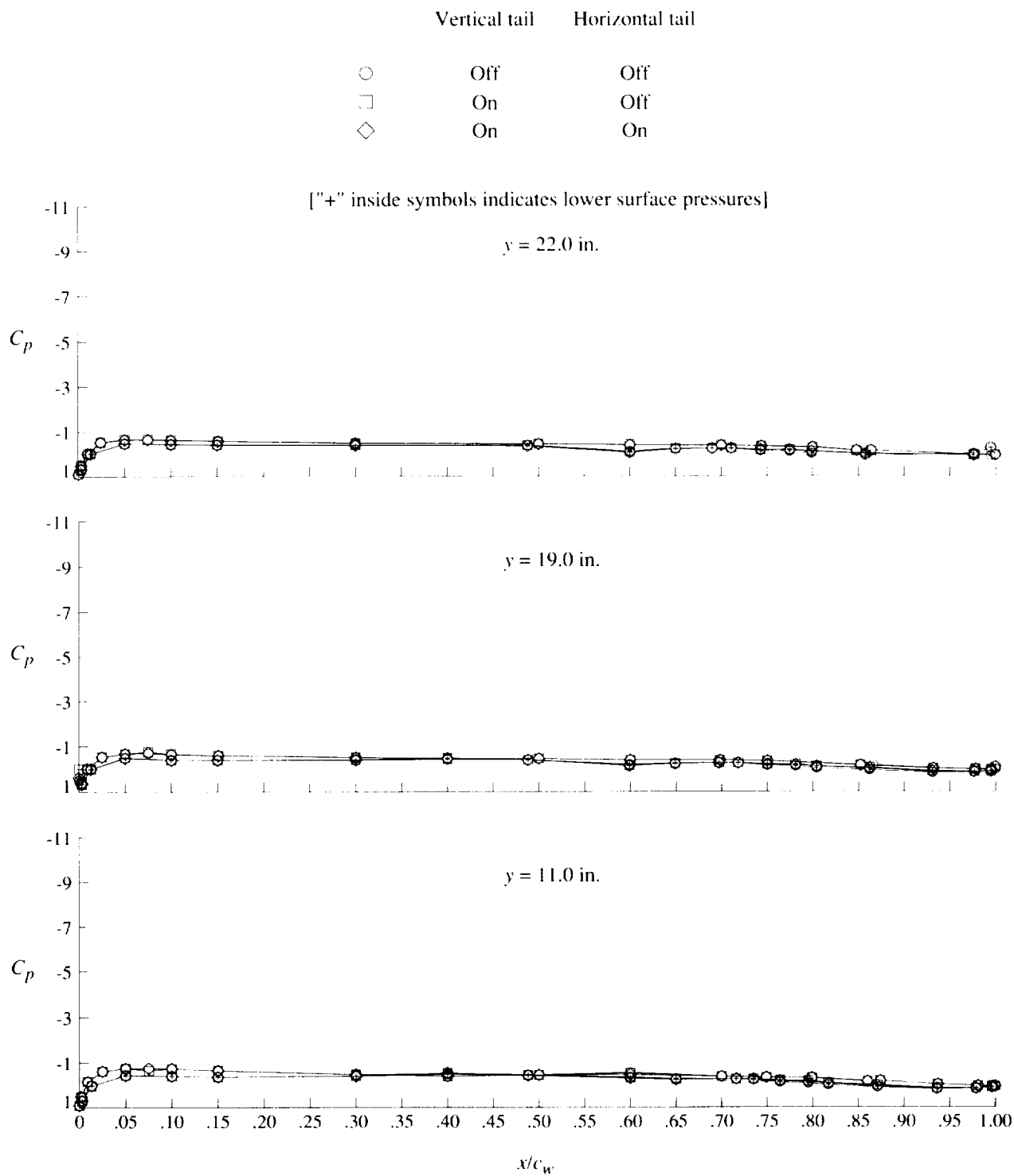
○	Off	Off
□	On	Off
◇	On	On

["+" inside symbols indicates lower surface pressures]



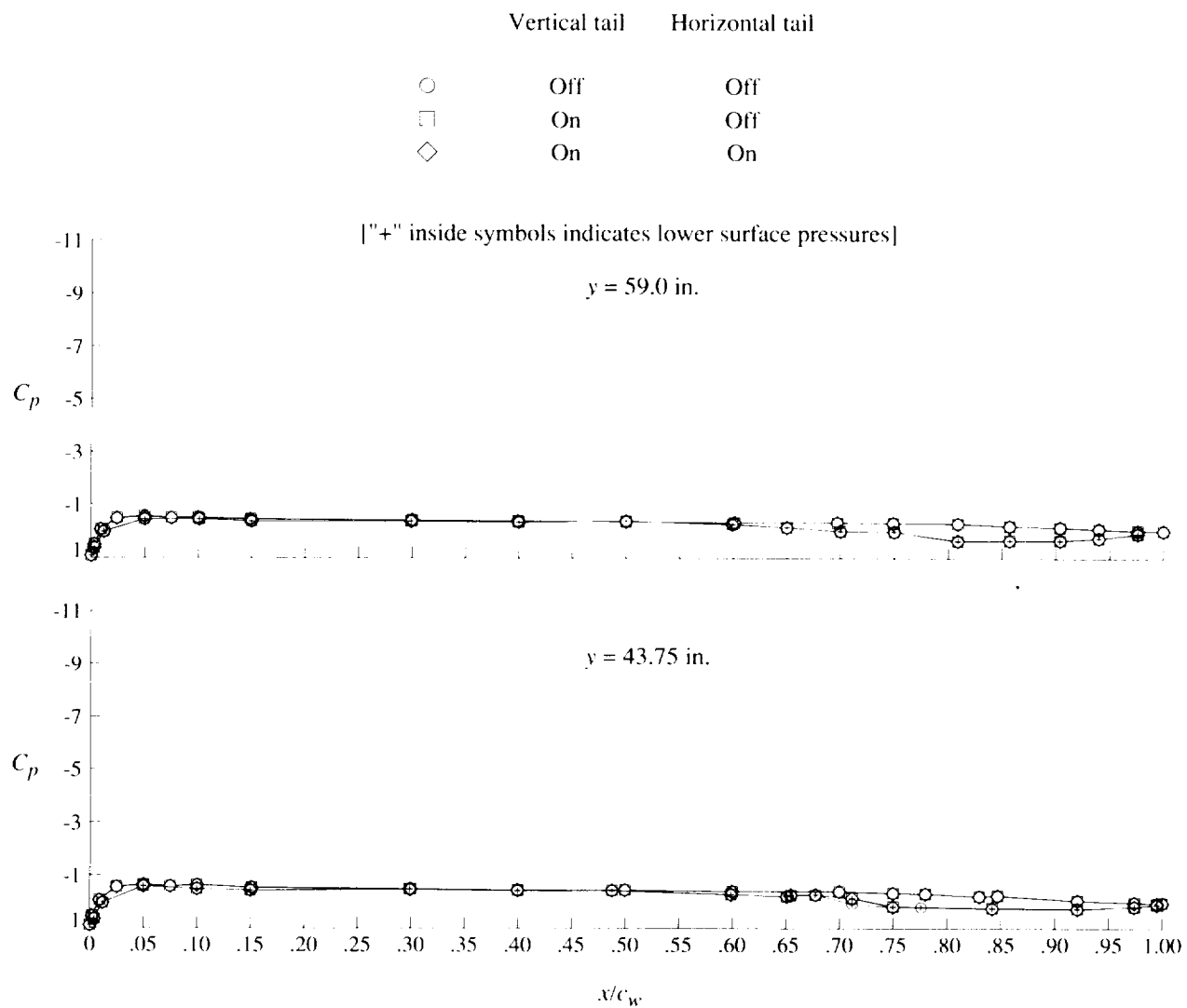
(b) Concluded.

Figure 41. Continued.



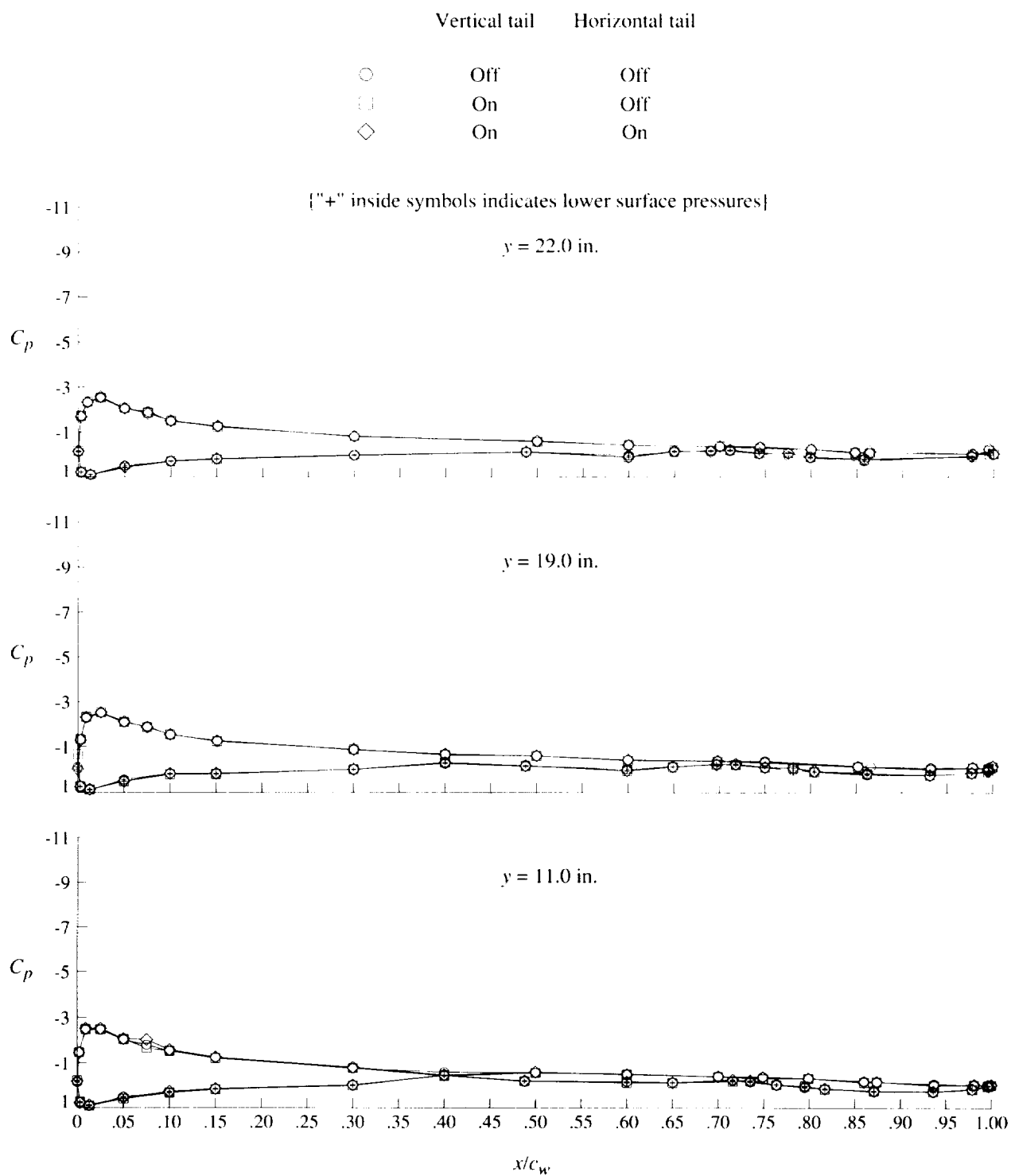
(c) $q = 60$ psf; $\alpha = 0^\circ$.

Figure 41. Continued.



(c) Concluded.

Figure 41. Continued.



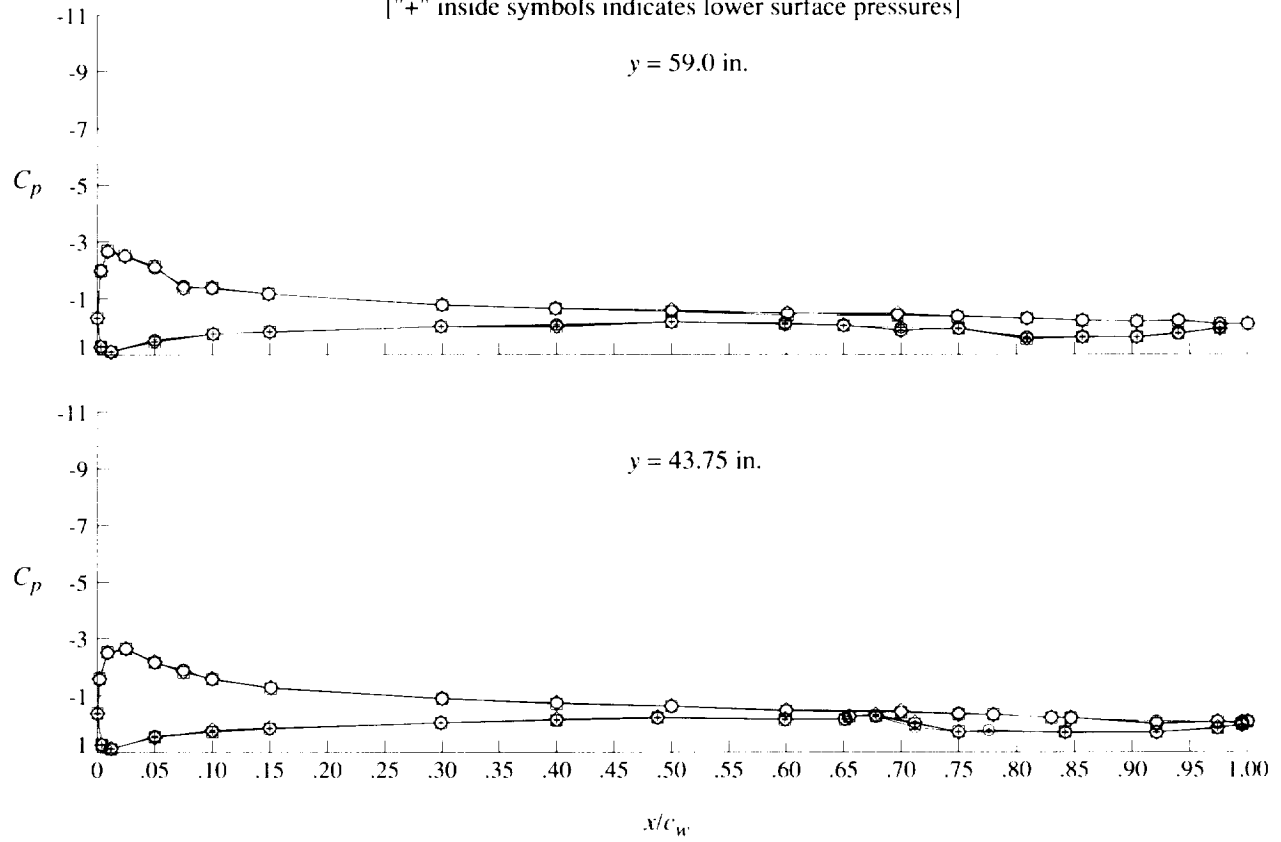
(d) $q = 20$ psf; $\alpha = 8^\circ$.

Figure 41. Continued.

Vertical tail Horizontal tail

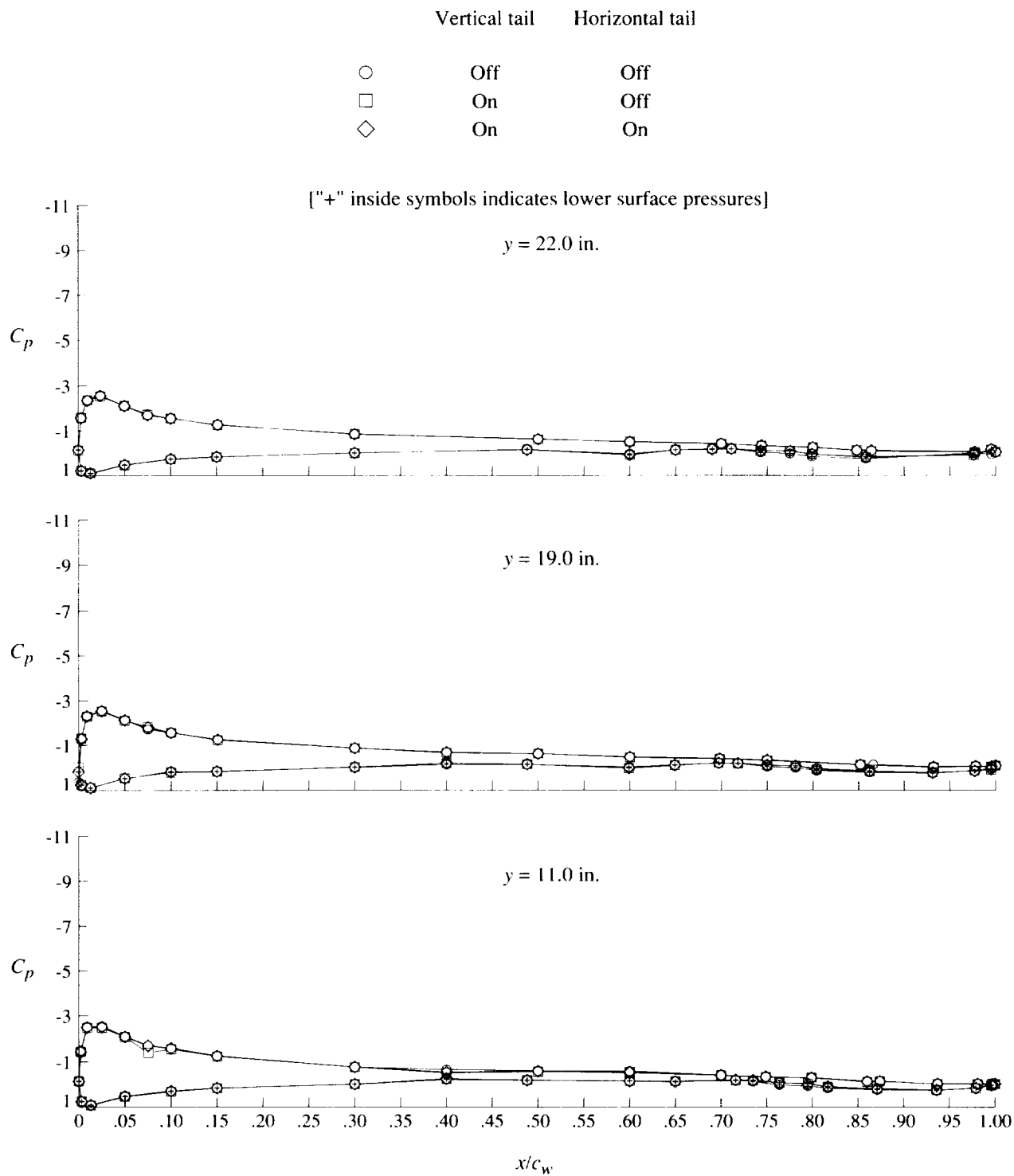
○	Off	Off
□	On	Off
◇	On	On

["+" inside symbols indicates lower surface pressures]



(d) Concluded.

Figure 41. Continued.



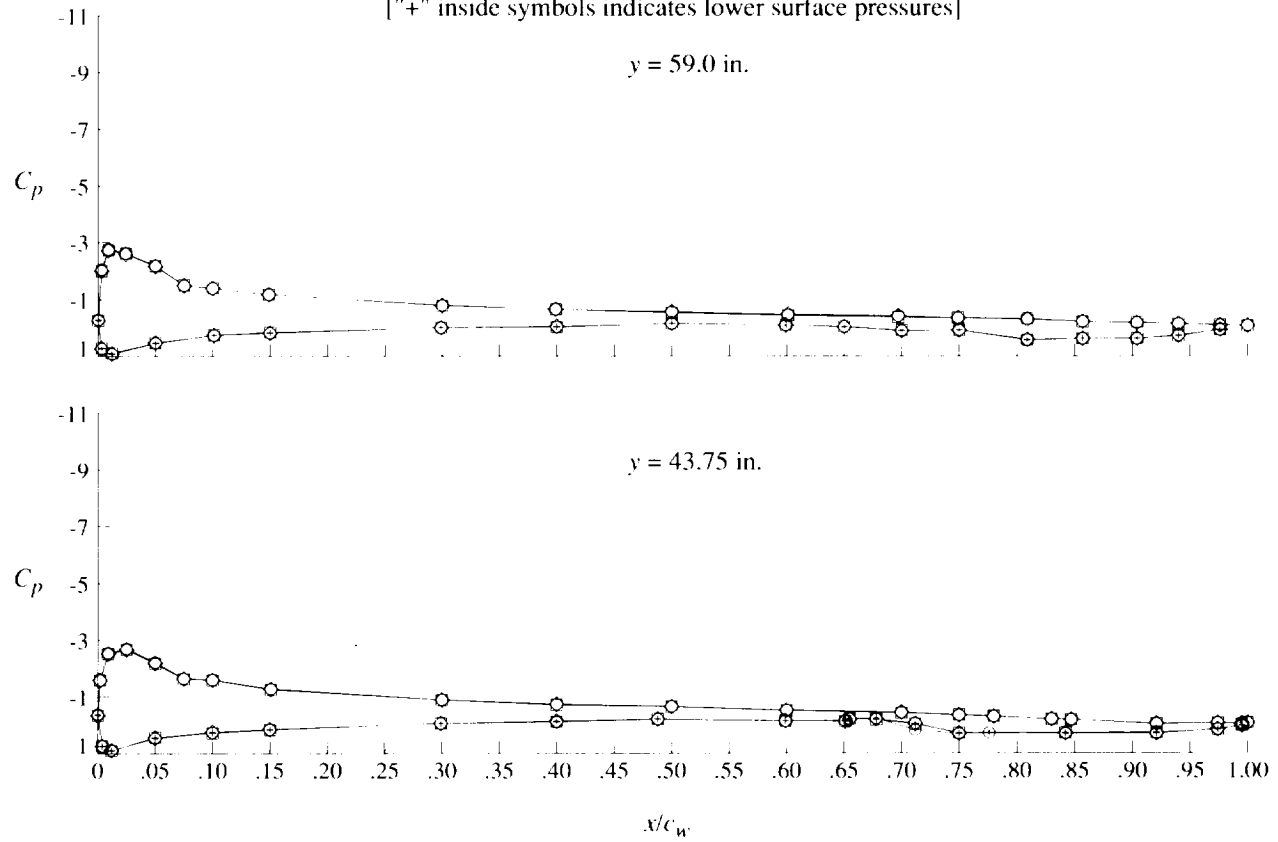
(e) $q = 40$ psf; $\alpha = 8^\circ$.

Figure 41. Continued.

Vertical tail Horizontal tail

○	Off	Off
□	On	Off
◇	On	On

["+" inside symbols indicates lower surface pressures]



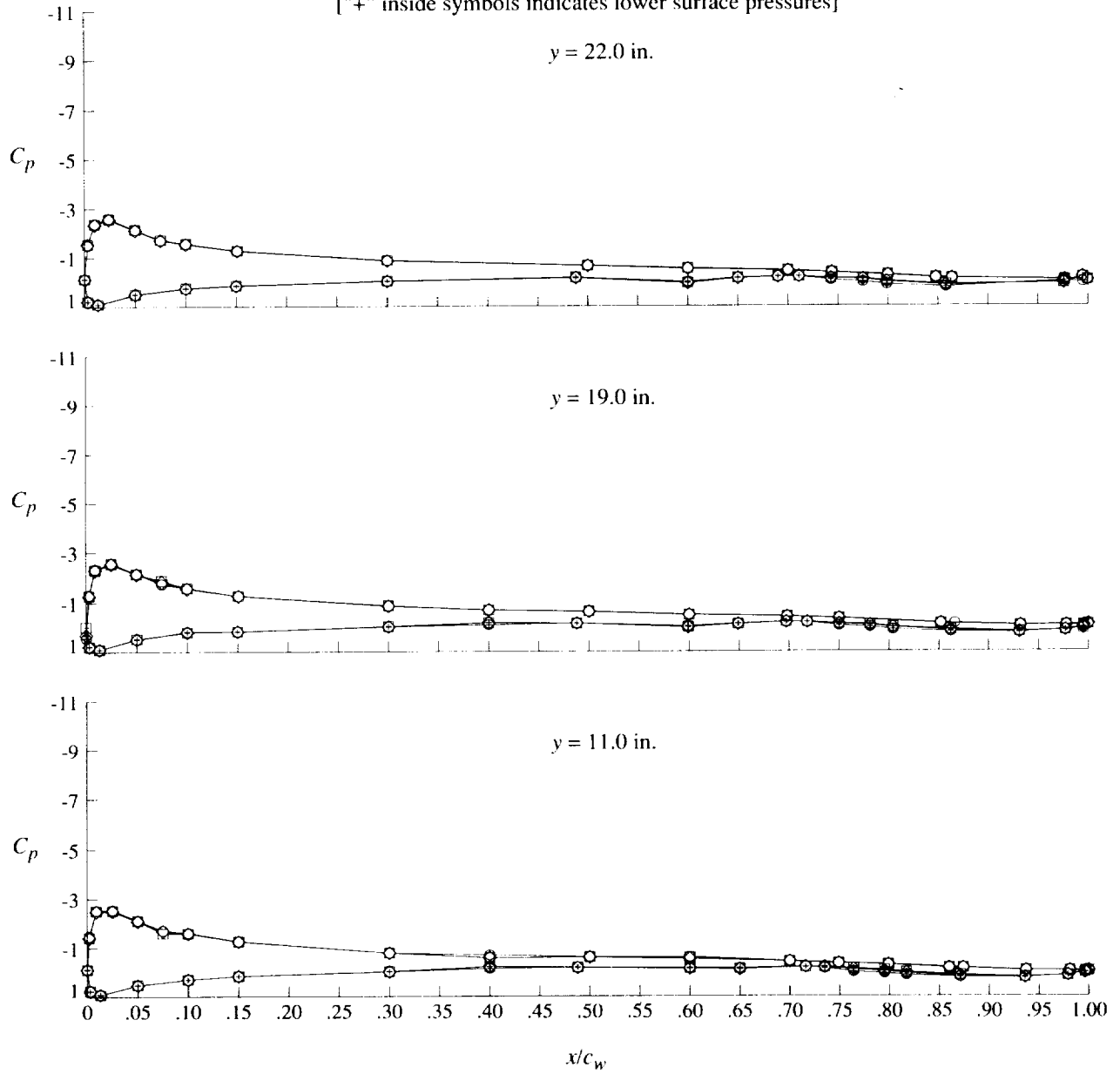
(e) Concluded.

Figure 41. Continued.

Vertical tail Horizontal tail

○	Off	Off
□	On	Off
◇	On	On

["+" inside symbols indicates lower surface pressures]



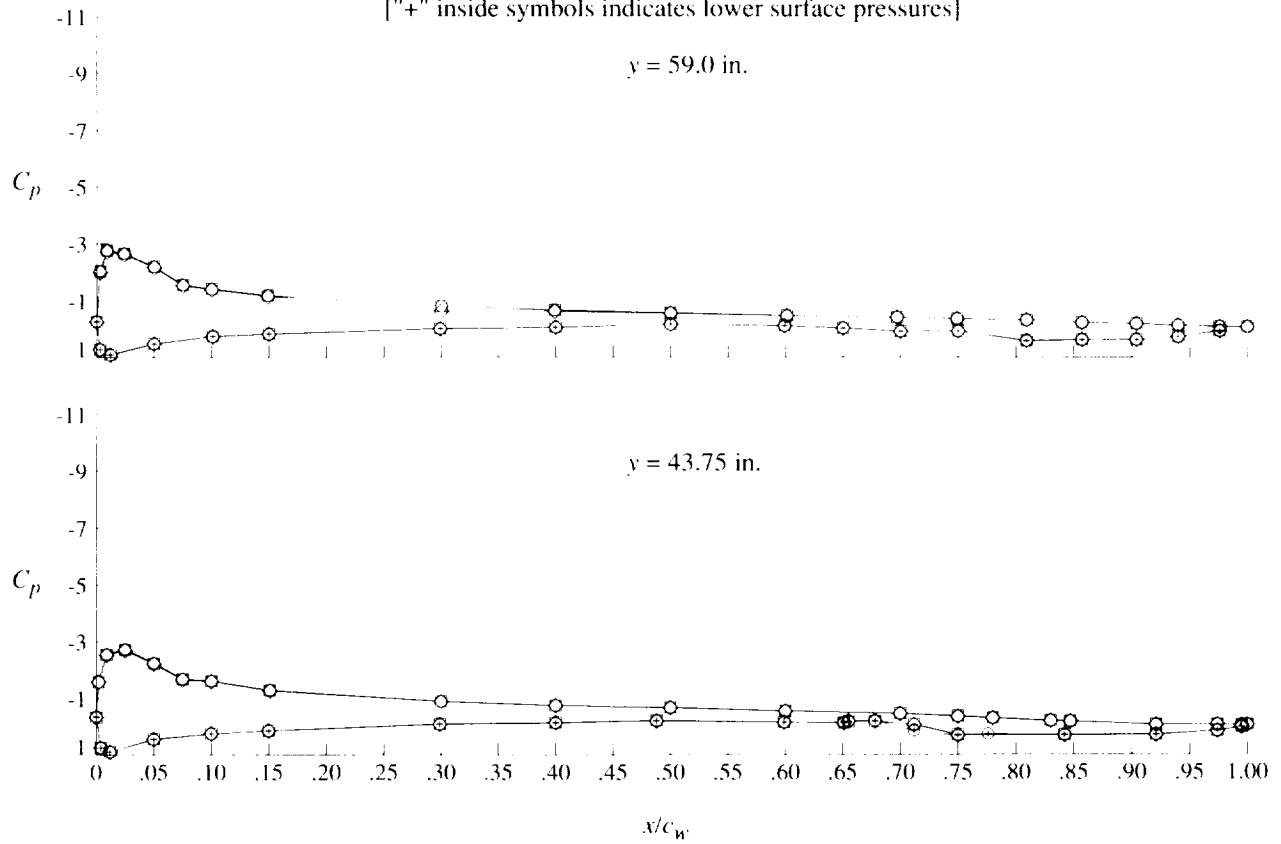
(f) $q = 60$ psf; $\alpha = 8^\circ$.

Figure 41. Continued.

Vertical tail Horizontal tail

○	Off	Off
□	On	Off
◇	On	On

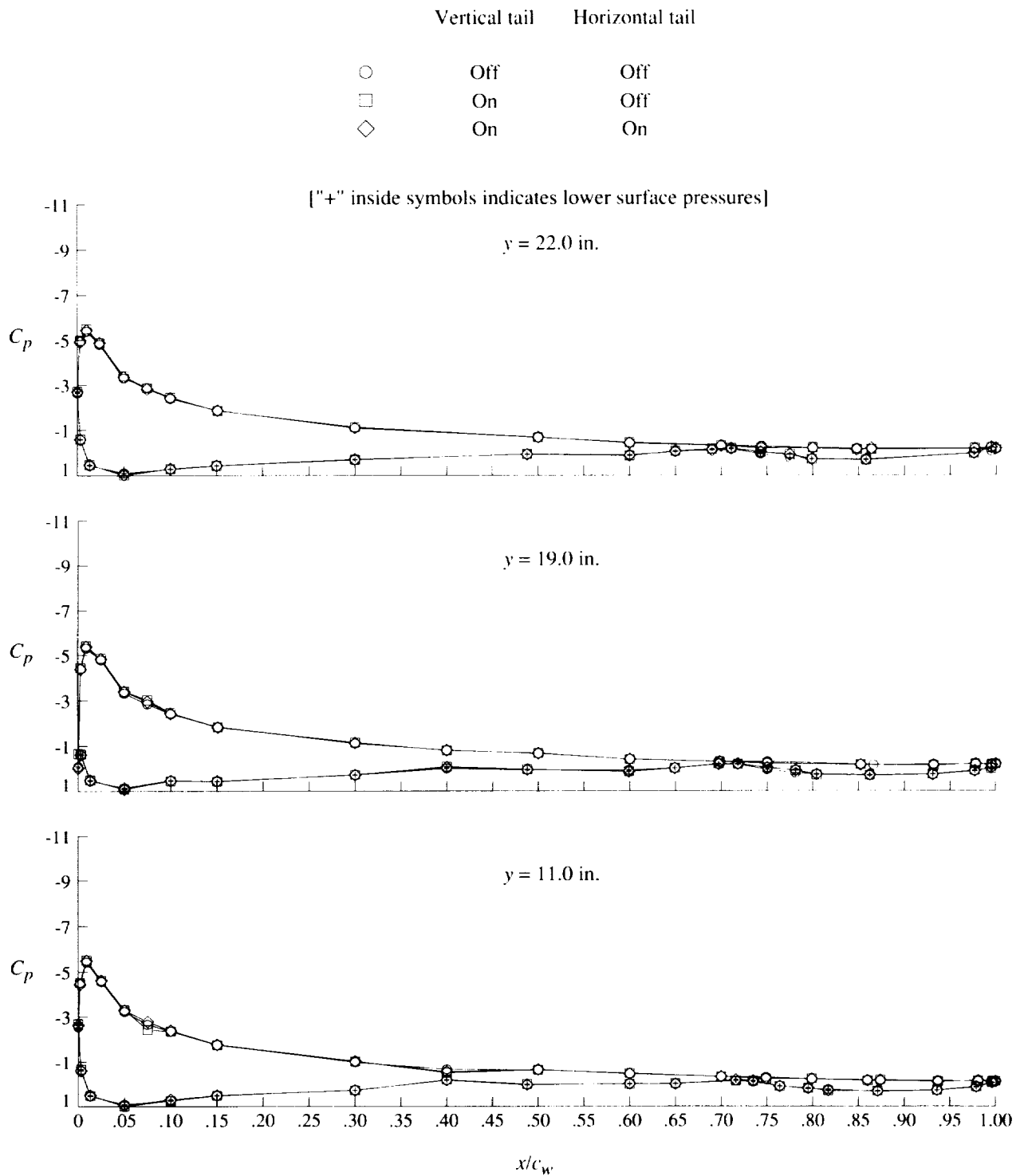
["+" inside symbols indicates lower surface pressures]



(f) Concluded.

Figure 41. Continued.

C-5



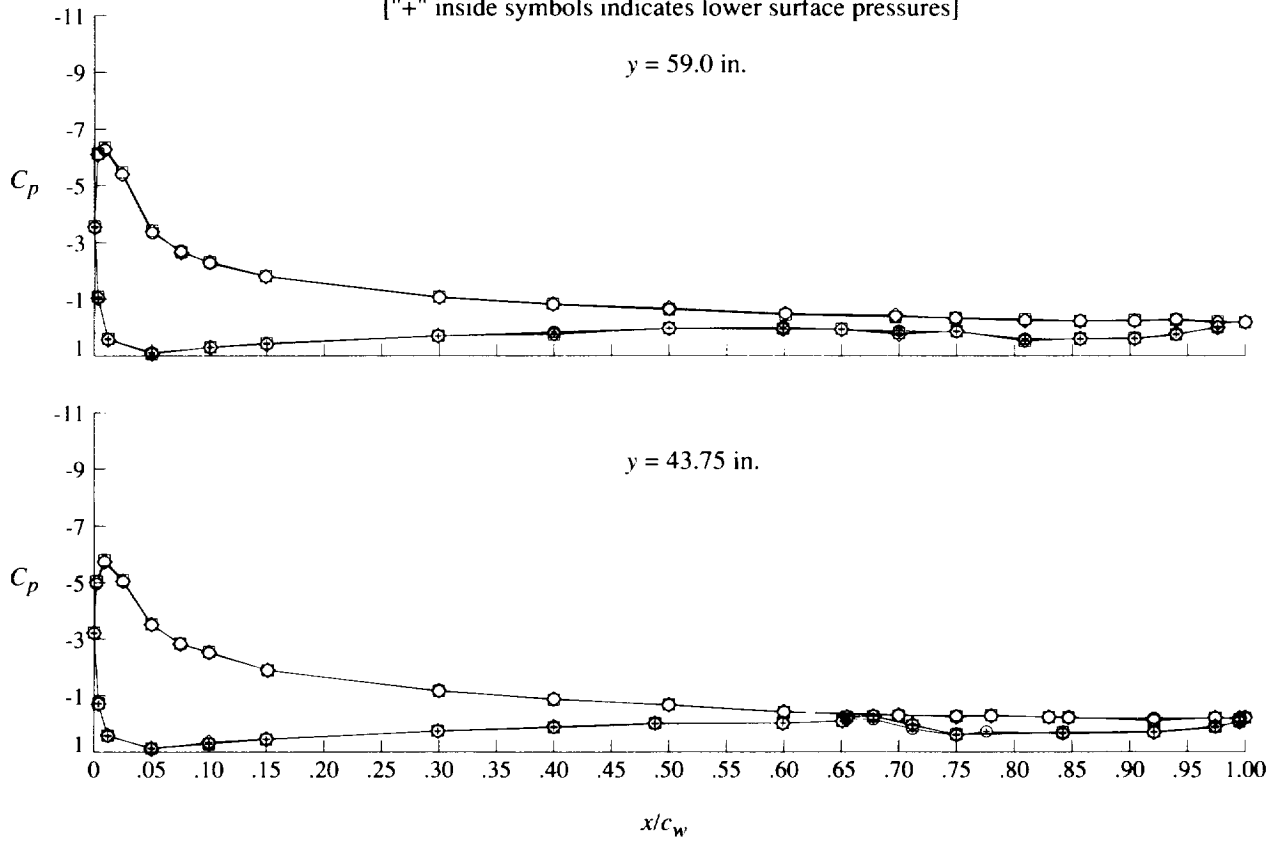
(g) $q = 20$ psf; $\alpha = 16^\circ$.

Figure 41. Continued.

Vertical tail Horizontal tail

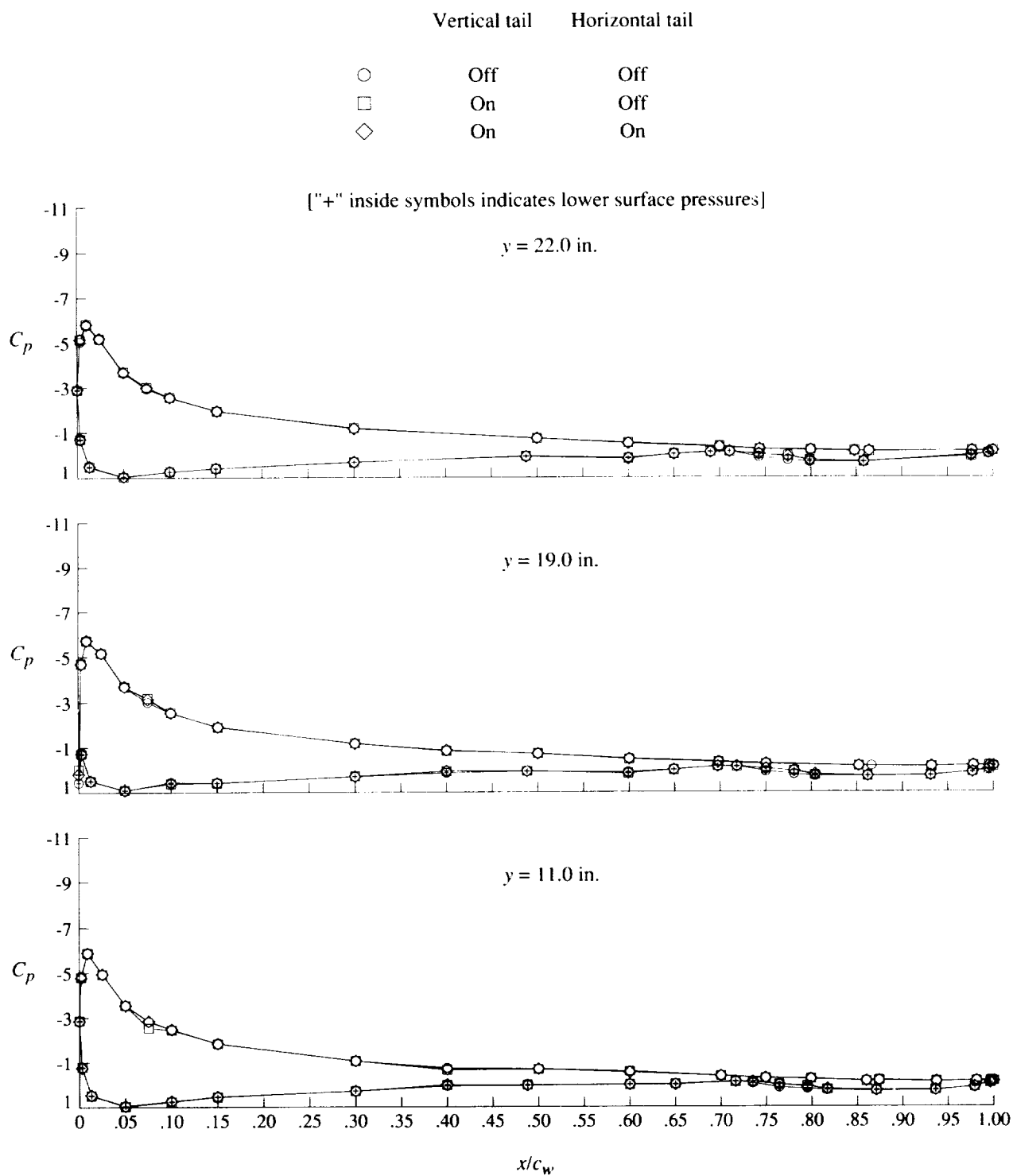
○	Off	Off
□	On	Off
◇	On	On

["+" inside symbols indicates lower surface pressures]



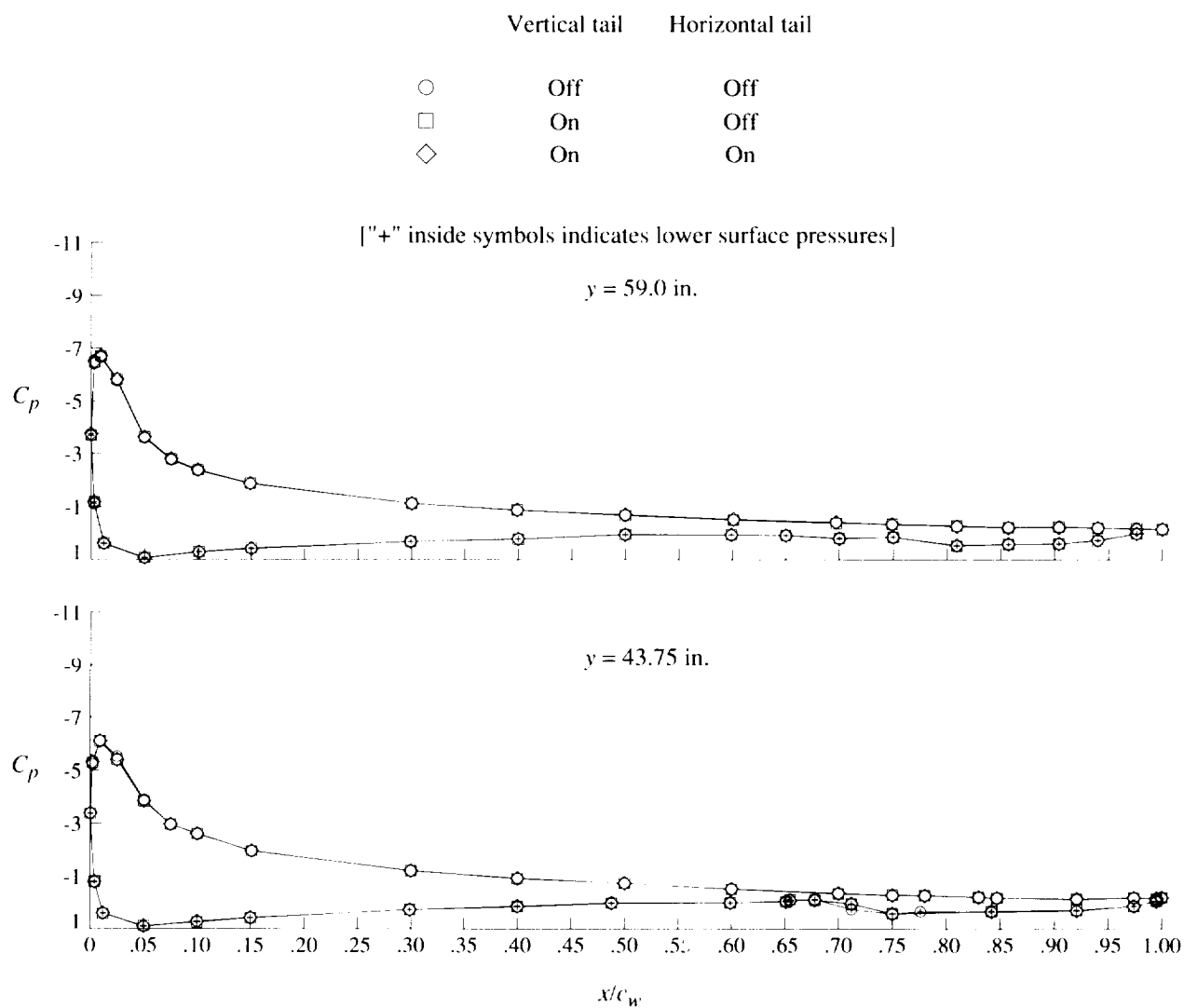
(g) Concluded.

Figure 41. Continued.



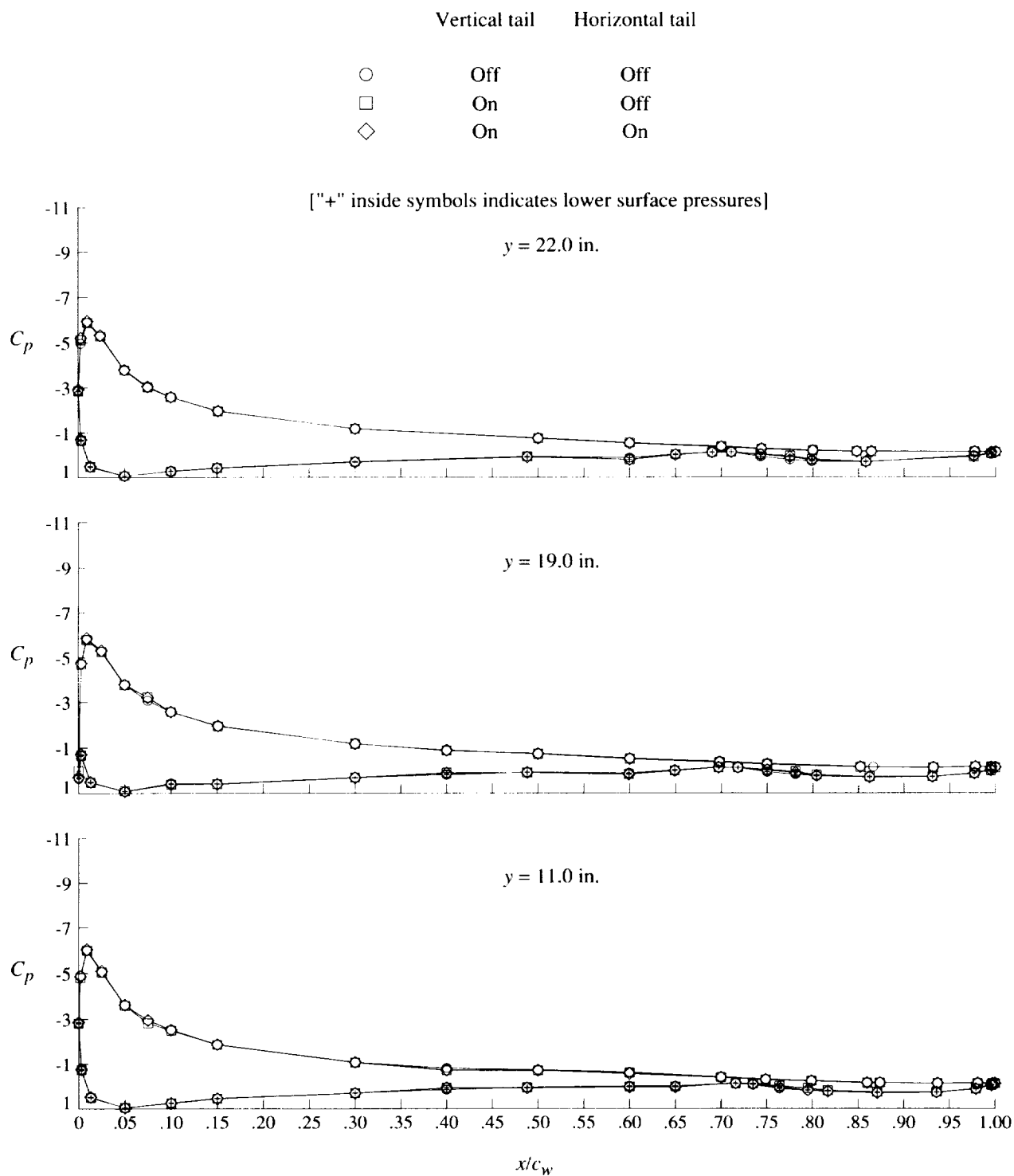
(h) $q = 40 \text{ psf}$; $\alpha = 16^\circ$.

Figure 41. Continued.



(h) Concluded.

Figure 41. Continued.



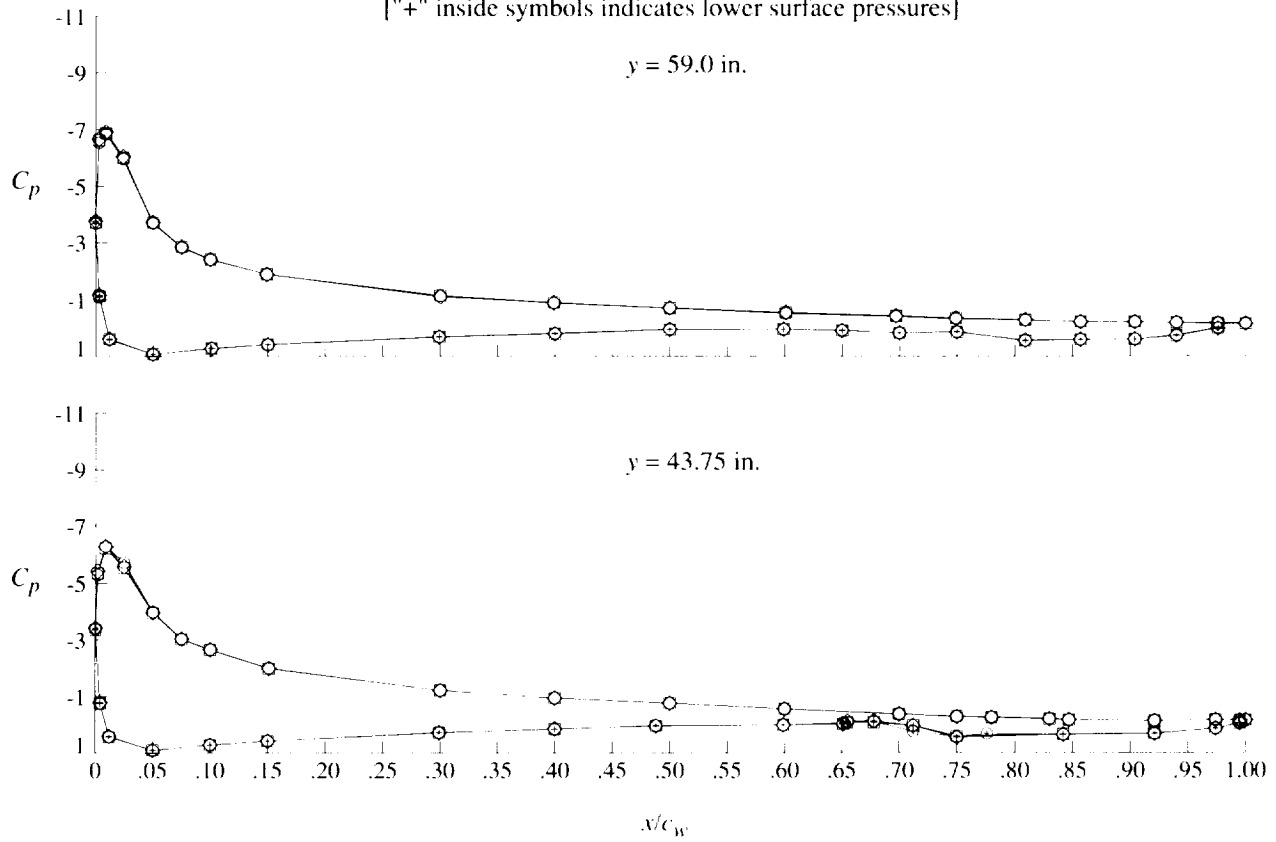
(i) $q = 60 \text{ psf}$; $\alpha = 16^\circ$.

Figure 41. Continued.

Vertical tail Horizontal tail

○	Off	Off
□	On	Off
◇	On	On

["+" inside symbols indicates lower surface pressures]



(i) Concluded.

Figure 41. Concluded.

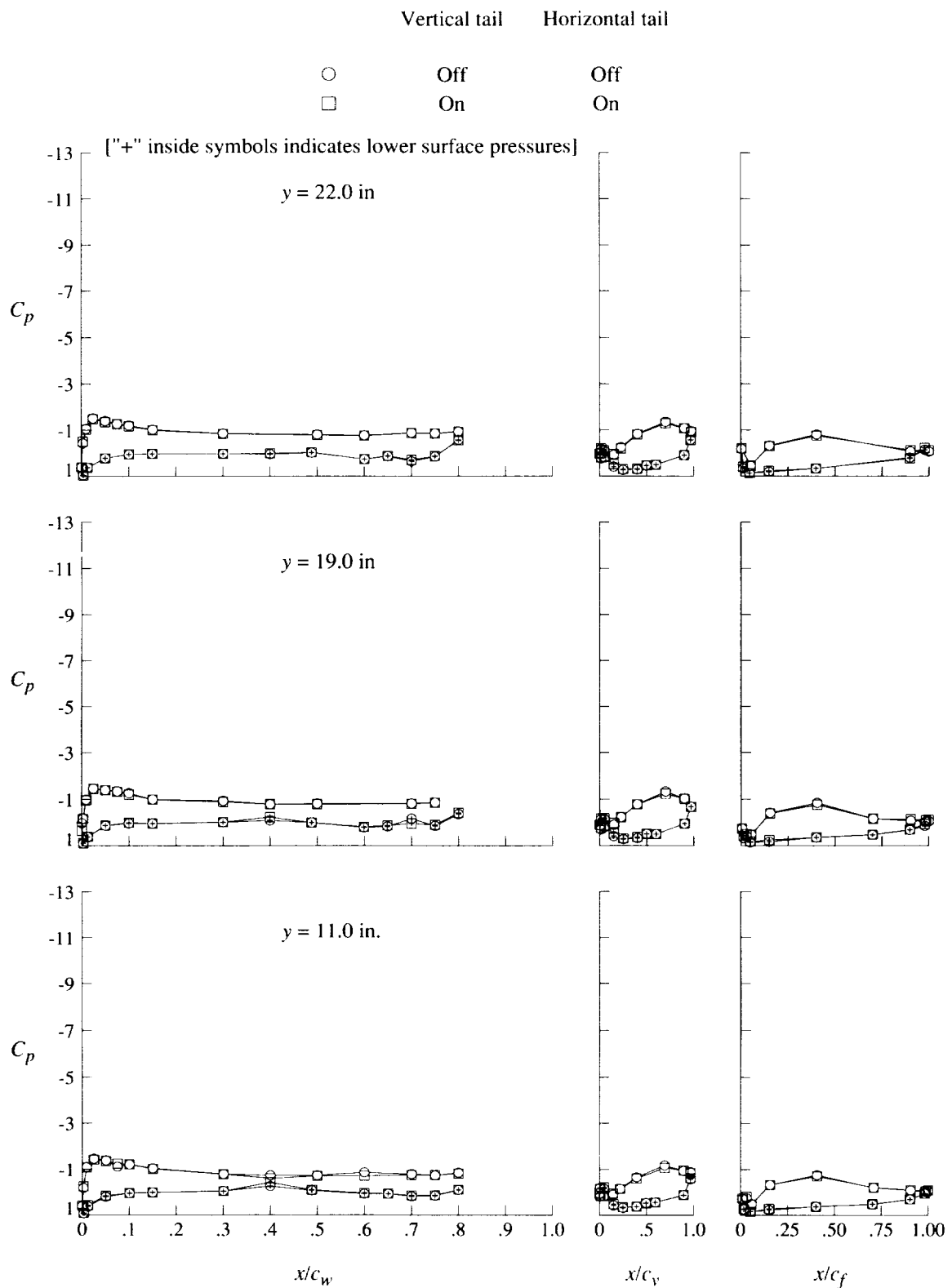
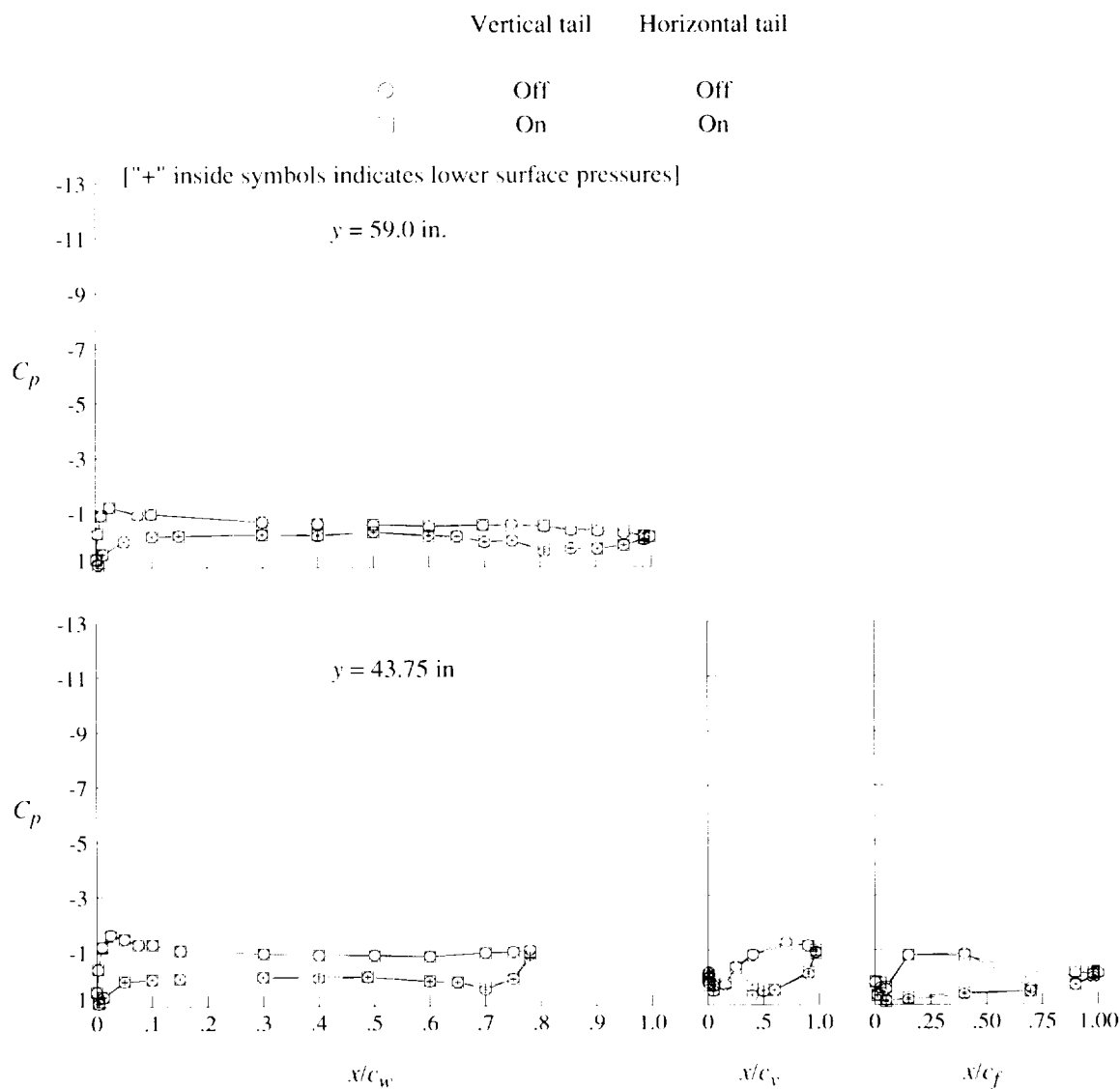
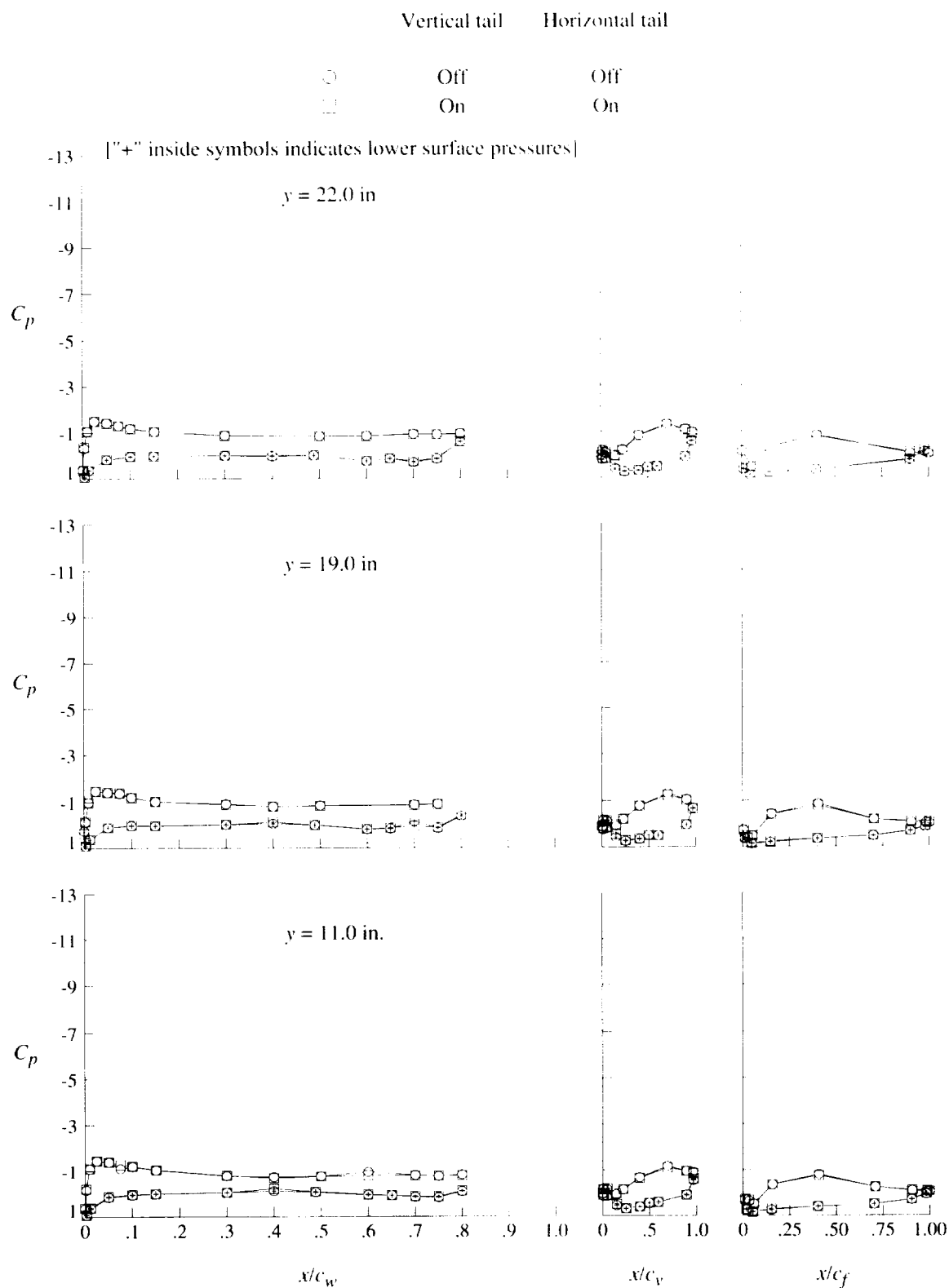


Figure 42. Effect of empennage on pressure distributions for flaps-only configuration at $\delta_f = 30^\circ$.



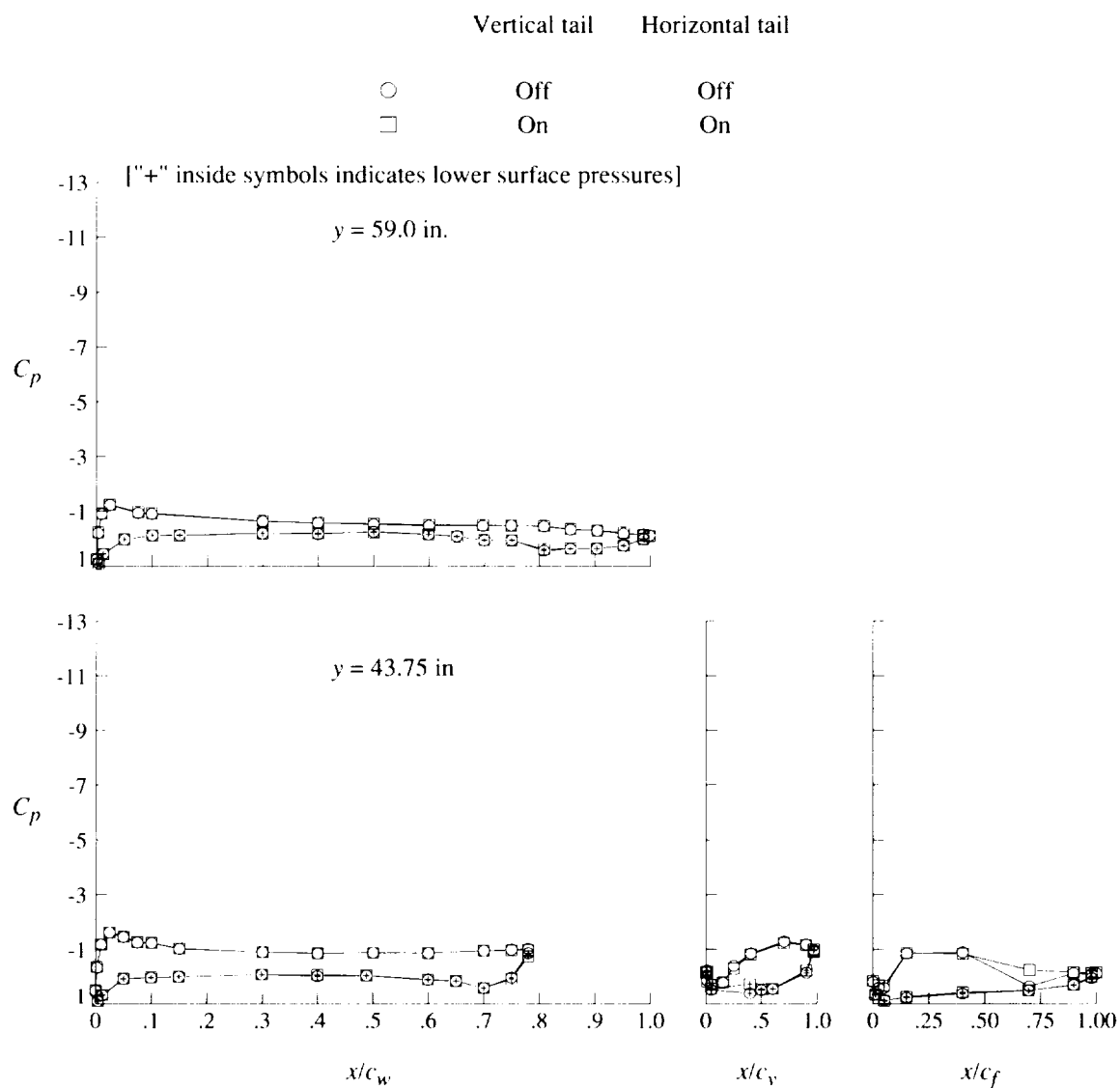
(a) Concluded.

Figure 42. Continued.



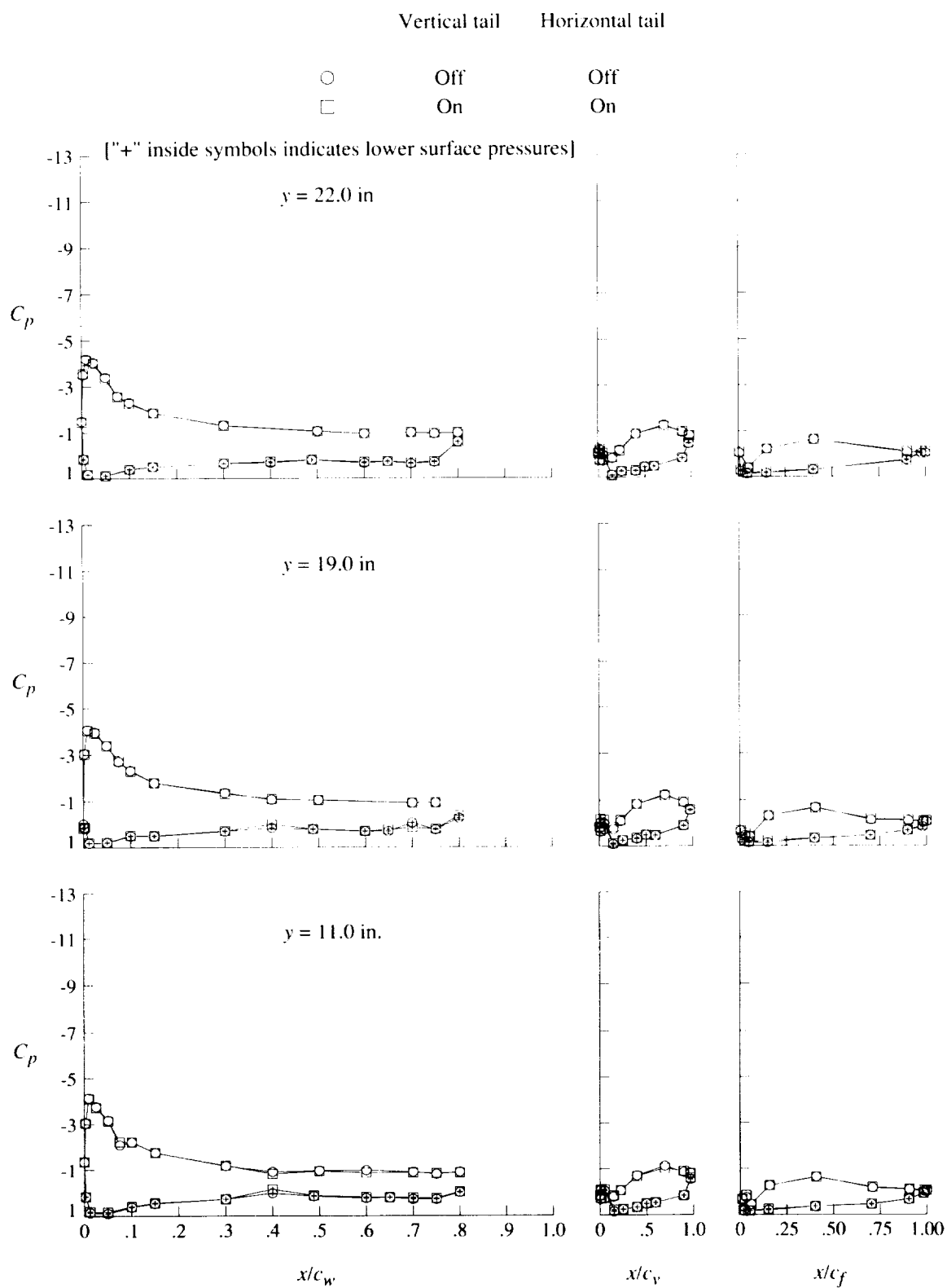
(b) $q = 40 \text{ psf}$; $\alpha = 0^\circ$.

Figure 42. Continued.



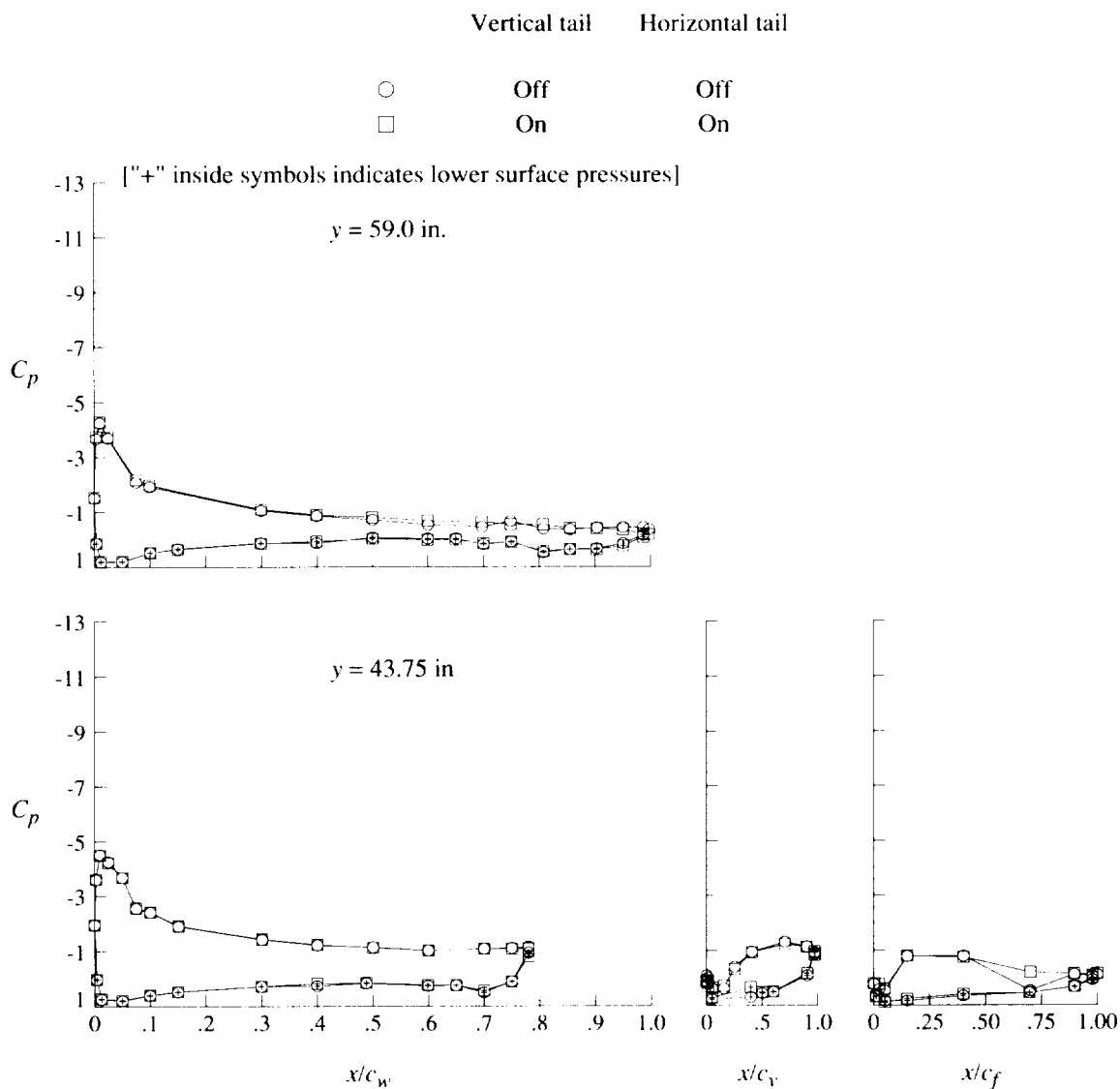
(b) Concluded.

Figure 42. Continued.



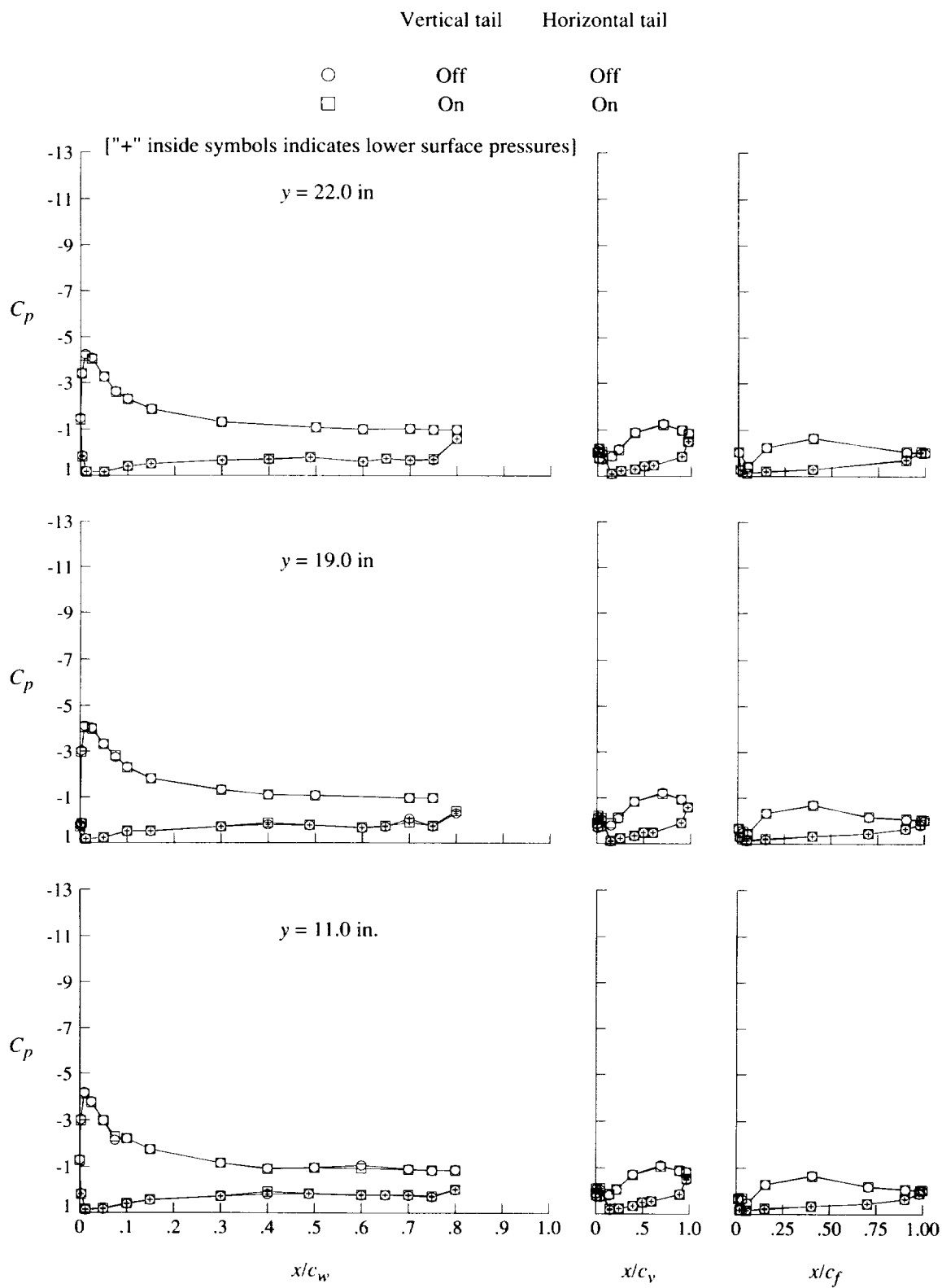
(c) $q = 20 \text{ psf}$; $\alpha = 8^\circ$.

Figure 42. Continued.



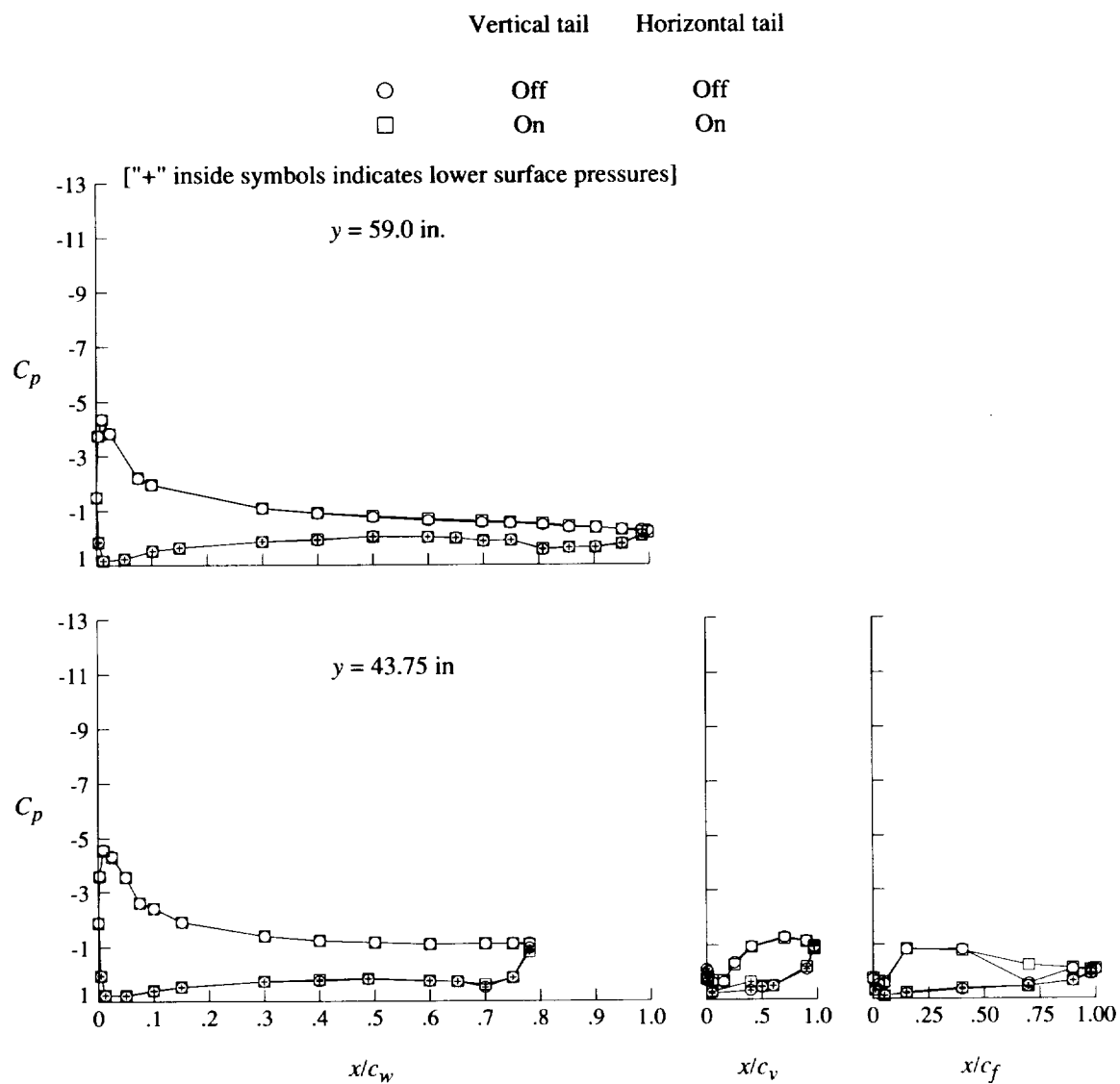
(c) Concluded.

Figure 42. Continued.



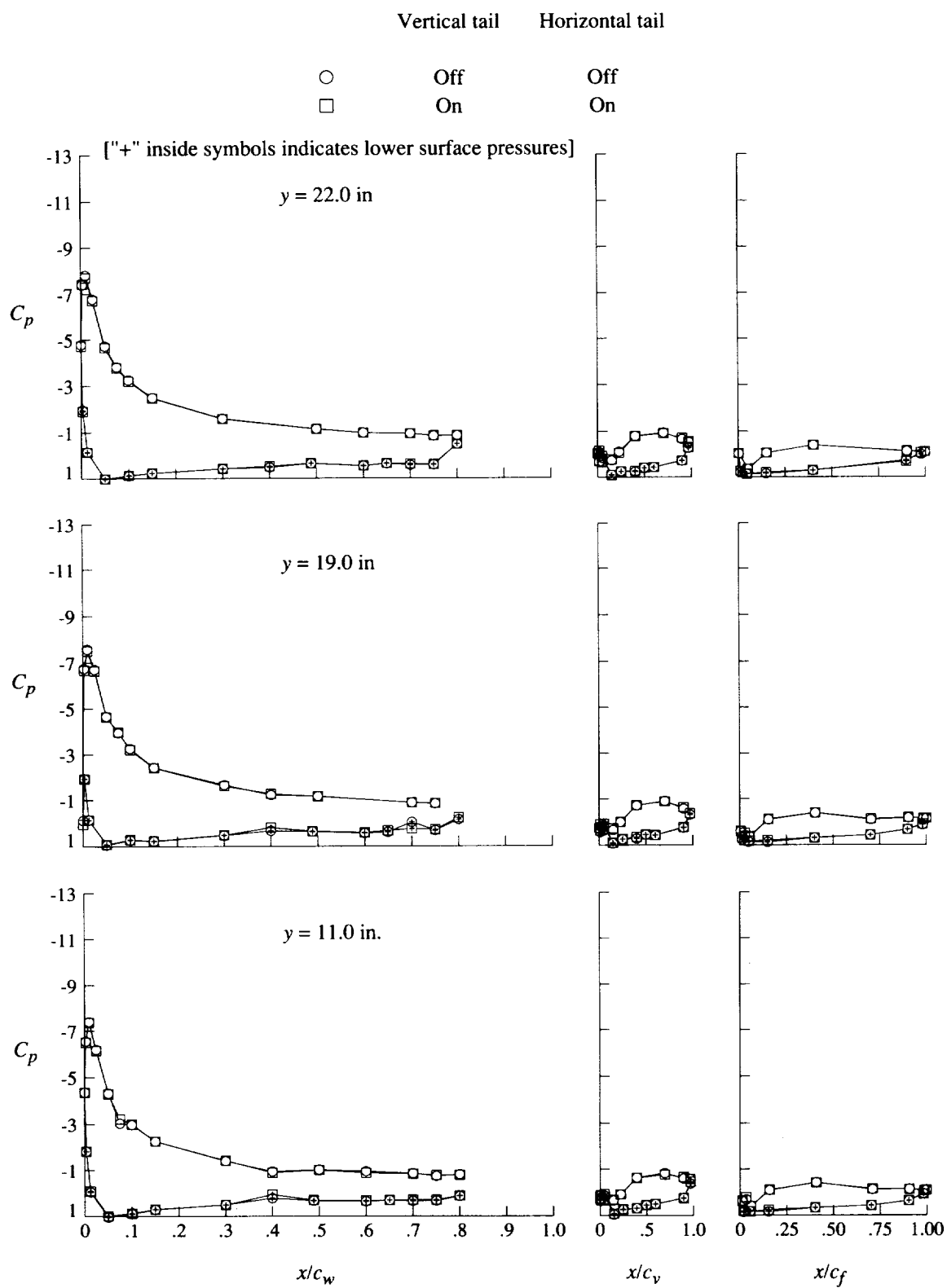
(d) $q = 40$ psf; $\alpha = 8^\circ$.

Figure 42. Continued.



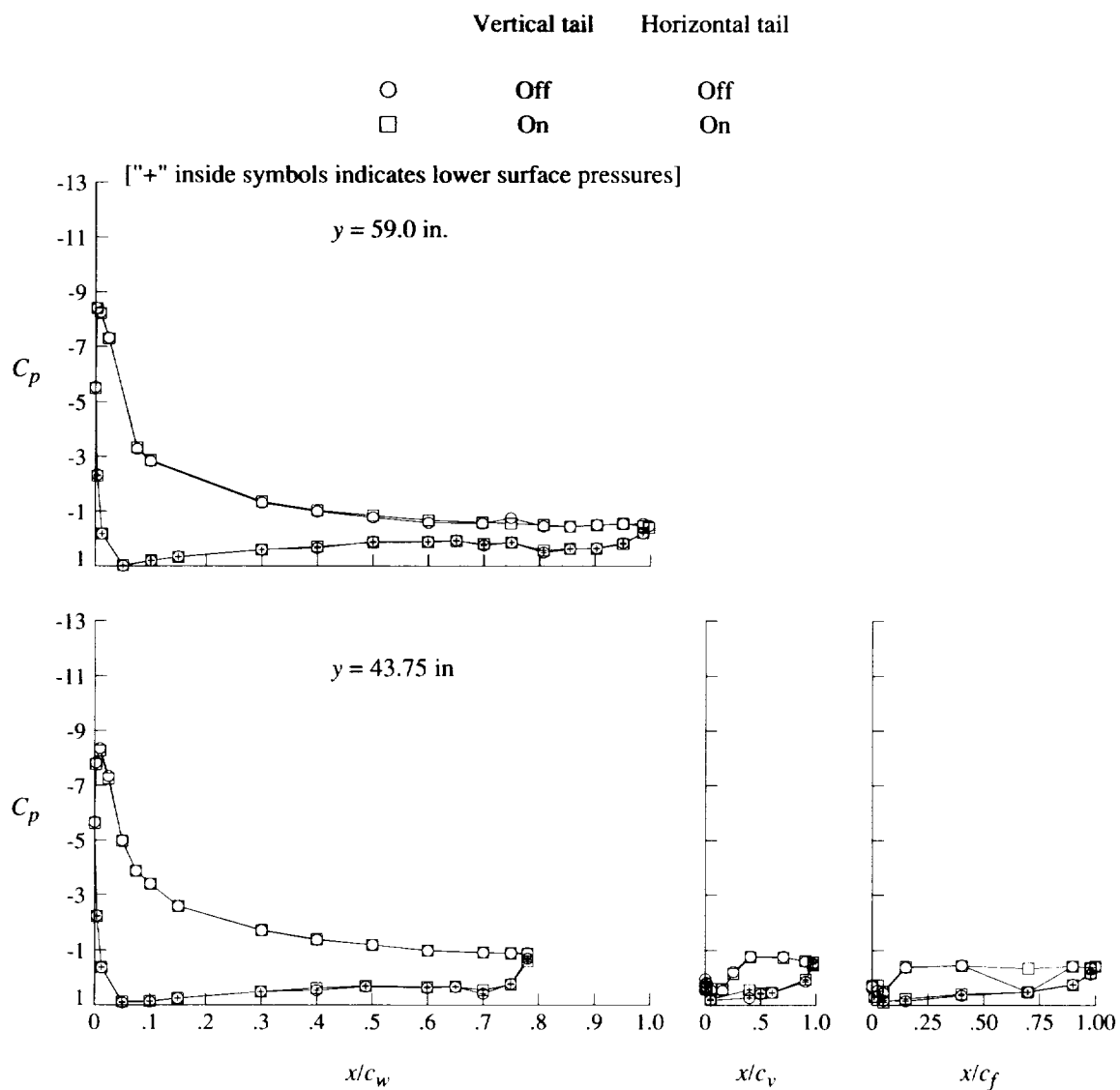
(d) Concluded.

Figure 42. Continued.



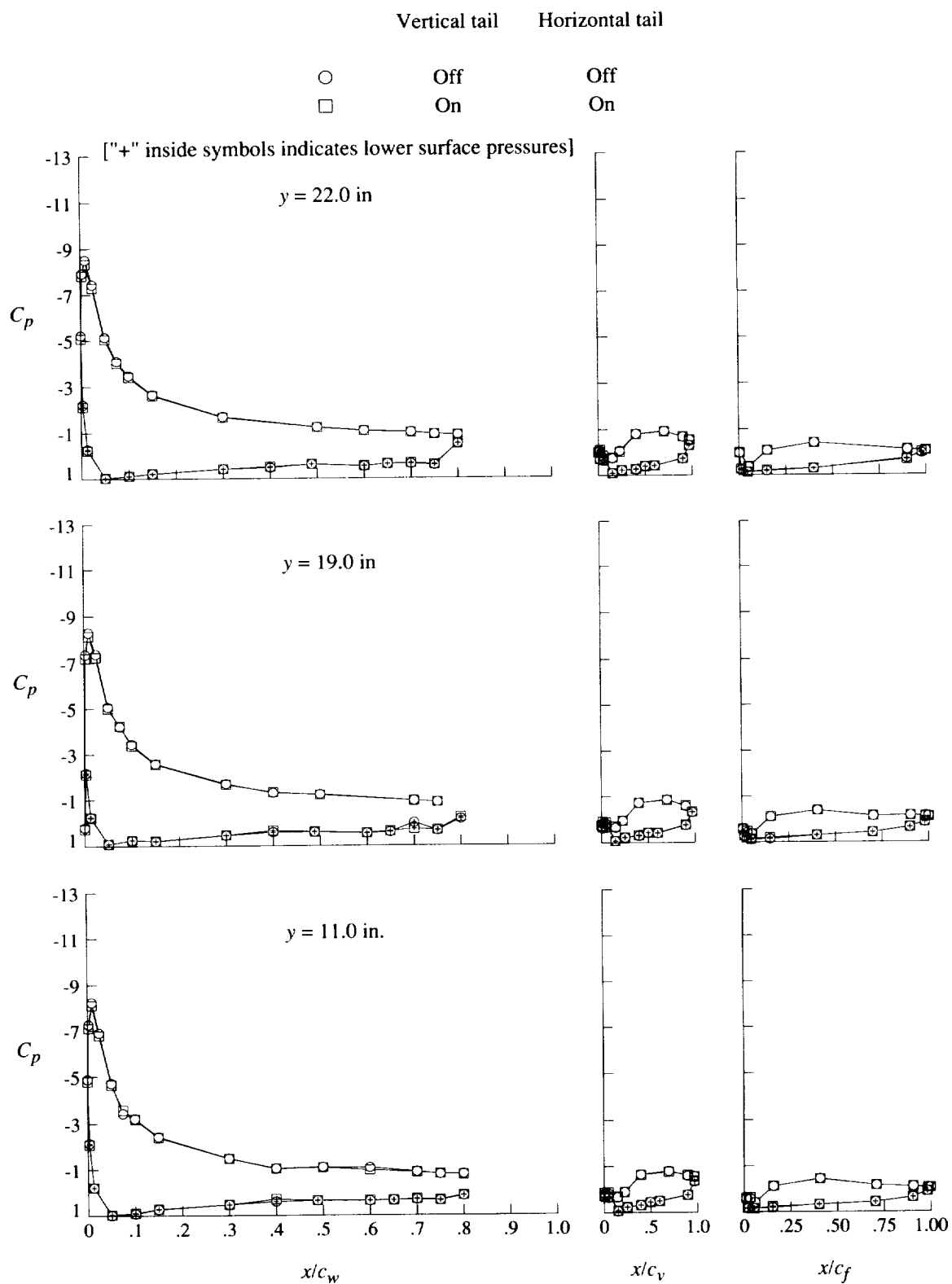
(e) $q = 20$ psf; $\alpha = 16^\circ$.

Figure 42. Continued.



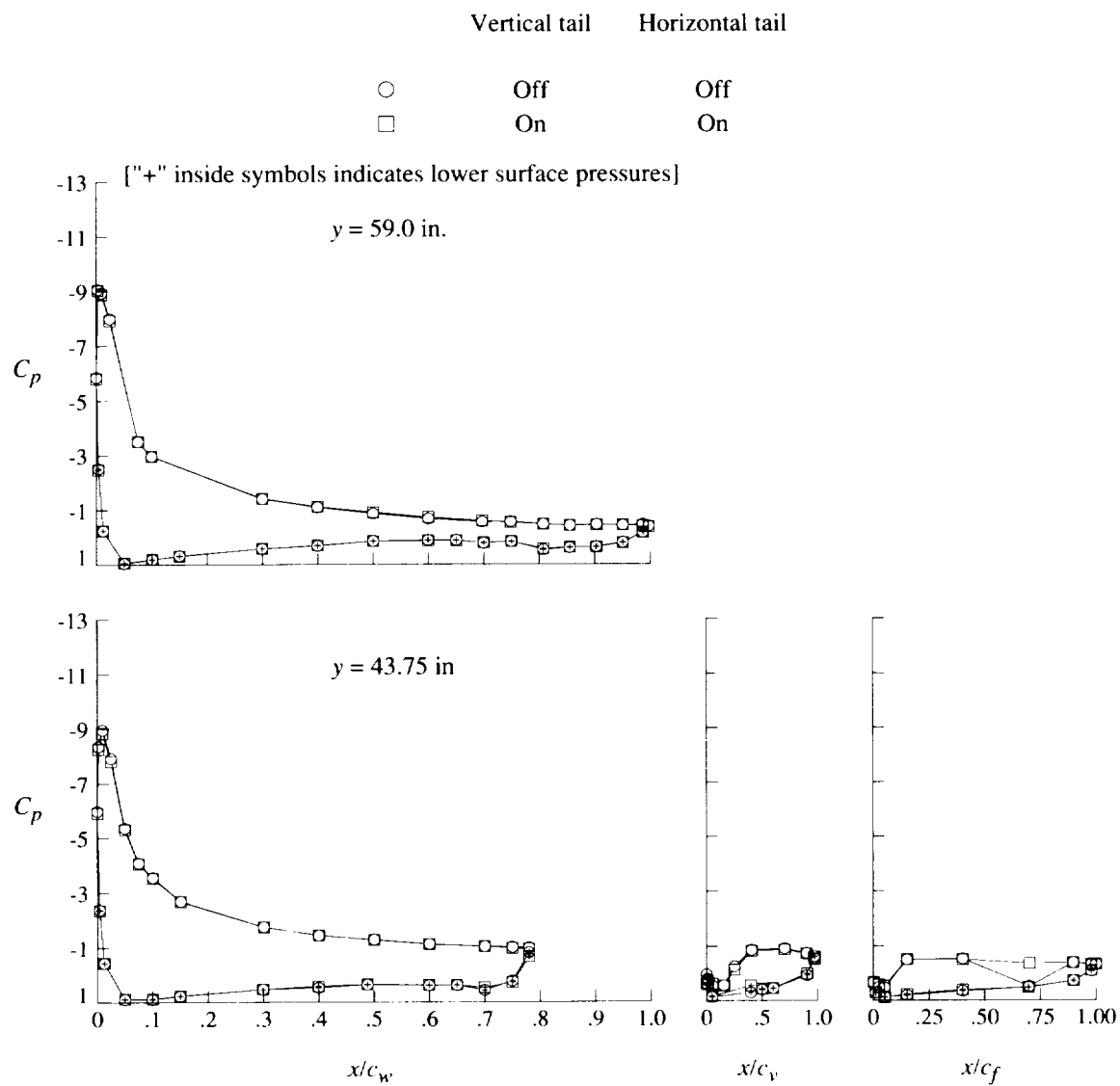
(e) Concluded.

Figure 42. Continued.



(f) $q = 40$ psf; $\alpha = 16^\circ$.

Figure 42. Continued.



(f) Concluded.

Figure 42. Concluded.

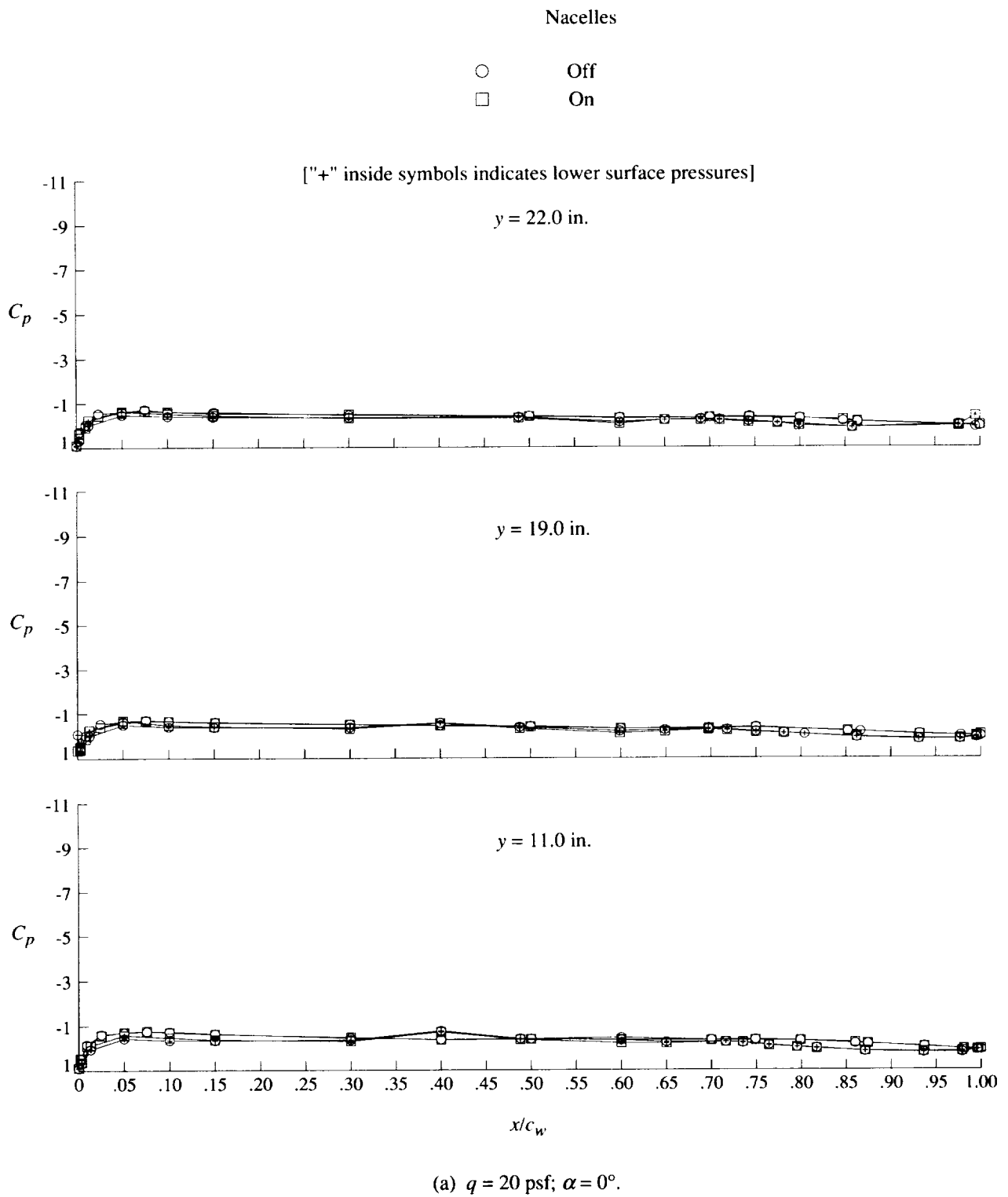
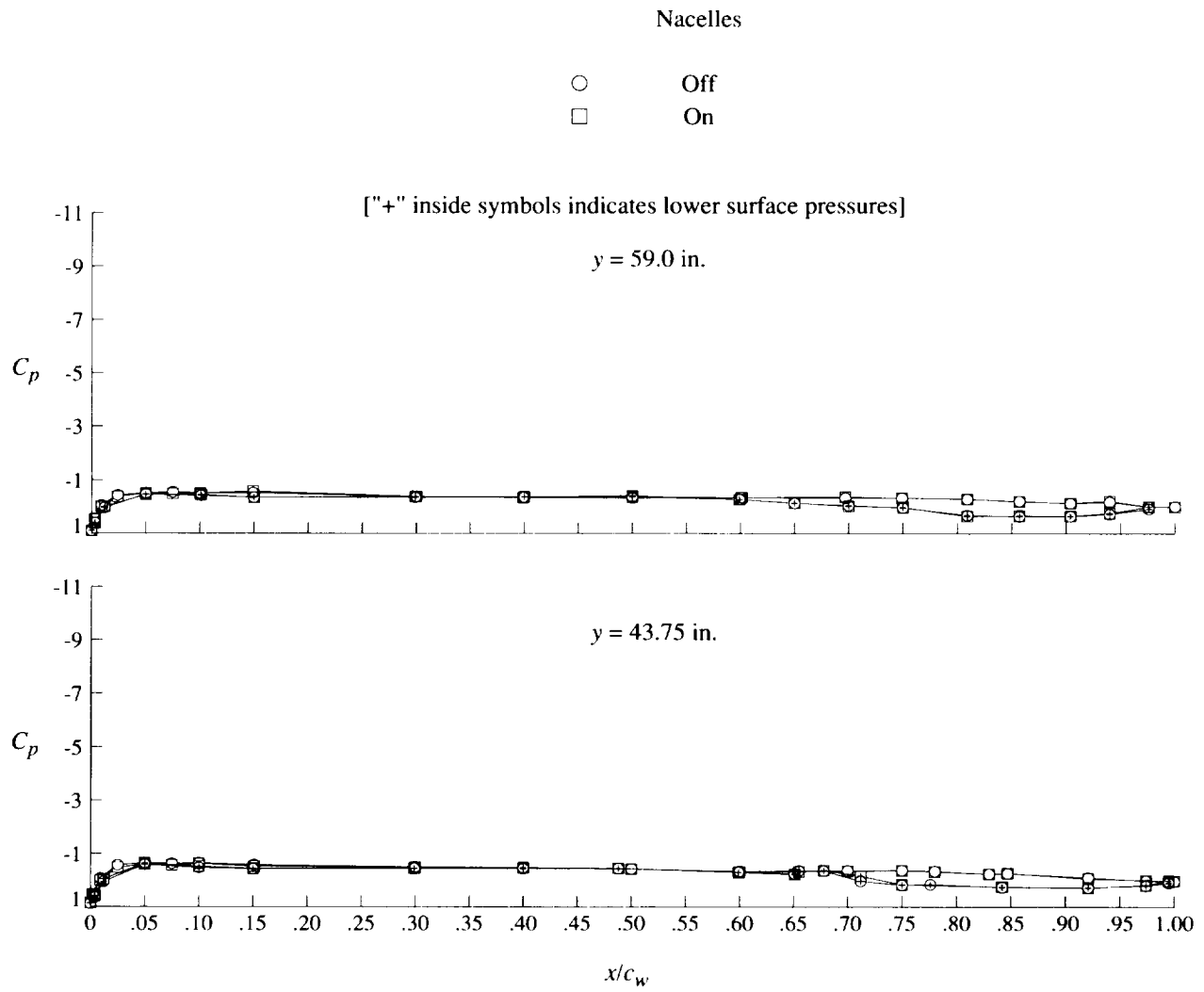
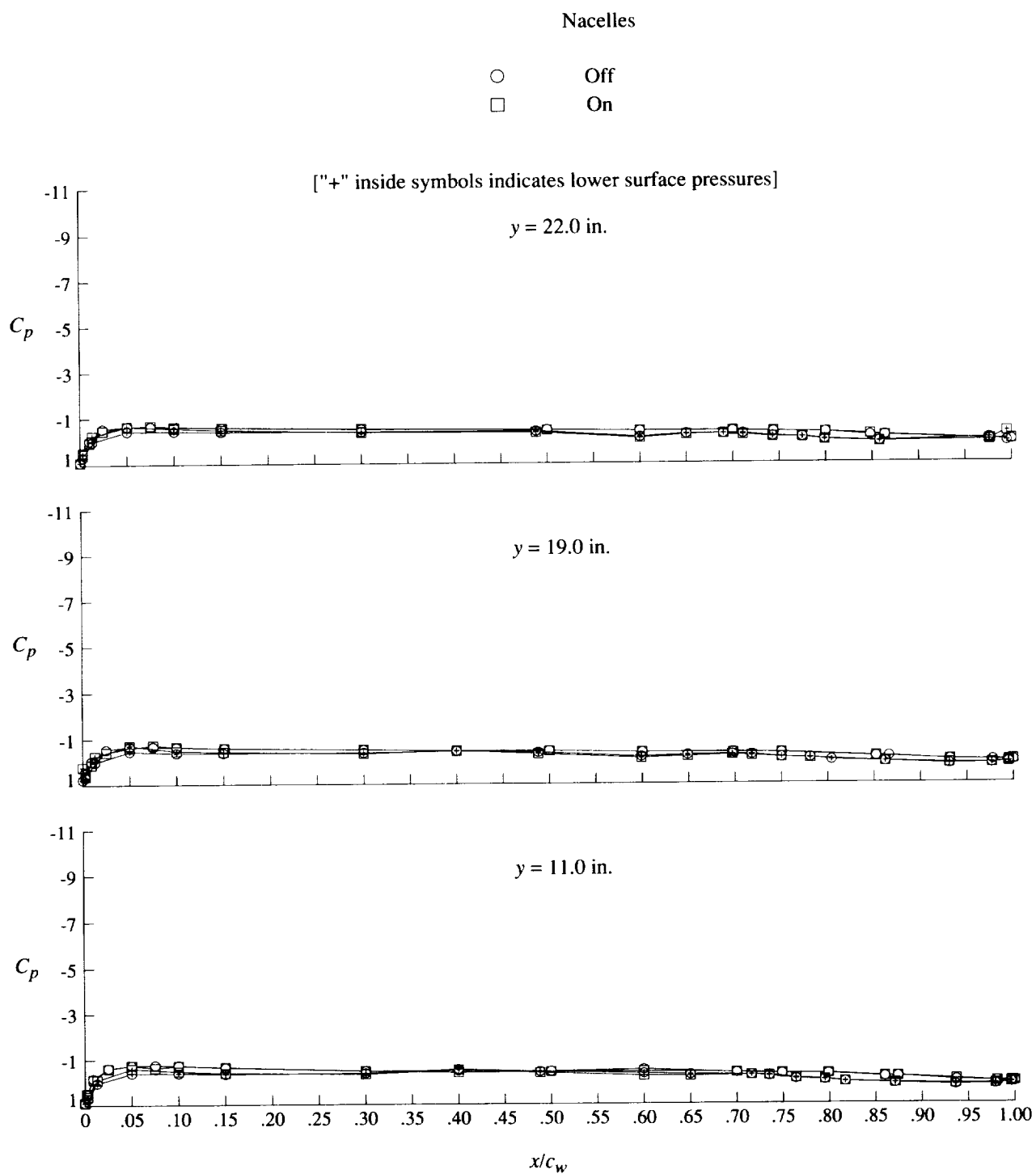


Figure 43. Effect of unpowered engine nacelles on pressure distributions for cruise configuration.



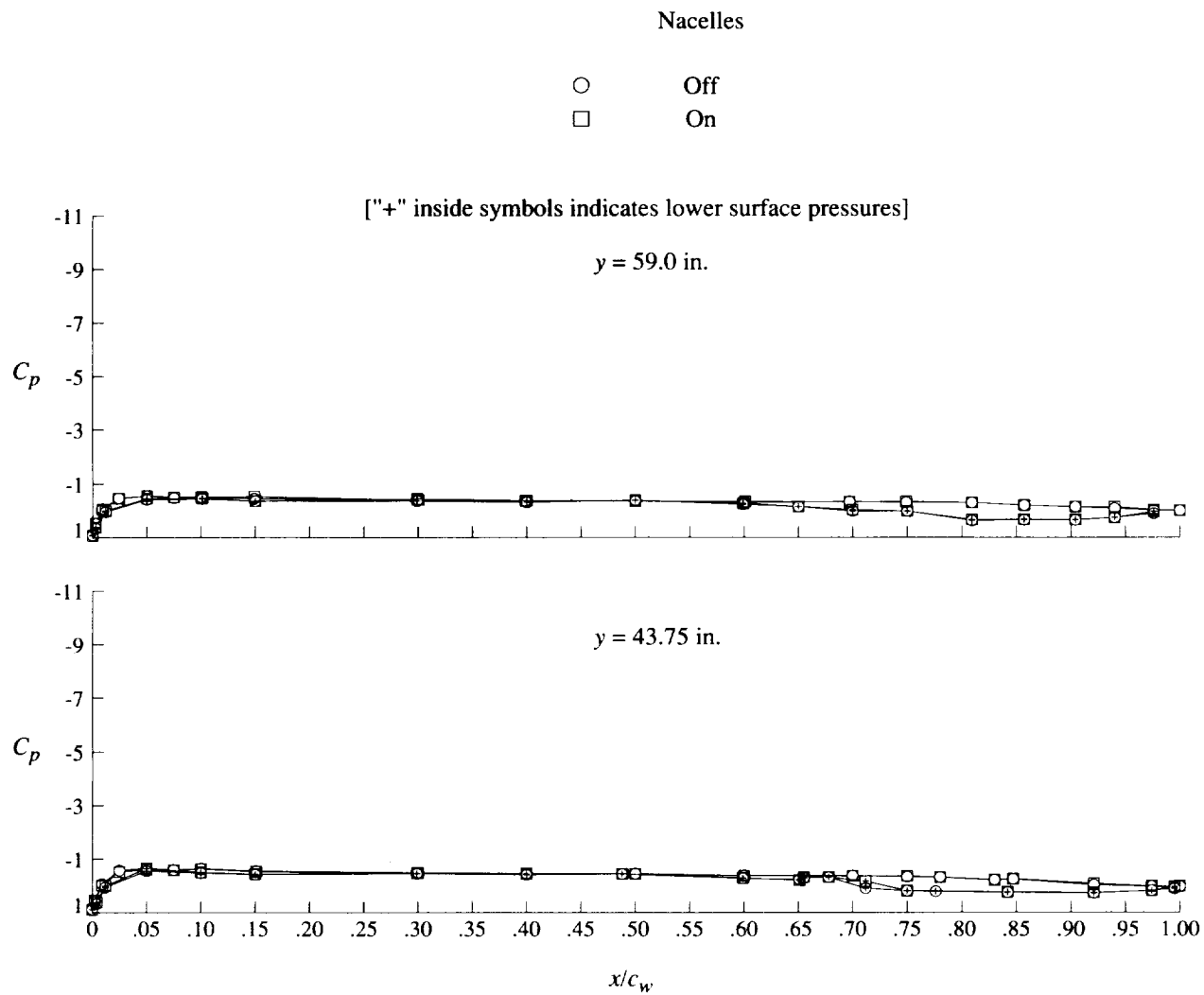
(a) Concluded.

Figure 43. Continued.



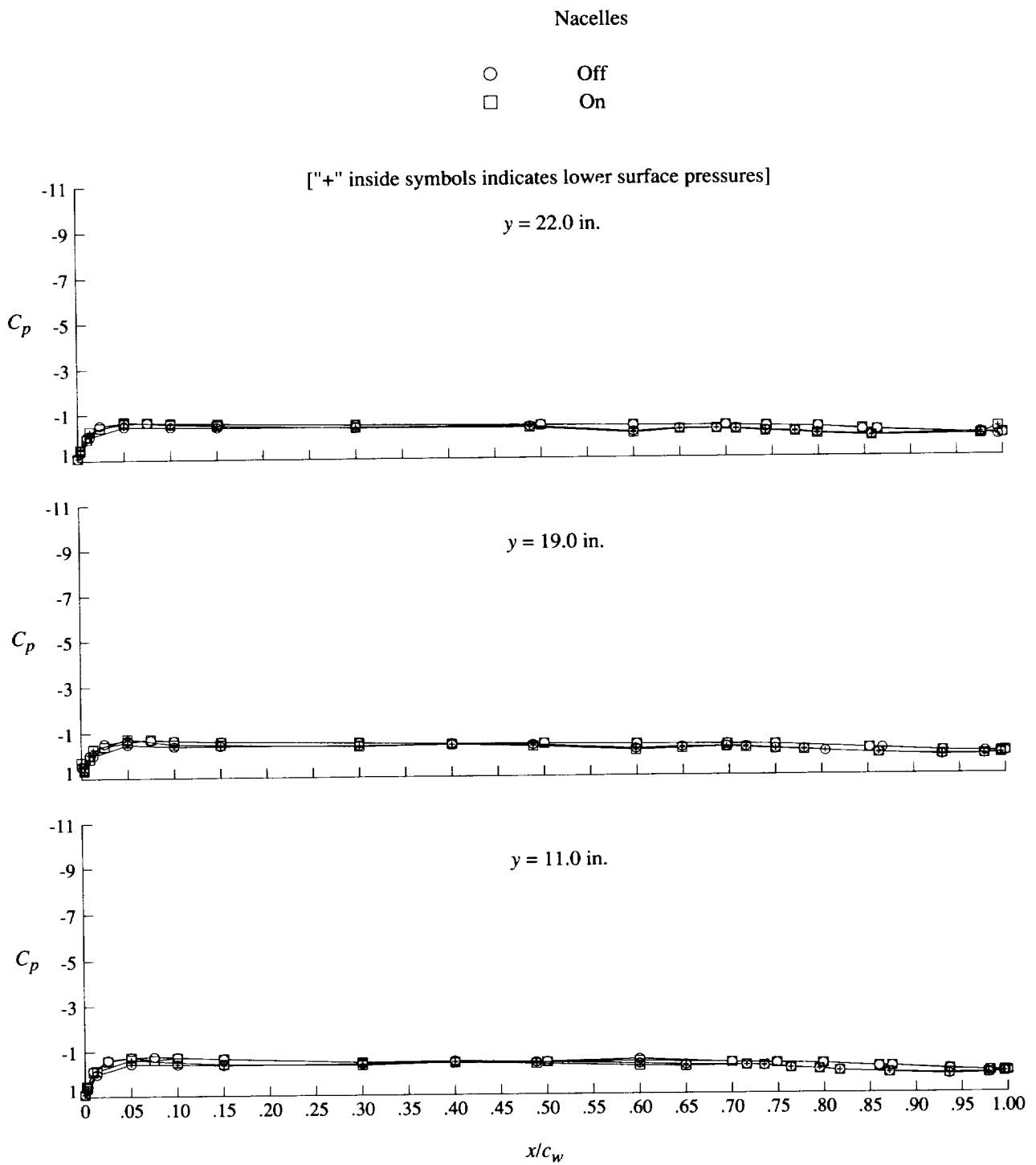
(b) $q = 40$ psf; $\alpha = 0^\circ$.

Figure 43. Continued.



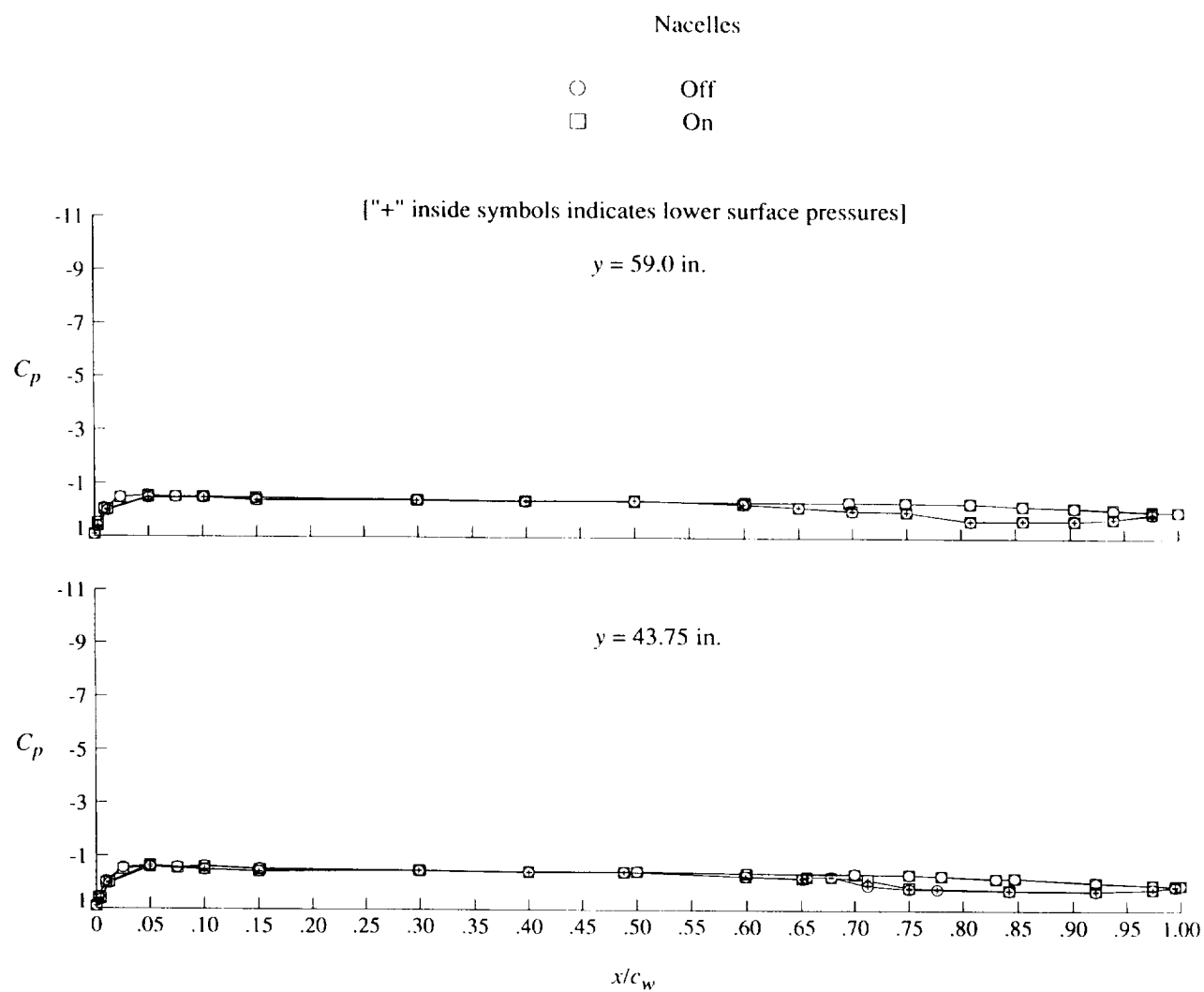
(b) Concluded.

Figure 43. Continued.



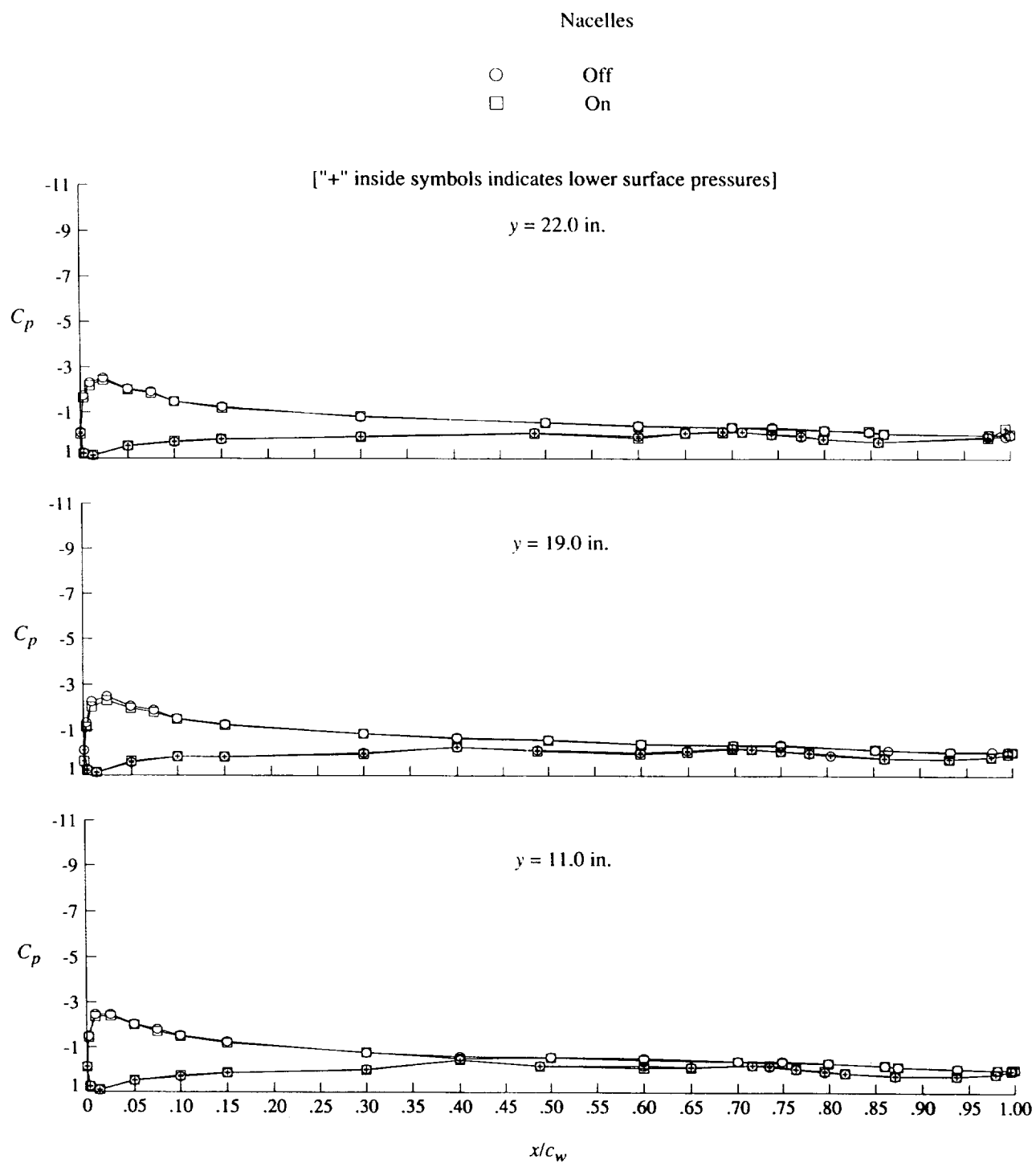
(c) $q = 60$ psf; $\alpha = 0^\circ$.

Figure 43. Continued.



(c) Concluded.

Figure 43. Continued.



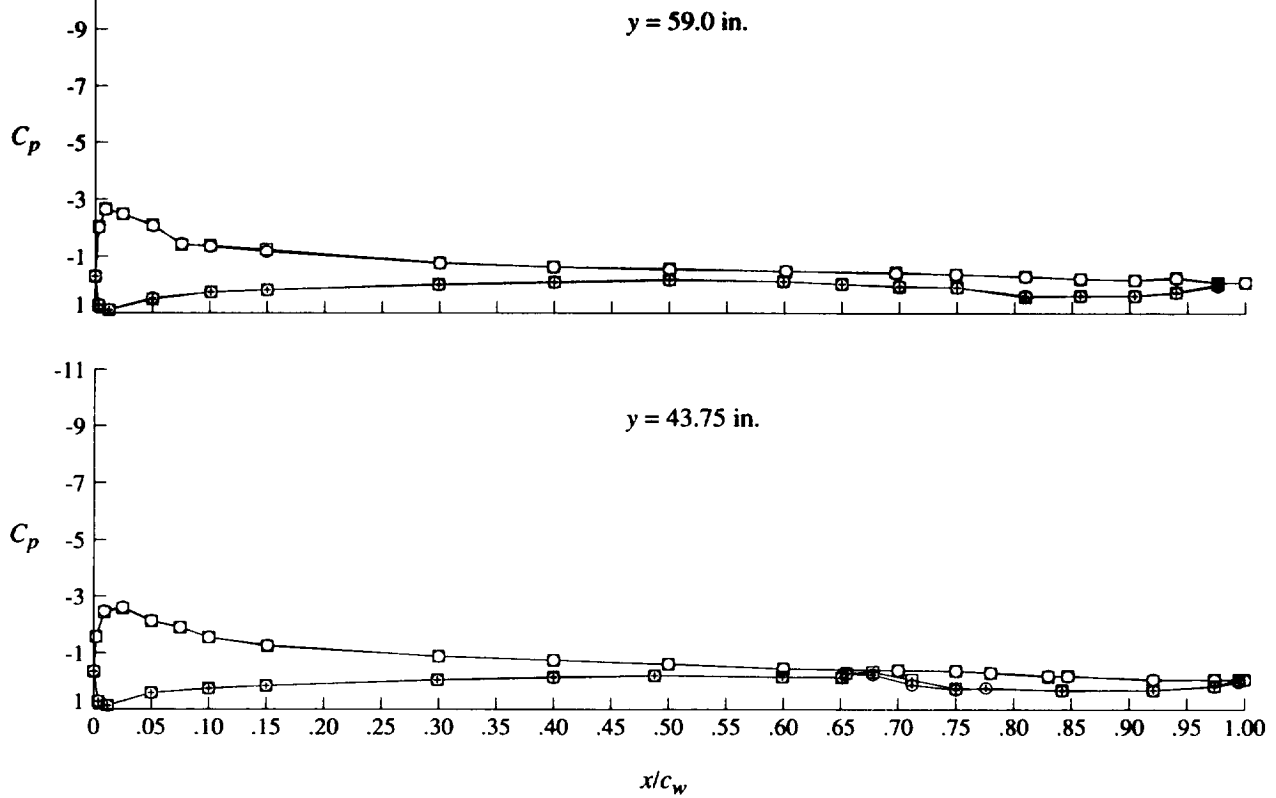
(d) $q = 20$ psf; $\alpha = 8^\circ$.

Figure 43. Continued.

Nacelles

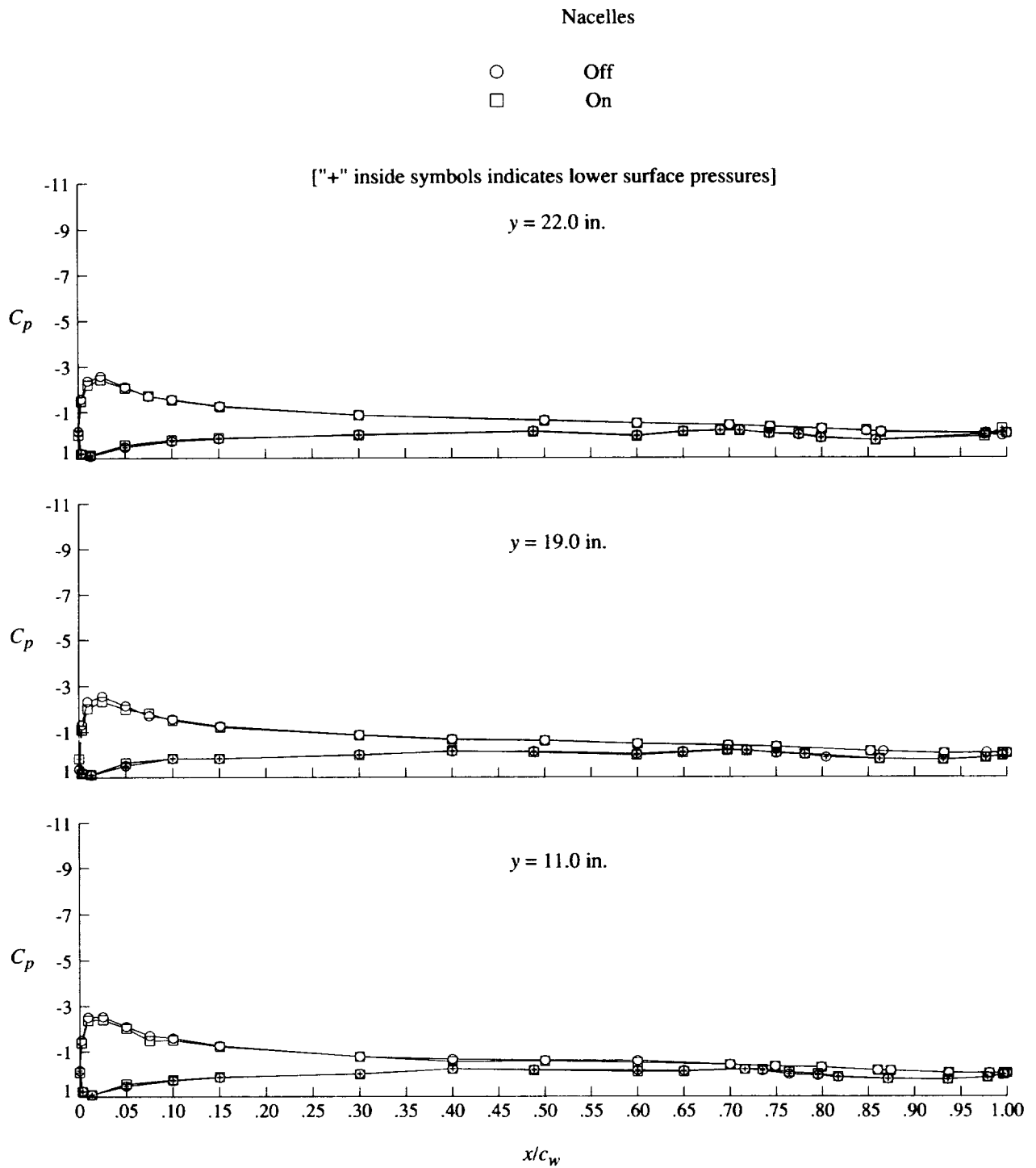
- Off
- On

["+" inside symbols indicates lower surface pressures]



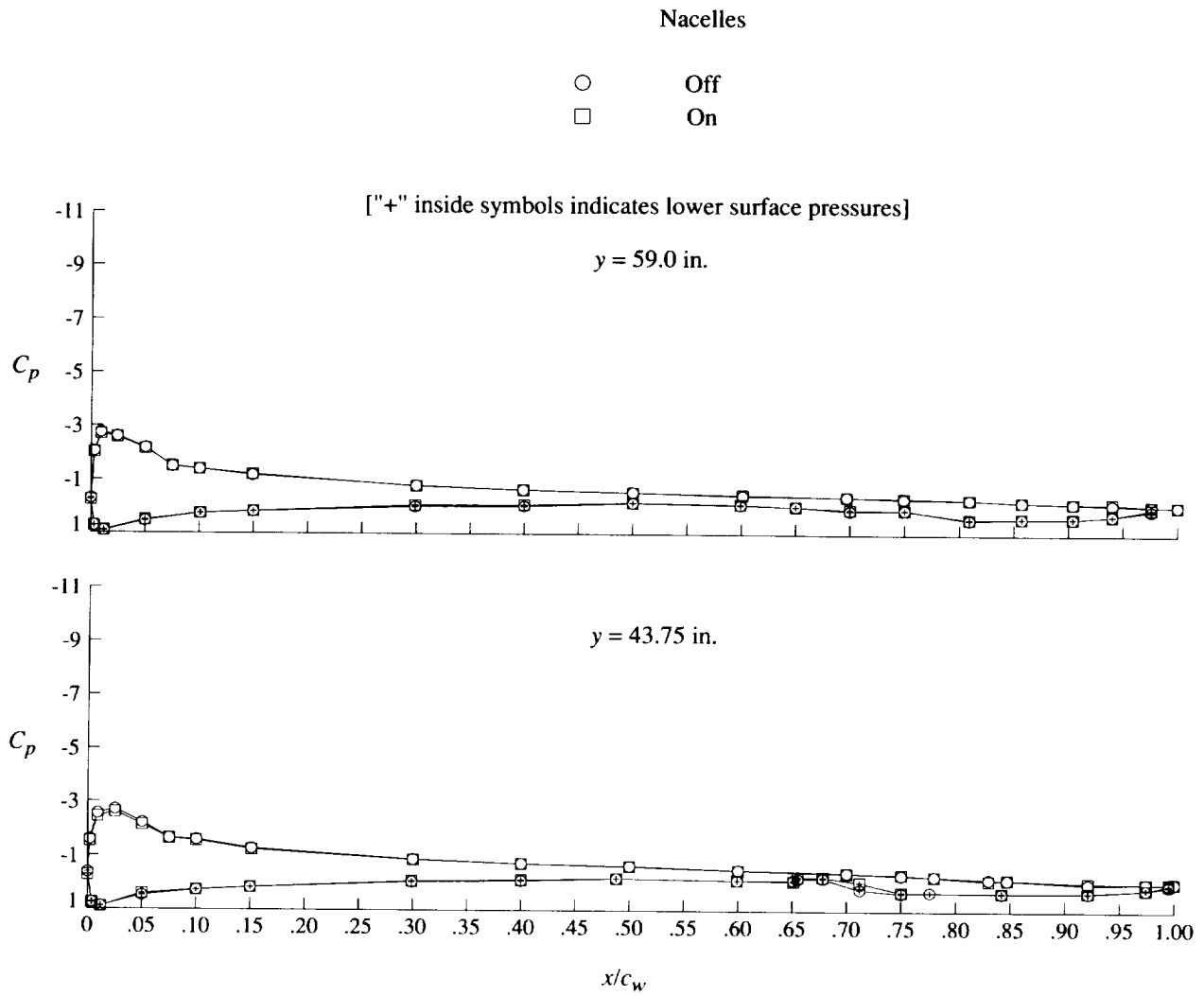
(d) Concluded.

Figure 43. Continued.



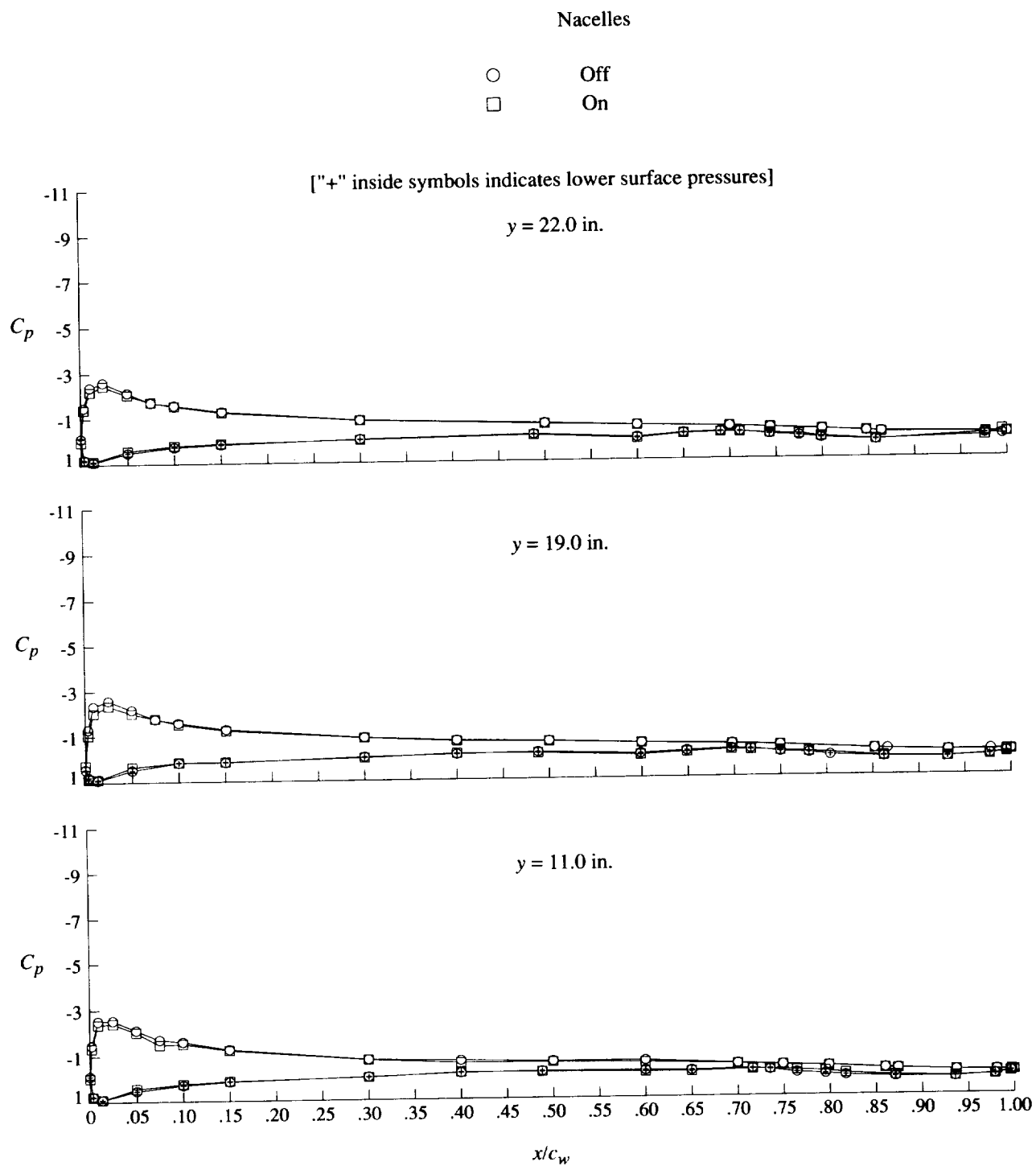
(e) $q = 40$ psf; $\alpha = 8^\circ$.

Figure 43. Continued.



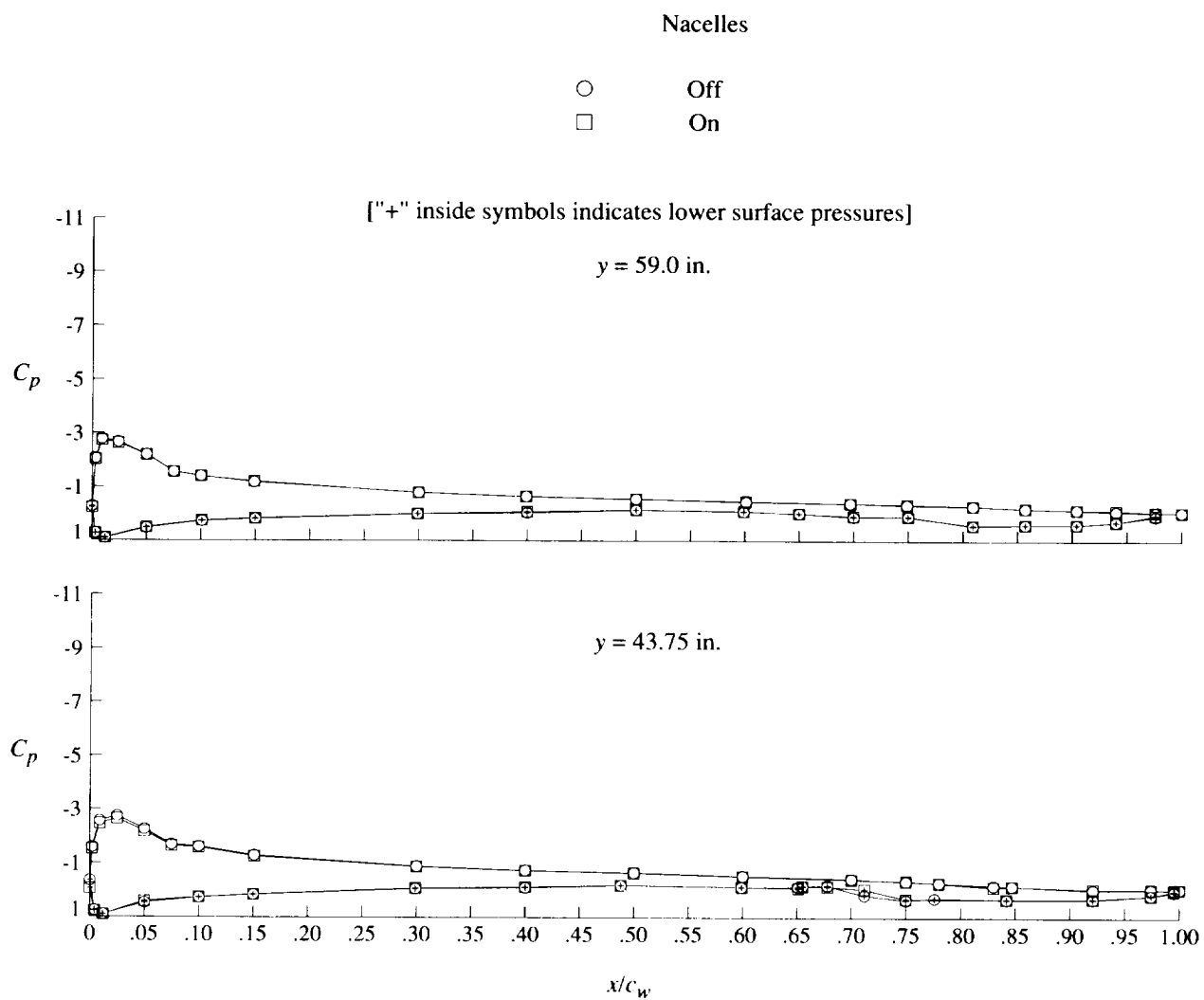
(e) Concluded.

Figure 43. Continued.



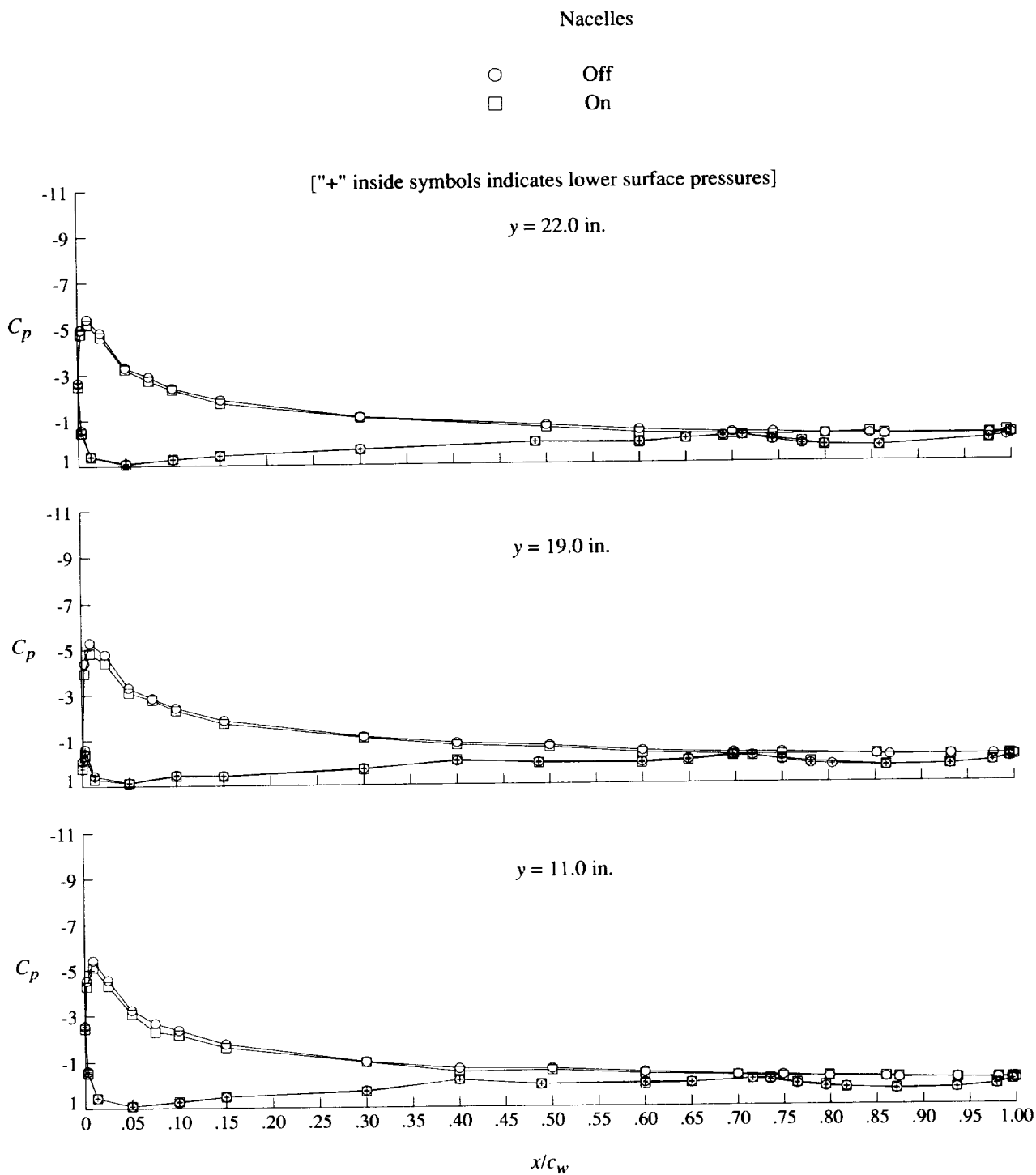
(f) $q = 60$ psf; $\alpha = 8^\circ$.

Figure 43. Continued.



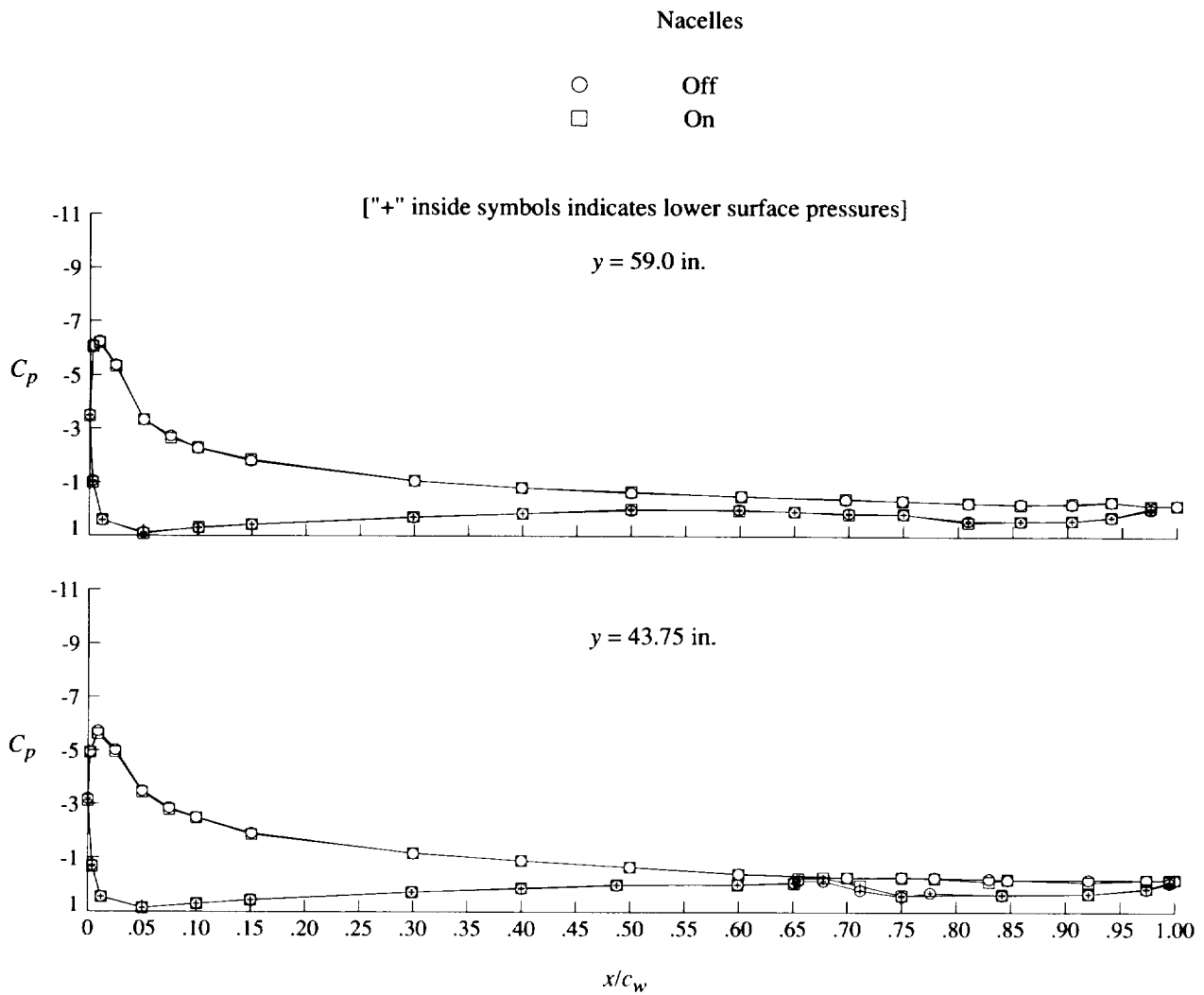
(f) Concluded.

Figure 43. Continued.



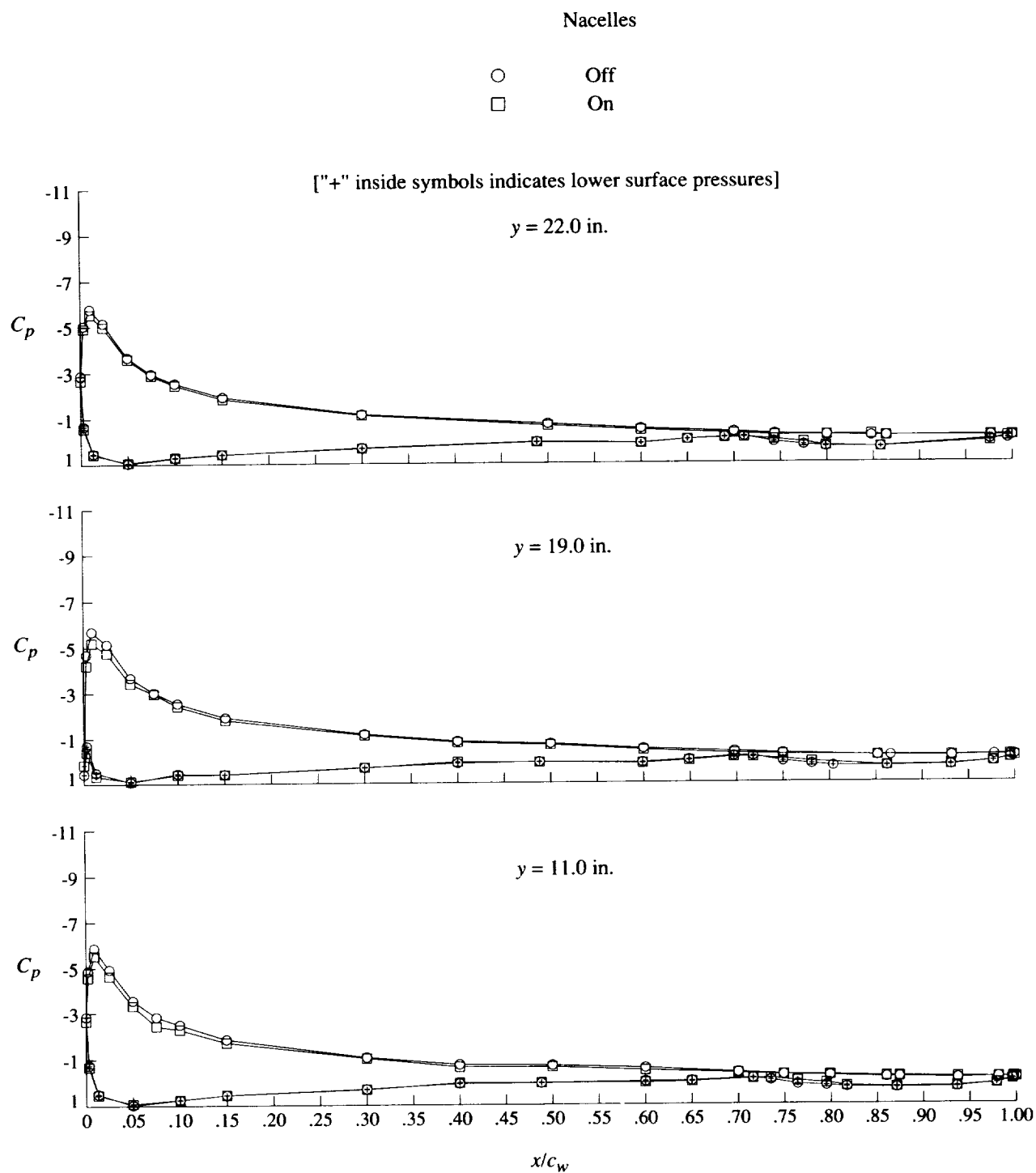
(g) $q = 20$ psf; $\alpha = 16^\circ$.

Figure 43. Continued.



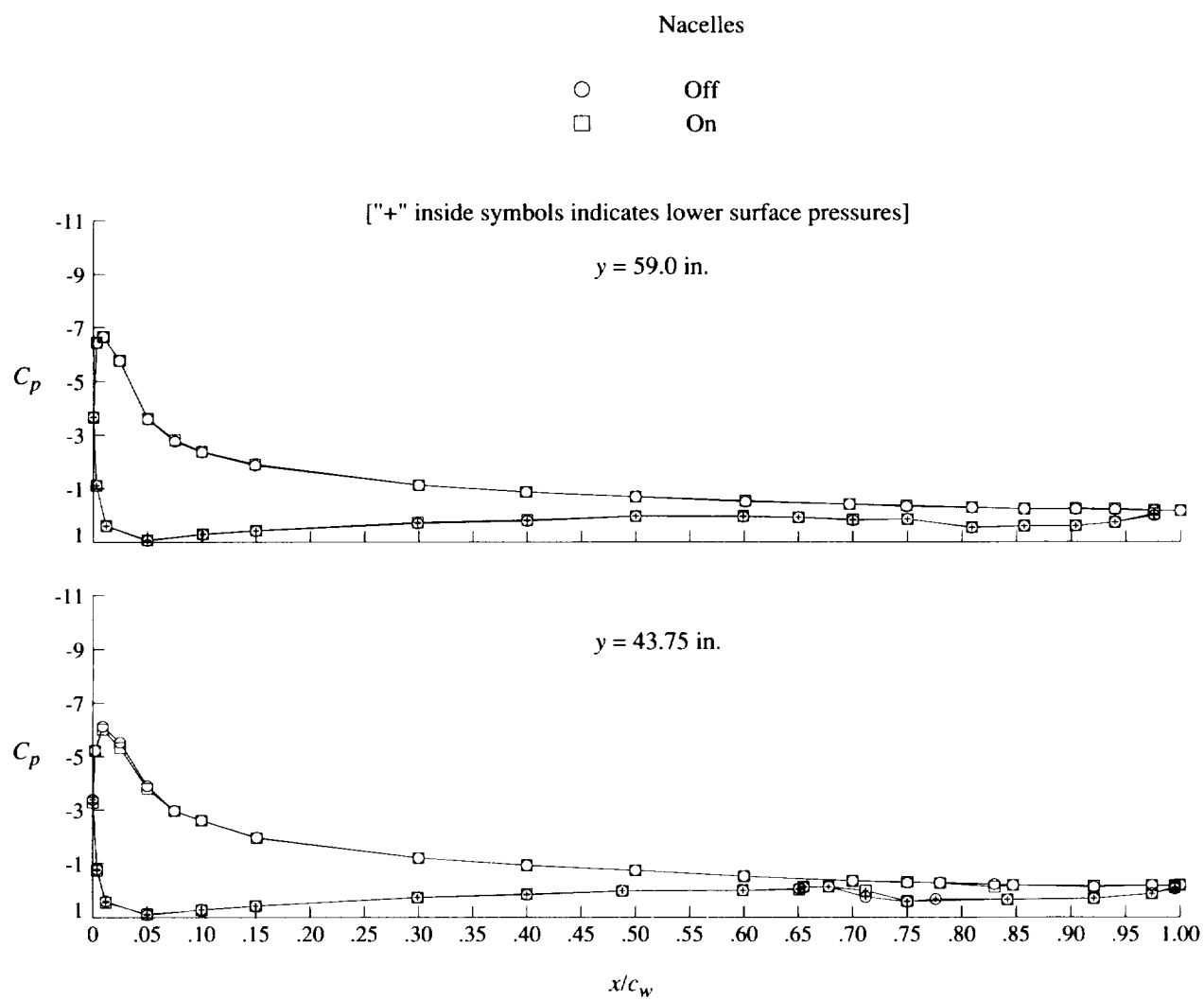
(g) Concluded.

Figure 43. Continued.



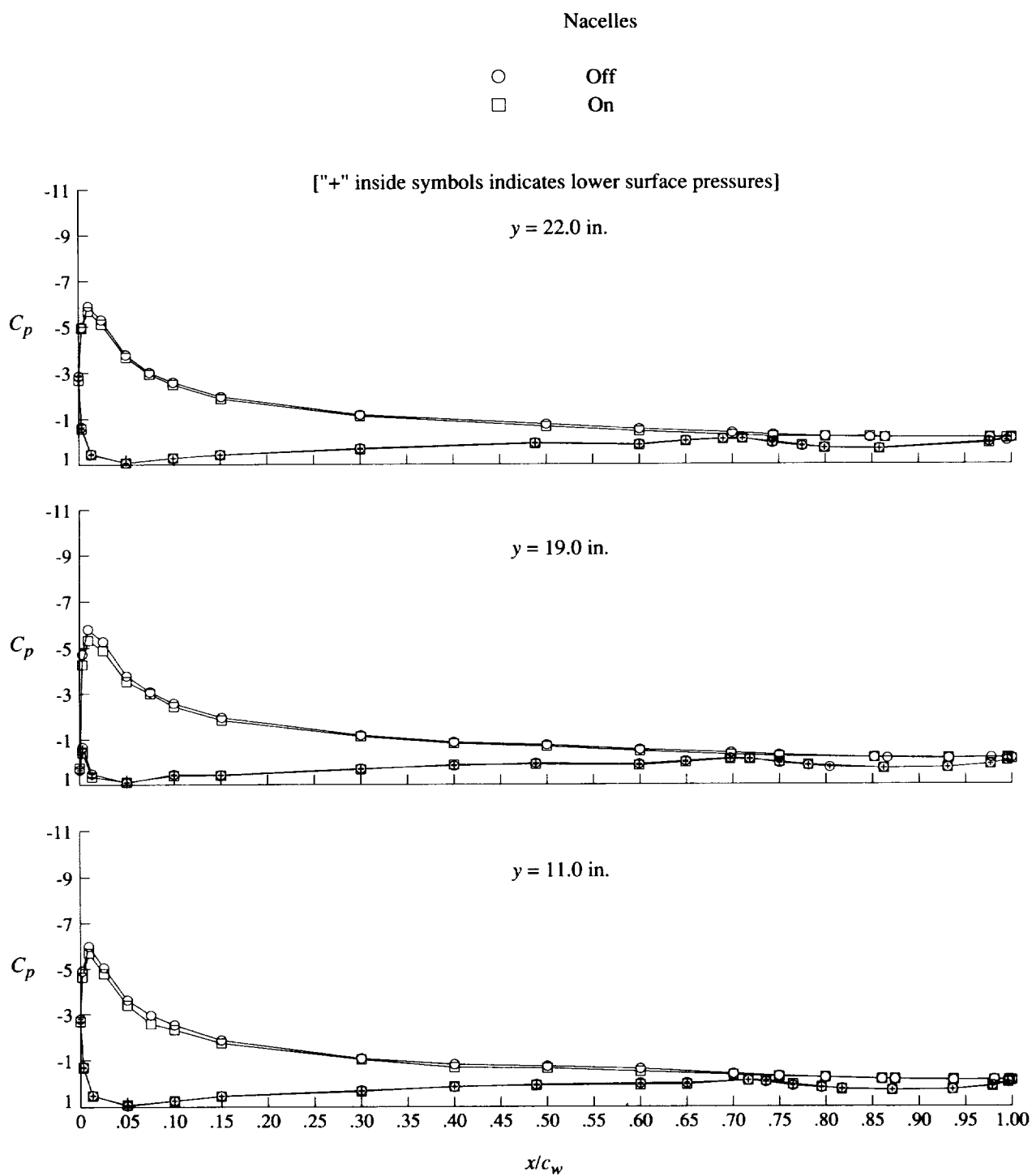
(h) $q = 40$ psf; $\alpha = 16^\circ$.

Figure 43. Continued.



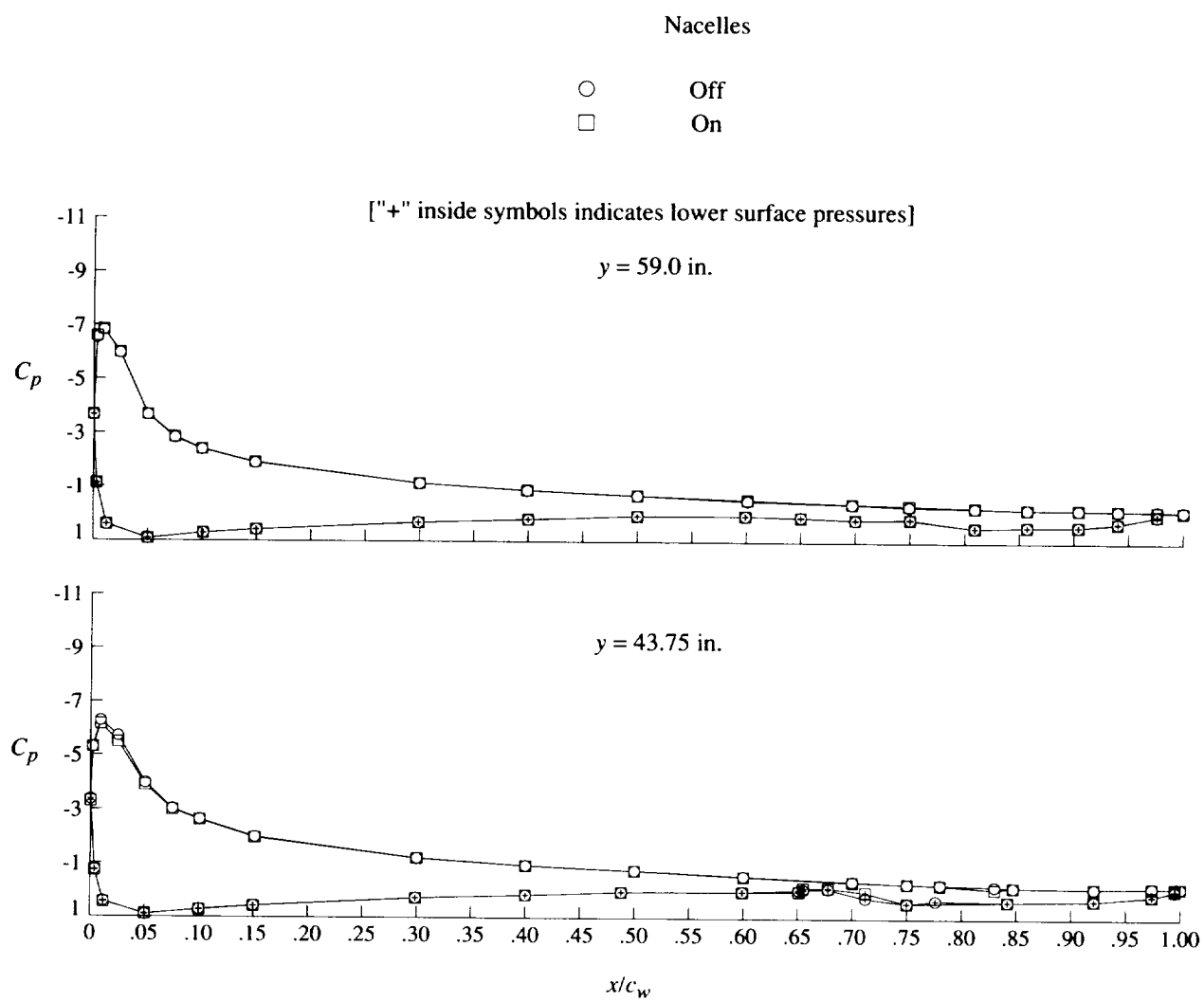
(h) Concluded.

Figure 43. Continued.



(i) $q = 60$ psf; $\alpha = 16^\circ$.

Figure 43. Continued.



(i) Concluded.

Figure 43. Concluded.

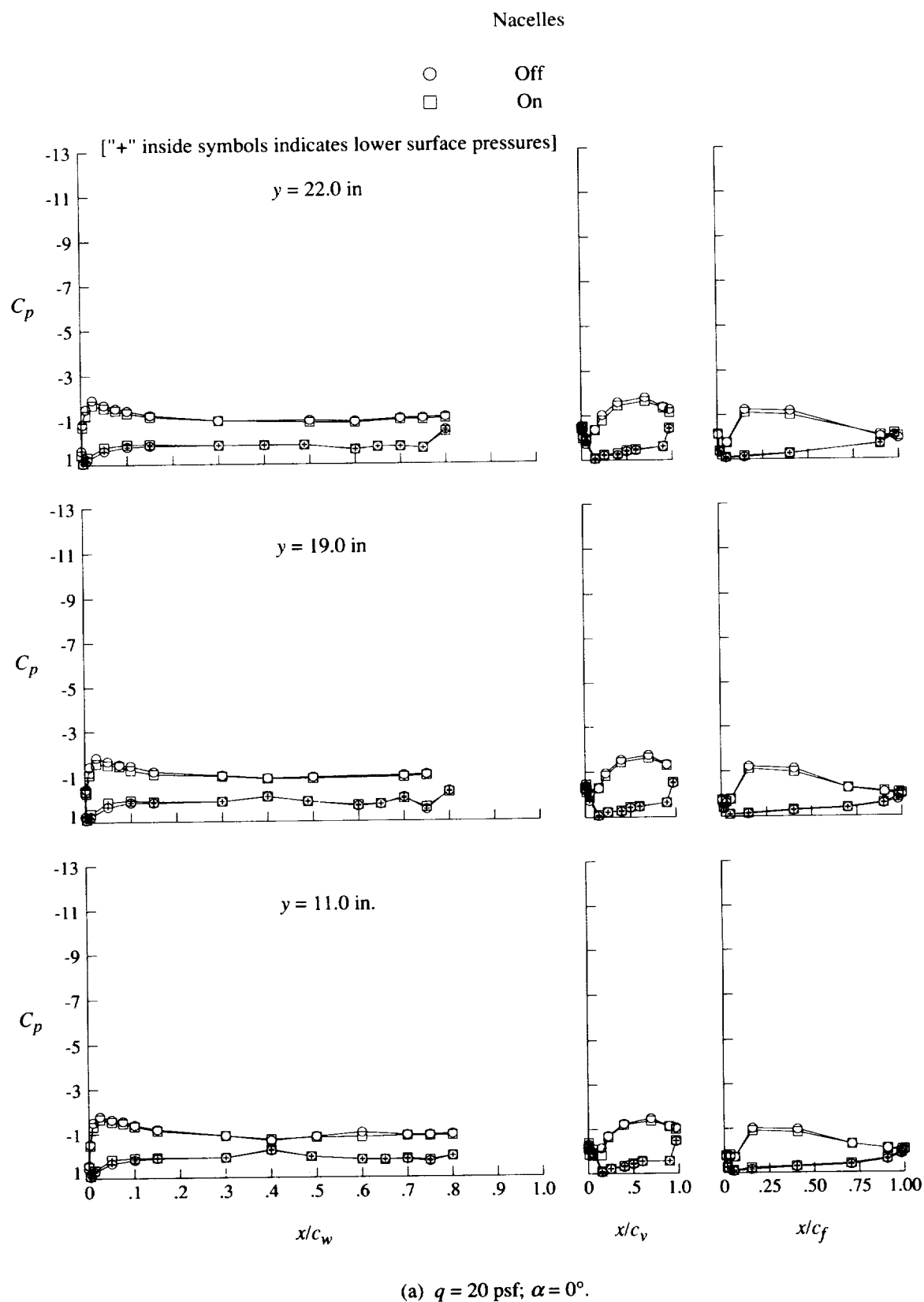
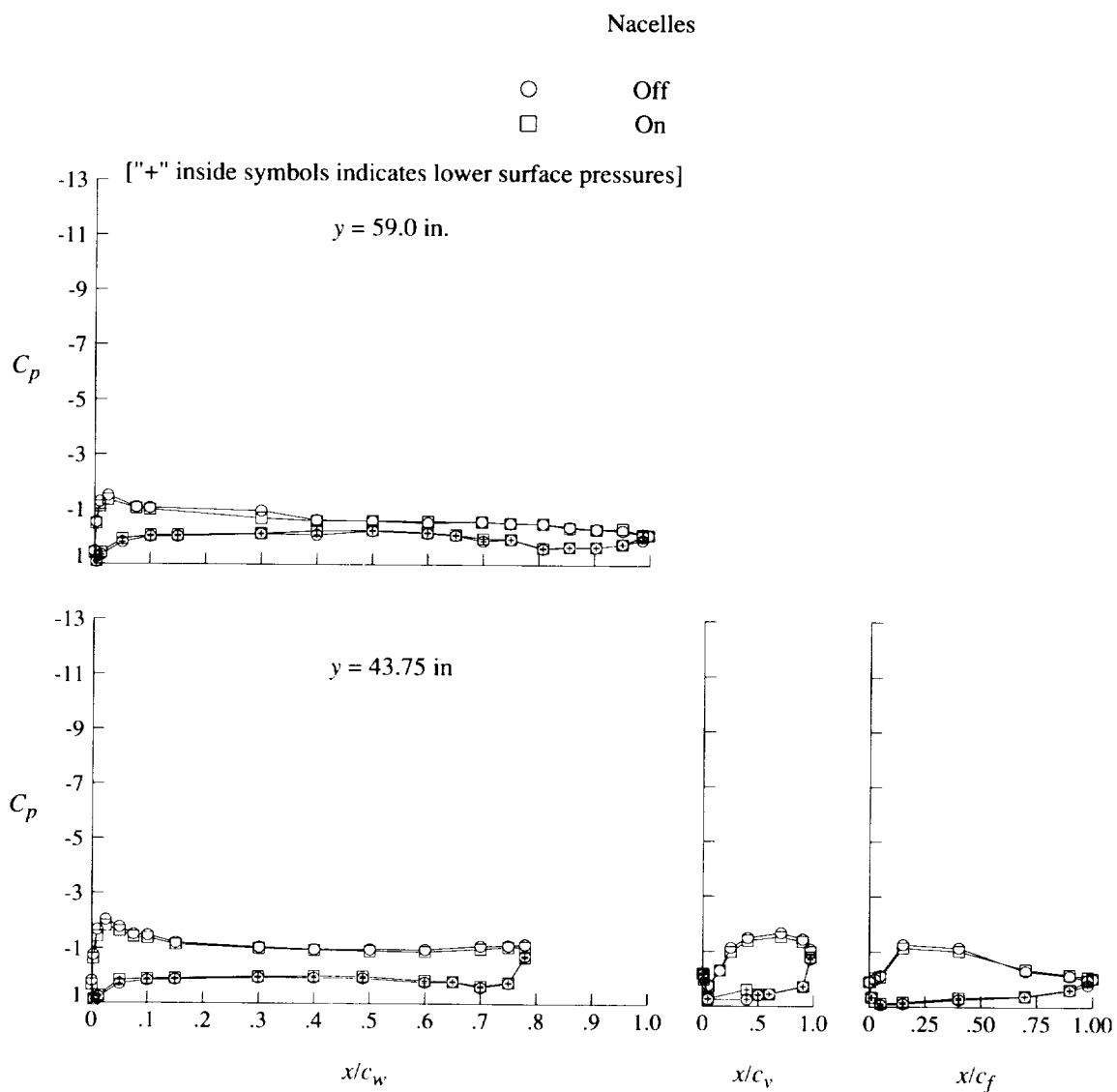
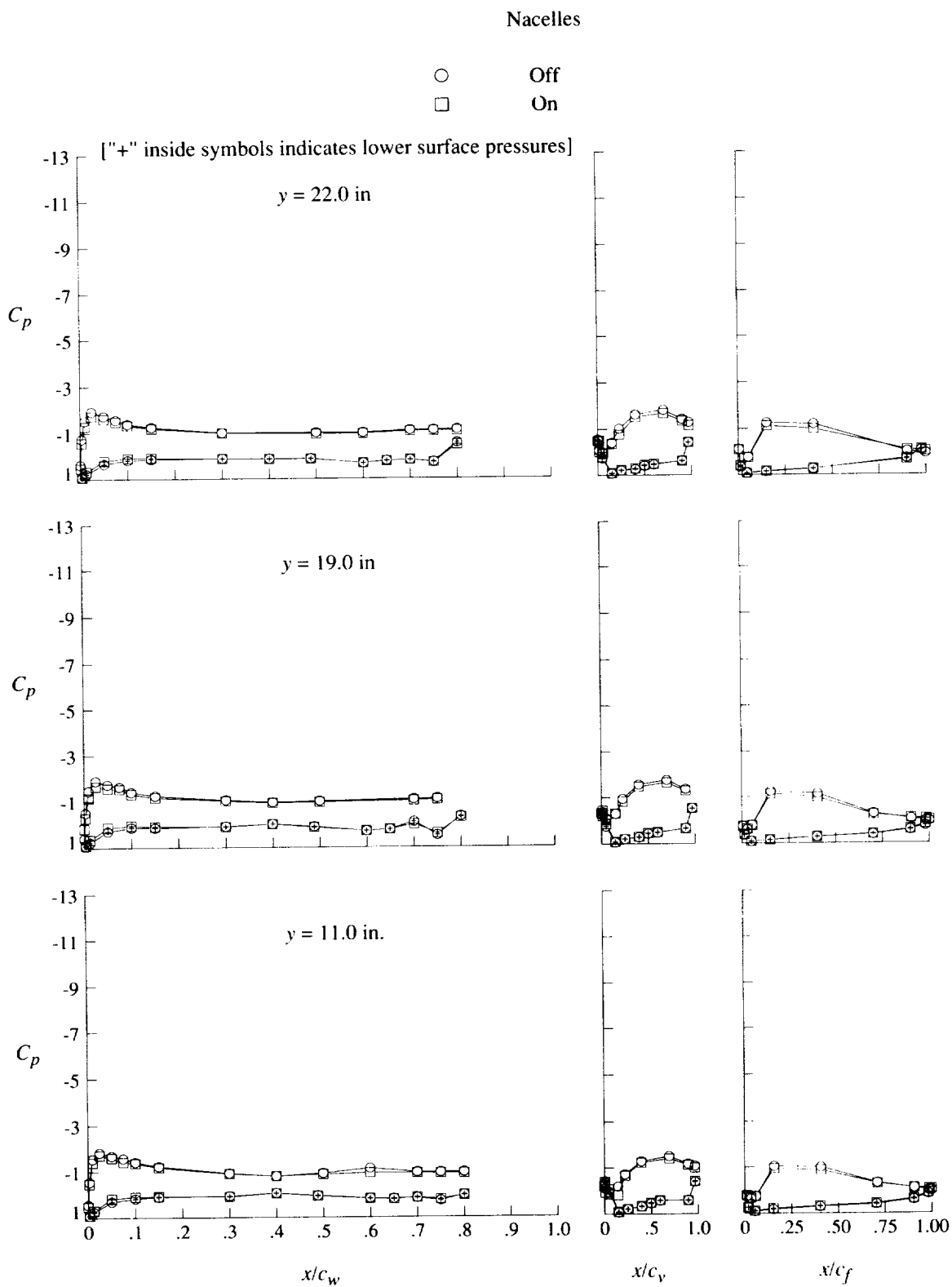


Figure 44. Effect of unpowered engine nacelles on pressure distributions for flaps-only configuration at $\delta_f = 40^\circ$.



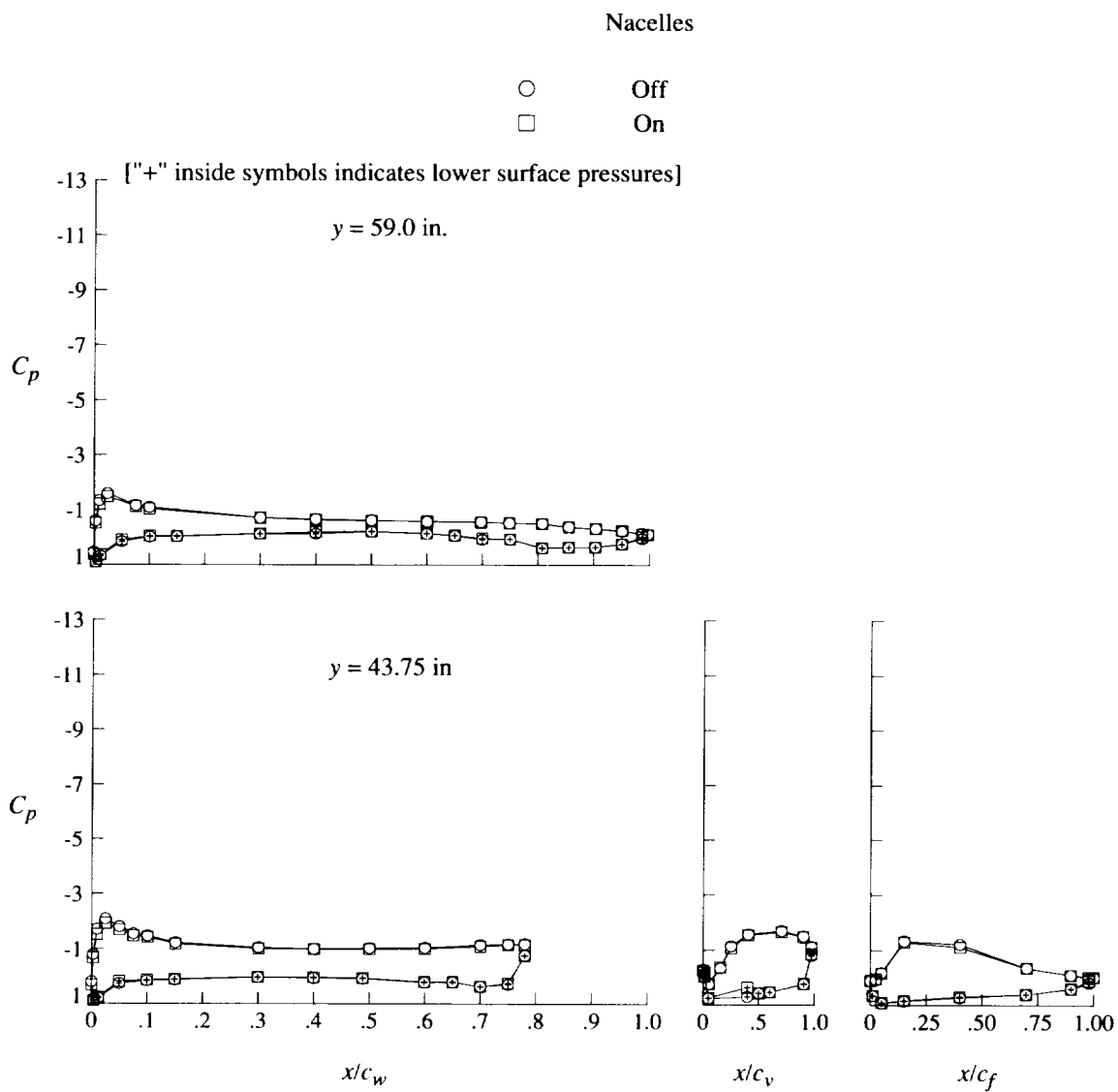
(a) Concluded.

Figure 44. Continued.



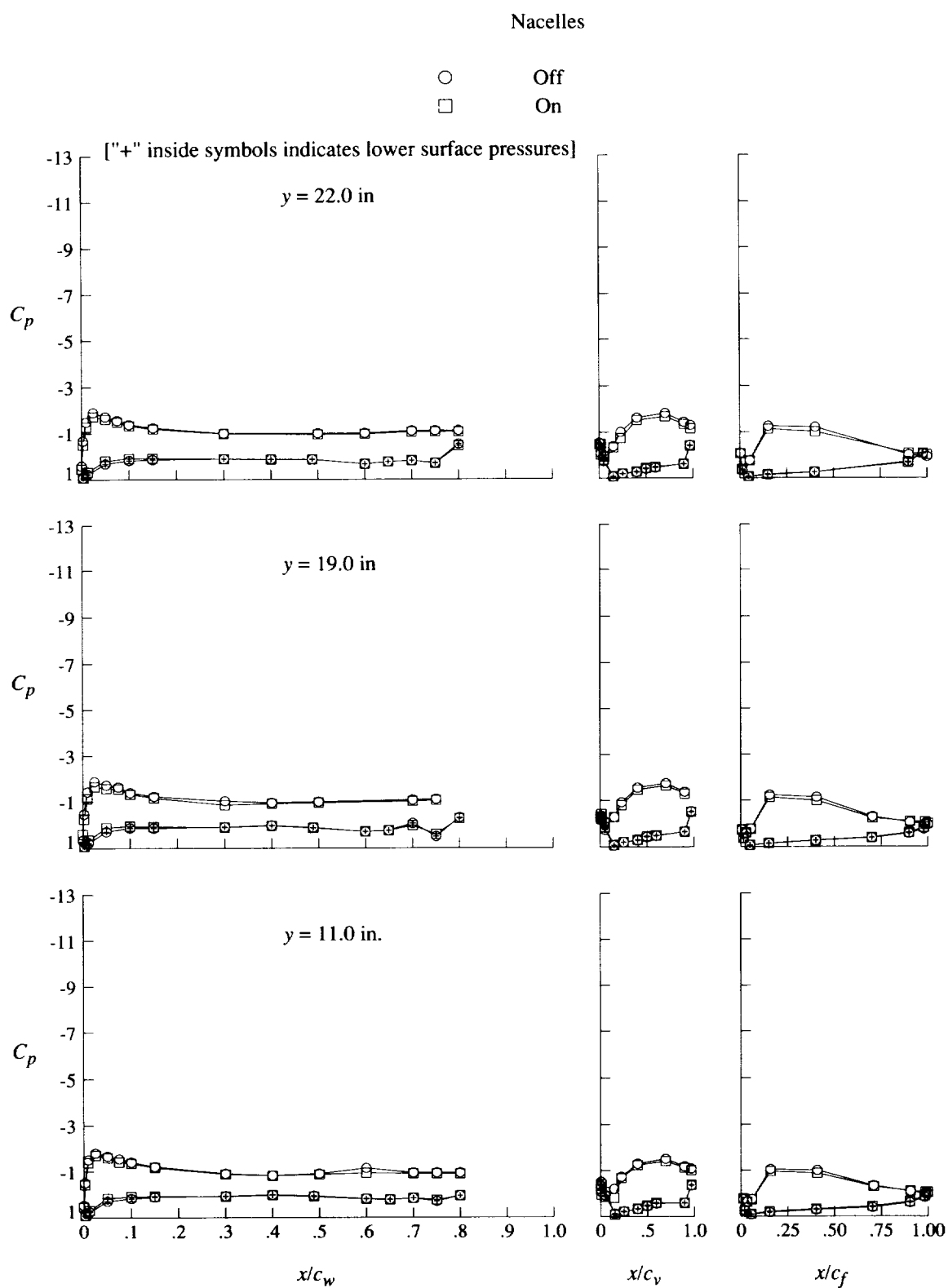
(b) $q = 40$ psf; $\alpha = 0^\circ$.

Figure 44. Continued.



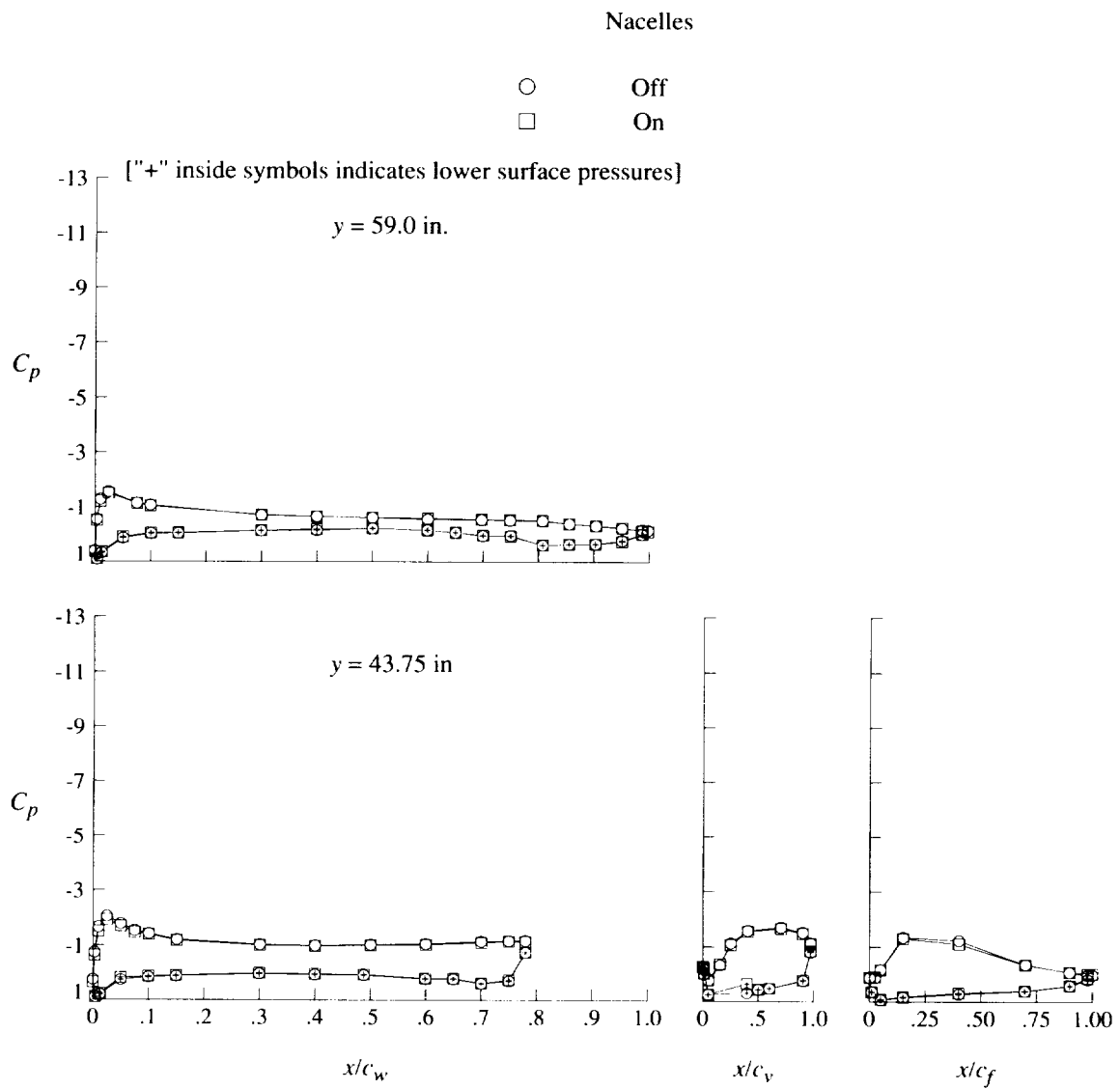
(b) Concluded.

Figure 44. Continued.



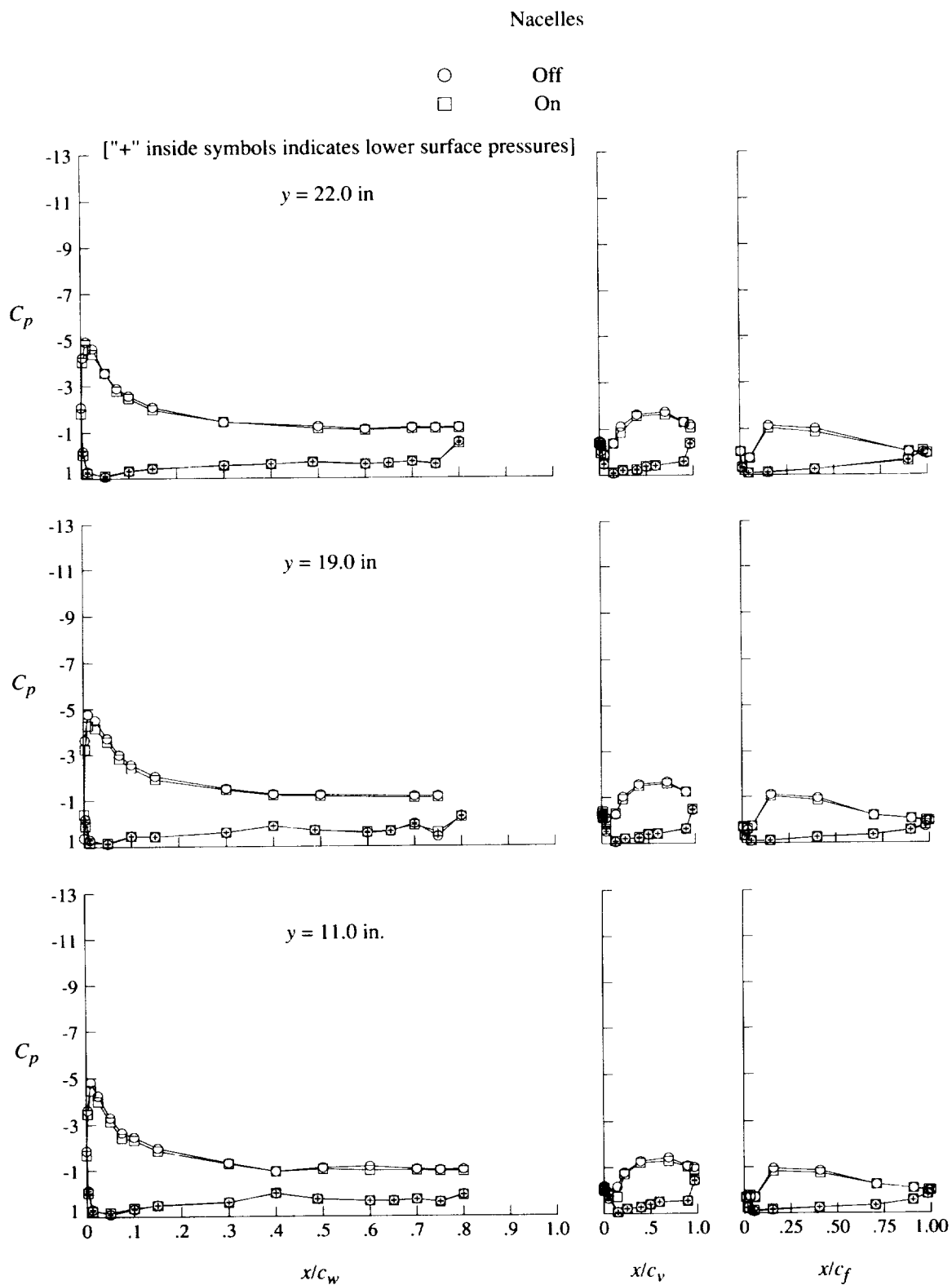
(c) $q = 60$ psf; $\alpha = 0^\circ$.

Figure 44. Continued.



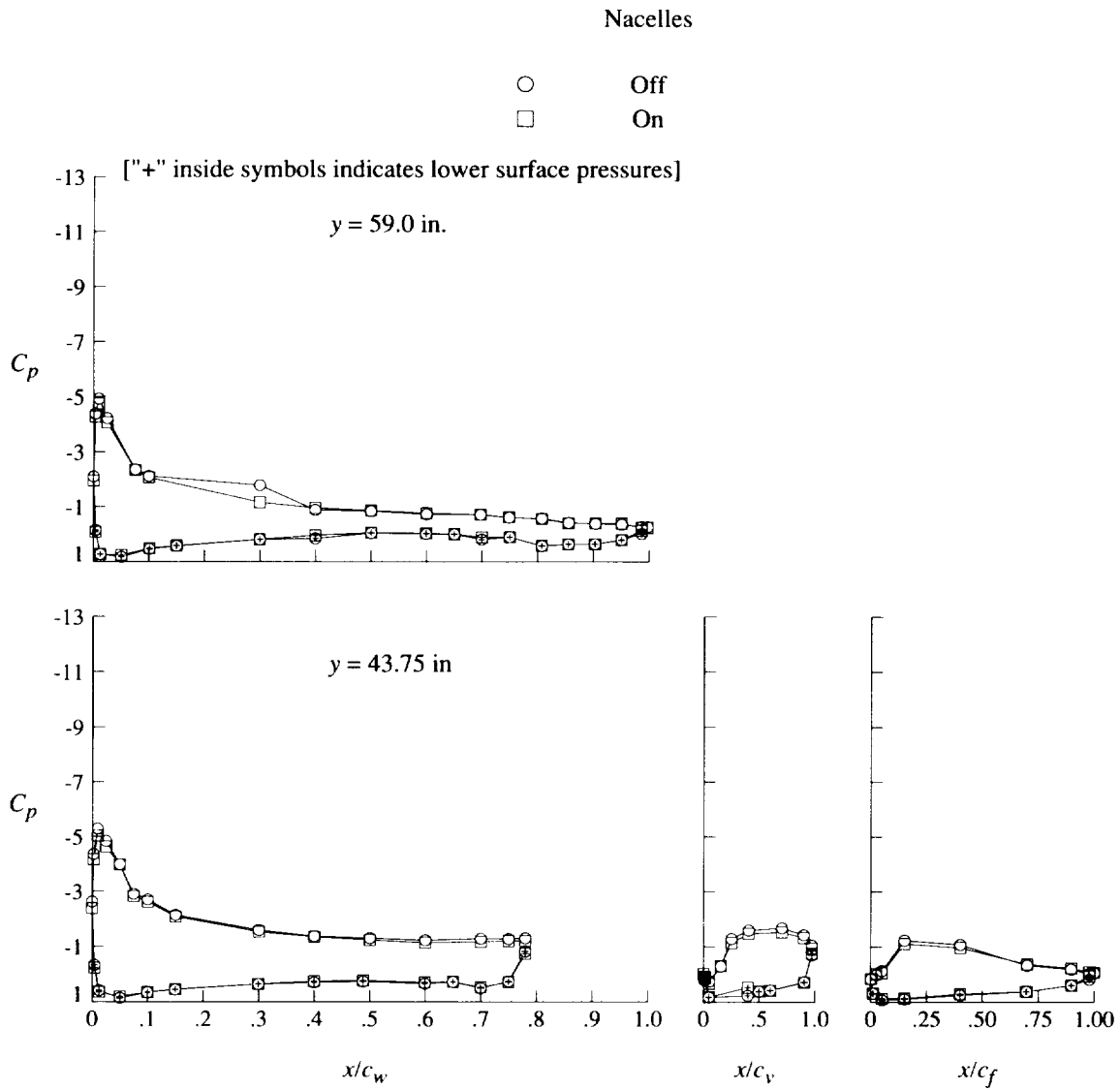
(c) Concluded.

Figure 44. Continued.



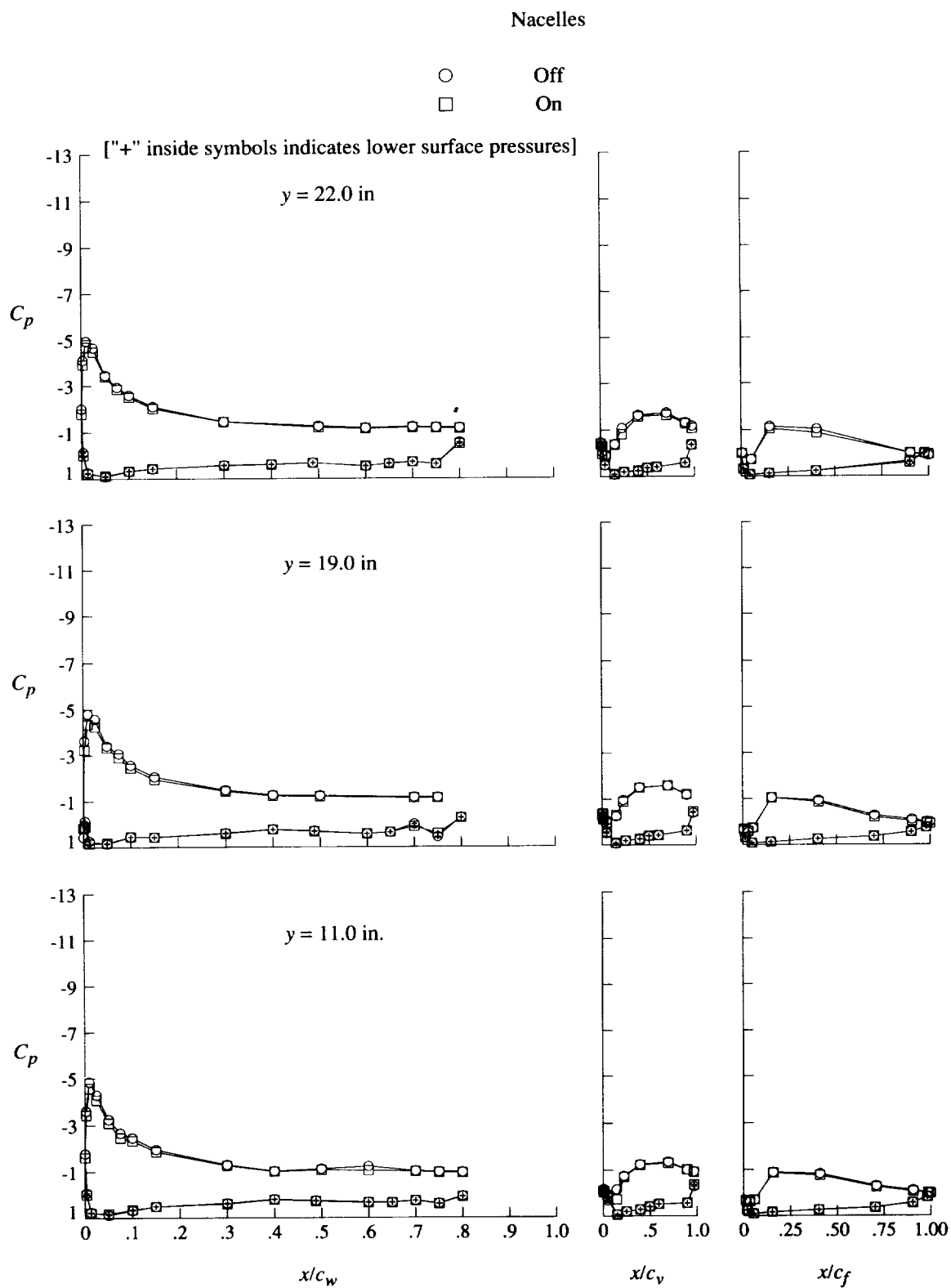
(d) $q = 20$ psf; $\alpha = 8^\circ$.

Figure 44. Continued.



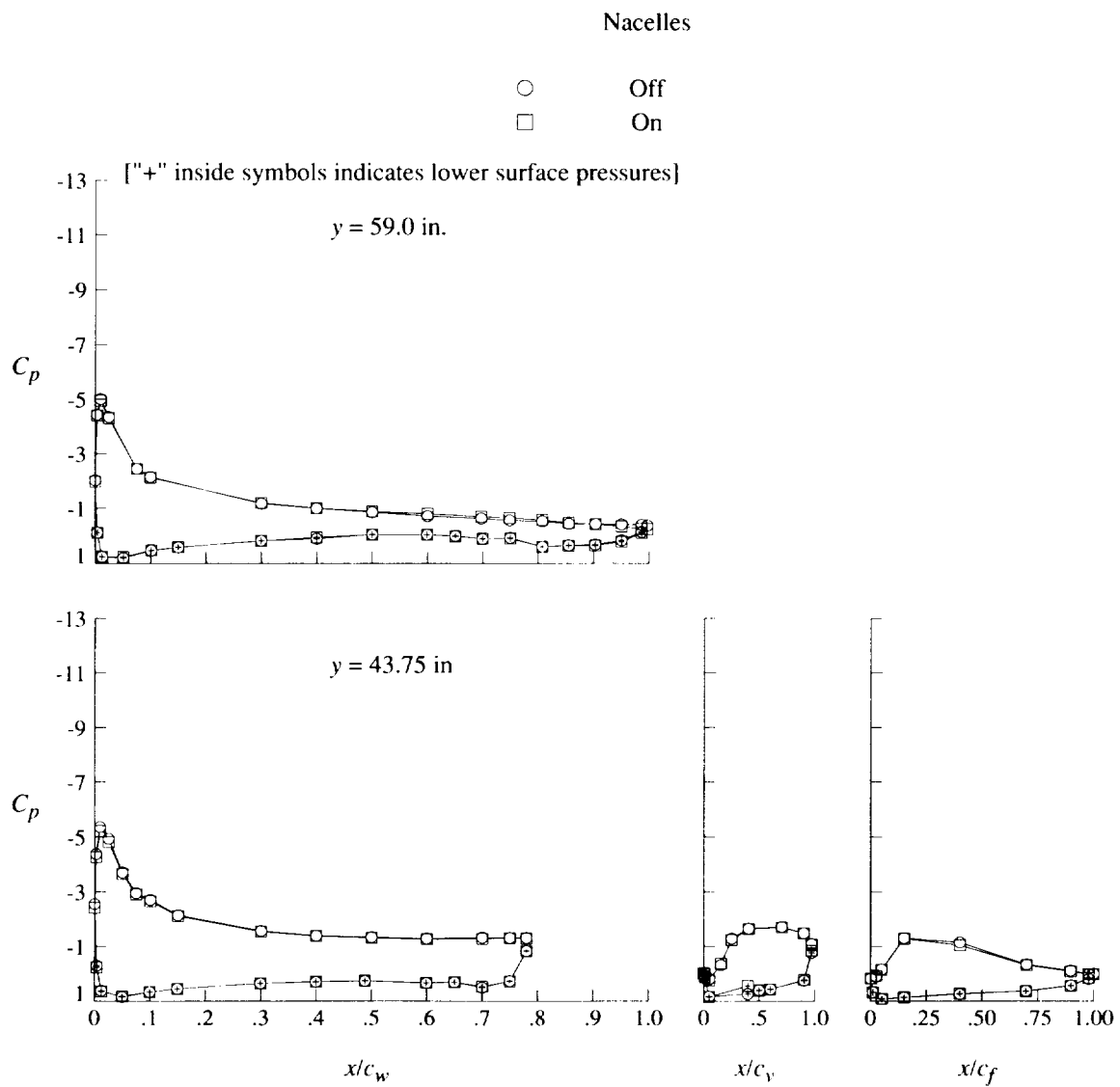
(d) Concluded.

Figure 44. Continued.



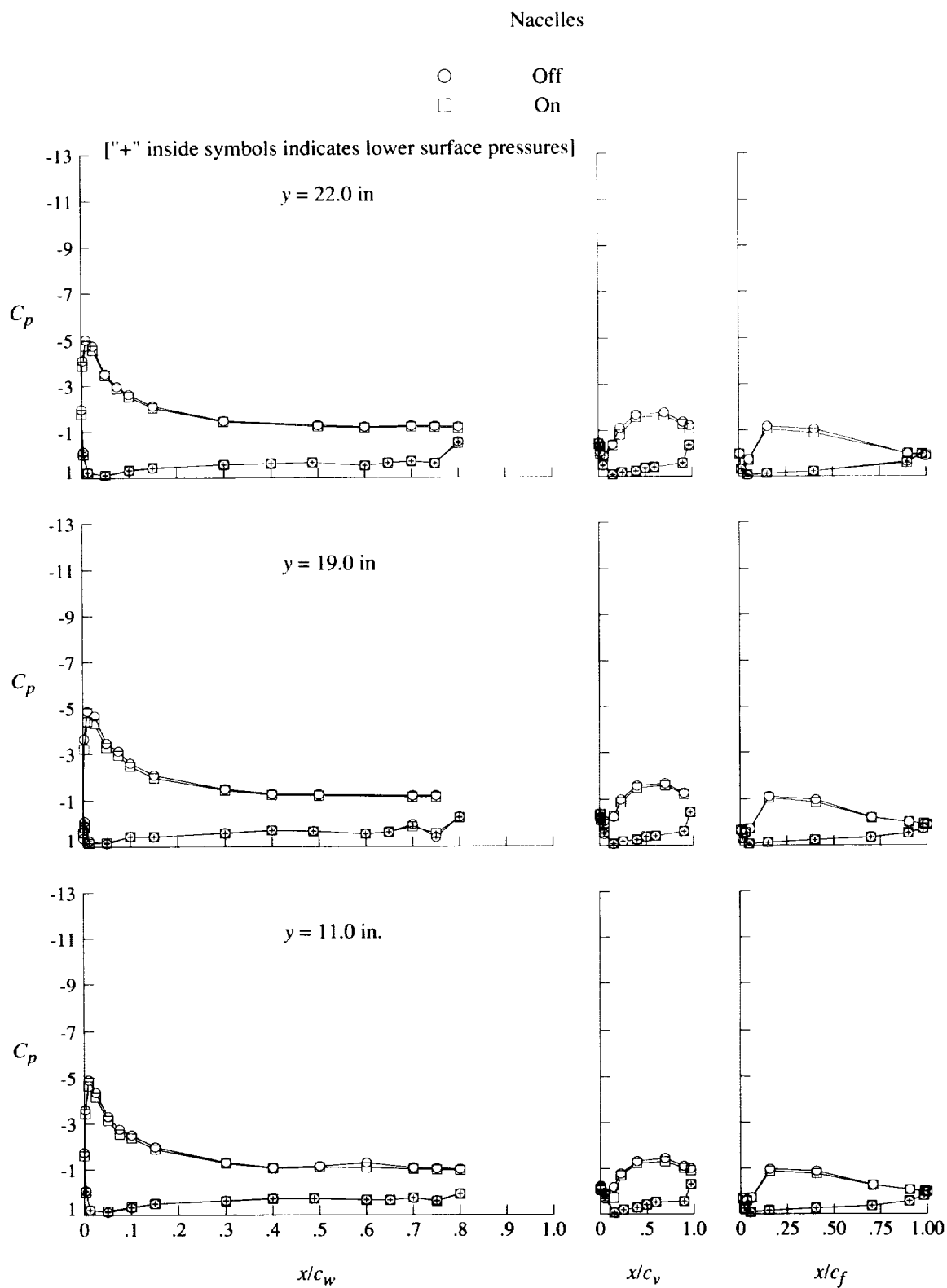
(e) $q = 40$ psf; $\alpha = 8^\circ$.

Figure 44. Continued.



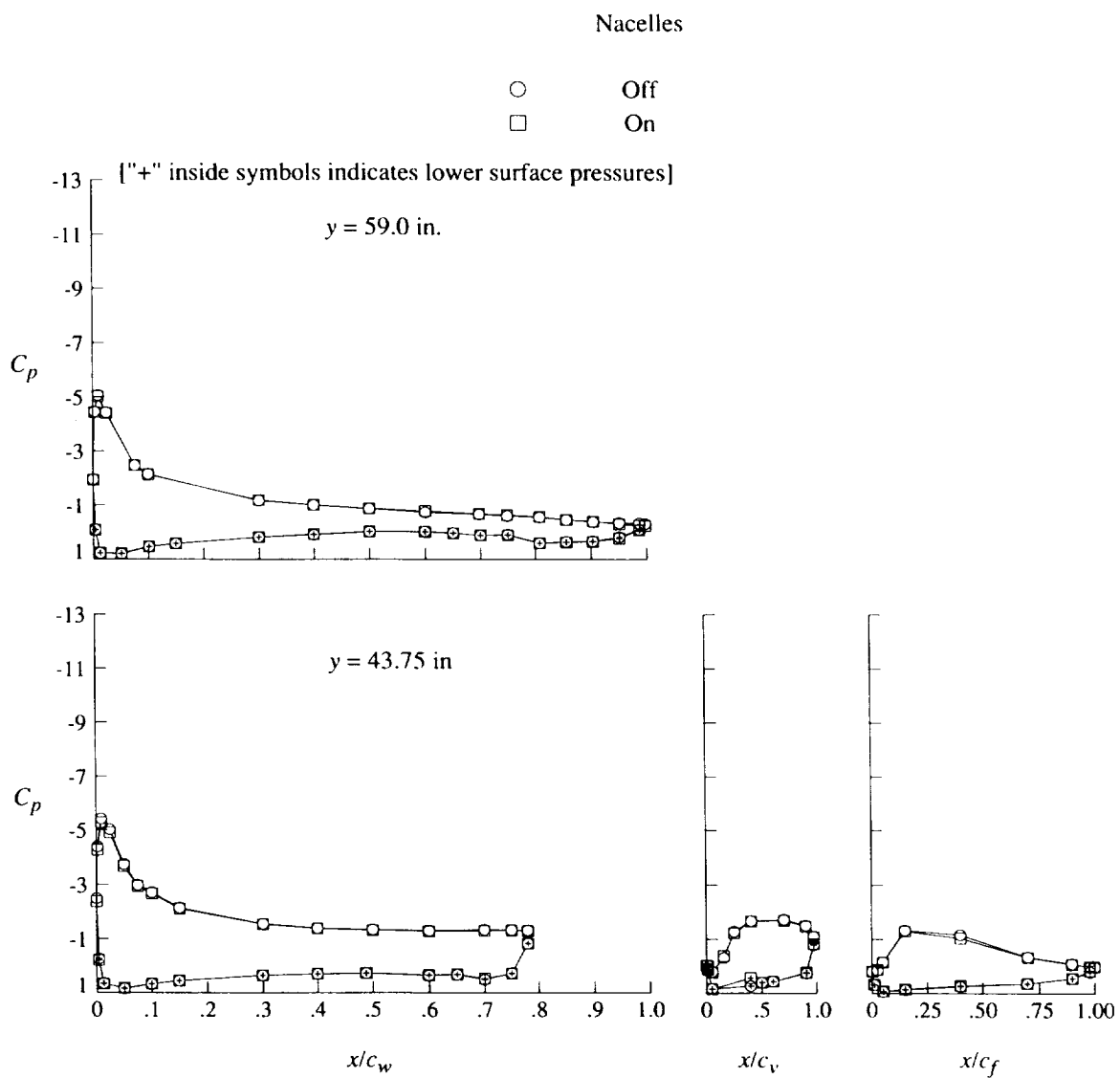
(e) Concluded.

Figure 44. Continued.



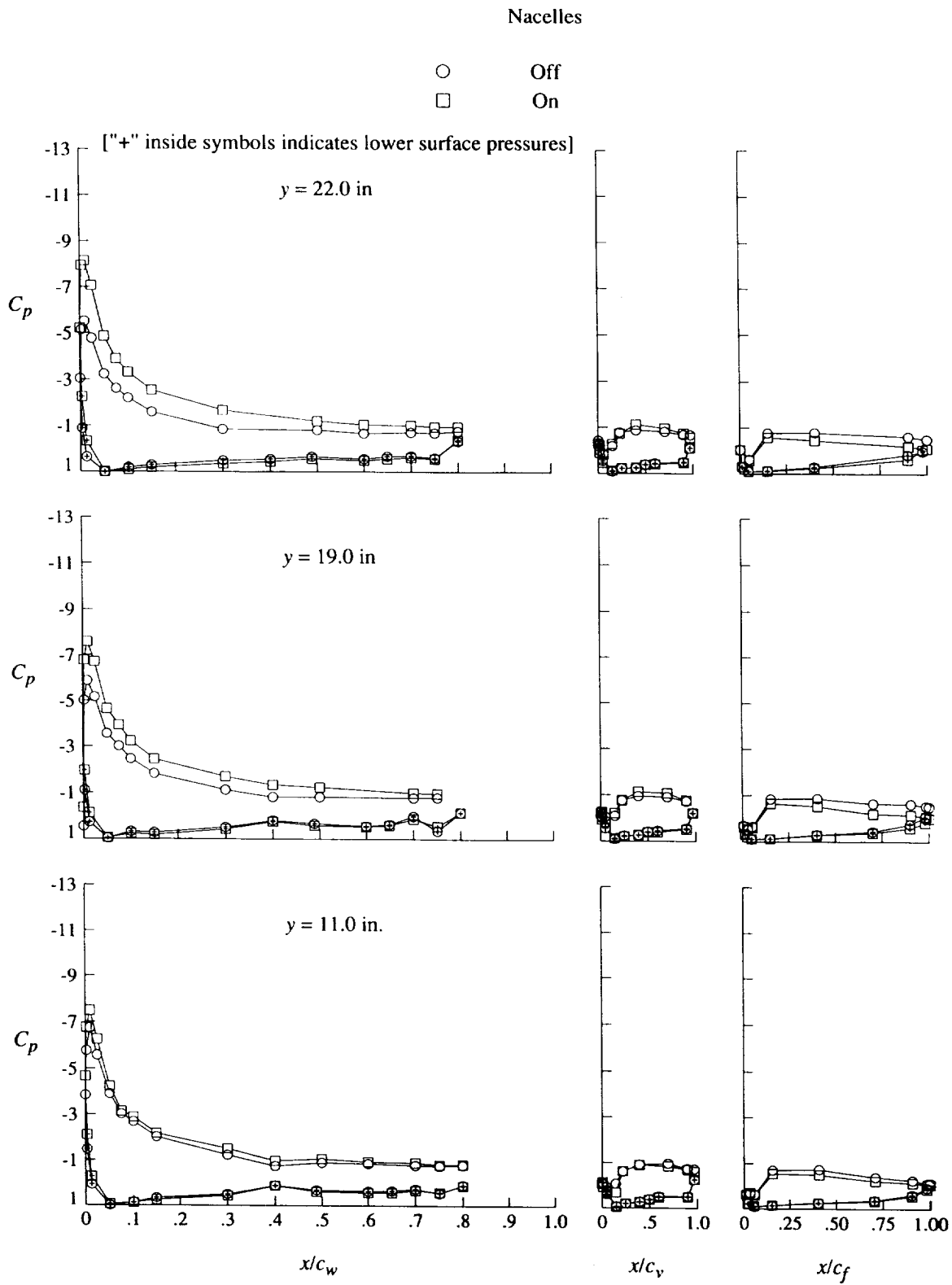
(f) $q = 60$ psf; $\alpha = 8^\circ$.

Figure 44. Continued.



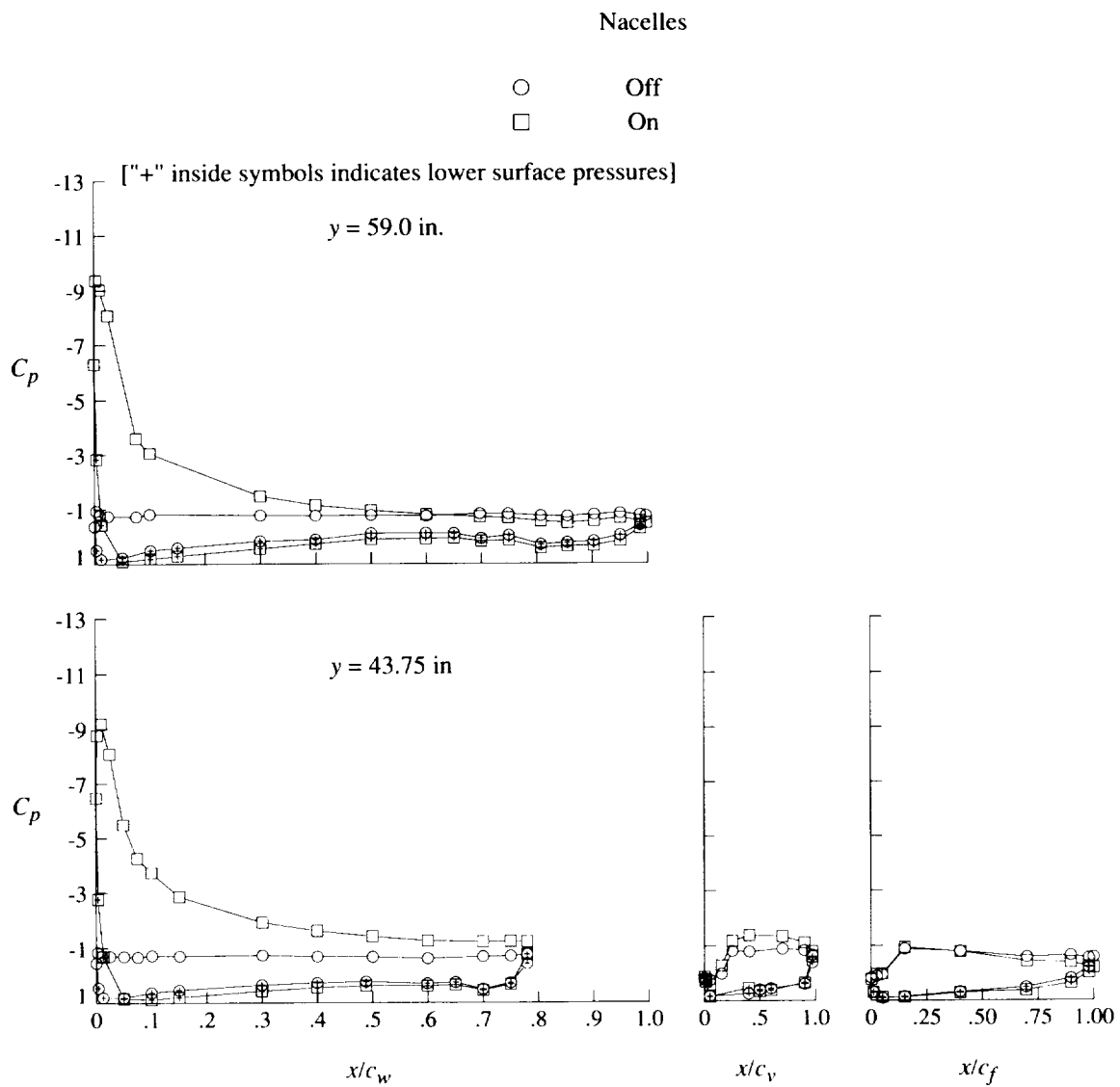
(f) Concluded.

Figure 44. Continued.



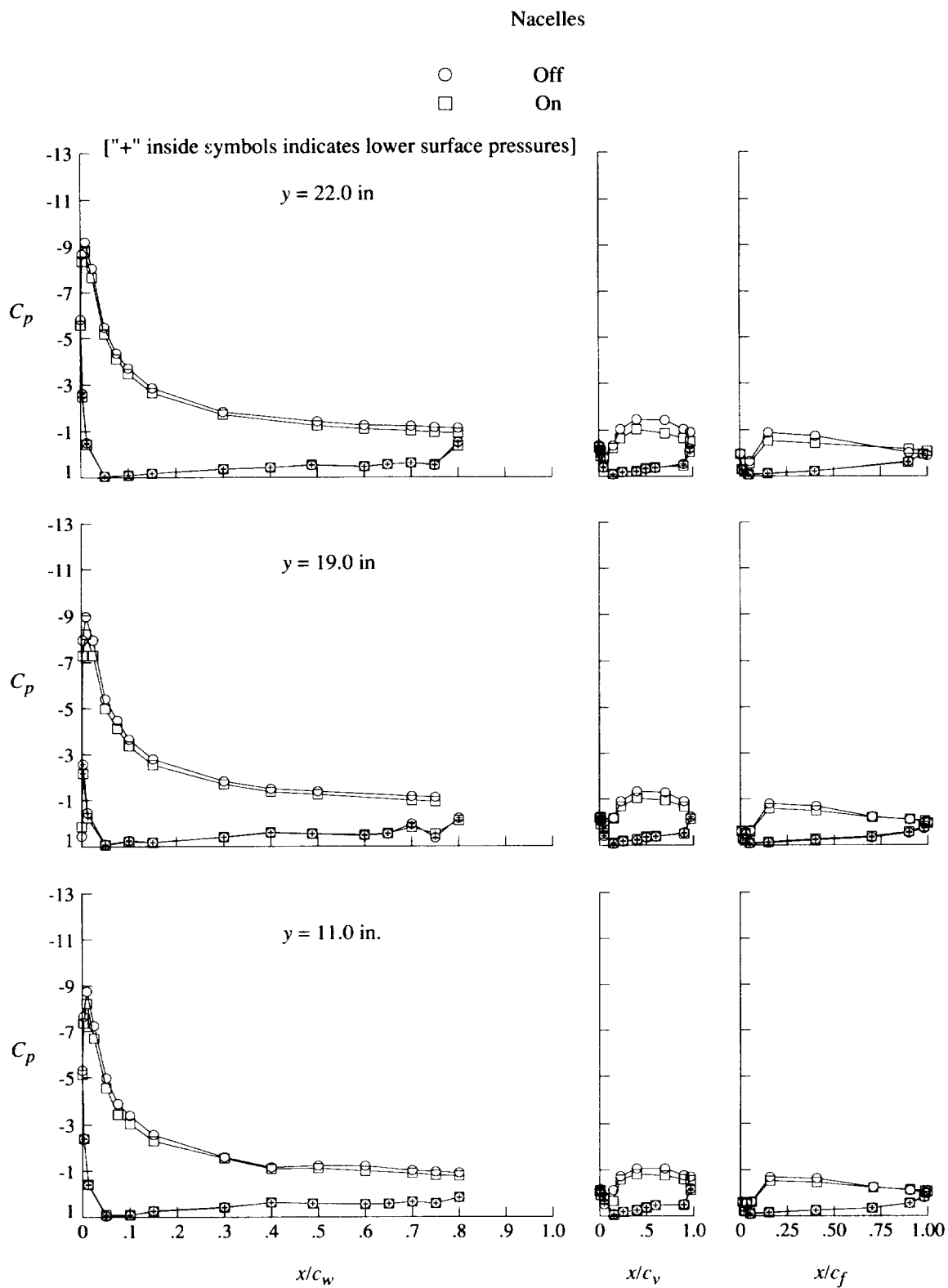
(g) $q = 20$ psf; $\alpha = 16^\circ$.

Figure 44. Continued.



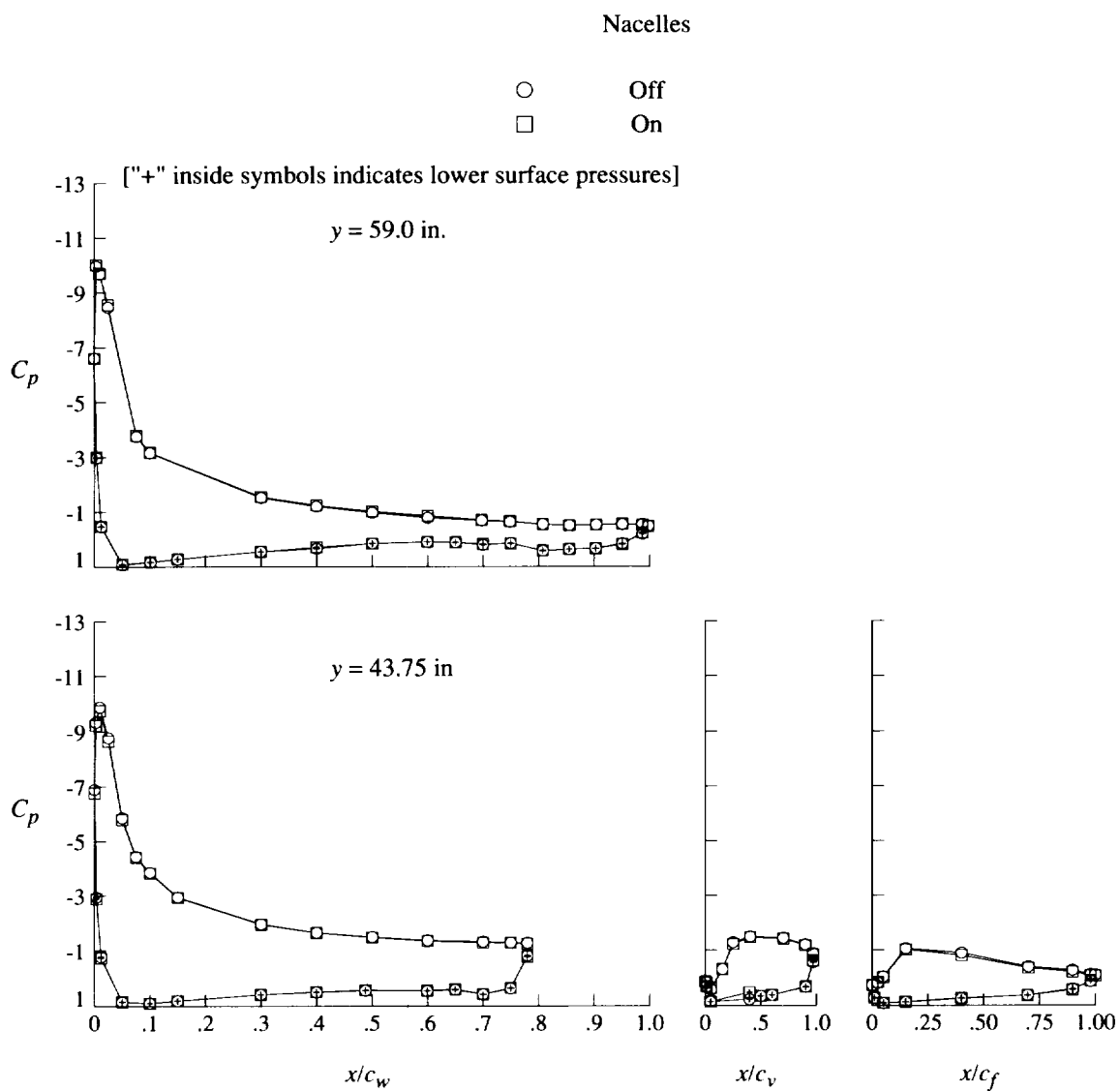
(g) Concluded.

Figure 44. Continued.



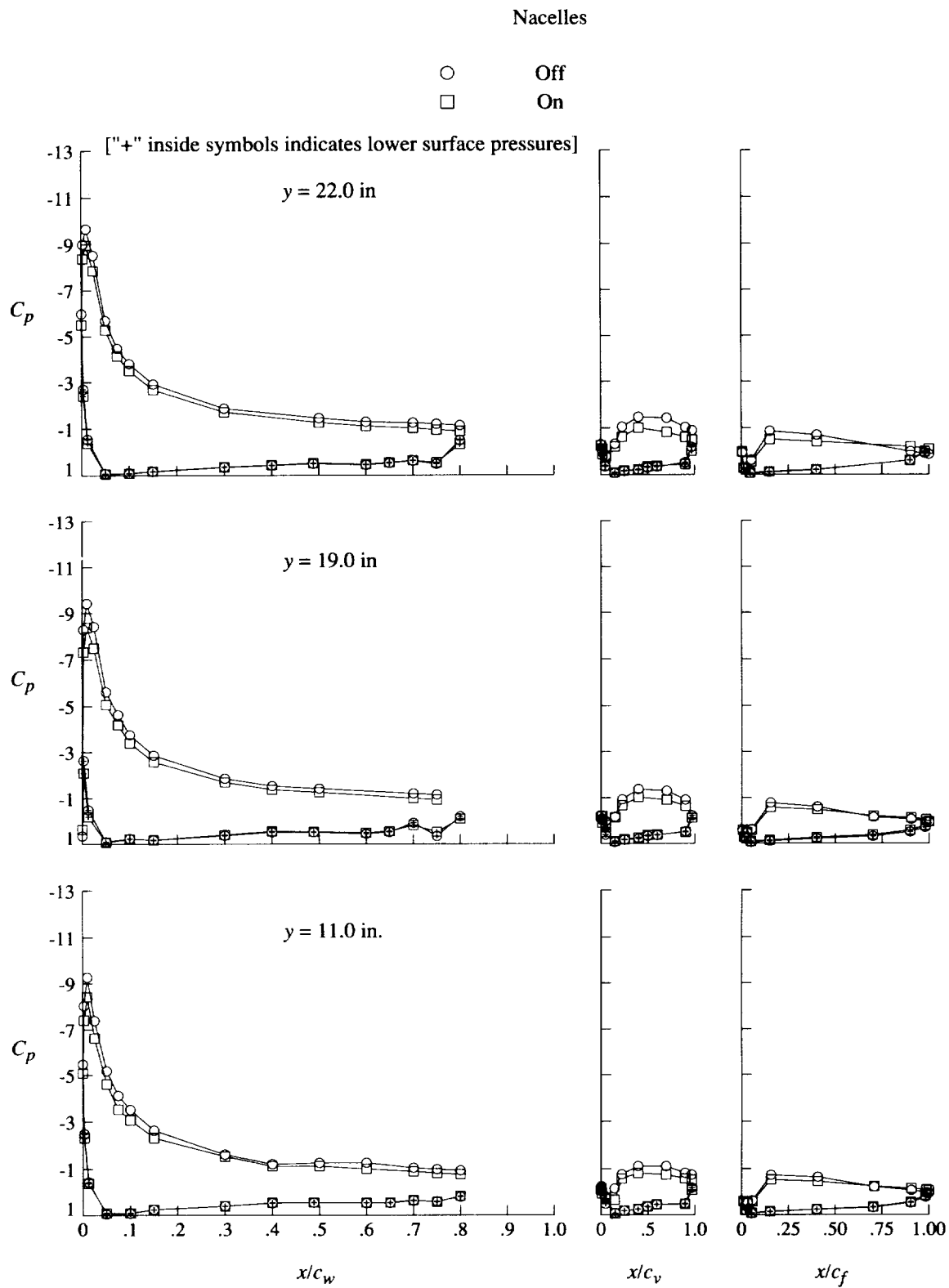
(h) $q = 40$ psf; $\alpha = 16^\circ$.

Figure 44. Continued.



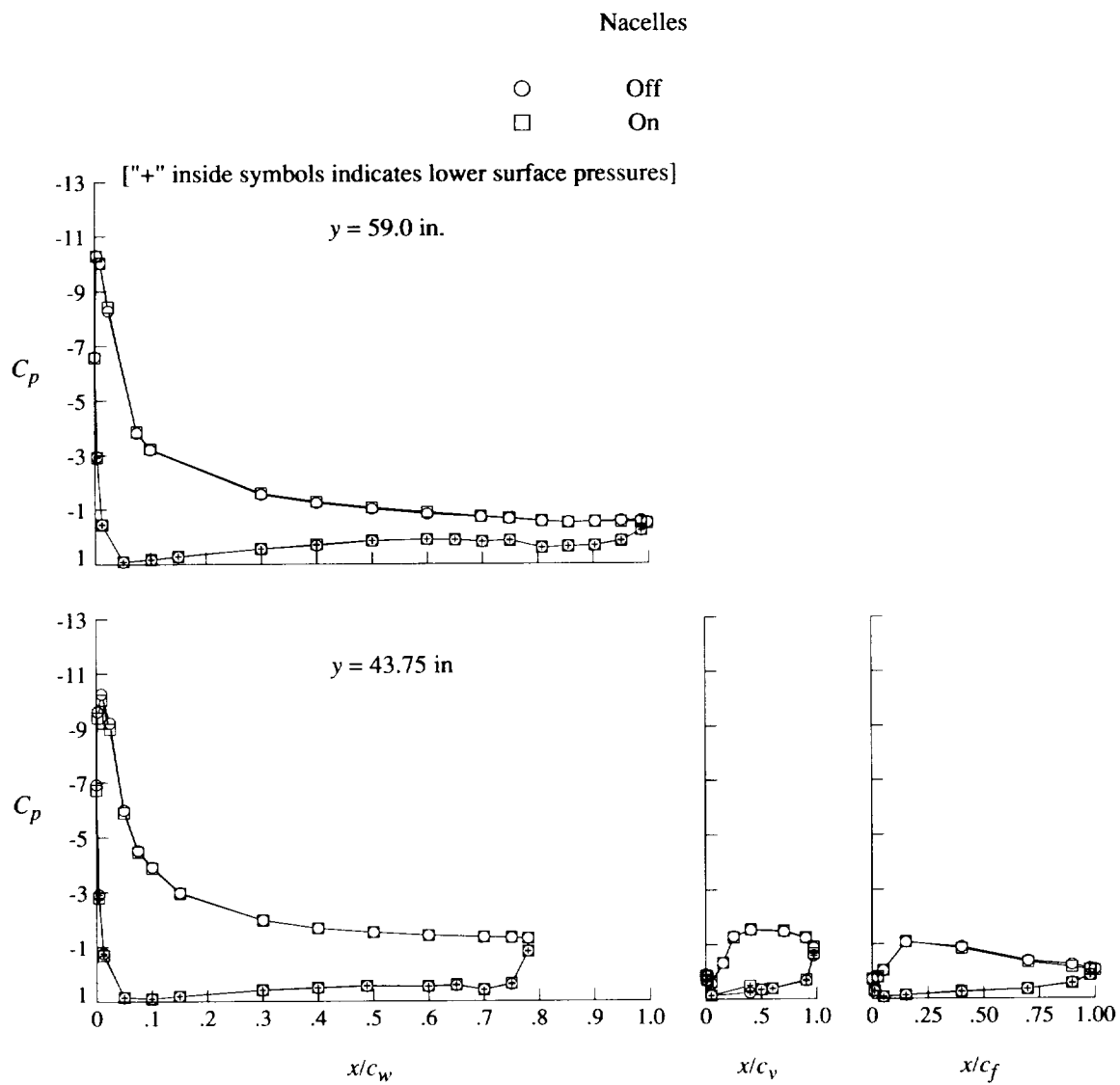
(h) Concluded.

Figure 44. Continued.



(i) $q = 60$ psf; $\alpha = 16^\circ$.

Figure 44. Continued.



(i) Concluded.

Figure 44. Concluded.

REPORT DOCUMENTATION PAGE			Form Approved OMB No. 0704-0188	
Public reporting burden for this collection of information is estimated to average 1 hour per response, including the time for reviewing instructions, searching existing data sources, gathering and maintaining the data needed, and completing and reviewing the collection of information. Send comments regarding this burden estimate or any other aspect of this collection of information, including suggestions for reducing this burden, to Washington Headquarters Services, Directorate for Information Operations and Reports, 1215 Jefferson Davis Highway, Suite 1204, Arlington, VA 22202-4302, and to the Office of Management and Budget, Paperwork Reduction Project (0704-0188), Washington, DC 20503.				
1. AGENCY USE ONLY (Leave blank)	2. REPORT DATE January 1995	3. REPORT TYPE AND DATES COVERED Technical Memorandum		
4. TITLE AND SUBTITLE Wing Pressure Distributions From Subsonic Tests of a High-Wing Transport Model		5. FUNDING NUMBERS WU 505-59-10-13		
6. AUTHOR(S) Zachary T. Applin, Garl L. Gentry, Jr., and M. A. Takallu				
7. PERFORMING ORGANIZATION NAME(S) AND ADDRESS(ES) NASA Langley Research Center Hampton, VA 23681-0001		8. PERFORMING ORGANIZATION REPORT NUMBER L-17380		
9. SPONSORING/MONITORING AGENCY NAME(S) AND ADDRESS(ES) National Aeronautics and Space Administration Washington, DC 20546-0001		10. SPONSORING/MONITORING AGENCY REPORT NUMBER NASA TM-4583		
11. SUPPLEMENTARY NOTES Applin and Gentry: Langley Research Center, Hampton, VA; Takallu: Lockheed Engineering & Sciences Company, Hampton, VA.				
12a. DISTRIBUTION/AVAILABILITY STATEMENT Unclassified-Unlimited Subject Category 02 Availability: NASA CASI (301) 621-0390		12b. DISTRIBUTION CODE		
13. ABSTRACT (Maximum 200 words) A wind tunnel investigation was conducted on a generic, high-wing transport model in the Langley 14- by 22-Foot Subsonic Tunnel. This report contains pressure data that document effects of various model configurations and free-stream conditions on wing pressure distributions. The untwisted wing incorporated a full-span, leading-edge Krueger flap and a part-span, double-slotted trailing-edge flap system. The trailing-edge flap was tested at four different deflection angles (20°, 30°, 40°, and 60°). Four wing configurations were tested: cruise, flaps only, Krueger flap only, and high lift (Krueger flap and flaps deployed). Tests were conducted at free-stream dynamic pressures of 20 psf to 60 psf with corresponding chord Reynolds numbers of 1.22×10^6 to 2.11×10^6 and Mach numbers of 0.12 to 0.20. The angles of attack presented range from 0° to 20° and were determined by wing configuration. The angle of sideslip ranged from -20° to 20°. In general, pressure distributions were relatively insensitive to free-stream speed with exceptions primarily at high angles of attack or high flap deflections. Increasing trailing-edge flap deflection increased suction pressures on the wing and improved flow on the flaps. The leading-edge Krueger flap significantly reduced peak suction pressures and steep gradients on the wing at high angles of attack. Installation of the empennage had no effect on wing pressure distributions. Unpowered engine nacelles reduced suction pressures on the wing and the flaps.				
14. SUBJECT TERMS Pressure distributions; High lift; High wing; Subsonic transport			15. NUMBER OF PAGES 440	
			16. PRICE CODE A19	
17. SECURITY CLASSIFICATION OF REPORT Unclassified	18. SECURITY CLASSIFICATION OF THIS PAGE Unclassified	19. SECURITY CLASSIFICATION OF ABSTRACT Unclassified	20. LIMITATION OF ABSTRACT	

